



French Society
for Soil Mechanics and
Geotechnical Engineering

International Society
for Soil Mechanics and
Geotechnical Engineering



Paris, France

18TH INTERNATIONAL CONFERENCE ON SOIL MECHANICS AND GEOTECHNICAL ENGINEERING

PROCEEDINGS OF THE TC207 WORKSHOP ON SOIL-STRUCTURE INTERACTION AND RETAINING WALLS

4 September 2013

CHALLENGES & INNOVATIONS IN GEOTECHNICS

➔ www.paris2013-icsmge.org



2-6 September, 2013

Partners:



18TH INTERNATIONAL CONFERENCE
ON SOIL MECHANICS
AND GEOTECHNICAL ENGINEERING

**PROCEEDINGS OF THE WORKSHOP
ON SOIL-STRUCTURE INTERACTION
AND RETAINING WALLS**

Edited by: V.M. Ulitsky, M.B. Lisyuk

Paris, France
4 September 2013

Proceedings of the Technical Meeting TC207 – Workshop on Soil-Structure Interaction and Retaining Walls

www.tc207ssi.org

The text of the various papers in this collection was set individually by typists under the supervision of each of the authors concerned.

All rights reserved. No part of this publication may be reproduced, stored or transmitted in any form without the written permission of the Publisher.

Published by: Georeconstruction Group of Companies
190005 Russia, Saint Petersburg, Izmaylovsky prospekt 4

ISBN 978-5-9902005-7-9

PREFACE

Materials of the last two major ISSMGE conferences on geotechnical engineering (Osaka 2005 and Alexandria 2009) testify to increasing importance of the actively working ISSMGE TC 207 “Soil-Structure Interaction and Retaining Walls”. A further proof of that is the decision by the Organizing Committee of the upcoming 18th ICSMGE Conference in Paris to hold two sessions under the aegis of TC207. Papers accepted for these sessions are devoted to a broad range of subjects directly related to complex calculative analysis of the system “soil-foundation-superstructure”. This area is important for further development of geotechnical engineering as a science responsible for defining degrees of risk, including the risk involved in estimation of stability of protective walls and retaining structures.

Practical importance of such calculations defeated all expectations formulated at an ISSMGE International Conference, which had taken place in the beginning of the century in Istanbul. During that conference, a special session featuring four invited lectures had been organized, one of the lectures being entrusted to the first author of this Preface. The lecture was pivoted on the importance of soil-structure interaction and retaining walls, with special reference to reconstruction and development of historic cities.

It becomes apparent from the materials published in the present collection, that the tasks of this research direction have extended into the domain of real design practice. A series of publications appeared, in which authors convincingly demonstrated convergence of calculative predictions and real stress-strain state not only for subsoils, but also for overground and underground structures. This relevance was ever so more strongly reinforced in the minds of TC 207 members during their technical meetings in Madrid, St. Petersburg, Moscow, Athens, Dubrovnik and Rostock. Additionally, in 2005 and 2008 in St. Petersburg, the State Transport University hosted two conferences devoted to the subject in question, in which specialists from 47 countries took part, and that also, albeit indirectly, points towards significance of the topics dealt with by our Technical Committee.

It is possible to note some features of growing accuracy in this research area. In 2002 a paper by Professor Schweiger was released, in which an analysis of various approaches to calculations and related software testified to the following:

1. Almost all numerical predictions (of which in the paper 16 were mentioned) of ground stability around a deep excavation in Berlin contradicted real monitoring data.
2. The fact of the studied numerical predictions having run completely amok testified to the danger or impossibility of using them in real design practice.
3. Certain errors can, in principle, be caused by insufficiency of initial soil data, with some data in a number of calculations showing incorrect correlations.
4. It is necessary to collect well-documented practical examples which will allow choosing appropriate numerical prediction techniques.

We hope, that such well-documented examples will be offered to colleagues for the purposes of testing the available software and perfecting their numerical representations.

In this aspect the materials presented for the present workshop will be of special interest. We believe that in conjunction with the published volumes of the Conference Proceedings, they will advance methods of solving geotechnical problems developed by TC 207 to a new international level, allowing expert designers to make use of the practically verified methods in real projects.

In this respect, the title of the paper by Professor R. Frank, published in this collection, “Eurocode 7 on Geotechnical Design: a Code for Soil-Structure Interaction” appears to us particularly remarkable. It means that one of the leading developers of Eurocodes confirms the importance of our TC 207. Our subsequent work within the framework of TC 207 should be directed towards perfection of European and other codes, irrespective of a status or size of any world’s region or country. In this respect, the Guidelines on Soil-Structure Interaction developed by our Technical Committee are of paramount significance.

At a recent session of the ISSMGE Board, our idea of holding a TC 207 lecture devoted to Professor Gregory Tschebotarioff was supported unanimously. This well-known American geotechnical engineer was born in Russia and studied in the oldest technical school of St. Petersburg – the Transport University. Considering his ideas, he would have been closer than anyone to the TC 207’s range of working subjects. In one of his classical works entitled “Foundations, Retaining and Earth Structures” he says: “No deformation of the soil surface beneath a structure can take place without a corresponding deformation of both the foundation and the superstructure above it ... The supporting soil, the foundation and superstructure form one single unit and should therefore be considered as a whole”. Unfortunately, in his day and age there was no computational facility to fully account for that consideration.

However, these days we are in possession of powerful software complexes serving practical design with the capability of translating all modern realities, including those of high-rise buildings and underground structures, into the language of mathematics.

V. Ulitsky
Chair of TC207

M. Lisyuk
Co-Chair of TC207

MEMBERS OF TECHNICAL COMMITTEE 207
“SOIL-STRUCTURE INTERACTION AND RETAINING WALLS”
ISSMGE

V.M. Ulitsky, Russia (Chairman)
M.B. Lisyuk, Russia (Co-chairman)
W. Van Impe, Belgium
K. Shashkin, Russia
C. Haberfield, Australia
Y. El-Mossallamy, Egypt
R. Katzenbach, Germany
W. Bilfinger, France
L. Andresen, Norway
H. St. John, UK
R. Finno, USA
F. Liu, China
N. Petrović, Croatia
J. Kos, Czech Republic
K. Avellan, Finland
C. Jacquard, France
J. Sze, Hong Kong
V. Balakumar, India
M. Latha, India
N.K. Samadhiya, India
O. al-Farouk Salem al-Damluji, Iraq
H. Hazarika, Japan
G.A. Sultanov, Kazakhstan
M. Korff, Netherlands
G. Horodecki, Poland
F. Roman, Romania
Z.G. Ter-Martirosyan, Russia
V.C.W. Ong, Singapore
A.R. Walker, Singapore
P. Morrison, UK
I. Sokolić, Croatia
M. Favre, France
J.M. Fernández Vincent, Argentina
O. Biligin, USA
J. Couck, Belgium
C. di Prisco, Italy
G. Gottardi, Italy
A.M. Kayana, Norway
B. Moczar, Hungary
J. Moreno, Spain
P. Pantelidis, Greece
L. Vollmert, Germany
A. Norkus, Lithuania

Table of contents

SOIL-STRUCTURE INTERACTION

<i>V.M. Ulitsky, K.G. Shashkin, V.A. Shashkin, M.V. Dunaeva</i> Solution of Limited Equilibrium Problems Using the Finite Element Method.....	10
<i>Omar Al-Farouk S. Al-Damluji, Husain M. Husain & Rafa'a M. Abbas</i> A Nonlinear Dynamic Interaction Algorithm of Elasto-Viscoplastic Concrete Structures with Coupled Saturated Soils	26
<i>I.V. Anirudhan, S.V. Ramaswamy</i> Revisiting a Full Raft Foundation Constructed on Soft Clay	38
<i>K. Avellan</i> Limit State Design for Strengthening the Foundations of St. John's Church of Tartu, Estonia Using Pretested Drilled Spiral Piles.....	50
<i>V.Balakumar, I.V.Anirudhan</i> A Study on the Interactive Behavior of Piled raft on Sand	64
<i>Werner Bilfinger, Thaís L. Dada & Pedro C. R. Silva</i> Vertical Pile Stiffness: Pile Load Test Data Base Analyses.....	76
<i>R.E. Dashko & A.V. Shidlovskaya</i> Concept of Cities Multicomponent Underground Space as a Factor of Enhancing Safety of its Exploration	83
<i>R. Frank</i> Eurocode 7 on 'Geotechnical Design': a Code for Soil-Structure Interaction	97
<i>C.M. Haberfield</i> Analysis of Tall Tower Footing Systems	107
<i>Xinye HAN, Takashi KIYOTA, Fumio TATSUOKA</i> Pullout Characteristics of Geocells Embedded in Gravelly Soil Backfill	120
<i>Hemanta Hazarika, Tadashi Hara, Hideo Furuichi</i> Soil-Structure Interaction During Earthquake and Tsunami – Two Case Studies from the Latest Disaster in Japan.....	131

<i>R. Katzenbach & S. Leppla</i> Soil-Structure Interaction of Large Storage Constructions.....	143
<i>A.Z. Khasanov, Z. A. Khasanov, F. F. Zekhniev</i> Strengthening of the Beds And Foundations of the Tilla-Kori Mosque of the Registan Ensemble in Samarkand.....	150
<i>S.A. Kudryavtsev, Y.B. Berestyanyy, T.U. Valtseva, R.G. Mihailin, D.G. Tsvigunov</i> Designs of the Railway Roadbed of Thawing Permafrost Soils in Condition of the Far East	156
<i>G. Madhavi Latha, P. Santhanakumar</i> Shaking Table Studies on Reinforced Modular Block and Rigid Faced Walls	163
<i>Ilizar T. Mirsayapov & Irina V. Koroleva</i> Calculation Models of Bearing Capacity and Deformation of Reinforced Soil Bases	179
<i>C.W. Ong, C. F. Leung, K.Y. Yong</i> Understanding Long-Term Effect of Tunnel-Soil Interaction	189
<i>Pavan Kumar, Madhav Madhira</i> Inclined Reinforcement-Backfill Interactions to Transverse Pull.....	202
<i>Paramonov V.N., Kravchenko P.A.</i> Bearing Capacity of Piles in a “Soil-Pile-Structure” System	214
<i>Prathyusha, J., Uday, V.K. and Singh, D.N.</i> Determination of Cracking characteristics of Soils for Various Geotechnical Engineering Problems.....	219
<i>B. Pallavi Ravishankar</i> Finite Element Modelling to Study Soil Structure Interaction of Asymmetrical Tall Building	225
<i>I.I. Sakharov, V.N. Paramonov</i> Reciprocal Influence of Inclined Subway Tunnels Constructed by Means of Artificial Freezing and Above-Ground Structures.....	231
<i>N.K. Samadhiya & Kumar Venkatesh, A.D. Pandey</i> Behaviour of Barrage Foundation Due to Presence of Rock Including Soil-Structure Interaction.....	241
<i>V.A. Vasenin</i> Evaluating Current Movements of the Earth Surface for the Purposes of Proving Referential Integrity of the Principal Markers in the Levelling Network of St. Petersburg and Definition of Long-Term Settlements of Buildings and Structures	247

RETAINING WALLS

Ö. Bilgin

Analysis of Lateral Earth Pressures on Anchored Sheet Pile Walls
Using Conventional and Finite Element Methods..... 268

Fang LIU, Mingjing JIANG, Wei ZHOU, Hiroaki NAKAYAMA

Differential Earth Pressure Against Combined Sheet Pile Walls:
Full-Scale Tests and Numerical Simulations..... 282

I. Sokolić

Numerical Modelling of Anchored Retaining Structures
in Medium Stiff to Stiff Soils 294

Y. El-Mossallamy, A. Wahbi, M. Farouk, W. Ibrahim

Deep Pit Excavation in Special Geotechnical Conditions..... 313

GUIDELINES FOR SOIL-STRUCTURE INTERACTION: FIRST DRAFT FOR DISCUSSIONS AND FURTHER DEVELOPMENT

*V.M. Ulitsky, A.G. Shashkin, K.G. Shashkin, V.A. Shashkin, M.B. Lisyuk, V.N. Paramonov,
V.A. Vasenin*

Soil-Structure Interaction..... 323

SOIL-STRUCTURE INTERACTION

THE EDITORS' PREFACE

The 8th of May, 2011 is the day on which we mark 100 years anniversary of the birth of Professor V. G. Berezantsev, an outstanding expert in the field of soil mechanics, an erstwhile long-standing head of Subsoil and Foundation Department of Leningrad Transport University. Professor V. G. Berezantsev belonged to that splendid constellation of scientists who shaped Russian soil mechanics as a science. V. G. Berezantsev's *oeuvre* have remained important decades later. To this day he is one of the Russian experts most frequently

quoted internationally. A special slot in the scholar's heritage is occupied by works on the theory of limited equilibrium. In our age of computer advancement when, owing to computational facility, achievements of soil mechanics have entered daily practice of design, questions of adequate solution of limited equilibrium problems with numerical methods require due attention. The paper, offered to readers' attention, considers these very questions and, consequently, in the year of the centenary anniversary of V. G. Berezantsev the authors dedicate it to the memory of this outstanding scientist.

Solution of Limited Equilibrium Problems Using the Finite Element Method

V.M. Ulitsky

St. Petersburg State Transport University, Russia, ulitsky.vladimir@gmail.com

K.G. Shashkin

Georeconstruction Engineering Co, St.Petersburg, Russia

V.A. Shashkin, M.V. Dunaeva

St.Petersburg University for Civil Engineering and Architecture, an undergraduate, St.Petersburg, Russia

ABSTRACT: The paper deals with transition of subsoil deformation problems into problems of limited equilibrium. The authors compare solutions based on the finite element method with numerical and analytical solutions, according to the theory of limited equilibrium. The authors likewise single out main factors capable to influence shapes of «load-settlement» curves for plate load tests performed on ideal elastoplastic subsoil.

1. INTRODUCTION

Solution of limited equilibrium problems to define bearing capacity of various foundations has a long history. Exact solutions for the case of weightless soil were obtained in early 20th century by L. Prandtl (1921) [1] and H.Reissner (1924) [2]. For a practical case of subsoil with non-zero specific weight, an angle of internal friction and cohesion, K. Terzaghi (1943) [3] formulated the classical trinomial formula:

$$p_u = N_c c + N_q q + \frac{1}{2} N_\gamma b \gamma, \quad (1)$$

in which factors N_c , N_q and N_γ are defined depending on values of angle of internal friction. According to L.Prandtl's solution [1]:

$$N_q = \frac{1 + \sin \phi}{1 - \sin \phi} e^{\pi \tan \phi}$$

$$N_c = (N_q - 1) \operatorname{ctg} \phi.$$

However, to define factor N_γ appears considerably more difficult. A methodology of solution for this problem in flat setting was formulated by V.V.Sokolovsky (1942) [4]. V.G. Berezantsev generalized this problem for the axisymmetric case [5]. The issues of defining bearing capacity of a foundation with account of the actual weight of soil are dealt with in works

by H. Meyerhof (1951) [6], Y. Hansen (1970) [7] and A. Vesic (1975) [8]. The fundamental theoretical solutions were obtained by D. Drucker (1952) [9]. For the case of ideally elastoplastic material with associated law of plastic yield he formulated theorems of the upper and the lower boundaries within which the value of the ultimate load must be placed.

Recently, solutions of limited equilibrium problems were fruitfully tackled by A.M. Karaulov (2002) [10], V.G. Fedorovsky (2005) [11], K.V. Korolev (2010) [12] and others.

In the book by the latter author we find a formula for factor N_γ , obtained by means of approximating numerical solutions of limited equilibrium equations:

$$N_\gamma = 1.66 \operatorname{tg} \phi e^{4.66 \operatorname{tg}^2 \phi}$$

which yields the factor values close to the ones contained in the Russian codes.

It should be noted that the factors N_γ given in domestic normative documents and in [12], will reflect a solution with existence of surcharge and an angle of internal friction provided that:

$$q' = \frac{q + c \cdot \operatorname{ctg} \phi}{\gamma b} > 1$$

As q' approaches zero, dependence of $p_u(q)$ gains nonlinear character, and correspondingly as it is noted in [11, 12], the formula (1) becomes fundamentally wrong (see Fig. 1). Therefore, the factors N_γ given in [12] as well as in Russian domestic regulative codes, correspond to the linear section of dependence $p_u(q)$ and are not true for the case of a plate on the surface or at small depth in the loose (friable) medium.

The problem of defining bearing capacity of a plate on the surface of friable medium (at q' tending towards zero) has long been out of bounds for an accurate theoretical solution. In view of the difficulties, related to accounting for the actual weight, a big number of approximate values of factor N_γ were obtained, the differences between some of them sometimes being enormous, especially for any angles of internal friction higher than 30° . As noted in the work by S. Sloan [14], «in situ experiments to define bearing capacity of foundations on sands were not able to answer the question as to which of the N_γ values obtained theoretically were true. First and foremost it is related to the difficulty in defining the true angle of internal friction for calculating bearing capacity when comparing in situ results and the obtained formula. Secondly, this is related to the difficulty in defining the scale effect. Besides, the existing theories assume that N_γ factor grows at a significant rate with increase in the angle of internal friction. Therefore it appears improbable that in situ tests can answer the question as to which of N_γ values are true». Thus, according to S. Sloan, the question of the value of N_γ factor for a foundation on the surface of a loose medium should be solved rather by means of theoretical solutions, than by means of in situ tests. Even more sharply the question of obtaining correct N_γ values is formulated in the paper by S. Martin [15]. For the notorious N_γ problem the author posits a question to the effect that instead of a set of very different multiple solutions we should devise the uniform exact solution, at least for the problem with the associated yield law for which the uniqueness of its solution has been proved by the corresponding theorem.

In the publications by S. Sloan, et al. (2002, 2004) [13,14] the authors provide a mathematical basis for solution of limited equilibrium

problems by a finite element method, which allows to receive a numerical solution for the « N_γ predicament». In the publications by S. Martin (2004) [15] this problem is solved by the method of characteristics. The author had written a rather simple programme called ABC (=Analysis of Bearing Capacity) which is freely available to use on the Internet and is very convenient for solving practical applications. As affirmed in that paper [15] the method of characteristics gives the exact “no nonsense” solution of the problem in question can be obtained; the paper also contains values of the N_γ factor for various angles of internal friction. S. Sloan, et al [14] obtained, by solving the problem of limited equilibrium with a finite element method, values of factor N_γ for the upper and the lower limits, being only around 3.4 % different from each. The values of N_γ obtained by S. Martin, are well within the boundaries calculated by S. Sloan. The paper by V.G. Fedorovsky [11] contains the exact solution of a more general problem, dealing with inclined loading action rendered onto a plate. In a specific case for an ideally rough plate and vertical loading, factors N_γ almost precisely coincide with the results contained in S. Martin’s paper and are well within the boundaries expressed in the paper by S. Sloan.

Thus, an analysis of these works allows to argue that for the factor N_γ in case of the foundation on loose (friable) subsoil the exact solution has been finally achieved. Pursuing various methodologies, the authors of [11, 14, 15] arrived practically at identical values of factor N_γ .

At this point it should be noted that for the problem of a plate on a surface of noncohesive medium, the values of N_γ according to works by S. Martin, S. Sloan and V.G.Fedorovsky are considerably lower than the values given in domestic regulative codes. The reason for this divergence is the fact that for the specific problem of unembedded plate in noncohesive medium the factor N_γ , strictly speaking, is not an independent factor in formula (1), but is itself a function of the surcharge value, because the $p_u(q')$ function becomes nonlinear (Fig. 1).

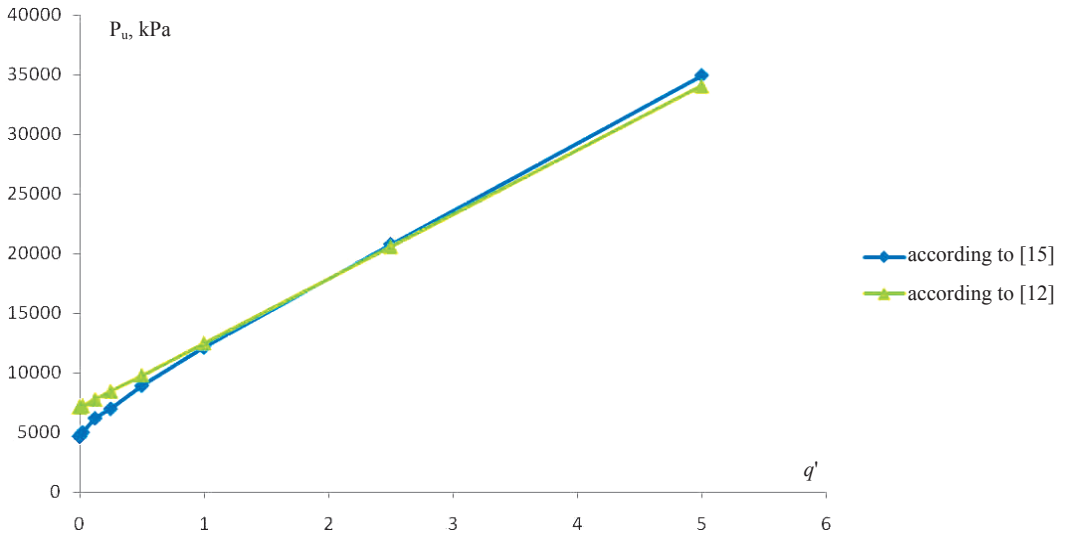


Fig. 1. Dependence of $p_u(q')$ at $\varphi = 45^\circ$ and $c=0$ according to the approximation [12] and according to the exact solution [15].

Table 1

Theoretical		Angle of internal friction φ								
		5°	10°	15°	20°	25°	30°	35°	40°	45°
CII 50-101-2004*		0.4	1.2	2.7	5.76	11.74	24.78	55	132.02	355.22
Eurocode 7 (Vesić)		0.1	0.52	1.58	3.94	9	20.1	45.24	106.04	267.74
Sloan	Upper boundary	0.120	0.456	1.238	2.961	6.738	15.237	35.649	88.390	240.880
	Lower boundary	0.115	0.434	1.178	2.822	6.431	14.567	33.951	83.327	224.945
Martin, Fedorovsky		0.11	0.43	1.18	2.84	6.49	14.76	34.48	85.58	234.3

* The factor according to Russian Construction Code CII 50-101-2004 is in agreement with formula (1)

The factors according to S. Martin, S. Sloan and V.G. Fedorovsky in comparison with those contained in domestic and foreign regulative codes are given in Table 1 and in Fig. 2. Here it should be noted that in domestic publications which contain formulas similar to (1), a factor of $\frac{1}{2}$ at N_γ is usually included in the N_γ value, and that is why for the sake of uniformity, the

factor N_γ , according to Construction Code 50-101-2004, is expressed as in (1) above. Considering existence of exact solutions for N_γ at $q' < 1$, it appears reasonable to restrict application of usual N_γ at $q' < 1$. For this section it would be worthwhile to use a more exact approximation of the nonlinear section of $p_u(q')$ dependence in comparison with K.Tertzagi's formula (1).

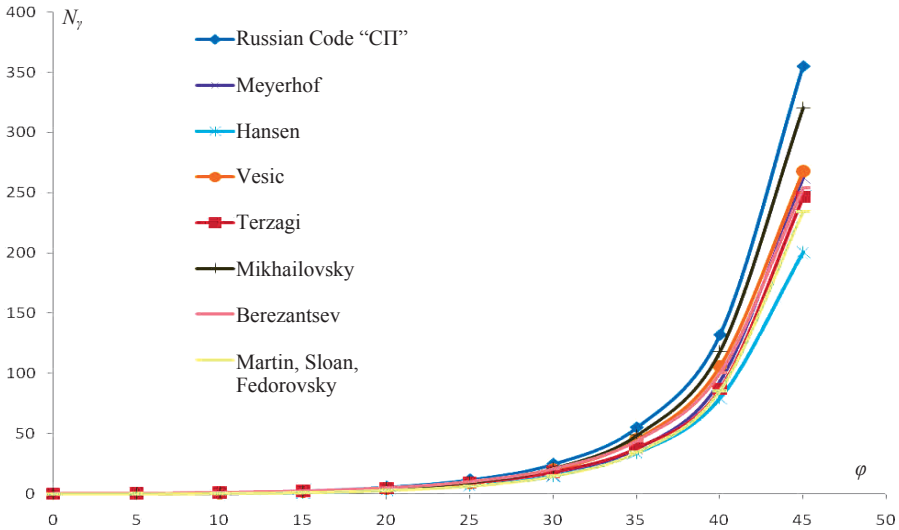


Fig. 2. Comparison of values of factor N_γ calculated based on various solutions.

2. THE ISSUE OF «LOCKING» IN SOLUTIONS OF LIMITED EQUILIBRIUM PROBLEMS BY FINITE ELEMENTS METHOD USING ELASTOPLASTIC MODELS.

Unlike the approach used by S. Sloan, which essentially is using the finite elements method (FEM) for solution of limited equilibrium equations, below we will dwell on using the FEM for more traditional elastoplastic problems of subsoil deformation. Such problems are usually solved using the method of movements with an application of iterative algorithm to account for physical nonlinearity. The most frequently used is the solution method with a constant matrix (the so-called method of initial stresses). In this case the iterative process can be represented as:

$$K \delta x = f - f_m(x_{k-1}), x_k = x_{k-1} + \delta x, \quad (2)$$

where K – matrix of system's strength, f – vector of external forces, $f_m(x)$ – internal forces in an element, calculated depending on movements of x according to the physical model of the material.

It is obvious that in solving the pressed plate problem the «load-settlement» curve should have a vertical section corresponding to the maximum load on the foundation. Thus, the problem of calculating deformations of the

subsoil below the foundation should automatically transform into the problem of limited equilibrium.

Meanwhile on the way of this transition there is a large number of theoretical and practical issues. The first complex of such issues is connected with the so-called "locking" of the elastoplastic solution. This issue was identified by S. Sloan and M. Randolph (1982) [16] and A.B.Fadeev (1987) [17]. Specifically, the problematic situation is that when using the defined law of plastic yield (associated or not associated, as the case may be, for example, coextensive), restrictions are imposed on the system of degrees of freedom, and this imposition may preclude using certain form functions in the elements. The works quoted above give theoretical reasons concerning the type of functions that the form of the final element should have so as to avoid "locking". Significantly though, for problems in flat setting, elements of the first order (with linear functions of their form) are considered permissible.

However, practical experience of solving real problems shows the opposite. When solving problems of pressing in the plate by the finite element method using elements of the first order the «load-settlement» curve never quite reaches a straight vertical line, i.e. the solution does not allow to calculate the maximum load. In particular, such incorrect solutions are given and

subjected to fair criticism in the book by K.V. Korolev [12]. And yet, this book [12] explains the deviation of the final element solution from conditions of equilibrium as the reason for incorrectness of that solution which, in our opinion, is wrong. In reality, the condition of equilibrium for finite elements is fulfilled automatically; moreover, the iterative process (2) actually minimizes the discord between the external and internal forces. Further on we will demonstrate that the FEM actually allows to receive solutions which concord with the theory of limited equilibrium, excluding the need to search for basic discrepancies in the FEM.

Nevertheless, the reason for the divergence between the final element solution and the

theory of limited equilibrium using elements of the first order needs identification. Let us remember that a possible solution is to use elements not of the first, but of a higher order with functions of a form according to the 2nd and the 3rd degrees. Such elements are used in the well-known PLAXIS software as well as in many other tools for numerical analysis. When solving problems of pressing in of the plate using elements of a higher order no "locking" of the solution can be identified. Then where does the fault lie when we use elements of the first order? In what follows below we attempt to offer an explanation.

Let us consider a final element scheme consisting of 4th nodes. Let us impart to this scheme movements as shown in Fig-s. 3a and 3b.

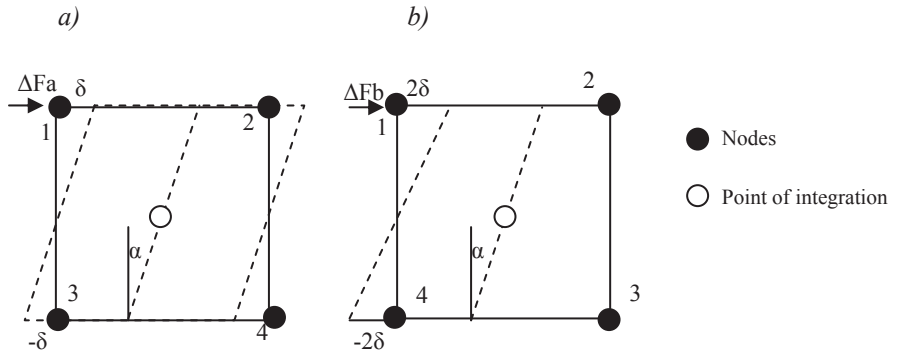


Fig. 3. Illustration to assess the reason for "locking" of the finite element solution.

Let us assume that within a final element functions of form are set by equations of the first order, and the point of integration is in the middle. Then in the integration point for Fig-s 3a and 3b:

$$\Delta\gamma_{xy_a} = \frac{\partial u}{\partial y} = tg\alpha = \Delta\gamma_{xy_b}, \Delta\varepsilon_x = \Delta\varepsilon_y = 0$$

Let stresses in the element be equal to the ultimate:

$$\tau_a = \tau_b = \tau_{lim}.$$

It is possible to express the iteration process (2) in a different form:

$$K(x_k) = f - f_m(x_{k-1}) + Kx_{k-1} = f + \Delta f_k,$$

where Δf_k – is the addition into the vector of the right parts, calculated based on the difference

between increments of "elastic" stresses in the element and the allowed stresses in the element according to the model of the material.

Increment of "elastic" stresses at the assumed increment of movement δ will be:

$$\Delta\tau_a = G\Delta\gamma_{xy_a} = \Delta\tau_b = G\gamma_{xy_b}.$$

As the stress has already reached the ultimate, all additions of "elastic" stresses should be moved into the vector of forces:

$$\Delta F_a = \Delta F_b = B^T \begin{Bmatrix} 0 \\ 0 \\ \Delta\tau \end{Bmatrix} V,$$

where B – the matrix of derivatives from functions of form, V – the area of the element.

As for the drawings 3a and 3b matrices B are identical, additions to the vector of forces

will be also calculated as identical. On the other hand, the elastic increment of the vector of forces can be calculated according to the FEM ideology as the product of the system strength matrix and the assumed movements:

$$\Delta F_e = K\delta = \begin{bmatrix} K_{11} & K_{12} & K_{13} & K_{14} \\ K_{21} & K_{22} & K_{23} & K_{24} \\ K_{31} & K_{32} & K_{33} & K_{34} \\ K_{41} & K_{42} & K_{43} & K_{44} \end{bmatrix} \begin{Bmatrix} \delta_1 \\ \delta_2 \\ \delta_3 \\ \delta_4 \end{Bmatrix}$$

For option 1a in the first node:

$$\Delta F_{ea1} = K_{11}\delta + K_{12}\delta - K_{13}\delta - K_{14}\delta.$$

For option 1b in the first node:

$$\Delta F_{eb1} = K_{11}2\delta - K_{13}2\delta.$$

If in matrix $K_{11} \neq K_{12}$ (the diagonal element is always bigger than the non-diagonal), then $\Delta F_{ea} \neq \Delta F_{eb}$. However, as stress is equal to the limit stress $\tau_a = \tau_b = \tau_{lim}$, the increment of total forces should be equal to zero: $\Delta F_b - \Delta F_a = 0$. This condition cannot be fulfilled, as for the option 3a and 3b the add-ons in the right part of ΔF are equal, but increments of elastic forces ΔF_b are different.

Thus, the reason for "locking" of the elasto-plastic solution when using elements of the first order is that the different deformations of finite elements 3a and 3b correspond to the identical field of stresses, which leads to the identical (and, as such, incorrect for one of the options) increment of the vector of the right parts in the iterative process. When solving the problem of pressing in of the plate a part of the elements in the zones under the plate edge work according to the scheme similar to Fig. 3b. As a result, the zone of plastic deformations in the final element solution become isolated in the space underneath the foundation and do not emerge on the surface, as, indeed, it should happen according to the limited equilibrium theory. In case we used elements of a higher order the quantity of integration points increases, allowing to more accurately collate the kind of deformation of the element and the stress in points of integration thus avoiding the "locking" of deformations.

From the given considerations an idea appears as to how it is possible to "adjust" the elements of the first order, adapting them for the solution of limited equilibrium problems. Indeed, the problem of deformations "locking"

is related to the loss of information on a type of the deformed condition in transition from the vector of movements (for example in Fig. 3 the element has 8 degrees of freedom) to stresses (3 components of stress in a flat problem) and back to the vector of loads (again 8 degrees of freedom). In order to correctly calculate the vector of forces, without having lost the kind of deformed condition, it is necessary or to increase the quantity of points of integration, or to calculate the add-on to the vector of the right parts, using the vector of forces directly. To make it happen is possible in the following way.

Let it be necessary to calculate the misfit of the vector of forces for the iterative process (2). Let us calculate the stresses in the element according to the physical model $\sigma_m(x) = \sigma_v - \sigma_D$, consisting of volumetric and deviatoric stresses. Let us calculate also "elastic" stresses $\sigma^e = DBx$ which also consist of volumetric and deviatoric stresses

$$\sigma^e = \sigma_{ev} + \sigma_{eD}.$$

Now let us calculate the vector of "elastic" right parts for an element $f = Kx$, where K - a matrix of strength of the element, and divide the forces into "volumetric" and "deviatoric":

$$f_v = B^T \sigma_{ev} V, \quad f_D = f - f_v.$$

The vector of forces corresponding to the physical model is possible to express as follows:

$$f_m(x) = \frac{\sigma_v}{\sigma_{ev}} f_v + \frac{\sigma_D}{\sigma_{eD}} f_D \quad (3)$$

When using expression (3) we calculate the vector of forces according to the physical model directly according to the vector of "elastic" forces, whereby the information on the type of deformation is not lost. When using expression (3), various options for the yield surface can be used (including the six-sided surface according to Coulomb-Mohr criterion), however the surface of the plastic potential is assumed as being circular around the hydrostatic axis, because the vector of strain increment is always directed towards it.

Let us consider a solution of the test problem performed with elements of the first order with *FEM models* software, using expression (3) and with elements of the second order performed with other available software. Comparison of results is given in Fig. 4. As shown

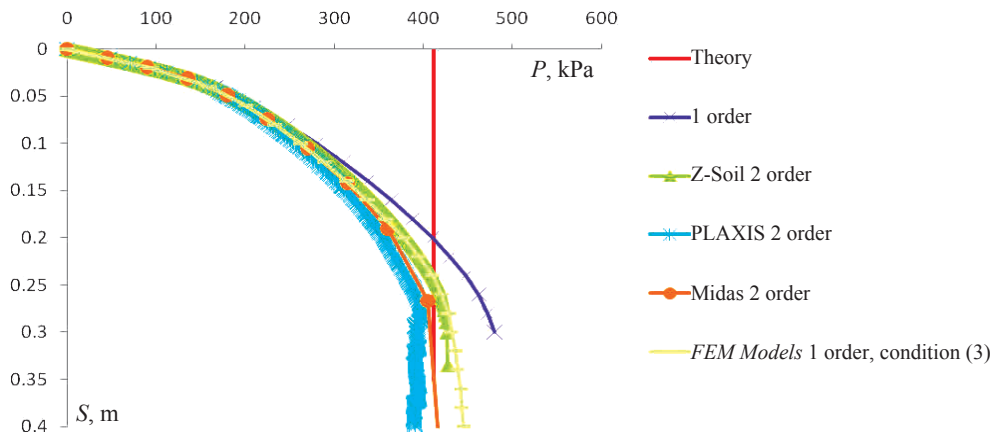


Fig. 4. Comparison of solutions of the plate problem at $c = 20$ kPa, $\varphi = 20^\circ$ at width of plate 2 m using elements of the 1st and the 2nd orders.

by the Figure, the condition (3) allows to get rid of problems with "locking" of solution when using elements of the 1st order and to receive the correct solution, identical to computation results with various other software using elements of the 2nd order. Fig. 4 also shows that when solving the problem without expression (3) not only the maximum load on the foundation, but also the entire graph «load-settlement» in its prelimit condition is incorrect.

Thus, it is possible to draw a conclusion that the problematic issues related to obtaining the ultimate bearing capacity, described in [12], are connected not with FEM shortcomings, but with aspects of solving this problem with finite elements of the 1st order. Use of these elements for solution of geotechnical problems is possible only when using special integration techniques for the vector of forces, for example, the expression (3). Otherwise elements of the first order yield incorrect values of maximum load and incorrect deformations in the prelimit condition.

Unfortunately, this peculiarity of elements of the first order has not been given due attention in literature, and there are currently some finite element software products (the most famous of them being "Lyre"), solving geotechnical problems using elements of the first order without any adjustments.

3. ESTABLISHING FACTORS WHICH INFLUENCE THE OUTLINE OF «LOAD-SETTLEMENT» CURVES IN SOLUTIONS OF PLATE PROBLEMS.

In spite of the fact that the problem of settlement of the plate on the surface of an elastoplastic medium has been thoroughly researched, in the literature published to date it is rather difficult to find description of factors which influence the outline of «load-settlement» curves even in the most elementary case featuring various modifications of the ideally elastoplastic Coulomb-Mohr models. It needs to be said, however, that these factors are not at all obvious. «Load-settlement» curves are influenced by the following factors:

1. Strain modulus of soil and the size of the area calculated (the obvious factors).
2. Value of Poisson ratio (also, generally, an obvious factor, as it defines the second elastic constant of the material).
3. Type of deformation (the drained or undrained statement of the problem). This factor is connected with factor 2 above as the undrained statement corresponds to Poisson ratio roughly equivalent to 0,5.
4. The kind of plastic yield: associated or non-associated (for example, coextensive) law of plastic yield. This factor strongly influences the outline of «load-settlement» curves.

5. The initial stress which is usually characterized by factor of lateral pressure K_0 . Some software products utilizing elastoplastic models based on Coulomb-Mohr criterion do not allow to adjust K_0 at the stage of natural stress, which renders them unsuitable for solution of geotechnical problems.
6. Specifics of yield surface.

On this last factor it is necessary to dwell in more detail. "It needs no ghosts to tell us" that in various finite element based software codes, the developers used models with different yield surfaces close to the classical Coulomb-Mohr criterion. For example, in the so-called Druker-Prager model instead of the six-faceted Coulomb-Mohr pyramid a conic surface (Fig. 5) is used.

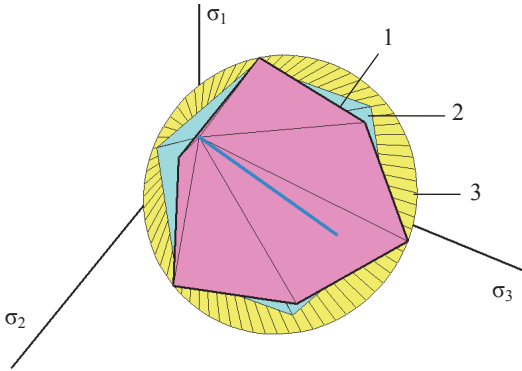


Fig. 5. Comparison of the limiting surfaces positions: 1 – based on Coulomb-Mohr condition, 2 – according to $q_{lim} = Mp$ (4), 3 – according to Druker-Prager's model.

Based on results of solving finite elements problems it appears that the conic surface *drawn*

outside the Coulomb-Mohr pyramid yields a considerably higher bearing capacity, than obtained through the classical Coulomb-Mohr criterion (Fig. 6). On the other hand the conic surface *drawn inside* Coulomb-Mohr pyramid does not meet the strength criterion $\sigma_2 = \sigma_3$, i.e. at usual tension in triaxial tests. Resulting from this a user of Druker-Prager model faces a dilemma: either to considerably overestimate the bearing capacity of his subsoil in comparison with classical solutions, or to disregard the possibility of modelling triaxial tests. Unfortunately, this problem of selecting parameters for Druker-Prager model is poorly reflected in literature and is not realized by the majority of designers.

Another example of a deviation from the Coulomb-Mohr surface is the models of Cam Clay type. These models are traditionally built in coordinates $p = (\sigma_1 + \sigma_2 + \sigma_3)/3$, as well as in $q = (\sigma_1 - \sigma_3)/2$. In these axes it is possible to draw the line

$$q_{lim} = Mp. \quad (4)$$

At $M = \frac{3 \sin \phi}{3 - \sin \phi}$ this line corresponds to

Coulomb-Mohr criterion, but under one condition: $\sigma_2 = \sigma_3$. On the whole, the criterion (4) gives a pyramid which is a bit different to the pyramid of Coulomb-Mohr (Fig. 5). Resulting from a solution of an ideally elastoplastic problem with criterion (4) we receive a considerably other «load-settlement» curve and a different bearing capacity of the foundation, too (Fig. 6). Therefore, when using models of the Cam Clay type with criterion (4) it should be

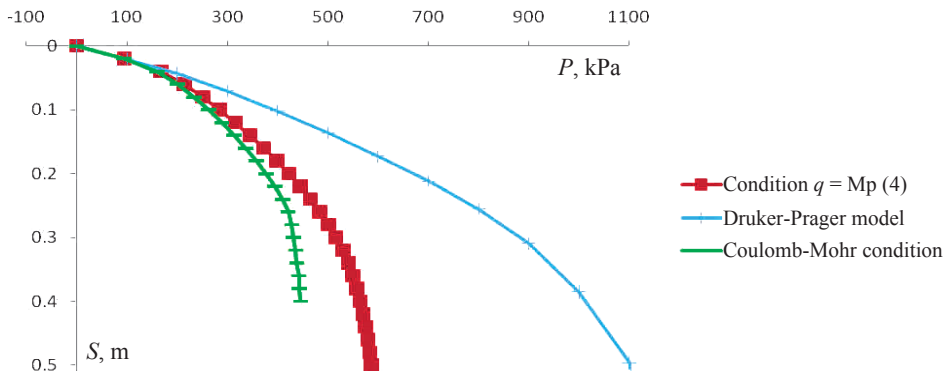


Fig. 6. Comparison of «load-settlement» curves using condition (4), according to Druker-Prager model (the cone drawn around the Coulomb pyramid) and according to the classical model with Coulomb-Mohr criterion.

borne in mind one obtains bearing capacity values slightly in excess of those obtained through solutions in terms of limited equilibrium theory.

Thus, it is necessary to draw attention of designers to multiple factors on which the «load-settlement» curve depends even when using the most elementary ideally elastoplastic model. When using more difficult models the number of factors significantly increases.

4. COMPARING FACTOR N_γ OBTAINED BY SOLVING ELASTOPLASTIC PROBLEMS AND THROUGH THE THEORY OF LIMITED EQUILIBRIUM

Let us compare factors N_γ obtained as results of solving elastoplastic problems and through various solutions in terms of theory of limited equilibrium. It should be noted that solution of elastoplastic problems which transform into problems of limited equilibrium is linked to a number of additional difficulties, apart from those already described in section 2 above. In particular, at angle of internal friction higher than 30° for to obtain the correct solution it is necessary to considerably increase solution accuracy. Trying to solve this problem using

PLAXIS at the angle of internal friction in excess of 30° we failed to obtain a satisfactory solution. The failure was connected to a strange behaviour of the autochoice algorithm for loading steps, which for unknown reasons starts dropping load during pressing of the plate, without reaching the maximum load values. The autochoice algorithm used in the program is not documented; the specifics of its behaviour (an increase of movements at loading reduction) are purely mathematical and are devoid of a physical sense. Correspondingly, selection of parameters for this algorithm can be done by users only through trial and error, which does not universally yield a positive result. The described features are an illustration of complexity of solving nonlinear problems even when using the most elementary models of soil mechanics.

In Fig. 7 we adduce a comparison of results for calculation of N_γ factors according to the FEM models software (using expression (3) for the elements of the first order) and according to solutions in terms of theory of limited equilibrium given in section 1 above. It is apparent from the comparison that the finite element method allows to receive solutions which are rather close to the values obtained by S. Sloan, S. Martin and V.G. Fedorovsky [14, 15, 11].

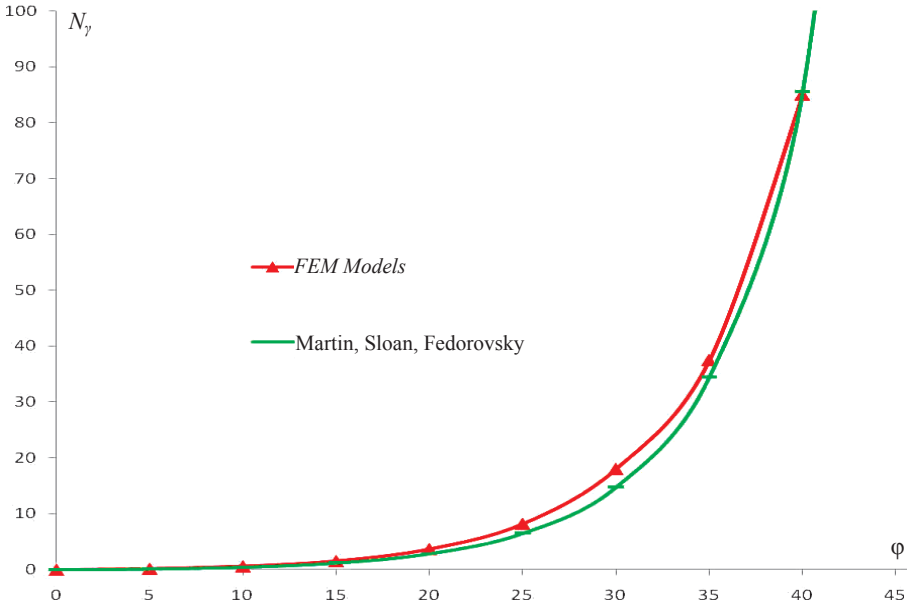
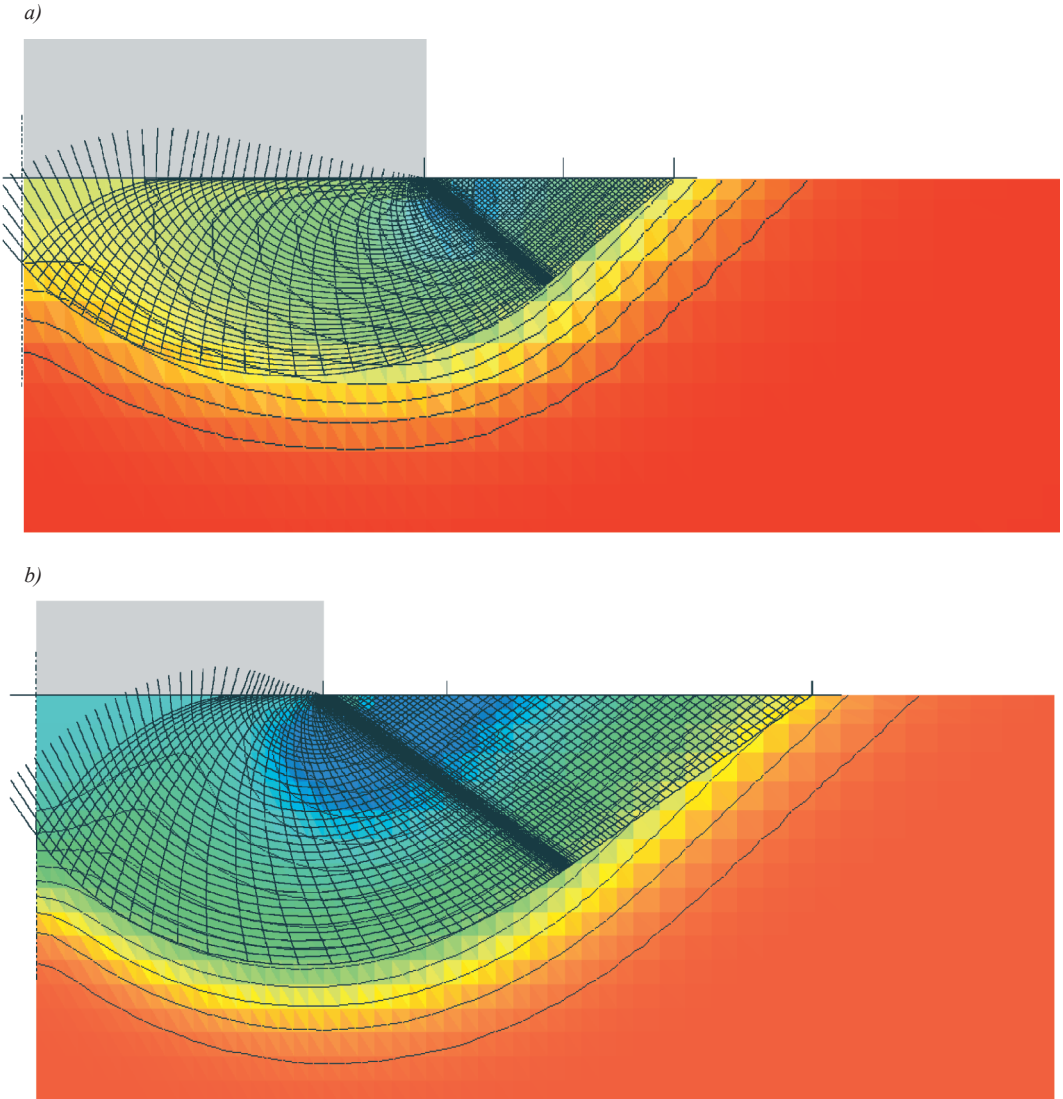


Fig. 7. Comparison of factor N_γ according to solutions of elastoplastic problems with “FEM models” software and according to solutions by S. Martin, S. Sloan, and V.G. Fedorovsky.

Fig. 8 contains comparison of the limited state areas obtained by solution of an elastoplastic problem through a finite element method and by the programme of S. Martin [15]. As visible from Fig. 8 (a,b) for angles of internal friction less than 25° , shear zones according to the theory of limited equilibrium and according to the numerical solution coincide rather closely. For higher values of the angle of internal friction we can observe a deviation of uplift

areas from the theoretical solution (Fig. 8c). This is probably related to the fact that for higher values of the angle of internal friction the limiting state is reached at higher values of movements. There, in the course of pressing in of the plate, the solution demonstrates formation of intermediate uplifts from under the plate edge, with the common uplift area forming only at the final stage. As a whole, the matter obviously requires further research.



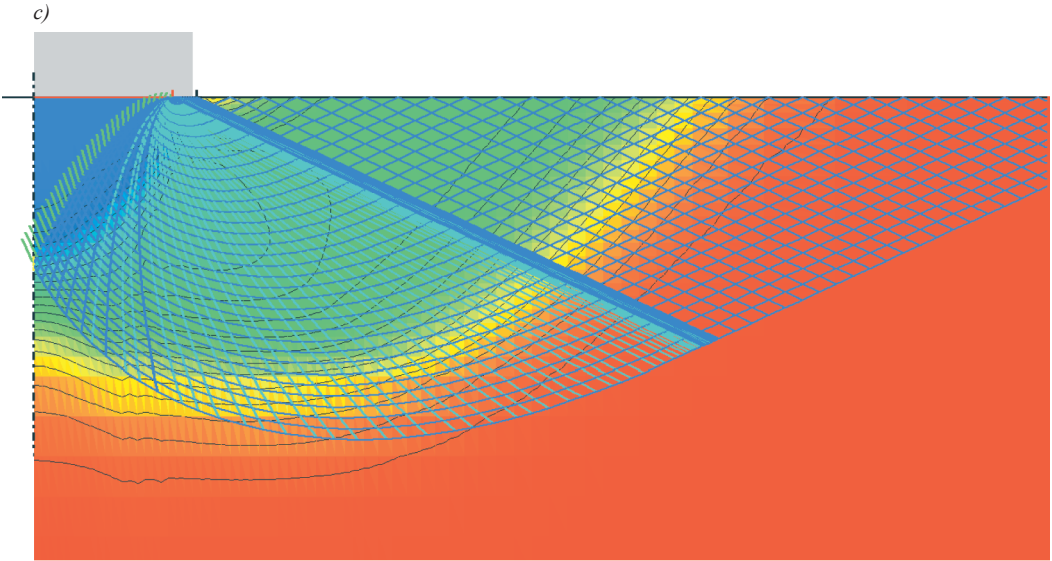


Fig. 8. Comparison of shear zones (maximum movements) according to solution of elastoplastic problems and according to the theory of limited equilibrium: *a)* $\varphi = 10^\circ$, *b)* $\varphi = 20^\circ$, *c)* $\varphi = 40^\circ$.

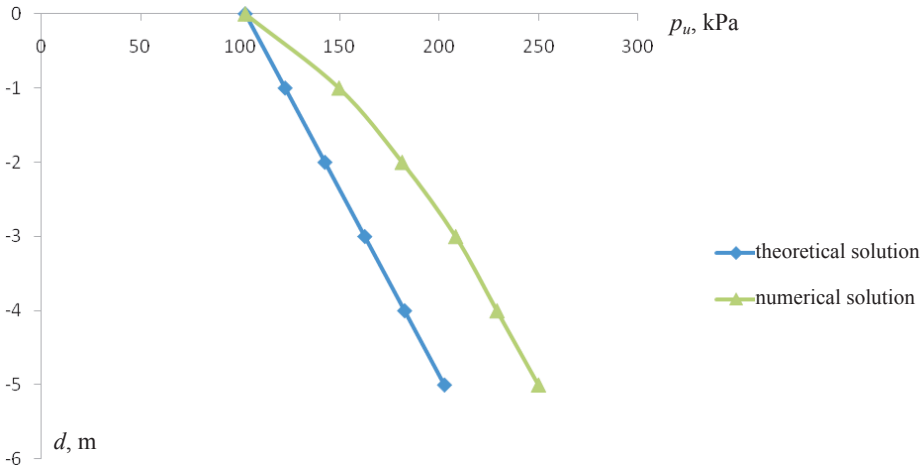


Fig. 9. Dependency of ultimate pressure on depth of the foundation d having width $b=2$ m at $c=20$ kPa, $\varphi = 0^\circ$

5. DEFINITION OF THE BEARING CAPACITY OF A DEEP FOUNDATION AND A FOUNDATION UNDER EX-CENTRIC LOAD

These problems were solved for an ideally cohesive medium (with a zero angle of internal friction). According to classical solutions, embedment of a foundation is accounted for

through addition of loading q on the surface, being equal to pressure of soil above the footing of a deep foundation. However, in reality, when embedment is increased, it is not only the loading of the subsoil near the foundation that starts to be important, but also strength of soil above the plate footing that leads to an increase of the maximum load in comparison with theoretical solutions (Fig. 9).

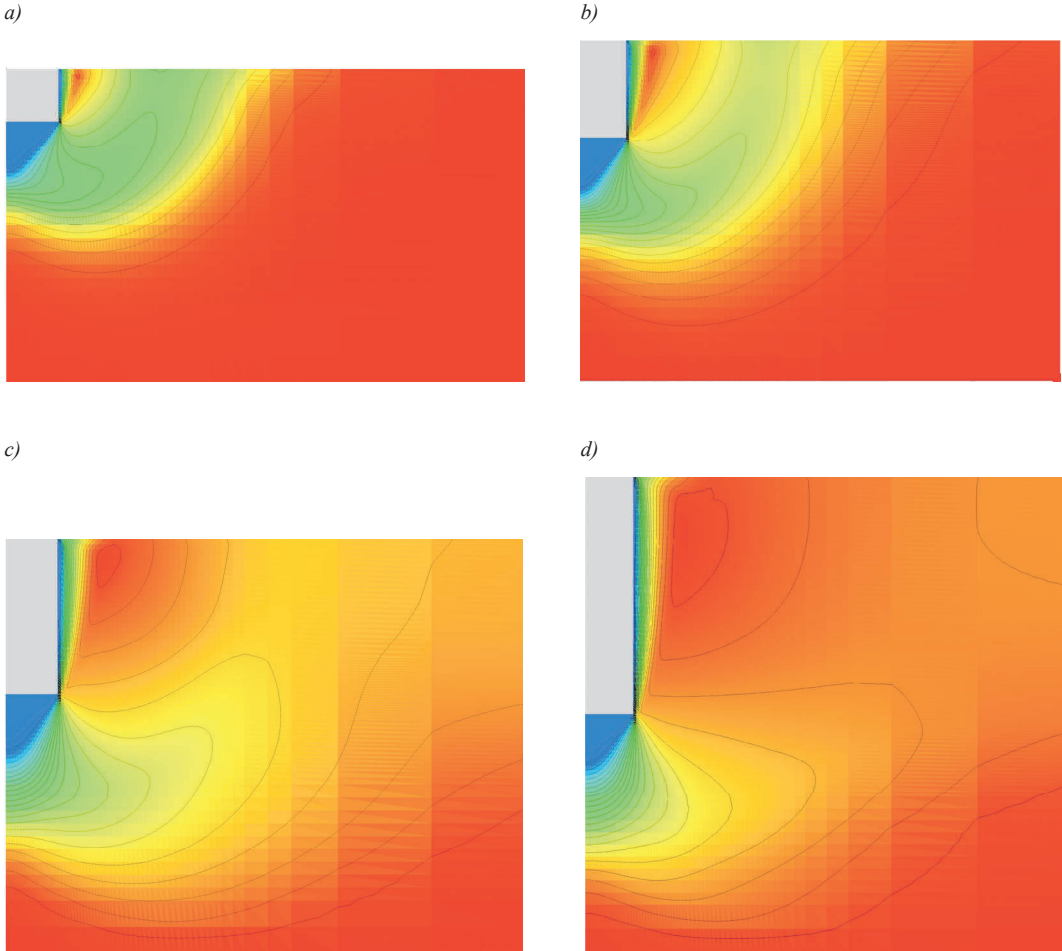


Fig. 10. Character of shear zones (maximum movements at the stage of losing stability) at various depths of foundation having width $b=2$ m, at $c=20$ kPa, $\varphi = 0^\circ$: a) 1 m, b) 2 m, c) 3 m, d) 5 m.

As is shown in Fig. 10, *a*, at smaller foundation depths the shape of the occurring uplift is close to that of an unembedded foundation. If one increases embedment of the foundation the uplift area becomes less clearly defined. Additionally, it can be seen from Fig. 11 that an increase of the plate embedment is linked to an increase of linear behaviour zone on the «load-settlement» curve.

The account for eccentricity of loading application in domestic regulative codes is made by reduction of width of the calculated foundation $b' = b - 2e$, where e - eccentricity of loading

application. This approach is also quite justifiable at low eccentricity values (Fig. 12). However, when the point of loading application reaches the foundation edge, such approach leads to bearing capacity reducing to nought. At the same time it is obvious that when loading is located on the foundation's edge, the bearing capacity of the foundation should drop significantly, but will never be reduced to nought. It is precisely this dependency that the finite element solution shows (Fig. 12). The forms of losing stability at eccentric loading applications are given in Fig. 13.

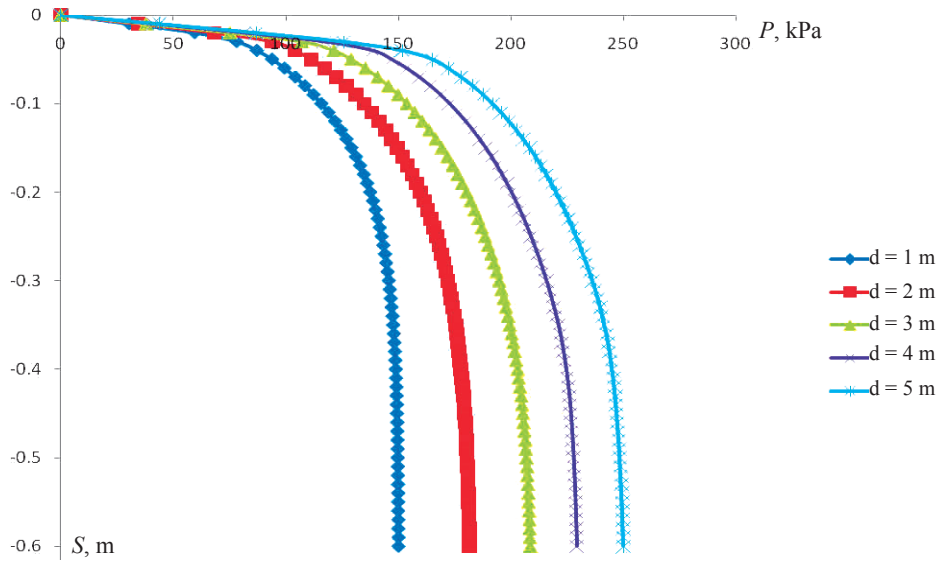


Fig. 11. Dependency of settlement S on load p at various foundation depths.

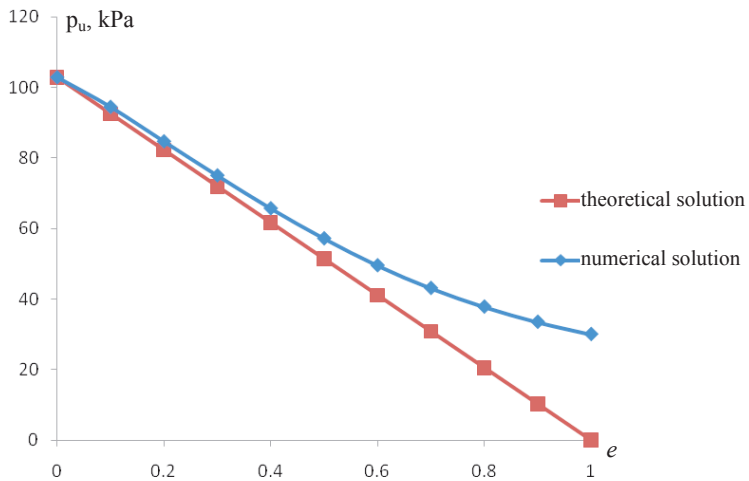


Fig. 12. Dependency of ultimate pressure on eccentricity of load application e for a foundation having width $b=2$ m, at $c=20$ kPa, $\varphi = 0^\circ$.

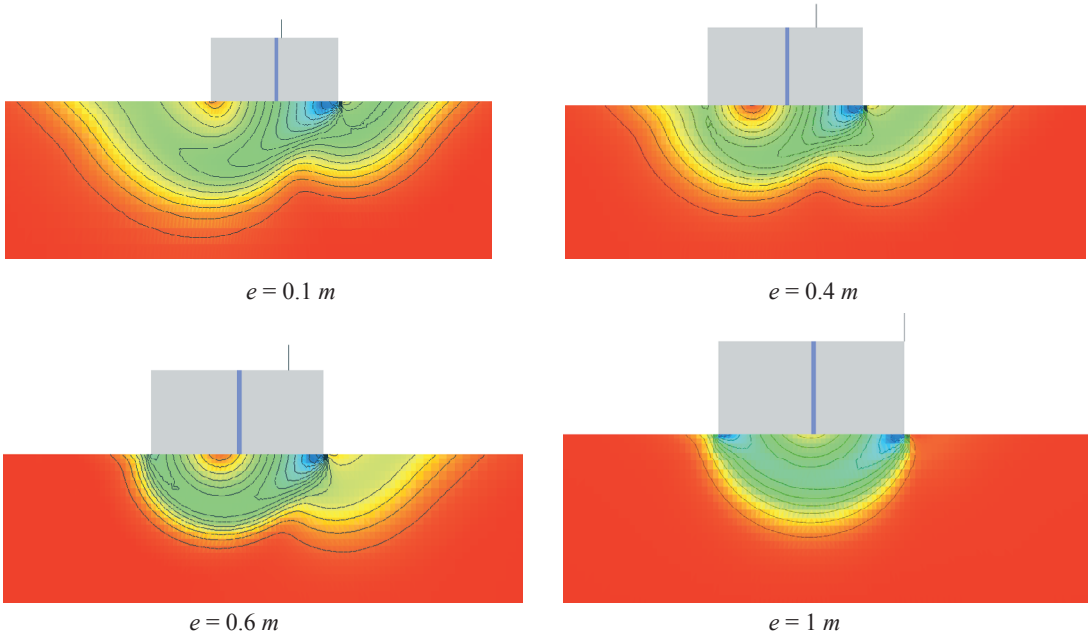


Fig. 13. Character of shear zones (maximum movements at loss of stability stage) at various values of eccentricity e for a foundation having width $b=2$ m, at $c=20$ kPa, $\varphi = 0^\circ$

6. CONCLUSIONS

1. For foundations on noncohesive subsoils at small levels of footing embedment it seems reasonable to introduce corrections into regulative codes based on the exact solutions obtained by S. Sloan, S. Martin and V.G. Fedorovsky. It is necessary also to impose restrictions on application of the common (as contained in the codes) factors N_γ in cases of small foundation embedments in noncohesive soils or to modify the traditionally applied trinomial formula, using more exact approximations to foundations at low embedment levels.

2. Solution of limited equilibrium problems with the finite element method allows to receive factor N_γ values close to solutions by S. Sloan, S. Martin and V.G. Fedorovsky. There, if a corresponding correction of calculation technique for defining internal forces is introduced, it is possible to use final elements with form functions of the first order. The reason for deformations "locking" with elements of the first order is information loss as to what form the deformation has on the way of calculating stresses on movements and the reverse transformation into the vector of forces. If used correctly, elements of the first order, as well as

elements of higher orders, allow to obtain transition of the problem of plate deformation to that of limited equilibrium.

3. Use of the finite elements method allows to specify details of stability loss in subsoil for a number of problems which have only an approximate solution according to the theory of limited equilibrium, in particular for problems of the embedded plate, with eccentricity of load application or with criteria of strength different to that of Coulomb-Mohr. In particular, when using models of Drucker-Prager and Cam Clay types it is necessary to bear in mind that the criteria of strength therein encoded differ from classical Coulomb-Mohr criterion and yield higher bearing capacity of the foundation, compared to solution within the theory of limited equilibrium.

REFERENCES

1. Prandtl, L., 1921. Über die Eindringungsfestigkeit (Harte) plastischer Baustoffe und die Festigkeit von Schneiden. *Zeitschrift für Angewandte Mathematik und Mechanik* 1 (1), 15–20.
2. Reissner, H., 1924. *Zum Erddruckproblem*. In: Biezend, C.B., Burgers, J.M. (Eds.), *Proc. First Congr. Appl. Mech.*, pp. 295–311.

3. Terzaghi, K., 1943. *Theoretical Soil Mechanics*. John Wiley & Sons, New York.
4. Соколовский В.В. *Статика сыпучей среды*. М.: Наука, 1960. 241 с.
5. Березанцев В.Г. *Осесимметричная задача теории предельного равновесия сыпучей среды*. М.: Гос изд-во технико-теоретич. Лит-ры, 1952. 120 с.
6. Meyerhof, G.G., 1951. *The ultimate bearing capacity of foundations*. *Geotechnique* 2 (4), 301–332.
7. Hansen, J.B., 1970. *A revised and extended formula for bearing capacity*. *Bulletin of the Danish Geotechnical Institute* 28, 5–11.
8. Vesic, A., 1975. *Bearing capacity of shallow foundations*. In: Winterkorn, H.F., Fang, H.Y. (Eds.), *Foundation Engineering Handbook*. Van Nostrand Reinhold, New York, pp. 121–147.
9. Drucker, D.C., Greenberg, W., Prager, W., 1952. *Extended limit design theorems for continuous media*. *Quarterly Journal of Applied Mathematics* 9, 381–389.
10. Караулов А.М. Несущая способность основания осесимметричных фундаментов. Новосибирск: Изд. СГУПС, 2002. 104с.
11. Федоровский В.Г. Несущая способность сыпучего основания ленточного фундамента при действии наклонной внецентренной нагрузки. // ОФМГ, 2005 №4, с 1-7.
12. Королев К.В. *Плоская задача теории предельного равновесия грунтов*. Новосибирск: Издательство СГУПС, 2010. 250 с.
13. Lyamin A. V. and Sloan S. W. *Lower bound limit analysis using non-linear programming*. // INTERNATIONAL JOURNAL FOR NUMERICAL METHODS IN ENGINEERING Int. J. Numer. Meth. Engng 2002; 55:573–611 (DOI: 10.1002/nme.511).
14. Hjjaj M., Lyamin A.V., Sloan S.W. *Numerical limit analysis solutions for the bearing capacity factor N_γ* .// *International Journal of Solids and Structures* 42 (2005).
15. Martin C.M. Exact bearing capacity calculations using the method of characteristics.
16. Sloan S.W. Randolph M.F. Numerical prediction of collapse loads using finite element methods // INTERNATIONAL JOURNAL FOR NUMERICAL AND ANALYTICAL METHODS IN GEOMECHANICS. VOL. 6. 41-16 (1982)
17. Фадеев А.Б. *Метод конечных элементов в геомеханике*. М.: Недра, 1987.

A Nonlinear Dynamic Interaction Algorithm of Elasto-Viscoplastic Concrete Structures with Coupled Saturated Soils

Omar Al-Farouk S. Al-Damluji

Former Chairman of Civil Engineering, University of Baghdad, omaraldamluji@gmail.com

Husain M. Husain & Rafa'a M. Abbas

University of Baghdad, rafaamaa@yahoo.com

ABSTRACT: The nonlinear response of concrete structures interacting with saturated soils due to different dynamic loadings and excitations is investigated. The soil is simulated as a two-phase saturated porous medium using a mixed (u-p) formulation. Solution algorithm adopted is based on field partitioning and staggered procedure to simulate the coupling problem.

A strain-rate sensitive elasto-viscoplastic model with progressive degradation of the strength and cracking is adopted for concrete material nonlinearity. A finite element computer program is developed. The results demonstrate that pore fluid-soil solid skeleton coupling affects the dynamic interaction between structures and the saturated foundation soil.

1. INTRODUCTION

Dynamic soil-structure interaction refers to the effects that the founding soil has on the dynamic response of the structure and, conversely, the effects of the structure on soil motion. The influence on the structural response often includes an amplification of the translational motion and the addition of damping from hysteretic action of the soil. Furthermore, radiation of energy away from the structure in the form of outward propagating soil waves (radiation damping) is usually encountered.

For the interaction problem between a structure and the saturated soil, the discretized model contains the structure and the soil body. These two parts are affecting each other through a common boundary (interface) between them. On the other hand, for the saturated foundation soil, it can be further modeled into a coupled two-phase saturated porous medium, i.e. soil skeleton and the entrapped pore water. Therefore, there are two kinds of coupling in the problems of dynamic interaction between structures and saturated soils:

- A coupling between the structure and the supporting saturated soil (soil-structure interaction), and
- A coupling between the soil solid skeleton and the pore water (two-phase behavior). For

such a case, the saturated porous medium can be viewed as consisting of two fields, i.e. the solid skeleton and the motive pore water with complete overlapping between the two fields.

The subject of dynamic soil-structure interaction has been an area of extensive research in the last few decades.

For the saturated foundation, fluid saturation of the porous skeleton introduces time dependence into the response when subjected to quasi-static or dynamic loading. However, for the cases in which some fluid flow can take place due to loading, there is an interaction between the skeleton strains and the pore fluid flow. The solution of these problems requires that the saturated porous medium be analyzed by incorporating the effect of the transient flow of the pore fluid through the solid skeleton voids.

Considering the interaction between the solid skeleton and the pore water, Biot (1956) developed a theory for the propagation of elastic waves in a porous saturated solid. Later, Biot (1962) extended his earlier theory of acoustic propagation in porous media to include anisotropy and viscoelasticity. Ghaboussi and Wilson (1972) presented the solution of the fully discretized equations for the linear case. Bazant and Krizek (1975) extended Biot's linear elastic theory to the nonlinear inelastic case. An incremental stress-strain relationship that takes

into account the nonlinearity of the soil was formulated. Zienkiewicz et al. (1980) and Zienkiewicz and Bettess (1982) presented a physical derivation of the governing equations for a two-phase porous medium. This formulation presented the basic models into which different constitutive relationships can be inserted when full analysis was used to study the validity of various approximations to Biot's equations. Prevost (1982) also extended Biot's theory and considered that the stress-strain behavior of the soil skeleton is nonlinear, anisotropic, hysteretic and path dependent. In this formulation, the soil was viewed as a multiphase medium and the theories of mixtures were used.

2. DYNAMIC EQUATIONS FOR THE TWO-PHASE POROUS SOIL MEDIUM

Biot (1962) presented a general set of equations governing the behavior of a saturated linear elastic solid under dynamic conditions. Biot's equations define the problem of dynamic fluid-solid interaction completely, and establishes a system with basic unknowns which can be numerically solved when suitable boundary and initial conditions are imposed on the domain (Ω). These equations can be used directly in the numerical solution as shown by Zienkiewicz and Shiomi (1984). This system is suitable for explicit time stepping computation as shown by Ghaboussi and Wilson (1972). However, in implicit computations, where a large system of algebraic equations arises, it is convenient to reduce the number of variables by neglecting the apparently small terms in these equations.

For medium speed phenomena, it is reasonable to assume that only the terms related to fluid acceleration are to be neglected. It is often preferable to reduce the problem by retaining u and p (solid displacement and pore water pressure) as the basic variables. This approximation, introduced by Zienkiewicz et al. (1980), is economical and convenient in numerical transient analysis. The final set of the governing equations for the (u-p) form are (Zienkiewicz and Bettess, 1982):

$$\sigma_{ij} = \sigma'_{ij} - \delta_{ij} p \quad (1)$$

$$d\varepsilon_{ij} = (du_{i,j} + du_{j,i})/2 \quad (2)$$

$$d\sigma'_{ij} = D_{ijkl}(d\varepsilon_{kl} - d\varepsilon_{kl}^0 + \delta_{kl} dp/3K_s) \quad (3)$$

$$\sigma_{ij,j} + \rho b_i = \rho \ddot{u}_i \quad (4)$$

$$(k_{ij} p_{,j})_{,i} - \dot{\varepsilon}_{ii} - (k_{ij} \rho_f b_i)_{,i} = -(k_{ij} \rho \ddot{u}_j)_{,i} + n\dot{p}/K_f + (1-n)\dot{p}/K_s - \dot{\sigma}'_{ii}/3K_s \quad (5)$$

where u_i is the displacement of the solid skeleton; p is the pore water pressure; n is the porosity of the soil and δ_{ij} is the Kronecker delta. Equation (1) is the effective stress definition in which σ_{ij} is the total Cauchy stress in the combined soil-fluid mixture, whereas σ'_{ij} is the effective stress used in soil mechanics. Equation (2) represents total strain definition in which $u_{i,j} = \partial u_i / \partial x_j$. Equation (3) is the constitutive law for the solid skeleton in which D_{ijkl} is the elasticity matrix; K_s is the average bulk modulus of the solid grains. Equation (4) is the equation of motion for the total system in which b_i is the body force acceleration; ρ is the mass density of the soil-fluid mixture and $\ddot{u} = \partial^2 u_i / \partial t^2$. Equation (5) is the equation of motion and mass balance of pore fluid flow in which ρ_f is the mass density of the pore fluid; K_f is the bulk modulus of the fluid; k_{ij} is Darcy's permeability coefficients and ε_{ii} is the total volumetric strain.

The above set defines the complete equation system for the solution of the problem defined provided that the necessary boundary conditions are specified. These boundary conditions are as follows (Zienkiewicz et al., 1999);

$$\text{For the solid phase: } -\Gamma = \Gamma_i U \Gamma_u$$

$$t = \bar{t} \quad \text{on } \Gamma_t \quad (6a)$$

$$u = \bar{u} \quad \text{on } \Gamma_u \quad (6b)$$

$$\text{For the fluid phase: } -\Gamma = \Gamma_p$$

$$p = \bar{p} \quad \text{on } \Gamma_p \quad (6c)$$

in which Γ is the prescribed boundary for solid and fluid phases. For the solid phase, \bar{t} and \bar{u} are specified surface tractions and displacements, respectively. For the fluid phase, \bar{p} is the specified pore fluid pressure.

3. FINITE ELEMENT FORMULATION

The governing Equations (4) and (5) are discretized in space by using the general procedure for finite element discretization of field vari-

ables. If complete saturation is assumed together with a linear form of the constitutive law, the set of governing equations can be reduced to the form given below in matrix notation (Paul, 1982):

$$\begin{bmatrix} M & 0 \\ -\hat{M} & 0 \end{bmatrix} \begin{Bmatrix} \ddot{\bar{u}} \\ \ddot{\bar{p}} \end{Bmatrix} + \begin{bmatrix} C & 0 \\ L^T & S \end{bmatrix} \begin{Bmatrix} \dot{\bar{u}} \\ \dot{\bar{p}} \end{Bmatrix} + \begin{bmatrix} K & -L \\ 0 & H \end{bmatrix} \begin{Bmatrix} \bar{u} \\ \bar{p} \end{Bmatrix} - \begin{Bmatrix} f_s \\ f_f \end{Bmatrix} = \begin{Bmatrix} 0 \\ 0 \end{Bmatrix} \quad (7)$$

where

$$M = \int_{\Omega} (N^u)^T \rho N^u d\Omega \quad (8)$$

$$K = \int_{\Omega} B^T DB d\Omega \quad (9)$$

$$S = \int_{\Omega} N^p \frac{1}{Q} N^p d\Omega \quad (10)$$

$$H = \int_{\Omega} (\nabla N^p)^T k \nabla N^p d\Omega \quad (11)$$

$$\hat{M} = \int_{\Omega} (N^p)^T \nabla^T (k \rho_f N^u) d\Omega \quad (12)$$

$$L = \int_{\Omega} B^T m N^p d\Omega \quad (13)$$

$$f_s = \int_{\Omega} (N^u)^T \rho b d\Omega + \int_{\Gamma_t} (N^u)^T \bar{t} d\Gamma \quad (14)$$

$$f_f = - \int_{\Omega} (N^p)^T \nabla^T (k \rho_f b) d\Omega + \int_{\Gamma_w} (N^p)^T \bar{q} d\Gamma \quad (15)$$

in which N^u and N^p represent appropriate shape functions which are used in the finite element method. K , M and C are the stiffness, mass and damping matrices for the solid phase, respectively. For the fluid phase, H and S are the permeability and compressibility matrices, respectively.

The coupling matrices L and M involve only interface integrals in which interpolation functions from either fields contribute. Vectors f_s and f_f include all prescribed loading terms and natural conditions. The constant Q in Equation (10) denotes the storage due to compressibility of the solid grains and fluid and it is defined as:

$$\frac{1}{Q} = \frac{n}{K_f} + \frac{\alpha_c - n}{K_s} \quad (16)$$

$$\text{and } \alpha_c = 1 - \frac{K_T}{K_s} \quad (17)$$

in which K_T is the bulk modulus associated with drained material. For most soils, $K_s \gg K_T$ and the value of α_c is close to unity.

4. SOLUTION ALGORITHM FOR THE COUPLED GOVERNING EQUATIONS

To complete the numerical solution, it is necessary to integrate the differential Equation (7) in time. For the problem under consideration where the two fields (solid skeleton and pore fluid) have different structures and properties, time integration of the governing equations can be best carried out using field partitioning (Zienkiewicz and Shiomi, 1984). The coefficient matrices in the coupled discretized equilibrium equations are non-symmetric. For such a case, the ‘‘staggered’’ solution procedure is most suitable in which the relevant equations are solved sequentially using previously extrapolated variables as follows:

1. The discretized equation for the solid skeleton is solved for the displacement increments using extrapolated values of (p) , and
2. The discretized equation for the pore pressure response is solved using predicted values of the displacement changes.

In the partition solution scheme, each set of the equations is solved separately. Considering two field problems, the system is divided into two, namely, (s) and (f) fields. The set of the differential equations, Equation (7), after spatial discretization can be expressed as (Paul, 1982):

$$M_s \ddot{u} + C_s \dot{u} + K_s u = f_s + f_{cs} \quad (18)$$

$$S_f \dot{p} + H_f p = f_f + f_{cf}$$

where

f_{cs} is the coupling force vector for the solid skeleton = Lp

f_{cf} is the coupling force vector for the pore fluid phase = $-L^T \dot{u} + \hat{M}\ddot{u}$

Here, the pore fluid and the solid skeleton are treated as separate fields coupled together through the contact boundaries. The two single field software analyzers are coupled through the coupling terms presented in the final discretized equation for the coupled fields.

In the adopted solution procedure for the problem of pore fluid-soil skeleton coupling, the incremental iterative equations for each field are linked together using the staggered field partition with the Newmark's predictor-corrector solution scheme

5. ELASTO-VISCOPLASTIC MODEL FOR CONCRETE

The behavior of concrete is complicated and any mathematical model simulating concrete material behavior must employ drastic idealizations. Physical evidence needs to be incorporated in the development of a realistic material model for concrete. This would include stiffness degradation during progressive cracking process, energy dissipation during load cycling and post-failure behavior, i.e. strain softening.

Although experimental data on dynamic behavior of concrete are rather scarce, and almost limited for multiaxial stress states, some features specific to dynamic behavior can be observed. Phenomena such as strain-rate sensitivity and progressive degradation of strength should be included in a material model intended to be used for transient analysis (Cervera et al., 1988).

Many material models based on plasticity theory are developed to represent concrete behavior such as linear elastic-plastic, nonlinear elastic, elasto-plastic, elasto-viscoplastic and the bounding surface models. It is well-known that any numerical model for concrete intended for transient analysis should be rate and history dependent. For transient dynamic analysis, an elasto-viscoplastic model presents a very good approximation for the behavior of a structural material with limited ductility, such as concrete.

In this research, the elasto-viscoplastic model proposed by Bic'anic' and Zienkiewicz (1983) is adopted to model the concrete behavior. This model, which includes strain-rate sensitivity and progressive degradation of strength, is implemented in the developed program to predict the transient response of the problems encountered in this work.

This model has two main differences when compared with the classical elasto-viscoplastic models (Cervera et al., 1988):

- i. *the fluidity parameter (γ) is not constant, and it is assumed to be dependent on the elastic strain rate.*

A sufficiently general expression for viscoplastic strain rate is given by the power law:

$$\dot{\epsilon}_{vp} = \gamma \left\langle \left(\frac{F}{\sigma_o} \right)^n \right\rangle \frac{\partial Q}{\partial \sigma} \quad (19)$$

in which

- Q = Q (σ, ϵ_{vp}, k) is the plastic potential,
- γ = fluidity parameter which can be dependent on some state variables such as time, total strain invariants etc, and
- F = positive monotonic increasing function
- σ_o = uniaxial yield stress

The fluidity parameter is related to the elastic strain rate through an exponential function of an effective elastic strain rate:

$$\gamma(\dot{\epsilon}_e) = a_o (\dot{\epsilon}_e^{eff})^{a_1} \quad (20)$$

where (a_o and a_1) are parameters which must be determined experimentally.

- ii. *a variable strength limit surface is introduced to monitor the damage caused by visco-plastic flow. If the stress point reaches the strength limit surface, then the degradation of the yield surface is initiated.*

During inelastic straining, both surfaces (F_o), the yield surface, and (F_f), the strength limit surface, change depending on the amount of accumulated damage, expressed as the viscoplastic energy density (W_p).

$$F_o(\sigma, \sigma_o(W_p, \kappa)) = 0$$

$$F_f(\sigma, \sigma_f(W_p)) = 0$$

where:

- $\sigma_o(W_p, \kappa)$: defines the change of the yield stress level in uniaxial compression,
- $\sigma_f(W_p)$: defines the change of the failure stress level in uniaxial compression σ_f ,
- WP: is the viscoplastic energy density

In this model, an exponential function will be used to describe the post-failure behavior. Therefore the function $\sigma_o(W_p, k)$ is defined by the expression:

$$\sigma_o(W_p, \kappa) = \alpha_1 f'_c \quad W_p \leq W_p^f$$

$$\sigma_o(W_p, \kappa) = \alpha_1 f'_c \exp(-\alpha_c \kappa) \quad W_p > W_p^f$$

where

- α_1 : defines the limit for elastic behavior,
- α_c : models the degradation after failure,
- f'_c : is the elastic limit strength of concrete,
- κ : is the viscoplastic work density in the softening range

The failure stress will be assumed to be a linear function of the viscoplastic energy density W_p^f , and the function $\sigma_f(W_p)$ is defined by the expression:

$$\sigma_f(W_p) = \beta_o f'_c (1 - \beta_1 W_p)$$

$$0 < W_p < W_p^f$$

The parameters (β_o and β_1) are determined from experiments and ($\beta_o f'_c$) is the compressive strength obtained with infinite load rates.

6. VERIFICATION

Based on the procedure presented above, a computer code has been developed for the analysis of the interaction of concrete structures and footings with two-phase saturated soils. It is a finite element computer program for the linear and nonlinear dynamic, two-dimensional plane and axisymmetric analyses. In this program, both one-phase (i.e. dry) and two-phase (i.e. saturated) soils are considered. Also, the transient response of a structural system in two-dimensional problems can be evaluated.

In the following, problems typical of soil-structure interaction are analyzed to investigate the nonlinear transient interaction of different concrete structures with saturated two-phase soils.

6.1. Concrete block subjected to vertical and horizontal impact pressures

Estorff (1991) and later Kim and Yun (2000) have analyzed the problem shown in Figure (1) of an elastic concrete block supported on a layered dry (one-phase) halfspace when subjected to impact pressure.

The transient load function shown in this figure consists of a rectangular impulse over a duration of ($5\Delta t$) is applied on the top of the

block either in vertical or in horizontal direction, in which Δt is 0.0008 sec. The vertical displacement at point (A) on the block is computed for the vertical load case, while the horizontal displacement at point (A) is computed for the horizontal load case.

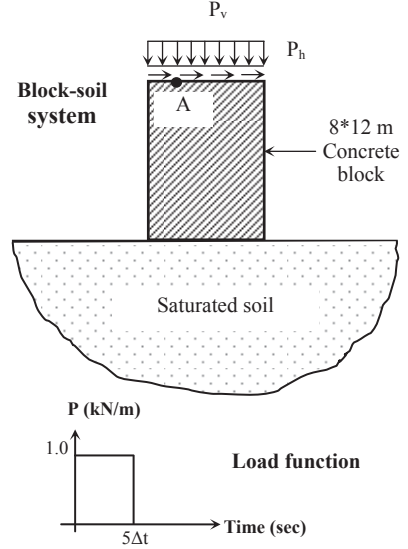


Figure 1. Concrete block-soil system and the loading function

In the present work, the dynamic behavior of the same block on saturated (two-phase) soil is studied. Furthermore, concrete material nonlinearity is included in the analysis. For finite element idealization, a rigid bedrock located away from the soil surface and an artificial lateral side boundaries are chosen to approximate the unbounded soil medium by a finite model. The rigid bedrock location is selected so that the ratio $h/b=20$, in which (h) is the depth of the soil stratum and (b) is half width of the block, to assure that the bedrock and the artificial side boundaries effect on the block response is minimal (Japon et al., 1997).

Results for the response of the block-soil system are shown in Figure (2) through (5). The response-time histories shown in these figures are plotted against the dimensionless time ($t_o = tv_s / b$), in which (v_s) is the shear wave velocity in the soil medium and (b) is the half width of the block base.

Figure (2) shows a comparison of the vertical displacement-time histories at point (A) for

the case of the dry and saturated soil media (uncoupled and coupled analyses). Also, excess pore pressure variation at 10m and 40m depth in the soil stratum due to vertical impact pressure is shown. This figure shows that coupled field analysis yields smaller values for the block response as would be expected since coupling increases the soil stiffness and the response of the coupled system is reduced. Figure (3) shows the same comparison made in Figure (2), but for the transient response due to a horizontal impact pressure. The same conclusion can be drawn for the coupled analysis response when compared with the uncoupled analysis.

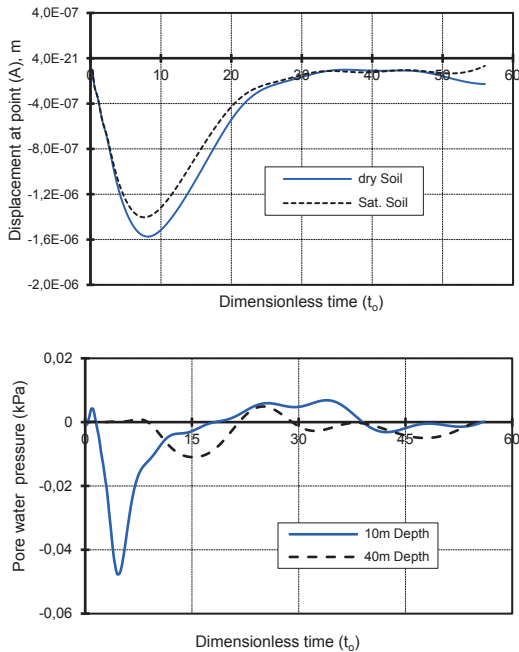


Figure 2. Transient response for the concrete block-soil system due to vertical impact pressure

Figure (4) shows the vertical and horizontal velocity-time histories at point (A) due to vertical and horizontal impact pressures. It is clear from this figures that the vertical velocity response is more rapidly damped out by the system when compared with the horizontal response component.

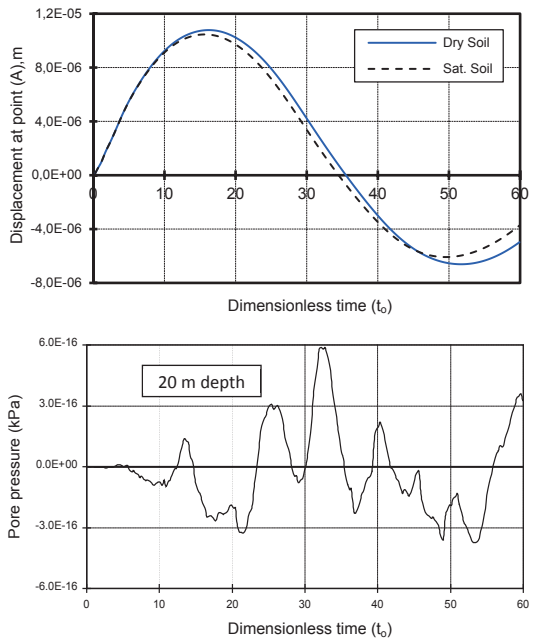


Figure 3. Transient response for the concrete block-soil system due to horizontal impact pressure

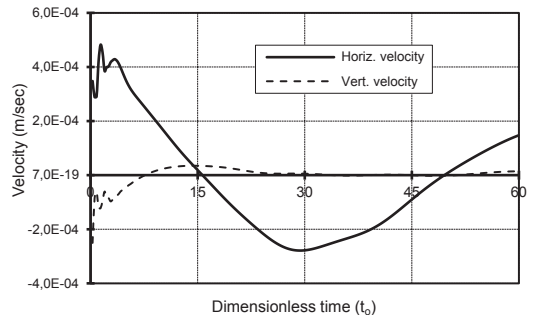


Figure 4. Velocity-time histories at point (A) due to vertical and horizontal impact pressures

Figure (5) shows the horizontal displacement and velocity-time histories at point (A) due to horizontal impact pressure when concrete plasticity is considered in the analysis. The comparison with the elastic block response reveals that the block response is decreased and the time period of the vibration is elongated when concrete plasticity is included. Cracking of concrete affects the stiffness of the structure, thus changing its fundamental period. Moreover, the transient block response greatly depends on its natural frequency, therefore the block response is changed due to cracking.

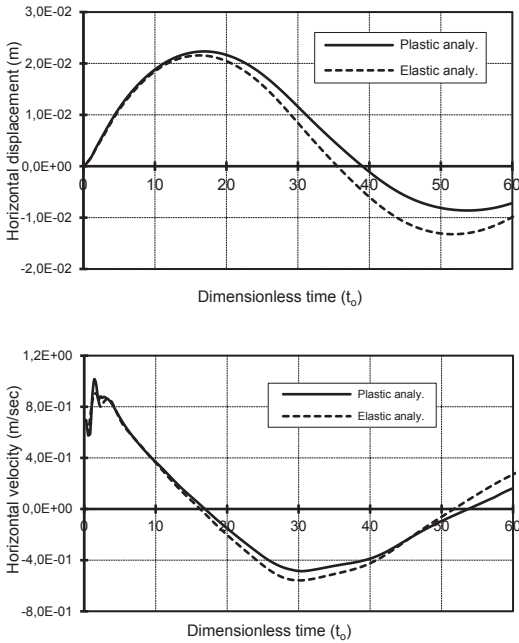


Figure 5. Nonlinear transient response at point (A) for the concrete block-saturated soil system

6.2. Concrete Tunnel Subjected to Transient Traffic Loads

Estorff (1991) and later Kim and Yun (2000) have analyzed the problem shown in Figure (6) of an elastic concrete tunnel embedded into a dry (one-phase) halfspace soil medium when subjected to transient traffic load.

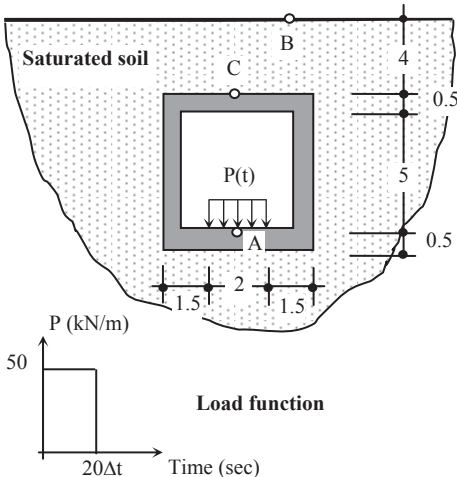


Figure 6. Concrete tunnel-soil system and the loading function

The dimensions of the rectangular concrete tunnel structure shown in Figure (6) are taken as $2b = 5\text{m}$, $h = 6\text{m}$ and the embedment depth is 4.0m . The transient traffic load of 50 kN/m^2 is idealized as a rectangular impulse pressure over time period of $(20\Delta t)$ and the time step is taken $\Delta t = 0.001\text{ sec}$.

In the present work, the dynamic behavior of the concrete tunnel embedded into saturated (two-phase) soil is studied. Furthermore, concrete material nonlinearity is included in the analysis. The founding soil medium is represented by a saturated soil stratum supported on rigid bedrock. For the finite element idealization, lateral side boundaries are artificially chosen away from the tunnel to minimize the “Box” effect due to wave reflections back into the model, also reflections are assumed to be sufficiently damped by material damping (Christian and Hall, 1982).

The tunnel lining and the soil skeleton is discretized by means of isoparametric plane strain elements, whereas the pore water in the saturated soil is idealized by isoparametric elements. Free drainage is permitted at the top soil surface. Also, impermeable boundaries are assumed along the interface between the tunnel lining and the surrounding soil medium.

To reveal the effect of soil saturation on the dynamic interaction, results for the vertical displacement at point (A) is shown in Figure (7), while pore water pressure variation below tunnel base is shown in Figure (8) for different tunnel lining stiffnesses. The response-time histories shown in these figures are plotted against the dimensionless time ($t_0 = tv_s / b$), in which (v_s) is the shear wave velocity in the soil medium and (b) is the half width of the tunnel.

Generally, the response of the system has decreased when the pore water pressure is taken into account in the analysis, i.e., coupled analysis. Also, pore water pressure variation greatly depends on tunnel stiffness.

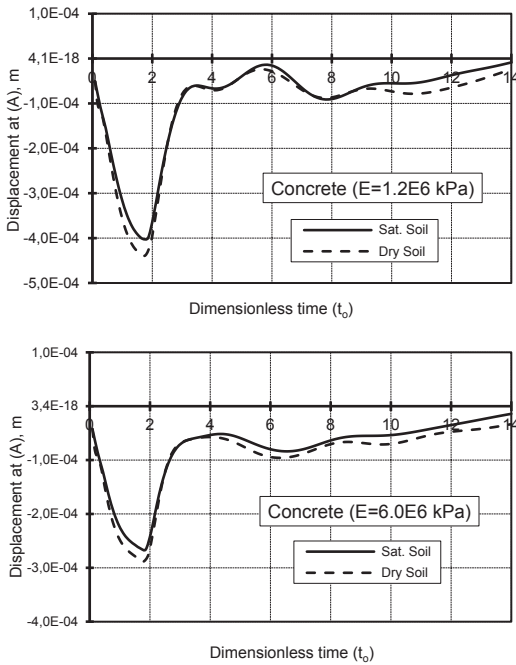


Figure 7. Transient vertical response at point (A) for the concrete tunnel-saturated soil system

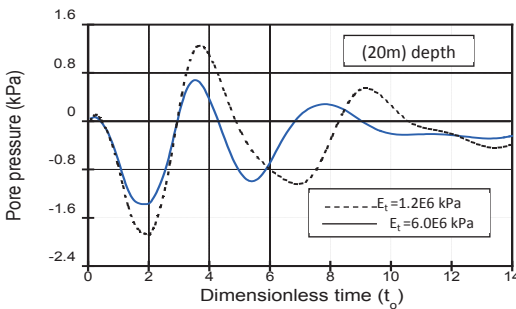


Figure 8. Pore water pressure-time history in the soil stratum at 20meter below tunnel base

To investigate material nonlinearity effect on the transient response of the tunnel, the elasto-viscoplastic model for the concrete material presented previously is implemented in the numerical analysis. Concrete with Young's modulus of 30×10^6 kPa is used in this verification.

Figure (9) depicts the vertical displacement-time history of the nonlinear concrete tunnel-soil system at point (A) when subjected to impulsive traffic loading shown in Figure (6).

Whereas, Figure (10) shows the vertical acceleration and velocity time histories at point C in the tunnel. Comparison between linear and nonlinear results for the concrete behavior is presented in these figures. The excess pore water pressure variation at different points in the soil stratum is presented in Figure (11).

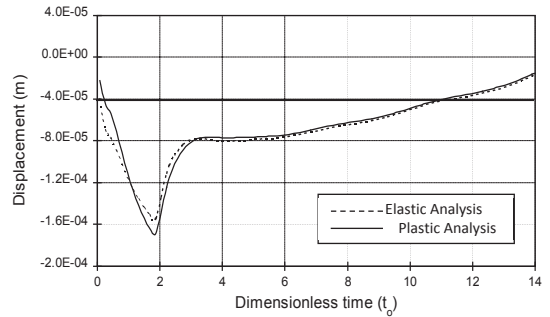


Figure 9. Nonlinear transient response at point (A) in the concrete tunnel-saturated soil system

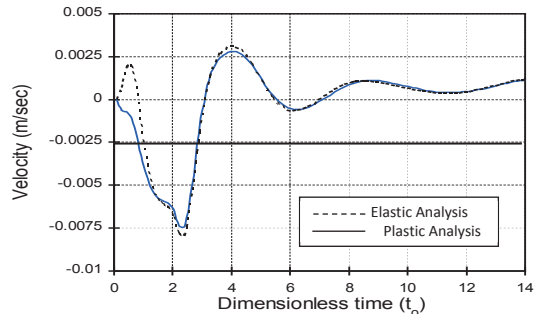
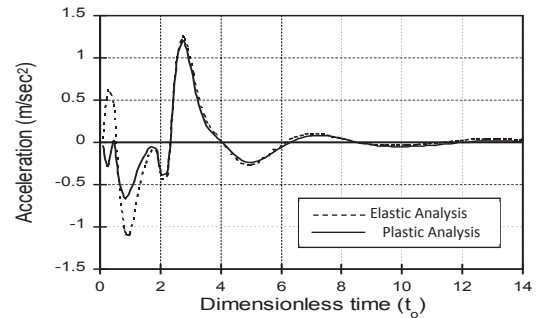


Figure 10. Vertical acceleration and velocity time histories at point (C)

It is observed that the acceleration and velocity peak values are reduced when concrete viscoplastic behavior is accounted for in the analysis. At the same time, Figure (11) shows that pore water pressure in the soil stratum is

increased due to concrete nonlinearity. This behavior is expected, since cracking of concrete reduces tunnel stiffness, and thus, changing the response of the tunnel and the soil. This conclusion is confirmed by the response characteristics observed in Figures (7) and (8) when tunnel lining stiffness is reduced.

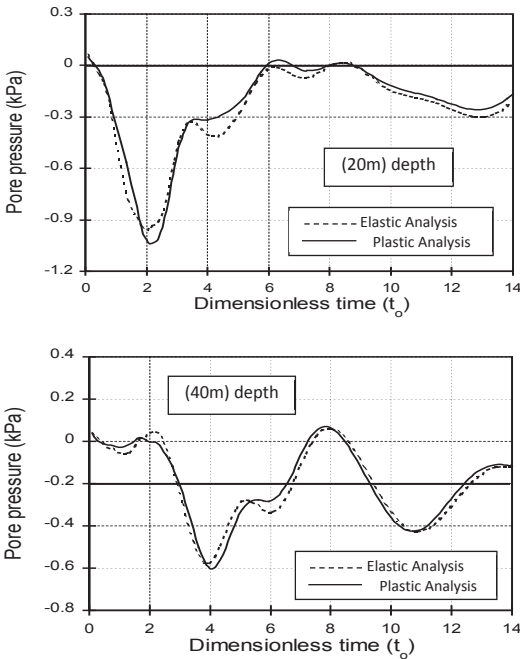


Figure 11. Transient pore water variation at different points in the saturated soil medium

6.3. A Concrete Gravity Dam Subjected to an Earthquake Base Excitation

In this application, the earthquake response of a concrete dam is studied and demonstrated with special emphasis on the two-phase behavior of the saturated soil medium on the dam-soil foundation interaction.

The geometry of the dam and the water reservoir are shown in Figure (12). The water and dam crest levels are taken to be 81.45m and 107.0m above the foundation level, respectively. The depth of the foundation layer is assumed to be 50.0 m below the dam base.

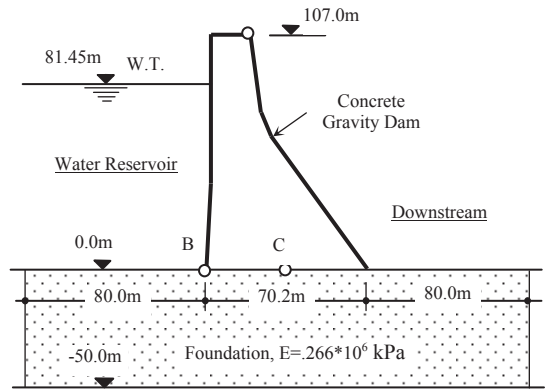


Figure 12. Geometry of the Concrete Gravity Dam

The gravity dam shown in Figure (12) was studied by Owen and Hinton (1980) when subjected to the sinseweep earthquake base excitation. The sinesweep analytic earthquake accelerogram with a maximum acceleration of (0.33g), which is equivalent to El-Centro N-S accelerogram, is shown in Figure (13).

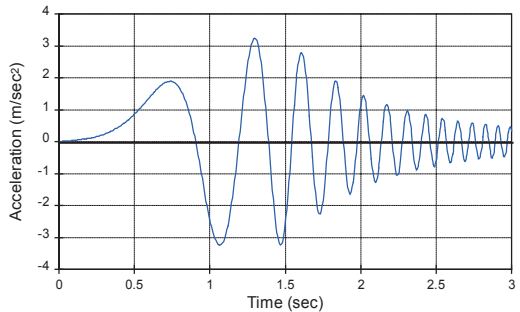


Figure 13. Johnson-Epstein sinesweep earthquake accelerogram

For finite element idealization, both the gravity dam and the foundation are modeled by two-dimensional plane strain elements, whereas the pore water in the foundation layer is represented by isoparametric elements. The model base is assumed to be impermeable, whereas side boundaries are represented by horizontal rollers free to move horizontally to allow for lateral movements during earthquake excitations. Water flow across side boundaries is prevented and only vertical water drainage is allowed. The influence of the reservoir water on the dynamic behavior of the dam is considered by taking into account the mass of the water

attached to upstream face of the dam. The simple representation of "added mass" with concentrated masses is used.

For the dam-foundation system shown in Figure (13), response time histories for the transient horizontal and vertical displacements at the dam crest level (point A) are shown in Figure (14). Response for both cases of saturated and dry foundation media are presented in this figure.

Figure (15) shows the transient response time histories for the vertical acceleration at point (A). Acceleration response curves are presented for both cases of saturated and dry foundations. Excess pore water pressure variation time-history at mid dam base level is presented in Figure (16).

Comparison presented in Figures (14) and (15) reveals that dam response and the accelerations of the two-phase (saturated) model are substantially lower than those of the single-phase (dry) model. This behavior is the result of the higher damping introduced in the system by the pore fluid-soil skeleton interaction.

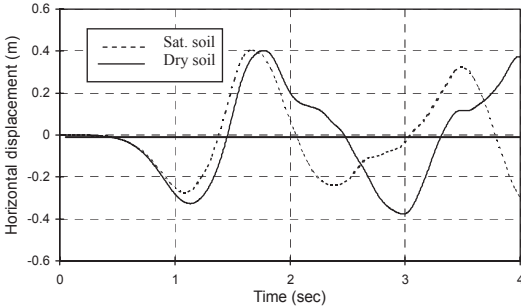


Figure 14. Horizontal and vertical displacement time histories at the dam crest level (point A)

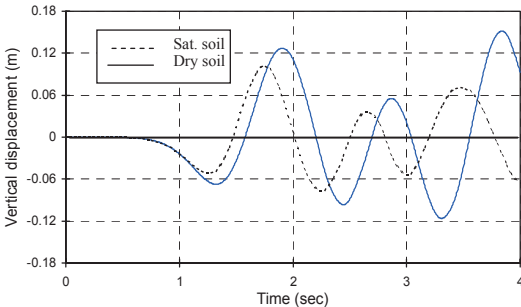


Figure 14. Continued

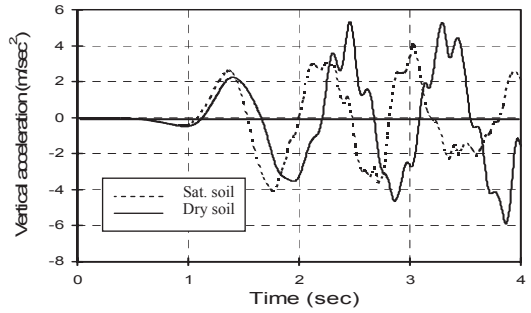


Figure 15. Vertical acceleration time histories at the dam crest level (point A)

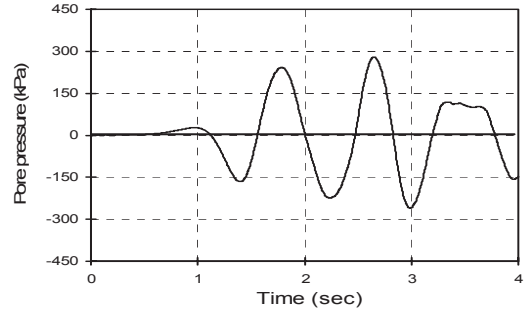


Figure 16. Excess pore water pressure variation time history at dam mid base level

Figure (17) depicts the nonlinear transient displacement response of the dam-soil system at points A and B. The results presented in this figure show that the response of the dam-saturated soil system is decreased and the period of vibration is elongated when concrete nonlinearity is introduced in the coupled analysis. The response of the dam-soil system to a seismic excitation is greatly dependent on the dynamic characteristics of the structure, especially the natural frequencies. Therefore, a change in the natural frequency due to concrete cracking results in a different amount of energy being transferred to the system, and in this case, this change reduces the amplitude of the response.

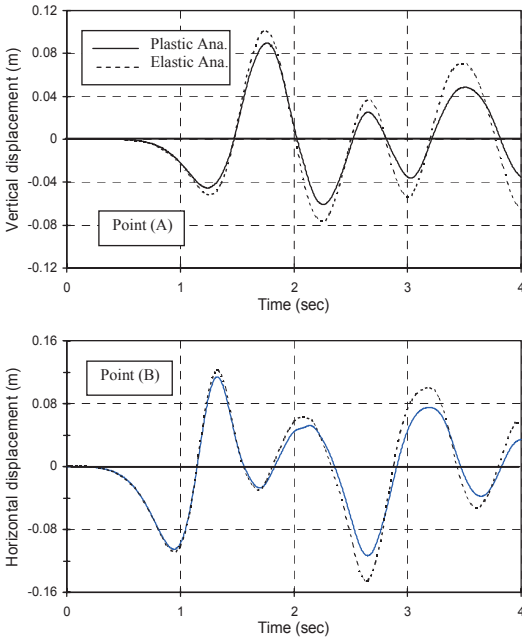


Figure 17. Nonlinear displacement time histories at the dam crest level (point A) and at base (point B)

Figure (18) depicts the nonlinear horizontal and vertical velocities at the dam base level (point B). Whereas, comparison of the excess pore water pressure response for the linear and nonlinear analysis is presented in Figure (19) for points at dam mid base level (point C) and at bed rock level (point D) in the soil stratum

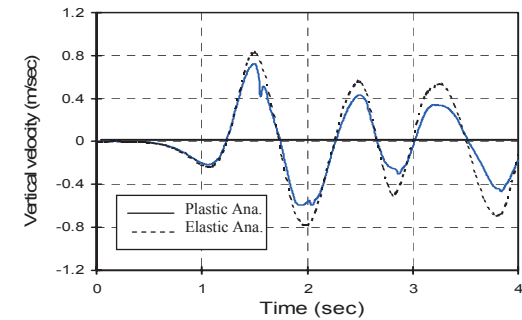


Figure 18. Nonlinear velocity time histories at the dam base level (point B)

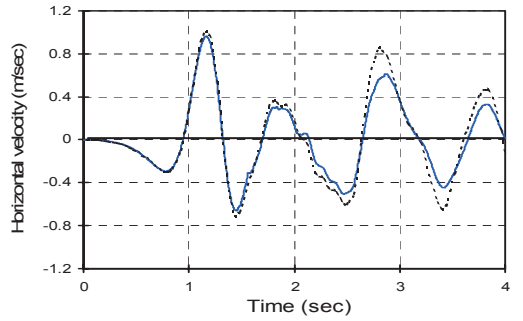


Figure 18. Continued

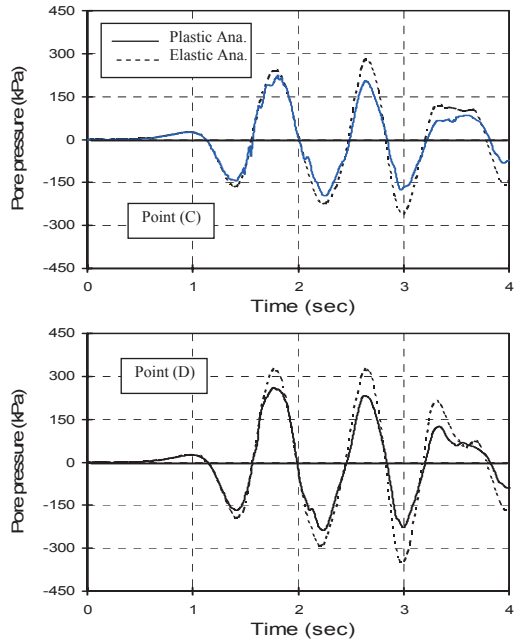


Figure 19. Nonlinear pore water pressure variation at different points in the foundation stratum

7. CONCLUSIONS

The dynamic response of concrete structures interacting with saturated soils is investigated. The saturated soil is viewed as a two-phase porous medium in which the approximate mixed (u-p) formulation is used to simulate the coupling between the soil skeleton and pore water and to predict the transient behavior of the concrete structures and the supporting saturated foundation.

Based on the adopted staggered field partitioning solution scheme, a finite element code is developed for the interaction analysis between structures and saturated soils. The efficiency of the developed program is demonstrated by solving various problems.

The results demonstrated that pore fluid-solid skeleton coupling greatly affects the dynamic response of concrete structures when supported by saturated foundation as compared with dry foundation medium. There is a maximum reduction of about 30% in the structural responses, when the soil two-phase behavior is accounted for in the analysis. Also, results demonstrated that the excess pore water pressure is reduced when structural stiffness is increased. Concrete material nonlinearity affects the dynamic response of the structures and the foundation medium in terms of acceleration, velocity and displacements.

Generally, time periods of vibration are shortened and damping is increased for structures interacting with saturated soils.

REFERENCES

- Bazant, Z. & Krizek, R. 1975. Saturated sand as an inelastic two-phase medium. *Journal of the Engineering Mechanics Division*, ASCE, Vol. 101, No. 4, pp. 317-332.
- Bic'anic', N. and Zienkiewicz, O.C. 1983. Constitutive model for concrete under dynamic loading. *Journal of Earthquake Engineering and Structural Dynamics*, Vol. 11, pp. 689-710.
- Biot, M. 1956. Theory of propagation of elastic waves in a fluid saturated porous solid. *Journal of the Acoustical Society of America*, Vol. 28, No. 2, pp. 168-191.
- Biot, M. 1962. Mechanics of deformation and acoustic propagation in porous media. *Journal of the Acoustical Society of America*, Vol. 34, No. 4, pp. 1482-1498.
- Cervera, M., Hinton, E., Bonet, J. and Bic'anic', N. 1988. Nonlinear transient dynamic analysis of three-dimensional structures: a finite element program for steel and reinforced concrete", Chapter 7 in "Numerical Methods and Software for Dynamic Analysis of Plates and Shells", Edited by E. Hinton, Pineridge Press, U.K.
- Christian, J.T. and Hall. J.R. 1982. Soil-structure interaction problems. *Proceeding of the Fourth International Conference on Numerical Methods in Geomechanics*, Edmonton-Canada.
- Estorff O. 1991. Dynamic response of elastic blocks by time domain BEM and FEM. *Computers and Structures*, Vol. 38, No. 3, pp. 289-300.
- Ghaboussi, J. & Wilson, E. 1972. Variational formulation of dynamics of fluid-saturated porous elastic solids. *Journal of the Engineering Mechanics Division*, ASCE, Vol. 98, No. 4, pp. 947-963.
- Japon, B., Gallego, R. & Dominguez, J. 1997. Dynamic stiffness of foundations on saturated poroelastic soils. *Journal of the Engineering Mechanics*, ASCE, Vol. 123, No. 11, pp. 1121-1129.
- Kim, K. & Yun, C. 2000. Time-domain soil-structure interaction analysis in two-dimensional medium based on analytical frequency-dependent infinite elements. *International Journal for Numerical Methods in Engineering*, Vol. 47, pp. 1241-1261.
- Owen, D. and Hinton, E. 1980. Finite Elements in Plasticity: Theory and Practice, *Pineridge Press*, Swansea, U.K.
- Paul, D. 1982. Efficient dynamic solutions for single and coupled multiple field problems. Ph.D. Thesis, *University College*, Swansea.
- Prevost, J. 1982. Nonlinear transient phenomena in saturated porous media. *Journal of Computer Methods in Applied Mechanics and Engineering*, Vol. 20, pp. 3-18.
- Zienkiewicz, O. & Bettess, P. 1982. Soils and other saturated media under transient dynamic conditions; General formulation and the validity of various simplifying assumptions. Chapter 1 in "Soil Mechanics-Transient and Cyclic Loads", Edited by G.N. Pande and O.C. Zienkiewicz, pp. 1-16.
- Zienkiewicz, O., Chang, C. & Bettess, P. 1980. Drained, undrained, consolidating and dynamic behavior assumptions in soils. *Geotechnique*, Vol. 30, No. 4, pp. 385-395.
- Zienkiewicz, O., Chan, A., Pastor, M., Schrefler, B. & Shiomi, T. 1999. Computational Geomechanics with Special Reference to Earthquake Engineering. *John Wiley and Sons Ltd*.
- Zienkiewicz, O. & Shiomi, T. 1984. Dynamic behavior of saturated porous media; the generalized Biot formulation and its numerical solution. *International Journal for Numerical and Analytical Methods in Geomechanics*, vol. 8, pp. 71-96.

Revisiting a Full Raft Foundation Constructed on Soft Clay

I.V. Anirudhan

Consultant, Geotechnical Solutions, Chennai, anirudhen@eth.net

S.V. Ramaswamy

Retd Professor, Anna University, Chennai, prof.svramaswamy@gmail.com

ABSTRACT: A two storey institution building in south Madras, India, was constructed over a full raft foundation below which 7.5m thick soft clay existed. One year later an extension of same length supported on piles resting on weathered rock was added. Shortly after this construction, a differential settlement of 32mm was noticed. Time settlement record for a period of about five years was collected and concluded that a significant part of primary consolidation had occurred. The observed settlement was 135mm. The building on raft continued to settle and recorded little more than 450mm settlement apart from 100mm tilt in the next 25 years. This paper compares the estimated and observed time settlement data. The time-settlement did not follow conventional primary consolidation pattern. Possibility of undrained creep and plastic flow is reviewed.

1. INTRODUCTION

It is generally accepted that a well designed raft foundation with the rigidity provided by the structure supported by it can tolerate large settlements provided the angular distortions are within the limits. The literature also provides numerous examples of satisfactory (at least structurally) performance of full raft foundation supporting RCC frames and other type of superstructure in spite of very large settlements.

The relevant Indian Code of Practice for Design and Construction of Foundations in Soils: General Requirements (third revision) (1986), in its Table 1 permits 125mm total settlement for a raft foundation resting in plastic clay and supporting RC or steel framed construction. It also recommends a limiting differential settlement and corresponding angular distortion. There is no stipulation to the permissible tilt of a full raft foundation.

The rigidity of full raft foundation system with respect to the supporting ground has significant influence on the contact pressure distribution below the full raft. When the soil is very weak, the relative rigidity of foundation tends to increase leading to large contact stress in the vicinity of raft edges. It is possible that the rigid foundation is considered flexible due to an overestimation of soil modulus, and the

possibility of large contact stress along the edges is overlooked. Where the soil is highly plastic soft clay, beyond a certain limiting stress, plastic flow may begin. Plastic flow below the foundation edges may not be considered if the rigid behaviour of the full raft foundation is overlooked.

Poor performance of spread footing resulted tilting of an overhead water tank, and hence it was decided to adopt full raft foundation for the two storied institution building. This construction over a subsoil stratum of 7.50m thick soft clay was completed in 1979. The construction of an extension of the same building that was taken up during the next year was however supported on pile foundation, since the building on raft foundation started settling immediately after construction.

Just after the construction of this extension supported on piles founded on weathered igneous rock, relative movement of the portion supported by full raft foundation became noticeable. The settlement recorded for a period of about five years thereafter was 135mm. The settlement observations were made assuming that the portion supported by the pile foundation did not experience any settlement. There is no any time settlement record for a period of about one and half years after the construction of full raft. A study in 1985 (Kumaradev, 1986)

concluded that a significant amount of primary consolidation settlement was complete and roughly 120mm more settlement on account of remaining primary consolidation and the secondary compression could be expected. Absence of any sign of structural distress in the structure led to the conclusion that the foundation was safe and sound even after allowing for the remaining settlement.

However, the full raft foundation continued to settle and recorded little over 450mm settlement in 2009 (differential with respect to the portion on pile foundation). A tilt of 100mm to 120mm was also noticed making a total settlement of about 570mm in the opposite side. Even though there was no structural damage in any part of the structures except minor damage to the parapet wall, the excessive settlement, and more importantly, the tilt were of concern. Attempt is made in this paper to trace back the possible performance during the initial stages based on a fresh settlement analysis using additional geotechnical data obtained for the study. There is a lack of full-fledged data on structural as well as geotechnical details of the raft foundation system and also on the time settlement record in the very initial stages just after the completion of the structure. Most of the data for this present analysis was obtained from 1985 study (Kumaradev, 1986).

The present review suggests that there could have been certain amount of undrained creep / visco-plastic deformation of soft clay during the first few years. The stress levels in the soft plastic clay are favourable for such yielding. The problem is more acute towards south east corner where the soil was always wet and marshy leading to tilt towards this direction. Part of this study was presented by Anirudhan and Ramaswamy (2012).

2. SOIL PROFILE AND FOUNDATION

The subsoil comprised a thin layer of desiccated clay crust followed by about 7.50m thick soft to very soft high plasticity silty clay. The weak stratum is immediately followed by highly weathered charnockite rock.

Stiffened raft system with average effective raft thickness of roughly 500mm was used as foundation. The full raft with beams, columns and the supported frame of three floors is rigid

and the relative rigidity of the foundation is very significant. The building is 21.60m long and 12.70m wide and the construction was completed in the beginning of 1979. The sub-soil profile proper of the building location is presented in Figure 1. The foundation system is schematically presented in Figure 2.

1.0	Stiff sandy clay	
1.2	Greyish soft silty clay	Data collected for the present study
2.0	SPT N = 2 to 3 NMC= 51% to 62.5%	Compression Ratio CR = 0.255 Recompression Ratio RR = 0.025 Preconsolidation Pressure = 55 to 65kPa
3.0	LL = 64% to 68% PI=43% to 44%	Coefficient of consolidation c_v up to 100kPa is 0.68 m ² /year
4.0	LI = 0.68 to 0.80 c_u = 12 to 15 kPa	
5.0	Greyish soft silty clay	Compression Ratio CR = 0.300 Recompression Ratio RR = 0.030 Preconsolidation Pressure = 50kPa
6.0	SPT N = zero NMC= 51% to 62.5%	Coefficient of consolidation c_v up to 100kPa is 0.68 m ² /year
7.0	LL = 85% to 100% PI=55% to 68%	
8.0	LI = 0.80 to 0.90 c_u = 9 to 10 kPa	
9.0	Details same as top soft clay layer	Details same as top soft clay layer
9.6		
10.0	Completely weathered disintegrated rock, SPT N >100	
11.0		

Figure 1. Sub-soil Conditions at the Building Location (Kumaradev, 1986) and Additional Data during Present Study

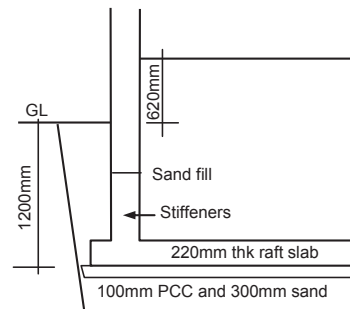


Figure 2. Foundation Adopted for the Building (Kumaradev, 1986)

3. TIME SETTLEMENT RECORDS

The 21.60m long extension to this structure was supported by bored cast in-situ piles founded in weathered rock. This construction on piles was completed in the middle of 1980. Soon after the completion of the extended portion on the piles,

relative settlement was noticed between the structure on raft foundation and that on the piles. The first settlement recording of the raft foundation was made on 15-10-1980, presumably with respect to a zero reference established on 4-9-1980 (Kumaradev, 1986). The observed settlement during this very short period of 41 days was 32mm. The next observation was made on 3-7-1981, 261 days after the previous observation and the observed additional settlement was only 11mm. Time settlement observations were made till 23-06-1985 and summary of such observation is given in Table 1 and a graphical representation is made in Figure 3. These observations were made on the assumption that the pile foundation is not moving after its initial settlements during the construction.

Table 1 Time Settlement Records (Kumaradev,1986)

Date	Cum time			Observed Sett mm
	Days	Years	Weeks	
04-09-1980	458*	1.25	64.53	0
15-10-1980	499	1.37	70.31	32
03-07-1981	760	2.08	107.08	43
19-02-1982	991	2.72	139.63	53
03-12-1982	1278	3.50	180.07	75
27-05-1983	1453	3.98	204.73	95
30-06-1985	2218	6.08	312.52	135

*Assuming that the construction was completed in January 1979 and full occupancy by June 1979 (Kumaradev, 1986).

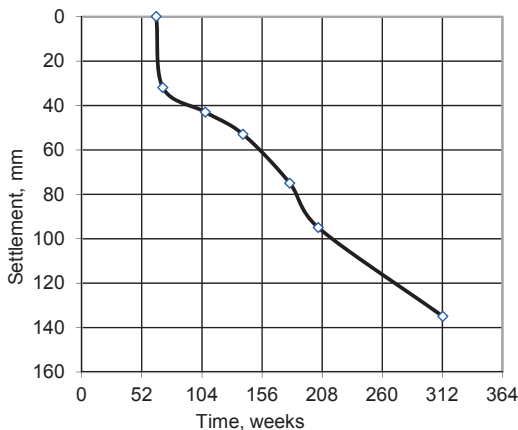


Figure 3. Time Settlement Plot

The differential settlement between the buildings as observed on 23-6-1985 is shown in Figure 4. The sunshades at the top levels of the building are roughly 100mm thick and the offset between these sunshades is very close to the finally observed settlement of 135mm. It was gathered that the sunshades of both the structures were cast at the same level and later observed that they were moving apart that triggered serious settlement observations.

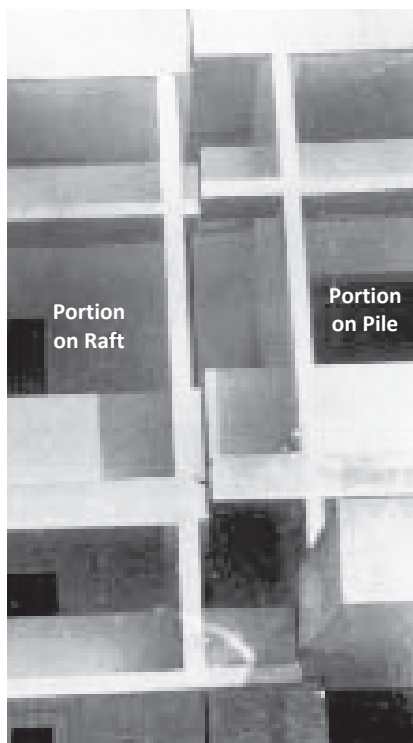


Figure 4. Differential Settlement between Raft Foundation and Pile Foundation, 30-06-1985 (Kumaradev, 1987)

There is no time - settlement record of the full raft during the first 1.50years. Even though the records states that the zero reference was made on 04-09-1980, it is surprising that the settlement recorded was 32mm in just 41 days in spite of the structure being in use for more than one and half years. It is also noticed that the measured rate of settlement for a period of next four years is increasing. The rate of settlement between different observations is shown in Table 2.

Table 2 Rate of Settlement during the First 6 Years

Time, months		Settlement, mm		Rate of settlement mm/ m
Total	Incr.	Total	Incr.	
16.41	1.35*	32	32	23.74
24.99	8.58	43	11	1.28
32.58	7.59	53	10	1.32
42.02	9.44	75	22	2.33
47.77	5.75	95	20	3.48
72.92	25.15	135	40	1.59

*with respect to date of start of observation.

4. REQUIREMENT OF FURTHER STUDY

The 1985 study estimated a total consolidation settlement of about 290mm for the raft foundation. These estimations were made using the laboratory oedometer test results and also using the results of screw plate tests conducted in the field. Study estimated that roughly 40mm settlement could have occurred before the start of the observation and adding this settlement, the total of about 175mm as observed in 1985 was on expected lines. The study concluded that another 120mm could be expected during the next 20 years suggesting a total of 295mm.

The 1985 study, however, did not give any particular importance to sudden increase in the settlement at a rate of 23.7mm per month during the start of observations (after a gap of roughly one and half years after construction) and also to the increased rate of settlement for more than three and half years thereafter.

The foundation however continued to settle and the amount of relative settlement between the raft foundation and the structure on piles as on 23-12-2009 was little over 450mm as shown in Figure 5.

Acknowledging the fact that there were no records of the settlement occurred during the first one and half years, the actual settlement should have been more than 500mm. The photograph presented in Figure 6 was taken on 3 December 2012 and practically there is no further relative settlement between the structures during these three years. The top parapet wall was repaired in the recent past. The settlement towards opposite side of the building (rear side) is more and both the photographs show a tilt towards rear side. The settlement in the rear side could be about 520mm (more than 600 including the unobserved settlement). Actual settlement records in the rear side are not available with the authors.

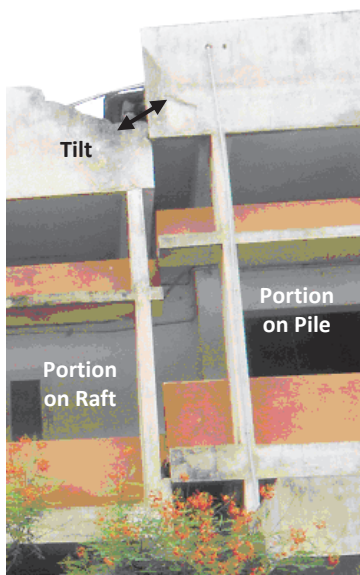


Figure 5. Differential Settlement as on 23-12-2009

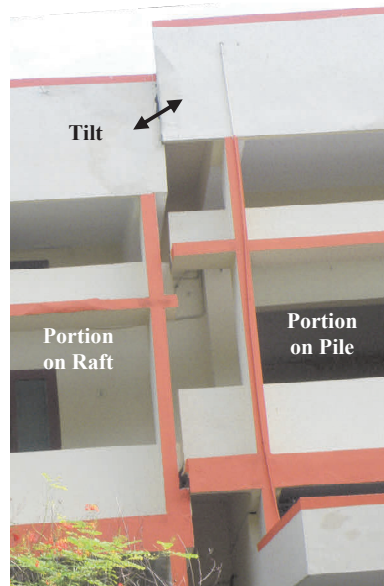


Figure 6. Differential Settlement as on 03-12-2012

Roughly 225mm additional settlement to the foundation caused worries with regard to the safety of the structure even though there were no signs of major structural defects except breaking of the parapet wall at the terrace level. About 120mm tilt towards rear side and close to the portion on piles was also of concern. There was a need for closer study of the performance.

5. ADDITIONAL INVESTIGATION AND SETTLEMENT ESTIMATION

The subsoil comprises three soft clay layers, the top and bottom ones being marginally stiffer. The middle layer between 4.0m and 7.0m is highly plastic and softer. Three numbers of one dimensional consolidation tests (incremental loading method, IL) conducted on undisturbed samples from the top clay layer recorded average coefficient of consolidation c_v equal to 0.68 $m^2/year$ corresponding to the stress level 80kPa to 100kPa. Both square root time and log time procedures were used to arrive at this average value. The sample collected from deeper level at 4.0m was infested with mica flakes and shells and the results from this one dimensional consolidation tests were not very consistent. Relatively low coefficient of consolidation is determined from this test. The compression ratio is also relatively high. The top layers recorded compression ratio CR $[=c_v/(1+e_0)]$ is 0.24 to 0.27. Based on the quality of test results and the nature of soft clay present here, the compressibility and consolidation parameters were judiciously selected for further analysis.

The maximum pre-consolidation pressure for the clay is in the range of 50kPa to 70 kPa. The field curve fitting suggested by Schmertmann is used for estimating the pre-consolidation pressure. The clay is 'under-consolidated' at some levels when the average ground water table is at about 1.50m below the ground level. However, considering the present c_v values and the age of the deposit, the clay below 3.0m is taken as normally consolidated under the present average effective overburden. The clay above 3.0m is very marginally desiccated or has attained certain amount of quasi pre-consolidation (Bjerrum, 1967).

The average load intensity on the raft level including that of the additional fill to reach the plinth level is estimated as 46 kPa. The actual

average load intensity during the service period is expected to range between 40kPa and 50kPa. The estimated settlement of 21.6m x 12.7m full raft with 46kPa is 345mm, out of which more than 95% is consolidation settlement. The estimated settlements under 40kPa and 50kPa are 302mm and 372mm respectively. The soil layers were subdivided into 1.00m to 1.50m thick layers and conventional one dimensional consolidation solutions recommended by Terzaghi is used for the estimation. The stress distribution below the raft is derived from Boussinesque's solution and the effect of rigidity of raft on the soil structure interaction is accounted by approximating the evened out settlement as 80% of that of the settlement estimated at centre. The time required for 90% consolidation is estimated as 18 years that is also close to that was reported in the 1985 study. It is thus expected that roughly 310mm (total) settlement could have been realised by the year 1997.

The 1985 study estimated 290mm total settlement. These two estimations can be said comparable as the 1985 assessment was made with an average load intensity of 400kPa. The average load intensity at the foundation level assumed in the estimations is considered to be very reasonable. Ladd and DeGroot (2003) recommends constant rate of strain, CRS, testing procedure for better evaluation of compression ratio CR when the soil is very soft producing an 'S' shape strain-log p curve. The CR obtained by CRS procedure is 30 to 80% more than that obtained by conventional IL procedure. However, here the soil has produced typical strain-log p curves, the field curve correction suggested by Schmertmann is expected to provide reasonably accurate results. The field curve fitting procedure produces roughly 30% larger CR than that is estimated by conventional curve fitting procedure. Moreover, both the independent studies produced comparable results. Hence, there is no need to revisit the compression and consolidation parameters. The reasons for more than 200mm excess settlement lie elsewhere.

6. TIME SETTLEMENT PREDICTION

The presence of 300mm thick sand layer fill that connects to the side filling and the com-

pletely weathered rock formation below the clay layer offered two-way drainage and sinusoidal pore water pressure variation is assumed in the analysis. The time factors T_v corresponding to each settlement observation date are accordingly estimated. Probable degree of consolidation and the amount of theoretical consolidation settlement corresponding to each of these observation date are worked out and compared it with the actual settlement observed. The summary of such estimation is presented in Table 3.

Table 3 Time – Consolidation Estimations

Date	Cum time		Obs. Sett mm	T_v
	Days	Years		
04-09-1980	458*	1.25	-	0.060
15-10-1980	499	1.37	32	0.065
03-07-1981	760	2.08	43	0.099
19-02-1982	991	2.72	53	0.129
03-12-1982	1278	3.50	75	0.166
27-05-1983	1453	3.98	95	0.189
30-06-1985	2218	6.08	135	0.289
04-04-1997	6513	17.9	-	0.847
23-12-2009	11160	30.58	450	1.5062

Date	U%	Exp. Sett, mm	Def. in Sett., mm
04-09-1980		95.0	-95.0
15-10-1980	0.275	99.2	-67.2
03-07-1981	0.287	122.4	-79.4
19-02-1982	0.355	139.8	-86.8
03-12-1982	0.405	158.7	-83.7
27-05-1983	0.460	169.1	-74.1
30-06-1985	0.490	207.7	-72.7
04-04-1997	0.602	310.4	(90%)
23-12-2009	0.960	337.0	+113.0

The last column of Table 3 is the amount deficient in the observed settlement if one considers that the observed settlement was from consolidation. The average deficiency is 80mm. Thus, if, for a moment, one assumes that the recorded settlements were due to primary consolidation, there is this 80mm un-noticed consolidation settlement during the first one and half years.

7. FURTHER REVIEW OF SETTLEMENT RECORDS

Asaoka (1978) proposed an ultimate settlement prediction method by using settlement monitoring data and curve fitting. In this procedure, the settlement records redefined with equal time intervals are used to make a plot between the settlement corresponding to time t_n and the settlement corresponding to the just previous observation at time t_{n-1} . The straight line plot thus prepared will converge to 45degree line and the settlement at this merging point is considered as the ultimate settlement. The advantage with this plotting procedure is that the observation can be from any point of time. The time settlement record of about 4 years was redefined at equal time interval and the Asaoka plot thus created is shown in Figure 7. The observed plot is found diverging from the 45degree line even though the settlement observations were made under reasonably uniform loading. This performance is in tune with the increasing rate of settlement described in Table 2.

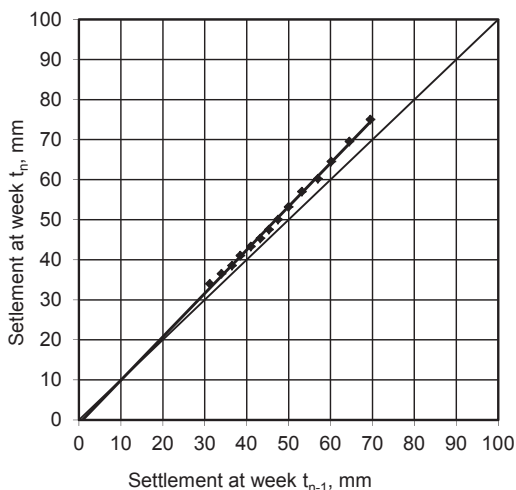


Figure 7. Asaoka Plot of Time Settlement during Initial Stages

There is also the very large, but unexplained, rate of settlement in the initial stage of observation that started one and half year after the construction. The observed time

settlement during the first 3.5 years does not appear as consolidation settlement. Interestingly, the last part of the observed time settlement data, more specifically after 3.5 years from construction, suggests consolidation process when represented by Asaoka plot (Figure 8).

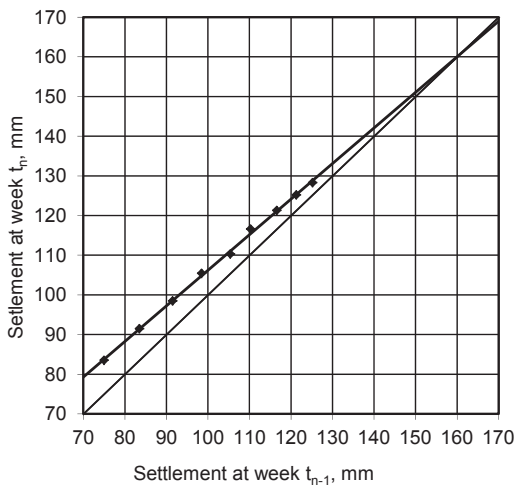


Figure 8. Asaoka Plot of Time Settlement during Final Stages of 5 Year Observation

8. HYPOTHESIS 1 - PURE CONSOLIDATION CASE

When the time settlement records are reviewed again considering about 80mm consolidation settlement during the first one and half year period without any observation, the time settlement plot may look like the curve C in Figure 9. This curve is plotted adding roughly 80mm settlement that was estimated ‘unobserved’ during the first one and half years.

The curve B is the actual time settlement record that was started after a gap of one and half year from the completion of construction. The curve A in Figure 9 is the time settlement plot theoretically estimated using one dimensional consolidation solutions (Table 3).

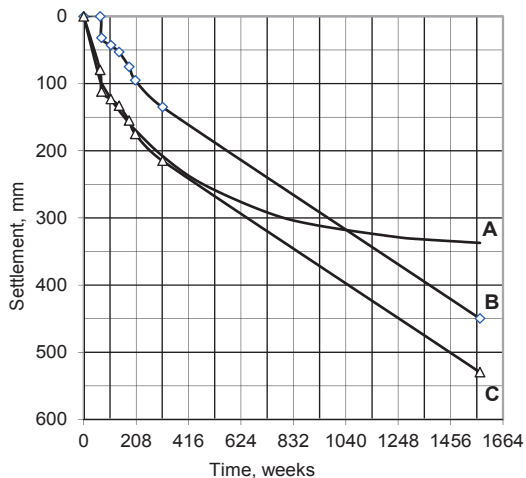


Figure 9. Observed and Predicted Time Settlement Plots

The increasing rate of settlement in the initial stages is not very prominent here when plotted for a very large elapsed time. It is interesting to note the time - settlement pattern closely following the theoretically estimated time-settlement plot. However, it significantly deviates from the theoretical estimations after about 350 weeks (about 7 years). The excess settlement that recorded after 1560 weeks (30 years) is about 200mm. There is also another 100mm to 120mm settlement towards the tilted corner.

The average rate of secondary compression ratio estimated for a stress level of 80 to 100 kPa from log time plots is about 8×10^{-3} , i.e. roughly 0.03 times the compression ratio. The secondary compression of 7.50m thick clay during 18 years to 30 years is estimated as about 15mm. When the ‘unobserved’ settlement of 80mm is added to 450mm settlement observed in 2009, the total settlement including the secondary compression shall be 530mm. The estimated total settlement including secondary compression is 360mm and there is roughly 170mm settlement in excess of possible consolidation settlement.

Skepton AW and Bjerrum L (1957) showcase time settlement records of three buildings on normally consolidated Chicago clay. All these time settlement plots follow the typical consolidation settlement pattern very similar to the curve A in Figure 9. Skempton (1957) acknowledges that the time settlement estimation from the theory of one dimensional

consolidation have shown tolerable agreement with the observations. It is hence difficult to explain the non-asymptotic progression of the observed settlement (curves B and C in Figure 9) for a foundation in normally consolidated clay. Any plastic deformation after such significant consolidation is possible only when there is drastic increase in the load intensity, which was not the case here. Deformations in soft clay such as immediate settlement, visco plastic deformation / undrained creep, plastic yield, etc. are more likely to happen when the soil is relatively virgin than after undergoing consolidation settlement over a significant period. Degradation in the undrained modulus after plastic yield is also possible.

9. HYPOTHESIS 2 – UNDRAINED CREEP / PLASTIC YIELD

The increasing rate of settlement in the initial four to five years (Table 2) suggests that there could have been deformation other than consolidation settlement during this period. Immediate settlement in the soft clay and sand layer are not considered here as these components are expected to happen during the construction stage. Other deformations in soft plastic clays are prolonged undrained creep which is a time dependent phenomena and plastic flow arising out of high stress increments. It will be interesting to compare the observed rate of settlement with the predicted average rate of settlement presented in Table 4.

Table 4. Comparison of Predicted and Observed Time – Settlement Rate

Time, months		Rate of settlement - observed	Rate of Settlement- Predicted
Total	Incr.	mm/ month	mm/ month
0	0		0
15.06	12.03		7.90
16.41	1.35	23.74	3.09
24.99	8.58	1.28	2.71
32.58	7.59	1.32	2.29
42.02	9.44	2.33	2.00
47.77	5.75	3.48	1.82
72.92	25.15	1.59	1.54

Even though there is a sudden drop in the rate of settlement after about 2 months of observation, the rate is increasing for the next three and half years. However, this observed rate is only half of that predicted for the corresponding period at least in the beginning. This erratic settlement pattern is sufficient to suggest that the settlement observed in the first four to five years is predominantly undrained and the actual consolidation started towards the end of 1985 study. This hypothesis is presented in Figure 10. Unfortunately, there is no record of time settlement data during 1985-2009 period to give justification to this hypothesis. It is also debatable that such undrained creep and visco plastic deformation may put the consolidation process completely in abeyance.

Notwithstanding these limitations, this is the most likely scenario especially when the stress levels in the soft plastic clay are far exceeding the elastic limits.

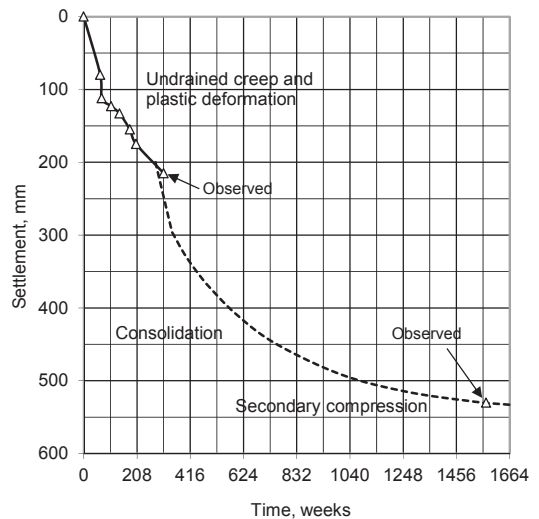


Figure 10. Hypothetical Creep and Consolidation in Time Scale

9.1 Plastic Yield

The conditions are favourable for undrained creep and other plastic deformations. Normally, when the stress levels in the soft clay are not exceeding 33% (FS=3) to 40% (FS=2.5) of the ultimate bearing capacity, large creep and plastic yield can not take place. It is established

by Ladd and Lambe (1964) that the modulus E at stress levels corresponding to factor of safety 1.5 is less than half of the E at stress levels corresponding to Factor of safety 3. There is a strong possibility that very large undrained shear strain will occur when the factor of safety is less than 1.5. Table 5 illustrates the stress levels at different depths below the raft foundation under study.

Table 5 Factor of Safety against Yield in Each Layer

Depth, m		c_u	$6.2 c_u$	Δp	Ratio $6.2c_u/\Delta p$
From	to	kPa	kPa	kPa	
1.60	2.00	14.8	91.6	45.3	2.02
2.00	3.00	14.8	91.6	45.1	2.03
3.00	3.60	12.8	79.4	44.6	<u>1.78</u>
3.60	4.00	10.8	67.2	44.1	<u>1.52</u>
4.00	5.00	8.9	55.0	43.0	<u>1.28</u>
5.00	6.00	8.9	55.0	41.0	<u>1.34</u>
6.00	7.00	8.9	55.0	38.5	<u>1.43</u>
7.00	8.00	14.8	91.6	35.8	2.56
8.00	9.00	17.7	109.9	33.1	3.32

It is evident that plastic yield had occurred between 3.60m and 7.00m depths since the stress levels are sufficiently large to initiate plastic yield.

9.2 Visco Plastic Deformation

Even though a detailed study on visco plastic deformation requires more data for analyzing a suitable model, a very rough review of possible visco-plastic deformation is made by comparing the stress ratio in the field and the critical stress ratio. The effective angle of friction ϕ' for this soft clay is reported as 20° (Robinson, 2012) and could be marginally smaller for the highly plastic clay. The stress ratio q/p' (David, 1990) at different soil layers along the depth is worked out as 0.86 at the top and 0.44 at the deepest level (Table 6). This estimation is made attributing soil structure interaction and certain increase in the contact stress along the periphery. However, a further increase of 20% in the contact stress will produce stress ratio of the order of 0.90 to 0.48. The critical stress ratio can be taken as $\phi'/25$, and the limiting stress ratio in the present case is 0.80. Hence the top

2.0m thick clay below the raft is likely to undergo visco-plastic deformation.

Table 6 Estimation of Stress Ratio, $k_0=1-\sin\phi$,
 $\sigma_3=k.p_0', \sigma_1=p_0'+\Delta p$

Depth from GL, m		p_0'	$p_0'+\Delta p$	q	p'	q/p'
From	to	kPa	kPa	kPa	kPa	Ratio
1.60	2.00	19.8	65.1	30.6	33.4	0.91
2.00	3.00	25.0	70.1	31.3	37.3	0.84
3.00	3.60	30.9	75.5	32.0	41.7	0.77
3.60	4.00	34.5	78.6	32.3	44.3	0.73
4.00	5.00	39.5	82.5	32.6	47.7	0.68
5.00	6.00	46.5	87.4	32.5	52.3	0.62
6.00	7.00	53.4	91.9	32.2	56.6	0.57
7.00	8.00	60.3	96.2	31.8	60.9	0.52
8.00	9.00	67.6	100.6	31.4	65.4	0.48

9.3 Undrained Creep

The time dependent shear deformation is usually referred as deviatoric creep or shear creep. Mitchell (1968) suggests the following expression for creep deformation.

$$\frac{d\varepsilon}{dt} = Ae^{\alpha D} \left(\frac{t_1}{t} \right)^m \quad (1)$$

where A and m are material constants, α and D are functions of stress, geometry, thickness of the creeping material, etc, t is time at which creep starts and t_1 is the time under consideration. This equation is obtained mainly based on creep during undrained triaxial shear tests on saturated clays and secondary consolidation during drained tests. The time dependent creep deformation $\varepsilon(t)$ can be expressed as,

$$\varepsilon(t) = ct^n \quad (2)$$

where c and n are material constants. Creep deformation $\varepsilon(t)$ can be expressed in terms of creep compliance $D(t)$ and applied stress σ as,

$$\varepsilon(t) = D(t)\sigma \quad (3)$$

where $D(t)$ is shear creep compliance and σ is the stress increment.

No change in stress distribution will occur under time independent loading. Hence the visco-elastic problem can be converted to a

quasi-elastic problem by replacing the elastic constants by time dependent moduli (Ramaswamy and Vaidyanathan, 1977). Hence the solution to the visco elastic problem can be obtained by replacing E with D(t) in the solution to the elastic problem.

With an assumption that the entire settlement observed during the first three and half years is from undrained creep, initially the material constant 'n' is determined. Using the 'n' thus determined the parameter K is determined. Time is measured from the start of observation and not from the start of loading.

$$32\text{mm} = K \times (0.1125\text{yrs})^n$$

$$\text{Log}(32) = \text{Log } K + n \text{Log } (0.112)$$

$$75\text{mm} = K \times (2.246 \text{ yrs})^n$$

$$\text{Log}(75) = \text{Log } K + n \text{Log } (2.246)$$

n' is determined as 0.28446 by curve shifting.

Substituting this 'n' in one of the equations, K is determined as 59.575

Using the 'n' and 'K' thus determined, the creep that was not measured during the first one and half years is estimated. Where y_0 is the creep before start of observation,

$$32 + y_0 = 59.575 (1.3675\text{yrs})^{0.28446} = 65.122 \text{ mm}$$

$$75 + y_0 = 59.575 (3.50\text{yrs})^{0.28446} = 85.09 \text{ mm}$$

y_0 is determined as 33.1mm and 10.1mm respectively, whereas both should have been same.

By trial and error, the 'n' and K are determined so that the both the y_0 are equal. The final 'n' and 'K' are 0.59974 and 47.05 respectively.

The material constant 'n' is in the normal range of saturated clayey deposits, the parameter K is found to be relatively large for the expected range of undrained modulus. The undrained creep is calculated by substituting the modulus E by 1/D(t) where D(t) is $(1/E_u)(t)^n$ in the idealized strain influence procedure suggested by Schmertmann for settlement under rigid foundation (Tomlinson, 2008). Two range of undrained modulus is used in the estimation viz $E=250c_u$ and $E=500c_u$ (Ladd, 1964). The results of these estimations

along with the creep estimated using the 'n' and K earlier determined are presented in Figure 11.

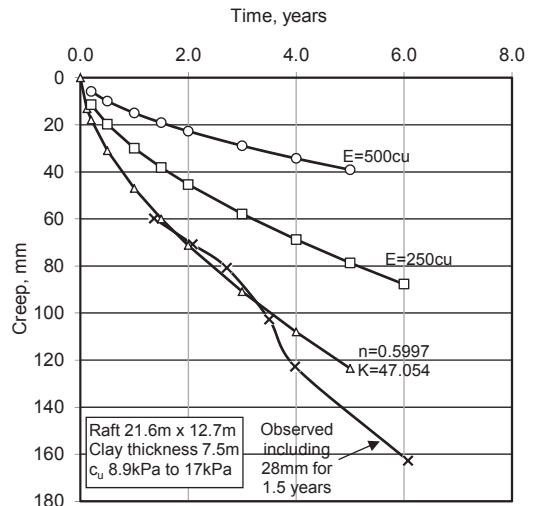


Figure 11 Estimated Undrained Creep

The actual modulus under the present stress levels could be between 250cu and 500cu and the creep of 7.50m thick clay during three and half to four years may be of the order of 40mm, whereas the total settlement observed is more than 90mm. The undrained creep is about 40% to 50% more than the secondary creep according to studies by Bolton (2012). This will quantify the undrained creep as about 30mm. The K determined from the estimation by strain influence procedure is about 22 (corresponding to the units considered). This K is only half of the value determined assuming that the estimated settlement is entirely due to undrained creep.

Considering the possible range of undrained creep as 30mm to 40mm that could have happened during the initial stages after loading, there is a significant amount of plastic yield experienced by the soft to very soft clay below the founding level.

10. TILT TOWARDS REAR SIDE AND PRESENT STATUS OF THE STRUCTURE

The rear side of the building has a varying ground profile. The overburden towards the far end of the structure is more or less equal to that

present in the front side, while the ground is low lying towards the portion on pile foundation. Even though the ground very close to the structure is only marginally lower from that in the front side, it dips down rapidly to roughly 1.20m. This area collects rainwater and remains marshy during most of the period.

A deficiency of 15kPa in the effective overburden pressure due to lower ground level and high ground water table, increases the stress ratio to 1.23 immediately below the raft and 0.80 at 3.00m below the raft level significantly increasing the possibility of visco plastic deformation. Reduction in the effective overburden pressure within the very soft clay between 3.0m and 6.0m makes this clay more prone to plastic yield as the incremental load is with factor of safety 1.20 to 1.40. The building tilted towards this side even though the thickness of clay layer is reasonably uniform.

The actual tilt of the structure towards rear side is not measured and not available for the review. It is assumed from the present position of the structure that the total settlement towards the rear could be 100mm to 150mm more than that in the front side as deduced from the photograph presented in Figure 6.

The observed final settlement in the front side is little over 450mm. Roughly 80mm settlement observed during the first three years and certain amount of 'unnoticed settlement' for some months after the construction are possibly due to undrained creep (estimated as 40mm) and partly due to plastic deformation of the soft clay immediately below the raft. Out of the remaining observed settlement of 370mm, the primary consolidation component is estimated as 345mm. The secondary compression (drained creep) may account for 15mm to 20mm as the structure is in place for a period more than thirty years.

On the other hand, the soft clay under the rear side of the building is expected to have experienced more plastic deformation due to less overburden, especially whenever the ground water table was high, causing the tilt.

11. CONCLUSIONS

Time settlement record available for a two storey institutional building constructed in the late seventies and freshly obtained one dimen-

sional consolidation test results are used to study the behavior of the full raft foundation resting in soft clay. The differential settlement between piled structure and the structure on raft did not increase during December 2009 to December 2012.

Significant increase in the rate of settlement during the first five year settlement observations suggests that the observed settlement is not attributable to primary consolidation. The unnoticed settlement during the initial months of no observation and about 80mm settlement recorded in the first three years may be attributed to undrained creep and plastic deformation. The primary consolidation starts after three to three and half years and accounts for roughly 340mm settlement in the next 15 years or so. The remaining 20mm to 30mm settlement is attributable to secondary compression (drained creep).

It may be possible that the idealized strain influence procedure for settlement by Schmermann can be used for estimating the undrained creep. The modulus E in the procedure may be replaced by $1/D(t)$ where $D(t)$ is $(1/E_v)(t)^n$. The 'n' is a material constant that can be determined by any suitable creep tests.

The rear side of the building has relatively less overburden and the land is marshy during most of the period. The possibility of visco plastic deformation in the soft clay here is much more and the excess settlement and tilt observed towards this side can be explained.

The ratio between ultimate bearing capacity and the incremental load at different levels is 1.28 to 2.02, much below a desirable value of 3.00 that would ensure against plastic deformation.

Design of full raft foundation resting on soft plastic clay cannot be treated as simple consolidation settlement problem. The increase in contact stress levels due to large difference in the stiffness of soil and the foundation is of utmost importance.

12. REFERENCES

- Anirudhan I.V. and Ramaswamy S.V. (2012), 'Performance of Full Raft Foundation Constructed on Clay', *Proceedings Fourth International Seminar on Forensic Geotechnical Engi-*

- neering, Bangalore, India, Ed. Dr. GL Sivakumar Babu, Dr. V.V.S. Rao, Dr. M.R. Madhav
- Asaoka, A. (1978), 'Observational Procedure of settlement Prediction', *Soil and Foundations, Japanese Society of Soil Mechanics and Foundation Engineering*, Vol 18, No: 4, 87-101
- Bjerrum, L (1967), 'Engineering Geology of Norwegian normally consolidated marine clays as related to settlements of buildings', 7th Rankine Lecture, *Geotechnique* 17(2), 81-118
- Bolton M.D. (2012), 'Performance-based design in geotechnical engineering', 52nd Rankine Lecture, Institution of Civil Engineers, London.
- Bureau of Indian Standards (1986): IS 1904, Indian Standard Code of Practice for *Design and Construction of Foundations in Soils: General Requirements* (Third Revision), Table 1
- David M.W. (1990), *Soil Behaviour and Critical State Soil Mechanics*, Digital re-print, 2009, Cambridge University Press, 420-422.
- Kumardev, V. (1986), Settlement Analysis of Two Storied Building Founded on Soft Clay Deposit, *M.E. Thesis*, Anna University, Chennai.
- Ladd C.C. (1964), 'Stress-Strain Modulus of Clay in Undrained Shear', *Journal of the Soil Mechanics and Foundations Division*, Proceedings of ASCE, September, 1964, 127-156
- Ladd C.C. and DeGroot Don J (2003), 'Recommended Practice for Soft Ground Characterisation: Arthur Casagrande Lecture', 12th Panamerican Conference on Soil Mechanics and Geotechnical Engineering, MIT, Cambridge.
- Ramaswamy, S.V. and Vaidyanathan, R. (1977), 'Settlement of Footings on Compacted Clays,' *International Symposium on Soil Structure Interaction*, Roorkee, India, January 1977.
- Robinson R.G. (2012), Unpublished data on soft clay in the region.
- Singh, A. and Mitchell, J.K. (1968), 'General Stress, Strain Time Function for Soils,' *Journal of Soil Mechanics and Foundations Division*, ASCE, Vol. 94, No. SM1, 21-46
- Skempton A.W. and Bjerrum L (1957), 'A Contribution to the Settlement Analysis of Foundations on Clay', *Geotechnique* (7) 168-178
- Tomlinson, M.J. and Woodward J. (2008), *Pile Design and Construction Practice*, Fifth ed. by Taylor & Francis, Sec. 5.3.2, 270.

Limit State Design for Strengthening the Foundations of St. John's Church of Tartu, Estonia Using Prestested Drilled Spiral Piles

K. Avellan

KAREG Consulting Engineers, Helsinki, Finland, kari.avellan@kareg.com

ABSTRACT: This article discusses the use of an original working method for the extensive underpinning of St. John's Church in Tartu, Estonia where a church destroyed during the Second World War had to be underpinned and wherein a line of columns had to be rebuilt. A new working and design method was developed for the project. The method focuses on the practical theory of how to design (geotechnically and structurally) a floating piled strip foundation using only one method based on ultimate limit state (ULS) and serviceability limit state (SLS). The method takes the following into account as geotechnical requirements: contact pressure, total settlement and angular distortions; and as structural requirements: admissible plastic rotations, end moments due to displacement angle, as well as control of cracking.

1. INTRODUCTION

1.1. The case of St. John's Church of Tartu

The strengthening of foundations for St. John's Church of Tartu, which originates from the 14th century, was a project of historic significance which presented many challenges. To underpin the foundations of this massive structure, original solutions had to be devised throughout the work period. The innovative piling technique developed by the author and the phases of the underpinning of St. John's church have been discussed in previous articles (Avellan & Lange 1997, Avellan & Maanas 2001, Avellan & Lange 2008, Avellan 2013).

1.2. Conditions of St. John's post WWII

In 1944 the church burned down and remained in ruins for the whole period of the Soviet occupation. Shoring was undertaken in subsequent years, and during the following decades several plans for the restoration of the church were drawn up. Some practical measures connected to the restoration of the church were already taken during the late Soviet era, including some surveying of the building done in the 1970s (Altoa 1994).

Figures 2, 3, and 4 show the state of the church before strengthening in the 1990s.

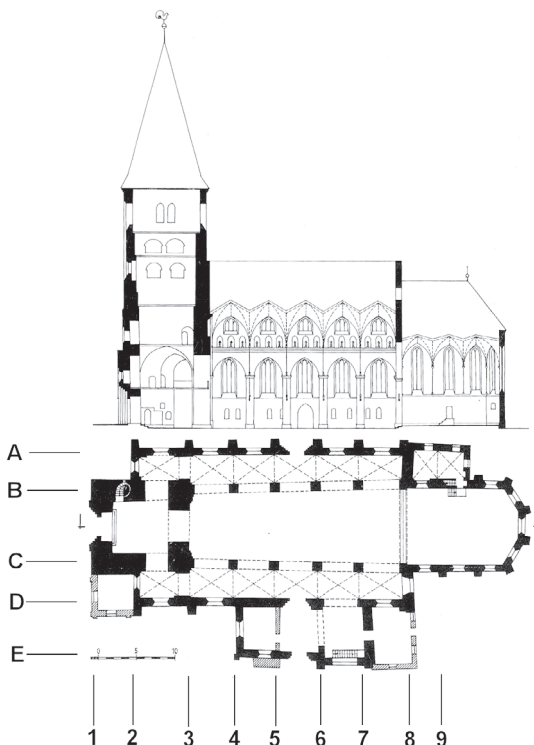
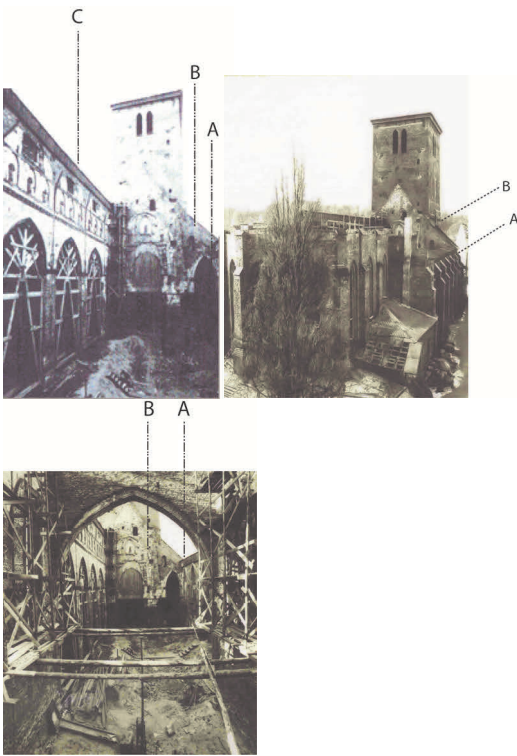


Figure 1. Plan and section of St. John's Church, pre WWII.



Figures 2, 3, 4. St. John's Church before the strengthening work. Line A is on the right side without roof. Line B had to be entirely rebuilt (see Fig. 6).

2. REASONS FOR STRENGTHENING THE FOUNDATIONS

The existing foundations of the church are on massive stones, which themselves sit on wooden rafts. The height of the stone setting is approximately 3 m. On the lowest parts of the building, situated in the south-western and south-eastern corners, the stone setting is 1.5-2 m high. On the top layer these stones are joined together with mortar, but at the lower level the joints are filled only with sand. The double wooden raft under the stone setting was made from Ø 30-40 cm wood trunks. The ground under the church consists of a variety of different soil layers. The approximate thicknesses of the soil layers under the wooden rafts are shown in Figure 5.

The consolidation process of the loose sandy silt layer has ended because of its thickness (5 m) and time-lapse (more than five hundred years). On the south side of the church, under line E, is a clay layer which is still consolidating (Fig. 6). The outside earth surface of the church

has risen in the past because of the addition of "cultural layers."

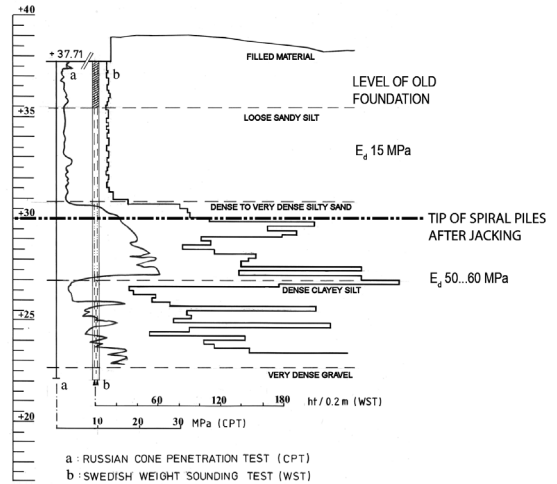


Figure 5. Russian cone penetration test (CPT) and Swedish weight sounding test (WST). Soil explorations results at sample point near the church wall.

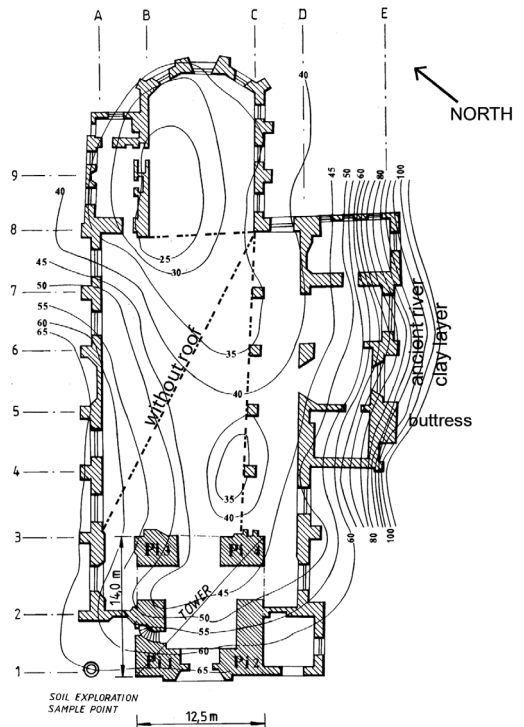


Figure 6. Contour lines of settlement (mm) in the area of the church during the years 1963-87 (Avellan & Lange 1997). Line A is on the left side without roof. Line B, where the columns were destroyed, had to be completely rebuilt.

During recent decades, the building began to sink because of the lowering of the ground water table. In the last few years before the strengthening work was started, the water level had dropped below the level of the wooden rafts. As the result, the rafts had begun to rot, thus accelerating the sinking process. The settlement map in the church area for the period from 1963 to 1987 is shown in Figure 6 as contour lines.

Work to stop the sinking of the church began by strengthening the foundations from 1993-96. The last supporting structures and concrete pours were realized in early 1996. The foundations of the choir were not underpinned since they lie on hard soil and were not considered to be in immediate need of strengthening.

3. UNDERPINNING METHODS

The foundations of the church were underpinned by piling, using jacked piles and drilled spiral piles. These pile types were employed because, in its fragile state, the building would not tolerate the vibrations of driven piles. The layer of dense to very dense silty sand starting at approximately 6 m below the old foundation level was chosen as the bearing stratum as the first 4 - 5 m layer of loose sandy silt (tufa layer) did not have enough bearing capacity. Additionally, the old block foundation could not have withstood the greater forces which would have been needed to jack piles through the compact silty sand layer.

3.1. Underpinning of the Tower

The church tower is built of brick, it's outer dimensions are 12,5 m × 14 m. The height of this part is 38 m from ground level. Previously a wooden spire rested atop the tower, giving it a total height of 60 m above ground level. The spire was destroyed during the Second World War and was later reconstructed as part of the restoration program.

At it's base, the tower is divided into four pillars, P1...P4, two of which measure 7,5m × 3m, and the others approximately 4m × 3.5m.

The foundation work was completed for each leg by joining it to a reinforced-concrete raft foundation, thus creating a partly 'floating piled raft.' This raft was realized by casting

section by section and providing bond connections with individual piles. The rationale for making the rafts part by part for each leg was to avoid dangerous cavity situations and bearing failures.

A concrete wall with thickness of 300 mm and height of 1200 mm shown in Fig. 7 was fabricated at the outer perimeter of the concrete slab. An empty space (Fig. 7) was left so as to give archaeologists and engineers a chance to study the accomplished work "in situ" in the future. All visible steel parts located in this space were painted against corrosion. The strengthening work was executed by following the anastylis principle. One principal objective of the work was to conserve the authenticity of the old structures as much as possible.

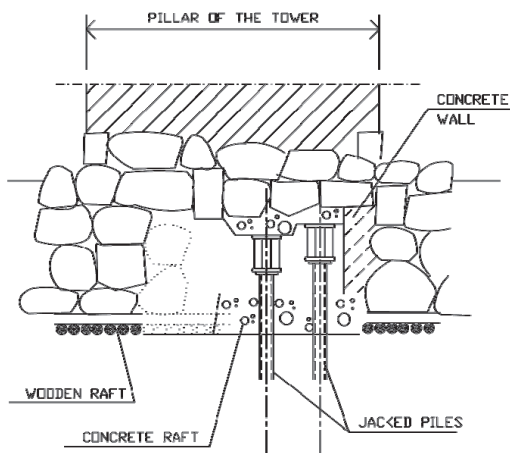


Figure 7. Empty cavity space for future observation (Avellan & Maanas 2001).

The rate of settlement and horizontal displacements, particularly those of the tower, were measured throughout the strengthening process. As a result of the construction technique, the overall settlement of the tower was only 18 to 20 mm (Fig. 8).

The settlement in other parts of the building during the strengthening work was monitored by levelling. According to the measurements, the inclination in other parts of the building was considerably less in comparison to that of the tower, as a result of continuous walls. In special places such as line A without roof, rebuilt columns in line B and columns in line C were underpinned using drilled spiral piles.

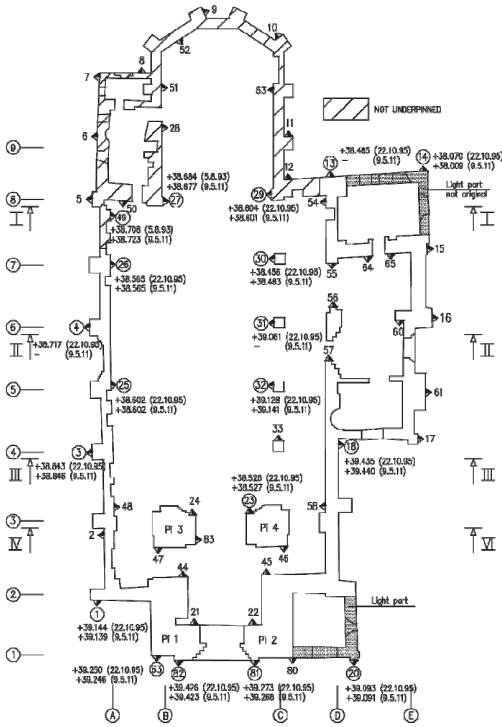


Figure 8. Settlement as a function of time in levelling points. Note: in line C, levelling in points 4 to 7 on 22.10.1995 was done prior to pretesting.



Figure 9. Simple screw driving equipment for drilled spiral piles.

Underpinnings at lines A and B were made with drilled spiral piles. The steel piles had a diameter of 218 mm and a thickness of 10 mm. The first section (1m) had a welded spiral 25 mm \times 10 mm. The spiral piles were embedded in the soil by twirling. The joints of the spiral drilled piles were made by welding the parts together and jacking them. The completed piles were filled with concrete. The total length of the piles on line A varied from 5.5 m to 6.5 m. A practical and simple technique and equipment was devised to enable the assembly of the spiral drilled piles by screwing in very limited work-spaces. All the parts of the necessary equipment could be equipment could be carried by workmen. The scope of work on line A has been discussed further in previous articles.

4. LINE B

4.1. Introduction

Nowadays there are several software programs to evaluate the interaction of soil, foundations, and structures. There is, however, a lack of examples of manual calculation methods by which it is possible to verify the other calculations, or which can be used directly for estimating soil-foundation interaction.

Because of the mentioned lack of precedent, the author developed a simple design method based on his former research work (Avellan 1992, 1994), on practical experience (Avellan & Lange 1997, Avellan & Maanas 2001, Avellan & Lange 2008, Avellan 2013), and on his Doctoral thesis work (Avellan 2011).

The result is a simple design method based on the lower and upper bond sentence of plasticity theory, where a piled, floating strip foundation lying on frictional soil can be designed geo-technically and structurally using a single method based on the ultimate limit state (ULS) and serviceability limit state (SLS). The geotechnical part of the procedure takes account of the following requirements: bearing capacity, mean settlement, pile settlements and angular distortions. The structural part of the procedure takes account of the following requirements: admissible plastic rotations, end and field moments to respective rotations, end moments resulting from angular distortions, and control of cracking.

4.2. Geotechnical Background of the Method

The method requires the value of the foundation settlement. Depending on the soil characteristics, the value of mean settlement can be estimated by settlement calculations. In the case of frictional soils, the settlement can be predicted using penetration testing as in the methods of Schultze & Sherif (1973) and Burland & Burbridge (1985). To be sure about the functionality of the piles, a special pretesting procedure was invented.

The soil layer, from dense to very dense silty sand, has about the same thickness (~ 4 m) but the upper level of the layer is slightly inclined. The area surrounding the church has in praxis the same geological strata. The outcome of the procedures in line A with special tested piles Nos. 220 and 222 indicate that using the same procedure for the piles in line B the allowable maximum load in SLS, according to DIN 1054, can be 400 kN. The safety factor gamma is defined as:

$$\gamma = \frac{602 \text{ kN} + 645 \text{ kN}}{2} \cdot \frac{1}{400 \text{ kN}} = 1.56 \quad (1)$$

The allowable load of 400 kN is less than the creep load $Q_c = 525 \text{ kN}$ (Fig. 8). The safety factor of creep is then:

$$\gamma = \frac{525 \text{ kN}}{400 \text{ kN}} = 1.31 \quad (2)$$

The maximum allowable load used on the installed spiral drilled piles was 375kN.

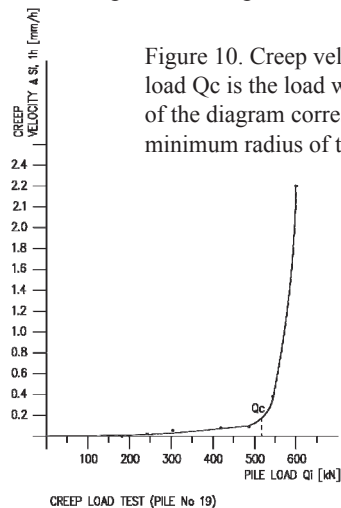


Figure 10. Creep velocity in the creep load Q_c is the load which the curvature of the diagram corresponds to the minimum radius of the curvature.

The pretesting procedure is illustrated in Figures 11 and 12, which also includes the end jacking procedure. The pressure was held constant for 15 minutes at each step and the settlement was measured at 3 intervals (5, 10, and 15 min). When the pressure of 450 bar (644 kN) decreased in 5 minutes by less than 50 bar (72 kN) to 400 bar (572 kN), the end jacking could start.

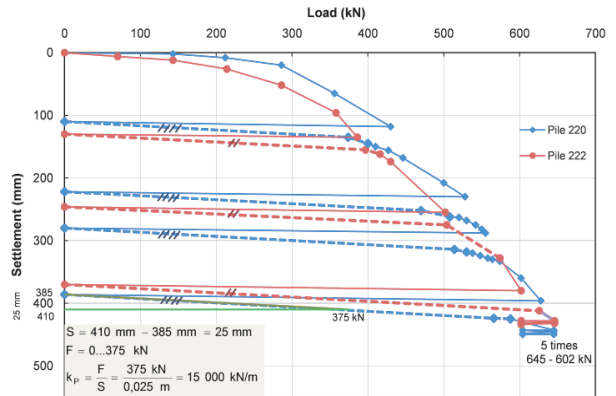


Figure 11. Line A. Load-settlement diagrams of special tested drilled spiral piles Nos 220 and 222 showing the repeated load cycling between 645-602 kN and at the end of the pretesting procedure. A parallel line in the pretesting diagrams justifies the evaluation of the spring coefficient, kP.

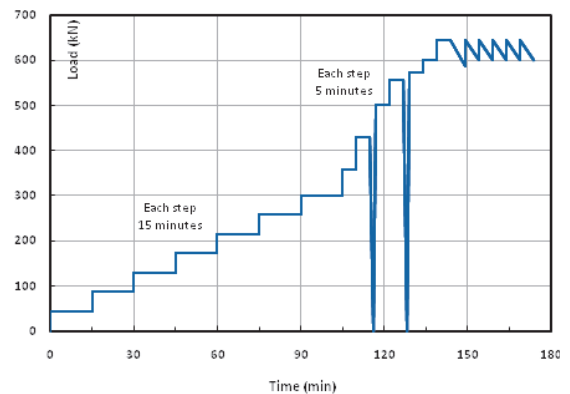


Figure 12. Time intervals for test loading of each of the drilled spiral piles in line A.

All of the installed drilled spiral piles in line A went through the pretesting procedure with end jacking to ensure their functionality (Fig. 12).

4.3. Columns of Line B

The columns and the roof in line B of St. John's church were totally destroyed during World War II and had to be rebuilt. Because of the lack of a sufficient counterweight of the spiral piles in line B, the work had to be done using the piles as springs. The rebuilt columns and arches loaded the foundations later on. The load was eccentric because of the presence of one side arch.

The piles, foundations, and loads of line B are shown in Figures 13 through 17.

5. LIMIT STATE DESIGN OF A STRIP FOUNDATION

The bearing resistance of a strip foundation resting on frictional soil is a special case of soil plasticity and a case of 3-dimensional passive pressure. The ultimate contact pressure q_u , the soil pressure with a safety factor of 1, is a special ULS-case. Thus the bearing capacity and ultimate contact pressure are functions of passive pressure.

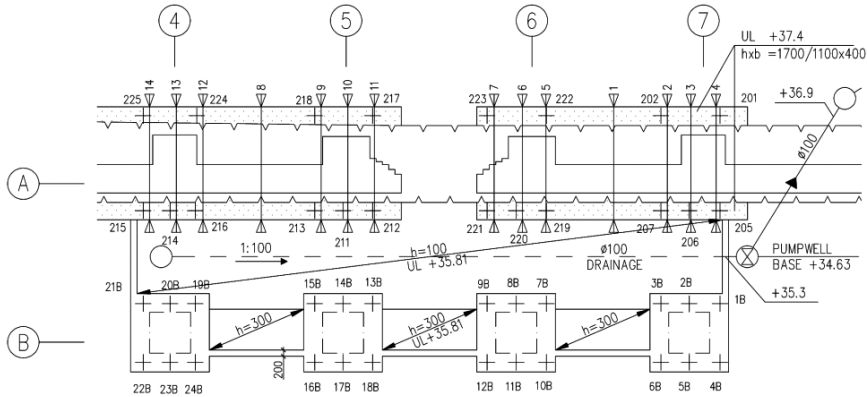


Figure 13. Line B in St. John's Church. Piled foundations of reconstructed columns and foundation of wall for burial chamber.

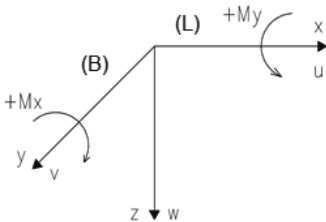


Figure 14. Line B. Coordinate system, displacements and direction of positive moments.

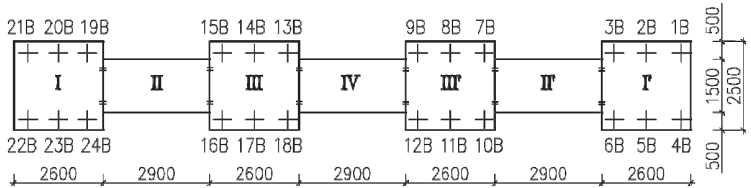


Figure 15. Line B in St. John's Church (overhead view) work joints and piles.

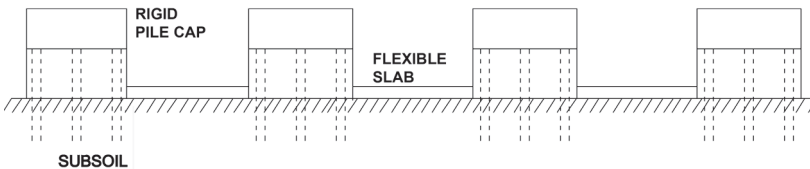


Figure 16. A) Section in direction x of line B in St. John's Church and piles.

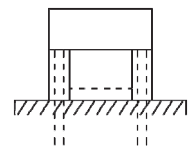


Figure 17. B) Section in direction y of line B, foundation and piles.

Horn (1970) found the relationship shown in Fig. 18 between the ratio $P_{p(s)} / P_p$ and S/S_f to be non-linear. He investigated the relationship between passive pressure and horizontal wall movements by test-loading rigid wall parts ($h/b < 3.33$) against frictional earth. The elastic-plastic model according to the author (Fig. 18) is based on that the elastic-plastic pressure-settlement relationship includes an elastic behaviour up to the settlement ratio $S_k / S_f = 0.2$. For this settlement ratio the passive pressure $P_{p(s)}$ is 0.7 times the passive pressure at failure P_p .

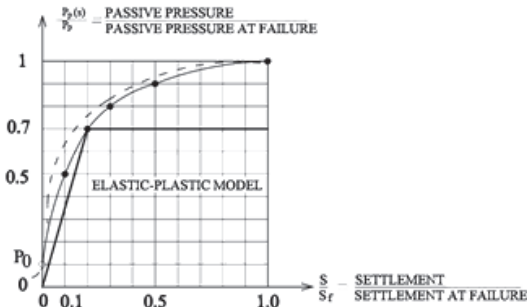


Figure 18. Elastic-Plastic model according to the author and based on the investigations of Horn (1970) (Avellan 1992, 1994).

By means of the lower bound theorem, it is possible to choose such a distribution of contact pressure which shall satisfy the requirement of equilibrium in all individual parts. The mean contact pressure due to loads (p_{od}) shall not exceed the mean design contact pressure (q_{od}) of substructure (Fig. 19).

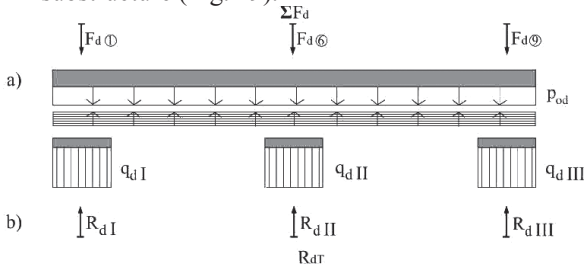


Figure 19. Strip foundation, design loads, and design contact pressure of superstructure b) Separate parts, resistant contact pressures q_d and resistances of substructure R (Avellan 1992, 1994).

The distribution of contact pressure for the ULS analysis can be taken into account by

choosing contact pressures according to the following conditions. This ensures that the lower bound theorem becomes fulfilled in the ULS in the simplest manner for the minimally effective foundation, i.e. $p_d \leq q_d$ (Fig. 20).

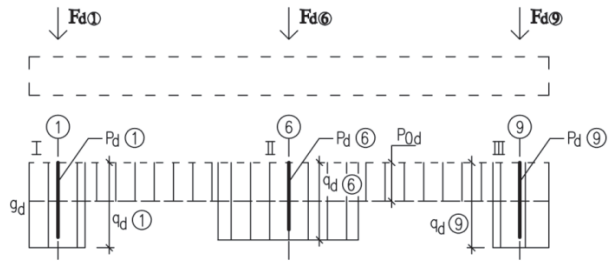


Figure 20. Contact pressure q_d of parts I, II, and III and contact pressure p_{od} of total foundation (Avellan 1992, 1994).

In addition, the distribution of the contact pressure $p_d(x)$ must be applied in such a way that the mean contact pressure is p_{od} in Figure 21. It is also possible to use the settlements of different foundations in the distribution of the contact pressure, $p_d(x)$.

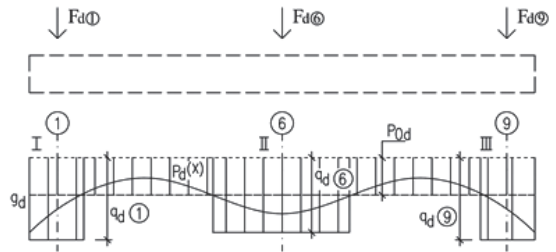
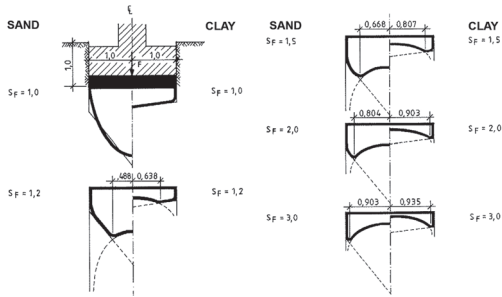


Figure 21. Balanced contact pressure $p_d(x)$ (Avellan 1992, 1994).

In homogenous frictional soil conditions the contact pressure (in ULS) can be expected to be uniformly distributed in accordance with Brinch Hansen (1961) and Schultze (1961).

- The mean contact design pressure q_{od} for the strip foundation length L_0 is determined for the whole strip foundation using the formula of Brinch Hansen (1961);
- The design contact pressure in direction y (B) is distributed uniformly due to safety factor 1.6 and according to Schultze, as in Figure 22:



$$q_d = \frac{q_u}{1.6} \quad (3)$$

Figure 22. Distribution of soil contact pressure and settlement under a rigid strip foundation due to safety factor S_F (Schultze 1961).

A strip foundation can be designed in geotechnical and structural ultimate limit states in accordance with the chart presented in Figure 23. According to the design procedure, the first values to be determined are the forces acting on the foundation resulting from the superstructure. The dimensions of the footing and foundation depth, D , are subsequently defined.

Because the ratio p_{0d}/q_{0d} due to load from superstructure, p_{0d} , and design contact pressure of substructure, q_{0d} , correspond to the ratio of $P_p(s)/P_p$, the ratio of settlement S_k and settlement at failure, S_f , can be defined by the ratio p_{0d}/q_{0d} , which is marked as S_{sq} yielding thus:

$$S_{sq} = \frac{p_{0d}}{q_{0d}} = \frac{\frac{\sum F_d}{L_0 \cdot B}}{\frac{\sum R_d}{L_0 \cdot B}}, \quad (4)$$

A settlement examination required for the feasibility of the strip foundation is carried out. As the contact pressure, q , is used, the design value

$$q_d = \frac{q_u}{\gamma} \quad (5)$$

where

q_u – is the soil pressure at failure and
 γ – is the overall safety factor representing a combination of safety factors (in this case 1.6). Note $1/1.6 = 0.625 < 0.7$.

If p_{0d}/q_{0d} is greater than 0.7, that means that piles and/or piled floating strip foundation are required.

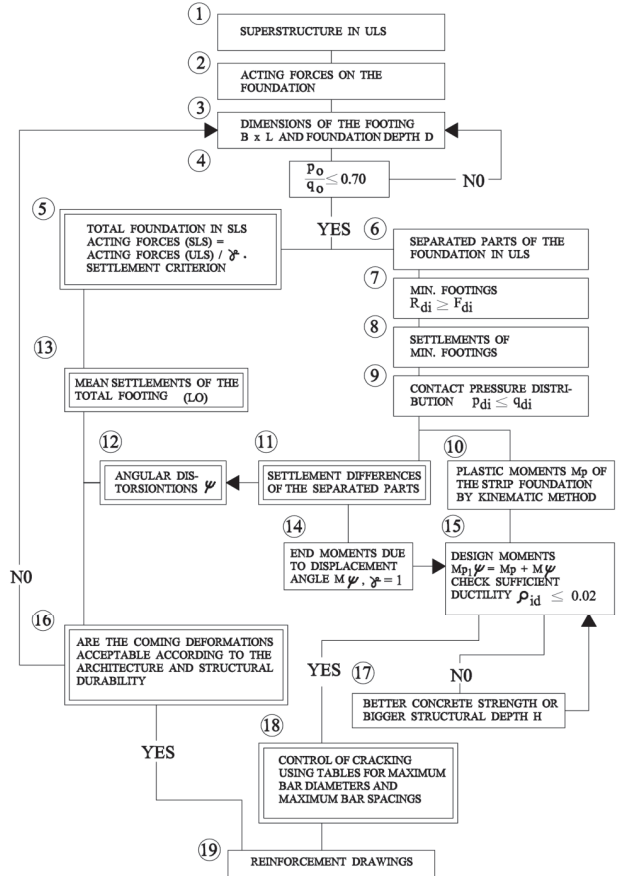


Figure 23. Geotechnical and structural design procedure in limit states for strip foundation. Double lines around boxes represent serviceability state (Avellan 1992, 1994).

6. DESIGN PROCEDURE IN ULS

6.1. Soil-foundation-pile interaction in ULS

First the theory is used for soil-foundation-pile interaction in ULS and then the theory is expanded for soil-foundation-pile-slab interaction in ULS. Characteristic loads in SLS (F_k) are multiplied by a safety factor, γ ($=1.4$) to get design loads in ULS (F_d). The design load (for example on piles 22B...24B is 515.3 kN when the arch is finished. The allowable load is due the end jacking 415 kN/1.3 = 319 kN. The pretesting and end-jacking process differs little

compared to the process used in line A. In line B, the pretesting process consisted of forces, load steps and jacking times as in line A up to 415 kN then to zero and from 450 kN to zero and the end-jacking procedure consisted of forces of 450 kN and 415 kN, and the sum of settlement was the same, $\leq 10\text{mm}$.

In spite of the reality (φ is 28° and c 10kN/m^2), the soil under the foundation was handled as pure frictional soil. Using the empirical correlation between the Swedish weight sounding test, we use $\varphi = 29^\circ$ as the frictional angle of the soil and a deformation modulus (E_d) of $15\,000\text{ kN/m}^2$ (Bergdahl & Eriksson 1983).

According to Brinch Hansen (1961), the contact pressure of the substructure q_u is 173.4 kN/m^2 . Note that the breadth of the foundation (B_{eff}), due to the eccentricity of the arch to be built and vertical load, is 1.71 m , and then:

$$q_d = \frac{q_u}{1.6} = \frac{173.4}{1.6} = 108.4\text{ kN/m}^2, \quad (6)$$

Using the well-known formula of Schleicher (1926), and expanded by Gordunov-Posanov (Tsytoovich 1981), the settlement, S_{FI} is 9.7mm . The subgrade reaction (K_{FA}) and spring coefficient (k_{F}) are:

$$K_{\text{FA}} = \frac{q_d}{S_{\text{F}}} \quad (7)$$

$$k_{\text{F}} = K_{\text{FA}} \cdot A_{\text{F}} = 49\,685\text{ kN/m} \quad (8)$$

A_{F} is the effective sub-area of the foundation (slab). The total spring coefficient (k_{PT}) for the three piles is:

$$k_{\text{PT}} = \Sigma k_{\text{p}} = 3 \cdot k_{\text{p}} \quad \text{and} \quad k_{\text{p}} \quad \text{is} \quad 15\,000\text{ kN/m} \quad (\text{Figure 11}),$$

$$\Sigma k_{\text{p}} = 3 \cdot 15\,000\text{ kN/m} = 45\,000\text{ kN/m}.$$

Compatibility:

$$\begin{cases} S_{\text{F}} = S_{\text{p}} \\ Q_{\text{F}} + \Sigma F_{\text{dp}} = V_{\text{dp}} \end{cases} \quad (9)$$

$$\begin{cases} S_{\text{F}} = \frac{Q_{\text{F}}}{k_{\text{F}}} \\ S_{\text{dp}} = \frac{\Sigma F_{\text{dp}}}{\Sigma k_{\text{p}}} \end{cases} \quad (10)$$

$$Q_{\text{F}} = V_{\text{dp}} - \Sigma F_{\text{dp}} \quad (11)$$

$$\frac{V_{\text{dp}} - \Sigma F_{\text{dp}}}{k_{\text{F}}} = \frac{\Sigma F_{\text{dp}}}{\Sigma k_{\text{p}}} \quad (12)$$

$$\frac{\Sigma k_{\text{p}}}{k_{\text{F}}} \cdot V_{\text{dp}} = \Sigma F_{\text{dp}} \cdot \left(1 + \frac{\Sigma k_{\text{p}}}{k_{\text{F}}} \right) \quad (13)$$

$$\Sigma F_{\text{dp}} = \frac{\Sigma k_{\text{p}}}{1 + \frac{\Sigma k_{\text{p}}}{k_{\text{F}}}} \cdot V_{\text{dp}} \quad (14)$$

(Resistance of the piles, every pile is pre-tested and end-jacked.)

$$F_{\text{dp}} = \frac{\Sigma F_{\text{dp}}}{3} = 244.9\text{ kN} < \frac{415}{1.1} \sim 377\text{ kN} < (15)$$

$< 400\text{kN}$

$$\Sigma F_{\text{dp}} = \frac{45\,000}{49\,685} \cdot 1\,546.0\text{ kN} = 734.8\text{ kN} \quad (16)$$

The settlement of the piles is $S_{\text{p}} = 16.3\text{ mm}$ and the settlement of the foundation is:

$$S_{\text{F}} = \frac{V_{\text{dp}} - \Sigma F_{\text{dp}}}{k_{\text{F}}} = \frac{1\,546.0 - 734.8}{49\,685} = 16.3\text{ mm} \quad (17)$$

From Figure 18, we see:

$$\frac{S_{\text{F}}}{S_{\text{f}}} = \frac{16.3\text{ mm}}{54\text{ mm}} = 0.30; \quad q_{\text{dF}} \approx (18)$$

$$\approx 0.80 \cdot 173.4\text{ kN/m}^2 = 138.7\text{ kN/m}^2$$

$$\gamma = \frac{173.4}{138.7} = 1.25 \quad (19)$$

Piles have enough resistance but for limiting theoretical settlements we study the calculation in ULS to the influence of slabs.

6.2. Soil-foundation-pile-slab interaction in ULS

The piles, foundation I, and slab II can be calculated using the same procedure already used in Section 6.1.

$q_{dII} = 139.9 \text{ kN/m}^2$, Note B_{eff} , is 1.21 m
 $q_{dII} = 87.4 \text{ kN/m}^2$
 $S_{II} = 7.4\text{mm}$, Note B_{eff} , is 1.21 m

Using the theory presented in section 5 of this article, we get as the contact pressure the q_d and $p_d(x)$ curves (Fig. 24B). The design model for the kinematic method of plasticity theory is explained in Figure 24C. The contact pressure of slab II is divided into a uniform part (Fig. 24D) and a triangular part (Fig. 24E).

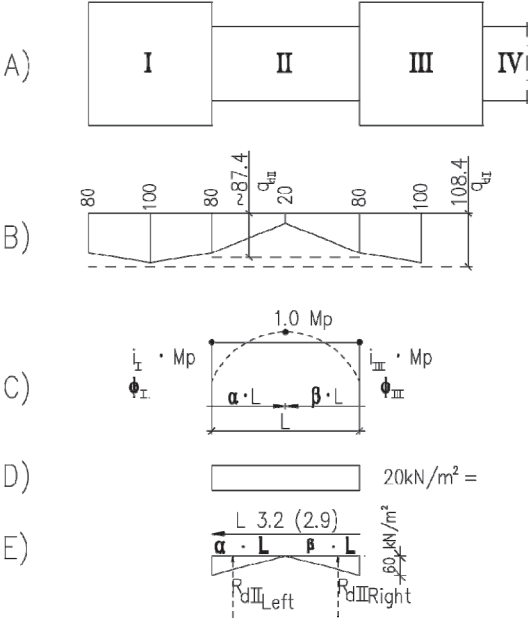


Figure 24. A) Structural system seen from the top. B) Contact pressure $p_d(x)$ under the structure. C) Slab II: Plastic moment distribution. D) Slab II: Contact pressure, uniformly distributed part. E) Slab II: Contact pressure, triangularly distributed part and its resistances.

$$W_i = i_I \cdot \varphi + 1.0 \cdot M_p(\varphi_I + \varphi_{II}) + i_{III} \cdot M_p \cdot \varphi_{III} \quad (20)$$

W_i is virtual internal work of slab II. For an iteration process we assume $\alpha = 0.45$ and $\beta = 0.55$.

$$i_I = 0.5 \text{ and } i_{III} = 1.5$$

$$W_i = 0.5 M_p \cdot 0.694 + 1.0 M_p \cdot 1.26 + 1.5 M_p \cdot 0.568 = 2.46,$$

and virtual external work is

$$W_e = 20 \cdot 3.2 \cdot 0.5 + 43.2 \cdot 1/3 + 52.8 \cdot 1/3 = 32 + 14.39 + 17.58 = 63.97,$$

$$W_i = W_e.$$

$$M_p = \frac{64.0}{2.46} = 26.0 \text{ kNm} \quad \text{and}$$

$$M_{p,III} = 39.0 \text{ kNm}. \quad (21)$$

This corresponds to $\alpha \cdot L \cong 1.44 \text{ m}$.

The free body diagram (Fig. 25) includes only one unknown, namely $\alpha \cdot L$, which can be solved by the principle of virtual work. $Q_{s, \text{uniform}}$ is the resultant of uniform contact pressure and $Q_{s, \text{triangular}}$ is the resultant of triangular contact pressure.

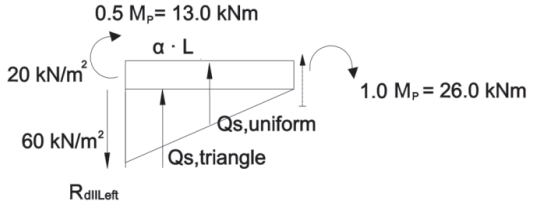


Figure 25. Free body diagram of the left part of slab II.

$$W_e = \alpha \cdot L \cdot 20 \cdot \frac{1}{2} + 30 \cdot \alpha \cdot L \cdot 0.333 = 20 \cdot \alpha \cdot L,$$

$$W_i = \frac{1}{\alpha \cdot L} \cdot 13.0 + 26.0 \cdot \frac{1}{\alpha \cdot L} = \frac{39.0}{\alpha \cdot L},$$

$$W_i = W_e. \quad (22)$$

and we get

$$\alpha \cdot L = 1.40 \sim 1.44.$$

The value of $R_{II,Left}$ can be solved by equilibrium. The eccentricity of $F_{dII,Left}$ over foundation I can be ignored.

$$(13.0 \text{ kN/m} + 26.0 \text{ kN/m}) - R_{dII,Left} \cdot 1.44 \text{ m} +$$

$$+ Q_{S, \text{triangle}} \cdot 0.96 + \frac{Q_{s, \text{uniform}} \cdot 1.44}{2} = 0,$$

$$39.0 + 43.2 \cdot 0.96 + 20.74 = R_{dII,Left} \cdot 1.44 \text{ m},$$

$$R_{dII,Left} = 70.3 \text{ kN per 1 m}. \quad (23)$$

Steel area, cracking and rotation capacity:

Steel area (A_s)

K35, $f_{cd} = 16.3 \text{ MN/m}^2$, A III (A400HW),
 $f_{vd} = 333 \text{ MN/m}^2$ and $d = 259 \text{ mm}$.

$$m = \frac{0.0390}{1.0 \cdot 0.259 \cdot 0.259 \cdot 16.3} = 0.0357,$$

$$A_s = 0.036 \cdot 1000 \cdot 259 \cdot \frac{16.3}{333} = 456.4 \text{ mm}^2.$$

Cracking

$\phi 12 \text{ c } 200$ (565 mm^2), high – bond bar

$$\delta_{sk} \sim \left(\frac{333}{1.4} \cdot \frac{456}{565} \right) \cong 192 \text{ MN/m}^2 < 200 \text{ MN/m}^2. \quad (24)$$

Steel stress in SLS is acceptable.

$$\rho_s = \frac{A_s}{B \cdot d}, \quad (25)$$

$$\frac{565}{1000 \cdot 259} = 0.002 < 0.02.$$

Rotation capacity is sufficient.

6.3. Settlements of foundations I and III

Using the same procedure as in section 6.1, we calculate the settlements of foundations I and III:

Foundation I

$$V_{dp} = 1.4 \cdot 1104.3 \text{ kN} - 70.3 \text{ kN/m} \cdot 1.21 \text{ m} = 1461.0 \text{ kN},$$

$$p_d(x) = 90 \text{ kN/m}^2, \text{ mean pressure (Fig. 24B).}$$

$$s_F = \frac{90 \cdot 1.71 \cdot 0.91}{15000} \cdot 0.865 \cdot 10^3 \text{ mm} = 8.1 \text{ mm}.$$

$$K_{FA} = \frac{90 \text{ kN/m}^2}{0.0081 \text{ m}} = 11111 \text{ kN/m}^3,$$

$$k_F = 11111 \text{ kN/m}^3 \cdot 1.71 \text{ m} \cdot 2.6 \text{ m} = 49400 \text{ kN/m}.$$

$$\Sigma F_{dp} = \frac{45000}{1 + \frac{49400}{45000}} \cdot 1461.0 \text{ kN} = 696.4 \text{ kN},$$

$$F_{dp} = \frac{\Sigma F_{dp}}{3} = 232.1 \text{ kN} < \frac{415}{1.1} = 377 \text{ kN}. \quad (26)$$

$$S_p = 15.5 \text{ mm},$$

$$S_F = \frac{V_{dp} - \Sigma F_{dp}}{k_F} = \frac{1461.0 \text{ kN} - 696.4 \text{ kN}}{49400 \text{ kN/m}} = 0.0156 \text{ m} = 15.5 \text{ mm}$$

$$\frac{S_F}{S_f} = \frac{15.5 \text{ mm}}{54.0 \text{ mm}} = 0.29.$$

$$q_{dFI} \sim 0.77 \cdot 173.4 \text{ kN/m}^2 = 133.5 \text{ kN/m}^2.$$

$$\gamma_d = \frac{173.4 \text{ kN/m}^2}{133.5 \text{ kN/m}^2} = 1.30,$$

$$\gamma_k = 1.82.$$

Using the same procedure, we get Foundation III:

$$S_p = 14.3 \text{ mm}$$

6.4. Angular distortion and end moments resulting from angular distortion

The settlement difference in slab II in SLS is:

$$S_{FI} - S_{FIII} = \frac{15.5 \text{ mm} - 14.3 \text{ mm}}{1.4} = 0.86 \text{ mm} = 0.86 \cdot 10^{-3} \text{ m} \quad (27)$$

The angular distortion Ψ_k in SLS is:

$$\Psi_k = \frac{S_{FI} - S_{FII}}{L_{SLABII}} = \frac{0.86 \cdot 10^{-3} \text{ m}}{3.2 \text{ m}} = \frac{1}{3721}. \quad (28)$$

The end moment M_Ψ reduces the plastic moment M_{PIII} but increases M_{PI} . $M_{\Psi d}$ is based on Ψ_k (partial safety factor $\gamma_d = 1$).

$$M_{\Psi Rigid} = \frac{6 \cdot E_c \cdot I_c}{L^2} \cdot \Delta \quad (29)$$

Because of the testing of the drilled spiral piles, slab II was loaded by backfilling 3...4 weeks after the concreting work was finished.

$$\varphi(\infty, t_0) \text{ is } \sim 2.4$$

$$E_c = \frac{5000 \sqrt{K}}{1 + 2.4} = 8700 \text{ MPa},$$

$$M_{\Psi Rigid} = \frac{6 \cdot 8700 \cdot 10^3 \cdot 0.00145 \cdot 0.85 \cdot 10^{-3}}{3.2 \cdot 3.2} = 6.28 \text{ kNm},$$

$$M_{dl} = M_{pl} + M_{\psi I} = (13.0 + 6.28) \text{ kNm} = 19.28 \text{ kNm} < 39.0 \text{ kNm}$$

Eccentricity can be ignored.

$$M_{dIII} = M_{pIII} + M_{\psi III} = 39.0 \text{ kNm} - 6.28 \text{ kNm} = 32.7 \text{ kNm} < 39.0 \text{ kNm} \quad (30)$$

Thus, the structure has sufficient resistance and ductility.

7. SOIL-FOUNDATION-PILE INTERACTION IN SLS

For the reason that the reader can compare the results in SLS and ULS, the values used in SLS-calculations are given as follows:

$$q_k = q_d = 108.4 \text{ kN/m}^2 \text{ as in section 6.1}$$

$$S_F = 9.7 \text{ mm}$$

$$k_F = 49\,685 \text{ kN/m as in 6.1}$$

$$\sum k_p = 45\,000 \text{ kN/m as in 6.1}$$

$$F_{kP} = 174.9 \text{ kN} < 300 \text{ kN} = F_{adm}$$

The settlement of the piles is $S_F = 11.7 \text{ mm}$ and the settlement of the foundation is:

$$S_F = \frac{V_{kP} - \sum F_{kP}}{k_F} = \frac{1104.3 - 524.8}{49\,685} = 11.7 \text{ mm} \quad (31)$$

Now we have to prove that the designed soil pressure is smaller than q_u . We have used q_{kF} as $q_u/1.6 = 0.625 q_u$. We notice (Fig. 18) that the calculated settlement, 9.7 mm is about 0.18 times the settlement at failure (S_f), which means that S_f is about 54 mm. According to SLS, S_F is 11.7 mm and less than $S_f = 54 \text{ mm}$. The S_F/S_f ratio is 0.22 and then q_{kF} is 0.72 times q_u (Fig. 18, non-linear line).

$$0.72 \cdot 173.4 \text{ kN/m}^2 = 124.8 \text{ kN/m}^2,$$

$$\gamma = \frac{173.4 \text{ kN/m}^2}{124.8 \text{ kN/m}^2} = 1.39.$$

The piles have enough resistance, but for limiting theoretical settlements we study the calculation in ULS to see the influence of slabs.

8. CONCLUSIONS

This article has three goals. One goal of is to clarify how to design a strip foundation when contact pressure is calculated as the ultimate

soil bearing pressure divided by a safety factor and the forces acting from the superstructure are calculated in ULS. The article includes the application of the upper bound theorem sentence to the strip foundation. Furthermore, the bearing capacities are determined using the formula of Brinch Hansen and the contact pressure distribution in the fictitious ULS was roughly determined according to the settlement calculations of theoretically separated minimum foundations. The plastic moments of the structure are calculated by the kinematic method. The angular distortions are calculated using settlements which were estimated applying the contact pressure distribution in the ULS divided by a safety factor. Thus the settlement and the angular distortion were considered to be the criteria of the serviceability state.

Another goal was to clarify the design method of the piled floating strip foundation in SLS and ULS. Finally, the third goal was to prove the reliability of the pretesting and end-jacking procedure employed.

8.1. Thematic conclusions

1. Creep load of drilled spiral pile

The creep load of the drilled spiral pile without pretesting and end-jacking procedure

The creep load of the jacked drilled spiral piles is 525 kN, which means that the soil pressure under the tip is 13.9 MPa and under the spiral tip 9.3 MPa. Because of jetting the skin friction has no or only a minor influence on the tip resistance.

The creep load tested of drilled spiral pile with pretesting and end-jacking procedure

The monitoring of levelling points indicates no significant settlement. Therefore the creep load of pretested and end-jacked drilled spiral pile is higher than 525 kN.

2. Settlement of drilled spiral pile

On account of the pretesting and end-jacking procedure in axis A by the author, the settlement of the drilled spiral pile can be estimated to be 5 mm, which means 20 % of 25 mm (Fig. 11). This estimation is based on levelling

(Fig. 8). The maximum settlement in the above-mentioned sixteen years has been 5 mm. The surveying accuracy between levelling points is 0.5 mm. The reason for the small settlements is probably soil hardening which occurred as a result of the use of the author's pretesting and end-jacking procedure. The technique referred to has also been used in the 2000's in foundations of high-rise buildings (H. Brandl 2005).

3. Soil-foundation interaction

Settlement of Soil

The Schleicher-Tsytoovich formula provides high settlement values and therefore yields results which can be considered too conservative. It was not possible in this study to clarify the stress influence of the weight and the long-term influence of the weight of the medieval church on the soil.

The author has used the same safety factor of 1.6 for estimating the settlement of the soil, in spite of the serviceability state or ULS. According to the author's opinion, this satisfies normal cases, when the soil stratum is homogenous, as is the case around St. John's Church in Tartu. If the soil strata is not homogenous, the author's method may be used with a greater safety factor. In principle, the author's "separate foundations" method for soil-foundation-pile interaction and for the piled floating strip foundation automatically takes care of limit states (ULS and SLS).

A small point of criticism in this article may be the employment of the curve of Horn (Fig. 18), which is based on experimental studies. It is nevertheless only employed to check the contact pressure after the settlement of the piled foundation and thus, in the author's opinion, has no practical influence on the author's method.

Soil-foundation-pile interaction in ULS (Line B)

The safety factor of piles in SLS:

- the calculated piled load in ULS is 244.9 kN
- the partial safety factor for the loads of the superstructure is 1.4
- the real safety factor in SLS is

$$1.4 \cdot \frac{1.3 \cdot 319.2 \text{ kN}}{244.9 \text{ kN}} = 2.37,$$

The safety factor of the bearing capacity of the soil in SLS:

- the calculated safety factor is $1.4 \times 1.25 = 1.75$.

Soil-foundation-pile-slab interaction in ULS (Line B)

The safety factor of piles in SLS:

- the calculated pile load of foundation I in ULS is 232.1 kN
- the real safety factor is

$$1.4 \cdot \frac{1.3 \cdot 319.2 \text{ kN}}{232.1 \text{ kN}} = 2.50,$$

- the calculated pile load of foundation III in ULS is 214.8 kN
- the real safety factor is

$$1.4 \cdot \frac{1.3 \cdot 319.2 \text{ kN}}{214.8 \text{ kN}} = 2.70.$$

The safety factors for the bearing capacity of the soil are $\gamma_{kI} = 1.82$ and $\gamma_{kIII} = 1.89$.

4. Safety factor in geotechnical and structural design

Soil-foundation-pile design calculations can be made in the same geotechnical and structural process using the method described in ULS in Section 6.1. With the use of the author's method the settlement (S_{kF}) in SLS is 11.7 mm (chapter 7) and the settlement in ULS (S_{dF}) is 16.3 mm (Section 6.1). As previously mentioned (S_{dF}), (S_{kF}) the partial safety factor is 1.4 for the superstructure.

The ratio of settlement in ULS (S_{dF}) and in SLS (S_{kF}) is:

$$\frac{16.3 \text{ mm}}{11.7 \text{ mm}} = 1.39.$$

The non-linearity of soil ($q_{dF} \sim 0,8 q_u > 0,7 q_u$) has no practical influence and thus the ratio of S_{Fd} and S_{Fk} is practically the same as the partial safety factor of 1.4 for the superstructure S_{kF} and S_{dF} .

As noted in the thematical conclusions the safety factors of piles of Soil-Foundation-Pile interaction are linear. The theoretical safety factor of the bearing capacities of foundations is slightly different because of non-linearity in

Fig. 18. In his Licentiate Thesis (Avellan 1992) and in an article (Avellan 1994) based on the Licentiate Thesis (Avellan 1992), the author has shown that with the use of the author's method the bending moments in SLS are nearly the same in spite of the calculation according to the method of foundation on Winkler-springs, compressibility method or the author's method.

9. REFERENCES

- Altoa, K. 1994. *St. John's of Tartu*. Tallinn: St. John's of Tartu Foundation and the Estonian heritage society.
- Avellan, K. 2013. *Drilled spiral piles in St. John's Church of Tartu, Estonia*. (Emilo Bilotta & al ed. Geotechnical Engineering for the Preservation of Monuments and Historic Sites. London. Taylor & Francis Group. 149-156
- Avellan, K. 2011. Limit state design for strengthening foundations of historic buildings using pretested drilled spiral piles with special reference to St. John's Church in Tartu. Doctoral thesis. University of Oulu, Faculty of Technology. Acta Universitatis Ouluensis, C Technica 392.
- Avellan, K. 1992. *Geotechnical and Structural Ultimate Limit State Design of Foundations Resting on Soil*. Licentiate thesis. Helsinki University of Technology, Faculty of Civil and Environmental Engineering.
- Avellan, K. & Lange K., St. John's Church, Tartu, Estonia – Underpinning of tower. (C. Viggiani ed.) Geotechnical Engineering for Preservation of Monuments and Historic Sites. Proceedings of the International Symposium on Geotechnical Engineering for the Preservation of Monuments and Historic Sites. Naples 3-4 October 1996, 521-525.
- Avellan, K. & Maanas, M. Strengthening the foundations of St. John's Church in Tartu, Estonia. *Proceedings of the Fifteenth International Conference on Soil Mechanics and Geotechnical Engineering*. Istanbul, 27-31 August 2001, 1687-1690.
- Bergdahl, U. & Eriksson, U. 1983. Bestämning av jordegenskaper med sondering – en literturstudie. Linköping. *Statens Geotekniska Institut. Rapport 22*. In Swedish. (Estimation of soil characteristics from penetration test results. Literature survey. *Swedish Geotechnical Institute. Report 22*.)
- Brandl H. (2005) Cyclic preloading of piles to minimize (differential) settlements of high-rise buildings. *Slovak Journal of Civil Engineering*. 2005/3: 1-12.
- Burland, JB. & Burbidge, MC. 1985. *Settlements of foundations on sands and gravel*. *Proceedings, Part 1*, 78. UK, Institution of Civil Engineers: 1325-1381.
- CEB-FIP Model Code 1990: design code. Comité Euro-International du Béton. August 1993. Thomas Telford Services Ltd.
- DIN 1054 (1976) Baugrund – Zulässige Belastung des Baugrunds. In German. (Subsoil; permissible loading of subsoil. German code, November 1976. Berlin, Beuth Verlag.)
- Drucker, D. & Prager, W. 1952. "Soil Mechanics and plastic analysis or limit design." *Quarterly of Applied Mathematics*, Vol X, No 1: 157-165.
- FIP recommendations (1984) Practical design of reinforced and prestressed concrete structures based on the CEB-FIP model code (MC78). London, Thomas Telford Limited.
- Horn, A. 1970. *Sohlfreibung und räumlicher Erdwiderstand bei massive Gründungen in nichtbindigen Böden*. Strassenbau und Strassenverkehrstechnik. Heft 110. Bonn. Bundesminister für Verkehr. (Sohlfriktion and 3-dimensional earth resistance with massive foundations in non-cohesive soil. Block 110. Federal Ministry of Transport, Building and Urban Environment.)
- ISO 13822:2010, Bases for design of structures – Assessment of existing structures, Annex I (informative) Heritage structures.
- Iwasaki Y (2005), Technical Session 4c: Preservation of Historic Sites, 16th World Conference on Soil Mechanics and Geotechnical Engineering, September 12-16, 2005, Osaka, Japan. (Also on the web <http://www.webforum.com/tc19/home/page.asp?sid=207&mid=2&PageId=22885>.)
- Iwasaki Y & Tsatsanifos C (2006) Geotechnical Aspects on Preservation of Monuments and Introduction to the Authenticity of Soils and Foundations. Presentation during the ICOMOS / ISCARSAH Workshop. Lefkosia, Cyprus, 24 February, 2006.
- Neal, B. 1970. *The plastic methods of structural analysis*. Great Britain, Norwich. Barnes & Noble Inc.
- Schultze, E. 1961. Distribution of stress beneath a rigid foundation. Proc. 5th International Conference on Soil Mechanics. Paris: 807-813.
- Schultze, E. & Sherif, G. 1973. Prediction of settlements from evaluated settlement observations for sand. Moscow. Pro
- Schleicher, F. 1926. *Zur Theorie des Baugrundes*. Der Bauingenieur. Heft 48: 931-935, Heft 49: 949-952. (*The theory of the ground*. The Civil Engineer. Block 48:931-935, Block 49, 949-952.)
- Tsytoovich, N. 1981. *Soil Mechanics*. Moscow. English translation Mir Publishers.

A Study on the Interactive Behavior of Piled raft on Sand

V.Balakumar

Senior consultant, Simplex Infrastructures Limited, Chennai, India vb_kumar2002@yahoo.com

I.V.Anirudhan

Director, Geotechnical solutions Chennai India. anirudhen@eth.net

ABSTRACT: The interaction behavior piled raft foundation was studied through 1g model tests, numerical method and observational study. The study has established that the interaction is mainly due to the enhancement of the confining stress due to the resistance offered by the grain columns. It was found that the pile group at higher settlement behaved like soil reinforcement reducing the raft settlement, and the stiffness at the elasto plastic and plastic stage indicates that the system behaves like an unpiled raft with enhanced carrying capacity. The observational study has shown that the behavior is similar in that the pile group acts as floating piles even in the case of closely spaced piles.

1. INTRODUCTION

The design of the foundation systems to support tall and heavily loaded structures need to consider both long term and short term settlements. The existing codes of practice have recommended certain values of permissible total and differential settlement depending upon the nature and the functional requirements of the structures. However the designers had always felt that the safety and the performance of the structure cannot be assured when the structure is permitted to settle, however small the settlement would be. This is mainly because of the complications involved in the settlement oriented design which require an accurate evaluation of in-situ parameters such as elastic modulus etc. This has resulted in the designers adopting designs that eliminate the settlement rather than reducing it. The concept of settlement reduction came to vogue after Burland (1995) established that deep foundation elements namely the piles could be used with the raft as settlement reducer. This has led to the advent of the combined piled raft foundation system.

The combined piled raft foundation system is a skilful geotechnical concept which attempts to strike a balance between the cost and the performance by allowing a settlement close to

the permissible value, ensuring the safety and serviceability of the structure.

The piled raft foundation system transfers the load by a load sharing process and the analyses of the interaction to understand this behavior is more complicated due to the three dimensional nature of the problem. The geotechnical design of this foundation system requires the consideration of not only the capacity of the pile elements and raft elements individually but also the combined capacity and interaction under serviceability loading and ultimate loading.

The analyses of the piled raft foundation system is more complicated due to the three dimensional nature of the problem. Even the most sophisticated numerical procedure with a highly advanced material model needs certain amount of dilution in the rigors of the analyses so that the model becomes computationally viable. Even the Further it has been reported that (Poulos, 2008) the observed results and the computed results even in the case of a well monitored proto type piled raft vary widely due to many reasons.

2. OBJECTIVE

The behavior of piled raft has been studied adopting various methods namely analytical and

numerical modeling (Prokoso and Kulhawy, 2001; Russo, 2001) centrifuge modeling, (Horikoshi and Randolph, 1995), 1g model studies (Kim et al., 2001; Turik and Katzenbach 2003; Balakumar, 2008), and by monitoring the proto type piled raft (Yamashita et al., 2010; Poulos, 2009 ; Katzenbach et al., 2000) and such studies have provided a wealth of information on various aspects on the behavior of piled raft on over consolidated clay bed. Still it is felt that a comprehensive study is required particularly on the interaction behavior, combining the observational method, numerical modeling and small scale model studies, particularly in the case of piled raft placed on sand. This paper presents the results of such a study.

3. SCOPE OF STUDY

Extensive research work on the behavior of piled raft with sand as bed material was carried out in Anna University by the first author and this is being further extended by the authors of this paper now. The studies have been carried out based on 1g model tests and numerical modeling; during this period a 12 storied building was designed and supported on piled raft and the behavior was monitored during construction and after construction for a period of 760 days. In addition the load settlement data collected by the second author during the hydro testing of storage tanks were also analysed. The paper presents the results of the study bringing out certain important aspects of the interaction behavior between the elements of the piled raft namely the raft, pile and the soil.

4. SMALL SCALE MODEL STUDIES

In order to understand the complex behavior of the piled raft as a whole, it is essential to study the behavior of the individual constituents under different stages of loading and the corresponding settlement. In this case the entire pile group is treated as one element as individual pile design depends upon the load shared by the group. As Murrey and Geddes (1989) have pointed out, although, the 1g model studies may not truly represent the field conditions the results obtained from the 1g model tests produce very valuable data regarding the behaviour pattern. These data coupled with the numerical

analyses and existing data can produce very important information which can form the basis for further works.

Keeping the above in mind, a series of 1g model tests were conducted on the Circular, Square, and rectangular shaped piled raft under varying bed density conditions, namely loose medium dense and dense conditions. Poorly graded local Palar sand was used for preparing the bed by sand raining process; the process was calibrated earlier, tested for consistency of results and was adopted. The least lateral dimension of the raft was kept constant namely 200 mm (dia in the case of circular raft and size in the case of square raft). Figure 1 presents the variation of angle of internal friction with the relative density. In the present discussion the results of the tests conducted on circular piled raft on medium dense sand bed is considered.

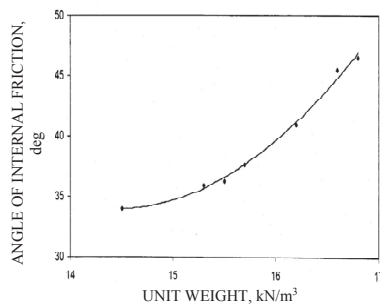


Figure 1. Variation of angle of internal friction with unit weight

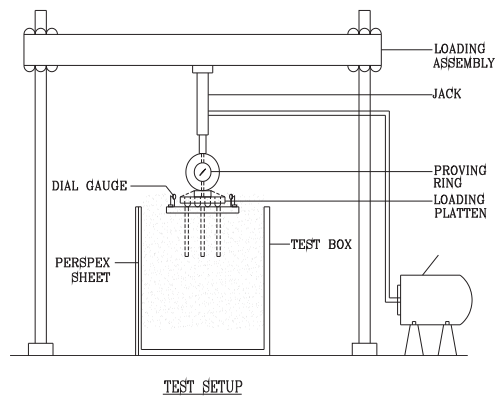


Figure 2. General arrangement of experimental set up

The Figure 2 presents the test set up. The raft diameter was 200mm and the thickness was 8mm. The piles were 10mm dia 160mm long and the pile – raft area ratio was 4.9%. The piles were arranged in a radial fashion. Extensive parametric studies carried out on this subject (Balakumar, 2008) has revealed that when the d/t ratio (d is the diameter of the pile and t is raft thickness) is close to unity the piled raft performance is at the optimum irrespective of the shape of the piled raft, and hence the results for this study were chosen from this part. Tests were conducted on unpiled raft, free standing pile group and piled raft. In the present paper the results of circular piled raft tested on medium dense bed is taken as the response in all the other cases was identical.

5. RESULTS, ANALYSES AND DISCUSSIONS

5.1. The Load Settlement Response

Figure 3a presents the characterized load settlement response of circular piled raft and the corresponding unpiled raft. In the present analyses, it can be seen that the ratio of the pile length to the diameter is kept as either unity or 0.8. Since in all the studies the raft dimension was kept constant, it was decided to represent the important levels of settlement in terms of the raft diameter.

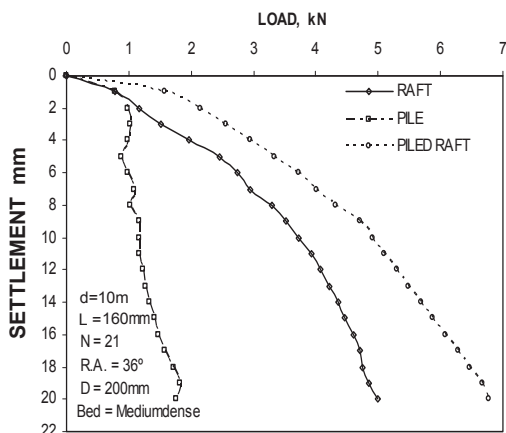


Figure 3a. Characteristic response of Plain raft and piled raft (medium sand)

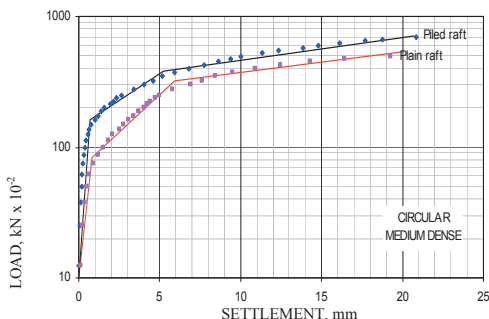


Figure 3b. Load – settlement response of plain raft, piled raft and pile group of piled raft in medium dense sand.

It is evident that the response has three phases namely OA, AB and BC represented in figure 3b. The initial response OA exhibits a very high stiffness. The settlement of 1.0 mm observed at point A is 0.5% of the least lateral dimension of the piled raft. At this settlement level the load taken by the piled raft is 100% higher than the load taken by the unpiled raft corresponding to the same settlement. Beyond this level of settlement the rate of fall of stiffness increases with the increase in the load gradually. This stage is observed upto a settlement level of 5mm to 6mm (AB) which is 3% of the least lateral dimension of the raft. As the applied load increase further, this settlement level the rate of fall of stiffness increases rapidly even for a small increase in the load, and the load taken by the piled raft for the same settlement still remains higher than that of the unpiled raft

For the model studies a settlement level of 20mm which is 10% of the least lateral dimensions of the raft is taken as failure settlement. Accordingly the settlement levels are represented as a percentage of the raft dimension. Accordingly the stage OA was upto 1% of the raft size the stage AB is up to 3% of the raft dimension.

Table 1 presents the variation of stiffness at the milestone settlement levels of 2mm, 6mm and 20mm for the piled and unpiled raft. It is seen from the table 1 that the stiffness reduces rapidly with the increase in the settlement. At 20mm settlement the stiffness of the piled raft is almost equal to that of unpiled raft. This means that the pile group in the initial stages provides a

very high stiffness which progressively reduces and finally the system has the stiffness equal to that of un-piled raft, still taking a higher load than the un-piled raft.

Table 1. Comparison of stiffness of plain and piled raft for various settlements
(D = 200mm, t = 8mm, L = 160mm and d = 10mm, and N = 21)

Bed	Phase OA (N/mm)		Phase AB (N/mm)		Phase BC (N/mm)	
	Plain	Piled	Plain	Piled	Plain	Piled
Loose	195	380	137	197	98	130
Medium	600	1100	467	633	255	345
Dense	800	1700	617	800	314	410

5.2. Behavior of pile group of piled raft

The influence of the pile group of piled raft is studied through a parameter named load sharing ratio which is defined as the ratio of the load taken by the pile group to the total load taken by the piled raft at any given settlement designated as α_{pr} which is mathematically defined as

$$\alpha_{pr} = \frac{Q_p}{Q_{pr}} \quad (1)$$

Where $Q_p = Q_{pr} - Q_r$ and Q_r = load shared by the raft at the same settlement.

The α_{pr} is plotted against the settlement and is presented in Figure 4 typically for the circular piled raft. It is clearly seen that at the initial stages the load shared by the pile group is very high upto a settlement level of around 2mm and this corresponds to the stage OA in the characterization curve. At this stage the stiffness is very high. As the settlement increases the load sharing ratio reduces upto a settlement level of 6mm (stage AB) and thereafter the value reduces rapidly and from a settlement level of around 10mm the load sharing ratio remains more or less constant indicating that the pile

group helps the raft to take a higher load keeping the settlement less than that of the un-piled raft. This establishes the fact that in the initial stages the pile group provides the required stiffness by taking a higher proportion of the load and at the later stage acts similar to soil reinforcement for the raft to take a higher load at a settlement far less than the un-piled raft.

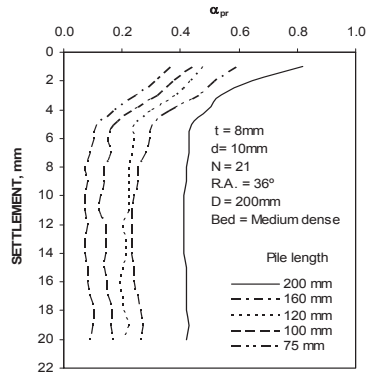


Figure 4. Settlement v/s LS ratio α_{PR} for 10mm dia pile.

5.3. Mechanics of Pile group behavior from 1g model tests

In order to understand this, the behavior of free standing pile group (raft not in contact with the bed) is compared with the load settlement response of pile group of piled raft. The plot is given in Figure 5.

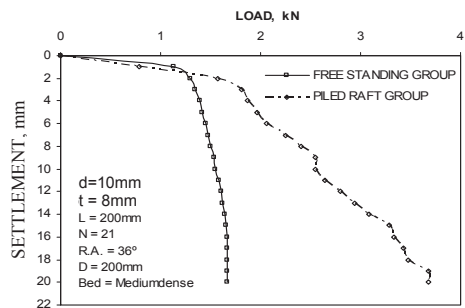


Figure 5. Comparison of load – settlement response of free standing pile group of piled raft.

It is seen that in the case of free standing pile group the pile group exhibits a very high stiffness upto a settlement level of 1.2 to 1.4mm wherein the friction is fully mobilized. Subsequently, even for a small increase in the load the

stiffness of the pile group reduces rapidly indicating a sudden failure. But in the case of pile group of piled raft, the system takes a much higher load (nearly 50% more) for the same settlement and the rate of fall of stiffness is gradual. The behavior is similar to elastic work hardening behavior

In the settlement problem this behavior suggests that with the increase of strain the mobilization of the stress is a function of effective soil grain contacts which increases, unlike a general increase in the intergranular stress on a constant number of grain contacts. It can be interpreted that when the strata is under compressive stress, the load is transmitted by internal columnar grain structure and when the limiting load is reached more and more columns begin to support the load, each having approximately the same yield load. This appears to be the reason for the high stiffness in the initial stages of loading in the case of piled raft. As the load is applied on the raft the intergranular resistance increases leading to the enhancement of the confining stress in the upper region leading to the pile group sharing a higher proportion of the load. As the applied pressure increases the enhanced inter-granular resistance enhances the raft stiffness with the piles functioning as soil reinforcement; hence the system takes a much higher load compared to that of the unpliled raft. The behavior is similar to the concept expressed by Fleming (1992).

5.4. Quantitative assessment of interaction

Although the interaction behaviour has been qualitatively established, quantification has to be done through a suitable parameter in non-dimensional form. Randolph (1993) in his studies had expressed the interaction between the pile and the cap considering the average displacements beneath the cap due to the loading on the pile, and down the center line of the pile due to the cap. Clancy [1993] had later established the raft pile interaction factor α and based on this, more rigorous analyses were conducted to show that the value is constant as the number of piles increases. The value suggested was around 0.8. The interaction factor is expressed as

$$K_{pr} = \frac{K_p + (1 - 2\alpha_{pr}) K_r}{1 - \alpha_{pr}^2 (K_r / K_p)} \quad (2)$$

Where, K_{pr} is the stiffness of the piled raft, K_p is the stiffness of the pile group, and K_r is the stiffness of the raft. All measured at the same settlement level. α_{pr} is the interaction factor.

Based on the parametric studies conducted through the 1g model tests the stiffness of the individual elements namely the raft (K_r) and the pile group as pier K_p and the piled raft K_{pr} were computed at different settlement levels using Excel programme and the value of α_{pr} was computed for various pile lengths, pile-raft area ratio in the case of circular piled raft and pile spacing in the case of circular piled raft. It is to be noted here that the number of piles were varied keeping the raft dimension constant.

5.5. Effect of pile length

Table 1 presents the variation of the interaction factor with the pile length at different settlement level. At a settlement level of 2mm the interaction factor is unity mainly because the pile group shares the maximum load due to the high intergranular stress created. As the settlement level increases the interaction factor reduces and at 20mm the value is the least.

Table 2. variation in length (8mm raft and 10mm pile)

Settlement (mm)	α_{pr} for various length (mm)			
	200	160	120	100
2	1.14	0.91	1.04	0.50
10	0.81	0.68	0.45	0.43
20	0.84	0.52	0.41	0.38

It is seen from the Table that when the pile length is equal to the raft width or 0.8 times the raft width the interaction factor varies from 0.5 to 1.0. At a settlement level of 10mm which is the end of elasto plastic stage the interaction factor varies from 0.60 to 0.80 close to the value suggested by Randolph(1994).

5.6. Effect of pile – raft area ratio

The variation of the interaction factor with pile raft area ratio is given in Table 3. The variation shows identical trend. When the pile raft area ratio is very high (9.25% with 37 piles) the interaction factor varies from 0.8 to 1.2 indicating that the piled raft has a tendency to behave as a fully piled system. When the area ratio is 5.25% (21 piles) the variation is from 0.4 to 0.8. When the area ratio is small the interaction factor is also small. It is seen that at a settlement level of 10mm when the load settlement response takes elasto plastic stage the interaction factor varies from 0.6 to 0.8 depending on the concentration of piles.

Table 3. Variation in radial angle / pile raft area ratio

Settlement (mm)	α_{pr} for various Pile raft area ratio			
	9.25	6.25	5.25	4.25
2	1.14	0.67	0.59	0.40
10	0.89	0.57	0.45	0.17
20	0.58	0.30	0.30	0.18

5.7. Effect of pile spacing– Square piled raft

The variation of the interaction factor with pile spacing varying from 4d to 7.5d shows identical trend as in the table 4. In the case of 4d spacing the interaction factor at a settlement level of 10mm is around 0.7.

Table 4. α_{pr} in square raft

Settlement (mm)	α_{pr} for various of spacing of piles		
	4d	6d	7.5d
2	1.12	0.57	0.47
10	0.71	0.45	0.37
20	0.60	0.35	0.17

At 2mm settlement level the interaction factor is more than unity indicating that the system behaves as fully piled. At the same time when the spacing changes from 4d to 6d and 7.5d the interaction factor varies from 0.45 to 0.7. From the above study it is seen that when the number of piles, length and the spacing is close, the interaction factor is nearly unity at the initial settlement level of 2mm and reduces at higher

pile spacing, shorter length and lesser number of piles. This behaviour indicates that when the load level is such that the entire friction is mobilized the interaction factor reduces but the system takes higher load compared to that of un- piled raft. However at a settlement level where the load settlement response reaches elasto - plastic level irrespective of the shape of the piled raft the interaction factor varies from 0.6 to 0.8 which is close to the value predicted by Randolph (1993) namely 0.8. The overall variation of the interaction factor under identical condition of EP/ES as 100 predicted by Randolph (1993) is 0.59 to 0.75 and based on the 1g model tests is 0.5 to 1.0. which is more or less in close agreement. However the variation observed is mainly due to the variation in procedure adopted. The study by Randolph is based on numerical modelling and the present study is based on ig model with bed material as sand. However under certain optimum conditions the variation is similar to what has been obtained by Randolph.

It is seen from the study that the variation in the interaction factor computed reduces when the settlement level becomes higher. When the length of the pile and the least lateral dimension of the raft remains equal the interaction factor remains the highest and when the length of the pile to raft diameter is 0.8 the interaction factor remains in the range of 0.5 to 0.9. Similarly in the case of square raft, when the spacing is 4d (d – diameter of the pile) the values are close to the values observed in the case of circular piled raft, with the pile length varying from 0.8D to 1D (D is the diameter of the raft), indicating that the spacing and length play very important role in influencing the behavior.

6. NUMERICAL MODEL BEHAVIOR

Figure 6 and Figure 7 present the quarter model of the circular piled raft under study using the finite element code Ansys. The finite element modeling was done utilizing the symmetry of the circular piled raft model, and so the quarter model was used for the study.

Figure 7 presents the raft contact stress at the initial stages of loading namely 2.1kN and at the final load of 8.1 kN. The load taken by the raft was computed taking the average stress and the percentage was evaluated as a function of the

applied load. It is seen that the load shared by the raft increases from 35% to 65 %.

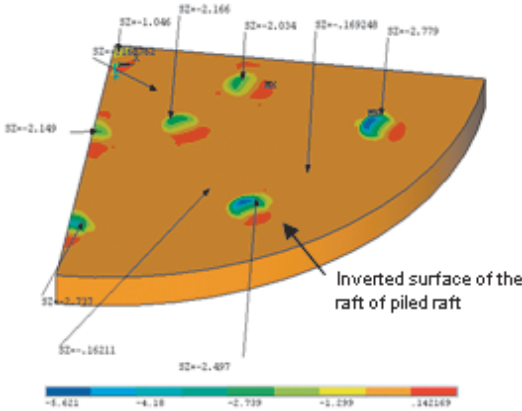


Figure 6. Vertical stress at typical locations of the raft for the load of 8.10 kN (settlement = 17.80mm)

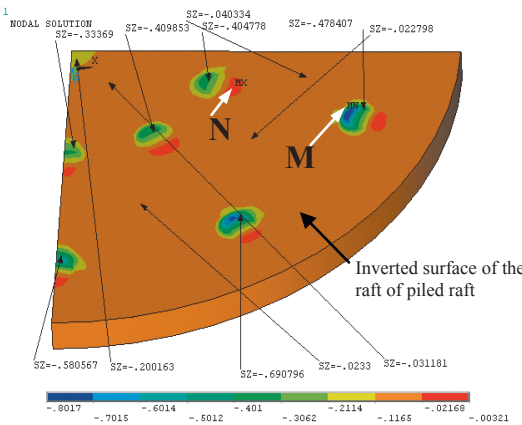


Figure 7. Raft contact stress at typical locations of the raft for the load of 2.1kN (settlement = 1.80mm)

Figures 8a and 8b presents the head stress distribution and the tip stress distribution. It was found that the load taken by the pile increased from centre to outer. Similar observation was made by Horikoshi and Randolph also. A study of the head stress and the tip stress indicate that the tip stress was found to be around 31% of the head stress. However at the final load the ratio of head stress and tip stress was of the order of 11% 9% to 10 and 17% to 19% for the central pile ,inner ring and the outer ring.

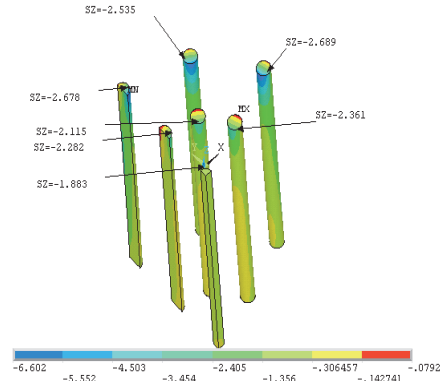


Figure 8a. Pile Head stress for the load of 8.1 kN (settlement = 17.8mm)

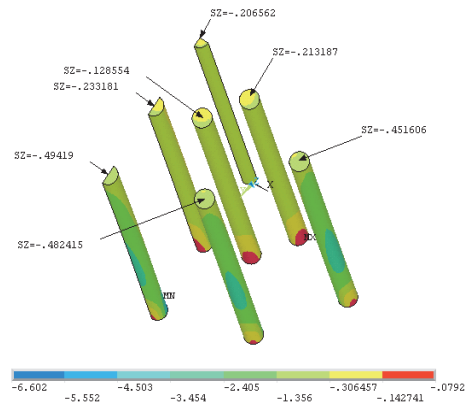


Figure 8b. Stresses in pile tips for the load of 8.1 kN (settlement = 17.8mm)

In each of these cases the difference between the head and the tip load show the shaft stress and the shaft stress variation over the length of the pile is as presented in the Figures 9a and 9b. The increase in the frictional load even at a higher settlement as the load increase is mainly due to the interaction of the raft – soil which increases the confining stress generated in the soil between the piles due to the load transferred from the raft to the soil.

It is seen from the study that as the loading increases the proportion of the load transferred to the pile decreases but the reduction in the load sharing ratio is very small for the load at which the plastic deformation stage namely the stage BC of the characterization curve. It is also seen that beyond the length ratio of 0.6 to 0.8 L (L- length of the pile) the shaft stress mobilized

is very small indicating that the pile group functions as floating piles and the confining stress does not get enhanced beyond this level. This particular length ratio is in agreement with the observations of Vesic. Further, it can be said that the increase in the raft contact stress and the mobilization of the shaft stress from $0.8L$, upwards clearly indicates that enhancement of the confining stress is effective upto $0.8L$ when the length of the pile is equal to the raft dia/ least lateral dimension of the raft.

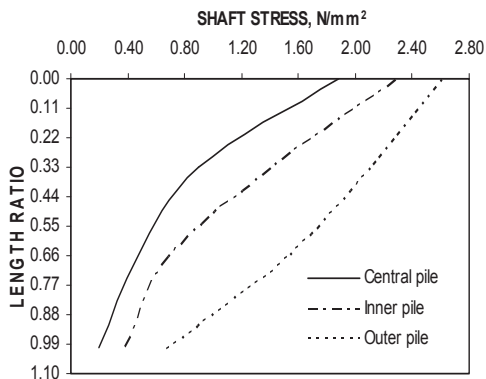


Figure 9a. Variation of stress along the shaft of typical piles along the centre line of raft for 8.10kN

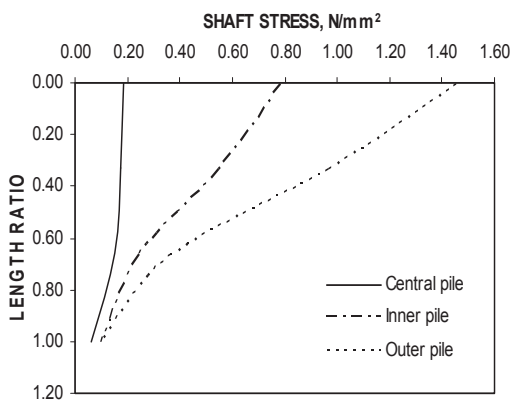


Figure 9b. Variation of stress along the shaft of typical piles along the centre line of raft for 2.10kN

7. OBSERVATIONAL STUDIES

It is a known fact that the results of the observational study are more authentic although as said earlier in certain cases the variation between the

observed values and computed values is higher. Therefore the behavior trend observed in the small scale and the analytical study is compared with the observation of two case histories to establish the predicted behavior. In order to validate the interaction behavior the results of two cases of observational studies have been taken for comparison.

One is related to a commercial cum residential apartment having a basement plus 11 stories supported on piled raft and the other relates to a 33meter diameter storage tank placed on a pile supported raft. The results obtained from the hydro testing of the tank More details of this study is presented elsewhere (Balakumar and Anirudhan, 2012). In both the cases although the nature of the pile layout and the loading patterns were different the behavior trend of the foundation system was similar to that of the results obtained from the 1g model studies In both these cases the loading and the deformation was elastic and linear.

7.1. Commercial cum Residential apartment – Palace Regency

Figure given in the Appendix A presents the pile and column layout of the building. It is seen that the individual columns have been provided with pile group and a raft is cast to serve as the basement. The foot prints of the building measures 32meter X 25meter and the column load ranges from 1075 kN to 2870kN. The piles were 600mm dia 93 numbers terminated on a medium dense to dense sand layer. The raft was 600mm thick. The entire structure was completed in 460 days.

The soil profile and the procedure adopted for monitoring etc are explained in an earlier publication (Balakumar and Ilamparuthy, 2008). The piled raft was modeled numerically adopting the FEA software Ansys. It was decided to carry out linear analyses mainly because the strain level around the pile foundation is very small particularly under the working loads. Hence most of the piled raft problems can be dealt with using the elastic analyses adopting the moduli from small strain considerations. Based on the analyses typical head load and the tip loads are presented in the Figure 10a, 10b. It is seen that the tip load is far less than the head load indicating that the load shared by the pile

has been transferred by friction indicating that the pile group has functioned as floating pile.

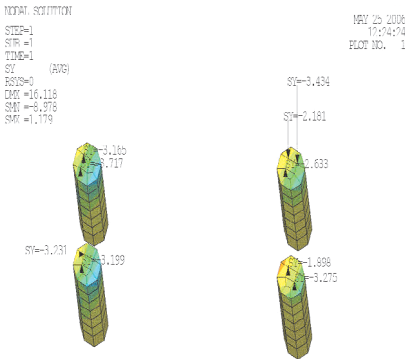


Figure 10a. Typical head stress values

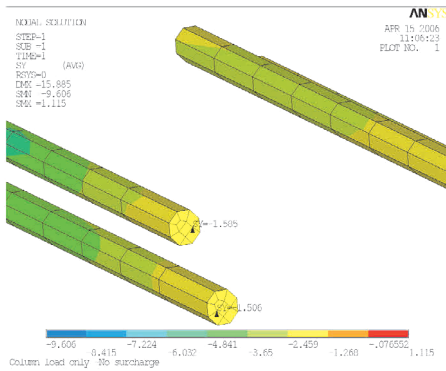


Figure 10b. Typical tip stress values

The Figure11 presents the load shared in the form of block. The percentage of tip load was found to vary from 20% to 30%. The tip resistance of the pile in the central row was found to be higher mainly because of the higher confinement effect was found to be more in the center than in the edges. This behavior is identical to what was found in the numerical analyses.

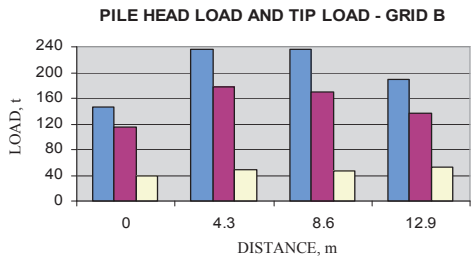
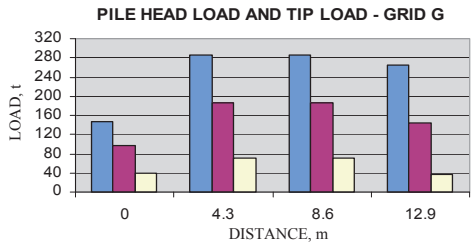
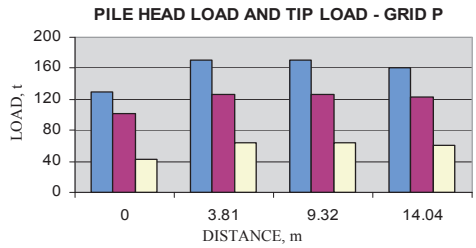


Figure 11. The Head Load – Tip Load Distribution with the column load (continue...)

7.2. Study on the Pile Supported Raft of the Storage Tank

The 33 meter diameter ammonia storage tank located in one of the storage tank farm of a petrochemical project was subjected to hydro test.

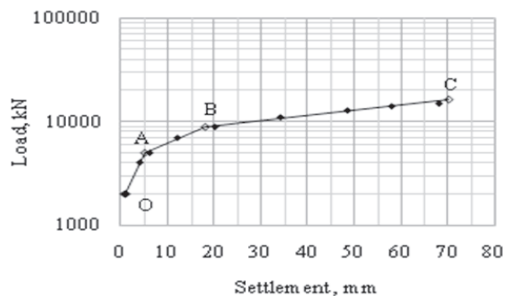


Figure 12. Typical characterized Load Settlement Response – Ammonia Tank

The pile supported raft comprised of 437 piles of 450mm diameter 9m long with lower 6m passing through medium dense to dense strata The raft was 400mm thick. The observed load settlement response is given Figure 12. The entire pile group was considered as equivalent pier.

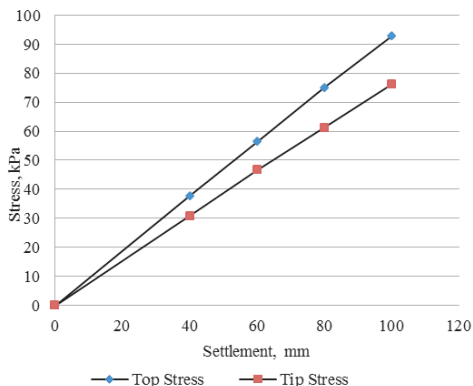


Figure 13. Stress at raft and tip.

The equivalent pier modulus is given as

$$E_{eq} = E_s + (E_p - E_s) * A_t / A_g \quad (3)$$

Wherein E_{eq} is the equivalent pier modulus, E_p is the elastic modulus of the pile E_s is the elastic modulus of the soil A_t is the total cross sectional area of the piles and A_g is the gross area of the pile group. The model was analyzed using Plaxis 2D software as an axi-symmetric problem. In this particular case as the system was a fully piled and the spacing was 2.5 d, where d is the diameter of the pile. An average soil modulus was taken 1.87 E04kpa was taken and the modulus for the piles were taken based on the concrete grade namely M25. Considering the closely spaced pile group the equivalent pier diameter was taken as 32m with 9meter depth and the analyses was done. Figure 13 presents the shaft stress distribution over the length of the pile. It is seen that the variation between the top stress and the tip stress increases with the increase in the settlement. The difference between the top stress and the tip stress although not appreciable the trend in the difference indicates that as the settlement increases the pier tends to behave as a ductile element or floating pile. This behavior trend indicates that

even in the case of closely spaced fully piled pile supported raft system also there is a certain amount of load sharing and a tendency for sharing the applied load. However it is to be noted that in this particular case the pile length is much shorter than the raft dimension .The hydro test load which was of the order of 17.5kN /m² must have had a very deep influence zone and perhaps this is the reason why the difference between the head stress and the tip stress was small unlike the other cases.

8. CONCLUSIONS

The interaction behavior of piled raft was studied through a series of 1g model tests and the results are compared with the numerical analyses. The non-dimensional interaction factor which is a function of the pile group, raft and the piled raft stiffness was evaluated under various parametric conditions. It was established that that the columnar grains contribute to the enhancement of the confining stress leading to the higher pile group stiffness and to the increased capacity of the whole system which is more or less in line what was proposed by Fleming (1985).

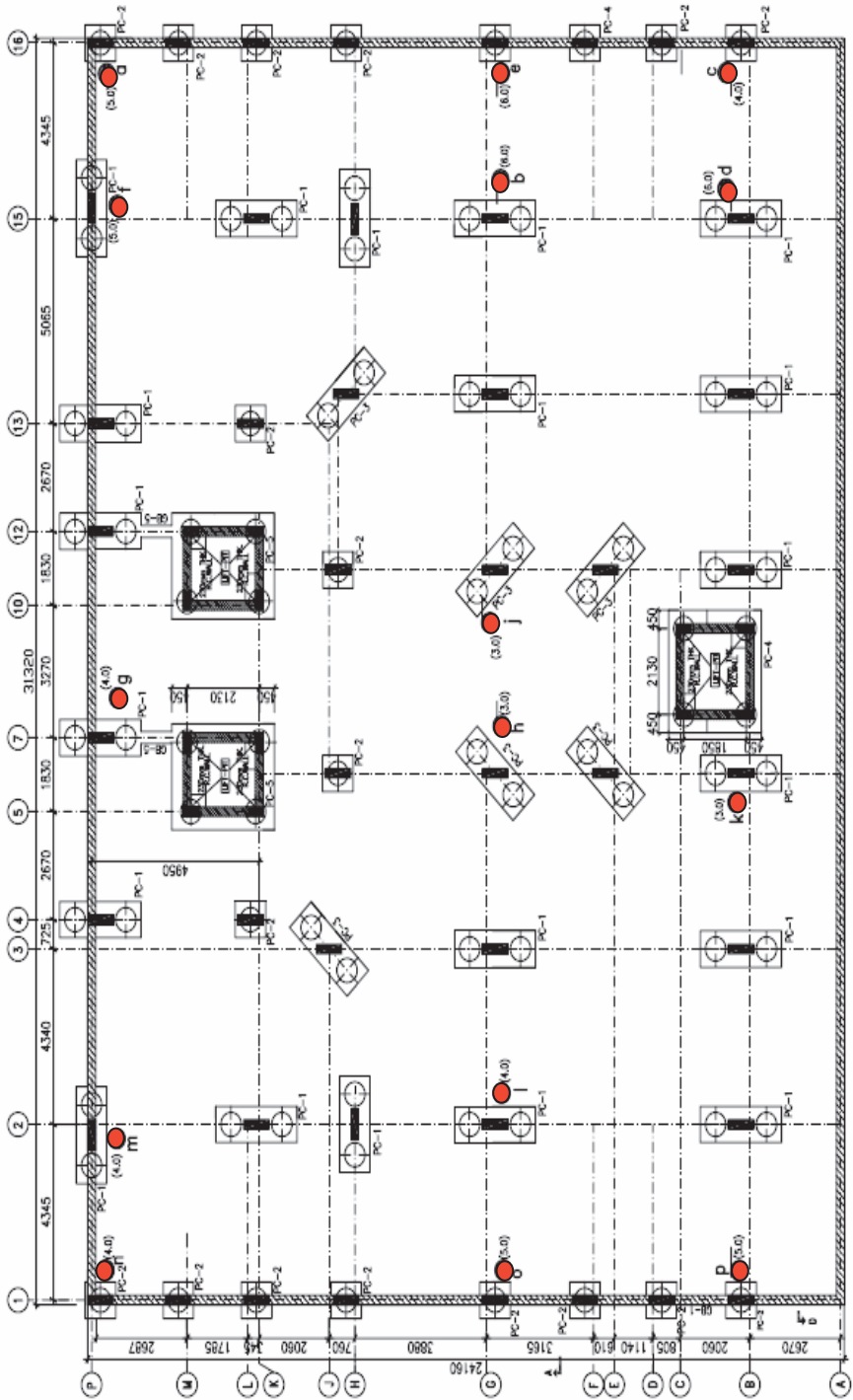
The interaction factor was computed from the model tests and were compared with the values predicted by Randolph. The variation was found to be somewhat wider but perhaps within an acceptable level as the method of study was different. However broadly the value varies from 0.6 to 0.8 at the elasto plastic stage corresponding to a settlement level of 8mm to 10mm in the model tests, which is in close agreement with predicted value with numerical analyses by Randolph although the method of study was different..

The interaction behavior observed in the case of 1g model tests and its numerical analyses was compared with two case studies one being a designed piled raft and the other being a fully piled pile supported raft. In either case the piles and the pile group had a tendency to exhibit a ductile behaviour. Even under a fully piled condition, there existed a load sharing behavior. The entire study has established that under favorable circumstances the piled raft behaves like a shallow foundation and the pile group acts like a soil reinforcement and the combined system of soil-pile reduces the raft settlement.

9. REFERENCES

- Balakumar V. 2008. Experimental Studies of Model Piled Raft on Sand and Field Study of Prototype Behaviour. *PhD. Thesis, Anna University, Chennai*.
- Burland J. B. 1995. Piles as Settlement Reducer. *18th Italian Congress on Soil Mech.*, Pavia.
- Clancy, P. 1993. *Numerical Analysis of Piled Raft Foundations, University of Western Australia*.
- Fleming, W.G.K. 1992. *Geotechnique*, vol.42, No.3, pp 411 – 619.
- Harry G Poulos. 2009. Tall building and deep foundations-middle east challenges. *Proceedings of the 17th International Conference on Soil Mechanics and Geotechnical Engineering*, pp 3173 – 3205.
- Katzenbach R., Arslan V. and Moorman ch. 2000. Numerical Stimulations of Combined Piled Raft Foundations for the New High Rise Building. *Max in Frankfurt am main*, *Proc. 2nd Int. Conf. on Soil Structure Interaction in Urban Civil Engineering*.
- Kim K.N., Lee S.K., Chung C.K., Kim M.N. and Lee H. 2001. Optimal Pile Arrangement for Minimizing Differential Settlements in Piled Raft Foundations. *Computers and Geotechniques*, Vol. 28, pp. 235 – 253.
- Murray E.J. and J.D.Geddes. 1989. Resistance of passive inclined anchors in cohesionless medium. *Geotechnique*, vol. 39, No.3, pp 417 – 431.
- Prokoso W.A. and Kulhawy F.H. 2001. Contribution of Piled Raft Foundation. *Journal of Geotechnical and Geoenvironmental Engineering*, ASCE, pp. 17-24.
- Poulos H. G. 2008. The Piled Foundation for the Burj Dubai – Design and Performance. *IGS – Ferroco Terzaghi Oration*.
- Randolph M.F. 1994. Design Methods for Pile Group and Piled Rafts. *Proc. 13th International Conference on Soil Mechanics and Foundation Engineering, New Delhi*, pp. 5, 61-82.
- Russo G. 1998. Numerical Analyses of Piled Rafts. *Intl. Jnl. Num. and Anl. Methods in Geomech*, Vol. 22, pp. 477-493.
- Turek J. and Katzenbach R. 2003. Small Scale Model Tests with Combined Piled Raft Foundations. *Proceedings of the 4th International Seminar on Deep foundations on Bored and Augured piles, Ghent, Belgium*, pp. 409-413.
- Yamashita K, Hamada J, Yamada T. 2010. Field Measurements on Piled Rafts with Grid-Form Deep Mixing Walls on Soft Ground. *Geotechnical Engineering-SEAGS*. Vol.42, No 2.
- Y. M. El Mossallamy, B. Lutz, and R. Durrwang. 2009. Special aspects related to the behavior of the piled raft foundations. *Proc.of the 17th Intl.Conf. on SoilMechanics and Foundation Engineering*. pp1366-1369.

APPENDIX - A



● — SETTLEMENT MARKER

Lay out of piles and settlement markers

Vertical Pile Stiffness: Pile Load Test Data Base Analyses

Werner Bilfinger, Thaís L. Dada & Pedro C. R. Silva
Vecttor Projetos Ltda., São Paulo, Brazil, werner@vecttor.com.br

ABSTRACT: In foundation engineering ultimate bearing capacity plays an important role. But with increasing complexity and size of structures and foundation, load-settlement behavior is also becoming increasingly important. Particularly in soil structure interaction analysis, foundation stiffness is an important input parameter. This paper presents results of 76 vertical static pile load tests, where pile stiffness is analyzed as a function of the normalized load. A tentative normalized stiffness range, valid for working loads (lower than 50% of the failure load) is proposed.

1. INTRODUCTION

Ultimate bearing capacity is the main issue in foundation engineering. For piles, several methods of ultimate load predictions are available. However, for soil structure interaction, load-settlement behavior is an equally important parameter, but much less prediction methods are available.

This paper presents a simplified approach to estimate vertical pile stiffness, based on results of 76 pile load tests.

This paper includes:

- A brief summary of pile load test types and their analysis;
- The presentation of a database of 76 static load tests;
- Analyses of the load-settlement behaviour, normalizing load and settlement;
- Some conclusions related to the results and proposition of typical pile-soil stiffness values.

2. BACKGROUND

Pile ultimate load prediction, as stated above, is one of the main issues of foundation engineering. Prediction methods are based on site and laboratory soil investigations, and different estimation methods are available. However, the

variability of prediction method results is relatively high. Briaud and Tucker (1988) present COV (coefficient of variation) for predicted \times calculated ultimate bearing capacities between 0.38 and 0.74, for different bearing capacity methods. Similar variabilities (COV) are presented by Décourt (1982), Bilfinger (2002), Rausche et al (2004), Su (2006), and several other authors.

The prediction of load-settlement behaviour is even more complicated and results are normally very variable, influenced by a number of different parameters.

Figure 1 presents the results of 76 pile load tests and confirms that the pile behaviour is extremely variable, especially at loads close to failure.

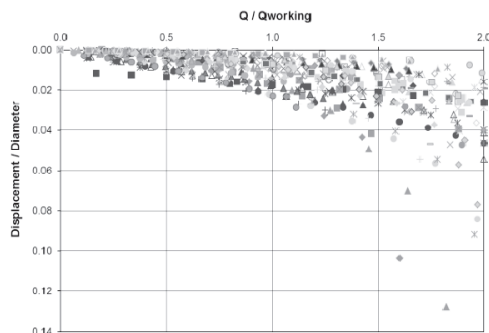


Figure 1. Normalized pile load test results.

It can also be seen that, for loads close to the working load, settlements are low, less than 2% of pile diameter. The use of pile diameter to normalize pile settlement is questionable, but, due to the lack of other simple parameters, it has been a relatively common simplification to correlate settlements to pile diameter.

Considering the above mentioned difficulties to predict pile load-deflection and, on the other hand, the above mentioned behavior, in this paper a simplified approach to estimate pile-soil stiffness for soil structure analyses is proposed, based solely on pile load test results.

3. LOAD TEST DATABASE

Static pile load tests are the best way to evaluate load-settlement behavior. Several standards and test methodologies deal with this topic. The database used for this paper is based on a number of static load tests, performed on piles using slow maintained load. Almost all load tests were performed in Brazil, mainly in the states of São Paulo and Rio de Janeiro. Geological environments of the load tests included soft quaternary sediments, tertiary sediments and residual soils.

Following pile types were included in the database; however, most of the piles are driven pre-cast concrete piles:

- Driven pre-cast concrete piles (diameter from 15 to 80 cm);
- Driven steel profiles (equivalent diameter from 46 to 80 cm);
- Bored piles (diameter from 60 to 80 cm);
- Root piles (diameter from 29 to 40 cm).

The database includes piles that actually failed according to Davison criteria (1973) and piles that did not fail, but reached twice their working load.

Failure loads were extrapolated, where possible, using 4 methodologies: Van de Veen (1953), Décourt (1996), Chin (1971), Massad (1986).

A summary of the data is presented in the Appendix. For identification in this paper, the piles where failure occurred are identified as Group A, and the piles where failures load was extrapolated and/or where unloading occurred reaching twice the working load, as Group B.

4. LOAD – SETTLEMENT BEHAVIOR OF PILES

A number of load-settlement prediction methods is available, like the methodologies presented in DGGT, 2012, or by Poulos & Davis, 1980. Figure 2 presents a number of load-settlement predictions for variable geotechnical conditions, using the method proposed by DGGT. The failure load was estimated using Davison's Criteria.

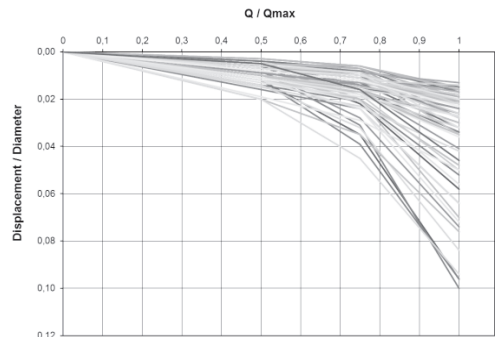


Figure 2. Load-settlement predictions, using the method proposed by DGGT.

It can be seen that load settlement behavior is variable and influenced by a number of factors. However, the number of parameters, as well as the variability associated to each of them, turns this type of prediction complicated and the results are associated to significant variability.

For soil structure interaction analysis, where the ultimate load is often of limited importance, displacements under working loads are a key factor: dividing the working load by the associated displacement, k – the stiffness of the pile-soil system can be obtained:

$$k = \frac{Q}{\delta}$$

Using this parameter, relatively simple soil-structure interaction analyses can easily be performed.

Several times, for this type of simplified analysis, pile-soil stiffness is estimated assuming some ratio with the elastic pile stiffness, EA / L . However, this approach, at least for the

analyzed database, does not yield compatible results.

Figure 3 presents the relation, for working loads, between the measured displacement and the estimated displacements using pile stiffness and correspondent load.

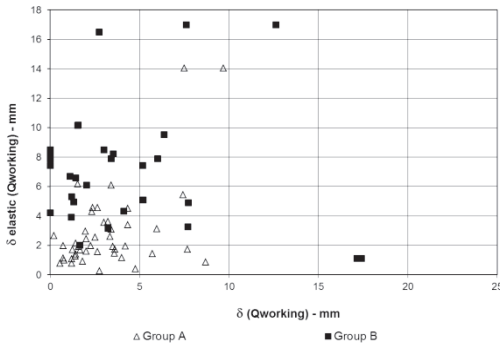


Figure 3. Ratio between the measured displacement and the estimated displacement assuming elastic pile compression

Figure 3 shows that there is no significant correlation between the elastic displacement and the actual measured displacement, for the used load test database.

5. DATABASE ANALYSES

The load-settlement behavior of the load tests of the presented database was analyzed to evaluate possible influence of following parameters:

- Pile type;
- Pile diameter;
- Pile length.

Pile displacement was normalized using pile diameter.

Figure 4 presents the ratio between the normalized pile settlement and pile diameter, considering different pile types and Groups A and B.

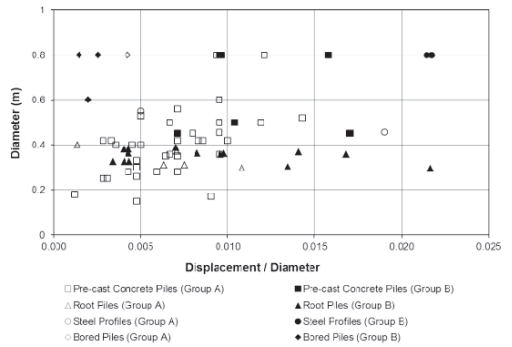


Figure 4. Ratio between the normalized displacement and pile diameter.

It can be seen that there is no clear relation between pile diameter and normalized displacement. It can also be seen that this conclusion is valid for the different pile types.

Figure 5 presents the ratio between the normalized pile settlement and pile length, considering different pile types and Groups A and B.

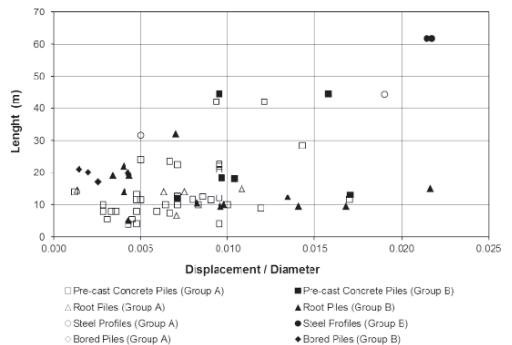


Figure 5. Ratio between the normalized displacement and pile length.

For long piles, where probably superficial soils are soft and compressible, the normalized displacements are higher. However, a clear ratio cannot be determined.

For shorter piles, it can be seen that there is no clear relation between pile length and normalized displacement. It can also be seen that this conclusion is valid for different pile types.

Similar evaluations were performed for different geological environments and no relation between load-settlements behavior could be established.

Figure 6 presents the distribution of normalized displacement for Groups A and B, considering respectively, settlement at 50% of the failure load and 50% of the estimated maximum load.

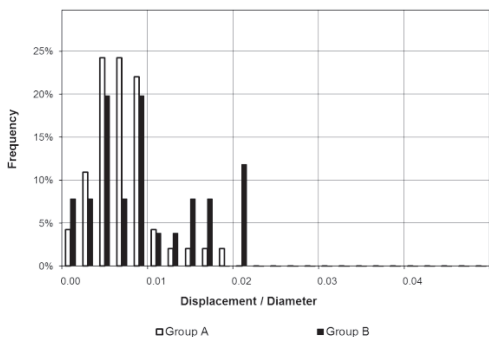


Figure 6. Normalized displacement distribution for 50% of maximum load, for Groups A and B

Figure 7 presents similar results, considering 75% of the maximum load.

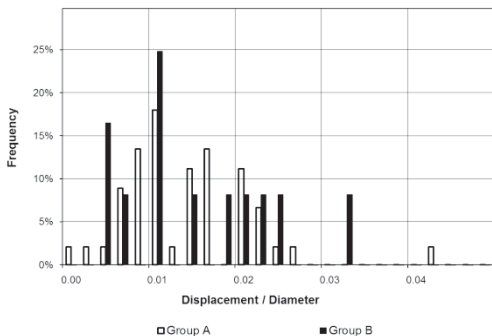


Figure 7. Normalized displacement distribution for 75% of maximum load, for Groups A and B

Tables 1 and 2 present, respectively, average and COV for the values presented in Figures 6 and 7.

Table 1. Normalized displacements for 50% of maximum load

	Group A	Group B	All values
Range	0,12–1,90%	0,15-2,18%	0,12-2,18%
Average	0.73%	0.98%	0.84%
COV	51,4%	65,7%	58,5%

Table 2. Normalized displacements for 75% of maximum load

	Group A	Group B	All values
Range	0,34-4,29%	0,47-3,23%	0,34-4,29%
Average	1.50%	1.54%	1.54%
COV	48,5%	56,9%	48,7%

It can be seen that there is no significant difference between piles of Group A and Group B. Variability can be considered relatively high, but in the same order of magnitude, as the values of usual ultimate bearing capacity estimation methods, meaning that predictions based on the empirically determined values above are associated to variabilities in the same order of magnitude than theoretical or semi-empirical methods to estimate ultimate bearing capacity.

Based on these results, the stiffness of pile-soil system, for working loads, can be estimated using following simplified methodology:

- Estimate necessary working load Q . This estimative is based on structural analyses;
- Using the necessary working load, estimate pile diameter D . This estimative can be performed using average working stresses in the piles, like, for example, 5 MPa in bored and CFA piles, or 6 to 8 MPa, in driven piles;
- Estimate probable settlement for the working load: $d = 0,0084 \times D$;
- Estimate pile-soil stiffness: $k = Q/d$.

Using the data from table 1, it is possible to estimate a range of possible values, considering the obtained range or a statistical approach using a COV of 58,5%.

Additionally, based on the data of tables 1 and 2, and the measured normalized pile settlements at ultimate bearing capacity of the piles of Group A, it is also possible to estimate a simplified load-settlement curve for piles. The average settlements at failure of Group A piles occurs at 3,6% of pile diameter, with a COV of 45,5%. Figure 8 summarizes these results.

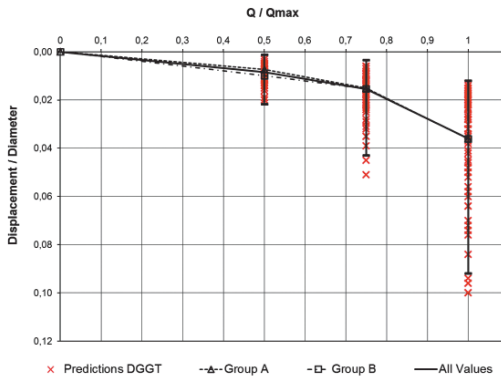


Figure 8. Normalized load-settlement behavior, based on the used data-base. The graph includes also the range of measured values, as well as the range of values using DGGT (2012) methodology predictions.

Figure 8 includes also the range of values of predictions using DGGT (2012). It can be seen that there is good agreement between the empirical values and predictions based on geotechnical parameters.

6. CONCLUSIONS

Based on the results presented in the previous items, some conclusions can be drawn:

- Pile displacement prediction is complicated and usual methods, that assume a direct ratio between displacement and structural pile stiffness, showed not to be reliable, at least for the analyzed data-base;
- Normalized pile displacements cannot be directly related to pile diameter or pile length, considering the analyzed data-base;
- For the analyzed database, for 50% of the maximum load, normalized pile displacements vary between 0,12% and 2,18%, with an average value of 0,84% and a COV of 58,5%.

These values can be used to estimate pile-soil stiffness for simplified soil-structure interaction analysis, as presented in item 5.

Using these values, the normalized displacements for 75% and 100% of the maximum load, a simplified load-settlement curve can also be estimated.

It is important to emphasize that the presented data should be considered only for simplified and preliminary analyses. The variability of results shows that this empirical approach based on a limited number of load tests, may be valid for preliminary calculations, but should never substitute site specific evaluations for final design.

7. REFERENCES

- Bilfinger, W. 2002. Safety criteria of foundations of driven piles using field control methods. PhD Thesis. Polytechnic School, University of São Paulo (in Portuguese).
- Briaud, J. L., Tucker, L. M. 1988. Measured and Predicted Axial Response of 98 Piles. *J. Geotech. Eng. ASCE*, v. 114.
- Chin, F. K. 1970. Estimation of the ultimate load of piles not carried to failure. *Proceedings of the Second Southeast Asian Conference on Soil Engineering*, pp. 81-90.
- Davisson, M.T. 1972. High capacity piles. *Proceedings of Lecture Series on Innovations in Foundation Construction, American Society of Civil Engineers, ASCE, Illinois Section, Chicago*, pp. 81-112.
- Décourt, L. 1982. Prediction of the Bearing Capacity of Piles based exclusively on N values of the SPT. *2nd European Symposium On Penetration Testing*, Amsterdam.
- Décourt, L. 1996. A ruptura de fundações avaliada com base no conceito de rigidez. *SEFE III – 3^o Seminário de Engenharia de Fundações Especiais e Geotecnia*, Anais, São Paulo, pp. 215-224.
- DGGT. 2012. Empfehlungen des Arbeitskreises "Pfähle". Wilhelm Ernst & Sohn, Darmstadt.
- Massad, F. 1986. Notes on the interpretation of failure load from routine pile load tests. *Solos e Rochas*, Vol. 9, No. 1, pp. 33-36.
- Poulos, H. G. Davis, E. H. 1980. *Pile Foundation Analysis and Design*. New York, John Wiley and Sons, 307.
- Rausche, F., Robinson, B., and Likins, G. 2004. On the Prediction of Long Term Pile Capacity From End-of-Driving Information. *Current Practices and Future Trends in Deep Foundations*: pp. 77-95.
- Su, Y. 2006. Bayesian updating for improving the accuracy and precision of pile capacity predictions. *IAEG 2006*.

APPENDIX 1 – Summary of Pile Load Test Database

N°	Pile Type	Diameter (m)	Length (m)	Group	Qworking (kN)	Qmax (kN)	Displ./Diam. (50%.Qmax)	Displ./Diam. (75%.Qmax)	Displ./Diam. (100%.Qmax)
1	Driven Concrete	0,42	10,0	A	-	1330	0,008	0,021	0,027
2	Driven Concrete	0,60	12,0	A	-	1700	0,010	0,024	0,025
3	Driven Concrete	0,40	11,5	A	-	875	0,005	0,008	0,033
4	Driven Concrete	0,42	12,5	A	-	815	0,009	0,017	0,031
5	Driven Concrete	0,42	8,0	A	-	1100	0,003	0,006	0,012
6	Driven Concrete	0,42	8,0	A	-	935	0,003	0,007	0,026
7	Driven Concrete	0,40	8,0	A	-	1105	0,004	0,007	0,026
8	Driven Concrete	0,25	10,0	A	-	489	0,003	0,008	0,026
9	Driven Concrete	0,42	22,5	A	-	1100	0,007	0,014	0,023
10	Driven Concrete	0,35	10,0	A	-	955	0,006	0,011	0,034
11	Driven Concrete	0,15	4,0	A	-	250	0,005	0,010	0,047
12	Driven Concrete	0,33	11,5	A	-	717	0,005	0,012	0,041
13	Driven Concrete	0,50	4,0	A	-	980	0,010	0,015	0,019
14	Driven Concrete	0,30	13,3	A	-	568	0,005	0,009	0,040
15	Driven Concrete	0,50	18,0	B	-	2770	0,010	0,021	-
16	Driven Concrete	0,40	5,5	A	-	1060	0,005	0,012	0,025
17	Driven Concrete	0,42	10,0	A	-	1350	0,010	-	-
18	Driven Concrete	0,25	5,5	A	-	450	0,003	0,008	0,029
19	Driven Concrete	0,17	11,5	A	-	610	0,009	0,018	0,085
20	Driven Concrete	0,52	28,5	A	-	2024	0,014	0,024	0,052
21	Driven Steel	0,55	31,6	A	-	2110	0,005	0,010	0,015
22	Driven Concrete	0,50	9,0	A	-	3400	0,012	0,021	0,036
23	Driven Concrete	0,50	7,5	A	-	3400	0,007	0,013	0,030
24	Driven Concrete	0,18	14,0	A	-	243	0,001	0,006	0,068
25	Driven Concrete	0,26	8,0	A	-	567	0,005	0,012	0,041
26	Driven Concrete	0,35	12,8	A	-	960	0,007	0,014	0,030
27	Driven Concrete	0,28	3,9	A	-	620	0,004	0,012	0,029
28	Driven Concrete	0,28	8,0	A	-	645	0,006	0,014	0,037
29	Driven Concrete	0,28	12,7	A	-	595	0,007	0,012	0,042
30	Driven Concrete	0,53	24,0	A	-	2100	0,005	0,017	0,022
31	Driven Concrete	0,56	10,0	A	-	1420	0,007	0,011	0,020
32	Driven Concrete	0,46	21,0	A	-	1320	0,010	0,024	0,036
33	Driven Concrete	0,46	22,6	A	-	1620	0,010	0,026	0,042
34	Driven Concrete	0,36	23,5	A	-	975	0,007	0,021	0,052
35	Driven Concrete	0,36	22,0	A	-	1385	0,010	0,021	0,062
36	Driven Steel	0,46	44,4	A	-	3200	0,019	0,043	0,092
37	Root Pile	0,36	9,4	B	1300	-	-	-	-
38	Root Pile	0,36	9,4	B	1300	-	0,010	-	-
39	Root Pile	0,36	10,4	B	1300	-	-	-	-
40	Root Pile	0,36	10,4	B	1300	-	0,008	-	-
41	Root Pile	0,36	9,4	B	1300	-	-	-	-
42	Root Pile	0,36	9,4	B	1300	-	0,017	-	-
43	Root Pile	0,37	9,4	B	1300	-	-	-	-
44	Root Pile	0,37	9,4	B	1300	-	0,014	-	-
45	Root Pile	0,36	10,0	B	-	4189	-	-	-
46	Root Pile	0,36	10,0	B	-	4189	0,010	-	-
47	Driven Concrete	0,45	11,6	A	-	1200	0,008	0,015	0,026
48	Driven Concrete	0,45	11,6	A	-	1200	0,017	0,021	0,026
49	Driven Concrete	0,45	13,0	B	1000	-	0,017	0,025	-
50	Driven Concrete	0,45	12,0	B	1000	-	0,007	0,011	-
51	Driven Concrete	0,80	18,3	B	-	6751	0,010	-	-
52	Root Pile	0,38	22,0	B	1310	-	0,004	0,010	-
53	Root Pile	0,36	20,0	B	1310	-	0,004	0,010	-
54	Root Pile	0,31	14,0	A	-	1160	0,008	0,016	0,053
55	Root Pile	0,31	14,0	A	-	800	0,006	0,011	0,040
56	Root Pile	0,31	12,4	B	-	1276	0,013	0,024	-
57	Root Pile	0,30	15,0	A	-	840	0,011	0,025	0,046
58	Root Pile	0,29	15,0	B	-	2158	0,022	-	-
59	Root Pile	0,39	32,0	B	-	3052	0,007	-	-
60	Root Pile	0,33	19,0	B	-	1471	0,003	0,006	-
61	Root Pile	0,32	14,0	B	600	-	0,004	0,007	-
62	Root Pile	0,33	19,0	B	-	1448	0,004	0,018	-
63	Root Pile	0,37	6,6	A	-	1300	0,007	0,017	0,027
64	Root Pile	0,36	6,8	B	-	3237	-	-	-
65	Root Pile	0,38	5,0	B	700	-	0,004	-	-
66	Root Pile	0,40	14,5	A	-	340	0,001	0,003	0,022
67	Bored	0,80	17,0	B	4500	-	0,003	-	-
68	Driven Steel	0,80	61,7	B	2500	-	0,021	-	-
69	Driven Steel	0,80	61,7	B	2500	-	0,022	0,032	-
70	Driven Concrete	0,80	44,5	B	2500	-	0,016	-	-
71	Driven Concrete	0,80	44,5	B	2500	-	0,010	0,015	-
72	Driven Concrete	0,80	42,0	A	-	8400	0,009	-	0,041
73	Driven Concrete	0,80	42,0	A	-	8400	0,012	0,018	0,041
74	Bored	0,60	20,0	B	-	3746	0,002	-	-
75	Bored	0,80	21,0	B	-	4673	0,001	0,005	-
76	Bored	0,80	19,8	A	-	3950	0,004	0,009	0,021

APPENDIX 2 – Summary of Load Settlement Estimatives using DGGT (2012)

Diameter (m)	qc (Base)	qc (Shaft)		δ/ϕ	δ/ϕ	δ/ϕ
				50%.Quit	75%.Quit	100%.Quit
0,2	7,5	7,5	min	0,5%	1,6%	4,6%
			max	0,6%	2,2%	5,8%
	15	15	min	0,8%	2,8%	7,4%
			max	1,2%	3,5%	9,6%
	25	25	min	1,2%	3,9%	9,6%
			max	0,4%	0,7%	2,2%
0,4	7,5	7,5	min	0,4%	0,7%	2,2%
			max	0,5%	1,4%	2,6%
	15	15	min	0,7%	1,0%	2,8%
			max	1,0%	1,6%	3,4%
	25	25	min	0,9%	1,3%	3,2%
			max	1,2%	1,8%	3,8%
0,6	7,5	7,5	min	0,3%	0,6%	1,7%
			max	0,5%	1,0%	1,9%
	15	15	min	0,6%	1,0%	1,9%
			max	0,9%	1,3%	2,2%
	25	25	min	0,8%	1,2%	2,0%
			max	1,0%	1,5%	2,4%
0,8	7,5	7,5	min	0,3%	0,6%	1,5%
			max	0,5%	0,8%	1,5%
	15	15	min	0,7%	0,9%	1,3%
			max	0,7%	1,1%	1,7%
	25	25	min	0,7%	1,1%	1,6%
			max	0,8%	1,2%	1,8%
0,2	7,5	7,5	min	0,5%	2,0%	7,0%
			max	0,8%	3,1%	10,0%
0,4	7,5	7,5	min	0,5%	0,7%	2,8%
			max	0,8%	1,8%	3,5%
	15	15	min	1,0%	1,6%	4,1%
			max	1,4%	2,1%	5,2%
	25	25	min	1,2%	2,0%	4,8%
			max	1,6%	2,4%	6,4%
0,6	7,5	7,5	min	0,5%	0,7%	1,9%
			max	0,8%	1,2%	2,2%
	15	15	min	0,9%	1,4%	2,4%
			max	1,0%	1,6%	3,0%
	25	25	min	1,1%	1,7%	2,7%
			max	1,1%	1,7%	3,5%
0,8	7,5	7,5	min	0,5%	0,6%	1,6%
			max	0,6%	0,9%	1,8%
	15	15	min	0,8%	1,2%	1,8%
			max	0,8%	1,2%	2,1%
	25	25	min	1,0%	1,5%	2,0%
			max	0,8%	1,2%	1,4%
0,4	7,5	7,5	min	0,6%	0,9%	3,5%
			max	1,0%	2,0%	4,8%
	15	15	min	1,4%	2,5%	6,0%
			max	1,4%	3,2%	8,4%
	25	25	min	2,0%	3,5%	7,6%
			max	0,6%	0,9%	2,2%
0,6	7,5	7,5	min	0,6%	0,9%	2,2%
			max	0,8%	1,2%	2,8%
	15	15	min	1,2%	1,8%	3,2%
			max	1,9%	5,1%	10,0%
	25	25	min	1,5%	2,2%	3,6%
			max	1,2%	1,8%	5,0%
0,8	7,5	7,5	min	0,5%	0,9%	3,2%
			max	0,8%	1,2%	2,0%
	15	15	min	1,1%	1,6%	2,2%
			max	0,8%	1,2%	2,8%
	25	25	min	1,2%	1,7%	2,4%
			max	0,8%	1,4%	3,2%
0,4	7,5	7,5	min	0,8%	1,2%	4,6%
			max	1,2%	2,4%	6,4%
	15	15	min	2,0%	4,5%	9,4%
			max	0,7%	1,1%	2,6%
	25	25	min	1,1%	1,8%	3,6%
			max	1,5%	2,3%	4,2%
0,6	7,5	7,5	min	1,2%	2,1%	5,6%
			max	1,9%	2,9%	5,0%
	15	15	min	1,2%	2,4%	7,2%
			max	0,7%	1,0%	2,0%
	25	25	min	0,8%	1,2%	2,3%
			max	1,3%	1,9%	2,7%
0,8	7,5	7,5	min	0,9%	1,5%	3,7%
			max	0,9%	1,5%	3,7%
	15	15	min	1,4%	2,2%	3,0%
			max	0,9%	1,6%	4,5%
	25	25	min	1,4%	2,2%	3,0%
			max	0,9%	1,6%	4,5%

Concept of cities multicomponent underground space as a factor of enhancing safety of its exploration

R.E. Dashko & A.V. Shidlovskaya

National Mineral Resources University, regda2002@mail.ru, shidanna@bk.ru

ABSTRACT: The underground space is considered as a multicomponent system (sand-with-clay and organic soils, groundwater, natural and alien microbiota, biochemical and deep gases, construction materials). The high degree of groundwater contamination with organic and inorganic contaminants generates active development of nature and alien biocenoses. The impact of peculiar contamination on soils degradation, their bearing capacity reduction in the bases of buildings, and, also, the effect of contamination on biochemical aggression of underground space medium, leading to the intensive destruction of bearing construction have been analyzed.

1. INTRODUCTION

Nowadays exploration and use of the underground space of cities is conducted in the following aspects:

- Location of transport infrastructure (metro systems, subways, highway tunnels, deep foundations of bridges etc.);
- Work of underground parts of civil and industrial structures with shallow and deep foundations and various footing areas;
- Construction and usage of utilities including household and storm sewage heating, water supply etc. characterized by large variability of their depth;
- Usage of underground structures for special purposes.

Comprehensive exploration and use of the underground space has apparent economic benefits due to long-term service of underground structures. Well-thought constructive solutions usually lead to reduction of costs of their safe usage, preservation of land resources for their future use for different purposes, reduction of heat energy consumption, limitation of costs of the environment protection.

There is a prospective direction of multi-level exploration and use of the underground space in the global practice. There is experience of French urban architects who developed a

concept of 3-level exploration of the underground space of Paris at different depths taking into account functional particularities of structures being designed.

Today's system of deep lining of utilities in large-diameter tunnels has been existing in cities of Europe, USA and Canada for 40 years, it considerably relieves the upper zone of the underground space and improves environmental state of the underground space. These underground tunnels encase not only the sewage system but also majority of city utility networks. Deep tunnels for utility networks for different purposes have been successfully used in Paris, London, Madrid, Stockholm, Brussels etc. Today deep headers are being designed and constructed in St. Petersburg. American experts in the field of underground exploration have designed and used deep tunnels for multiple purposes which can serve as transport systems, heating lines, treatment facilities etc.

Exploration and use of the underground space in cities of USA, Europe, Japan, South-East Asian, some states of Latin America (firstly, Brazil) resulted in the fact that most of warehouses, refrigerators, garages, restaurants, cafes, gyms, swimming pools, sometimes educational establishments and even churches have been constructed and successfully function under the ground level.

Modern trends of active exploration and use of the underground space of cities should be based, first and foremost, on the safety requirements in the processes of deep pit excavation, lining transportation structures and objects for special use including deep sewage headers as well as development of fields of natural resources in complex mining-geological conditions, burial of extremely hazardous industrial waste in geological strata. This condition requires comprehensive interdisciplinary approach to solution of this important problem of modern civilization addressing to experts in related areas – engineers-geologists, geotechnical engineers, microbiologists etc.

The underground space is considered as a multi-component system which includes soils of different genesis; ground waters characterized by special hydrodynamic and hydro-chemical conditions; biochemical and deep gases; underground microbiota with account of its negative and positive activities including generation of biochemical gases (methane, nitrogen, hydrogen, hydrogen sulfide, ammonia, carbon dioxide etc.), quick soil formation, corrosion of construction materials of underground structures (fig. 1).

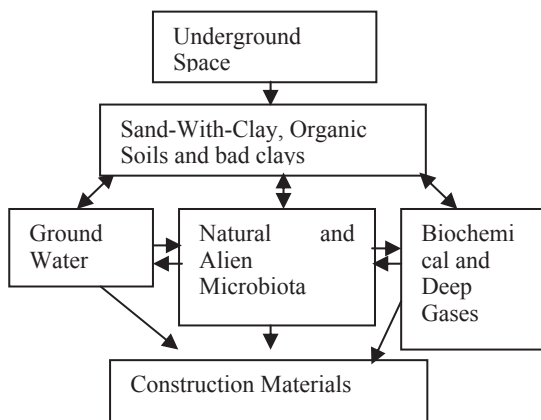


Figure 1. Underground space as a multi-component system.

Solution of the problem of design structural developments and different building construction technology adequacy to existing engineering-geological and geotechnical conditions taking into account nature and intensiveness of use of multi-component underground space is quite important.

Transition of structures in emergency and pre-emergency states during construction and use requires analyzing causes of such situations; attention should be paid not only to construction works technology violation but also to the period of use of a structure. Irreversible soil changes occur during use of a structure in the area of structural influence due to alteration of their stress-strain state as well as physical-chemical and biochemical factors which are not taken into account in theory and practice of engineering-geological and geotechnical investigations and, subsequently, at designing different building and structures.

According to the official data in Russia 63-71% of transitions of structures in emergency state are caused by factors acting in the period of objects usage because one important step – prediction of changing conditions of soil-structure interaction including negative transformation of content, state and physical-mechanical soil properties in time, change of stress-strain state of soils as well as development of hazardous engineering-geological processes - is missing.

2. GROUNDWATER AND ITS ROLE IN THE ASSESSMENT OF THE UNDERGROUND SPACE AS A MULTICOMPONENT SYSTEM

In theory and practice of geotechnical and engineering geological research the oxidation-reduction condition in underground space are not studied. Nevertheless, this aspect is crucial not only to the assessment of strength and consistency of clayey soils but also for biochemical processes such as gas generation and different types of corrosion.

In Saint-Petersburg underground space strongly marked reducing conditions have been registered. The value Eh of the groundwater is less than 0 mV and can decrease to -100 mV (tab. 1).

A crucial role in reducing Eh values of groundwater is played of natural and contamination organic compounds. In 1703 more than 50 % of the territory constituted a formation of peatbogs and peaty soils (fig. 2). Swamps are extremely important for geotechnical and engineering geological conditions. In the process of the city foundation (since 1703) and

construction work peat wasn't removed but, as well as large swamp, it was strewn over. For raising of the surface the soil dug out for construction needs, at the digging of new canals and at the deepening and clearing of rivers was often used.

Table 1. Variations in oxidation-reduction potential in groundwater some island of St. Petersburg historical centre.

Name of island	pH	Eh, mV	Notice
Zayachy	6.88-	(-107)-	Black
	7.11	(-94)	powder
Vasilievsky	6.84-	(-54)-	Smell of
	6.89	(-82)	H ₂ S, black powder
Petrogradsky	7.21-	(+85)-	Black
	7.38	(+17)	powder
Admiralteysky	7.13-	(+68)-	Black
	7.23	(-55)	powder

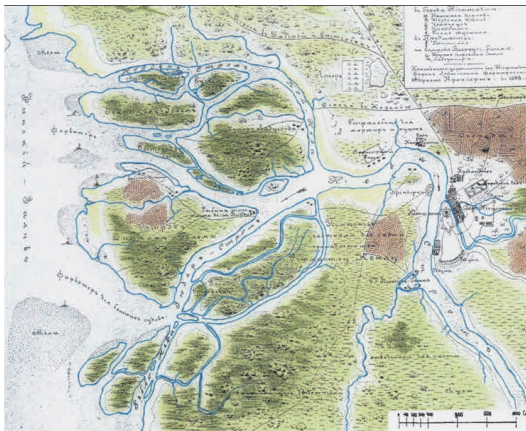


Figure 2. The scheme of marshlands within the future territory of St. Petersburg historical centre (according to the Swedish dates, 1698).

Sewage system is a one of most important factor in the active contamination of the groundwater by organic components. Regional sewerage in St. Petersburg came into exploitation only in the 30-ies of the XX c. In 1950 there existed in the city more than 86000 cesspools which were the permanent source of contamination of groundwaters. Now more than 50 % of underground communications have leakage according to official dates.

Consumer wastes sewers are known to have relatively stable composition - mineral contents is about 42%, organic - 58%. The index of oxygen biochemical consumption (OBC) reaches 85% of oxygen chemical consumption (OCC) index, insolubles are present as suspensions, their colloidal component being represented by albumens, fats, carbohydrates.

The organic compounds present in quantity of some milligrams per 1 liter are known to considerably change the value Eh - pH of water medium.

In strongly marked reducing conditions high content of ammonia, chlorine, bicarbonate ions and low contents of sulphates are defined. The section of some paleovalleys (as for example in Vasilyevsky Islands) shows ammonium contamination of underground waters at more than 50 meters depth; the same is fixed even at comparatively protected intermoraine aquifer.

Biotic contamination of water saturated soils leads to formation of hydrogen sulphide traces of which were identified below the ground water level. Hydrogen sulphide generation is derivative from activity of sulphate-reducing bacteria, common in the underground space of Saint Petersburg historical centre. In reduction conditions, formation of hydrogen sulphide and bivalent iron is accompanied by generation of hydrotrolite $FeS \cdot nH_2O$ in the form of black and dark grey powder which was found throughout the upper strata down to the moraine deposits of the aquiclude.

In anaerobic conditions the transition of metals of variable valence from oxidal to easily soluble protoxid forms is witnessed. First of all this refers to iron, its ferric oxidal combinations are cementing, as a rule, the clay deposits in St. Petersburg section. Iron reduction causes dispergation of clay soils and cementing bonds are destabilized. It is necessary to stress the fact that the most intensive iron reduction proceeds at the growing microbiological activity.

3. GEOTECHNICAL ASSESMENT OF BED CLAYS DURING DEVELOPING AND EXPLOITATION OF UNDERGROUND SPACE

The geological conditions of St. Petersburg call for in-depth studies of bed lithified Upper Vendian and Lower Cambrian clays that are

used as foundation base or construction surroundings for underground structures.

For over 50 years the Upper Vendian clays have been used as the construction surroundings for the underground stations and tunnels of St. Petersburg Metro system. The construction of subterranean sewage collectors began in the clays as early as the 1870s. Upper Vendian clays are regarded as the base layer for pile foundations of the surface structures. Lower Cambrian clays are used as the foundations for the buildings in the Southern suburbs of St. Petersburg and as the construction surroundings for Metro tunnels and sewage collectors in the Southern districts of the city.

The immediate plan is to use bed soils as foundations for the high rise buildings. The term ‘high rise building’ herein defines the structures exceeding 75 m (25 floors) in height with the height to width ratio of 3+. The engineering of these unique structures calls for a new approach to the related geotechnical research, soil investigation. The existing methods of research, as well as of engineering and construction of multi-storied industrial and civil structures, are not necessarily applicable to high rise buildings. The foundation base distributed pressure in high rise buildings can reach 1,5 MPa. The foundation zone of such structures can be 100+ meters deep, which makes it necessary to study the properties of the soils at the respective depths.

Since high rise buildings interact with the base in the same way as the loaded stiff stamp with a flexible base, the main assessment criteria for the stability of such structures are not just the ultimate settlement but also the heeling development through the changing properties of soils and/or eccentricity of load application.

3.1. Bed fissured clays properties

Within most of St. Petersburg territory the Upper Vendian clays are to be found under the layer of Quaternary soils. In the Southern part of the city the Vendian sediments are overlaid by the Lower Cambrian sandstones and clays.

One of the specific features of St. Petersburg traverse section are paleo valleys that run along the tectonic faults and fixate the subterranean relief of pre-Quaternary layers (Fig. 3). The depth of erosion into the bed soils determines

the thickness of Quaternary sediments and the specifics of the bed soils. Outside the buried valleys the upper boundary of bed soils can be traced to the depth of 20–25 m, sometimes even deeper; for the low erosion cut valleys (the cut of less than 30 m) the upper boundary of bed soils is fixated at the depth of less than 40 m, for the medium cut (30–60 m) at 90 m, for the deep erosion cut (60–90 m) at 120 m. Acclivous edges (2-18°) and considerable width (1800-3500 m) are typical for the paleo valleys.

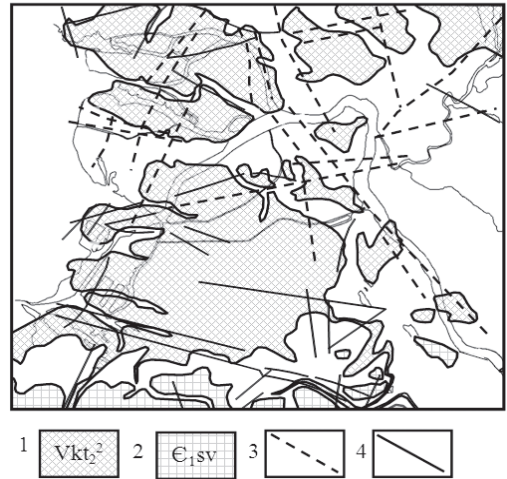


Figure 3. Location of the bed clays upper boundary and of tectonic fault lines in St. Petersburg

1- Upper Vendian clays at the depth of 15 to 30 m; 2 – Lower Cambrian clays at the depth of up to 20 m; 3 – estimated tectonic fault lines; 4 – existing tectonic fault lines.

The Upper Vendian and Lower Cambrian clays under consideration are marine sediments. The accumulation of the clays took place under placid tectonic conditions. The catagenetical transformations of the clays were influenced by several processes, (1) gravitational consolidation of the deposits through the pressure of overlays, (2) tectonic activity at the junction of the Russian Plate and the Baltic Basement and (3) change in thermodynamic and physico-chemical conditions.

The younger, Lower- and Upper Paleozoic sediments, 300—350 m thick, have created additional pressure of 6-7 MPa on the Cambrian and Vendian clays. Subsequently the overlays were eroded, which triggered the processes of regressive lithification and of transformation of layers that brought forth the change of their condition, composition and fissuring (Fig. 4).

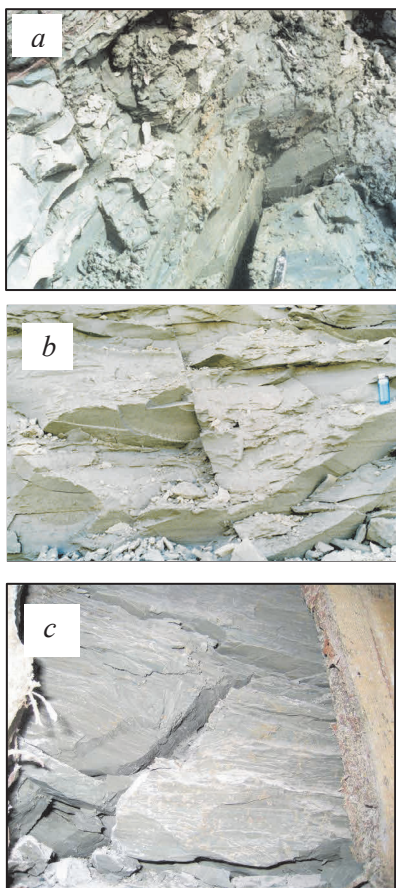


Figure 4. Fissured Lower Cambrian clays in a pit edge (a, b), Upper Vendian clays in a mine (c)

In the glacial periods the bed clays were covered by a thick (over 1000 m) layer of ice and experienced cyclical increase and decrease of stress corresponding to glacial and interglacial periods. In the postglacial and current periods the Vendian and the Cambrian clays covered by a thin layer of Quaternary sediments

go through regressive lithification or have surfaced (Low Cambrian clays).

A notable feature of the structuring of bed clays is their zoning according to physical-mechanical properties and to fissuring; the above is strongly linked to the influence of tectonic and non-tectonic factors.

The tectonic activity at the junction of the Russian Plate and the Baltic Basement manifests itself through tectonic fissures within the clays that form two main systems of North-Western and North-Eastern course; there also are sublateral and submeridional tectonic fissures. The fissures are of vertical or subvertical (70-80°) decline. The intensity of tectonic fissuring of the Upper Vendian and the Lower Cambrian clays reveals itself most clearly in the clusters of tectonic faults; that is confirmed by the intensity of intrushes while tunneling in St. Petersburg.

Lithogenic fissuring is clearly seen in the bed clays, and the thickness of layers between the horizontal fissures decreases from the lower to the upper boundary of the layer.

Non-tectonic fissuring is largely typical for the upper zone of the bed clays section. In the upper zone of the clays regressive lithogenesis, formation of fissures of elastic reaction and of weathering in alternating temperatures and in crystallization of salts took place. In the glacial (progressive lithogenic) period the fissures were formed through glaciotectionics (wedges traced to the depth of 20—25 m) and through frost weathering. In the zones of tectonic faults with the high degree of disintegration of clays, the weathering zones are at their deepest.

3.2. Physical and mechanical properties of bed clays

For the purpose of the analysis of their physical-mechanical properties, clays are treated as block fissured surroundings (Tab. 2).

Table 2. Depth-Related Changes of Fissuring and Water Content in Upper Vendian and Lower Cambrian Clays

Zone No	Layer No	Depth from upper boundary, m	Block size, m	Water content alteration, %
Upper Vendian Clays				
I	1	0-20	0,1-0,5	12-23
	2	20-40	0,5-0,7	10-20
II	3	40-60	0,7-1,0	10-19
	4	60-75	1,2	10-17
	5	>75	>1,2	9-15
Lower Cambrian Clays				
I	1	0-3	0,08-0,25	23-28
	2	3-10	0,25-0,40	21-25
	3	10-20	0,38-0,60	17-21
II	4	20-30	0,40-0,85	16-20
	5	30-40	0,60-0,90	16-19
	6	>40	1,0-1,40	15-18

The first 10—20 m of the clay section feature the minimal water contents and the lowest density. Fissuring decreases with depth, the size of blocks increases accordingly.

In analyzing the strength of bed clays under triaxial compression the difference in parameters is most vivid, especially in the sample cohesion versus in situ cohesion from various depths; the block fissured structuring of the layer is also taken into account. Such pattern is observed for the Upper Vendian clays. (Tab. 3).

Besides, the clays failure axial strain that leads to their destruction decreases with depth. The possibility of lateral strains development predetermines the opening of micro fissures that are particularly common in the upper zones; as the result the upper layers have much lower strength than the deeper horizons.

Table 3. Strength of Upper Vendian Clays in Various Zones.

Zone depth, m	Strength parameters			
	Cohesion (c), MPa		Angle of internal friction (φ), degrees	
	block	in situ	block	in situ
0-10	0,18* /0,14**	0,13 /0,05	5/2	5/2
10-20	0,30/0,05	0,12 /0,02	24/18	24/18
20-30	1,40/0,82	0,60 /0,33	22/11	22/11
30-40	2,04/1,10	1,82 /0,56	23/18	23/18
40-60	2,80/1,90	1,12 /0,62	23/19	23/19

Note: *- values for soils outside tectonic fault zones, ** - values for soils inside tectonic fault zones.

Laboratory tests only allows to assess the mechanical properties of clays in separate blocks with various strengths of structural bonds, degrees of silicification, micro fissuring. The results of the analysis vary dramatically depending on the equipment used. Thus, the tests where lateral strains can develop (with a stabilometer or an unconfined compression apparatus) show the decrease of shear strength by 30—50% versus the tests conducted without this equipment (using direct shear apparatus) (Dashko, 1985)

Incidentally, the strength values obtained in laboratory tests on small samples are higher than obtained in situ. The laboratory assessment of the influence of scale effect on the values of strength for the Lower Cambrian clays has shown that in bigger samples, with the constant height-to-diameter ratio of 2, gradual decrease of clay strength was registered (Tab. 4)

Table 4. Scale Effect Influence on the Strength of Lower Cambrian Clays (samples collected from the depth of 3-10 m)

Sample size, cm ²	20-26,5	40-48	98
Unconfined compression strength, MPa	0,70-	0,24-	0,105-
	0,92*	0,50	0,140
	0,81/6**	0,34/7	0,12/5

Note: *- minimal – maximal values, ** - average value/number of tests

The existing standards of clay deposits properties evaluation in St. Petersburg determine the shear strength parameters through nomograms that depend on consistency index and water content. Actually, fissured bed clays of the Upper Vend show no correlation between the consistency index (I_L) and shear strength parameters (c and ϕ) (Tab. 5).

Table 5. Consistency Index and Shear Strength Parameters of Upper Vendian Clays (Laboratory Tests).

Consistency index, I_L		
-0,25...-0,15	-0,15...0	0...0,15
Cohesion, c , MPa		
0,08...0,12	0,10...0,12	0,09...0,11
Angle of internal friction, ϕ , degrees		
8...10	4...16	0...16

Fissured rocks are characterized by asymmetrical of compressive stress σ_z depend on the angle of bedrocks fissuring (fig. 5).

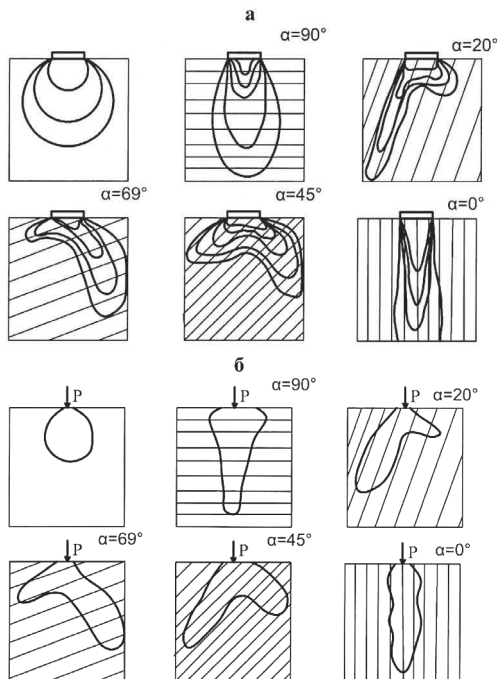


Figure 5. Isobar lines of compressive stress σ_z , obtained on the models (a) and by calculating (б), α - angle of fissure slope or layers relative to vertical (by Goodman)

In the fault zones and the adjacent paleo valleys the bed clays show the highest degree of fissuring and most variable physical and mechanical properties. Since the bed clays of St. Petersburg are fissured, the fissuring has to be taken into account for any structures that have bed clays for their foundation base or construction surroundings.

3.3. The assessment of fissuring bed clays for high-rise buildings

In engineering and construction of high responsibility level buildings in St. Petersburg the influence of fissuring on their maintainability has to be assessed from the following standpoints:

1. Fissuring of bed clays accounts for the much higher strength of small scale samples versus the large blocks of clay. Thus scale effect must be taken into account, i. e. the decrease of strength with the increase of volume of the deformed clay to a maximum value determined by the quasi continuity criteria; once it is reached, fissuring has no more influence on the strength of clay. The indispensable laboratory method of testing is the stabilometer test which allows to expose micro fissures in the samples through lateral expansion. Fissuring of clays has to be studied in the field (in situ) as well as in the laboratory.

2. The aspects of clay fissuring have to be taken into account in engineering, construction and maintenance of unique buildings of St. Petersburg. The standards for construction, geotechnical research, soil investigation must be updated accordingly.

4. ROLE AND CONSEQUENCES OF MICROBIOITA DURING DEVELOPING AND EXPLOITATION OF UNDERGROUND SPACE

Consideration and prediction of microbe activity deserves special attention at analysis and evaluation of transformation of the underground space components. In international and Russian practice the influence of microbiological factors is firstly considered in geo-ecological aspect, i.e. regarding safety for human, animal and plant health. The aspect of influence of natural and alien microbiota on change of content, state

and physical-mechanical soil properties, development of dangerous engineering-geological processes and biocorrosion requires additional studies.

Relevance of studying microbiota activity in the underground space and its impact on its main components was confirmed in the XX century in the framework of the International Symposium in Davos (1996) when a new direction of microbiology associated with the underground space "Subsurface Microbiology" was established.

Within the territory of St. Petersburg, formation and specific nature of engineering-geological conditions is linked with the location features of the city in the delta area of the river at low absolute altitudes of the land surface, which contributes to development of swamps and water-logging across most of the territory. The high degree of water content in the city underground profile and progressive contamination of groundwater and soils with organic and inorganic contaminants due to leakages from a variety of community pipe infrastructures generate prerequisites for active development of natural biocenoses living in marsh sediments, and also for alien microbiota from various technological sources.

4.1. Features of microbiota in the underground space

Microorganisms in the marsh sediments, including peat and sapropel, have a specific magnitude of vital activity, that of microbial mass, expressed in the number of cells per gram of substrate. Activity of microbiota depends on the degree of the organic material decomposition and the climatic conditions in which swamp biota develops. The greatest activity of microorganisms is characteristic of peats with a medium degree of decomposition. With the increasing degree of organic matter decomposition, the intensity of microbial activity decreases, and so do the number of microorganisms and diversity of physiological groups. The top of St. Petersburg's peatland, where transient conditions are registered – from oxidative to reducing ones ($Eh \approx +50$ mV, seldom lower), demonstrates the major groups of nitrifying bacteria with 10^2 to 10^4 cells per g of substrate. The midsection of the peat lands profile ($Eh = 0 \div +50$ mV) abounds in denitrifying bacteria,

with 10^6 cells per g of substrate; in the reduction conditions of the deep zones ($Eh < 0$ mV) there are active sulphate-reducing, anaerobic forms of cellulose-fermenting, ammonifying and methane-producing bacteria. In anaerobic conditions, the number of cells can vary from 10^3 – 10^4 to 10^6 – 10^7 cells per g of substrate.

Thus, the buried paludous sediments, as well as peatlands should be considered as permanent areal "bioreactors" in the upper layer of the underground space of the city, the downward filtration of groundwater thereof causing microbial contamination of the underlying sandy-clayey soils.

A second and very important source of the inflow of microorganisms into the subsurface is leaks from water disposal systems, primarily sewerage system, household waste dumps, as well as liquidated and existing cemeteries. The impact of all the above-mentioned linear, areal and point contaminants can be traced to a depth of 50–70 metres in the underground space of the city.

One millilitre of wastewater contains 10^7 – 10^8 cells of microorganisms. Sewage brings nutrients and energy substrates into the underground environment that are easily utilized by microorganisms, contributing to their development and growth.

An additional natural source of introduction of microbiota into the underground space of the city is gas-generating interglacial sandy-clayey deposits (QIII–QIV) of the Mikulin Interglacial Sea containing up to 20–22% of bituminous organic matter. Microbiological studies of these structures reveal the presence of a high number of anaerobic forms of microorganisms that are involved in natural biochemical generation of slightly soluble gases – methane, nitrogen, – and soluble ones, carbon dioxide, hydrogen sulphide. Deposition of slightly soluble gases in the underground environment leads to formation of high gas-dynamic pressure, which causes transfer of microorganisms in the gas flow. The zone of gas-generating strata and gas flows demonstrates active destruction of the load-bearing lining in underground railway tunnels.

Investigation of redistribution of microorganisms in water-saturated sand-clay soils shows that less than 10% of the total microbiota in the depth under study is present in the aqueous phase; most of the living and dead cells of

the microorganisms and their metabolic products are adsorbed on disperse particles, forming biofilms with a complex layered structure at the nanoscale.

It was recognised certain types of microorganisms in Quaternary sandy clayey soils of St. Petersburg contaminated with sewages and petroleum products over the period of more than 250 years (fig. 6).

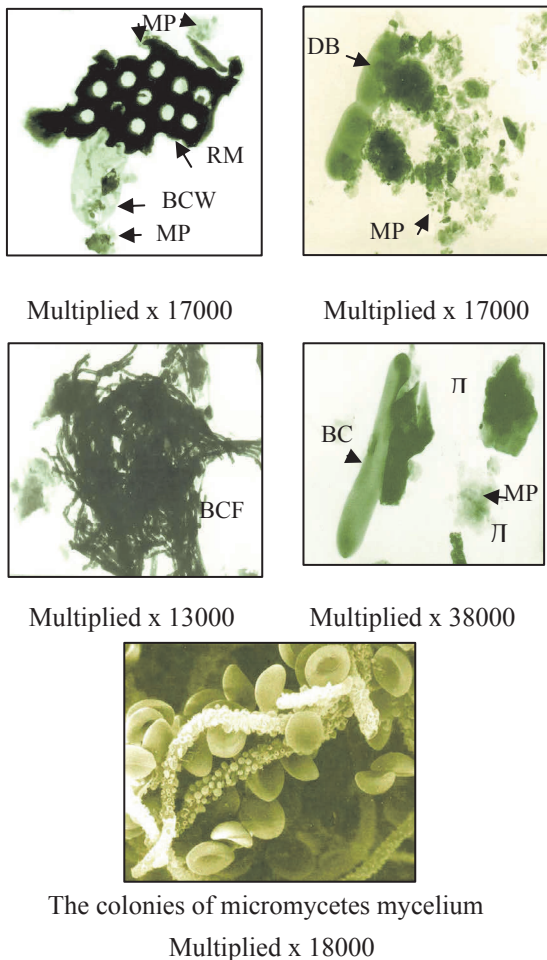


Figure 6. Microbiota in underground space of St. Petersburg historical centre. Samples taken from 6.0-40.0 m. MP – metabolic products, RM – residual microfungi, BCW – bacterial cellular wall – “cellular shade”, DBC – dividing bacterial cell, BCFC – bacterial colony of filiform cultures, BC – bacterial cell.

The activity of microorganisms in the deeper parts of the underground space section of the city should be analyzed from the following standpoints: transfer of microbiota with the ascending flow of high-pressure mineralized sodium chloride waters of the Lower-Kotlin aquifer through the thickness of fractured clay aquitards (the Upper-Kotlin clays of the Upper Vendian rocks) and inflow of microorganisms due to the transfer from the upper and most contaminated horizons, as well as local sources in the areas with gas flows.

4.2. Features of transformation of groundwater and sandy-clayey soils, with participation of microbiota

Vital activity of microorganisms is accompanied by accumulation of biomass of live and dead cells, as well as metabolic products of protein nature.

The total content of protein compounds is expressed by the index of the bacterial mass (BM), which we determine using the biochemical Bradford method:

$$BM = Blmo + Bdmo + BMpm,$$

where Blmo and Bdmo are protein values of live and dead cells of microorganisms, respectively; BMpm is protein products of their metabolism (T.N. Nizharadze, E.A. Pushnova, 1988).

Accumulation of BM depends on the availability of nutritional substrates, pH and Eh values of the environment, temperature and humidity regimes, as well as soil sorption capacity and gas production intensity.

Assessment of the accumulation of microbial activity using the value of BM for the Quaternary and Upper-Kotlin clays of the Vendian period, is based on the results of numerous definitions, depending on affinity of the cross section of the strata to contamination sources (Table 5).

Table 5. Variations in bacterial mass (BM) in the Quaternary and bedrocks, depending on the intensity of their contamination with sewage and petroleum products

Type of soil	Content of bacterial mass (BM), $\mu\text{g/g}$ in the areas of:		
	No contamination	Contamination via sewage (> 200 years) and oil products (> 60 years)	
Littorina Sea sediments mIVt			
Sandy loam with organic matter	25-30	75-151/114(14)	
Sands with organic matter		99-144/105(19)	
Lake-glacial deposits of the Baltic Ice Lake lgIIIvd ₃ ^b			
Clay loam	20-38	40-89/63(10)	
Ribbon clays		95-188/135(17)	
Luga moraine deposits gIIIvd ₃ lz			
Clay loam	10-20	72-129/94(12)	
Intermorainal deposits f,lg II-III			
Clay loam	15-10-35	80-125/98(5)	
Moscovian moraine deposits gIIms			
Clay loam	20	90-98/93(8)	
Upper-Kotlin clays of the Upper Vendian Vkt ₂ ²			
Bed clays	≤ 10	Outside paleovalleys	In slope part
		101-275/183 (15)	97-234/160 (12)

Of particular interest are moraine clay deposits in assessing stability of structures with pile foundations, where the above-mentioned soils are the bearing strata. The apparent reliability of moraine deposits is usually associated with high density and stable forms of consistency values. However, depending on the conditions of formation of moraines and connection to contamination zones, their consistency can change to less stable (Table 6).

Table 6. Physical and mechanical properties of clay moraines, depending on the redox conditions in the moraine thickness

Section	W, dimensionless	I_L	Strength parameters		E_o , MPa
			C, MPa	ϕ , degrees	
I	0.08-0.14	<0.25	>0.15-0.32	>15-25	$\geq 40-50$
II	0.14-0.17	0.25-0.45	0.04-0.07	6-10	2.4-4.3
III, IV	0.16-0.19	0.25-0.50	0.03-0.05	0-7	2.1-3.6

I – oxidizing zone moraine; II – moraine in transition or reduction conditions is crossed with lake-glacial deposits; III – moraine under reduction conditions, under a layer of Littorinal, lake-glacial deposits; IV – moraine under reduction conditions under swamps.

Under conditions of contamination via effluents containing organic compounds and microbiota, the most marked decline in the parameters of strength and modulus of total deformation occurs in the oxidizing zone moraines (Table 7).

Table 7. Variations in shear strength (c, ϕ) and modulus of total deformation (E_o) in moraines contaminated with organic matter microbiota

Parameters	E_o , MPa	ϕ , degrees	c, MPa
In oxidizing conditions, with BM background content <30 $\mu\text{g/g}$	> 25	>15	0.15-0.22
In a reducing environment, with BM 65–136 $\mu\text{g/g}$	2.0-8.0	<10	0.03-0.11

When moraines are polluted in the transient and reducing zones, a slower decline in their strength is observed. At numerous sites in the historic part of St. Petersburg, these deposits show a tendency to develop plastic deformations.

Intensification of microbe activity at such depths of the underground space is highly important for implementation construction projects of superstructures with considerable foundation areas, underground structures such as metro, deep headers etc. as well as reconstruction and restoration of heavy historical buildings which substrata are complicated with a large bulk of water and gas saturated soils. Models of quasi-plastic environments should be used for such microbe-affected clayey soils.

High levels of microbial infestation is also characteristic of sandy soils, when they are polluted. Increased BM in sands leads to an increase in their hydrophilicity, along with a sharp decrease in water gravity yield and permeability. As shown by field and laboratory studies, in the presence of adsorbed biomass on the sand grains and fine suspended matter colmatating the pore space, the filtration coefficient of the medium- and fine-grained sand is reduced to $n \cdot 10^{-2}$ and $n \cdot 10^{-4}$ m/day (at pressure gradients of 20). Removal of organic matter and biota in drying the sands leads to an increase in filtration coefficient up to 4–20 m/day.

With reduced filtration capacity, sands exhibit pronounced features of quicksands, emergence of ‘clots’ is observed, as well as instant slipping down of the walls in the well drilling process.

Significant decompaction of sands and their transition into the quicksand state is caused by accumulation in the depth of sandy soils of slightly soluble biochemical gases such as nitrogen, hydrogen and methane generated by micro-organisms. An important factor in increasing the mobility of the sands is the reduced angle of internal friction and water gravity yield. Activation of microbial activity and gradual accumulation of biomass in clayey soils translates them into the quasiplastic state.

Our research conducted in late XX century witnessed that even negligible content of microbe mass comprising tens and hundredths of soil mkg/g ($n \cdot 10^{-3}$ – $n \cdot 10^{-2}$ %) has negative

impact of permeability, strength and strain capacity of the affected sands. Microbe-affected sands become quick soils that complicate carrying out of construction works and require to be taken into consideration at developing technological schemes of advancement in such soils.

4.3. Biocorrosion in the underground space

Processes of biochemical corrosion of materials which occur with direct involvement of micro-organisms become highly significant. Relevance of research in this field is proven by emerging and intensive development of new scientific directions such as ‘Geo-microbiology’, ‘Construction microbiology’, ‘Geo-micology’, ‘Microbiology of the Underground Space’ in recent years.

Biocorrosion can proceed at the expense of: 1) direct effect produced by metabolism products, first of all such gases as CO_2 , NH_3 , H_2S and also organic and non-organic acids formation; 2) organic products formation creating a medium which acts as corrosion reactions catalyst; 3) corrosion reactions can proceed as part of microorganic metabolic cycle (Rogers, Liechtenstein, 1968).

Biocorrosion aggressiveness of the underground environment is formed due to accumulation of products of bacterial metabolism, carbon dioxide, hydrogen sulphide, mineral and organic acids, as well as enzymes. In addition, microorganisms are capable of retrieving the missing elements necessary for their vital activity, from the crystal lattice of minerals. As studies show, the processes of biological corrosion affect all types of building materials including concrete, reinforced concrete, metals, ceramics and wood. According to the data of different investigators from 50 to 70 % of all corrosion losses are ascribed to microorganisms. Biocorrosion is most active in building materials which is are under tension.

The key destructors of building materials include bacteria, micromycetes and actinomycetes, attacking them in different ways.

Emergence of acidic environments is associated with the activity of nitrifying bacteria (Nitrosomonas and Nitrobacter), which oxidize ammonia or ammonium entering in sufficient quantity the underground space with sewage effluents, to nitrous and nitric acids: $\text{NH}_4^+ +$

$11/2O_2 \rightarrow NO_2^- + 2H^+ + H_2O$, $NO_2^- + 1/2O_2 \rightarrow NO_3^-$. These acids cause destruction of cements and carbonates, as well as certain clay minerals.

Among the bacteria growing in an aerobic environment, and creating an acidic environment, thione bacteria (genus *Thiobacillus*) have particularly destructive properties. Thiobacteria play a major role in oxidation of sulphides to sulphuric acid ($HS^- + 2O_2 \rightarrow H^+ + SO_4^{2-}$, $S_2O_3^{2-} + 2O_2 + H_2O \rightarrow 2H^+ + 2SO_4^{2-}$), which in case of exposure to metals becomes an electrolyte on their surface, and activates electrocorrosion processes, followed by oxidation of Fe^{2+} to Fe^{3+} . Thiobacteria grow at low pH values, but can also continue their activities under alkaline conditions. Of the greatest danger for porous materials are bacteria *Thiobacillus thiooxidans*, which are able to generate sulphuric acid.

Also actively involved in destruction of porous building materials in the transition (microaerophilic) redox conditions are denitrifying bacteria, the main representative of which being *Pseudomonas denitrificans*. Denitrification occurs in two stages:

- 1) reduction of nitrates to nitrites;
- 2) reduction of nitrites to free nitrogen.

Typically, in building structures this process is completed with the first stage. The energy source for these bacteria is organic matter. In addition to nitrites and N_2 , biochemical reactions also produce NH_3 and aggressively acting CO_2 as a respiration product of microorganisms.

It is known that the corrosion of metals was noticeably intensified in reducing medium in which ammonium forming bacteria are actively propagating. On the base of studying anaerobic biocorrosion mechanism a theory of metal cathodic depolarization was worked out. Water medium containing Fe^{2+} ions, dissolved oxygen and carbonic gas, and ammonium salts or nitrates at pH = 5-6 is optimal for ferrobacteria propagating. These bacteria are actively propagating at Fe^{2+} oxidation, which leads to corrosion of metal construction placed lower than ground water level in aerobic conditions.

Biocorrosion of materials is greatly enhanced if the bacteria develop in conjunction with fungal cultures that break down wood, consisting of cellulose (major component), lignin, pectins, gums, tannins, proteins and other compounds. The most common decomposition of wood is caused by the following

micromycetes: *Chaetomium*, *Stachybotrys*, *Stysanus* *Trichoderma*, *Cladosporium*, *Stemphyllium*, *Fusarium*. Activators of fungal corrosion can grow and develop with a high moisture content of wood, in aerobic, more seldom anaerobic conditions, and destroy cements and metals as a result of formation of acidic environments.

Tests conducted by microbiologist in 2003-2009 (Vlasov D.Yu.) confirmed a defining role played by microorganisms (micromycetes and bacteria) in integrity degradation of Peter and Paul Cathedral's construction materials in Saint-Petersburg. The samples studied revealed presence of 39 types of micromycetes, among which the greatest diversity of species was identified for genus *Penicillium* (10 species) (figure 7). The majority of micromycetes identified in various samples of construction materials are classified as active decomposers of construction materials.

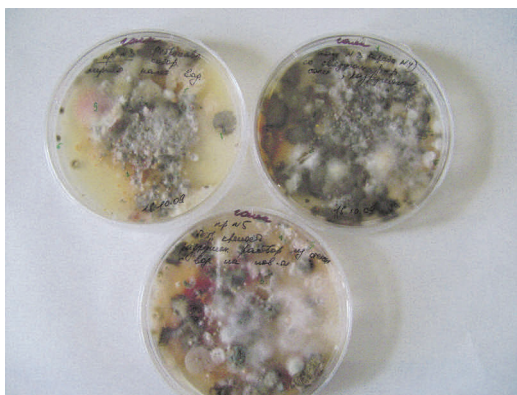


Figure 7. The mycology analyze of samples from Peter and Paul Cathedral's construction materials (Petri dish).

Corrosion of underground escalator constructional materials in Saint-Petersburg has been investigated since 2005. A detailed study and numerical analyses of escalator tunnel constructional materials were carried out to reveal biological defeat and destruction of concrete and grey iron as a result of microbiota destructive activity (figure 8).



Figure 8. Active biocorrosion of reinforced-concrete tubing of Saint-Petersburg Metro systems

A considerable role of biocorrosion in degradation of the Cheboksary Hydropower Plant concrete constructions is ascertained using the results of investigating the chemical composition of aqueous extracts from destroyed concrete samples and sinter forms, chemical composition features of the water from piezometers and the water basin and the results of microbiological analysis of the destroyed construction materials. The main forms of concrete degradation of overfall dam and turbine hall building are shown on the figure 9.

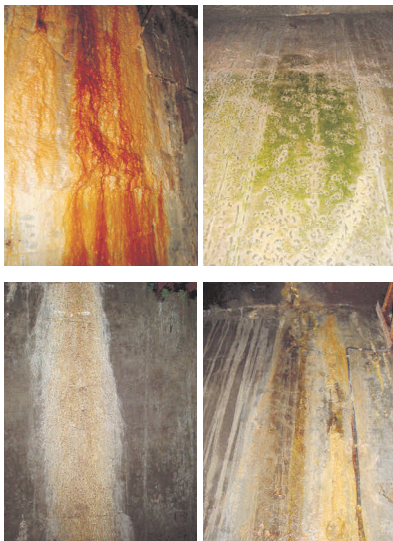


Figure 9. The different types of biocorrosion in degradation of the Cheboksary Hydropower Plant concrete constructions

Microbiosis is also found in underground tunnels construction materials (blaster) in Paris St. Lasare train station. It was known that the train station St.Lasare was constructed in 1837 and was exploited during 176 years.

Both of construction materials samples are characterized by high quantities of saprophyte bacteria – more than 10^6 CFU per gram. The quantity of oligotrophic bacteria is very high and can increase to $6 \times 10^5 - 10^6$ CFU per gram that shows the high duration of biodestruction processes and presence of big quantities of organic matter (Table 8).

Table 8. Microbiosis in the construction materials of St. Lasare train station (Paris)

Samples №	Quantity of microorganisms, CFU (colony-forming unit) per gram				
	Total quantity of saprophyte	Oligotrophic bacteria	Actinomyces	Thiobacteria	Micromycetes
Plaster № 1	$5,7 \times 10^6$	$4,5 \times 10^5$	$4,3 \times 10^4$	no more than 10^3	less than 5×10^2
Plaster № 2	$6,1 \times 10^6$	$2,1 \times 10^6$	$2,1 \times 10^4$	no more than 10^3	$3,0 \times 10^3$

Microbiota of plaster № 1 consist mainly of bacteria (beige, orange and yellow colony) and gram-positive Kokken (white and pink colony). The quantity of micromycetes is low.

Microbiota of plaster № 1 consist of dominant bacillus (genus Bacillus) – white colony on the picture (Figure 10).

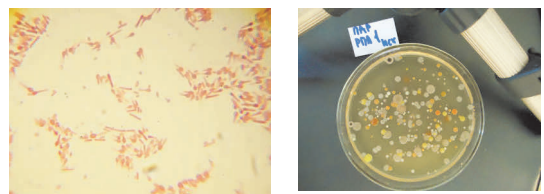


Figure 10. Microbiota in the construction materials of St. Lasare train station (Paris)

5. CONCLUSION

In engineering geology and geotechnics the research has to be assessed from the following main standpoints.

1. Fissuring of bed clays accounts for the much higher strength of small scale samples versus the large blocks of clay. Thus scale effect must be taken into account, i. e. the decrease of strength with the increase of volume of the deformed clay to a maximum value determined by the quasi continuity criteria; once it is reached, fissuring has no more influence on the strength of clay. The indispensable laboratory method of testing is the stabilometer test which allows to expose micro fissures in the samples through lateral expansion. Fissuring of clays has to be studied in the field (in situ) as well as in the laboratory.

2. The aspects of clay fissuring have to be taken into account in engineering, construction and maintenance of unique buildings of St. Petersburg. The standards for construction, geotechnical research, soil investigation must be updated accordingly.

3. Negative effects due to growth in the number of cells of microorganisms and their metabolites, biochemical activity leading to negative transformations in the state and properties of soils, gas generation, formation of gas-dynamic pressure and development of quick-sands, thixotropic soils, deep degradation of concretes, mortars, metals (iron, steel), ceramics and wood.

4. Positive role of microorganisms, which manifests itself in self-purification and self-regulation of polluted groundwater, especially with non-toxic contamination by organic compounds – petroleum hydrocarbons (pH); in the presence of a rich biocenosis, a complete degradation of pH is observed; the most active self-cleaning of groundwater from pH is observed when their content does not exceed 50–80 mg/L.

The microbial factor in the study of engineering and geological conditions of the underground space of cities and industrial regions in their development and utilization has not been reflected in the existing regulations or in predicting long-term sustainability of surface and underground facilities. This position should be

entered into subsequent regulations and guidelines.

6. REFERENCES

- Bagrintseva, K. I. 1982. Treshchinnovatost osadochnyh porod (Sedimentary rocks fissuring). M., Nedra. 256 p. (In Russian).
- Dashko, R.E. 2011. Microbiota in underground space: role and consequences. *Environmental Geosciences and Engineering Survey for Territory Protection and Population safety. International conference EngeoPro-2011*: 517-521.
- Dashko, R.E. et al. 2011. Geotechnical Assessment of Bed clays as Foundation and unique constructions projects in Saint-Petersburg. *Environmental Geosciences and Engineering Survey for Territory Protection and Population safety. International conference EngeoPro-2011*: 521-525.
- Dashko, R.E. 2003. Problems of Geoecology in Geotechnics, *Reconstruction of historic towns and geotechnical construction*: Vol.1: 95-106. Saint-Petersburg.
- Lengeler, J et al. 2005. *Sovremennaya mikrobiologiya. Prokarioty: V 2 tomah*. Moscow: Mir.
- Dashko R.E., Shidlovskaya A.V., Aleksandrova O.Yu. Rol' mikrobioty v inzhenernoj geologii i geoekologii: istoriya voprosa i rezul'taty eksperimental'nyh issledovanij // *Sergeevskie chteniya*. M., GEOS, 2004, vyp. 6., s.48-52 (Dashko, R.E., Shidlovskaya, A.V., Alexandrova, O.Yu. The role of microbiota in engineering geology and Geoecology: background and experimental results // *Sergeevskie readings*. Moscow, GEOS, 2004, vol. 6, p.48-52)

Eurocode 7 on 'Geotechnical design': a Code for Soil-Structure Interaction

R. Frank

Université Paris-Est, Navier, Ecole nationale des ponts et chaussées – CERMES, France

ABSTRACT: Eurocode 7 on 'Geotechnical design' is actively being implemented throughout Europe. In particular, Part 1 devoted to the 'General rules' (Part 1) was published by CEN in 2004 and National Annexes have been prepared for implementation in the various European countries. After describing shortly the history of the development of Eurocode 7, and giving the main contents, some aspects of particular interest to the soil-structure interaction modelling are described: design approaches (DA1, DA2 and DA3) for ULS verifications in persistent and transient design situations, SLS verifications and allowable movements of foundations.

1. INTRODUCTION

The Structural Eurocodes are design codes for buildings, bridges and other civil engineering structures. They are based on the Limit State Design (LSD) approach used in conjunction with a partial factor method. They consist of 10 sets of standards: 'Eurocode: Basis of structural design' (EN 1990) and Eurocodes 1 to 9 (EN 1991 to EN 1999; EN is for 'European Norm')

Eurocodes 2, 3, 4, 5, 6 and 9 are 'material' Eurocodes, i.e. relevant to a given material (reinforced concrete, steel, etc.). EN 1990 (Basis of design), Eurocode 1 (Actions), Eurocode 7 (Geotechnical design) and Eurocode 8 (Earthquake resistance) are relevant to all types of construction, whatever the material.

Eurocode 7 should be used for all the problems of interaction of structures with the ground (soils and rocks), through foundations or retaining structures. It allows the calculation of the geotechnical actions on the structures, as well the resistances of the ground submitted to the actions from the structures. It also gives all the prescriptions and rules of good practice for conducting the geotechnical part of a structural project or, more generally speaking, a purely geotechnical project.

Eurocode 7 consists of two parts:

EN 1997-1 Geotechnical design - Part 1: General rules (CEN, 2004)

EN 1997-2 Geotechnical design - Part 2: Ground investigation and testing (CEN, 2007)

In this paper, only Eurocode 7 – Part 1 on 'General rules' is mentioned.

The development of Eurocode 7 – Part 1 has been strongly linked to the development of EN 1990: 'Eurocode: Basis of structural design' (CEN, 2002) and the format for verifying ground-structure interaction problems is, of course, common to both documents.

After describing shortly the history of the development of Eurocode 7, and giving the main contents of the document, this Paper comments some aspects directly linked to soil-structure interaction, without recalling all the principles of LSD and of the partial factor method used.

2. DEVELOPMENT OF EUROCODE 7 AND MAIN CONTENTS

2.1. History and implementation

The first Eurocode 7 Group, in charge of drafting a European standard on geotechnical design, was created in 1981. It was composed of repre-

sentatives of the Member Societies of ISSMGE of the 10 countries forming the European Community at that time. A first model code on general rules for geotechnical design (corresponding to Eurocode 7- Part 1) was published in 1990.

In 1990, the task of drafting design codes for buildings and civil engineering works was transferred to the Comité Européen de Normalisation (CEN, European Committee for Standardization) and CEN/TC 250 (Technical Committee 250) in charge of all the 'Structural Eurocodes' was created. In particular, SC 7, Sub-Committee 7, is in charge of Eurocode 7 on 'Geotechnical design'. Note that CEN is composed of the national standard bodies of a number of European countries (in 2013, 33 countries are members, i.e. 27 countries of EU, plus 3 countries of EFTA, Croatia, FYR of Macedonia and Turkey).

In 1993, SC 7 adopted the ENV 1997-1 pre-standard: 'Geotechnical design - Part 1: General Rules'. It was clear, at that time, that (much) more work still needed to be done before reaching a full European standard (EN) acceptable to all members of CEN. An important fact helped in obtaining a positive vote for the conversion into an EN (May 1997). It was the recognition by CEN/TC 250 that geotechnical design is unique and cannot be considered to be the same as other design practices needed in the construction industry. The models commonly used vary from one country to the other and cannot be harmonised easily, simply because the geologies are different and form the rationale for the so-called 'local traditions'... This recognition is confirmed by a resolution taken by TC 250 (Resolution N 87, 1996): '*CEN/TC 250 accepts the principle that ENV 1997-1 might be devoted exclusively to the fundamental rules of geotechnical design and be supplemented by national standards*'.

The work for the conversion of ENV 1997-1 into EN 1997-1 'Geotechnical design – Part 1: General rules' was performed from 1997 to 2003. The positive vote on the versions in the 3 working languages of CEN (English, French and German) was obtained in 2004 (the vote was nearly unanimous: 26 countries out of 28 expressed a positive vote). CEN finally published Eurocode 7 – Part 1 (EN 1997-1) in November 2004 (CEN, 2004).

The publication of a Eurocode Part by each national standardisation body, in the official language(s) of the country, is to be accompanied by a National Annex. The role of the National Annex is to indicate the decisions corresponding to the so-called "Nationally Determined Parameters (NDPs)". The National Annex can also give a 'normative' status to one or to several of the 'informative' Annexes, i.e. it (they) will be mandatory in the corresponding country.

As mentioned above, each country is also free to supplement the general rules of Eurocode 7 by national application standards, in order to specify the calculation models and design rules to be applied in the country. Whatever their contents they will have to respect in all aspects the principles of Eurocode 7.

The 'legal' status of standards/norms is different in each country and the regulatory bodies of the various countries have an important role to play for the implementation of the Eurocodes. A 'Guidance Paper' has been elaborated by the European Commission to co-ordinate the implementation of the Eurocodes into the national regulations. (CE, 2003a). The European Commission has also issued a strong recommendation to the Member States inviting them to adopt the Eurocodes in their regulations (CE, 2003b).

2.2. Contents of the document

Eurocode 7 - Part 1: 'General rules' is a rather general document giving only the principles for geotechnical design inside the general framework of LSD. These principles are relevant to the calculation of the geotechnical actions on the structural elements in contact with the ground (footings, piles, basement walls, etc.), as well as to the deformations and resistances of the ground submitted to the actions from the structures. Some detailed design rules or calculation models, i.e. precise formulae or charts are only given in informative Annexes. Eurocode 7 – Part 1 includes the following sections (CEN, 2004):

- Section 1 General
- Section 2 Basis of geotechnical design
- Section 3 Geotechnical data
- Section 4 Supervision of construction monitoring and maintenance
- Section 5 Fill, dewatering, ground

improvement and reinforcement

- Section 6 Spread foundations
- Section 7 Pile foundations
- Section 8 Anchorages
- Section 9 Retaining structures
- Section 10 Hydraulic failure
- Section 11 Overall stability
- Section 12 Embankments

A number of Annexes are included. They are all informative, except for Annex A which is 'normative' (i.e. mandatory). They are the following :

Annex A (normative) Partial and correlation factors for ultimate limit states and recommended values

Annex B Background information on partial factors for Design Approaches 1, 2 3

Annex C Sample procedures to determine limit values of earth pressures on vertical walls

Annex D A sample analytical method for bearing resistance calculation

Annex E A sample semi-empirical method for bearing resistance estimation

Annex F Sample methods for settlement evaluation

Annex G A sample method for deriving presumed bearing resistance for spread foundations on rock

Annex H Limiting values of structural deformation and foundation movement

Annex J Checklist for construction supervision and performance monitoring

Annex A is important, as it gives the partial factors for ULS in persistent and transient design situations ('fundamental combinations'), as well as correlation factors for the characteristic values of pile bearing capacity. But the numerical values for the partial or correlation factors given in Annex A are only recommended values. These values can be changed in the National Annex. All other Annexes are informative (i.e. not mandatory in the normative sense). Some of them, though, contain valuable material which can be accepted, in the near future, by most of the countries.

3. SOME ASPECTS OF SOIL-STRUCTURE INTERACTION

3.1. General

It can be argued that the whole of Eurocode 7 is devoted to soil-structure interactions, as its first role is to provide the geotechnical rules for the structures designed with the so-called system of 'Structural' Eurocodes (see Introduction above).

From the viewpoint of the structure, Eurocode 7 provides the principles for determining the geotechnical actions (noted P in Figures 1 to 3 in section 3.2 below, where only vertical equilibrium is considered). The geotechnical (P) and structural (G and Q) actions and the "reactions" from the ground (noted E), in turn, allow to check the resistance and/or the deformation of the structural element in contact with the ground. From the viewpoint of the ground, Eurocode 7 deals not only with the geotechnical actions on the structural element (P), but also with the deformations of the ground and its resistances (R) corresponding to the "reactions" (E). The "reactions" (E) are the forces provided by the ground, which equilibrate both the structural actions (G and Q) and the geotechnical actions on the structure (P) ($E = -V$ in Figures 1 to 3). The values of the resistances of the ground correspond to the limiting values for the "reactions" in ultimate limit states verifications (ULS), i.e. $E \leq R$ must be satisfied.

This assumes that the loads on the structural element have been determined previously. Soil-structure interaction studies, in the pure sense, aim precisely at determining the loads and the displacements of the structural elements in contact with the ground. They take into account, of course, both the stiffness of the ground and the stiffness of the structure (see, for instance, Frank, 1991). Most often they use numerical methods (finite element method, load transfer functions, etc). The way to apply numerical methods in geotechnical engineering is not really the subject of Eurocode 7. Nevertheless, it comprises a large number of recommendations relevant to their use. It can even be noted that many of the requirements of Eurocode 7 are not practicable without recourse to numerical modelling, e.g. those relevant to the determination of the displacements of foundations.

In the following, the approaches advocated by Eurocode 7, for the ultimate limit state (ULS) verifications are described (i.e. sets of partial factors to be used for G, Q, P and R). The requirements for serviceability limit state (SLS) verifications and allowable movements of foundations, which are relevant to the displacements of foundations, are also considered.

3.2. ULS verifications

The ultimate limit states (ULS) to be checked are defined, in the following manner, by Eurocode 7 – Part 1, consistently with ‘Eurocode: Basis of structural design’ (CEN, 2002) (clause 2.4.7.1 in EN 1997-1) :

‘(1)P Where relevant, it shall be verified that the following limit states are not exceeded:

- loss of equilibrium of the structure or the ground, considered as a rigid body, in which the strengths of structural materials and the ground are insignificant in providing resistance (EQU);
- internal failure or excessive deformation of the structure or structural elements, including footings, piles, basement walls, etc., in which the strength of structural materials is significant in providing resistance (STR);
- failure or excessive deformation of the ground, in which the strength of soil or rock is significant in providing resistance (GEO);
- loss of equilibrium of the structure or the ground due to uplift by water pressure (buoyancy) or other vertical actions (UPL);
- hydraulic heave, internal erosion and piping in the ground caused by hydraulic gradients (HYD).

NOTE: Limit state GEO is often critical to the sizing of structural elements involved in foundations or retaining structures and sometimes to the strength of structural elements.’

The ultimate limit states should be verified for the combinations of actions corresponding to the following design situations (see EN 1990, CEN, 2002) :

- permanent and transient (the corresponding combinations are called ‘fundamental’);
- accidental ;
- seismic (see also Eurocode 8 - Part 5, i.e. EN 1998-5).

The design values of the actions and the combinations of actions are defined in EN 1990 (partial factors γ for the actions and factors ψ for the accompanying variable actions).

For the soil-structure interaction, STR and GEO are the relevant ultimate limit states (in the case of foundations submitted to uplift by vertical forces, UPL must also be checked). For STR/GEO, EN 1997-1 writes (clause 2.4.7.3.1(1)P) : ‘... it shall be verified that

$$E_d \leq R_d \quad (2.5)$$

where: E_d is the design value of the effects of all the actions, R_d is the design value of the corresponding resistance.’

The debate about the format for checking the STR and GEO ultimate limit states was relevant to the persistent and transient design situations. This debate follows from the formulation in the pre-standard ENV 1997-1 which inferred that STR and GEO had to be checked for two formats of combinations of actions, i.e. for Cases B and C, as they were called at that time. B was aimed at checking the uncertainty on the loads coming from the structure, and C the uncertainty on the resistance of the ground. Some geotechnical engineers were in favour of this double check, as others preferred having to use only one single format of combinations of actions (for more details, see, for instance, Frank and Magnan, 1999).

The consensus reached opened the way to three different Design Approaches (DA 1, DA 2 and DA 3). The choice is left to national determination, i.e. each country can state in its National Annex, the Design Approach(es) to be used for each type of geotechnical structure (spread foundations, pile foundations, retaining structures, slopes or overall stability).

The three Design Approaches are the following (clause A1.3.1 in EN 1990) :

‘(5) Design of structural members (footings, piles, basement walls, etc.) (STR) involving geotechnical actions and the resistance of the ground (GEO) should be verified using one of the following three approaches supplemented, for geotechnical actions and resistances, by EN 1997 :

Approach 1: Applying in separate calculations design values from Table A1.2(C) and Table A1.2(B) to the geotechnical actions as well as the other actions on/from the structure. In common cases, the sizing of foundations is

governed by Table A1.2(C) and the structural resistance is governed by Table A1.2(B) ;

Note : In some cases, application of these tables is more complex, see EN 1997.

Approach 2 : Applying design values from Table A1.2(B) to the geotechnical actions as well as the other actions on/from the structure ;

Approach 3 : Applying design values from Table A1.2(C) to the geotechnical actions and, simultaneously, applying partial factors from Table A1.2(B) to the other actions on/from the structure. Note : The use of approaches 1, 2 or 3 is chosen in the National annex.'

Tables 1 and 2 give, in a simplified manner, the recommended values for buildings taken from Tables A1.2(B) and A1.2(C) of EN 1990 (CEN, 2002). The recommended values given may also be modified by National decision. Note that, for continuity with the ENVs, the sets of partial factors are noted 'Set B' and 'Set C'.

Table 1. Recommended values for partial factors for actions on buildings (STR/GEO, Set B)

Action	Symbol	Value		
		Eq. (6.10)	Eq. (6.10a)	Eq. (6.10b)
Permanent				
-unfavour ⁽¹⁾	γ_{Gsup}	1.35	1.35	1.15 ⁽²⁾
-favour ⁽¹⁾		1.00	1.00	1.00
Variable				
-unfavour	γ_Q	1.50	1.5 ψ_0	1.50
-favour		0	0	0
(1) all permanent actions from one source are multiplied by γ_{Gsup} or by γ_{Ginf} .				
(2) value of ξ is 0.85, so that $0.85\gamma_{Gsup} = 0.85 \times 1.35 \cong 1.15$.				
Note 1 : choice between expression 6.10 or expressions 6.10a and 6.10b used together, is by National decision				
Note 2: γ_G and γ_Q may be subdivided into γ_g and γ_q and the model uncertainty factor γ_{sd} . $\gamma_{sd} = 1.15$ is recommended.				

Table 2. Recommended values for partial factors for actions on buildings (STR/GEO, Set C)

Action	Symbol	Value
Permanent actions		
- unfavourable	$\gamma_{G,sup}$	1.00
- favourable	$\gamma_{G,inf}$	1.00
Variable actions		
- unfavourable	γ_Q	1.30
- favourable		0

In other words, Design Approach 1 (DA1) is the double check procedure coming from the ENV 1997-1 (B+C verification). Design Approaches 2 (DA 2) and 3 (DA 3) are new procedures using a single format of combinations of actions. DA 2 is elaborated with 'resistance factors' for the ground (RFA), as DA 3 makes uses of 'material factors' for the ground (MFA).

Whatever the Design Approach selected, it is to be noted that STR and GEO ULS are checked with the same values of partial factors, i.e. with the same combinations of actions.

Two important remarks should be made at this point :

- with regard to the choice between Eq. 6.10 or Eqs 6.10a and 6.10b of EN 1990 (see table 1 for set B), Eurocode 7 only mentions Eq. 6.10 (table A.3 in the note to paragraph A.3(1)P of Annex A in EN 1997-1). This derives from the fact that there is no experience on the use of Eqs 6.10a et 6.10b in geotechnical engineering...

- for DA 2 and DA 3, the partial factors can be applied either on the actions or on the effects of the actions (they are noted γ_F and γ_E , respectively). This is relevant to the factors of set B and of set C (unfavourable variable actions).

Table 3 gives the link between Sets B and C and the corresponding sets of factors for geotechnical actions and resistances : Sets M1 and M2 for material properties (e.g. shear strength parameters c' , ϕ' , c_u , etc.) and Sets R1, R2, R3 and R4 for total resistances (e.g. bearing capacity, etc.). These sets are defined in Annex A of Eurocode 7 – Part 1. As mentioned above, Annex A also gives their recommended values which may be set differently by the National Annex. Note that the recommended values for the partial factors γ_M on material properties in Set M1 are always equal to 1.0.

Table 3. STR/GEO limit states. Partial factors to be used according to EN 1997-1

Design Approach	Actions on/from the structure	Geotechnical	
		Actions	Resistances
1	B	B and M1	M1 and R1
	C	C and M2	M2 and R1 or M1 and R4*
2	B	B and M1	M1 and R2
3	B	C and M2	M2 and R3
*for piles and anchorages			

Figures 1, 2 and 3, as well as their captions, illustrate the situation for each of the three Design Approaches. On these figures, index 'd' indicates a design value with a partial factor γ different from 1.0 and index 'k' indicates a value equal to the characteristic value. The values recommended by EN 1997-1 are used and, for simplicity, only vertical equilibrium is considered and only unfavourable actions have been shown in these figures.

In DA 1, the first format (combination 1, former case B) applies safety mainly on actions, while the factors on resistances have recommended values equal to 1.0 (Sets M1 and R1) or near 1.0 (Set R1 in the case of axially loaded piles and anchorages); in the second format imposed by DA 1 (combination 2, former case C), the shear strength parameters are always factored for the calculation of geotechnical actions and sometimes factored for the calculation of resistances (Set M2); in the case of axially loaded piles and anchorages, the total resistance is directly factored by applying Set R4. In DA 2, safety is applied both on the actions (Set B) and on the total ground resistance (Set R2). In DA 3, safety is applied both on the actions (Set B for the actions coming from the structure and Set M2 for the properties of the ground acting on the structure, i.e. for the geotechnical actions) and on the geotechnical resistances (Set M2 for the elementary properties; the recommended values for Set R3 for the total geotechnical resistance is always equal to 1.0, except for piles in tension and anchorages for which they are equal to 1.1).

More details on the use of the three Design Approaches for persistent and transient situa-

tions are given, for instance, in Frank et al. (2004).

Figures 1 to 3 also show some specific features of geotechnical design compared to structural design:

- some geotechnical actions depend on the ground resistance (e.g. earth pressures against retaining walls; downdrag on piles);
- some geotechnical resistances, on the other hand, depend on the actions (e.g. bearing capacity of shallow foundations under eccentric or inclined loads).

Thus, actions and resistances, cannot always be completely separated.

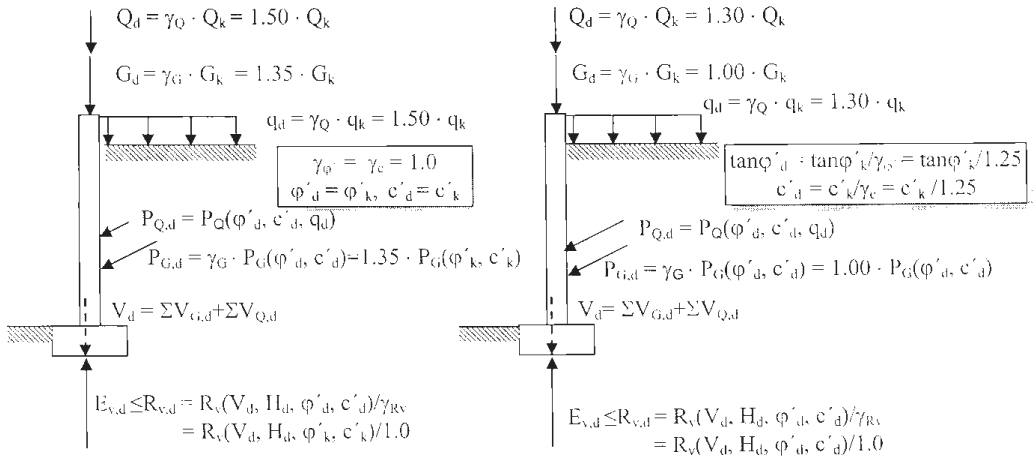
With regard to the design values for accidental situations, Eurocode 7 only states that (clause 2.4.7.1 in EN 1997-1) : '*(3) All values of partial factors for actions or the effects of actions in accidental situations should normally be taken equal to 1,0. All values of partial factors for resistances should then be selected according to the particular circumstances of the accidental situation.*

NOTE The values of the partial factors may be set by the National annex.'

3.3. Verification of serviceability limit states (SLS)

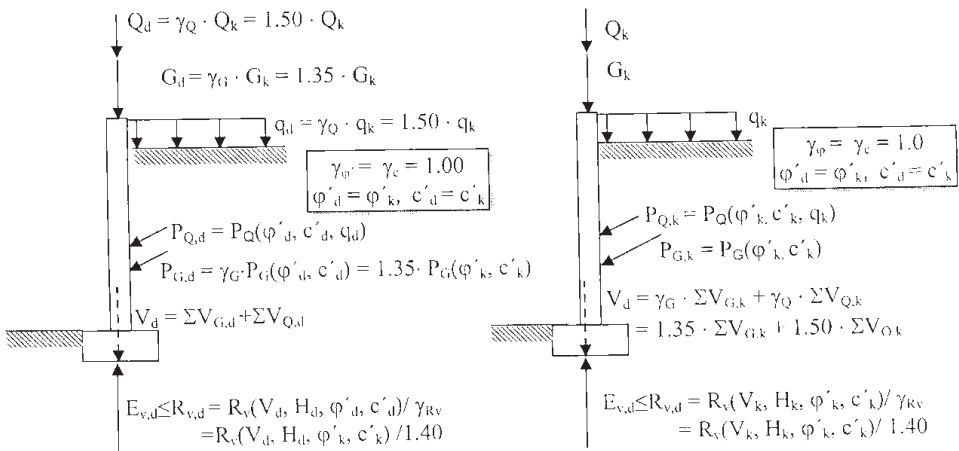
The main discussions during the development of Eurocode 7 were about the format for verifying ULS in permanent and transient situations. However, the verification of serviceability limit states (SLS) is an issue equally important in contemporary geotechnical design. This issue is fully recognised by Eurocode 7 which indeed often refers to displacement calculations of foundations and retaining structures, while common geotechnical practice mainly sought so far to master serviceability by limiting the bearing capacity or by limiting the shear strength mobilisation of the ground to relatively low values.

The verification of SLS in the real sense proposed by Eurocode 7 (prediction of displacements of foundations) is certainly going to gain importance in the near future. For the time being, it is an aspect which is too often neglected in common geotechnical practice.



Note : for simplicity, only vertical equilibrium is considered and only unfavourable actions are shown.

Figure 1. Design Approach 1 - Combination 1 (left), Combination 2 (right) (after Frank et al., 2004)



Note : for simplicity, only vertical equilibrium is considered and only unfavourable actions are shown.

Figure 2. Design Approach 2 - Factoring the actions at the source (left), factoring effects of actions (right; Design Approach DA2*) (after Frank et al., 2004)

Eurocode 7 - Part 1 repeats the formulation of EN 1990 (clause 2.4.8, EN 1997-1) :

(1) *P Verification for serviceability limit states in the ground or in a structural section, element or connection, shall either require that:*

$$E_d \leq C_d \quad (2.10)$$

or be done through the method given in 2.4.8(4).

(2) *Values of partial factors for serviceability limit states should normally be taken equal to 1.0.*

NOTE The values of the partial factors may be set by the National annex.'

with E_d the design value of the effect of actions and C_d the limiting value (serviceability criterion) of the design value of effect of actions. At the same time, Eurocode 7 introduces immediately the possibility to keep the traditional approach mentioned above (clause 2.4.8) :

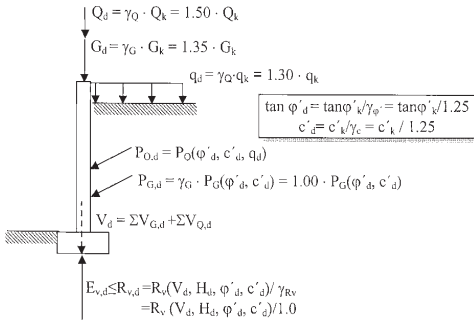


Figure 3. Design Approach 3 (after Frank et al., 2004)

'(4) It may be verified that a sufficiently low fraction of the ground strength is mobilised to keep deformations within the required serviceability limits, provided this simplified approach is restricted to design situations where:

- a value of the deformation is not required to check the serviceability limit state;
- established comparable experience exists with similar ground, structures and application method.'

This clause is to be linked to the one dealing with the design methods of spread foundations (paragraph 6.4(5)P in EN 1997-1) :

'(5)P One of the following design methods shall be used for spread foundations:

- a direct method, in which separate analyses are carried out for each limit state. When checking against an ultimate limit state, the calculation shall model as closely as possible the failure mechanism, which is envisaged. When checking against a serviceability limit state, a settlement calculation shall be used;
- an indirect method using comparable experience and the results of field or laboratory measurements or observations, and chosen in relation to serviceability limit state loads so as to satisfy the requirements of all relevant limit states;
- a prescriptive method in which a presumed bearing resistance is used (see 2.5).'

Indeed, the indirect method 'chosen in relation to serviceability limit state loads' comes to applying the traditional method of designing the bearing capacity of spread foundations, i.e. a simple calculation comparing the applied loads for serviceability limit states to a limit load divided by a global factor of safety high enough (usually around 3). Of course, as indicated in

Eurocode 7, this can only be valid if there is no need to assess the settlement of the foundation and if conventional structures with well known ground conditions are dealt with.

Paragraph 2.4.8(2) of Eurocode 7 – Part 1, reproduced above, indicating that partial factors for SLS are normally taken equal to 1.0 (in other words that the design values of the various quantities are taken equal to their characteristic values), applies to the actions in the characteristic, frequent or quasi-permanent combinations (see EN 1990), as well as to the geotechnical properties, such as the modulus of deformation. It should be noted that, for determining the differential settlement for instance, sets of lower characteristic values and upper characteristic values can be chosen in order to take account of the ground variability.

With regard to the use of the combinations of actions for SLS, EN 1990 provides (in editorial notes) some guidelines which are summarised in table 4 (clause 6.5.3 in EN 1990).

Table 4. Recommended combinations of actions for checking serviceability limit states SLS

Combination of actions	Use according to EN 1990
Characteristic	Irreversible limit states
Frequent	Reversible limit states
Quasi permanent	Long term effect and appearance

When applying equation 2.10 of Eurocode 7 - Part 1 (see paragraph 2.4.8(1)P reproduced above), it appears that the frequent and quasi-permanent combinations should be recommended ; on the contrary, in the case of the alternative method allowed by 2.4.8(4), the characteristic (or 'rare') combination should be used, because the experience gained in the past was rather for loads near this type of combination.

The last general paragraph in Eurocode 7 – Part 1 about SLS, deals again with the 'displacement approach'. It states that (clause 2.4.8 in EN 1997-1) :

'(5)P A limiting value for a particular deformation is the value at which a serviceability limit state, such as unacceptable cracking or

jamming of doors, is deemed to occur in the supported structure. This limiting value shall be agreed during the design of the supported structure.'

The application of these general clauses is detailed further down in Eurocode 7 - Part 1 for each geotechnical structure (in the Sections for spread foundations, pile foundations, retaining structures, overall stability and embankments). It is interesting to note that the document insists on the difficulty to predict displacements with accuracy (in the present state of geotechnical engineering knowledge, of course!).

3.4. Limiting values of displacements of foundations

The knowledge of limiting allowable displacements of foundations is a subject of prime importance, even though it is not often explicitly addressed. These limiting values depend primarily on the nature of the supported structure, but it has also been a point of interest for geotechnical engineering for a long time, as well (a summary of data collected for buildings and bridges is given e.g. by Frank, 1991).

The limiting values of movements of foundations is the subject, in particular, of clause 2.4.9, as well as of Annex H (informative) of Eurocode 7 – Part 1. It is noted that clause 2.4.9 contains 4 rather strong principles, i.e. paragraphs (1)P to (4)P. The first one says :

(1)P In foundation design, limiting values shall be established for the foundation movements.

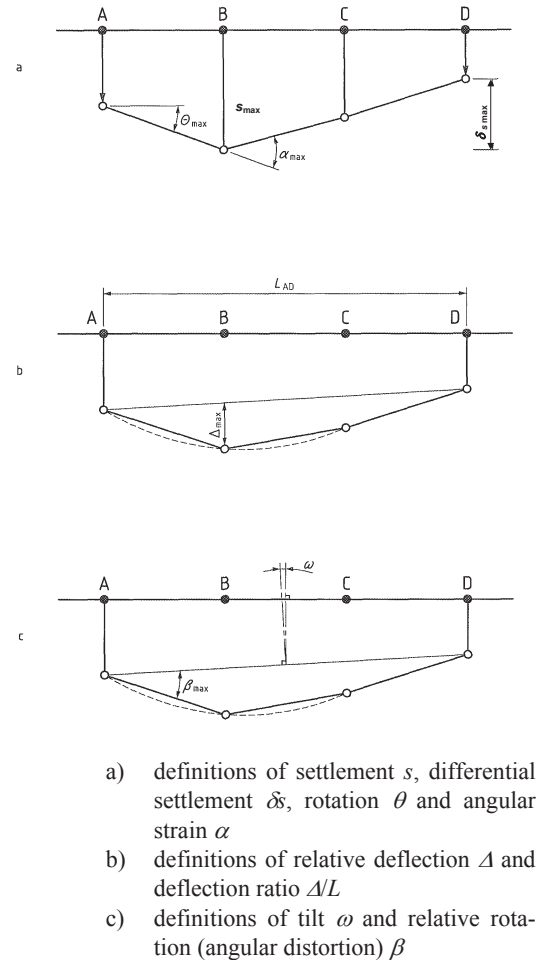
NOTE Permitted foundation movements may be set by the National annex.'

Furthermore, it seems that not only SLS are concerned (see above) but also ULS...(because movements of foundations can trigger an ULS in the supported structure).

Eurocode 7 lists a number of factors which should be considered when establishing the limiting values of movements. It is important that these limiting values are established in a realistic manner, by close collaboration between the geotechnical engineer and the structural engineer. If the values are too much severe, they will usually lead to uneconomical designs.

Figure 5 defines the parameters used to quantify movements and deformations of structures. This figure, originally proposed by Burland and

Wroth (1975) for buildings is reproduced in Annex H of Eurocode 7 – Part 1.



- a) definitions of settlement s , differential settlement δ_s , rotation θ and angular strain α
- b) definitions of relative deflection Δ and deflection ratio Δ/L
- c) definitions of tilt ω and relative rotation (angular distortion) β

Figure 4. Definitions of foundation movements and deformations of structures (CEN, 2004, after Burland and Wroth, 1975)

Annex H (informative) quotes the following limits after Burland et al. (1977):

- for open framed structures, infilled frames and load bearing or continuous brick walls : maximum relative rotations between about 1/2000 and about 1/300 to prevent the occurrence of a SLS in the structure ;

- for many structures, a maximum relative rotation $\beta = 1/500$ is acceptable for SLS and $\beta = 1/150$ for ULS ;

- these figures are for a for a sagging mode (as in figure 4) ; for a hogging mode they should be halved;

- for normal structures with isolated foundations, total settlements up to 50 mm are often acceptable.

Obviously these values can only serve as a guide, in the absence of other indications on the limiting values for the deformation of the structure. They apply to routine buildings with uniform loading intensity. They should be used with great caution when the structure is not ordinary (i.e. the case of most bridges) or when the loading is not uniform.

4. CONCLUSION

The implementation of the 'Structural' Eurocodes in the various countries will prove to be very important for the whole construction industry. Eurocode 7 is devoted to all the geotechnical aspects of structural design. It is meant to be a tool not only to help European geotechnical engineers speak the same technical language, but also a necessary tool for the dialogue between geotechnical engineers and structural engineers.

It is felt that Eurocode 7 will promote research, in particular in the field of soil-structure interactions. One of the great challenges of contemporary geotechnical engineering is precisely the development of rational methods for predicting the movements of foundations, in order to design safe and more economical structures.

5. REFERENCES

Burland, J.B., Broms, B.B. and De Mello, V.F.B. 1977. Behaviour of foundations and structures. *Proc. 9th Int. Conf. Soil Mechs & Fdn Engng*, Tokyo, vol. 2, pp. 495-546.

Burland J.B. and Wroth C.P. 1975. Settlement of buildings and associated damage. Review Paper, Session V, *Proc. Conf. Settlement of Structures*, Cambridge, Pentech Press, London, pp. 611-654..

CE 2003a. *Guidance Paper L. Application and use of the Eurocodes*. ref.: CONSTRUCT 03/629 Rev.1 (27 November 2003), European Commission, Brussels.

CE 2003b. Recommendation on the implementation and use of Eurocodes (2003/887/EC). *Official*

Journal of the European Union, 19.12.2003, EN, L 332/62 &63.

CEN 2002. *Eurocode: Basis of structural design. European standard*. EN 1990 : 2002. European Committee for Standardization: Brussels.

CEN 2004. *Eurocode 7: Geotechnical design - Part 1: General rules*. EN 1997-1:2004 (E), (F) and (G), November 2004, European Committee for Standardization: Brussels.

CEN 2007. *Eurocode 7: Geotechnical design - Part 2: Ground investigation and testing*. EN 1997-2:2007 (E), March 2007, European Committee for Standardization: Brussels.

Frank R. 1991. Quelques développements récents sur le comportement des fondations superficielles. Rapport général, Session 3, in: *Comptes rendus 10ème Cong. Européen Méca. Sols et Tr. Fond.*, Florence, vol. 3, pp. 1003-1030. English version: Some recent developments on the behaviour of shallow foundations. General report, *Proc. 10th European Conf. Soil Mechs & Fdn Engng*, Florence, vol. 4, 1994, pp. 1115-1141.

Frank R., Bauduin C., Driscoll R., Kavvas M., Krebs Ovesen N., Orr T. , Schuppener B. 2004. *Designer's guide to EN 1997 Eurocode 7 – Geotechnical design*. Thomas Telford, London.

Frank, R. & Magnan J.P. 1999. Quelques réflexions sur la vérification des états limites ultimes suivant l'Eurocode 7 (in French - A few thoughts about ultimate limit states verifications following Eurocode 7). Workshop on the Eurocodes, *Proc. 12th European conf. soil mechs. & geot. engng*, Amsterdam, Vol. 3, pp. 2179-2183 .

ANALYSIS OF TALL TOWER FOOTING SYSTEMS

C.M. Haberfield
Golder Associates Pty Ltd

ABSTRACT: Most tall buildings are supported on piled rafts and/or deep bored cast-in-situ piles. Good engineering design requires foundation structure interaction analysis and a clear understanding of the factors controlling the performance of the footing system. These rely on a sound understanding of the ground characteristics and individual and group pile performance, including adequate collection of data and testing. This paper focuses on what is required to achieve a reliable estimate of footing system performance using foundation structure interaction analysis. It highlights the importance of accurate inputs into the analyses, especially in respect to the stiffness characteristics of the ground and the load displacement performance of individual piles.

INTRODUCTION

Recent experience with footing design for tall buildings (e.g Nakheel tower in Dubai, the Gate of Kuwait in Kuwait, the City Centre project in Bahrain and Eureka Tower and Freshwater Place in Melbourne) has shown the benefits that can be achieved regarding footing system design when advanced foundation structure interaction analysis are utilized. However, the success or otherwise of these analysis is highly dependent on a number of factors other than the analysis undertaken, including sufficient knowledge of the subsurface geology, engineering behaviour and properties of the soil and rock on which the structure is built and the quality of construction.

The footing systems for these types of projects generally include the use of deep bored cast-in-situ piles or barrettes (piles of rectangular cross-section) founding in relatively incompressible material such as very dense or hard soil or weak rock. Many use piled rafts where the piles, while acting to support the load, are primarily used to reduce settlements. A clear understanding of the factors controlling the behaviour of the footing system is needed to enable a good engineering design to be achieved. This starts with a sound understanding of the ground characteristics and individual pile per-

formance, including adequate collection of data and testing. The best footing solution can then be found using suitable foundation structure interaction analyses. This process, when successfully carried out can lead to lower construction costs, better constructability and shortened construction time.

THE DESIGN PROCESS

As the performance of a footing system depends on both design and construction, it is important that the design process considers potential construction effects. The preliminary design of a footing system typically comprises a number of steps as follows:

- i. Preliminary considerations including desk study to identify likely founding conditions including groundwater aspects, consideration of likely structural form and design actions, availability of suitable piling contractors and available piling equipment
- ii. Development of a concept design of footing and basement retention system incorporating preliminary assessment of pile type, diameters and lengths, raft thickness, basement requirements and

support, dewatering aspects and so on. This may include development of a risk register to identify potential geotechnical risks and their mitigation and some preliminary simplified analysis to confirm assessment.

- iii. Development and completion of a ground investigation to obtain site specific data on stratigraphy and soil and rock properties for design and construction. The ground investigation may comprise several stages depending on availability of site access, complexity of subsurface conditions and availability of insitu test equipment.
- iv. Development of geological and geotechnical models of the site and assessment of design soil and rock properties
- v. Foundation structure interaction analysis and design of the footing and basement retention system to estimate pile and raft actions (axial and lateral loads, bending moments and shear forces, horizontal and vertical displacements).

FOOTING SYSTEM DESIGN

The footing system concept design and the ground investigation programme need to consider the potential factors that could affect the performance of the footing system.

For a typical pile-supported footing system, it is necessary to consider both individual pile, pile group and raft performance. These require consideration of the behaviour of the ground immediately beneath the surface raft or footing, along the pile shaft, and at and beneath the pile toe (Figure 1). Immediately beneath the surface raft or footing, the important factors are strength for bearing capacity and stiffness for settlement and interaction effects. Along the pile shaft, of most interest are strength for bearing, excavatability and stability; stiffness for settlement and interaction effects; geology and permeability for pile stability and pile shaft resistance. At the pile toe all the above factors for the pile shaft are present and in addition the pile end bearing is of interest. Below the toe, stiffness for settlement of

the overall footing system is important to at least a depth of twice the building width.

Due to the significant column loads, footings for large structures commonly comprise large diameter cast-insitu piles founding in relatively incompressible, very dense or hard soil or rock. Traditionally, such piles have been installed using bored pile techniques. However, more recently with the advent of larger piling rigs with significantly greater torque, large diameter continuous flight auger (CFA) piles for large structures is becoming common.

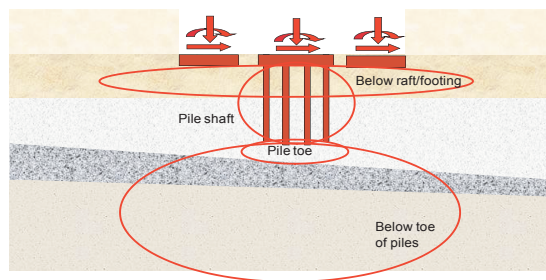


Figure 1: Areas of interest for footing design

For footings comprising cast-insitu piles, construction issues include the structural integrity of the pile shaft and the nature of the contact between the base and sides of the pile excavation and the pile concrete. The geotechnical design issues include the detailed interface properties, the boundary conditions and soil/rock properties including the impact of fissures or discontinuities within the soil/rock mass. An understanding is needed of the strength, stiffness, permeability, geology and mineralogy of the rock/soil mass. This can lead to solving design issues of bearing capacity, serviceability, excavatability and stability of the piles that make up the footing system.

A footing system can comprise a few to in excess of many hundreds of individual piles, groups of piles supporting pile caps or piles supporting shallow footings or rafts (e.g. piled raft). In such instances the interactions between piles and other foundation components can be significant and analyses which consider such interactions are required for the design of the footing system. This is particularly important for the design of tall buildings supported on a piled raft and founding in hard soil or weak rock. The interac-

tions are usually not of significance if the piles found in medium to high strength rock as settlements and interactions are generally small.

The problem, which is common to all footing systems, is to be able to estimate displacements at serviceability loads. Whilst ultimate strength of the footing system is important and requires consideration, it is rarely a critical factor. The areas of interest with respect to the assessment of footing system displacement are shown in Figure 1. These areas of interest extend well beyond the soil/rock adjacent to individual piles and or raft and can incorporate the ground to (at least) a depth of twice the building width. The ground investigation may therefore need to extend not only over (at least) the plan area of the building but potentially to a depth of at least twice the building width.

The design of the footing system will usually rely on the results of soil structure interaction analyses. There are many proven, hand calculation methods and computer based analytical tools available to estimate the load versus displacement performance of individual piles, pile groups and overall footing systems and which provide a quantitative assessment of foundation structure interaction which is required for design of the footing system and the load bearing elements of the structure. The more complex computer based tools (e.g. non-linear continuum (e.g. PLAXIS2D and 3D, FLAC2D and 3D) and discontinuum (e.g. UDEC, 3DEC) methods), in particular, are very powerful when used competently and the results are tempered with experience and judgement. However, although these tools are in general relatively easy to use, they are open to misuse especially if the analyst is inexperienced or does not have a good understanding of soil and rock properties, construction methods, numerical methods, plasticity, soil and rock behaviour and constitutive modelling.

It is beyond the scope of this paper to provide a summary of the many analysis methods that are available and how they can be used in serviceability based design. A common misconception is that discontinuum methods (e.g. UDEC) are required to model foundation structure interaction problems (e.g. footings and retention systems) in fractured rock. This is not the case.

Reasonable results can usually be obtained from continuum models (e.g. PLAXIS and FLAC) provided reasonable and representative rock mass properties (which account for the structure in the rock) are assumed. In particular, the modelling of discontinuities is generally not required for piled footings subjected to axial load as the impact of the discontinuities can be incorporated into the rock mass properties. For some situations however where failure to a free surface can occur; e.g. laterally loaded piles or retention piles, the orientation of discontinuities present in the rock mass may need to be considered. Many of the continuum methods that are commercially available allow a small number of discontinuities to be included in the analysis. For most applications the introduction of one to a few discontinuities into the model is sufficient to account for most credible and critical joint configurations.

One aspect that all the various analysis (both continuum and discontinuum) methods have in common is that to obtain meaningful results, appropriate input parameters (particularly for rock strength and deformation properties) need to be used. As in most applications the strength and deformation properties of the rock mass may not be known with sufficient confidence, it is good practice and prudent to undertake analyses assuming a range of credible properties for the rock mass. In some applications, probabilistic analysis may need to be undertaken to better quantify the potential for unfavourable settlement and rotation (e.g. under wind load) of the footing system.

The principal factors affecting the performance of footing systems include both design and construction issues. The performance of the footing system will depend on the performance of individual piles within that system, their interaction with one another and with the raft and/or other footings. Understanding the performance of single (isolated) piles is therefore a key factor to understanding the performance of the entire footing system. In addition, load testing of a completed footing system can only practically be achieved on individual piles. Confidence in the performance of the entire footing system can only be obtained by confirmation of individual pile performance and displacement monitoring during construction of the superstructure.

For the reasons set out above, the satisfactory design of a footing system relies on:

- i) a well-considered ground investigation that allows development of accurate geological and geotechnical models of the subsurface and measurement/estimation of relevant soil and rock properties over the area of influence of the footing system.
- ii) accurate analysis of the performance of single piles, pile groups and overall footing system
- iii) an understanding of potential construction issues which can impact on pile performance and therefore impact on pile design assumptions

The first two of these items are considered in further detail below.

GROUND INVESTIGATION AND PROPERTY ESTIMATION

The design of the ground investigation should only be undertaken following a desktop study of available information, development of a preliminary geological model and the development of a preliminary concept design. This will allow the ground investigation to be designed so that it targets the most relevant areas with respect to footing analysis and design. Considerations may be given to depth, number and location of boreholes and requirements for laboratory and insitu testing to allow estimation of relevant soil and rock properties. For some localities where the geology is relatively well defined and simple, there may be benefit in reducing the number of boreholes in lieu of a more intensive programme of targeted insitu testing. At other sites, in localities of complex geology, a greater number of boreholes may be required, but this should not be at the expense of the laboratory or insitu testing programme.

The following comments relate to the assessment of geological and geotechnical models and estimation of relevant soil and rock properties.

Geological and Geotechnical model

Assessment of soil and rock properties for analysis and design should only be undertaken after the development of an adequate subsurface

model of the site which is based on a reasonable understanding of the geology and geological history of the site. This may require an understanding of formation processes, how geological structures are developed and how subsequent factors affect the extent and depth of weathering. Without a reasonable understanding of the geology of the site, any assessment of stratigraphy, rock structure and/or rock properties could be seriously in error.

One example of this was for the 1000 m plus Nakheel Tower in Dubai. Geotechnical investigations at the site by others indicated that the weak calcareous rock underlying the site was highly fractured. This had implications for the assessment of mass modulus and strength and hence on the design of the footing system and estimate of displacements. The geological history of the area indicated the rock to be relatively young (Holocene age) and was unlikely to have experienced any activity which would have caused the rock to be fractured. The fractures observed in the core were attributed to the double tube coring methods used for the ground investigation. Subsequent ground investigation using triple tube methods showed the rock to be massive. Figure 2 compares the rock core obtained from double and triple tube coring for the Nakheel Tower project.



Figure 2. Triple tube (top) and double tube (bottom) core barrel drilling

Ground Investigation

The geological model can provide a significant insight into the behaviour of the rock and of the rock properties. Confirmation of rock properties is usually obtained from the results of appropriate laboratory testing. However, the results of laboratory testing depend critically on the quality of the samples. This applies equally to tube samples in soil and core samples in rock. The sample quality can be significantly affected by the drilling method and the type of core barrel used in soft rocks, where stress relief and slaking may be important. Careful sealing, storage, transport and test preparation are also important if representative material properties are to be established by laboratory testing.

Rock samples should be tested as close to saturation as practical as like soil, their strength and stiffness properties depend on the degree of saturation. This should also apply (in general) to rocks that have been sampled above the water table. It is also important to maintain the insitu water content of rocks if testing or observation of samples is to be relied upon. Rock samples that have been allowed to dry out and are then resaturated for testing may not be representative.

Even with the best sampling, sealing, storage and transporting practices, rock core samples will still undergo stress relief and disturbance. This is particularly evident in weak rocks sampled from depth. For the Nakheel Tower project, rock samples from up to 200 m depth were retrieved for laboratory testing. The recovered core samples (from below about 30 m depth) were observed to delaminate within minutes of being brought to the surface. This was attributed to the low permeability and low strength of the rock, the significant depth from which they were recovered and the sudden loss of confinement and water pressures as the core was sampled and brought to the surface. The samples were essentially blown apart by the internal pore water pressures. The delamination has an obvious and significant impact on the strength and deformation properties of the rock. Figure 3 compares the strength and modulus values measured in uniaxial compressive strength tests with those calculated from pressuremeter tests at the Nakheel Tower site. The modulus and strength parameters measured in laboratory tests are

significantly lower than calculated from insitu pressuremeter tests. Subsequent bi-directional load tests on test barrettes installed at the site confirmed the higher modulus and strength values calculated from the pressuremeter testing (Haberfield and Paul, 2011). Whilst carefully conducted insitu testing usually causes some disturbance and stress relief, the effects are much less than that can occur with rock samples obtained from coring. For this reason, in situ testing usually provides better estimates of properties for analysis and design. However, this does not mean that laboratory testing should not be carried out, even when extensive in situ testing has been undertaken. Laboratory tests can provide significant insight into the nature and constitutive behaviour of the rock which is difficult to obtain from insitu testing.

Unfortunately, the amount of laboratory and in situ testing undertaken for many projects is less than ideal. For some projects, standard penetration testing may be the only insitu test that is undertaken. In the authors view, standard penetration testing in hard soil and soft rock is of little if any value and the practice should be discontinued in favour of more advanced insitu tests.

The relative merits of carrying out more advanced insitu testing such as insitu pressuremeter testing, crosshole seismic testing and static load testing and more advanced laboratory testing such as triaxial testing and direct shear testing are carried out on relatively rare occasions. The additional information obtained from such testing not only provides better estimates of rock and soil strength and deformation properties but also provides a better basis for assessing practical footing construction procedures and construction risks.

Unfortunately, some geotechnical professionals express the opinion that there is no benefit in carrying out more advanced testing to better establish the strength and stiffness parameters of the rock. Instead, they argue that a satisfactory footing design can be based on “experience” and a visual assessment of the rock. As a result, the design of the footing system is generally overly-conservative and can result in over-designed foundations, often at significant cost to the project, and in some cases the foundations may be impractical to build.

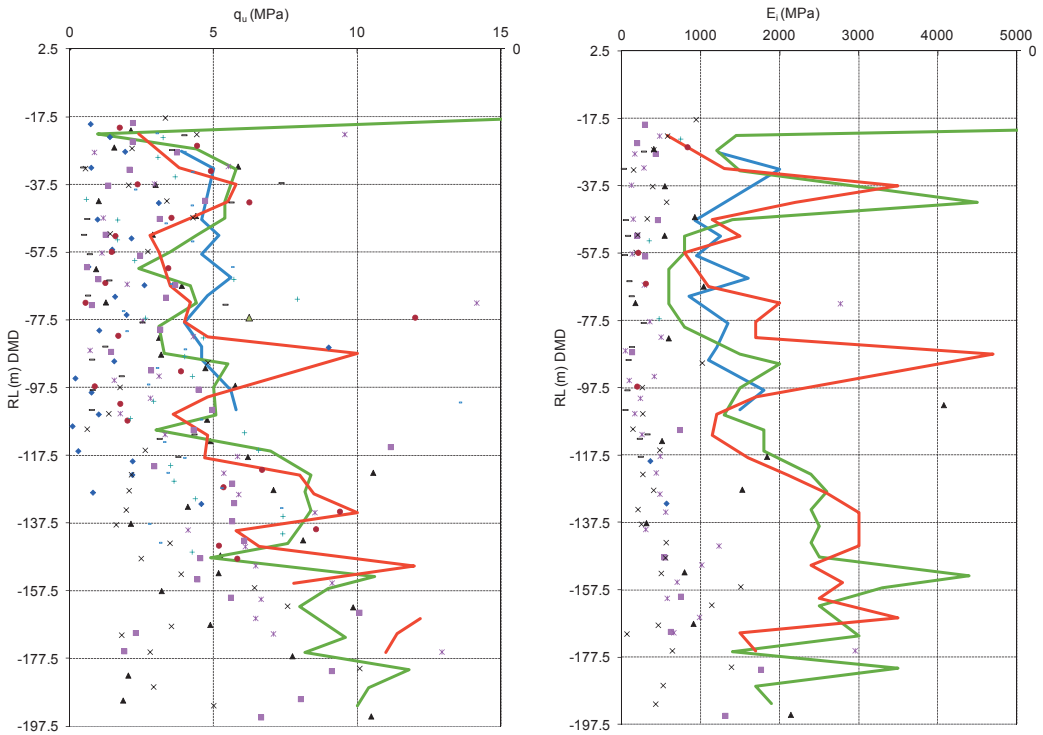


Figure 3. Comparison of strength (q_u) and deformation parameters (E_i) from laboratory tests (points) and insitu pressuremeter tests (lines).

Ground investigations that include only basic and limited testing (e.g. SPT and point load strength testing) are often attractive to the owner as they are inexpensive. However, for the relatively small additional cost to conduct a more thorough ground investigation with a reasonable component of insitu and laboratory testing, significant savings can be made in the construction of the foundations (Haberfield, 2012). Couple this with on-site presence during construction by experienced geotechnical professionals (to log pile holes, confirm raft subgrade and carry out appropriate testing for example), a lower cost and lower risk foundation solution is generally achievable.

More extensive and appropriate ground investigations allow a better assessment of rock properties, which in turn allow a serviceability design based approach to be undertaken (rather than the working stress method). A serviceability based analysis/design approach allows an improved understanding of individual pile and footing

system performance and construction techniques to be more fully utilised, and coupled with observations during footing construction, can reduce the risk and costs associated with installation of such footing systems.

The question arises therefore as to what laboratory and in situ tests are available and practical for testing of hard soil and rock to allow a reasonable estimate of strength and deformation properties? What are the limitations of these tests and how are the test results best interpreted to obtain the rock properties required for analysis and design?

Laboratory testing for intact strength and modulus

Point load index testing is commonly used to estimate the strength of rock materials. The test results however show a large scatter and are of limited benefit in estimating the strength or modulus of weak rocks. Greater benefit is

generally achieved by undertaking unconfined compressive strength (UCS) testing of the rock core. If the rock core is too fractured for UCS testing, then (additional) insitu testing should be undertaken instead of placing reliance on point load strength testing.

Unconfined or uniaxial compressive strength testing can (if undertaken correctly) provide a useful measure of strength but can be affected by the sample preparation (particularly saturation) and the testing rate adopted. All unconfined compressive strength tests (especially on weak rocks) should be carried out on samples that are as close to fully saturated as practical (usually obtained by soaking the samples in a bucket of water for 24 hours) and tested at a displacement rate that results in failure over at least 15 minutes. Experience has shown that even partial drying of samples can have a significant impact on strength and modulus measurements. The testing of saturated samples may preclude the use of strain gauges to measure intact modulus and a device which measures displacement over the middle third of the sample may be required. Modulus values calculated from end platen displacements can provide a significant underestimate of the actual intact rock modulus. If end platen measurements are used, a tangent modulus from the steepest gradient of the load vs displacement response should be calculated.

Triaxial testing has been used to measure rock and soil strength and may be better suited for soft rocks and rocks that slake when placed in water. Effective stress triaxial tests (consolidated drained and consolidated undrained with pore pressure measurements) can be used to obtain estimates of effective strength properties. However such tests should be single staged as the development of a failure plane in the first stage of the test can have a significant impact on the strength measured in later stages. In most applications which relate to the design of footing systems, the effective strength parameters of the rock are usually of minor importance and may not need to be tested for. As stated above, it is the rock modulus that is of primary importance.

Various laboratory methods are available to measure the intact rock modulus of rock in compression. The results show that, as for soils (e.g. Carter, 2006), the value measured is strain-

dependent and strain-rate dependent. Figure 4 shows the results of Young's modulus measurements for a carbonate-cemented siltstone using resonant column and cyclic triaxial testing. The resonant column test results included in Figure 4 may be an underestimate of the true small strain modulus due to equipment compliance issues with the test apparatus when testing material of relatively high stiffness. Such compliance issues are common with most laboratory based stiffness measurements of weak rock and hard soil and need to be considered in the assessment of the test results.

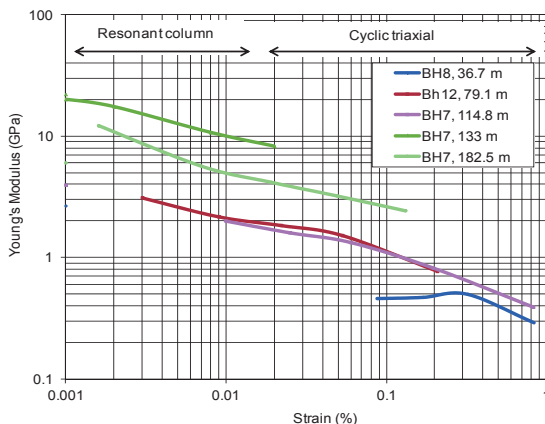


Figure 4. Young's modulus versus strain level for carbonate siltstone

The choice of a modulus for design therefore depends on the likely strain level for the loading condition. Values for analysis of earthquake, wind or static loading will each require an assessment of the relevant strain level and hence the appropriate modulus. Strain levels will also vary around the footing, with higher strains occurring near loads or excavations and reducing away from the areas. Non-linear finite element programs commonly used for analysis of foundation structure interaction problems (eg PLAXIS and PLAXIS3D) include constitutive models that account for this variation in modulus with strain.

The oedometer test is commonly used to estimate the one-dimensional compression characteristics of soil. Such tests may also be suitable for estimating the near one-dimensional compression of the ground directly underlying the base of the footing system for a tall building founded in very

weak rock or hard soil. Such testing can also provide an indication of time dependent consolidation and creep settlements. Measurement of the modulus of relatively stiff materials such as hard clay and very weak rock in laboratory oedometer tests requires an appreciation of compliance effects and the application of high pressures (Haberfield, 2013). Oedometer testing of these materials requires direct measurement of compression of the sample to obtain a reasonable estimate of constrained modulus.

Assessment of mass strength and modulus from intact values

Rock mass (continuum) models can generally provide a reasonable and practical approach to most foundation structure interaction problems (e.g. footings and retention systems) in fractured rock. In some applications however, e.g. retention systems or laterally loaded piles, it may be necessary to introduce (usually a small number of) discontinuities into the model to account for critical planes of weakness in the rock mass. Use of continuum methods to assess stability of slopes and excavation and temporary support of underground spaces in fractured rock may need special consideration and may be better suited to discontinuum or blocky rock models.

Key inputs into the analysis of footing systems in rock masses is the selection of the rock mass strength, stiffness and dilation properties.

The Hoek-Brown criterion

One of the most flexible rock mass models is the Hoek-Brown Geological Strength Index (GSI) model. The generalised Hoek-Brown criterion was introduced in 1994 (Hoek, 1994) and incorporated both the original criterion for excellent to fair quality rock masses and the modified criterion for poor to very poor quality rock masses.

The Hoek-Brown GSI model is widely known and offers flexibility in its application to a wide range of rock mass quality. The two main inputs into the model are m_i and GSI - m_i is based on rock type whilst GSI is usually assessed visually from a set of charts which classify the rock mass according to rock structure (intact through blocky to disintegrated) and joint surface condition (from very good to very poor).

Whether the GSI is a suitable model for prediction of rock mass strength for large structures (and therefore its value in predicting bearing capacity) still requires confirmation.

Application of GSI to rock mass modulus prediction

Hoek and Diederichs (2006) have provided methods for empirical estimation of rock mass modulus. They established relationships between the rock mass modulus and GSI for a range of disturbance factors (D) between 0 and 1, based largely on analysis of published values from tests in China and Taiwan. Figure 5 shows the results expressed as the normalised modulus (E_m/E_i) against GSI. In the absence of direct measurement, the value of E_i can be established from UCS using proposed values of the modular ratio, MR (where $MR = E_i/UCS$).

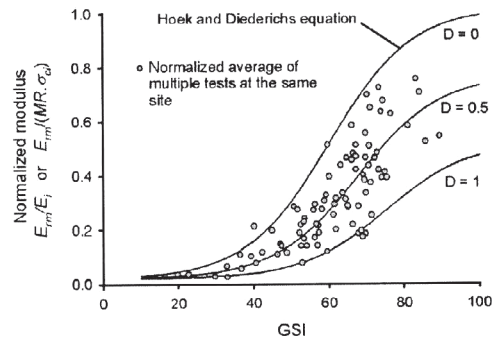


Figure 5. Normalised rock mass modulus versus GSI (Hoek and Diederichs, 2006)

Field measurement of rock mass modulus

Pressuremeter testing is commonly used to measure modulus and strength or hard soils and weak rock. However the interpretation of measurements is subject to a number of factors. These factors include the nature of the cavity expansion model adopted, the effects of radial cracking, disturbance and drainage. Modulus can be interpreted from the results of first loading or from any number of unload/reload loops. The first loading modulus is generally appropriate for analysis of piled foundations, whereas the unload/reload modulus is more appropriate for low strain applications such as in retaining wall design. A significant amount of information can

be gained from the shape of the pressuremeter curves. For example, tests results in fractured rock show greater curvature than in less fractured rock of the same intact rock strength and weathering. It is of benefit to compare pressuremeter curves from across a site to assess the relative strength and stiffness characteristics of the rock mass at different depths and locations.

The interpretation of strength from pressuremeter test results is not straight forward and requires experience and some subjectivity, and if possible confirmation through other tests. It also requires the test to be carried to significant strain levels which are commensurate with yielding of the rock mass. This is rarely possible in rocks with uniaxial strengths greater than about 5 MPa even when using a high pressure pressuremeter (20 MPa capacity). Assuming relatively high strain levels are achieved in the test does not necessarily mean a reasonable estimate of strength can be made. An assumption that the test is undrained and application of pressuremeter analyses used for clay may result in significant over-estimates of strength. On the other hand the application of

pressuremeter analyses for sand is also not applicable. Haberfield (1997) provides a curve fitting process which allows estimates of mass strength to be made, however these estimates are sensitive to a reasonable estimate of mass modulus. Significant over or under-estimates of strength can be made if the assumed modulus value is not reasonable. A reasonable estimate of insitu horizontal stress is not practical from most pressuremeter tests in hard soil and rock – such values must usually be assumed and can have a significant impact on strength assessment (and calculated performance of retention structures).

Benson and Haberfield (2003) compare the estimates of rock mass modulus for Melbourne siltstone from three methods of measurement. Figure 6 shows the modulus values measured from plate load tests, from pressuremeter tests and inferred from pile load tests. In these tests, the geotechnical strength was usually not reached. Where values of the UCS were available, the results were generally contained within the limits, $E = 50 q_u$ and $E = 400 q_u$. This is consistent with the range proposed from GSI by Hoek and Diederichs, (2006).

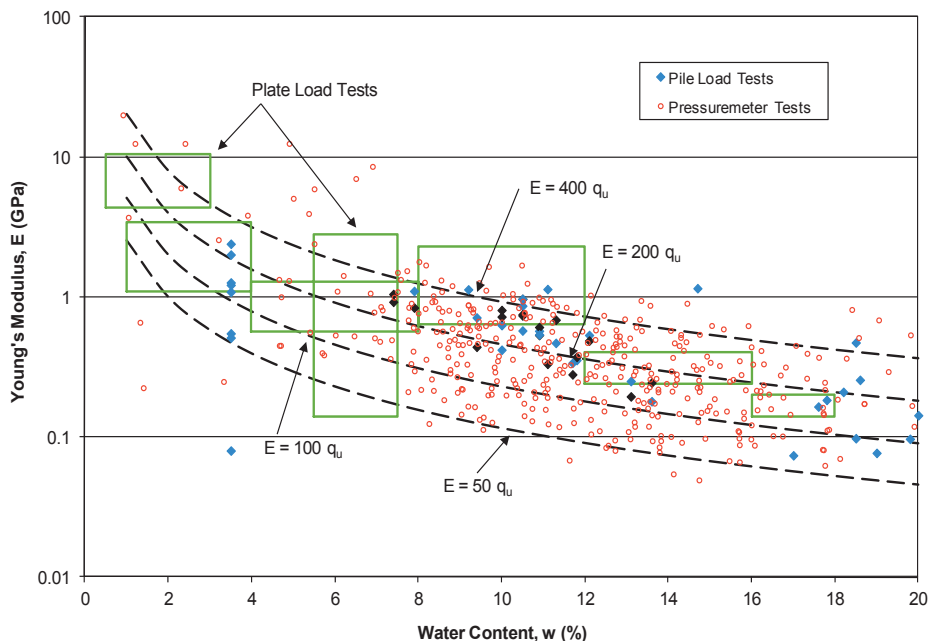


Figure 6. Young's modulus of Melbourne siltstone estimated from field tests (Benson and Haberfield, 2003)

An alternative method of estimating rock mass modulus was adopted at a site underlain by deeply weathered phyllite. The material proved impossible to sample for UCS or other testing, it slaked on exposure and pressuremeter testing was unsuccessful. Point load index tests on small pieces of core gave values of I_{s50} of less than 0.05 MPa. The design was for a bored pile footing system, albeit without much confidence in the design parameters for estimating settlement or on the ability to install the piles free from smear. On review of the footing system it was recommended that a precast pile be installed and dynamically (PDA) tested. From the interpretation of the PDA tests, a value of mass modulus was established. Subsequent analyses showed that the building could be supported on shallow footings on the very poor quality rock with acceptable settlements. Survey measurements undertaken during construction confirmed settlements within design estimates.

Cross-hole seismic and pressuremeter tests were used to measure mass modulus on a site underlain by carbonate-cemented siltstone. Figure 7a shows the results of these tests which were carried out to depths of up to 200 m. The small-strain cross-hole seismic tests gave estimates of

modulus which ranged between about 3 to 7 times those measured in the pressuremeter tests at the same depths. This difference is consistent with the effects of strain level on modulus, see Figure 4. To obtain a modulus value for engineering design adopting the strain levels appropriate to field behaviour, the cross-hole values were reduced by a factor of five. Figure 7b shows the correspondence between the reduced cross-hole seismic values and the pressuremeter results. Subsequent pile load tests confirmed the design modulus values.

Summary

The analysis of footing systems for large structures requires a good understanding of the soil deformation modulus at the appropriate strain level. Laboratory testing on core samples often underestimates the modulus because of stress relief and sample disturbance. In situ testing in these relatively competent materials is limited to pressuremeter testing, cross-hole seismic testing and pile load tests. The use of standard penetration tests should be discouraged as they are of little benefit and cone penetrometer testing is usually not practical.

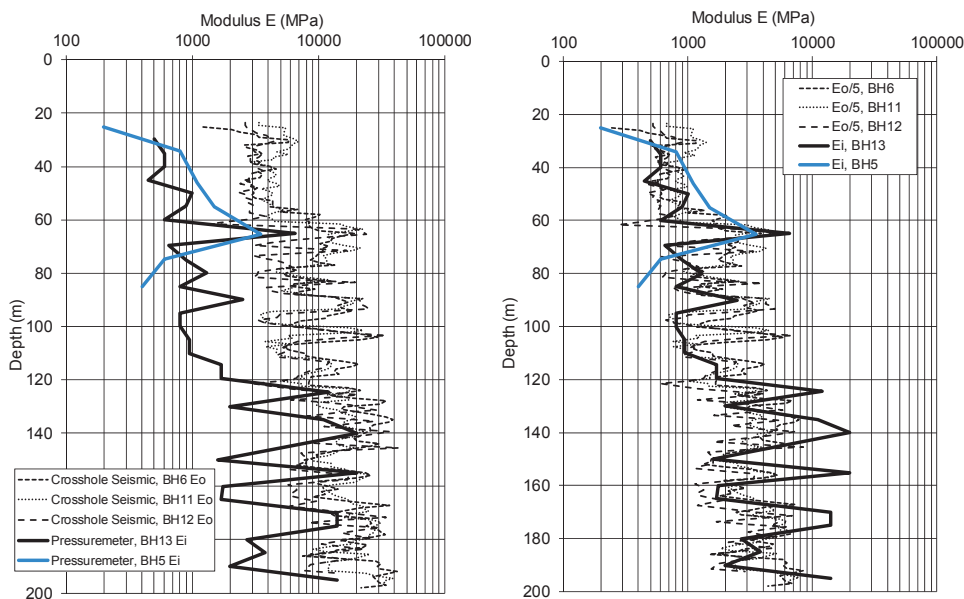


Figure 7a and b. Comparison of pressuremeter and cross-hole seismic modulus

A careful evaluation of the results of pressuremeter tests, cross-hole seismic tests and pile load tests can provide a consistent picture of deformation modulus which is a necessary input into analysis of the footing system. The measurement of mass strength is usually not practical.

As rock mass strength is usually not critical to footing design in hard soil and weak rock, reasonable estimates of mass strength properties can be made from laboratory unconfined compressive strength and triaxial tests coupled with empirical correlations which allow for mass effects; e.g. the GSI model.

CONSIDERATIONS FOR SINGLE PILES

The performance of a footing system is dependent on the performance of individual piles within the system and their interaction with one another.

For foundation structure interaction analyses, accurate simulation of individual pile load settlement performance is required to obtain a reasonable estimate of overall footing system performance. Fundamental aspects of pile performance that need to be considered are:

- i) The different mobilisation rates of shaft and base resistance (see Figure 8). Typically, ultimate shaft resistance is mobilised at pile displacements of about 1 % of pile diameter, whereas base resistance is not fully mobilised until displacements of at least 10 % of pile diameter if not higher if base debris is present.
- ii) Ultimate base resistance of piles in hard soil and rock can be many (>5 and of the order of 10 to 20) times the uniaxial compressive strength (q_u) of the intact soil/rock. For rocks with a $q_u > 2$ MPa, the concrete strength of the pile often governs the maximum design load of the pile. However, the displacements required to mobilise these loads can be significantly in excess of the serviceability requirements.

Due to the different mobilisation rates of shaft and base resistance, the performance of most piles at serviceability loads (SLS) is dependent

predominantly on the shear resistance developed at the interface between the concrete shaft and the surrounding soil/rock; i.e. shaft resistance. The base resistance also provides some resistance to the serviceability load, but in general its contribution is much less than shaft resistance (particularly for relatively long piles). For this reason it is common for piles in hard soil and weak rock to be designed such that serviceability loads are carried predominantly by shaft resistance, and that the available base resistance is only relied on for ultimate loads (ULS).

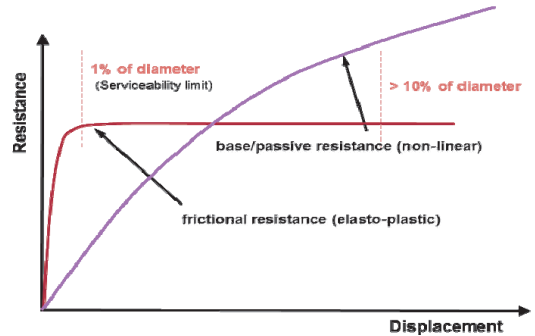


Figure 8. Rates of mobilisation of base and shaft resistance in piles

However, for large groups of piles and piled rafts this may not be valid. As shaft resistance relies on relative displacement between the pile and the ground, for large groups of piles or piled rafts this relative displacement may not occur until close to the toe of the piles. As a result, the upper part of the pile may not be providing any significant resistance to the applied load at serviceability load, but only develops as the piles approach ULS loads or beyond.

Shaft resistance

Shaft resistance depends on many factors including shaft diameter, rock/soil type, stiffness of the rock/soil mass, strength of the soil/rock and construction effects such as pile roughness, the thickness of smear zone or residual drilling fluid coating the pile shaft and the pressure imposed onto the soil/rock due to fluid concrete placement (e.g. Johnston, 1977; Williams and Pells, 1981; O'Neill and Hassan, 1994, Haberfield, 2000).

Shaft resistance is sensitive to a number of these parameters and as a result, pile performance can vary significantly from one site to another, even in the same soil/rock type. This provides an explanation for the large scatter observed in published correlations between shaft resistance and rock strength (e.g Williams, Johnston and Donald (1980) or Rowe and Armitage (1984)). As a result, shaft resistance vs displacement performance should be confirmed by appropriate pile load testing and if found to be significantly different than used in the design analysis, revision of the foundation structure interaction analysis carried out for the footing system may be required. For this reason, there is significant advantage in undertaking trial pile load tests during the design stage.

Base resistance

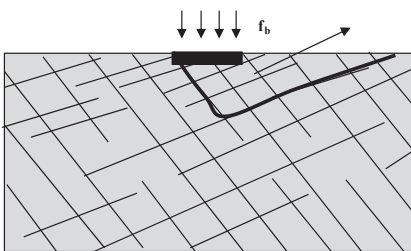
As bored piles are often of relatively large diameter, the resistance provided by the base of the pile can be substantial. However as set out below, the calculation of a meaningful base resistance for a bored pile founding in hard soil or rock is not straight forward.

Very few field pile load tests in rock achieve ultimate base resistance, this is not surprising if the possible failure mechanisms in jointed rock are considered. For surface footings, (Figure 9a), joints can provide a preferred failure surface and clearly they limit bearing capacity. In contrast, for piles (Figure 9b), there may not be a theoretical limit to bearing capacity as a failure surface does not propagate to the ground surface. The jointed rock mass is assumed to be a dense,

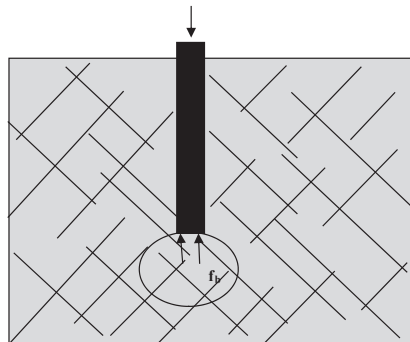
dilatant material. The stress bulb beneath the toe is confined by the stiffness of the surrounding rock, and dilation (as a result of shearing of the rock) increases this confining stress thereby increasing the resistance. This only occurs in relative dense dilatant rocks and hard soils and is not applicable to high void ratio rocks (e.g. carbonate rocks) or soils. The load that can be supported by the pile is controlled in practical cases by settlement (serviceability) and not by bearing capacity.

The above discussion has assumed that there is no debris at the base of the pile. This requires appropriate construction procedures to be implemented. The presence of base debris will not reduce the peak base resistance of the pile, but it will significantly increase the displacement required to mobilise the design base resistance. For this reason, it is imperative that bored piles are constructed with clean bases, or alternatively, the piles should be designed such that serviceability load can be safely carried by (factored) shaft resistance only.

Even if accepted base cleaning methods are adopted and carried out competently, it is likely that some debris will remain at the base of the pile. If concrete is placed with a tremie, some of this base debris may be carried away on the top of the rising concrete column, whilst the remainder will tend to be pushed to the edge of the pile base, potentially forming an annulus of debris material around the outer edge of the pile.



(a) footing or short pile



(b) long pile

Figure 9. Possible failure surface for shallow footings and piles in jointed rock

For this reason it is prudent to reduce the effective base area of the pile for serviceability calculations (unless a clean base can be ensured and confirmed). A reasonable and prudent assumption for design would be that 50 % of the base area is effective for serviceability calculations. The full base area may be used for ultimate limit state calculations, but the designer should be aware that the pile head settlement required to achieve this may be significant.

SUMMARY AND CONCLUSIONS

To obtain a reasonable estimate of footing system performance, foundation structure interaction analyses are required. For such analyses to be meaningful accurate geological and geotechnical models are required along with accurate estimates of relevant engineering properties. Also required is a good understanding of individual pile performance and the properties and construction effects that impact on their performance. Careful control of construction is necessary for the performance of cast-in-situ piles (and therefore the overall footing system) to achieve the design performance.

REFERENCES

- Benson, N. & Haberfield, C.M. (2003). *Assessment of rock mass modulus*. 10th International Congress on Rock Mechanics, Johannesburg, Sth Africa.
- Carter, J.P. (2006). *Who needs constitutive models*. EH Davis Memorial Lecture. Australian Geomechanics, Vol 41(2), June, 1-27.
- Haberfield, C.M. (1997). *Pressuremeter testing in weak rock and cemented sand*. Geotechnical Engineering Journal, Proceedings ICE, July, Vol. 125, 168-178.
- Haberfield, C.M. (2000). *Prediction of the initial normal stress in piles and anchors constructed using expansive cements*. International Journal for Numerical & Analytical Methods in Geomechanics, 24, 305-325.
- Haberfield, C.M. (2013). *Performance of footings in rock based on serviceability*. EH Davis Memorial Lecture. To be published in Australian Geomechanics.
- Haberfield C.M., Paul D.R. & Ervin M.C. (2008). Geotechnical design for the Nakheel Tall Tower, ISSMGE Bulletin, 2(4), 5-9.

- Hoek E. (1994). *Strength of rock and rock masses*, ISRM News Journal, 2(2) 4-16.
- Hoek, E. & Diederichs, M.S. (2006). *Empirical estimation of rock mass modulus*, International Journal of Rock Mechanics and Mining Sciences, 43, 203-215, Elsevier.
- Johnston, I.W. (1977). *Rock-socketing down under*. Contract Journal, 279: 53-53.
- O'Neill, M.W. & Hassan, K.M. (1994). *Drilled Shafts: Effects of Construction on Performance and Design Criteria*. Proceedings International Conference Design and Construction of Deep Foundations, Orlando, Florida: 137-187.
- Rowe, R.K. & Armitage, H.H. (1984). *The design of piles socketed into weak rock*. Report GEOT-11-84, University of Western Ontario, London, Canada.
- Williams, A.F. (1980). *The design and performance of piles socketed into weak rock*. Ph.D. Thesis, Monash University, Melbourne, Australia.
- Williams, A.F., Johnston, I.W. & Donald, I.B. (1980). *The design of socketed piles in weak rock*. International Conference on Structural Foundations on Rock. Sydney, Balkema, 327-347.
- Williams, A.F. & Pells, P.J.N. (1981). *Side resistance rock sockets in sandstone, mudstone and shale*. Canadian Geotechnical Journal, 18, 502-513.

Pullout Characteristics of Geocells Embedded in Gravelly Soil Backfill

Xinye HAN & Takashi KIYOTA

Institute of Industrial Science, University of Tokyo, Japan, hanxinye@iis.u-tokyo.ac.jp & kiyota@iis.u-tokyo.ac.jp

Fumio TATSUOKA

Department of Civil Engineering, Tokyo University of Science, Japan, tatsuoka@rs.noda.tus.ac.jp

ABSTRACT: In order to study whether geocell can be worked as tensile reinforcement in retaining walls, pullout tests were performed on two types of geocell models which have diamond-shaped cells and square-shaped cells embedded in three different compacted gravelly soils under the surcharge of 1 kPa at constant pullout rate. Different pullout behaviors were found due to the effect of in-plane geometry which can be explained by different pullout mechanisms. In addition, improvements on the pullout behavior of square-shaped geocell were studied by considering the influencing factors, such as arrangements of transverse members, height of transverse members, spacing between transverse members and the particle size backfill soils.

1. INTRODUCTION

Geocells, as a three-dimensional soil confinement system, have been widely applied in construction roads over soft soils, stabilization soils on embankments, protection steep slopes.

The common type of geocell has a diamond pattern, on which many studies were carried out mainly to check the function as base reinforcements subjected to vertical loads, such as roads, embankments and light houses. Bathurst and Karpurapu (1993), Rajagopal et al. (1999) and Mengelt et al. (2006) conducted triaxial compression tests to investigate the confinement effect of single geocell or multiple geocells. Many laboratory model tests were conducted to investigate the influencing factors for the performance of geocell-reinforced bases, such as geometric structures and dimensions, properties of geocell material and properties of infilled soil, loading methods, etc. Rea and Mitchell (1978), Shimizu and Inui (1990), Dash et al. (2001a, b) discussed the geometric factors on the performance of geocell-reinforced base and found that the optimum values of the geocell height/width ratio and the loading area width/geocell width ratio exist. Dash et al. (2001b) showed the bearing capacity of geocell-reinforced base increases as the density of infill soil increases. Mhaikar & Mandal (1992b,

1994) concluded that the geocell-reinforced base has better performance when geocells has a higher modulus.

However, the application of geocell as tensile reinforcement to soil structures, such as retaining walls, is relatively new due to the lack of related research. Ling et al. (2009) investigated the seismic performance of several soil retaining walls having a geocell facing by shaking table tests. The results showed that walls having a geocells facing are flexible exhibiting much better seismic performance than conventional type retaining walls. In addition, the performance of a retaining wall with the backfill reinforced with geocell layers is better than with geogrid layers.

In order to check whether geocell can be worked as tensile reinforcement, two types of geocell reinforcements which have diamond-shaped cells (traditional type geocell) and square-shaped cells (new developed geocell) were evaluated by pullout tests embedded in compacted gravelly soils. In addition, improvements on the pullout behavior of square-shaped geocell were studied by considering the influencing factors, such as arrangements of transverse members, height of transverse members, spacing between transverse members and the particle size effect of backfill soils.

2. TEST APPARATUS, PROCEDURES AND MATERIALS

2.1. Pullout Test Apparatus

Figure 1 shows the schematic diagram of pullout test apparatus that was developed at IIS, the University of Tokyo. The tests are carried out on plane-strain condition. The soil box is rectangular in shape and made of steel. The dimensions of inner soil box are 700mm (length) \times 400mm (width) \times 500mm (height). The opening size of the front wall could be changed for pulling out the geocell reinforcements with different heights. Leads shots are applied on the crest of the backfill to provide a surcharge of 1 kPa as a flexible top boundary, which is preferred for the purpose of measuring vertical deformation of backfill, which caused by the dilatancy of soils around the geocell reinforcements in the pullout process.

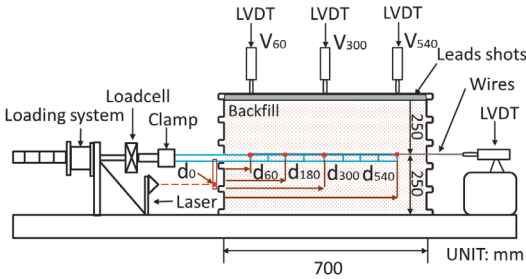


Figure 1. Schematic diagram of pullout test apparatus

2.2. Pullout Test Procedures

Gravels were poured into the soil box and compacted in 25 cm-thick sub-layers arranging geocell model at the prescribed level in the backfill. The target density of the backfill was 1.76g/cm³. As indicated in Fig. 1, the front horizontal displacement (d_0) was monitored by laser deformation transducer. The horizontal displacements along the geocell, for example, the locations at distances of 60 mm (d_{60}), 180 mm (d_{180}), 300 mm (d_{300}), and 540 mm (d_{540}) from the face of front wall were measured with linear variable differential transformers (LVDTs). Monitoring the horizontal displacements along the geocell reinforcement allows proper interpretation of the interface force transfer mechanism and provides appropriate

evaluation of the pullout resistance as well. Inextensible stainless wires were connected to the designated locations of geocell reinforcement to measure the horizontal displacements along the geocell reinforcement. The wires were protected by stiff tubes and connected to the LVDTs, which were mounted on the rear wall of soil box. In addition, the vertical deformation of the backfill surface at distances of 60 mm (V_{60}), 300 mm (V_{300}), and 540 mm (V_{540}) from the face of the front wall were also measured with three LVDTs. The tests were conducted by pulling out the geocell at a constant displacement rate of 2.5 mm/min using a precision jack driven by a motor. The pullout force was measured with a load cell. All instrumentations were linked to an electronic data logger which can scan the measurements at desired time intervals.

2.3. Soil Materials and Tested Geocell Models

The backfill soils used in this study were poorly graded sub-round gravelly soils, Gravel No.1, Gravel No.3 and Gravel No.5 (Fig. 2). Their particle sizes are 3~5 mm, 7~10 mm and 12~20 mm. As shown in Fig. 3, two models of geocell reinforcements were prepared: diamond-shaped geocell which is a conventional type geocell, and square-shaped geocell which is a new-developed type geocell. The diamond-shaped geocell reinforcement (DG) was 480 mm (length) \times 360 mm (width), having eight diamond-shaped cells in both longitudinal direction and transverse direction. The square-shaped geocell reinforcement (SG) was 480 mm (length) \times 350 mm (width), having eight square cells in the longitudinal direction and seven square cells in the transverse direction. The longitudinal members have a common height which is 20mm higher than transverse members. Five types of square-shaped geocell reinforcements with different heights were prepared. The full height (H) of transverse members is 12.5 mm (SG-1); 25 mm (SG-2); 40 mm (SG-3); 60 mm (SG-4); and 80 mm (SG-5). Both types of geocell reinforcements were made of polyethylene terephthalate (PET) covered with PVC for protection, having a thickness of 1 mm. The ultimate tensile strength of the material is 56kN/m at a strain of 20%. All test cases are summarized in Table 1.



Figure 2. Soil materials: (a) Gravel No.1; (b) Gravel No.3; (c) Gravel No.5;

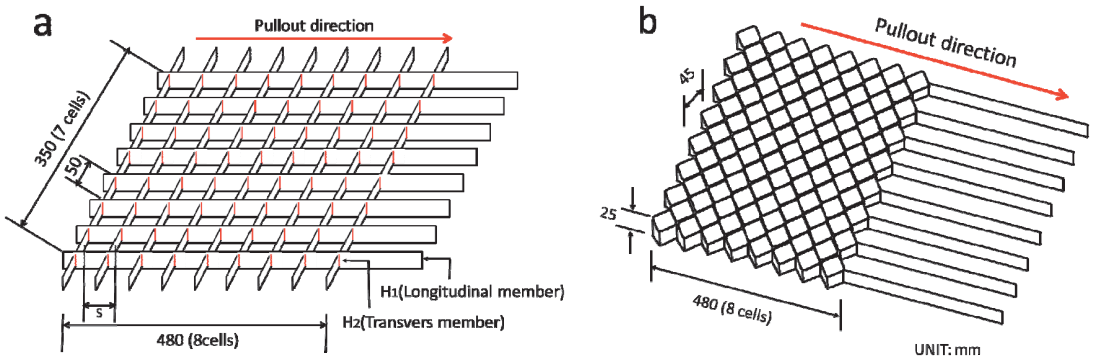


Figure 3. Schematic diagram of: (a) square-shaped geocell and (b) diamond-shaped geocell

Table 1. Test cases

Type of geocell	H	S	Backfill materials	Opening size of front wall
DG	25		Gravel No.1	46.5
SG-2	25	60		
SG-2(Preloading method)	25	60		
SG-2	25	60	Gravel No.3	100
SG-2(Preloading method)	25	60		
SG-1	12.5	60	Gravel No.1	
SG-2	25	60		
SG-2	25	120		
SG-3	40	60	Gravel No.3	
SG-2	25	60		
SG-3	40	60		
SG-4	60	60	Gravel No.5	
SG-2	25	60		
SG-3	40	60		
SG-4	60	60		
SG-5	80	60		

H: Height of transverse members; S: Spacing between transverse members; Unit: mm

3. RESULTS AND DISCUSSION

3.1. Effects of geometry of geocell

Typical pullout test results on square-shaped geocell and diamond-shaped geocell embedded in Gravel No.1 are presented in Fig. 4. The pullout resistance (P) versus horizontal displacement (d_{60}) is plotted in Fig. 4a, while the vertical displacement (V_{60}) of the backfill surface and horizontal displacement (d_{60}) of geocells is plotted in Fig. 4b.

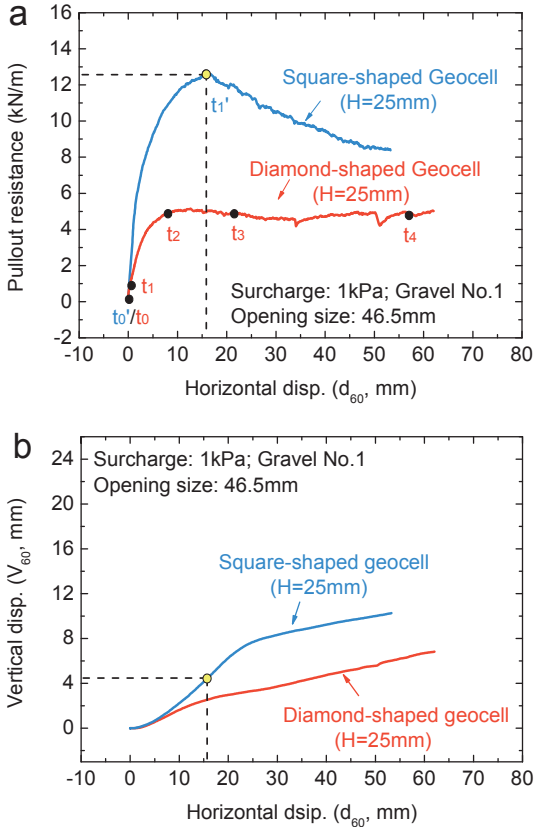


Figure 4. Typical pullout behaviors of square-shaped geocell and diamond-shaped geocell: (a) pullout resistance (P) against horizontal displacements (d_{60}); (b) relationship between vertical displacement (V_{60}) and horizontal displacement (d_{60})

It is found that square-shaped geocell shows both higher peak pullout resistance and higher initial stiffness than diamond-shaped geocell. It is interesting to note that, for square-shaped

geocell, with increasing pullout horizontal displacement (d_{60}) there is a high peak pullout resistance indicating a contribution from dilatancy of soil (Fig. 4b) around the geocell reinforcement, and then as pullout continues the resistance decreases to a residual state. The peak pullout resistance at 16mm horizontal displacement coincides with the steepest slope of the vertical-horizontal displacements curve (V_{60} - d_{60}) (Fig. 4b). This behavior is quite similar to the typical behaviour of granular dense soils which indicates that the dilatant contribution equals the work done against the normal stress as pullout progresses, thereby increasing the pullout resistance, as pullout continues, the shear zone around the geocell reinforcement eventually achieves to a stable state-sliding state, in which the pullout resistance reaches residual state. While for diamond-shaped geocell, the dilatant contribution is lower than square-shaped geocell (Fig. 4b), which is associated with the value of the pullout resistance is lower than square-shaped geocell in both peak state and residual state (Fig. 4a). These differences are due likely to the different geometries of the geocell, in particular the shape of aperture (Fig. 3).

Figure 5 represents the distribution of the local horizontal displacements of the geocell reinforcements for different values of the applied pullout forces, and the slope of the curve represents the local strain. It is found that, for square-shaped geocell (Fig. 5a), two different phases are observed to characterize the pullout behavior of the reinforcement from the soil: (1) In Phase 1 (force-transfer phase), the local strain increases as the pullout force increases, which indicates that the tensile force is progressively transferred to the geocells and the each cell provides its passive anchorage resistance or shear resistance (which will be discussed later in this paper) consecutively from the front cells near the point of pullout load application to the end cells until the peak pullout state ($P=12.59\text{kN/m}$) of geocell reinforcement after which no increment of strain along the geocell reinforcement occurs. Note again, at peak state, the steepest slope of vertical-horizontal displacements curve (V_{60} - d_{60}) is reached (Fig. 4b); (2) In Phase 2 (sliding phase), two adjacent curves are parallel each other, indicating that the geocell reinforcement

move as a whole and the shear bands form where the residual shear force determines the residual pullout resistance.

In the case of diamond-shaped geocell (Fig. 5b), only Phase 1 (force-transfer phase) occurs. It is noteworthy to highlight that, due to large

deformation of diamond-shaped cell itself, the last node of geocell does not move at large displacement of the first node, which restricts the development of shear band along the geocell resulting in a lower peak resistance.

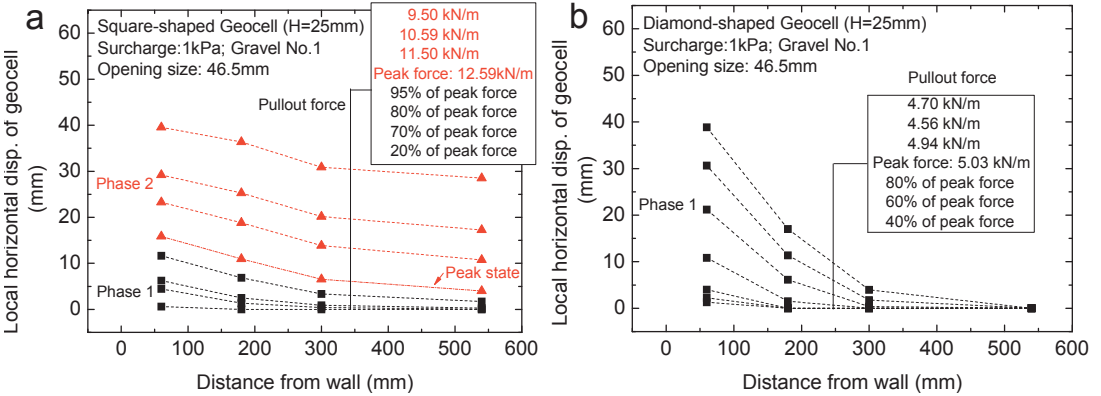


Figure 5. Local horizontal displacements at different pullout force levels: (a) square-shaped geocell and (b) diamond-shaped geocell

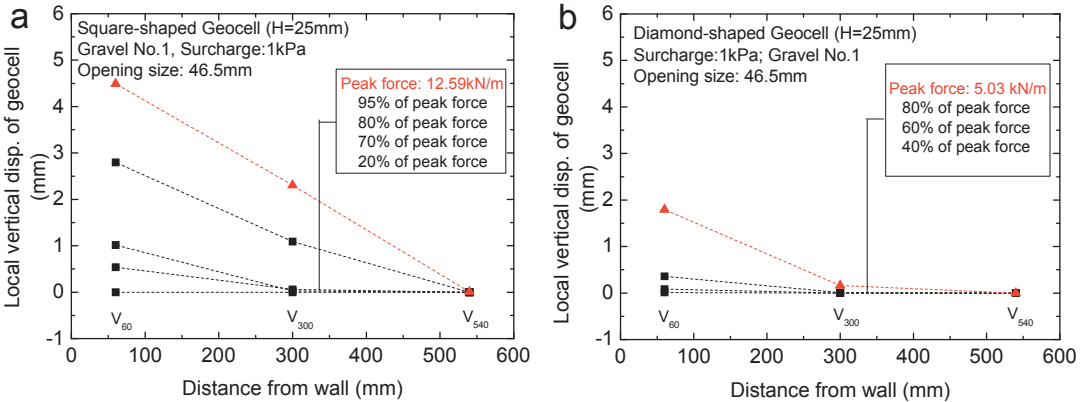


Figure 6. Local vertical displacements of backfill soil at different pullout force levels: (a) square-shaped geocell and (b) diamond-shaped geocell

Moreover, Fig.6 shows the distributions of vertical displacements of backfill surface (V_{60} , V_{300} and V_{540}), which caused by the dilatancy of soil around the geocell reinforcements in the pullout process, for different values of the applied pullout forces in Phase 1 (force-transfer phase). Apparently, for both types of geocell, vertical displacements of backfill surface along the geocell reinforcements are non-uniform, reducing with the distance from the front location (V_{60}) to the end location (V_{540}), which

reflects that stress state around geocell reinforcement is non-uniform since the extensibility of geocell. From this, it confirms that the pullout process is progressive and not all cells reach the sliding state at the same time, the front cells near the point of pullout load application may have been reached the sliding state even in Phase 1 (force-transfer phase).

For better illustrating the above pullout mechanism, Figs. 7 and 8 show schematic stress-deformation characteristics of diamond-

shaped geocell and square-shaped geocell varying with time when subjected to a pullout force. For diamond-shaped geocell (Figs. 4a and 7), from t_0 (initial state) to t_1 (the first state), the first diamond cell starts to deform and provide corresponding pullout resistance (Figs. 4a and 7c) until other cells reach the residual resistance state of the first cell. Afterwards from t_1 to t_2 , the second and the third cells deform and provide their pullout resistances until the rest cells reach the residual state of them. This procedure repeats from t_2 to t_3 until all cells work in the pullout Phase 1 (force-transfer phase). This deformation characteristics of diamond-shaped geocell can be characterized as progressive deformation in Phase 1 (force-transfer phase), which would induce the soil surrounding the diamond-shaped geocell not

fully mobilized, and therefore cause a lower peak pullout resistance and initial stiffness compared with the square-shaped geocell. However, as shown from Figs. 4a and 8, the square-shaped geocell only shows a slightly progressive deformation in Phase 1 (force-transfer phase) from t_0 (initial state) to t_1 (peak state). After that, all square cells work immediately which could provide larger peak pullout resistance and higher initial stiffness than diamond-shaped geocell. It is possible to observe the final deformation states of diamond-shaped geocell (Fig. 9a) and squared-shaped geocell (Fig. 9b), showing shrink deformation characteristics and non-shrink deformation characteristics close to the position of clamp, respectively.

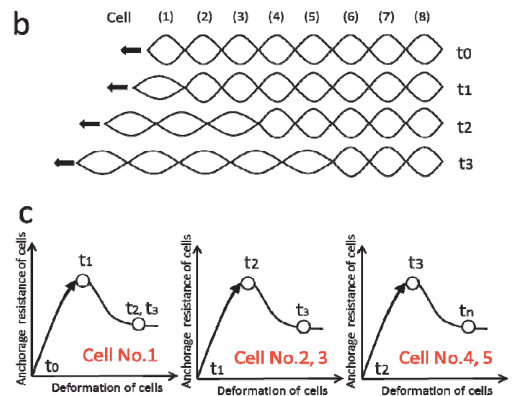
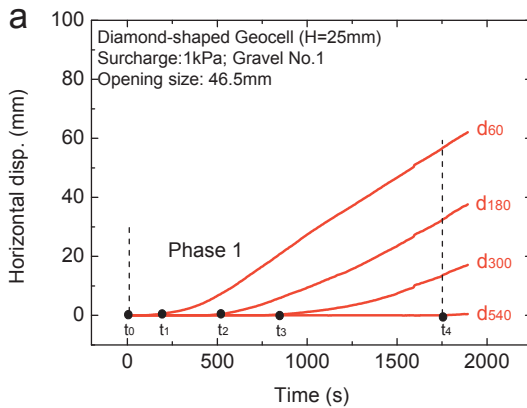


Figure 7. Schematic of stress-deformation characteristics of diamond-shaped geocell: (a) horizontal displacement versus time history; (b) and (c) schematic diagram of stress-deformation mechanism

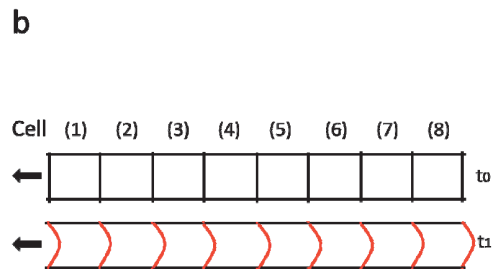
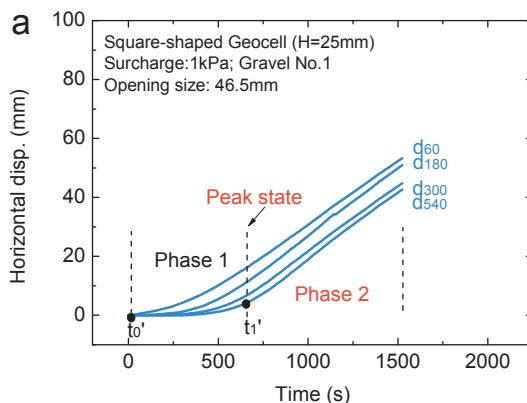


Figure 8. Schematic of stress-deformation characteristics of square-shaped geocell: (a) horizontal displacement versus time history; (b) schematic diagram of stress-deformation mechanism

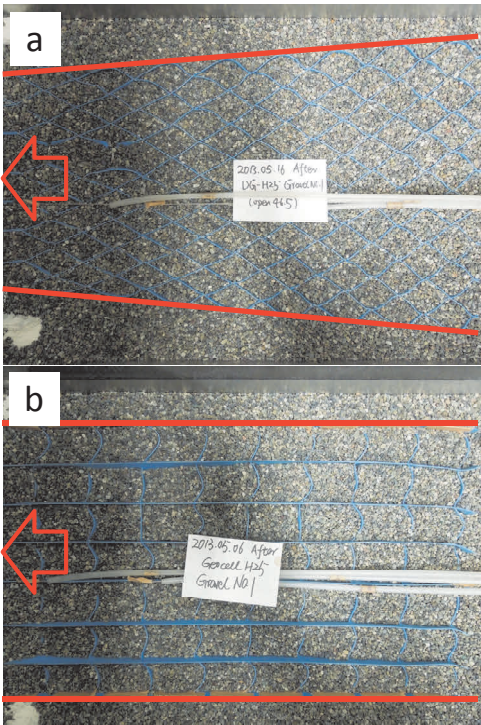


Figure 9. Final deformation states of: (a) diamond-shaped geocell and (b) square-shaped geocell

3.2. Enhancement of Initial Stiffness of Square-shaped geocell

With square-shaped geocell, the peak pullout resistance and initial stiffness are mainly determined by the anchorage resistance provided by transverse members or shear resistance around geocells in Phase 1 (force-transfer phase). In particular, initial stiffness would increase as an increase in the stiffness of transverse members, and also better initial arrangements of transverse members would also be of prime importance. As shown in Fig. 10, a preloading was applied at the value of residual strength in order to decrease the slackness of transverse members as presented in Fig. 11. From Fig. 12, with Gravel No.1, the initial pullout stiffness of square-shaped geocell increases significantly by preloading method, while from Fig. 13, with Gravel No.3, the initial pullout stiffness increases slightly. However, the preloading method has little influence on the peak resistance and residual resistance in both cases.

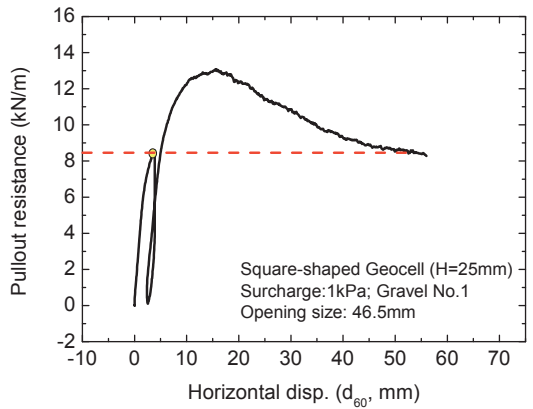


Figure 10. Preloading method for square-shaped geocell

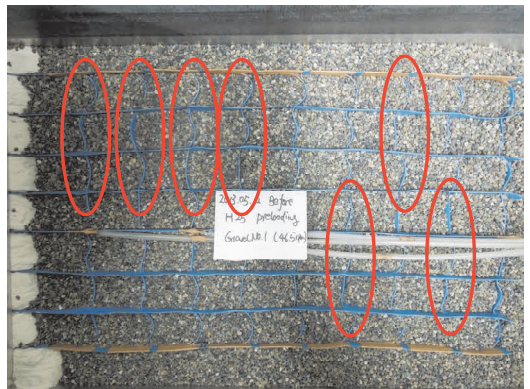


Figure 11. Arrangements of transverse cell members before test

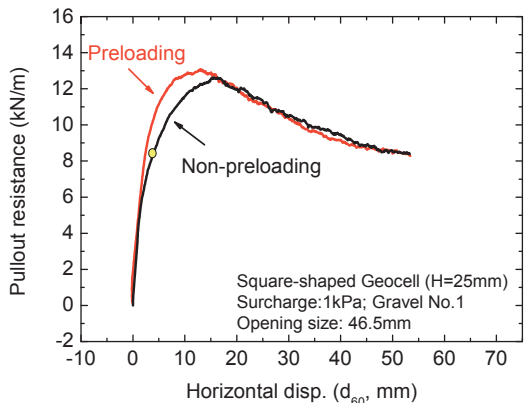


Figure 12. Enhancement of square-shaped geocell by preloading method with Gravel No.1

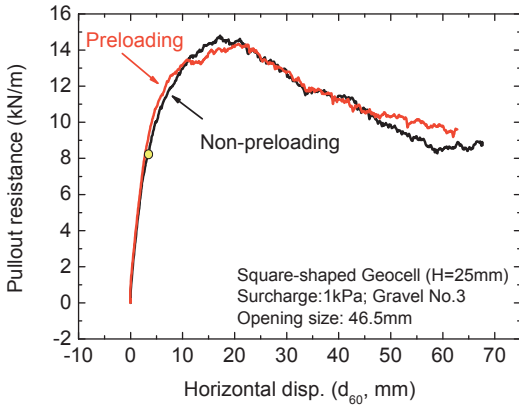


Figure 13. Enhancement of square-shaped geocell by preloading method with Gravel No.3

3.3. Effects of Height (H) and Spacing (S) between Transverse Members of Square-shaped Geocell

Apart from the soil properties, the height of geocell members (H) and the spacing (S) between transverse members would be key influential factors on interface mechanism. Fig. 14 compares pullout behaviors of square-shaped geocell with different member heights ($H=12.5\text{mm}$, $H=25\text{mm}$ and $H=40\text{mm}$) and the same spacing ($S=60\text{mm}$) between transverse members embedded in Gravel No.1 ($D_{50}=4\text{mm}$). It can be seen that the pullout resistance increases with an increase in the member height from 12.5mm to 25mm; however, with further increase in the member height, the pullout resistance exhibits only a very small increase. This can be attributed to the interference of transverse members restricting the development of anchorage resistance as the height increases from 25mm to 40mm. As can be seen that from Fig. 14b, the vertical displacements of backfill surface with height of 25mm and 40mm are similar, reflecting that same excessive normal stress activated on the soil-reinforcement interface, thereby inducing the same peak pullout resistance in these two cases. It is therefore considered that, when the member height is relative small ($H=12.5\text{mm}$), the peak pullout resistance is mainly determined by anchorage resistance provided by each transverse members; as the member height increases ($H=25\text{mm}$ and $H=40\text{mm}$), since the interference

of transverse members and thereby the restricted development of anchorage resistance, the geocell reinforcement moves like a block, in which the shear resistance of the shear bands that develop along the upper and bottom faces of geocell reinforcement would mainly determine the total pullout resistance.

When the spacing (S) between transverse members increases from 60mm to 120mm, both pullout resistance and vertical displacement of backfill surface almost keep the same (Fig. 15), which suggests that, the anchorage resistances provided by each transverse members are still interfered with each other, and the total pullout resistance is mainly determined by shear resistance.

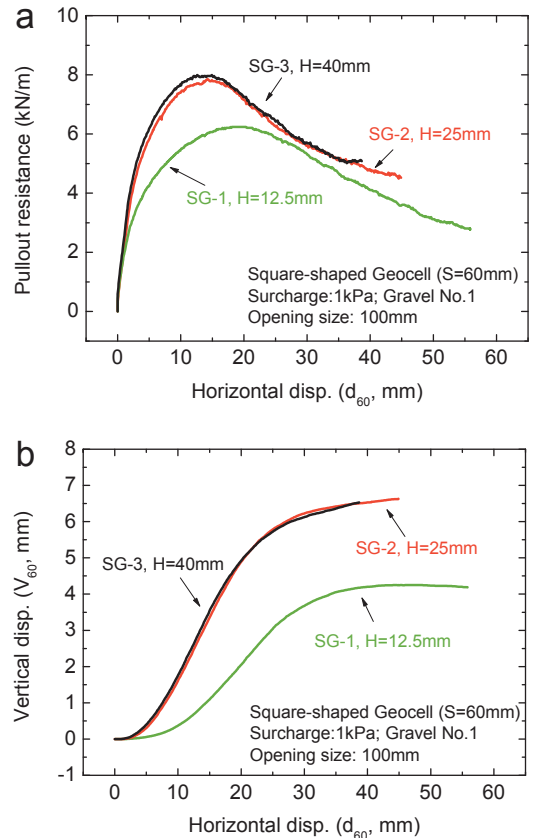


Figure 14. Pullout behaviors of square-shaped geocell with different heights: (a) pullout resistance (P) against horizontal displacements (d_{60}); (b) relationship between vertical displacement (V_{60}) and horizontal displacement (d_{60})

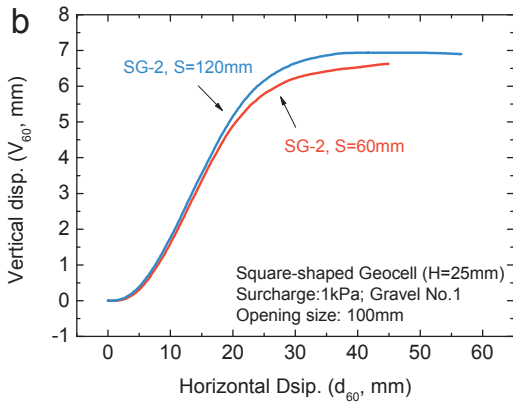
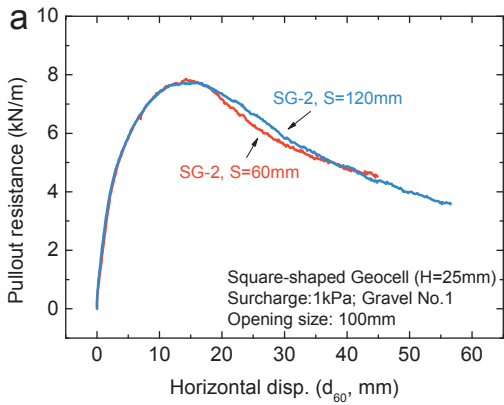


Figure 15. Pullout behaviors of square-shaped geocell with different spacing between transverse members: (a) pullout resistance (P) against horizontal displacements (d_{60}); (b) relationship between vertical displacement (V_{60}) and horizontal displacement (d_{60})

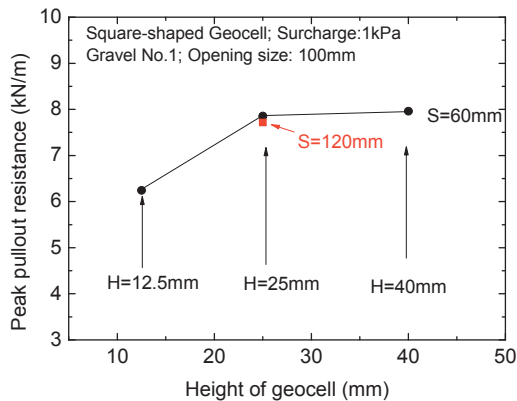


Figure 16. Influence of member height and spacing between transverse members on peak pullout resistance

Figure 16 summarizes the peak pullout resistances influenced by the factors of height (H) of geocell member and the spacing (S) between transverse members. It is revealed that as height of geocell member increases, the pullout resistance increases which is mainly determined by the anchorage resistance induced by passive pressure inside the cells. However, since the spacing (S) between transverse members has an interference effect on pullout interaction mechanism, there is a limit pullout resistance which is mainly determined by shear resistance of shear band.

3.4. Effects of Particle Size Relative to Height of Geocell

The effect of particle size relative to height of geocell is investigated by using square-shaped geocell with different member heights (H) but same spacing (S) between transverse members arranged in backfill Gravels No.1 ($D_{50}=4.5\text{mm}$), No. 3 ($D_{50}=8.5\text{mm}$) and No. 5 ($D_{50}=16\text{mm}$). It is clear to see that the pullout resistance increases with an increase in the member height from 12.5 mm to 25 mm in Fig. 14a, from 25 mm to 40 mm in Fig. 17a and from 25 mm to 60 mm in Fig. 17b. However, with further increase in the member height, the pullout resistance exhibits only a very small increase.

To analyze this trend, Fig. 18a summarizes the peak pullout resistance of square-shaped geocells (SG-1, SG-2, SG-3, SG-4 and SG-5) embedded in Gravel No.1, Gravel No.3 and Gravel No.5. It may be seen that, under otherwise the same conditions, the pullout resistance increases with an increase in the member height with the square-shaped geocell. However, there exists an upper limit with the pullout resistance that is reached when the height of member becomes a certain value that increases with an increase in the backfill particle diameter.

These test results suggest the following fundamental mechanism. As shown in Fig. 18b, the peak pullout resistance is equal to the smaller one of the following two types of resistance: 1) the shear resistance of the shear bands that develop along the upper and bottom faces of a geocell and the backfill, which is independent of the height of member and 2) the anchorage resistance induced by passive pressure developing inside the cells, which increases with an increase in the height of geocell. Therefore, as

the height of geocell increases, the total pullout resistance is first determined by the anchorage resistance and increases with an increase in the height of geocell. When the height of geocell reaches a certain value, due to the effect of interference of transverse members, the shear resistance finally determines the total pullout resistance. Then, the pullout resistance does not increase with further increase in the height of

geocell. Both shear resistance and anchorage resistance increase with an increase in the backfill particle size, therefore the pullout resistance does so. The test results show that the limit of the height of geocell at which the two types resistance become the same increase with an increase in the backfill particle size.

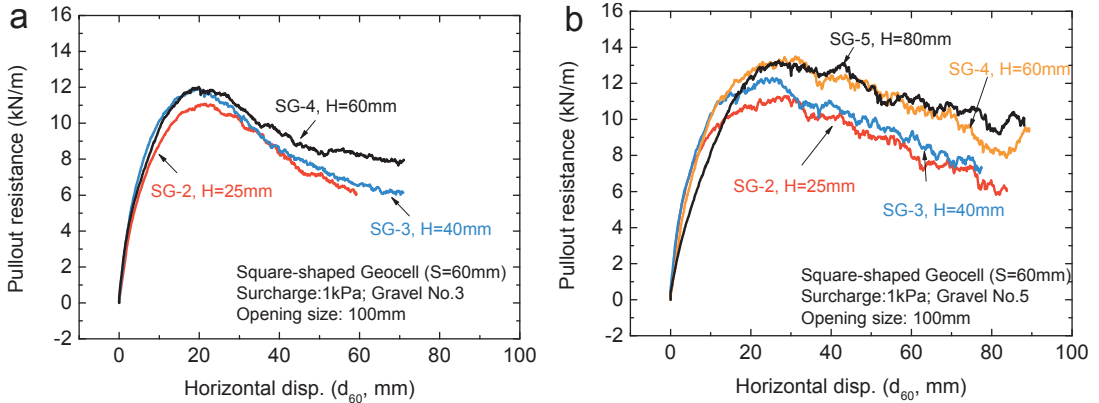


Figure 17. Pullout behaviors of square-shaped geocell with different heights embedded in: (a) Gravel No.3; (b) Gravel No.5

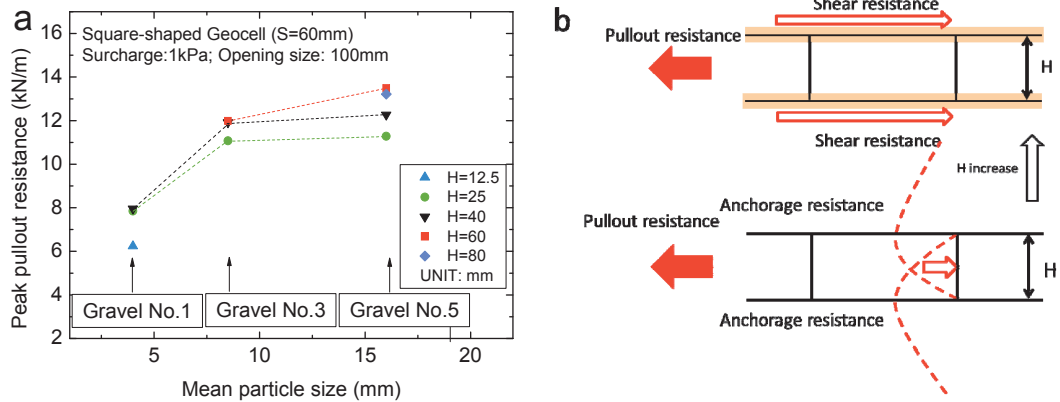


Figure 18. (a) Particle size effect on peak pullout resistance; and (b) schematic mechanisms of pullout resistance of geocell reinforcements embedded in the backfill

4. CONCLUSIONS

A series of pullout tests were conducted on small scaled models of square-shaped geocell as well as diamond-shaped geocell arranged in backfill of gravelly soils. By analyzing the data from these tests, the effects of the geometry of

cell, the height of transversal members, the spacing between transverse members and the backfill particle size on pullout resistance were evaluated. The main conclusions from this study are as follows:

- a) The square-shaped geocell exhibits much higher peak pullout resistance and higher initial stiffness than the diamond-shaped geocell.
- b) These differences are related to the effect of geometry of geocell on the mobilization of interface mechanisms. With diamond-shaped geocell, a large progressive mobilization of the interface interaction mechanism develops indicated as Phase I (force-transfer phase), which determine the total pullout resistance; on the other hand, square-shaped geocell firstly experiences slightly progressive deformation indicated as Phase 1 (force-transfer phase) in which passive anchorage resistance provided by transverse members or the shear resistance along the shear bands determines the total pullout resistance until the peak state, after that, in Phase 2 (sliding phase), the geocell reinforcement moves as a whole to reach the residual state where the shear bands form at larger pullout displacement.
- c) A preloading method was applied to reduce the slackness of transverse members of square-shaped geocell, and therefore enhance the initial stiffness.
- d) The pullout resistance is equal to the smaller value of: 1) the shear resistance of the shear bands along the upper and bottom faces of a geocell, which is independent of the height of geocell; and 2) the anchorage resistance induced by passive pressure developing inside the cells, which increases with an increase in the height of geocell. Therefore, as the height of geocell increases, the total pullout resistance is equal to the anchorage resistance and increases with an increase in the height of geocell. When the height of geocell reaches a certain value, due to the effect of interference of transverse members, the pullout resistance becomes the same as the shear resistance and does not increase with further increase in the height of geocell. Both shear resistance and anchorage resistance, therefore the pullout resistance, increase with an increase in the backfill particle size.
- e) However, the particle size effect was investigated by using square-shaped geocell with different heights but same spacing between transverse members. Since the spac-

ing between transverse members has an interference effect on the interface mechanism mobilization, the effect of spacing between transverse members should be further investigated and the optimum analysis for the geocell dimension relative to backfill particle size should also be confirmed in the future.

5. REFERENCES

- Bathurst, R.J. and Karpurapu. (1993), "Large scale triaxial compression testing of geocell reinforced granular soils." *Geotechnical testing journal-GTJODJ*, 16, 3, 296-303.
- Dash, S.K., Krishnaswamy, N.R., and Rajagopal, K. (2001a). "Bearing capacity of strip footings supported on geocell-reinforced sand." *Geotextiles and Geomembranes*, 19(4), 235-256.
- Dash, S.K., Rajagopal, K., and Krishnaswamy, N.R. (2001b). "Strip footing on geocell reinforced sand beds with additional planar reinforcement." *Geotextiles and Geomembranes*, 19(8), 529-538.
- Ling, H.I., Leshchinsky, D., Wang, J.P., Mohri, and Y., Rosen, A. (2009). Seismic response of geocell retaining walls: experimental studies. *ASCE Journal of Geotechnical and Geoenvironmental engineering*, 135, 515-524.
- Mengelt, M., Edil, T.B. and Benson, H.H. (2006), "resilient modulus and plastic deformation of soil confined in a geocell." *Geosynthetics International*, 13(5), 195-205.
- Mhaiskar, S.Y. and Mandal, J.N. (1992). "Comparison of a geocell and horizontal inclusion for paved road structure." *Proceedings of the International Symposium on Earth Reinforcement Practice*, 1, 641.
- Mhaiskar, S.Y. and Mandal, J.N. (1994). "Three dimensional geocell structure: performance under repetitive loads", *5th International Conference on Geotextile, Geomembranes and Related products*, Singapore, 155-158.
- Rajagopal, K., Krishnaswamy, N.R., and Latha, G.M. (1999). "Behavior of sand confined with single and multiple geocells." *Geotextiles and Geomembranes*, 17(13), 171-184.
- Rea, C. and Mitchell, K. (1978). "Sand reinforcement using paper grid cells." *Proceedings, Symposium on Earth Reinforcement*, ASCE Annual Convention, Pittsburgh, PA, 644-663.
- Shimizu, M. and Inui, T. (1990). "Increasing in the bearing capacity of ground with geotextile wall frame." *Geotextiles, Geomembranes and Related Products*, 254.

Soil-Structure Interaction during Earthquake and Tsunami – Two Case Studies from the Latest Disaster in Japan

Hemanta Hazarika

Kyushu University, Fukuoka, Japan, E-mail: hazarika@civil.kyushu-u.ac.jp

Tadashi Hara

Kochi University, Kochi, Japan, E-mail: haratd@kochi-u.ac.jp

Hideo Furuichi

Giken Seisakusho Co., Ltd., Tokyo, Japan, E-mail: furuichi@giken.com

ABSTRACT: A lot of coastal protection structures suffered heavy casualties due to the 2011 off the Pacific coast of Tohoku earthquake and the tsunami that followed. The purpose of this research was to confirm whether our age old perceptions on resisting capacity of rigid and heavy structures were correct, and how far it is fair to blame the scale of tsunami alone. To that end, site investigations and laboratory investigations were performed on two earth structures (a damaged coastal dike and a non-damaged retaining wall) in the southern central part of Iwate prefecture. Based on the investigation results, the interaction mechanism of the structures during the earthquake and tsunami were clarified.

1. BACKGROUND

The undersea mega thrust earthquake (magnitude $M_w = 9.0$) on March 11, 2011 was the most powerful known earthquake to have hit Japan, and one of the five most powerful earthquakes in the world overall since record-keeping by strong motion seismograph began in 1900. Several compound disasters (Hazarika, 2011) followed the earthquake including widespread liquefaction in a vastly wide area covering the prefectures of Aomori, Iwate, Miyagi, Fukushima, Ibaraki, Chiba, Kanagawa, Tochigi and in some parts of Tokyo metropolis. The extent of damage by the tsunami was irreparable, especially near the coastal area, due to more than 1 m of tectonic subsidence caused by the strong quake and the record breaking tsunami that easily overtopped many coastal structures. For many years to come, the long-term solutions and reconstruction will remain the challenging issues for the geotechnical engineers.

The tsunami caused damage to many river banks and railway embankments. According to investigation by the Ministry of Land, Infrastructure, Transport and Tourism (MILIT), Japan, there were more than 1195 damage in the river bank that Tohoku district maintenance office directly manages (MILIT, 2011). In the river mouth, the damage was mostly by the

tsunami. In the other parts of the river banks, the damage was mostly due to the subsidence by either earthquake motion or the liquefaction of soils in the levee body. According to investigation conducted by Hara et al. (2012) in southern central part of Iwate prefecture, the level of damage by the tsunami on river banks varies according to the structural forms, such as existence of surface covering, materials and topographical features. The overtopping tsunami caused sliding failures in many land development sites (Hara, 2011). On the other hand, according to the investigation conducted by Hazarika et al. (2012) in Aomori prefecture and northern part of Iwate prefecture, most of the damage of the river banks or coastal dikes was mainly due to scouring at the back of the structures. Scouring was caused not only by the overtopping tsunami itself, but also the force of the backrush of the tsunami (Hazarika et al., 2011).

A Japanese government panel is estimating that a 9.0 magnitude earthquake in the Nankai Trough region will do damage worth \$2.2 billion, a figure that is much higher than the \$177 million from the Great East Japan Earthquake of 2011. Scientists are predicting that the earthquake is due “in the not-too-distant future”, based on historical rough calculations. The report of central disaster mitigation council of

the ministry of Japan (Central Disaster Mitigation Council, 2003), states that about 2m of tectonic subsidence is expected in the Kochi area of Shikoku island, Japan, by that earthquake. In order to mitigate the damage from such future devastating earthquakes, it is necessary to take appropriate measures that can protect the infrastructures from the compound disasters instigated by the combined effect of events such as an earthquake, liquefaction, and tsunami. To realize that, what is needed most at this moment is to how to make use of the lessons that we civil engineers learned from the 2011 great east Japan disaster.



Figure 1. Tire retaining wall in Okirai



Figure 2. Collapsed sea wall in Okirai

While surveying the tsunami disaster areas immediately after the disaster, the authors were amazed to find a retaining wall (made of recycled tires) that miraculously survived the disaster (Fig. 1). Ironically, this tire retaining wall is located just about 150 m away (towards the land) from a completely collapsed sea wall (Fig. 2). The factory building situated on the

backfill ground of the retaining wall was damaged by the tsunami, and a natural slope nearby this tire retaining wall was eroded by the tsunami. Why this tire retaining wall was neither damaged by the earthquake nor by the inundation and erosion due to the tsunami was the source of investigations presented in this research. The authors also wanted to know, whether the cause of the damage to other structures were tsunami alone, and selected a damaged river levee as a target structure for that purpose.

This paper reports the results of the investigations conducted focusing on the structural and geotechnical aspects of a damaged river levee with concrete covering and a non-damaged retaining wall made of tires. It contains information based on the investigations conducted by the authors covering seismological, geotechnical and structural aspects of the two structures due to the tsunami using both the field survey and laboratory testing. As a part of the field survey, in-situ density test, dynamic cone penetration test, micro tremor measurement and surface wave exploration were conducted.

2. OUTLINE OF THE DISASTER IN THE SURVEYED AREAS

2.1. Earthquake records

The acceleration records of the earthquake at K-NET MYG010 station (Fig. 3) in the central Tohoku (Ishinomaki, Miyagi prefecture) shows that it contains two major events, and has long duration of shaking. Furumura et al. (2011) showed the rupture process of the main shock of the 2011 off the pacific coast of Tohoku Earthquake using the acceleration record obtained from K-NET and KiK-net (K-NET, 2011). According to their study, the first rupture occurred off Miyagi prefecture, and strong seismic waves were released all over Tohoku (phase1). After several tens of seconds, another massive rupture occurred and strong seismic waves were released (phase2). The third rupture occurred at the offshore near the northern Ibaraki, and strong seismic waves were radiated towards Ibaraki prefecture (phase3). The rupture property and the radiation characteristics of the third slip were different from those of the others.

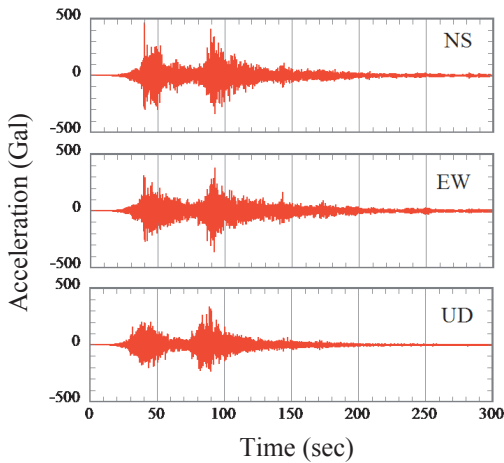
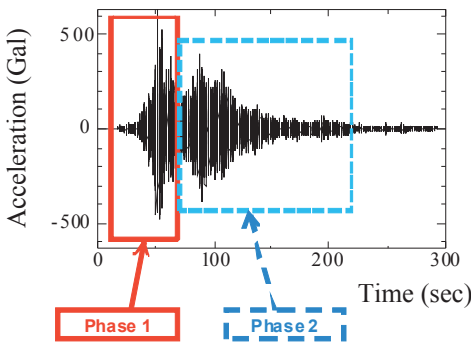
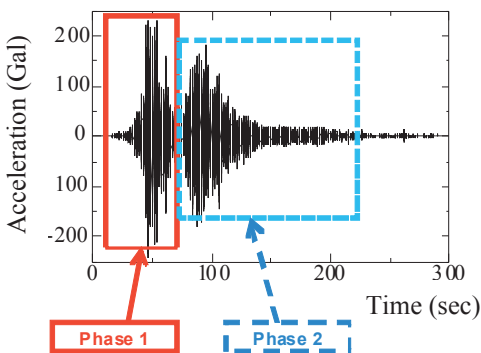


Figure 3. Acceleration record at Ishinomaki, Miyagi prefecture (K-NET MYG010)



(a) IWT007 (Kamaishi)



(b) IWT008 (Ofunato)

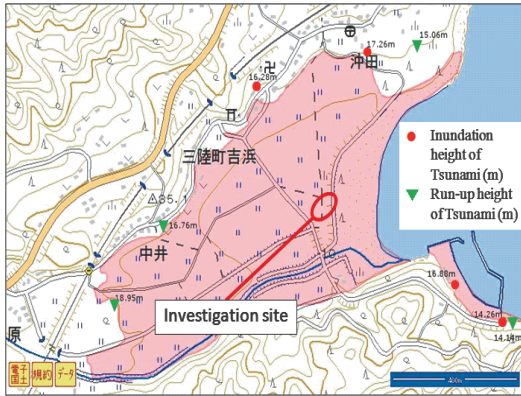
Figure 4. Acceleration records of the main shock recorded at K-NET

Fig. 4(a) shows the acceleration records of the main shock recorded at K-NET IWT007 station (at Kamaishi), which recorded maximum acceleration 741.6 Gal. Fig. 4(b) shows the acceleration records of the main shock recorded at K-NET IWT008 station (at Ofunato), which recorded maximum acceleration 387.0 Gal. In both the acceleration records, continuation time was over 220 seconds. Such long continuation time, a characteristic of the earthquake this time, was one of the reasons for the damage to more than 2000 river dikes and coastal dikes in the Tohoku region.

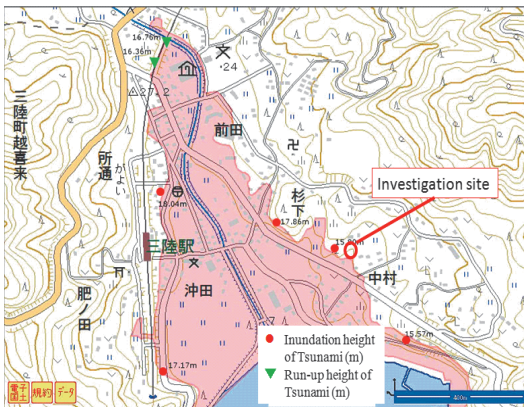
2.2 Tsunami records

Field surveys were conducted on two geotechnical structures located in Yoshihama area and Okirai area of Ofunato city, Iwate prefecture (Fig. 5). The surveys were conducted in two phases: the first phase was on May 3 and 4, 2011, and the second phase was six month after the disaster (September 12 and 13). Yoshihama area repeatedly suffered tsunami damage during the past big earthquakes. Due to complete collapse of the sea wall and the river levee by the tsunami this time, the tsunami easily entered and inundated the plain area. Due to strong shaking of the earthquake and tsunami that followed, the coastal dike at the mouth of Yoshihama river was completely damaged over a wide range with complete collapse of the concrete slabs and concrete blocks (Fig. 6). In some parts, more than 30 m displacement of the sea wall was observed. As compared to many other sea walls destroyed due to the tsunami located along the coastal area of the Tohoku region (Hara et al., 2012; Hazarika et al., 2012) the damage to this sea wall in Yoshihama was not due to the scouring or erosion.

It is worth mentioning here that during the first phase of our investigation (May, 2011), the paddy fields behind the sea wall were completely covered with deposited sands from the seashore, and the inundated waters were seen over a wide area. This is a classic example of the inundation due to tectonic subsidence.



(a) Yoshihama area



(a) Okirai area

Figure 5. Extent of tsunami inundation in the surveyed area



Figure 6. Damaged river dike in Yoshihama area

On the other hand, the whole of Okirai area was inundated completely by the tsunami. The casualties were greater in this area with 66 deaths and 30 missing people. As seen in Fig. 2, the concrete sea wall along the coastal line completely collapsed. As a result, the tsunami run-up washed away most of the wooden buildings in the area. The tsunami run-up was up to the third floor of the Okirai elementary school, which is located 200 m from the coastline. The tsunami run-up height in this location was found to be 16 m by the RTK- GPS survey conducted by the authors.

According to previous records, the tsunami run-up height in Sugishita area of Okirai was 11.6 m during the Showa Sanriku tsunami in 1933, and was 7.8 m during the Meiji Sanriku tsunami in 1896 (Shuto, 2011). Based on our surveying data using the total station, the tsunami run-up height this time was estimated to be 16.79 m, which is much higher than past tsunamis that inundated this area.

3. ANALYSIS OF DAMAGE TO TARGET STRUCTURES

3.1 Damage investigation

As a part of the site investigation, surveying, portable dynamic cone penetration test (PDCP), surface wave exploration and micro tremor measurement were conducted at two locations of Iwate prefecture. Disturbed soil samples were also collected from the sites and laboratory investigations were carried out.

PDCP is recognized widely as a standard method for obtaining dynamic characteristics of soils at the site by the Japanese Geotechnical Society (JGS 1433). In PDCP, a drop hammer weighing 5kg is allowed to fall through a rod from 50cm height, which enables the cone attached at the toe of the rod to penetrate into the ground. The number of blows (Nd) to penetrate every 10 cm of the ground measured. Nd is related to the N-value of the standard penetration test. In this study, using the relationship proposed by Okada (1992) for sandy soils, Nd values were converted to N-values. The location of the ground water table was judged from the wet condition of the rod immediately after termination of the test.

The surface wave exploration is a convenient method to obtain S-wave velocity distribution within the ground up to a depth of 10 m. This method measures and analyses the transmission of the surface wave (Rayleigh wave) that transmits near the ground surface. In this method, a wave is generated by striking the ground surface with a hammer. The generated wave propagates according to the surface and subsurface material conditions. During this investigation, in order to obtain the characteristics of the ground layer indirectly from the surface, the surface wave exploration was carried out together with the PDCP.

Micro tremor measurement has become a powerful tool for engineers to estimate the ground motion characteristics, amplification of ground motion in the soil deposits, microzonation and dynamic behavior of existing service structures. The micro tremor observations described in this study were carried out by portable micro tremor equipment (type New PIC). Measurements (2 horizontal and 1 vertical components) were conducted in velocity mode, which were recorded by the sensors. H/V Ratio is then calculated based on the smoothed ratio of horizontal to vertical Fourier spectra of the micro tremor data. The amplitude ratio calculated in this study was based on the method proposed by Nakamura (1989). The value corresponding to the peak represents the predominant frequency of the motion.

3.2 Details of Investigations at Yoshihama

3.2.1 Field survey

The plane view of the river dike damaged by the tsunami after the earthquake at Yoshihama area is shown in Fig. 7. PDCP (one location), the surface wave exploration (over a distance of 24 m) and the micro tremor (two locations) were carried out on the levee body.

Fig. 8(a) shows an estimated standard cross section of the embankment before the earthquake. The embankment is having the standard shape typically used in Japan with 5.15 m in height, 2.0 m in width at the crown, and 1:1.2 in gradient at the back. The structure of the sea wall consists of a concrete wall with counterfort on the river side, and a levee body with filled

soil covered with concrete blocks on the back side of the slope. Fig. 8(b) shows the N-value converted from Nd obtained from the PDCP test conducted on the soils of the levee body. The N-values of the fill soils ranged between 1 to 4, implying that the soil is very loose. However, the N-value increases along the bottom of the body, implying a dense state. From the PDCP test the ground water level was confirmed to be at 2 m below the ground surface. Therefore, it can be said that the fill soil was almost at the saturated state.

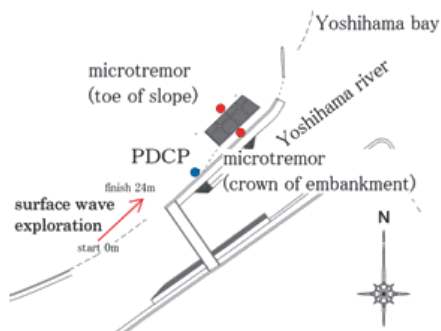
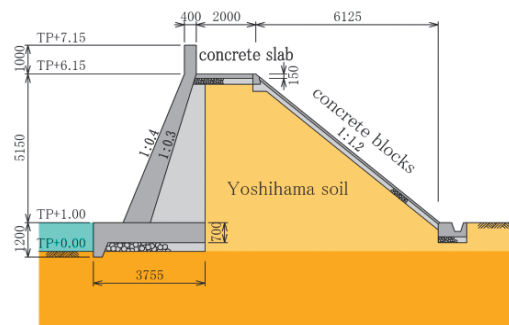
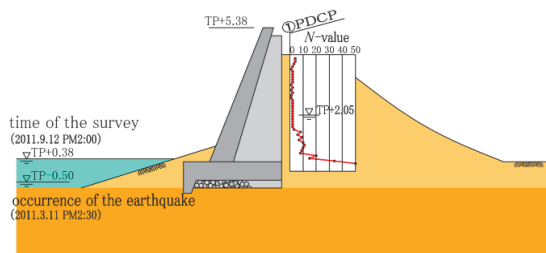


Figure 7. Location of the river dike damaged in Yoshihama area



(a) Before the earthquake



(b) After the earthquake

Figure 8. Estimated cross section of the dike

Fig. 9 shows the S-wave velocity distribution analyzed from the surface wave exploration data of the ground near the embankment. The S-wave velocity ranges from 200 to 250 m/s near the surface, and the converted N-value was about 20 (Imai & Tonouchi, 1982), which implies that the surface soil is very dense. Near the end of the measured zone, the S-wave velocity was found to be low. Based on the observations of the topography and the deposited sand due to tsunami, it can be said that the lower velocity was due to the reclaimed soils of restoration work.

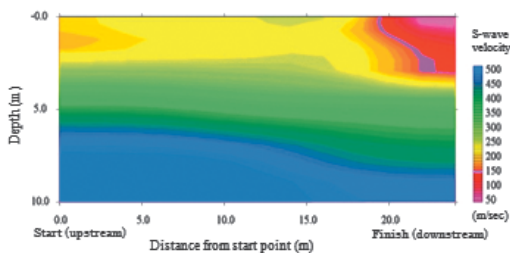


Figure 9. Distribution of S-wave velocity

The results of the micro tremor measurements are shown in Figs. 10(a) ~ (c). Measurements were made at the top as well as at the bottom of the embankment. On the surface of levee body, the predominant frequency of the soil deposits is 3.1 Hz (Fig. 10a). On the bottom of the levee body, the predominant frequency of soil deposits is between 4.0 to 6.0 Hz (Fig. 10b). Spectral ratio between the top and the bottom of the sloping side was found to be 2 Hz (Fig. 10c).

As observed in Fig. 9, the shear wave velocity is approximately 200 m/sec within 5 m from the surface layer. The predominant frequency of the site is 10 Hz. At the lower stream, the shear wave velocity of the surface wave within 5 m from the surface is below 100 m/sec. Thus, the result of the micro tremor measurements and the surface wave exploration shows a good agreement.

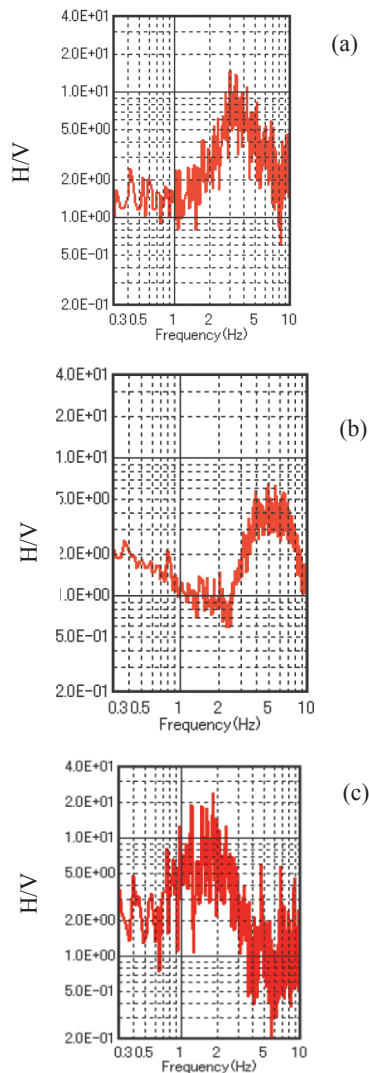


Figure 10. Results from the micro tremor observation

- (a) H/V-ratio at the surface, (b) H/V-ratio at the surface, (c) H/V-ratio at the surface

3.2.2 Laboratory testing

Physical testing and shear testing of soil samples collected at the investigation site in Yoshihama area (called Yoshihama soil hereafter). Test samples were found to be composed of gravelly soil that included gravel with a maximum grain diameter of 9.5 mm. The grain size distribution revealed that the samples contain gravel fraction of 12% and fine fraction of 20%.

Soils passing through 0.425 mm sieve had a plasticity index IP of 4.7, indicating some level of non-plasticity in the samples. In-situ wet density test of the soils at the site conducted using the core cut method (JGS 1613-2003) was obtained to be 1.46 g/cm³, and the degree of saturation was found to be 34.8%. The relative density of the embankment soils calculated using the JIS A1224 method was found to be 60%. Thus, there is a likelihood of liquefaction of the soils by the strong shaking during the earthquake. The shear strengths of the soils were determined using the cyclic triaxial shear test. In the triaxial apparatus used in this research, the specimen size was 50 mm in diameter and 100 mm in height. The soil specimens were prepared by the wet tamping method, because the other preparation methods such as air-pluviation or water-pluviation tend to intensify the segregation of soil particles for a well-graded granular soil. The relative density was adjusted by tamping to approximate target values at the site ($D_r = 60\%$). The specimen was saturated fully by supplying CO₂ gas and deaired water into the specimen. The specimen was isotropically consolidated by applying an effective stress of 49 kPa and maintaining the back-pressure at 98 kPa. The Skempton's B-value measured was greater than 0.96 in all the tests.

Fig. 11 shows the relation between the cyclic stress ratio $\sigma_d/2\sigma'_c$ and the number of cycles N_c from the undrained cyclic triaxial test when the double amplitude of the axial strain (DA) reached 2%, 5%, and 10% at the excess pore water pressure ratio of 0.95. It can be seen that the liquefaction strength has changed significantly with the increase in the number of cycles. Fig. 11 also shows liquefaction strength curves for various other alluvial sands and decomposed granite soil without fines (Hara et al., 2004). The liquefaction strength, R_{L20} of Yoshihama soil is found to be low (0.18) at $N_c = 20$. Comparing the R_{L20} values, one sees that Yoshihama soil has a lower strength than alluvial sand having the same relative density. The internal friction angle of Yoshihama soils was found to be 36.6 degree, which is close to value proposed by Nishida and Aoyama (1984) for undisturbed soils.

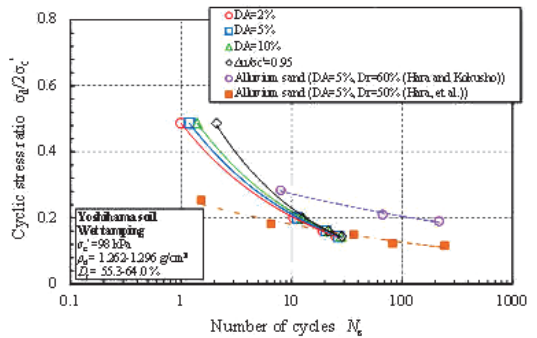


Figure 11. Results of cyclic triaxial test

Fig. 12 shows volumetric strain ε_v versus effective confining pressure σ'_c relationships obtained from the consolidation tests carried out after the undrained cyclic triaxial tests. The volumetric strain was found immediately after removing the load when DA reached 10%, based on the amount of drained water in a burette when specimens were returned to the drained state at the point of completion of the initial consolidation. Fig. 12 also shows the same relation at $D_r = 50\%$ for alluvial sand, alluvial gravel, and decomposed granite soil without fines. The change in volume for the Yoshihama soil after liquefaction was greater than for the alluvial sand and gravel containing hard grains or decomposed granite soil containing soft grains.

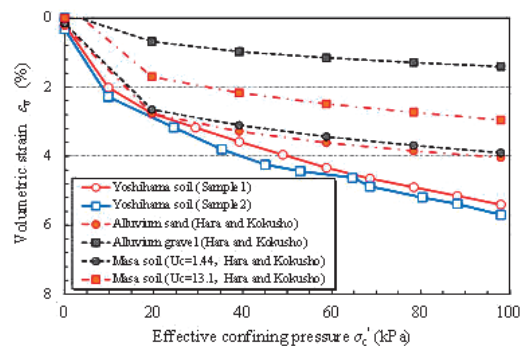


Figure 12. Results of the consolidation test

3.2.3 Soil-structure interaction mechanism

From the results of the site investigation on the coastal dike at Yoshihama area, it could be confirmed that the depth of dense layer in the

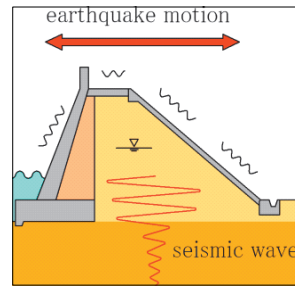
embankment was shallow; the fill soil was not compacted enough and was in loose state when the earthquake and the tsunami struck. Also, the water level within the levee body was high. On the other hand from the laboratory investigation on the sampled soil, it was found that the pore water pressure rose within the embankment due to the strong earthquake motion with long continuation time and the fill soils liquefied. Due to huge volume change resulting from liquefaction, the levee body subsided and this has led to the collapse of the structure. Furthermore, the tsunami, which followed the earthquake, led to further reduction of the strength of the levee body in spite of the existing concrete blocks at the back.

The collapse mechanism of the dike is illustrated in Figs. 13 (a) ~ (d). The top layer of the fill soils subsided largely by the action of cyclic loading during the earthquake as shown in Fig 13(a). This has resulted in the generation of voids and differential settlement between the levee crown and the concrete blocks as shown in Fig 13(b). Furthermore, as shown in Fig. 13(c), the vertical wall tilted due to extra force of the tsunami wave, and the inundated water entered into the levee body resulting in the scouring of the sides and the toe of the levee. Finally, as shown in Fig. 13(d), the backrush of the tsunami further deteriorated the strength of the levee due to scouring and the force due to backrush led to the complete collapse of the wall.

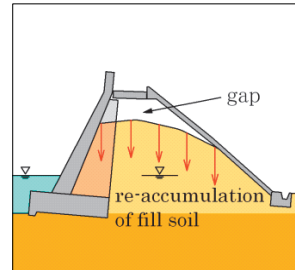
3.3 Details of investigations in Okirai

3.3.1 Field investigation and laboratory testing

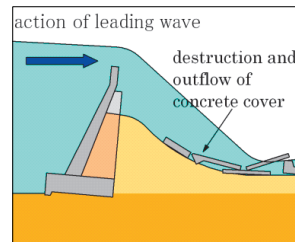
Fig. 14 shows the plane view of the tire retaining wall in Okirai. The figure also shows the locations of the various field surveys (in-situ density, PDCP test, surface wave exploration, and micro tremor measurement) that were conducted. Soils samples were also collected from the three locations (No.1, No.2, soil within tire).



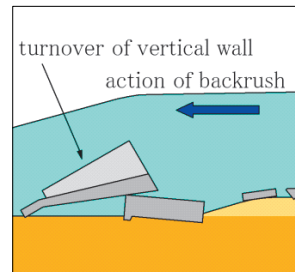
(a) Before the earthquake



(b) Just after the earthquake



(c) Effect of the leading wave



(d) Effect of the backrush

Figure 13. Mechanism of collapse of the dike

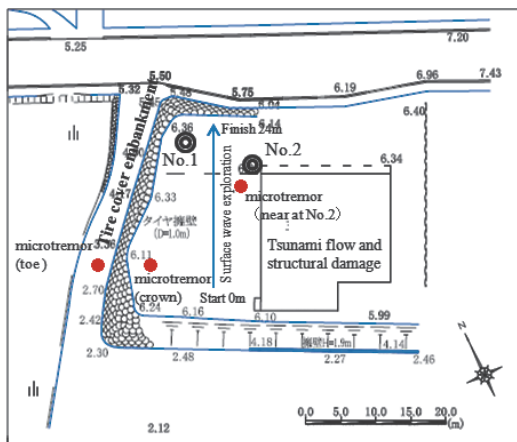


Figure 14. Location of retaining wall in Okirai

The distribution of S-wave velocity by surface wave exploration method conducted on the backfill soils is shown in Fig.15. As seen in the figure, beyond the depth of 10 m, S-wave velocity is greater than 220m/s implying a hard stratum near the sloping side. Within the depth of less than 10 m, stratum with 150~200 m/s of S-wave velocity exists. Since the average height of the retaining wall was 3.2 m with a maximum height of about 4 m, it can be said that as a whole, the backfill soil was in the loose state. Fig.15 also shows converted N-value obtained from the PDCP test. Converted N-value and S-wave velocity in general are showing the similar trend. The converted N-values to the depth of 0~70 cm are high, so it can be said that near the surface the backfill soil has a very high density. The higher density near the surface may be the result of influence of cyclic load experienced by the backfill soils due to parked cars, since the yard was used as a parking lot. On the other hand, converted N-value within the depth of 1~1.5 m is about 5. Therefore, if we consider that the backfill consists only of sandy soil, it can be said that in general the backfill soil was in loose state.

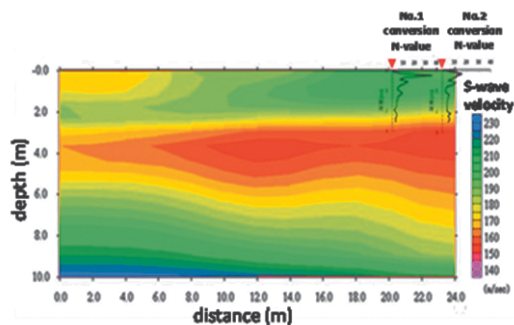
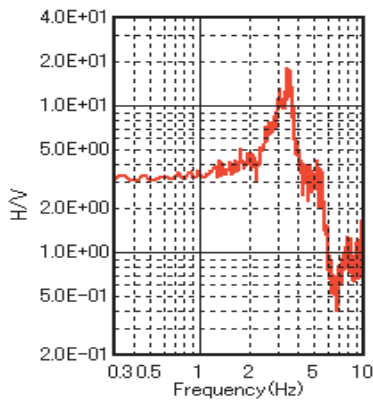


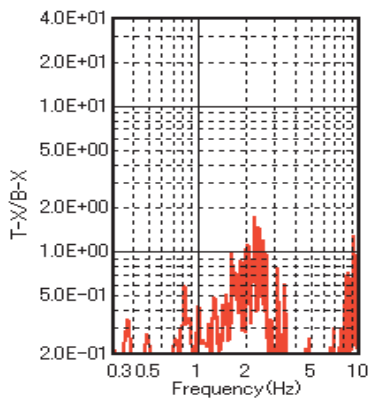
Figure 15. Distribution of S-wave velocity

Fig. 16 shows the results of the micro tremor measurements made at the top as well as at the bottom of the embankment. At location No. 2, the predominant frequency of H/V ratio of the soil deposits is 3.1 Hz (Fig. 16a). Spectral ratio between the top and the bottom of the sloping side was found to be 2.1 Hz (shown in Fig. 16b). The shear wave velocity from Fig. 15 was found to be approximately 200 m/sec beyond 10 m depth. The predominant frequency of site is 3.8 Hz. Therefore, it can be said that the result of the micro tremor measurements and the surface wave exploration is in good agreement.

Laboratory test was conducted for soils samples that were collected at the sites. The in-situ density of the backfill soil was measured using the core-cut method (JGS1613-2003). The values of in-situ wet density ρ_t at the two locations (No.1 and No.2) are almost the same (a little more than 1.5 g/cm³). From the laboratory testing the void ratio of the soil was found to be less than 1.1. The grain size distribution showed that the soils were well-grained. It can also be said that the soils are well compacted. On the other hand, it is found that the filled soils inside the tires are found to be of higher density, and thus can be said that they were compacted better. The angle of internal friction of the sample soil (collected within 30 cm from the surface) of the backfill ground is 45.7°, while it is 48.2° for the soil within the tires. Therefore, it can be said that near the surface both soils have high value of internal friction, because the wet density ρ_t is quite high.



(a) H/V-ratio at the surface

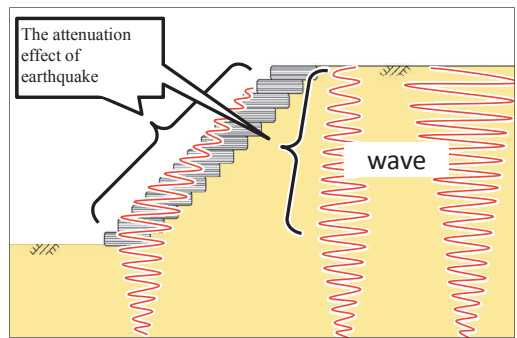


(b) Transfer function

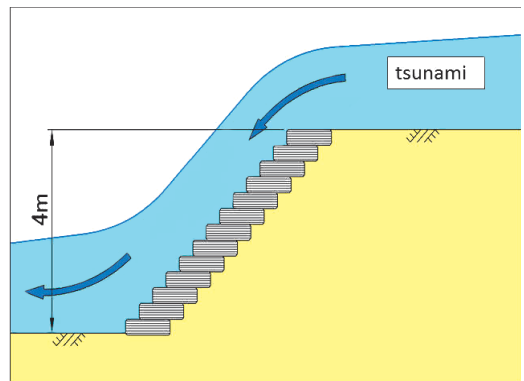
Figure 16. Micro tremor observations results

3.3.2 Soil-structure interaction mechanism

Fig. 17 illustrates the state of the tire retaining wall at the time of earthquake and tsunami. As seen from Fig. 17(a), the tire retaining wall has the confining effect (Fukutake & Horiuchi, 2007) which made the wall strong against earthquake, and this could prevent any sliding failure or surface failure of the backfill soils. On the other hand, permeable and flexible structures like the tire retaining wall can reduce the earth pressures and water pressures during earthquakes and tsunamis. In addition, the earthquake motion could be attenuated because of the seismic isolation characteristics of the tire and that prevented the failure of the backfill ground.



(a) During the earthquake



(b) During the tsunami

Figure 17. Interaction mechanism of the tire retaining wall at the time of earthquake and tsunami

On the other hand, tsunami entering from the backfill side damaged the building situated on the backfill ground and also eroded the natural slope opposite to the road parallel to the building. However, as shown in Fig. 17(b), the tire wall could prevent damage to the backfill as well as the sloping side of the backfill from scouring. The flexible structure could prevent any scouring of the wall at the bottom, a phenomenon which was prevalent in almost any sea walls, sea dikes, breakwaters and quay walls in many parts of Tohoku area due to the tsunami this time. The fact that tires are strong against scouring is evident from the fact that even during the backrush, the tsunami could not do any damage to the retaining wall. The hoop tension due to confinement, isolation effect and the anti-scouring effect is due to the high strength attributable to the hoop stress in each individual tire, and the high flexibility of the tire retaining wall.

The performance of the wall during the tsunami can be explained using the classic Newton's law, which is explained using Eq. (1) and Fig. 18 below.

$$F = \frac{mv}{\Delta t} \quad (1)$$

Where, F is the impact force acting on the structure, m is the approaching mass, v is the velocity with which the mass approaches the structure, and Δt is the time interval within which the mass acts on the structure.

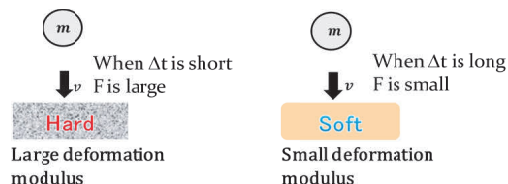


Figure 18. Impact force on structure depending on the structural materials

The force of impact will be less when the time interval will be large. Due to flexible nature of tires, the impact force will be acting for a comparatively longer time, which resulted in a lesser force acting on the structure. In addition, permeable nature of the structure, allows the force to dodge rather than bounce, which resulted in the good performance of the structure. This is a classic application of technique of Judo or sometimes in Sumo wrestling.

4. CONCLUSIONS

Field and laboratory investigations were carried out on two retaining structures located in the affected areas of the 2011 great east Japan disaster. Both the structures show contradictory behavior in their seismic resistant and tsunami resistant characteristics as far as the level of damage is concerned. Based on the investigations, the following conclusions could be drawn.

- (1) Dikes covered with concrete block in Yoshihama were damaged completely. The results show that subsidence related failure probably had taken place in the dike body with low soil density and high water table. Due to huge volume change resulting from liquefaction, the levee body

subsided and this has led to the collapse of the structure. Furthermore, the tsunami and the backrush led to further reduction of the strength of the levee body in spite of the existing concrete blocks at the back.

- (2) The tire retaining wall was not damaged in spite of the loose state of the backfill. Damage to the tire retaining wall could be prevented by the earthquake due to confinement effect. In addition, the flexibility inherent in tires made the earth pressure and water pressure reduce during the earthquake and the tsunami. The seismic isolation effect was the reason behind such good performance.

This research further revealed a shortcoming of our age old perception that any rigid and heavy structure will have strong resistance against impact forces such as earthquake and tsunami. However that conventional perception was proved to be wrong as evidenced by these two particular case studies presented here. After the 2011 great east Japan disaster, there has been a lot of attention on tsunami resistant characteristics of geotechnical structures. For example, development of ductile/resilient foundations that can protect the structures without collapse even if a tsunami of such scale attacks the structure. The case study of tire retaining structure is a good example of resilient and ductile structures. Studies are ongoing to investigate the behavior of the two structures described here through detailed numerical analysis and further field surveys.

It is high time that the civil engineers will throw away their conservative thinking, and put their knowledge and wisdom rather than convention in the development of new materials and techniques. Such approaches in design and construction will pave the way for preventing scouring, erosion and ultimate collapse of civil engineering structures in the future devastating earthquakes and tsunamis.

5. ACKNOWLEDGMENTS

The authors greatly appreciate the contributions of the following individuals in the in-situ testing and data analysis of this research: Dr. Minoru Yamanaka, Kagawa University; Prof. Tsuneo

Ohsumi, Tsukuba University; and Mr. Nozomu Kosaka, JAFEC U.S.A.

6. REFERENCES

- Central Disaster Mitigation Council. 2003. Report of the 16th Committee Meeting, Investigation Committee on Tonankai Earthquake and Nankai Earthquake, *Cabinet Office*, Government of Japan (in Japanese).
- Fukutake, K., and Horiuchi, S. 2007. Stacks of Tires for Earth Reinforcement Using Their Resistance to Hoop Tension and Land Reclamation Methods, *Scrap Tire Derived Geomaterials, Hazarika & Yasuhara (eds)*, Taylor and Francis, London, pp. 205-214.
- Furumura, T., Takemura, S., Noguchi, T., Takemoto, T., Maeda, K., and Padhy, S. 2011. Strong Ground Motions from the 2011 Off the Pacific Coast of Tohoku, Japan (Mw=9.0) Earthquake Obtained from a Dense Nation-wide Seismic Network, *Landslides*. Vol. 8, pp. 333-338.
- Hara, T. 2011. Relationship between geotechnical disaster and building, *Wood Industry*, Vol. 66, No. 11, pp. 492-497 (in Japanese).
- Hara, T., Kokusho, T. and Hiraoka, R. 2004. Undrained Strength of Gravelly Soils with Different Particle Gradations, *Proc. of the 13th World Conference on Earthquake Engineering*, Paper No.144, pp. 1-9.
- Hara, T., Okamura, M., Uzuoka, R., Ishihara Y. and Ueno, K. 2012. Damages to River Dikes Due to Tsunami in South-central Coastal Area of Iwate Prefecture in 2011 off the Pacific Coast of Tohoku Earthquake, *Japanese Geotechnical Journal*, Japanese Geotechnical Society, 7:1, pp. 25-36 (in Japanese).
- Hazarika, H. 2011. Infrastructural Damage and Lessons Learnt – A Review on the Aftermath of the March 11, 2011 Earthquake, *Keynote Lecture, Proc. of the 4th AUN/SeedNet Regional Conference on Geohazard Mitigation in ASEAN*, Phuket, Thailand, CD-ROM.
- Hazarika, H., Kasama, K., Suetsugu, D, Kataoka, S., and Yasufuku, N. 2012. Damage to Geotechnical Structures in Waterfront Areas of Northern Tohoku Due to the March 11, 2011 Tsunami Disaster, *Indian Geotechnical Journal*, Indian Geotechnical Society, Vol. 43, No. 2, pp. 137-152.
- Imai, T., and Tonouchi, K. 1982. Correlation of N-Value with S-Wave Velocity and Shear Modulus, *Proc. of the 2nd ESPT*, pp. 67-72.
- Kyoshin Network K-NET. 2011. National Research Institute for Earth Science and Disaster Prevention, <http://www.k-net.bosai.go.jp/>
- MILIT. 2011. Damage and Restoration of River and Coastal Structures due to the East Japan Disaster, *Water and Disaster Management Division*, Tohoku Regional Bureau, Ministry of Land, Infrastructure, Transport and Tourism, Sendai, Japan (in Japanese).
- Nakamura, Y. 1989. A Method for Dynamic Characteristics Estimation of Subsurface Using Micro tremor on the Ground Surface, *Quarterly Report of RTRI*, Vol. 30, No. 1, pp. 25-33.
- Nishida. K., and Aoyama, C. 1984. Classification System of Decompose Granite soil in Undisturbed State, *Journal of Japan Society of Civil Engineers*, Vol. 352, No. III-50, pp. 159-168 (in Japanese).
- Okada, K., Sugiyama, T., Noguchi, T., and Muraishi, N. 1992. A Correlation of Soil Strength between Different Sounding Tests on Embankment Surface, *Tsuchi to kiso*, Vol. 40, No. 4, pp. 11-16 (in Japanese).
- Shuto, N. 2011. History of Tsunami in Sanriku Area (Part 1): Information on Tsunami due to 2011 off the Pacific Coast of Tohoku Earthquake, *Joint Investigation Report of the 2011 off the Pacific Coast of Tohoku Earthquake*, <http://www.coastal.jp/ttj/index.php> (in Japanese)

Soil-structure-interaction of large storage constructions

R. Katzenbach & S. Leppla

Technische Universität Darmstadt, Institute and Laboratory of Geotechnics, Germany, katzenbach@geotechnik.tu-darmstadt.de

ABSTRACT: Qualified design and construction of any type of structure basis on the knowledge of the soil-structure-interaction. To investigate the soil-structure-interaction it is necessary to guarantee stability and serviceability of the structures during construction phase and service time. The paper presents the analysis of the soil-structure-interaction of a large storage construction for coal at a power station in Germany. The storage is a circular concrete construction with a diameter of about 125 m and a height in the centre of about 40 m. The analysis of the soil-structure-interaction includes the 3-dimensional modelling of the superstructure and the non-linear soil behaviour in a Finite-Element-simulation.

1. INTRODUCTION

The knowledge of the soil-structure-interaction is the basis for a qualified design and construction of any type of construction. To investigate the soil-structure-interaction it is necessary to guarantee stability and serviceability of the structures during construction phase and service time. In many cases for analysis of the soil-structure-interaction numerical methods as the Finite-Element-Method (FEM) are used considering the stiffness of the soil and of the superstructure. For verification of the numerical analysis and for quality assurance the observational method is applied (Peck 1969; Katzenbach et al. 2010).

The paper presents the analysis of the soil-structure-interaction of a large storage construction for coal at a power station in Germany. The analysis include the 3-dimensional modelling of the superstructure and the non-linear soil behaviour in a Finite-Element-simulation. The analysis showed that the original design of the superstructure had to be verified to minimise the displacements of the structure. Since the end of the construction the superstructure is monitored during the service time with geotechnical and geodetic measurement devices by means of the observational method.

2. PROJECT DISRCIPTION

2.1. Foundation system and superstructure

The coal storage of the power station is a circular concrete construction with a diameter of about 125 m and a height up to 40 m in the centre. For the power station 2 new storages with a distance of 5 m between each other are planned. Figure 1 shows the first storage after construction. The soil improvement for the second storage is in progress.



Figure 1. New circular coal storage at power station.

Both circular coal storages were planned with a 20.5 m high reinforced concrete wall with a thickness of 90 cm. At the top of the wall a circular reinforced concrete beam with a width

of 3.5 m and a height of 1.5 m is located. The wall has 32 stiffener walls every 11° with a thickness of 1 m for minimisation of the horizontal displacements. The circular reinforced concrete strip foundation was planned with a thickness of 2 m and a width of 10 m. The storage is covered with a steel construction.

First 2-dimensional, rotation-symmetric FE-simulations showed, that the horizontal displacements of the concrete wall were too large for the stability of the steel construction on top. So the width of the circular strip foundation was increased to 12 m. Additionally a soil improvement was planned consisting of a gravel layer with 1 m thickness and a deep compaction of the natural sand and gravel layer up to a depth where the clay layer is reached.

Figure 2 shows the cross section of the circular construction including the surrounding soil conditions and the located soil improvement.

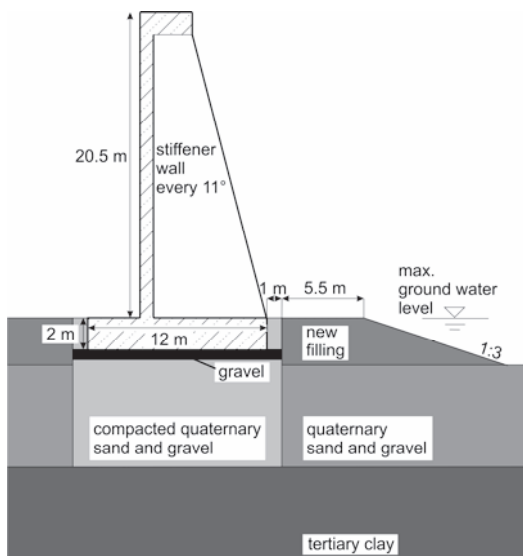


Figure 2. Cross section of the circular construction.

Due to the delicate steel roof construction especially the horizontal displacements of the top of the reinforced concrete wall had to be limited to guarantee the stability of the steel roof. Regarding this aspect the soil-structure-interaction has a very important role. The project is categorised into the Geotechnical

Category 3 of the Eurocode 7 (EC 7). This is the category for projects with a very high complexity. Based on the building legislation the building authorities involved independent experts of structural engineering and of geotechnical engineering for an independent peer review process (Katzenbach & Leppä 2013a & 2013b). Additionally the observational method with a monitoring program consisting of geodetic and geotechnical measurements was installed.

2.2. Soil and ground water conditions

The project area is located in the flood zone of a nearby river. Due to that fact the area of the storages is filled up to a height of 3.2 m. Artificial fillings and cohesive, clayey soil material was removed under the storages until the natural quaternary sand and gravel layer is reached.

The quaternary sand and gravel layer has a thickness of about 6 m to 9 m. Below the sand and gravel layer a tertiary, stiff clay layer is investigated with a thickness of several decameters. Table 1 shows the soil mechanical parameters of the quaternary sand and gravel and the tertiary clay.

Table 1. Mechanical parameters of the soil.

		quaternary sand and gravel	tertiary clay
weight γ	[kN/m ³]	20	20
weight γ'	[kN/m ³]	11	10
friction angle ϕ'	[°]	32,5	20
cohesion c'	[kN/m ²]	0	20
modulus of stiffness $E_s(z)$	[MN/m ²]	60-80	30-80

The mechanical soil parameters of the new 1 m thick gravel layer under the strip foundation and of the compacted natural sand and gravel layer are shown in Table 2.

Table 2. Mechanical parameters of the improved soil.

		new filling	compacted quaternary sand and gravel
weight γ	[kN/m ³]	20	20
weight γ'	[kN/m ³]	11	11
friction angle ϕ'	[°]	32,5	35
cohesion c'	[kN/m ²]	0	0
modulus of stiffness E_s	[MN/m ²]	45	80

The ground water table is directly influenced by the river and is close to the surface. In flood situations the water table will rise approximately up to the upper edge of the strip foundation.

3. INDEPENDENT PEER REVIEW PROCESS

As part of the 4-eye-principle the independent peer review is the basis for quality assurance. The process of independent peer review is shown in Figure 3.

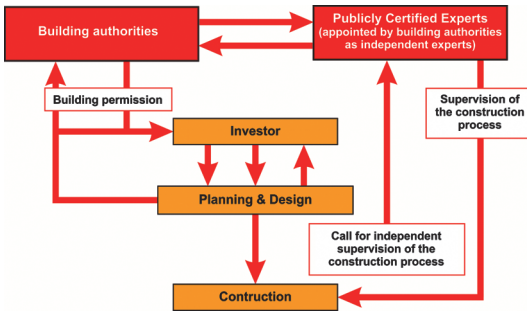


Figure 3. Independent peer review process.

It consists of 3 parts. The investor, the experts for planning and design and the construction company belong to the first part. Planning and design are done according to the requirements of the investor and all relevant documents to obtain the building permission are prepared.

The building authorities are the second part and are responsible for the building permission which is given to the investor.

The third part consists of the publicly certified experts. They are appointed by the building authorities but work as independent experts. They are responsible for the technical supervision of the planning, design and construction.

In order to achieve the license as a publicly certified expert for geotechnical engineering by the building authorities intensive studies of geotechnical engineering in university and large experiences in geotechnical engineering with special knowledge about the soil-structure-interaction are required.

The independent peer review by publicly certified experts for geotechnical engineering makes sure that all information including the results of the soil investigation consisting of laboratory and field tests and the boundary conditions defined for the geotechnical design are complete and correct.

In case of a defect or collapse the publicly certified expert for geotechnical engineering has to be involved as an independent expert to find out the reasons of the defect or damage and to develop a concept for stabilisation and reconstruction (Katzenbach et al. 2013c). For all difficult projects an independent peer review is essential for the successful realisation.

4. OBSERVATIONAL METHOD

The observational method is applied to projects with difficult boundary conditions for verification of the design during the construction and, if necessary, during service time. For example in the EC 7 the effect and the boundary conditions of the observational method are defined.

The application of the observational method is recommend for the following types of construction projects:

- very complicated/complex projects
- projects with a distinctive soil-structure-interaction, e.g. mixed shallow and deep foundations, retaining structures for deep excavations, Combined Pile-Raft Foundations (CPRFs)
- projects with a high and variable water pressure
- complex interaction situations consisting of ground, excavation and neighbouring buildings and structures

- projects with pore-water pressure reducing the stability
- projects on slopes

The observational method is always a combination of the common geotechnical investigations before and during the construction phase together with the theoretical modelling and a plan of contingency actions (Figure 4). Only monitoring to ensure the stability and the serviceability of the structure is not sufficient and, according to the standardisation, not permitted for this purpose.

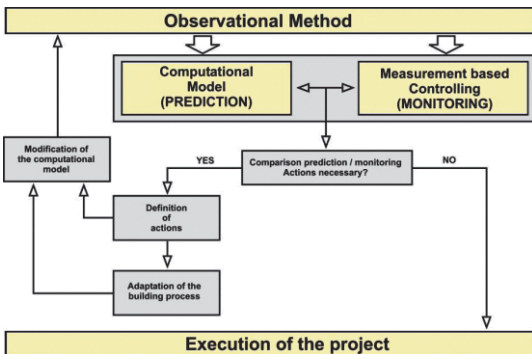


Figure 4. Observational method.

Overall the observational method is an institutionalised controlling instrument to verify the soil and rock mechanical modelling (Katzenbach et al. 1999a & 1999b; Rodatz et al. 1999).

The identification of all potential failure mechanisms is essential for defining the measurement concept. The concept has to be designed in that way that all these mechanisms can be observed. The measurements need to be of an adequate accuracy to allow the identification of critical tendencies. The required accuracy as well as the boundary values need to be identified within the design phase of the observational method.

Contingency actions need to be planned in the design phase of the observational method and depend on the ductility of the systems.

The observational method must not be seen as a potential alternative for a comprehensive soil investigation program. Additionally the observational method is a tool of quality assurance and allows the verification of the param-

eters and calculations applied in the design phase. The observational method helps to achieve an economic and save construction.

5. SOIL-STRUCTURE-INTERACTION

5.1. Analysis with FE-simulations

For the analysis of the interaction of the reinforced concrete structures and the soil numerical methods as the FEM are used. The non-linear elastoplastic soil behaviour was modelled using a modified Drucker-Prager cap model. The linear elastic material behaviour of the concrete was modelled using *Hook's Law*.

For verification of the first design of the foundation and the superstructure and the necessary soil conditions 2-dimensional rotation-symmetric FE-simulations were executed in an early planning stage. Figure 5 shows the FE-net of the 2-dimensional rotation-symmetric simulations. The simulation considered the coal storage with a height up to the top of the wall.

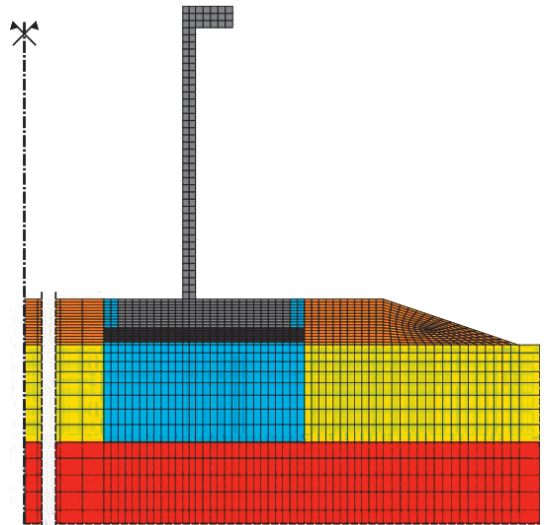


Figure 5. 2-dimensional, rotation-symmetric FE-simulation.

For the analysis of the interaction between both coal storages 3-dimensional non-linear FE-simulations were carried out. For analysing the worst case of coal storage the load impact on the construction was simulated as shown in

Figure 6. With this load constellation the biggest displacements of the structures are predicted.

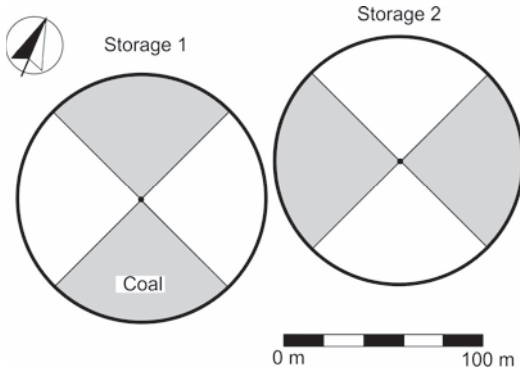


Figure 6. Coal storage for worst case simulation.

The 3-dimensional simulations had 261.000 elements with 155.000 nodes. The equation system has about 450.000 unknown values. Figure 7 shows the FE-model.

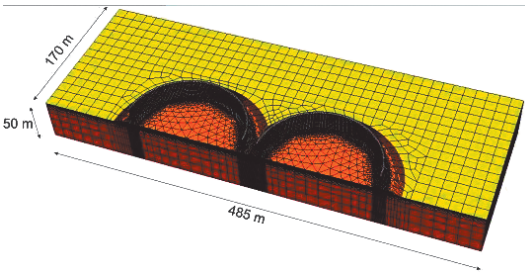


Figure 7. 3-dimensional FE-model.

5.2. Requirements for structural analysis

For the analysis of the superstructure the structural engineers had to consider the soil-structure-interaction. Regarding the delicate steel roof construction especially the horizontal subgrade reaction modulus $k_{s,h}$ was of interest. The horizontal subgrade reaction modulus $k_{s,h}$ defines a spring stiffness and depends on the stiffness of the soil, on the load impact and on the geometrie of the foundation system.

The horizontal subgrade reaction modulus is defined by Equation (1) as follows:

$$k_{s,h} = \tau/v_h \quad (1)$$

with: τ = shear stress under strip foundation [MN/m²]

v_h = horizontal displacement of the strip foundation [m]

Due to the close storage constructions and the different load constellations caused by the optional coal fillings the horizontal subgrade reaction modulus can only be determined by 3-dimensional, non-linear FE-simulations.

The results of the comprehensive FE-analysis gave for the Ultimate Limit State (ULS) a $k_{s,h} = 0.63 \text{ MN/m}^3$ and for the Serviceability Limit State (SLS) a $k_{s,h} = 0.83 \text{ MN/m}^3$.

6. APPLICATION OF THE OBSERVATIONAL METHOD

6.1. Monitoring program

Based on the requirements of the observational method a comprehensive monitoring program was installed. The measurement data is collected by the following measurement devices:

- 48 geodetic measurement points in 3 levels on the concrete wall (1.2 m, 3 m and on the top)
- 4 inclinometer under the strip foundation down to a depth of 40 m
- 4 extensometer (fivefold) under the strip foundation down to a depth of 40 m

For the evaluation of the stability and the serviceability especially the horizontal displacements at the top of the concrete wall are important.

For safety reasons and due to the long consolidation time of the tertiary clay at the moment the allowed height of coal stored is 14 m on the concrete wall, which is about 70 % of the maximum filling. This filling period will last until every part of the storage is filled more than one time. After that the allowed height of coal stored will be increased.

The geodetic measurement sections of the up to now constructed storage are displayed in Figure 8.

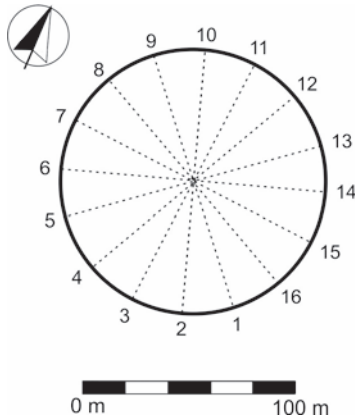


Figure 8. Geodetic measurement sections.

6.2. Measurement results

The maximum measured horizontal and vertical displacement of the reinforced concrete structure is shown in Figure 9. The coal was stored up to the height of 14 m at the wall. The maximum measured vertical displacement is up to 5 cm. The maximum measured horizontal displacement is up to 3.5 cm. The results of the numerical simulations are in the same range for this load situation.

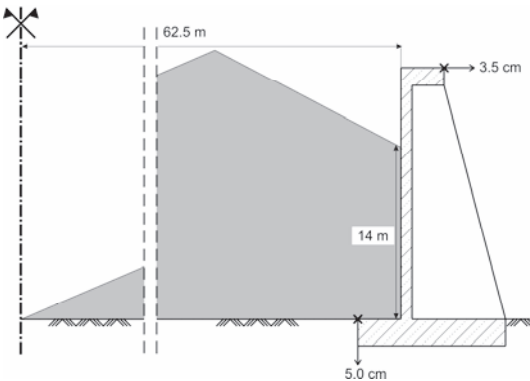


Figure 9. Maximum measured displacements.

The measured vertical displacements of the circular structure during the 4 last filling situations are displayed in Figure 10. The 4 successive filling situations show that the load impact on the soil leads to varying displacements along the superstructure. The displayed minimum displacements are caused by the former load situations.

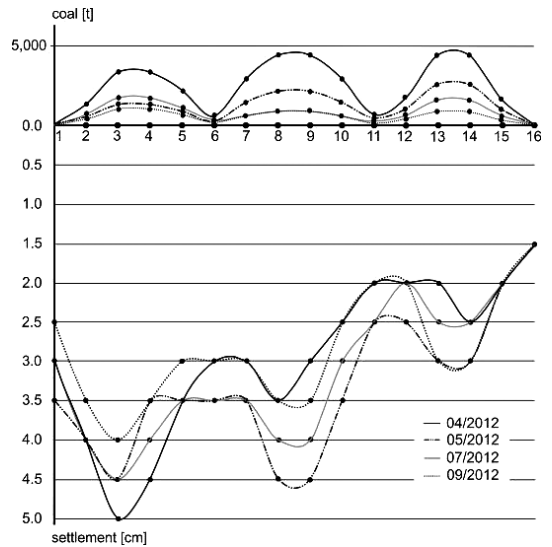


Figure 10. Measured vertical displacements along the superstructure.

7. CONCLUSIONS

The qualified analysis of the soil-structure-interaction of complex construction projects are the basis for a safe and economic design. These analysis include in most cases numerical simulations considering the non-linear behaviour of the soil.

The analysis of the soil-structure-interaction for the presented project defined the horizontal subgrade reaction modulus as a basis for the analysis and design of the superstructure. Nevertheless the predictions based on the numerical analysis have to be proofed by means of the observational method.

The comparison of the numerical results and the measured displacements shows a good accordance.

For the successful realisation of the project the following aspects are decisive:

- adequate soil investigation
- 3-dimensional, non-linear FE-simulation for the definition of the horizontal subgrade reaction modulus
- controlling of the predictions made during the analysis in the design stage by application of the observational method

- peer review by an independent, publicly certified expert for structural engineering
- peer review by an independent, publicly certified expert for geotechnical engineering

The decision of the building authorities to involve the independent, publicly certified experts for structural engineering and for geotechnical engineering in an early planning stage guaranteed a safe design and construction.

8. REFERENCES

CEN European Committee of Standardisation 2008. Eurocode 7: Geotechnical design – Part 1: General rules.

CEN European Committee of Standardisation 2008. Eurocode 7: Geotechnical design – Part 2: Ground investigation and testing.

Katzenbach, R., Bachmann, G., Leppla, S., Ramm, H. 2010. Chances and limitations of the observational method in geotechnical monitoring. 14th Danube-European Conference on Geotechnical Engineering, 2.-4. June, Bratislava, Slovakia, 13 p.

Katzenbach, R., Boley, C., Moormann, C., Rückert, A. 1999a. Rechtsrelevante Sicherheitsaspekte in der Geotechnik. Mitteilungen des Institutes und der Versuchsanstalt für Geotechnik der Technischen Universität Darmstadt, Heft 43, 71-96.

Katzenbach, R., Leppla, S. 2013a. Economic solutions for geotechnical challenges like super high-rise buildings and urban tunnelling. International Conference on “State of the art of pile foundation and pile case histories”, 2.-4 June, BAndung, Indonesia, A1-1-A1-12.

Katzenbach, R., Leppla, S. 2013b. Qualified soil investigation and the 4-Eye-Principle as basis for safety and serviceability of geotechnical constructions. 1st International Conference on Foundation and Soft Ground Engineering Challenges in MeKong Delta, 5. June, Thu Dau Mot University, Binh Duong City, Vietnam, 19-26.

Katzenbach, R., Leppla, S., Weidle, A. 2013: Aspects of management of soil risk. 4th International Seminar on Forensic Geotechnical Engineering, 10.-12. January, Bengaluru, India, 12 p.

Katzenbach, R., Schmitt, A., Turek, J. 1999b. Cooperation between the geotechnical and structural engineers – experiences from projects in Frankfurt. COST Action 7, Soil-Structure-

Interaction in urban civil engineering, 1.-2 October, Thessaloniki, Greece, 53-65.

Peck, R. B. 1969. Advantages and limitations of the Observational Method in applied soil mechanics. *Géotechnique*, 19 (2), 171-187.

Rodatz, W., Gattermann, J., Bergs, T. 1999. Results of five monitoring networks to measure loads and deformations at different quay wall constructions in the port of Hamburg. 5th International Symposium on Field Measurements in Geomechanics, 1.-3. December, Singapore, 4 p.

Strengthening Of The Beds And Foundations Of The Tilla-Kori Mosque Of The Registan Ensemble In Samarkand

A.Z. Khasanov

M. Ulugbek Samarkand Architectural and Civil-Engineering Institute, Samarkand, Uzbekistan

Z. A. Khasanov

Geofundamentproject Co. LTD. Samarkand, Uzbekistan

F. F. Zekhniev

N. M. Gersevanov Scientific-Research Institute of Foundations and Underground Structures, Moscow, Russia

ABSTRACT: Causes of the deformation of the universally known 17th century Tilla-Kori Mosque of the Registan ensemble in Samarkand are examined. Results of geomechanical investigations and geodesic observations, analysis, construction, and design of elements for the strengthening of the bed and foundation and their implementation are described.

Failures of architectural monuments are, as a rule, associated with processes that take place in the geologic medium. This, among other things, is the deformation of the soil bed due to tectonic processes in the earth's crust, gravitational, and internal loads, and processes resulting from man's activity, which are governed by characteristics of the historic infrastructure of the region where the monuments are located, and modern urban development.

The condition of the world-famous architectural monuments within the Registan ensemble in Samarkand has been observed since 1950. During the past 15–20 years, and particularly beginning in 1993, significant deformations of architectural forms and severe damages to the structures have been recorded, for example, the arches and columns of the galleries, and tilting of the minaret, raising question concerning strengthening of the beds and foundations of the entities that have been deformed.

As an architectural monument, the Tilla-Kori mosque was constructed in 1960–1964 on the site of former public houses, auxiliary spaces, rows of artisan shops, etc.

The monument building has a rectangular 145×155-m planform with an internal courtyard. The central dome section is 20×20 m around the outside, and the heights of the lower and upper domes are 16 and 30 m, respectively (Fig. 1). The southern and northern galleries

with planform dimensions of 30×17 and 24×17 m, respectively, are 5 m in height. All structures of the central dome weigh 66,000 kN, while those of the outer dome weigh in at 4,000 kN [1]. The basic geometric dimensions of the mosque are shown in Fig. 2.



Fig. 1. Western wall of Tilla-Kori mosque.

Geologic-engineering surveys have indicated that soils of anthropogenic origin reside

from the surface to a depth of 8-10 m, and are underlain to 30 m by loess clayey loams; the groundwater table sits at a depth of 15-16 m.

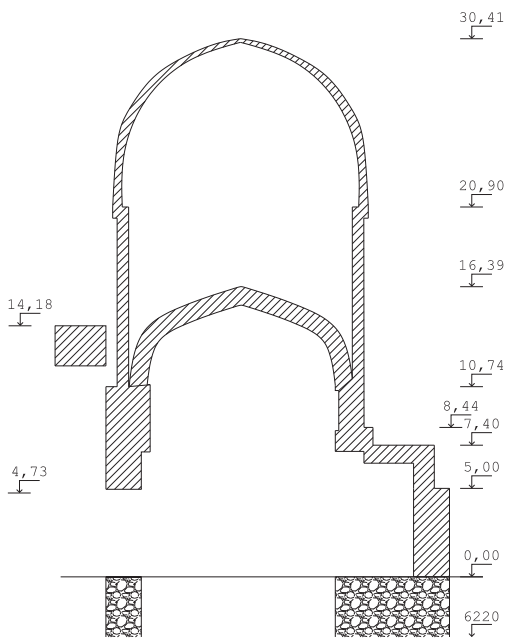


Fig. 2. Cross section of central domed portion of mosque.

Soils containing cultivated and urban deposits (GEE-1) are weakly structured, and are primarily clayey loams with inclusions of construction debris, organic material, and humus; they are highly porous with a void ratio $e > 0.9$ and density $\gamma < (1.3-1.4) \text{ g/cm}^3$. Remnants of foundations formed from kiln-fired brick in a clay mortar, or the brick covering of floors of older structures are encountered at various depths.

The moisture content of the soil ranges from 20 to 24% to a depth of 8 m diminishes to 16-18% below this depth where it is confined to the natural soil stratum. Its seasonal increase occurs in the surface zone of aeration.

The loess soils residing at depths of from 8-10 to 16 m macroporous, prone to slump-type settlement, and are slightly moist (GEE-2) with a plasticity index of 7-8%, void ratio of 0.85-0.92, dry density of 1.3-1.4 g/cm^3 and moisture content of 12-16%. The loess soils below 15-16 m, which corresponds to the groundwater table, and to an exposed depth of 30 m have consis-

tencies ranging from highly to slightly plastic (GEE-3).

Field tests of the soils by dynamic cone penetration, which were carried out from the face of a pit (-3.5 m) to a depth of 12 m indicated that the conditional dynamic resistance of the soil for GEE-1 varies from 0.16-0.20 to 0.90-1.08 MPa. Interlayers of the soils at a depth of 6-7 m were found to be particularly weak (Table 1).

Table 1.

Thickness	Soil	Depth of cone penetration, m	Conditional dynamic resistance, MPa	Lightweight zone								
				0.2	0.4	0.6	0.8	1.0	1.2	1.4		
9	Antropogenic	1.0										
		2.0										
		3.0										
		4.0		1.08								
		5.0		0.92								
		6.0		0.19								
		7.0		0.164								
		8.0		0.94								
		9.0		1.15								
		3	Loess	10.0		1.50						
11.0				1.55								
12.0				1.45								

Several series of plate tests were carried out beneath the foundation to determine the compression modulus of the soils. The plate was placed horizontally at a depth of 3-8 m in a deepened recess at a depth of 3-8 m. The tests revealed a compression modulus of 2.8 and 11.0 MPa under the outer walls of the northern and southern galleries, respectively, and 1.5 MPa under the central dome.

The foundation beneath the abutment in the central domed section of the mosque assumes a rectangular planform with outside dimensions of 20×23 m, and inside dimensions of 11×13 m. The foundation with a depth of embedment of 3.3 m from the surface of the ground consists of multilayer rub-blestone and brick masonry in a Ganchev (ancient procedure for the preparation of a binder formed from alabaster with the addition of loess soil) grout (Fig. 3). Masonry formed from large broken limestone rubble is placed to a height of 90-100 cm, and is topped-

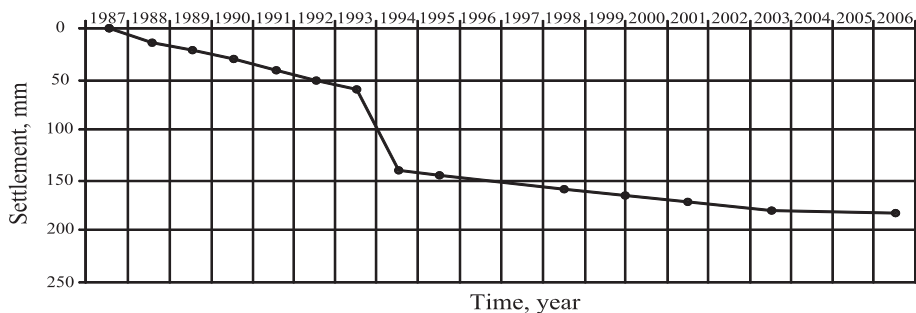


Fig. 4. Plot showing settlement of foundations under western wall from 1987 through 2006.

piles, and transferring a portion of the load onto the stronger loess soils. Deformations of the bed soils occur due to loads that exceed the limiting allowable values (the average pressure beneath the foundation of the abutments is more than 343 Pa). Degradation of the properties of the soils in the cultivated-urban deposits is possible as a result of the penetration of water, and an increase in their moisture content due to leakage from irrigation systems. Moreover, significant horizontal displacements of the foundations are observed in the central domed section, and along the western wall of the gallery (especially the northern gallery) due to surface displacement of the soil layer under the action of thrust and vertical loads imparted by the massive arches.

In this connection, the strengthened foundations should take up not only the vertical, but

also horizontal thrust loads. To determine the forces and degree of reinforcement of the piles and rafts, we analyzed their joint performance with the existing foundation.

The design called for an increase in the stiffness of the piles, and the installation of a retaining wall fabricated from a raft and six piles to take up the horizontal thrust forces.

All pile heads were connected by reinforced-concrete rafts of complex configuration at a level of 3.3-4.3 m. The walls of the foundation were waterproofed prior to back-filling.

Static field tests of two piles with a length of 12 m, shaft diameter of 80 cm, and a lower face expanded to 130 cm were conducted to determine the bearing capacity. A charging system with a load-carrying capacity of 3,000 kN on a metallic frame over a span of 6 m was fabricated for this purpose. The frame was bolt-

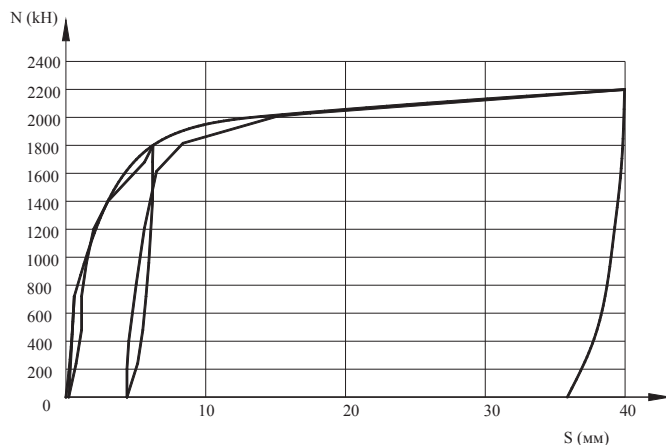


Fig. 5. Plot showing settlement of piles due to static loads.

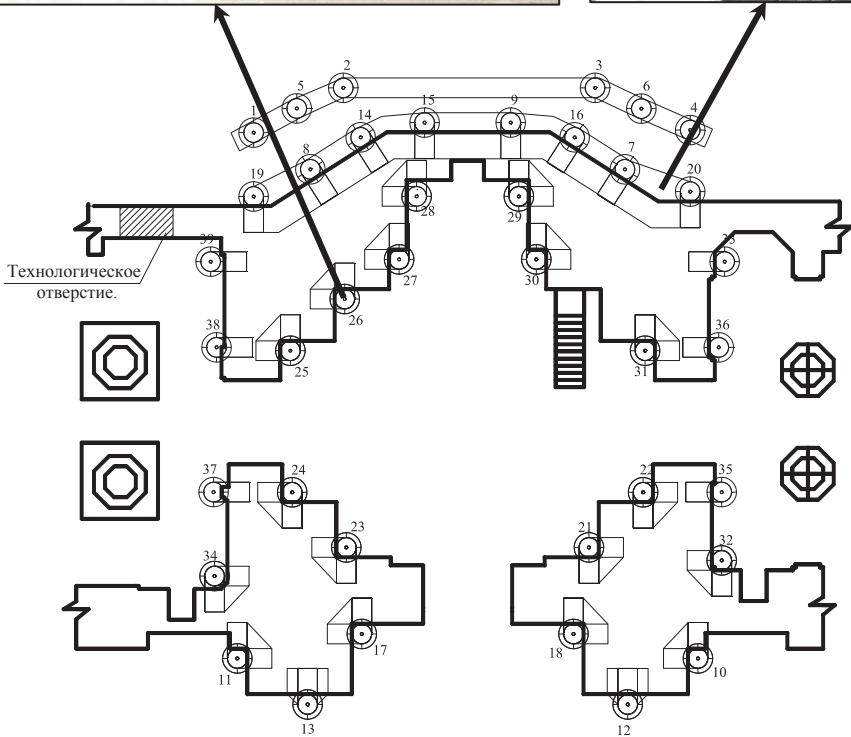


Fig. 6. Plan view of arrangement of piles, rafts, and retaining wall around perimeter of four abutments

connected to two anchor piles positioned at a distance of 5.6 m.

A 0.1-mm deformation after 20 min was adopted as conditional stabilization for the cast-in-place piles. The load was imparted in steps of 200 kN, and was brought to the critical load at which the limiting deformation of a pile ex-

ceeded 40 mm. The load amounted to 2,200-2,400 kN during the tests.

Figure 5 shows a plot of the settlements of the cast-in-place piles with the expanded base due to the static loads. The bearing capacity of a cast-in-place pile for the project was assumed to be 1,700 kN.

Due to the complexity of the procedure, strengthening of the bed and foundations was performed in two stages. The pile foundations were installed in the first stage, and the raft was connected to the reinforced-concrete retaining wall in the second.

The reinforced-concrete raft under a foundation was constructed between two piles. For safety and formulation of the procedure, it was decided to localize the opening of pits, dig under the foundation, assemble the reinforcement, and concrete the rafts. A pit 80-90-cm wide and 460 cm deep was excavated between the piles, and then back-filled with layer-by-layer compaction. The soils were wetted to the optimal moisture content of 18–20%, and compacted with a tamper.

A total of 38 cast-in-place piles and rafts, and a retaining wall were installed (Fig. 6). The construction operations were accompanied by geodetic measurement of the settlements and deformations of the structures. It is established that the deformations of the monument are currently stabilized (see Fig. 4).

CONCLUSIONS

1. Results of multiyear observations of the monument have demonstrated that bed deformations have been occurring over a long period. Significant deformations over the past 15-20 years have been associated with technogenic activity, and, as a consequence, an increase in the moisture content of the bed soils.

2. Weak cultivate-urban deposits 8-10 m thick, which cannot serve as a reliable bed due to their weak bearing capacity and high deformability, reside beneath the foundation of the monument.

3. Field tests of cast-in-place piles in the vicinity of the monument indicated that the load on the soil is approximately 2,200 kN instead of the 1,700 kN adopted in the design.

4. Strengthening of the beds and foundations by the method of underpinning with cast-in-place piles, and transfer of a portion of the load onto the stronger loess soils made it possible to stabilize their settlements as suggested by results of geotechnical monitoring.

Designs of the Railway Roadbed of Thawing Permafrost Soils in Condition of the Far East

S.A. Kudryavtsev, Y.B. Berestyanyy, T.U. Valtseva, R.G. Mihailin, D.G. Tsvigunov
Far Eastern State Transport University (FESTU), Khabarovsk, Russia

ABSTRACT: In developing more rational geotechnical solution we used the properties of strong and heat isolating materials.

Heat engineering calculations were done within annual cycle of freezing and thawing. The following years the depth of thawing will be increasing due to changing of thermo physical indexes of foundation soils that experience compressing loads of traffic and the embankment.

Stressed deformation calculations of the embankment were carried out at the beginning of exploitation in the process of the thawing as a result of traffic loads. They took into account the cycle of traffic. So, the final settlement will be greater than the calculated one.

The railway roadbed under construction on permafrost high-temperature soils is in the area of influence of the Bureya hydropower station, Russia. It was designed according to the second principle that admits thawing in basement under embankment.

The railway main road crosses the area with breaking occurrence of high- temperature permafrost soils with thawing. The engineering geological structure of railroad subgrade consists of peat, sandy loam, sandy soil and crushed stone rocks covering basic soils that are sandstones. In the river valleys there are a lot of swamps. They stretch along the detouring main road for 30% of its length while peat capacity is 2-3m deep. A specific feature of permafrost peat is a significant deformation due to icing in comparison with a thawed peat.

The geotechnical modeling was used for selecting a rational design of the railway roadbed on weak thawing subgrade. This was done on a programming complex "Finite Element Modeling designs" developed by geotechnicians in St.Petersburg.

The programming complex allows solving task of thermo-physical and stress deforming states of designs and their subgrade in three dimensional definitions. The «Termoground» mathematical model of freezing, frost heaving and thawing in annual FEM cycle was developed in three dimensional definitions as a part

of programming «FEM models» complex. It was designed according to analysis of currently existing patterns of freezing and thawing soils. This challenging geotechnical task is solved in two stages. The heat engineering task is solved on the first stage resulting in determining the temperature and damping fields for every period of time. On the second stage the task of determining stress deformation state of soils in subgrade is solved in freezing and thawing processes. They are described in «Termoground» module by the equation of thermo-conductivity taking into account the phases of ground water transformations within an interval of temperatures below zero for unstable thermal regime in a three dimensional picture of soils.

Several variants of roadbed designs were suggested for different engineering and geological conditions of different difficulty. They were developed with the help of up-to date geotechnologies and properties of geotechnical materials.

As an example of this, you can see the survey of the embankment 4.8m high that is located on a slope of 42% cross fall. In the foundation in the up-down direction there are: moss and plants layer of 0.3m deep, flowing sandy soil of 1.2m deep, permafrost sandy cryo-layered soils of up to 6.2m deep and massive cryo-conglomerates of low strength. The calculation scheme of the embankment is on Fig.1.

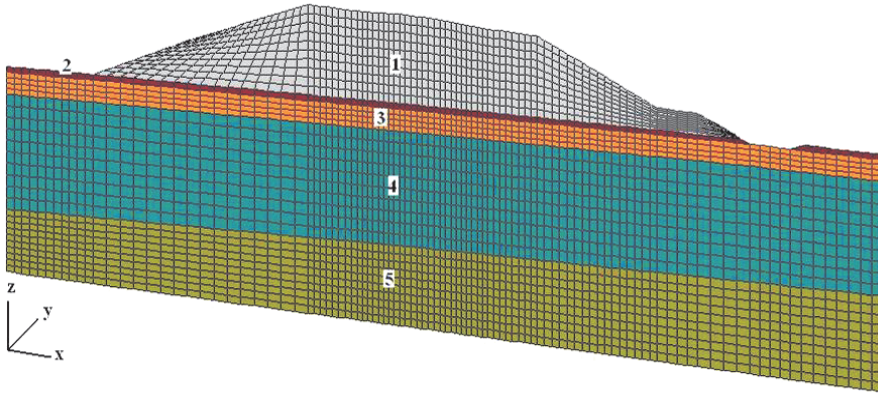


Fig.1. Calculation scheme of the embankment: 1 – body of the embankment (sand or pebble); 2 – moss and plants layer; 3 – flowing sandy soil; 4 – permafrost sandy soil; 5 – massive cryo-layered crushed rock conglomerates of low strength

As result of thermo physical calculations for the annual cycle, it was found that thawing of the embankment soil in September is up to 1.2m deep.

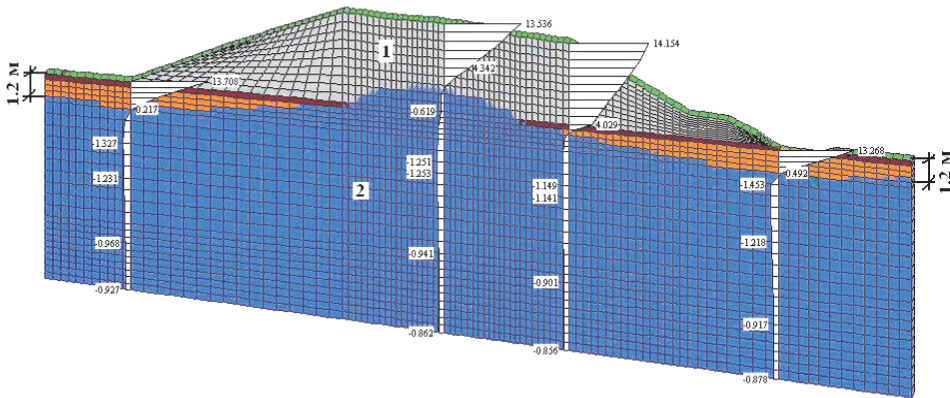


Fig.2. Diagram of temperatures spreading in the body and basement embankments in September: 1 – thawing soil; 2 – freezing soil

The largest thawing occurs on slopes from 0.5 to 1.2m high. Directly under the embankment axis the mark of permafrost rises in the body of the embankment up to 0.8m. The temperature of permafrost soil fluctuates from -0.6°C to -1.2°C . To keep the embankment soils in permafrost condition it is necessary to install warming with extrusion foaming polystyrene. It should be no less than 150mm thick in a projection in the main area of 11.5m long at the embankment subgrade and no less than 300mm thick in a projection on the slopes of 21.3m long. This way the temperature in the subgrade fluctuates from -0.6°C to 1.0°C .

In case of designing the embankment according to the second principle (with thawing of subgrade) vertical deformations of the embankment body and subgrade are no less than 42cm at the beginning of exploitation (Fig. 4-6). The biggest share of general settlement takes the compression of moss and plants layer and flowing sandy soil.

Due to the location of the embankment on the slopes the horizontal deformations of more them 12cm are developing in deep moss and plants layer at the subgrade of the slope (Fig. 7.), with shifting stresses in a body of the embankment being up to 70 kPa (Fig. 8.).

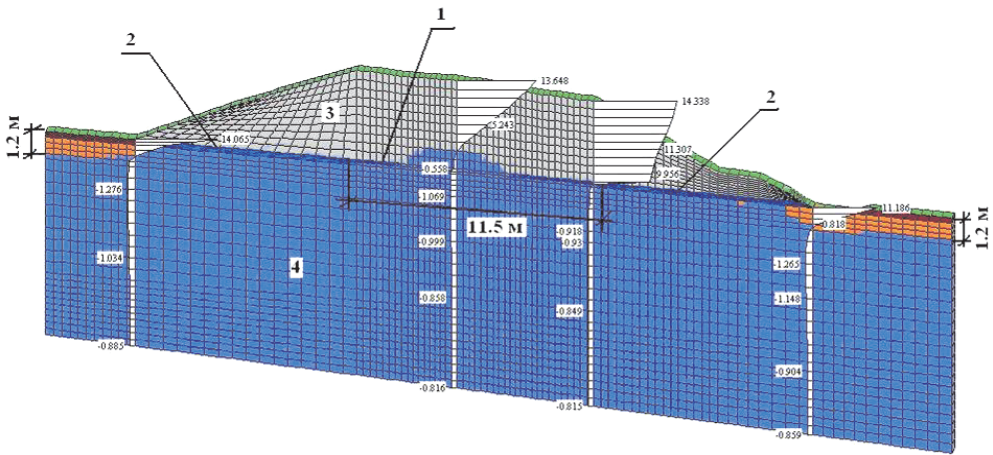


Fig.3. Diagram of temperatures spreading in the embankment body and subgrade with foot thermal insulation in September: 1- foaming polystyrene of 150mm thick; 2 – foaming polystyrene of 300mm thick; 3 – thawing soil; 4 – freezing soil.

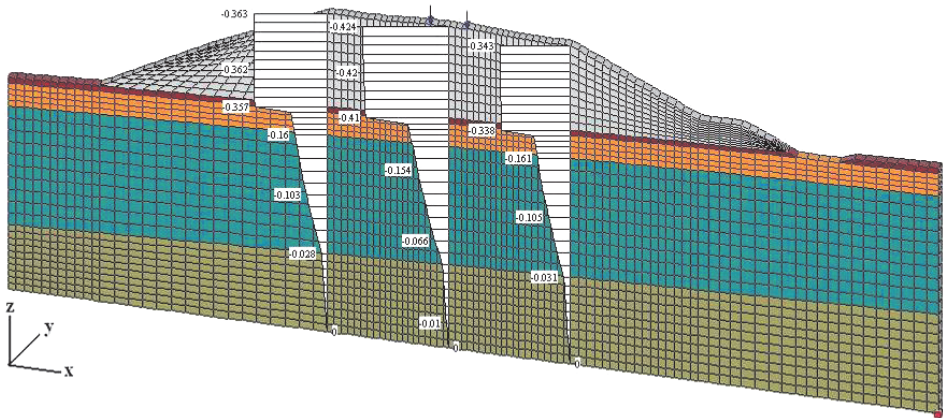


Fig.4. Diagram of vertical deformations in the body and subgrade embankment at the beginning of exploitation.

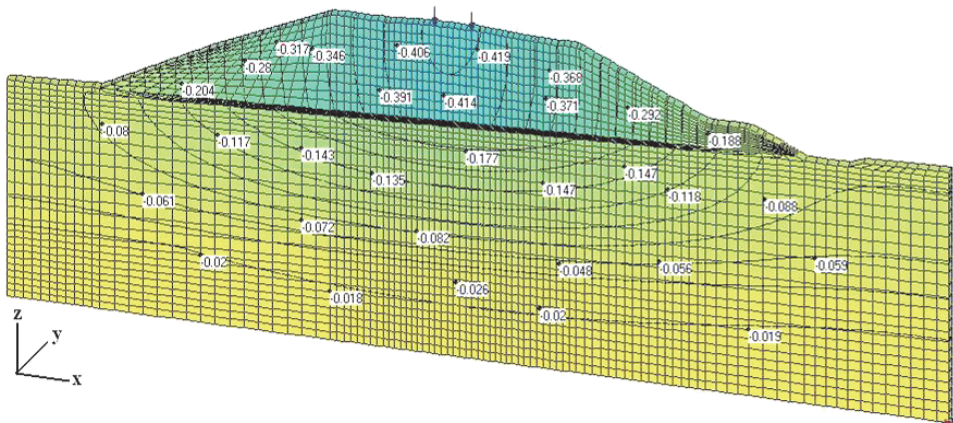


Fig.5. Isolines of vertical deformations in the body and subgrade embankment at the beginning of exploitation.

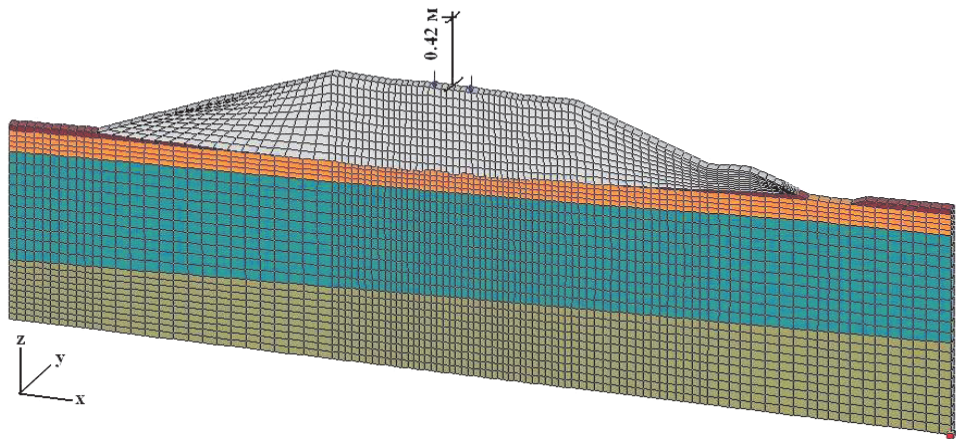


Fig.6. Deformation embankment scheme at the beginning of exploitation.

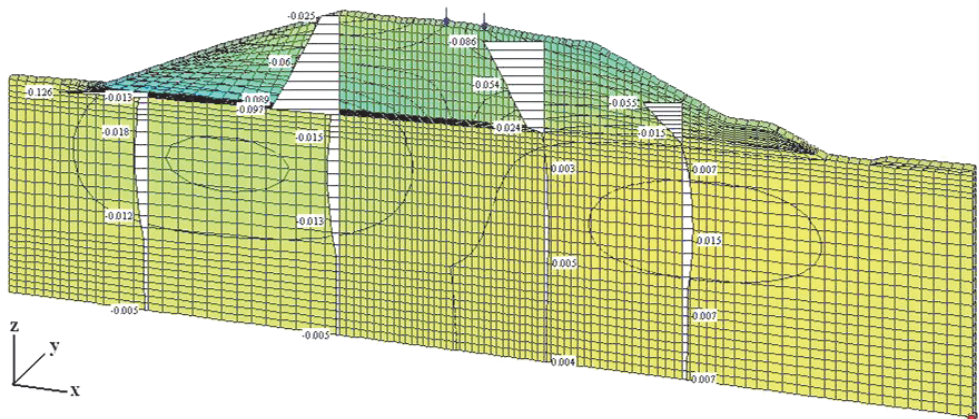


Fig.7. Isolines and diagram of horizontal deformations in the embankment body and subgrade for the period of exploitation.

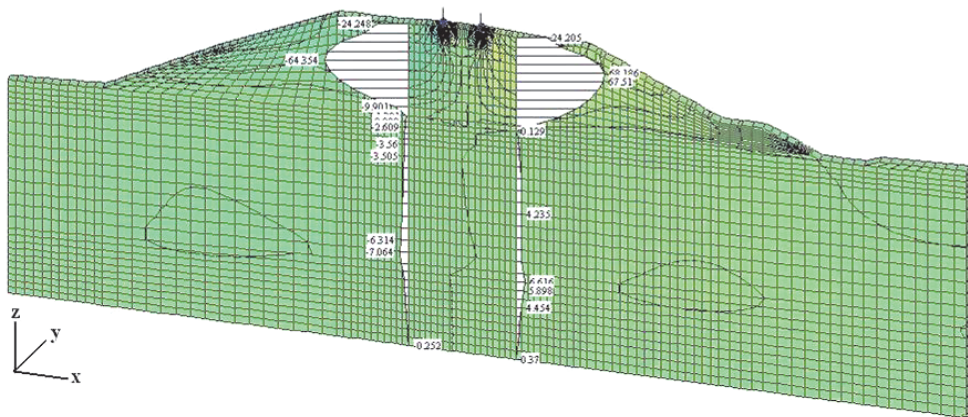


Fig.8. Isolines and diagram of horizontal stresses in the embankment body and subgrade for the period of exploitation.

The reinforced design of the embankment (Fig. 9.) is suggested to decrease vertical and horizontal deformation. It includes:

1. Laying the geomaterial along the foot of the body (no less than 6-10m) to reduce spreading of the embankment on the subgrade.
2. Designing a reinforced construction from reinforced cement piles of 7,7m long and pace of 2×2m as a stop to reduce horizontal deformation.

Vertical deformations in the embankment with the given reinforced design accounts for up to 39cm, so reducing is no less 7% (Fig. 10.)

With the given reinforced design the horizontal deformation achieves 5cm, so reducing accounts for up to 64% (Fig. 11, 12).

Stresses in the body of the embankment are up to 70 kPa (fig. 13.)

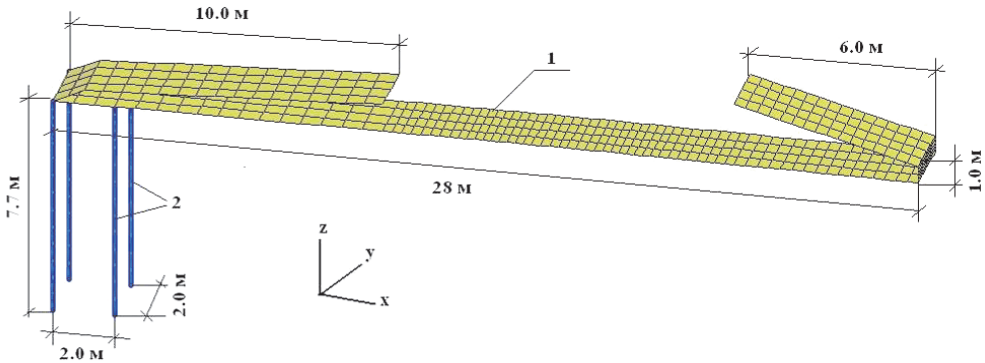


Fig.9. Reinforced embankment design: 1 – geomaterial; 2 – reinforced cement pies of 7,7m long and cross section of 20×20 cm

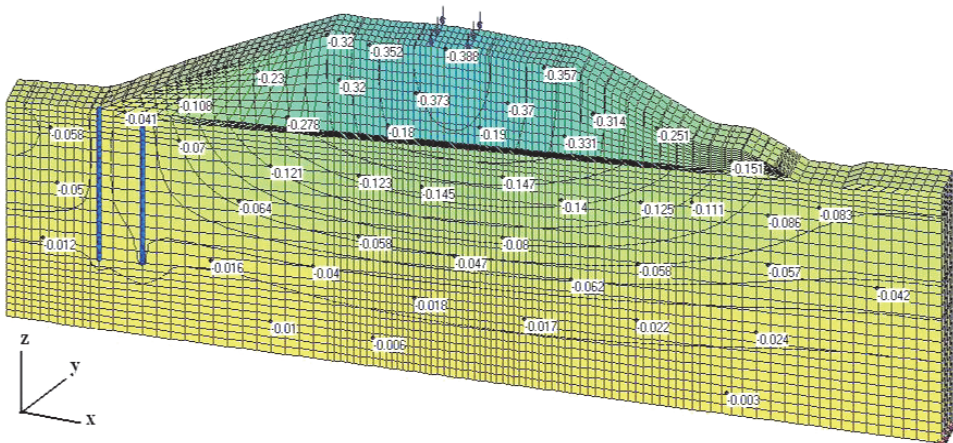


Fig.10 Isolines of vertical deformations in the body of reinforced embankment at the beginning of exploitation.

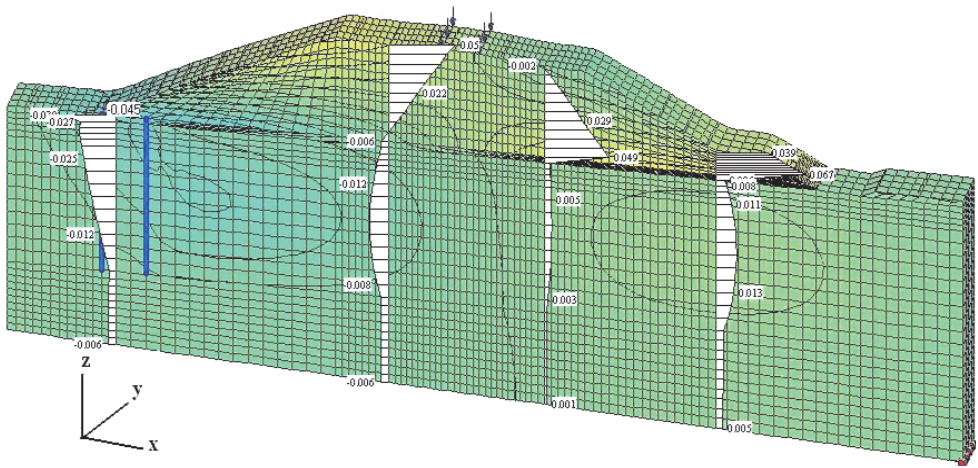


Fig. 11. Isolines of horizontal deformation of the body in the reinforced embankment and foundations for the period of exploitation.

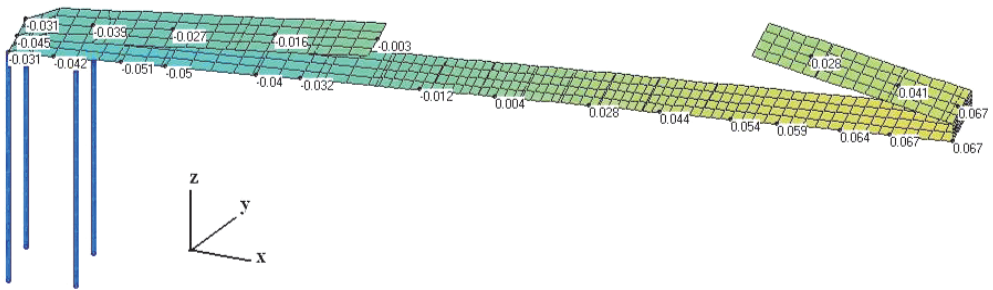


Fig. 12. Isolines of horizontal deformations in the reinforced embankment design.

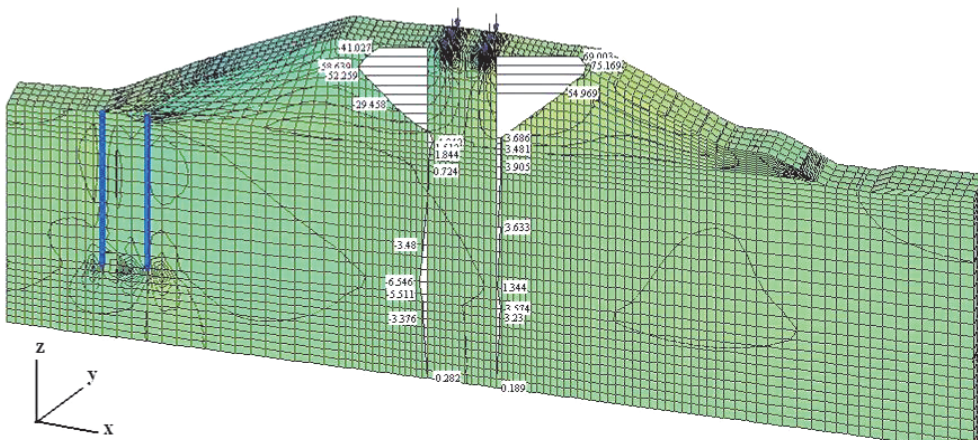


Fig.13. Diagram of horizontal stresses in the reinforced embankment design at the beginning of the exploitation.

ACKNOWLEDGEMENTS

The developed roadbed designs allow reducing horizontal deformations significantly and in some cases even eliminating vertical sediments in the embankment providing smooth settling in linear profile on railway distances. The suggested design solutions are not only more rational in technical aspect in comparison with conventional ones, but also economically more profitable as far as investments and exploitation costs.

REFERENCES

1. Kudryavtsev S.A., Berestyanyy U.B., Valtseva T.U., E.D. Goncharova, R.G. Mikhailin. Geotechnical. Vferials in designs of highways in cold regions of Far East. *Cold regions engineering 2009: cold regions impact on research, and construction: proceedings of the 14th international conference on cold regions engineering*, August 31- September 2, 2009, Duluth, Minnesota, USA. P.546-550.
2. Kudryavtsev S.A., Berestyanyy U.B., Valtseva T.U., Arshinskaya L.A., Zussupbekov A.Z. Developing design variants while strengthening roadbed with geomaterials and scrap tires on weak soil. *International workshop on scrap tire derived geomaterials. «Opportunities and challenges» National Institute for Land and Infrastructure Management*. Yokosuka, Japan. March 23-24, 2007. P.117.
3. Kudryavtsev S.A., Berestyanyy U.B., Valtseva T.U., Barsukova N.V. Practice of use of positive properties of geosynthetic materials on building objects in severe climatic conditions of the Far East of Russia. *1st International conference on new developments in geoenvironmental and geotechnical engineering*. November 9-11, 2006. University of Incheon. Korea. P. 423-427.
4. Kudryavtsev S.A., Paramonov V.N., Lisuk M.B. Numerical modeling of thawing railway embankments constructed on permafrost soil. *Asian Conference on Permafrost*. Abstracts. Lanzhou, China. August 7-9, 2006. P.53.

Shaking Table Studies on Reinforced Modular Block and Rigid Faced walls

G. Madhavi Latha

Associate Professor, Indian Institute of Science, Bangalore, madhavi@civil.iisc.ernet.in

P. Santhanakumar

Former M.E. Student, Indian Institute of Science, Bangalore, santhy.iisc@gmail.com

ABSTRACT: Shaking table tests on unreinforced and geosynthetic reinforced model retaining walls are discussed and compared in this paper. Rigid faced and modular block walls were constructed with geosynthetic layers placed at different elevations of the walls. Effect of backfill density, number of reinforcement layers, reinforcement type and frequency of shaking on wall performance was studied through different series of model tests. Performances of the walls were assessed in terms of wall displacement, crest settlement and acceleration amplification at different elevations and compared. Modular block walls performed better than the rigid faced walls for the same level of shaking. Type and quantity of reinforcement has significant effect on the seismic performance of both the types of walls.

1. INTRODUCTION

Retaining walls reinforced with geosynthetics performed satisfactorily during strong earthquakes as observed by several researchers (Juran and Christopher 1989; Kutter et al., 1990; Collin et al., 1992; Bathurst et al., 1993; Sandri, 1997; Tatsuoka et al., 1997). Collin et al. (1992) reported that Geosynthetic Reinforced Soil (GRS) walls survived the Loma Prieta earthquake of 1989 with estimated ground accelerations ranging from 0.3–0.7g. White and Holtz (1997) conducted a survey of three geosynthetic reinforced walls and four geosynthetic reinforced slopes after Northridge earthquake of 1994 to show that these walls and slopes were not subjected to any visual distress after the earthquake.

The use of Segmental or modular block Retaining Walls (SRW) that include dry-stacked concrete block units as the fascia system together with extensible sheets of polymeric materials (geosynthetics) that internally reinforce the retained soils and anchor the fascia has gained wide popularity in recent times. Studies on SRW in North America were reported by Bathurst and Simac (1994). Several other researchers (Cazzuffi and Rimoldi 1994; Gourc et al. 1990; Knutson 1990; Won 1994) reported the use of these structures in Europe, Scandinavia

and Australia. Use of modular block walls has tremendously increased all over the world during recent years. The distinguishing feature of these structures is the facing column that is constructed using mortarless modular concrete block units that are stacked to form a wall batter into the retained soils (typically 3 to 15° from vertical). Modular blocks of different shapes and sizes are available in market and are well explained by several researchers (Bathurst and Simac, 1994).

1.1. Shaking Table Tests

The use of scaled models in geotechnical engineering offers the advantage of simulating complex systems under controlled conditions, and the opportunity to gain insight into the fundamental mechanisms operating in these systems. In model testing, the boundary conditions of a particular problem are reproduced in a small scale model of the prototype. Studies on physical model help in providing better understanding of the behaviour of the prototype and the process leading to failure of the model at a real time can be directly observed. Different model studies available in geotechnical engineering are: Tilt table test, Centrifuge test (high-g tests), Hydraulic gradient tests and Shaking table tests (1-g tests). In the early years of geotechnical earthquake engineering, virtually

all physical model tests were performed on shaking tables. Shaking table research has provided valuable insight into liquefaction, post earthquake settlement, foundation response and soil-structure interaction and lateral earth pressure problems. Shaking table model represents the actual prototype soil rather than resorting to the smaller particle sizes often required for smaller scale model tests (Kramer 1996). Shaking table tests have the advantage of well controlled large amplitude, multi-axis input motions and easier experimental measurements and their use is justified if the purpose of the test is to validate the numerical model or to understand the basic failure mechanisms. Shaking table tests facilitate testing of relatively larger structures and model response can be physically observed in these tests along with measurements of response parameters. Laboratory model tests are very instrumental in studying the behavior of reinforced soil walls under controlled conditions. Shaking table tests in which the models of retaining walls are subjected to harmonic or random base acceleration are particularly useful in understanding the actual behaviour of these structures during earthquakes. However, most of the shaking table tests are conducted using reduced scale models in a 1g field (Bathurst et al. 2001; Koseki et al. 2003) that are possibly subjective to scale effects due to the influence of stress levels and the lack of reasonable scaling techniques.

Most of the model studies on seismic behavior of GRS walls have been performed on very small-scale models where scale effects are expected to have a major influence on measured response. Some examples include: Lo Grasso et al. (2005), H (model wall height) = 0.35 m; Watanabe et al. (2003), Kato et al. (2002) and Koseki et al. (1998), H = 0.5 m. There are also some seismic tests on larger models: El Emam and Bathurst (2004), Matsuo et al. (1998), Bathurst et al. (1996), H = 1 m; Sakaguchi (1996), H = 1.5 m and Ling et al. (2005), H = 2.8 m. However, the present study presents relative performance of rigid faced and modular block walls at varying earthquake shaking conditions, providing insights to the effect of various parameters on the seismic performance of these walls.

To understand the performance of geosynthetic reinforced soil (GRS) walls during strong shaking, a series of shaking table tests on reinforced soil model walls with dry sand backfill are performed in the present study. This research effort had the goals of providing insight into the seismic response of geosynthetic reinforced soil walls under controlled dynamic base shaking, with the variation of parameters like type of facing, backfill relative density, reinforcement layers, and frequency of base motion.

1.2. Literature review

Several studies on segmental retaining walls are available in literature. Bathurst et al. (1997) presented full scale tests on geosynthetic reinforced retaining walls constructed with a column of dry-stacked modular concrete units and wrapped-face. It was concluded that hard facing column is a structural element that acts to reduce the magnitude of strains that would otherwise develop in a wall with a flexible facing. Ramakrishnan et al (1998) presented shaking table test results of geotextile wrap faced and geotextile-reinforced segmental model retaining walls. Segmental retaining wall was found to sustain approximately twice the critical acceleration of the wrap-faced wall. Huang et al. (2003) used multi-wedge method based on Newmark's sliding block theory to analyze four geosynthetic reinforced modular block walls in the 1999 chi-chi earthquake. Ling et al. (2005) presented shaking table tests on three large scale 2.8 m high modular-block geosynthetic-reinforced soil walls subjected to significant shaking using the Kobe earthquake motions. The reinforcements used were polymeric geogrids, which were frictionally connected to the facing blocks having a front lip. It was observed that the wall performance under earthquake shaking could be improved by increasing the length of the top reinforcement layer, reducing vertical reinforcement spacing, and grouting the top blocks to ensure firm connection to the reinforcement. Lateral displacement was largest at the top of the wall and larger settlements occurred in the unreinforced zone of backfill.

Koerner and Soong (2001) carried out extensive survey of existing geosynthetic reinforced segmental walls and reported major

reasons for excessive deformations and collapse of some of these walls. Yoo and Jung (2006) investigated the case history of a failed geosynthetic reinforced segmental retaining wall in Korea. Finite element analysis of the wall and laboratory tests carried out on backfill and reinforcement revealed that the main reasons for failure were inappropriate design and low quality backfill, apart from the rainfall infiltration.

Liu (2012) carried out extensive finite element analysis of geosynthetic reinforced SRW and concluded that the deformation of reinforced soil zone was largely governed by reinforcement spacing and reinforcement stiffness, whereas the lateral displacement at the back of reinforced soil zone was governed by the reinforcement length.

2. LABORATORY MODEL TESTS

A computer controlled servo hydraulic single axis shaking table with payload capacity of 1000 kg and foot print of up to 1000 × 1000 mm was used in this study. To minimize the boundary effects on model structures, a laminar box was designed and built for the shaking table facility. Laminar box is a large sized shear box consisting of several horizontal layers, built such that the friction between the layers is minimized. The layers move relative to one another in accordance with the deformation of the soil inside. The laminar box used in this study is rectangular in cross section with inside dimensions of 500 × 1000 mm and 800 mm deep made up of fifteen rectangular hollow layers machined from solid aluminum compose. The gap between the successive layers is 2 mm and the bottommost layer is rigidly connected to the solid aluminum base of dimensions 800 × 1200 mm and 15 mm thickness. The layers were separated by linear roller bearings arranged to permit relative movement between the layers with minimum friction. Photograph of the laminar box mounted on the shaking table is shown in the Figure 1. Accelerometers, soil pressure sensors and Ultrasonic Displacement Sensors (USDT) were used for instrumenting the model retaining walls.



Figure 1. Laminar box mounted on shaking table

2.1. Materials used in experiments

Backfill material

Backfill material used for the model construction is locally available dry sand. The grain size distribution of the sand is shown in Figure 2. The sand is classified as poorly graded (SP) according to the Unified Soil Classification System. Physical properties of the sand are reported in Table 1.

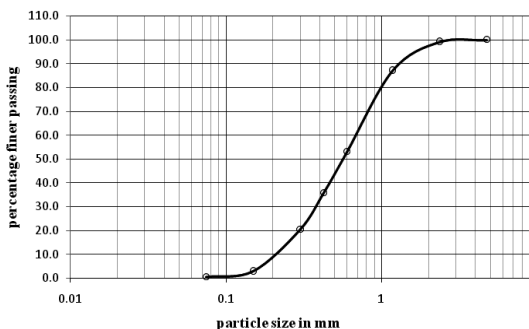


Figure 2. Grain size distribution of backfill sand

Table 1. Properties of backfill sand

D10	0.215 mm
D30	0.37 mm
D60	0.71 mm
Coefficient of uniformity C_u	3.30
Coefficient of curvature C_c	0.896
Specific gravity G	2.65
Maximum void ratio e_{max}	0.828
Minimum void ratio e_{min}	0.5022
Maximum unit weight γ_{dmax}	17.22 kN/m ³
Minimum unit weight γ_{dmin}	14.21 kN/m ³

Backfill sand is reinforced with two different types of geogrids, stronger biaxial geogrid (SG) and weaker biaxial geogrid (WG). These geogrids are made up of polypropylene, biaxially oriented integrally extruded geogrids with rigid junctions and stiff ribs. Properties of both the geogrids are presented in Table 2.

Table 2. Properties of geogrids

Property	WG	SG
Ultimate tensile strength (kN/m)	26	46
Yield point strain	16.27%	9.2%
Aperture size	35×35	30×30
Mass per unit area g/m ²	220	230

Modular Blocks

Concrete blocks used for model facing were 125mm wide × 100 mm long x 150 mm thick with a positive mechanical interlock in the form of concrete lip of 125 width × 25 mm length × 50 mm thickness located at the back bottom of each block. The modular block has a concrete thickness of 25 mm all around provided with a 75mm wide × 50 mm long × 150 mm hollow section at the centre. Similar type of hollow modular blocks with half of the width as mentioned above are also used for making the model retaining walls. The dimension details of the block are shown in Figure 3.

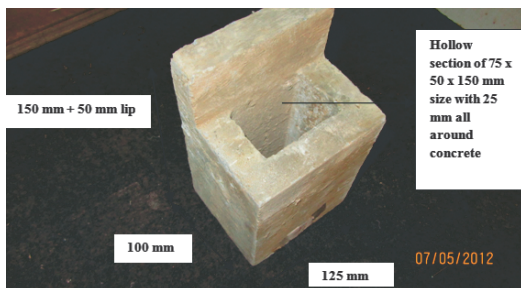


Figure 3. Dimensions of modular block

Modular concrete blocks were made according to the specifications of national concrete masonry association (NCMA), ASTM codes which are presented in the Table 3. The blocks were casted with high quality ordinary Portland cement of grade 53 for achieving minimum of 28 days characteristic compressive strength of 30 MPa. The maximum nominal aggregate size

used is 6 mm. The maximum water content used is 40% with a workability slump of 50-75 mm under severe exposure condition. The mix design ratio by weight is 1:1.2:2.36. The blocks were casted by moulds made up of wood coated with red oxide paint as shown in Figure 4. These blocks were reinforced with galvanised iron wires of 4 mm diameter with the reinforcement layout as shown in Figure 5. Properties of the modular block are presented in Table 4.



(a)



(b)



(c)

Figure 4. (a) Reinforcement layout (b) Mould with reinforcement for casting (c) Casting of hollow concrete modular blocks

Table 3. Specifications of modular blocks

Minimum compressive strength	30 MPa
Water adsorption	8 %
Dimension tolerance	3 mm
Maximum horizontal gap between erected units	3.25 mm

Table 4. Properties of modular block units

Compressive strength	35 MPa
Water adsorption	5.5%
Overall dimensions	125×100×150 mm / 64.5×100×150 mm
Hollow section	75×50×150mm / 14.5×50×150 mm
Weight of each unit	3.55 kg / 1.75 kg
Maximum aggregate size	6 mm
Sand	Zone II
Cement grade	OPC 53
Reinforcement	Galvanised iron wire of 4 mm diameter

2.2. Model construction

Model retaining walls were constructed in the laminar box to a size of 700 mm × 500 mm in plan and 600 mm height. All model walls are backfilled with sand, constructed in lifts of equal heights. Wall facing was either rigid or modular block facing.

Rigid faced wall models are constructed using 12 hollow rectangular steel box sections of 50 mm height and 25 mm width each bolted together using a vertical steel rod which is in turn bolted to the bottom plywood base to form a 600 mm high rigid panel of 25 mm thickness with a fixed bottom condition. The reinforcement materials are made to run through the rods firmly fixed between two rectangular box sections. A typical rigid facing wall is shown in Figure 5.

Modular block faced walls were made up of concrete blocks of size 125 mm × 100 mm × 150 mm with a positive mechanical interlock in the form of concrete lip of 125 mm × 25 mm × 50 mm located at the back bottom of each block. The model wall forms an inward batter of 7.2°. The bottommost layer of the wall is fixed to the wooden frame which in turn is firmly attached to the base. A typical modular faced model wall after construction is shown in Figure 6.



Figure 5. Typical rigid faced wall



Figure 6. Typical modular block wall

Backfill sand was placed in the laminar box using dry pluviation technique to achieve the uniform density. A series of trials with different heights of fall were made to achieve the desired density. In case of reinforced wall models, geosynthetic layers were placed at the specific depth while filling the backfill sand. The reinforcement length of 0.7H from the facing of the wall was maintained in all the tests. The schematics of typical reinforced rigid faced wall and modular block wall with instrumentation are shown in Figures 7 and 8 respectively.

The retaining wall models were subjected to specific sinusoidal motion of 20 cycles. Dynamic response of wall models in terms of accelerations, facing displacements, vertical displacements, horizontal soil pressure were measured using accelerometers, displacement sensors, soil pressure sensors respectively and the same were recorded using data acquisition system of the shaking table.

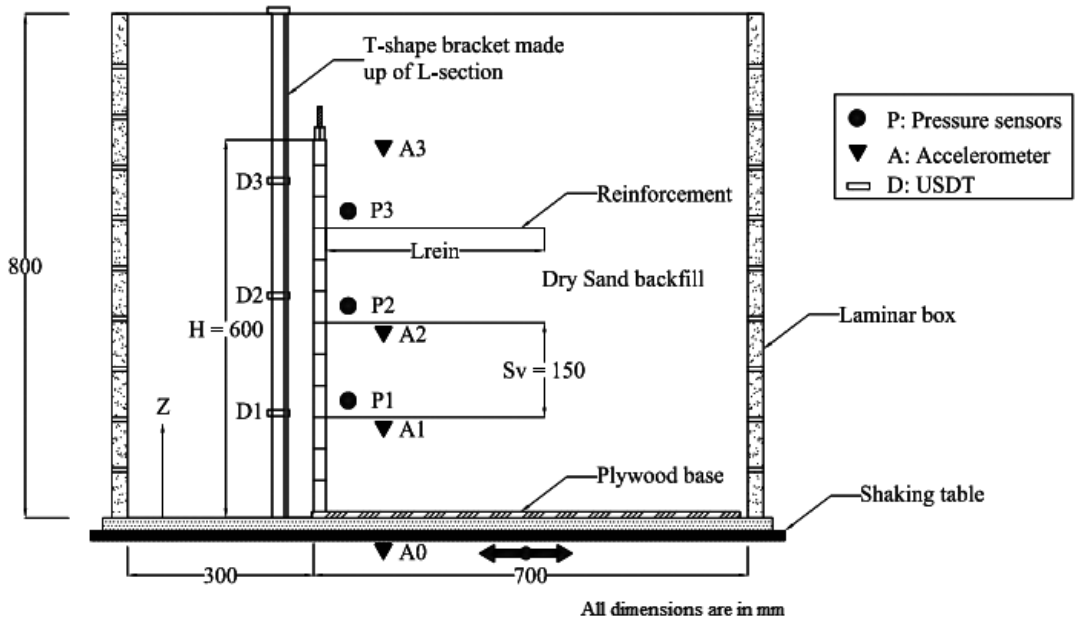


Figure 7. Schematic diagram of typical rigid faced wall configuration and instrumentation

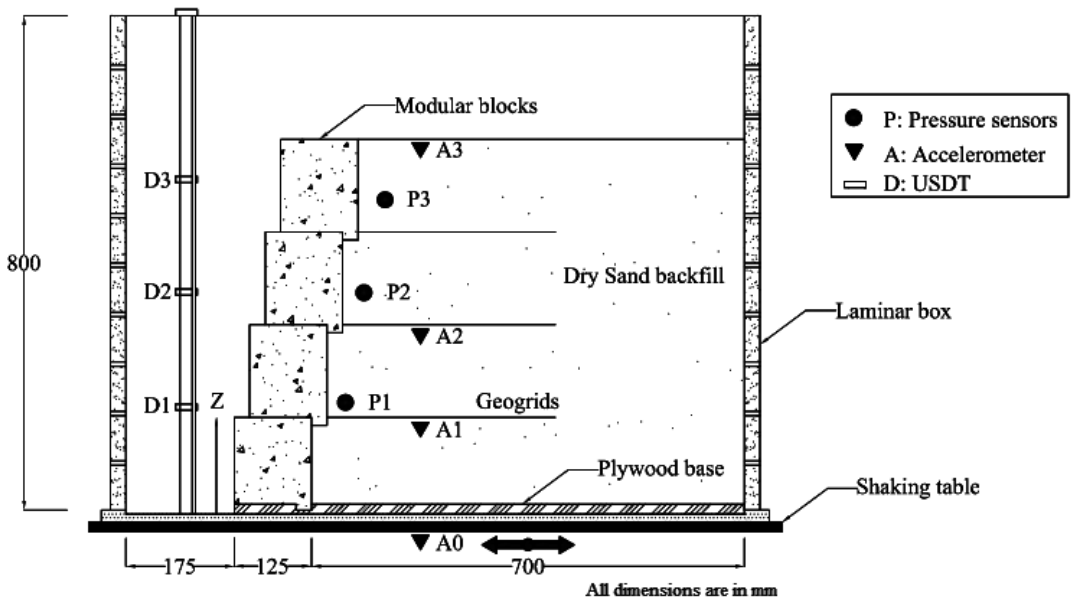


Figure 8. Schematic diagram of typical modular block faced wall configuration and instrumentation

3. RESULTS AND DISCUSSION

3.1. Tests on rigid faced walls

Rigid faced unreinforced and reinforced retaining walls were tested under acceleration of 0.3 g and frequency of 2 Hz for two different relative densities 47% and 65%. The models were built in laminar box. Parameters varied in the tests and the corresponding test codes are shown in Table 5.

Two types of reinforcements are used as discussed in previous section. The minimum reinforcement length (L_{rein}) of 0.7H (420 mm) corresponding to minimum required for reinforced earth structures (FHWA 2001) is maintained from the wall facing for all the tests. Out of the four accelerometers, one accelerometer A0 was fixed to the base of the shaking table.

Remaining three accelerometers A1, A2, A3 are embedded in backfill material at elevations 150, 300, 600 mm respectively from the base at a constant distance from 100 mm. Three soil pressure transducers P1, P2, P3 are placed inside the wall in contact with facing at elevations 175, 325, 475 mm respectively from the base. To measure the horizontal displacement of wall facing three USDTs D1, D2 and D3 are placed at elevations 200, 350, 500 mm respectively from the base. To measure the vertical displacement of the backfill sand one USDT D4 is placed at a distance 200 mm wall facing. The remaining vertical displacement along the length of the backfill material is measured using steel scale. Figure 9 shows the front and top views of the finished rigid faced wall model. All the wall models were subjected to a sinusoidal motion of 0.3 g and 2 Hz frequency.

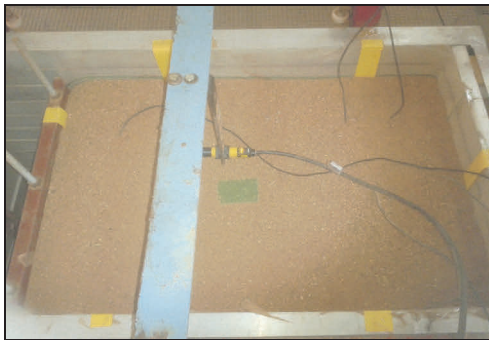
Table 5 Parameters varied and the corresponding test code

Sl. No.	Test code	Relative density (%)	Acceleration (g)	Frequency (Hz)	No of cycles	Type of reinforcement	No of layers
1	UT1	47	0.3	2	20	-	-
2	UT2	65	0.3	2	20	-	-
3	UT3	65	0.3	3	20	-	
4	UT5	65	0.3	5	20	-	
5	UT7	65	0.3	7	20	-	
6	RT1	47	0.3	2	20	WG*	2
7	RT2	47	0.3	2	20	WG	3
8	RT3	65	0.3	2	20	WG	2
9	RT4	65	0.3	2	20	WG	3
10	RT5	47	0.3	2	20	SG**	2
11	RT6	47	0.3	2	20	SG	3
12	RT7	65	0.3	2	20	SG	2
13	RT8	65	0.3	2	20	SG	3

WG*: Weaker biaxial geogrid & SG**: Stronger biaxial geogrid



(a) Front View



(b) Top view

Figure 9. Photographs of finished rigid faced wall

Effect of Backfill density

Effect of backfill density on wall performance of unreinforced and reinforced retaining model is studied by conducting tests at two different relative densities, 47% and 65%. The tests UT1 and UT2 represent tests on unreinforced wall models. A typical plot of horizontal displacement versus number of cycles is shown in Figure 10. Figure 11 shows the wall displacements, acceleration amplification and incremental pressure for unreinforced walls UT1 and UT2. The reduction in displacement as the relative density increases can be inferred from Figure 11 (a). The displacement observed in tests UT1 and UT2 are 22.33 mm and 18.22 mm respectively at D3.

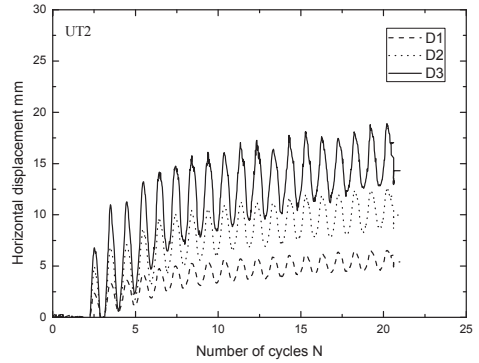


Figure 10. Variation of horizontal displacement with number of cycles

Acceleration response at different elevations of the walls is presented in terms of RMS acceleration amplification factors (RMSA amplification factors). These factors were calculated using the root mean square (RMS) method applied to the acceleration-time history for each accelerometer device. RMSA amplification factor is the ratio of RMS acceleration record value in the soil to the corresponding base RMS acceleration value. The RMSA amplification factor value for UT1 and UT2 are 1.12 and 1.25 respectively. The acceleration is amplified more at the top of the wall. The RMSA factor is relatively higher for denser sand compared to that of loose sand.

Incremental residual pressures observed at the end of dynamic excitation along the height of the wall in different rigid faced unreinforced model walls are presented in Figure 11 (c). No consistent trend in change in pressure with change in relative density of the backfill soil is noticed. The pressure sensors used in these tests are not sensitive enough to the small pressures exerted on the facing in these tests.

Vertical displacement of the backfill decreased 30% on increase in relative density of the backfill from 47% to 65%. Vertical displacement of the backfill increased as the distance from the wall is increased. This can be inferred from the plot shown in Figure 12 which compares the vertical displacement measured in tests UT1 and UT2.

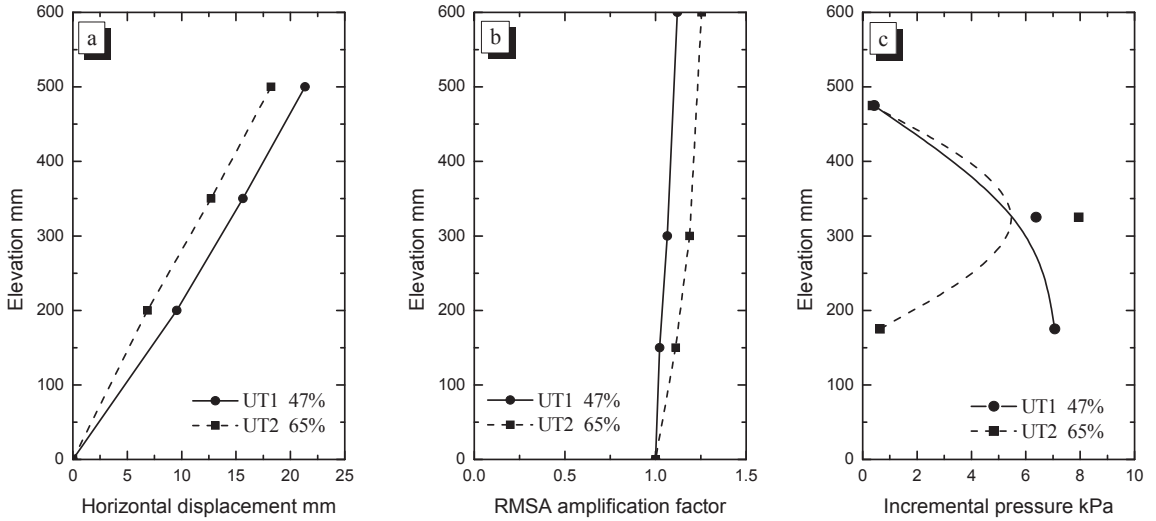


Figure 11. Response of rigid faced unreinforced walls for RD 47% and 65% at the end of 20 cycles for dynamic simulation of 0.3 g at 2 Hz (a) Wall displacement profiles (b) RMSA amplification factor (c) Incremental pressures

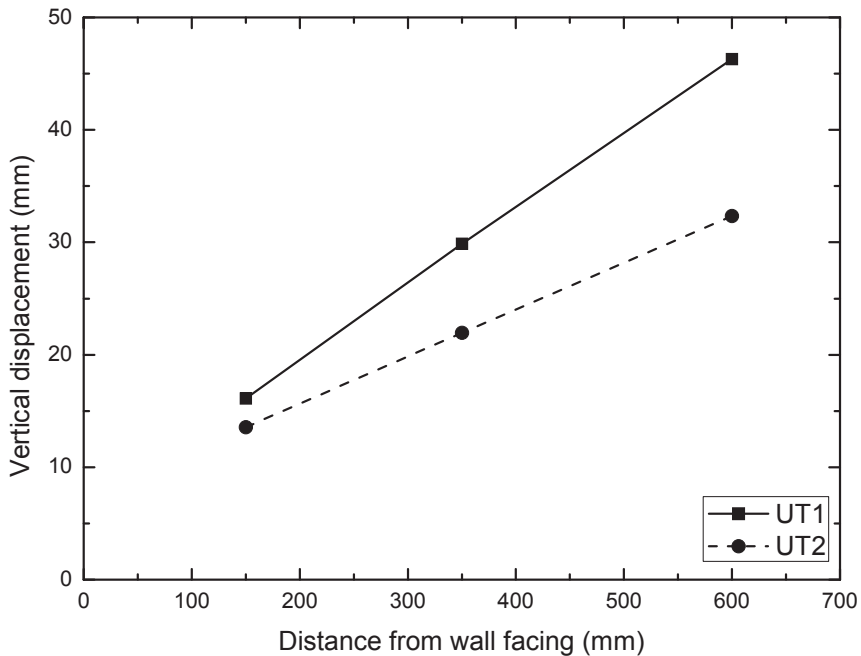


Figure 12. Vertical displacement of the backfill sand

Effect of Reinforcement

Model tests RT1 to RT8 are used to study the effect of inclusion of reinforcement on the performance of soil wall models. Figures 13 (a) to 13 (d) show the effect of inclusion of reinforcement on horizontal displacement of the wall. Wall displacement reduced significantly on inclusion of reinforcement. Maximum displacement of 22.33 mm observed in case of wall with backfill density of 47% (UT1) is reduced to a minimum of 1.68 mm upon inclusion of 3 layers of stronger geogrids. Similarly the maximum displacement of 18.22 mm observed in case of wall with backfill relative density of 65% (UT2) is reduced to a minimum of 1.56 mm on inclusion of 3 layers of SG.

The effect of number of reinforcement layers on horizontal displacement is shown in Figures 14 (a) to 14 (d). Following observations are made from this series of tests.

- i. In case of backfill relative density of 47%, the horizontal displacement of unreinforced wall is 22.33 mm. On inclusion of weaker geogrid of 2 layers and 3 layers the horizontal displacement reduced 7.23 mm and 6.37 mm respectively. Similarly the horizontal displacement reduced to 3.71 and 1.68 mm on inclusion of stronger geogrid of 2 layers and 3 layers respectively.
- ii. In case of backfill relative density of 65%, the horizontal displacement of unreinforced wall is 18.22 mm. On inclusion of weaker geogrid of 2 and 3 layers, the horizontal displacement reduced to 5.95 mm and 2.55 mm respectively. Similarly the horizontal displacement reduced to 1.82 mm and 1.56 mm on inclusion of stronger geogrid of 2 layers and 3 layers respectively.

Horizontal displacement of the wall reduced significantly with both the types of geogrids. But not much variation is observed in the performance of weaker and stronger geogrids. Following specific observations are made when the walls made with two types of geogrids are compared.

- i. As compared to unreinforced wall models, the reduction in horizontal displacements observed in case of walls reinforced with 2 and 3 layers of WG at backfill relative density of 47% are 67.6% and 72.4% respec-

tively. Similarly 83.33% and 92.47% reduction in horizontal displacements are observed in case of model walls reinforced with 2 and 3 layers of SG at backfill relative density of 47%.

- ii. As compared to unreinforced wall models, the reduction observed in case of walls reinforced with 2 and 3 layers of WG at backfill relative density of 65% are 67.3% and 86.04% respectively. Similarly 90.0% and 91.43% reduction on horizontal displacement are observed in case of walls reinforced with 2 and 3 layers of SG at backfill RD of 47%.

These observations infer that the difference in the performance of the walls with weaker as well as stronger geogrids with relative densities of 47% and 65% is not more than 10% either for 2 layers or 3 layers of reinforcement.

Effect of backfill density on reinforced wall is similar to that of unreinforced wall. Horizontal and vertical displacements of the wall decreased as the relative density of the wall is increased. This can be clearly observed from Figures 15 (a) to 15 (d). The RMSA amplification factor values are not affected by the inclusion of reinforcement. The RMSA amplification of the model backfill sand follows a similar pattern for unreinforced and reinforced walls of particular density. Figure 16 shows the response of model walls, RT1 to RT8 that are constructed with different reinforcing materials WG and SG. The horizontal displacement of the wall is reduced on using reinforcing materials of higher stiffness. From Figure 16, it is observed that horizontal displacement of wall using SG as reinforcement is lesser than in case of wall with WG as reinforcement.

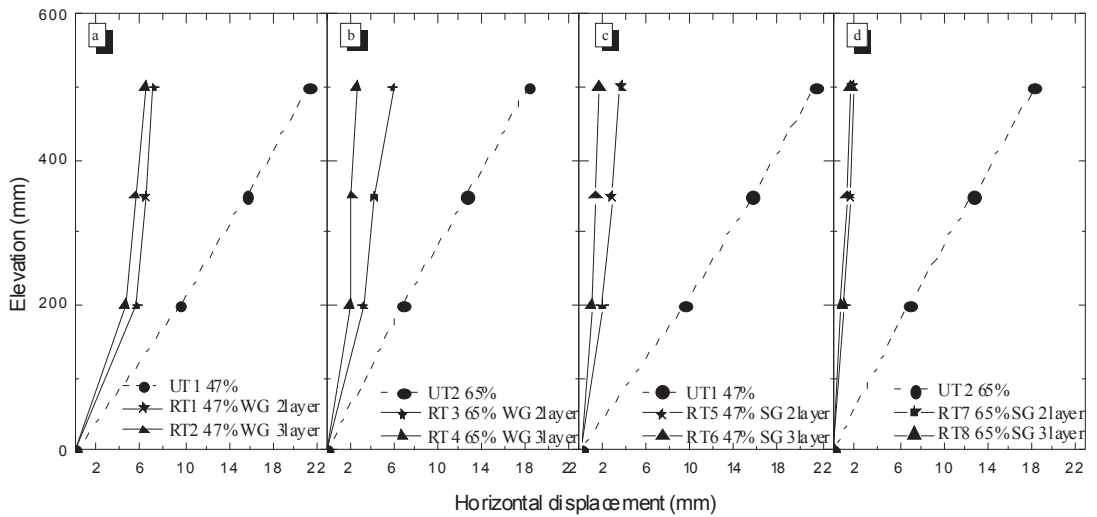


Figure 13 Effect of inclusion of reinforcement on horizontal displacement of wall
 a) RD 47% - WG b) RD 65% - WG c) RD 47% - SG d) RD 65% - SG

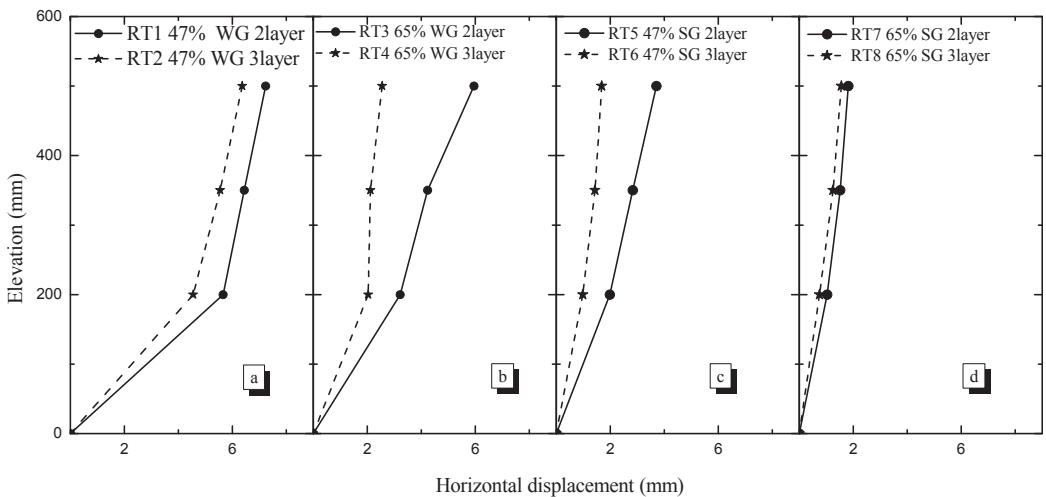


Figure 14 Effect of number of reinforcement layer on horizontal displacement of wall
 a) RD 47% - WG b) RD 65% - WG c) RD 47% - SG d) RD 65% - SG

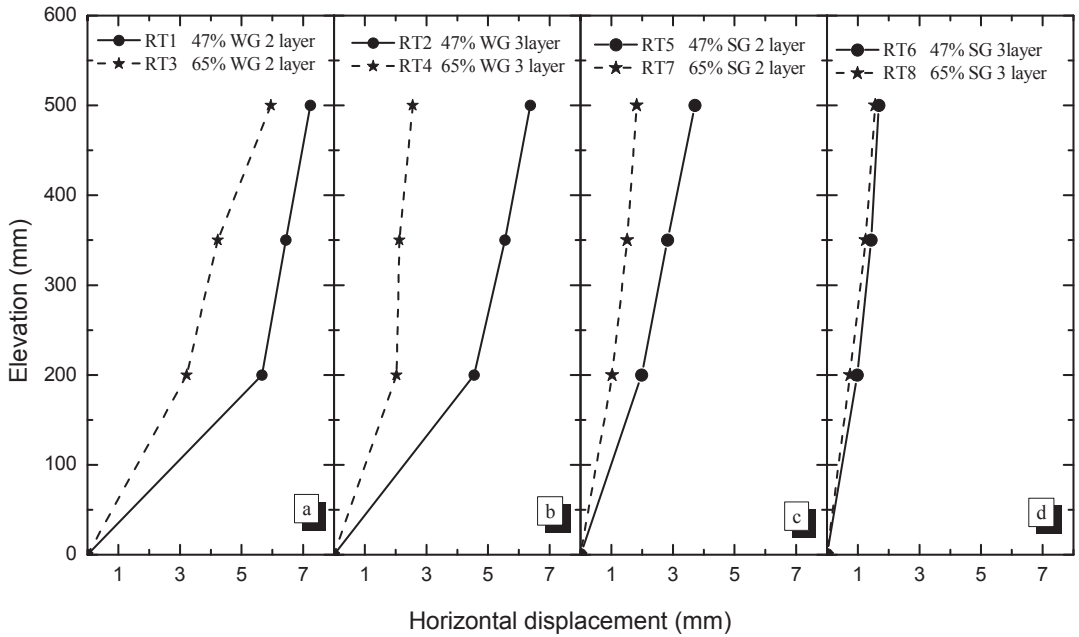


Figure 15 Effect of backfill density on horizontal displacement of reinforced soil wall models
a) RD 47% - WG b) RD 65% - WG c) RD 47% - SG d) RD 65% - SG

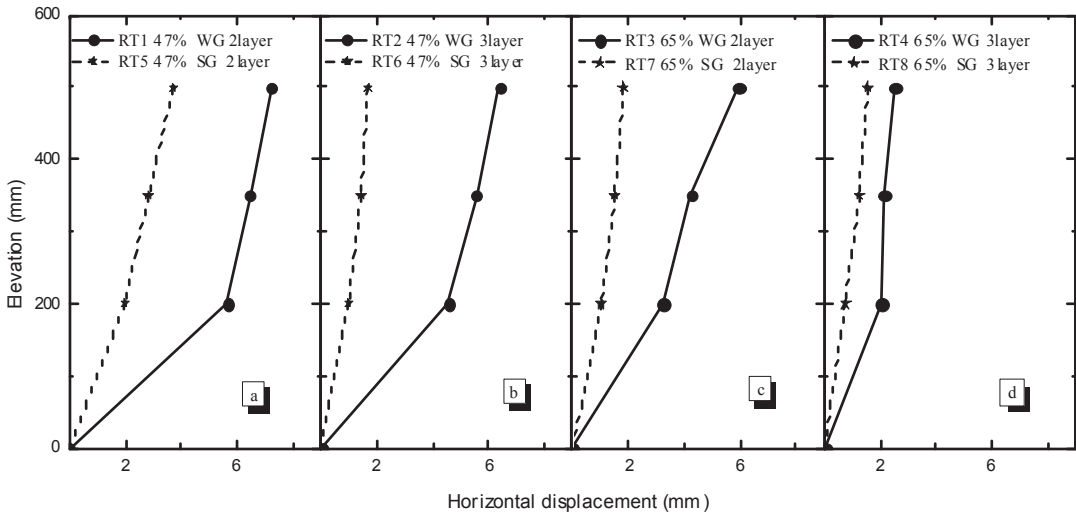


Figure 16 Effect of reinforcement type on horizontal displacement

3.2. Tests on modular block walls

Effect of Shaking frequency

Rigid faced unreinforced and reinforced retaining walls are tested under acceleration of 0.3 g and frequency of 2 Hz for two different relative densities of 47% and 65%. The models are built in laminar box. The parameters varied and the corresponding test codes are shown in Table 6. All the wall models are subjected to a sinusoidal motion of 0.3 g and 2 Hz frequency. WG is used as reinforcement in all the tests with modular blocks.

Table 6. Parameters varied in tests with modular block walls

Test code	Relative density (%)	No of layers
MUT1	47	-
MUT2	65	-
MRT3	47	2
MRT4	65	2
MRT5	47	3
MRT6	65	3

Tests with modular blocks showed qualitatively similar trends corresponding to the variations in relative density of the backfill, frequency of shaking and type and quantity of reinforcement. Comparison of performance of modular block walls with the performance of rigid faced wall yielded some very important insights into the difference in performance of these two types of walls. Details of these comparisons are presented in this section.

In case of unreinforced retaining models, face deformations are relatively very high in rigid faced walls when compared to modular block faced wall for the same backfill relative density. In case of backfill density of 47%, the wall face deformation is reduced from 21.33 mm to 14.65 mm on using modular block facing instead of rigid facing as shown in Figure 17 (a). In case of backfill density of 65%, wall deformation reduced from 18.22 mm to 6.14 mm on using modular block facing instead of rigid facing as shown in Figure 17 (b).

In case of reinforced retaining models with backfill density of 47%, on inclusion of 2 layers of weak geogrid, modular block faced wall performed better than the rigid faced wall. The displacement is 7.23 mm and 5.95 mm in case of rigid and modular facings respectively. The displacement is about 3.71 mm for rigid faced wall reinforced with two layers of stronger geogrid as presented in Figure 18 (a). On inclusion of 3 layers of weak geogrid, modular block faced wall performed better than the rigid faced wall. The displacement in this case is 6.37 mm and 1.34 mm for rigid and modular facings respectively. The rigid faced wall with 3 layers of stronger geogrid showed a displacement of 1.68 mm as shown in Figure 18 (b).

In case of reinforced retaining models with backfill density of 65%, on inclusion of 2 layers of weaker geogrid, modular block faced wall performed better than the rigid faced wall. The displacement is 5.95 mm and 5.33 mm in case of rigid and modular facings respectively. The displacement is about 1.82 mm for rigid faced wall reinforced with two layers of stronger geogrid as shown in Figure 19 (a). On inclusion of 3 layers of weaker geogrid, modular block faced wall performed better than the rigid faced wall. The displacements in this case are 2.55 mm and 0.95 mm for rigid and modular facings respectively. The rigid faced wall with 3 layers of stronger geogrid showed a displacement of 1.56 mm as shown in Figure 19 (b). The variation of RMSA value follows a similar trend for both rigid and modular faced walls. The inclusion of WG and SG reinforcement does not affect the RMSA value. This emphasizes the fact that the reinforcement is not enhancing the stiffness of the wall, though it is reducing the deformations.

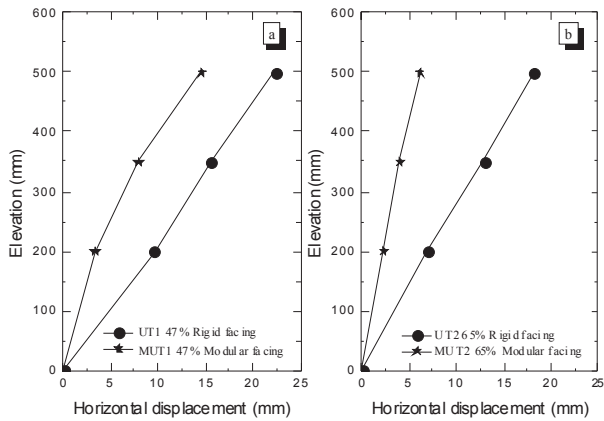


Figure 17 Variation of horizontal displacement with elevation for rigid and modular facing a) Relative density 47% b) Relative density 65%

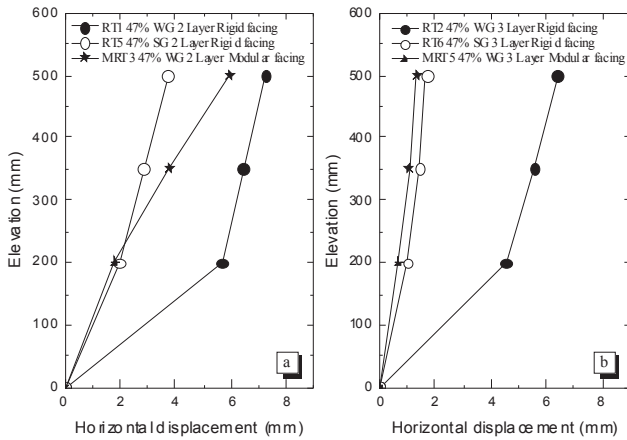


Figure 18 Variation of horizontal displacement with elevation for reinforced rigid and modular facing for Relative density 47% a) 2 layered system b) 3 layered system

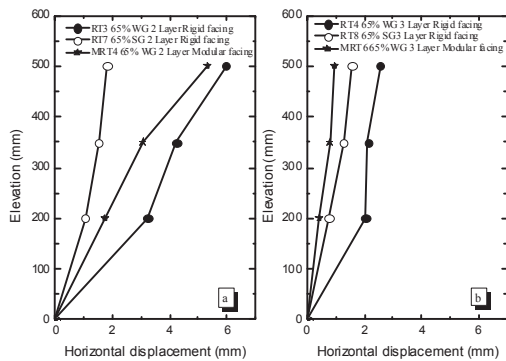


Figure 19 Variation of horizontal displacement with elevation for reinforced rigid and modular facing for Relative density 65% a) 2 layered system b) 3 layered system

4. CONCLUSIONS

Following major conclusions are drawn from the shaking table studies on unreinforced and reinforced rigid faced and modular block walls.

Displacements are more sensitive to relative density and decrease with increasing relative density, the effect being more pronounced in case of unreinforced walls than in reinforced ones.

Acceleration amplification is not varied significantly upon inclusion of reinforcement because geosynthetic reinforcement does not enhance the stiffness of the wall.

Vertical displacement of backfill sand increases as distance from wall facing increases

Horizontal displacement profile along the width of the wall for two adjacent modular blocks is similar.

In general, modular block faced wall performed far better than rigid faced wall in terms of wall displacements. The RMSA amplification factor is not affected by wall facing and reinforcement inclusion but was altered slightly with the variation in the relative density of the backfill.

5. REFERENCES

- Bathurst, R. J. and Simac, M. R. 1994. Geosynthetic reinforced segmental retaining wall structures in North America. Keynote Paper, *Proceedings of the 5th International Conference on Geotextiles, Geomembranes and Related Products*, Singapore, pp. 1275-1298.
- Bathurst, R. J., Cai, Z. & Pelletier M. J. 1996. Seismic design and performance of geosynthetic reinforced segmental retaining walls. *Proceedings of the 10th Annual Symposium of the Vancouver Geotechnical Society*, British Columbia, Canada. 26 p.
- Bathurst, R.J., Simac, M.R. & Berg, R.R. 1993. Review of the NCMA Segmental Retaining Wall Design Manual for Geosynthetic-Reinforced Structures. *Transportation Research Record*, Vol. 1414, pp. 16-25.
- Cazzuffi, D. & Rimoldi, P. 1994. The Italian Experience in Geosynthetics Reinforced Soil Retaining Wall with Vegetated and Concrete Facing. *Recent Case Histories of Permanent Geosynthetic-Reinforced Soil Retaining Walls*. Tatsuoka, F. & Leshchinsky, D. (eds.), Rotterdam, The Netherlands: Balkema, pp. 21-43
- Collin, J. G., Chouery-Curtis, V. E. & Berg, R. R. 1992. Field observations of reinforced soil structures under seismic loading. *Earth Reinforcement Practice*, Proceedings of the International Symposium on Earth Reinforcement Practice, IS-Kyushu '92, Kyushu, Japan, pp. 223-228.
- El-Emam, M. & Bathurst, R.J. 2004. Experimental design, instrumentation and interpretation of reinforced soil wall response using a shaking table, *International Journal of Physical Modelling in Geotechnics*, Vol. 4. No. 4, 13-32.
- Gourc, J.P., Gotteland, P. & Wilson-Jones, H. 1990. Cellular Retaining Walls Reinforced by Geosynthetics: Behaviour and Design. *Performance of Reinforced Soil Structures*, McGown, A., Yeo, K. & Andrawes, K. Z. (eds.), Proceedings of the International Reinforced Soil Conference held in Glasgow, Scotland, September 1990, pp. 41-45.
- Juran, I. & Christopher, B. 1989. Laboratory model study on reinforced soil retaining walls. *Journal of Geotechnical Eng.* Vol. 115, No. 7, pp. 905-926.
- Kato, N., Huang, C.C., Tateyama, M., Watanabe, K., Koseki, J. & Tatsuoka, F. 2002. Seismic stability of several types of retaining walls on sand slope., *Proc. of 7th International Conference on Geosynthetics*, Nice, Vol. 1, pp. 237-240.
- Knutson, A.F. 1990. Reinforced Soil Retaining Structures, Norwegian Experiences. *Proceedings of the Fourth International Conference on Geotextiles, Geomembranes and Related Products*, Rotterdam, The Netherlands: Balkema, Vol. 1, pp. 87-91
- Koerner, R. M. & Soong, T. Y. 2001. Geosynthetic Reinforced Segmental Retaining Walls. *Geotextiles and Geomembranes*, Vol. 19, No. 6, pp. 359-386.
- Koseki, J., Tatsuoka, F., Munaf, Y., Tateyama, M. & Kojima, K. 1998. A modified procedure to evaluate active earth pressure at high seismic loads. *Soils and Foundations*, Special Issue on Geotechnical Aspects of the January 17 1995 Hyogoken-Nambu Earthquake, Vol. 2, pp. 209-216.
- Kutter, B. L., Casey, J. A. & Romstad, K. M. 1990. Centrifuge modeling and field observations of dynamic behavior of reinforced soil and concrete cantilever retaining walls. *Proc., 4th U.S. Na-*

- tional Conf. on Earthquake Engineering*, pp. 663-672.
- Ling, H. I., Tatsuoka, F. & Tateyama, M. 1995. Simulating performance of GRS-RW by finite-element procedure. *Journal of Geotechnical Eng.*, Vol. 121, No. 4, pp. 330-340.
- Ling, H.I., Mohri, Y., Leshchinsky, D., Burke, C., Matsushima, K. & Liu, H. 2005. Large-scale shaking table tests on modular-block reinforced soil retaining walls. *Journal of Geotechnical and Geoenvironmental Engineering*, Vol. 131, No. 4, pp. 465-476
- Liu, H. 2012. Long-term lateral displacement of geosynthetic-reinforced soil segmental retaining walls. *Geotextiles and Geomembranes*, Vol. 32, pp. 18-27
- Lo Grasso, A.S., Maugeri, M. & Recalcati, P. 2005. Seismic behaviour of geosynthetic-reinforced slopes with overload by shaking table tests. *Slopes and Retaining Structures under Seismic and Static Conditions*, ASCE Geotechnical Special Publication No. 140, CDROM.
- Matsuo, O. Tsutsumi, T., Yokoyama, K. & Saito, Y. 1998. Shaking table tests and analyses of geosynthetic-reinforced soil retaining walls, *Geosynthetics International*, Vol. 5, pp. 97-126.
- Ramakrishnan, K., Budhu, M. & Britto, A. 1998. Laboratory Seismic Tests on Geotextile Wrap-Faced and Geotextile-Reinforced Segmental Retaining Walls. *Geosynthetics International*, Vol. 5, Nos. 1-2, pp. 55-71.
- Sakaguchi, M. 1996. A study of the seismic behavior of geosynthetic reinforced walls in Japan. *Geosynthetics International*, Vol. 3, No. 1, pp. 13-30.
- Sandri, D. 1997. A summary of reinforced soil structure performance in the greater Los Angeles area after the Northridge earthquake. *Mechanically stabilized backfill*, Wu, J. (ed.), Rotterdam, The Netherlands: Balkema, pp. 433-442.
- Tatsuoka, F., Koseki, J. & Tateyama, M. 1997. Performance of reinforced soil structures during the 1995 Hyogo-ken Nanbu Earthquake. *Earth reinforcement*, Ochiai, H. et al., (eds.), Rotterdam, The Netherlands: Balkema, pp. 973-1008.
- Watanabe, K., Munaf, Y., Koseki, J., Tateyama, M. & Kojima, K. 2003. Behaviors of several types of model retaining walls subjected to irregular excitation. *Soils and Foundations*, Vol. 43, No. 5, pp. 13-27.
- White, D.M. & Holtz, R.D. 1997. Performance of geosynthetic-reinforced slopes and walls during the Northridge, California Earthquake of January 17, 1994, *Earth Reinforcement*, Rotterdam, The Netherlands: Balkema, Vol. 2, pp. 965-972.
- Won, G.W., 1994. Use of Geosynthetic Reinforced Structures in Highway Engineering by the Roads and Traffic Authority (NSW). *Ground Modification Seminar No 3 - Geosynthetics in Road Engineering*, Sydney, Australia: University of Technology, Sydney, September 1994, 26 p.
- Yoo, C. & Jung, H. 2006. Case History of Geosynthetic Reinforced Segmental Retaining Wall Failure. *Journal of Geotech. Geoenviron. Eng.*, Vol. 132, No. 12, pp. 1538-1548.

Calculation models of bearing capacity and deformation of reinforced soil bases

Ilizar T. Mirsayapov & Irina V. Koroleva

Kazan State University of Architecture and Engineering, mirsayapov1@mail.ru, mirsayapov@yandex.ru

ABSTRACT: The article discusses design models bearing capacity and deformation of reinforced soil base vertical elements. Development of new analytical expressions of the mechanical condition of reinforced base with a joint deformation of the soil and reinforcing elements. Resistance reinforced base shift in the boundary zones formed of earth resistance by compression reinforcing elements and the resistance to bending of reinforcing elements. The bearing capacity of the soil under the reinforcing elements is determined from the strength of triaxial compression. The value of shear force, the perceived reinforcing elements is determined from the equation of equilibrium moments of the external and internal forces of the most loaded section of the reinforcing element, clamped through the shear plane of the soil. The resistance of reinforced soil compression in the middle part defined of the requirements of strength under triaxial compressive. Deformation of the reinforced base determined by the method of layer-stack surround the stress-strain state and joint deformation of the soil and reinforcing elements.

1. INTRODUCTION

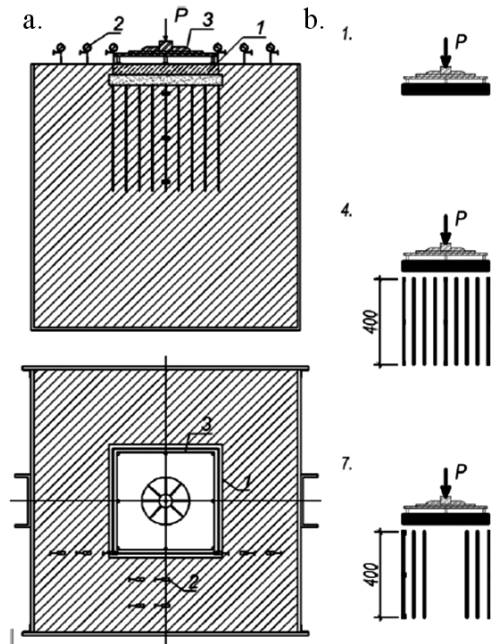
At high levels of stress in the ground at the base of reconstruction and strengthening of the bases and under unfavorable geotechnical conditions of construction sites one way to increase carrying capacity and reduce sediment bases is the vertical reinforcement of soil at the base of buildings.

Reinforced soil foundation is a combination of soil and reinforcing element, wherein the reinforcing elements of the base deformation conditions change, limiting soil deformation in both the vertical and horizontal direction, increasing the overall stability of the whole base.

2. RESULTS OF EXPERIMENTAL STUDIES

The laboratory and field pilot studies revealed that the reinforcement of the vertical elements increases the bearing capacity of base soil of 1,42 – 2,42 times and reduces the deformation of base at 1,25 – 3,15 times, depending on the characteristics of the reinforcement compared

with unreinforced base [Mirsayapov I.T. & Popov A.O., 2008] (Figure 1-3).



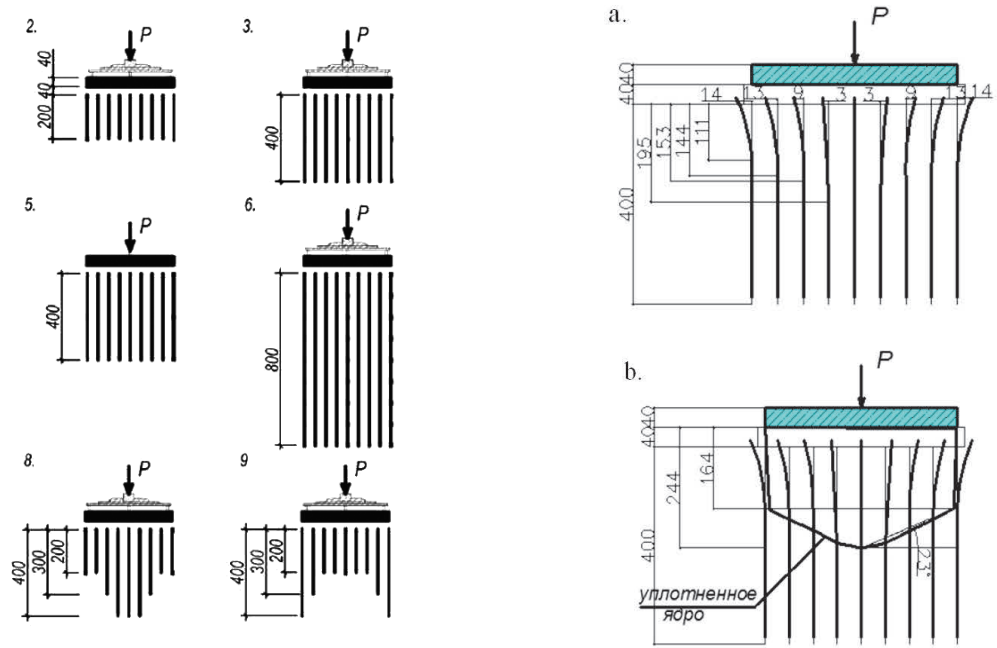


Figure 1. a – The scheme of the laboratory tests, b – The program of experimental studies

In the process of experimental studies been studied changes in stress-strain state in a variety of zones reinforced soil base [Mirsayapov I.T. & Popov A.O., 2010]:

- stresses in the soil and effort in reinforcing elements evolve at different rates throughout the test, with the most notable changes are in the stage of elastic deformation of soil;
- reinforcing elements apart axial compression have experienced bending and prepared deviation from the vertical, in which case the greatest horizontal displacements associated with the bending, observed in the reinforcing elements disposed in the extreme zones and the minimum horizontal movements have been recorded in the central zone;
- deviation from the vertical reinforcing elements associated with the formation and development of the regions of the shift with the bases loaded and the pressure of a plastically deformed zone of the soil.

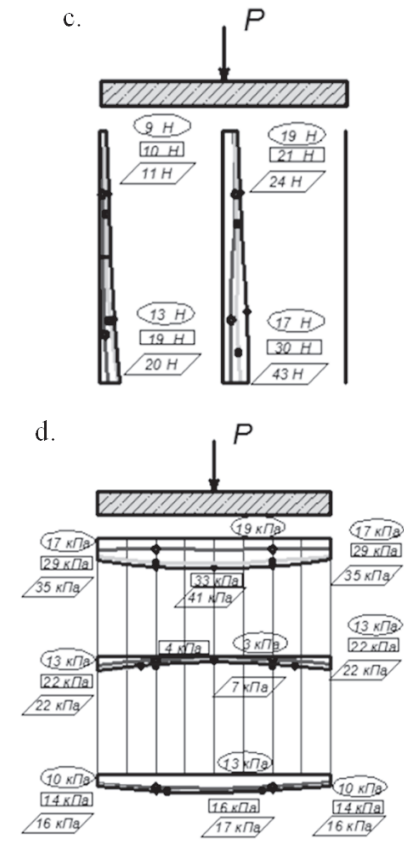


Figure 2. The results of laboratory tests
 a – The scheme deformation reinforcing elements,
 b – The efforts reinforcing elements,
 c – The scheme of education compacted core,
 d – The stress diagram in the soil base

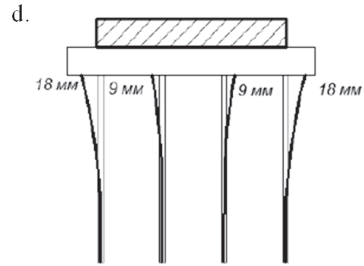
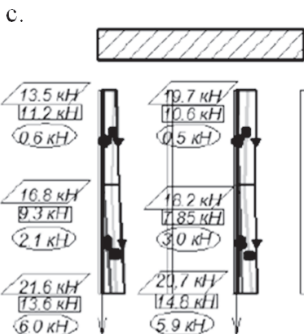
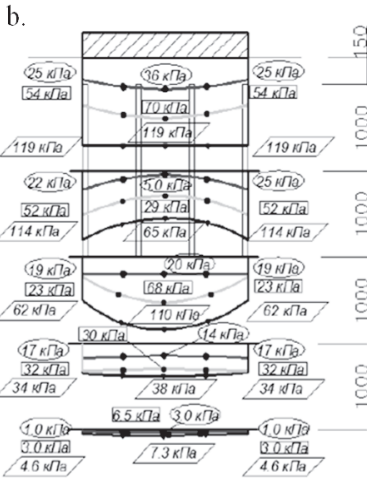
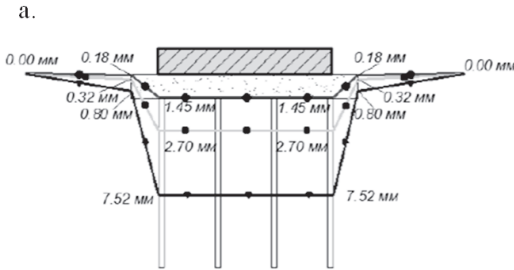


Figure 3. The results of field tests
 a – The strain diagram of the base soil,
 b – The stress diagram in the soil,
 c – The diagram efforts in reinforcing elements,
 d – The represents the deformation of the reinforcing elements

Thus, the resistance to compression reinforced base consists of resistance of the soil reinforcing elements under to compression and resistance to bending of reinforcing elements in the edge zones and resistance reinforced base to triaxial compression in the central zone.

3. ASSESSMENT THE BEARING CAPACITY OF REINFORCED SOIL BASE

Based on the analysis of the results of experimental studies, adopted the working hypothesis, according to which the resistance of reinforced array compressive force consists of flow resistance in triaxial to compression of the mean area and the shear resistance in the boundary zones (Figure 2-3).

Based on the proposed hypothesis about the mechanism of resistance, the condition of the bearing capacity of reinforced soil base can be written as:

$$P \leq \text{ctg } \varphi \cdot T + N_c, \quad (1)$$

where T – resistance of reinforced soil mass shift; N_c – reinforced soil mass resistance to compression in the middle part; φ – internal friction angle of reinforced soil.

The strength of reinforced soil base shift in the marginal zones of consists of the resistance to bending of reinforcing elements crossing the slip plane of soil and resistance to compression of the soil under the reinforcing elements. In

this case, the strength of the shear zone boundary is described by the equation:

$$T = R_a + R_{rp}, \quad (2)$$

where R_a – resistance to bending reinforcing element; R_{rp} – soil resistance to compression under the reinforcing elements.

The force perceivable by the bending of the reinforcing element, depends on the conditions of joint deformation of the element and the surrounding soil strength and deformation characteristics. At the same time reinforcing element is treated as a cantilever beam, clamped at the shear line of the foundation soil. The deformation of the reinforcing element below the shift is determined by both the beam on elastic foundation, for which it is very important are the deformation properties of the base. One measure of this property is the coefficient of the bed base. Coefficient of base soil foundation under the reinforcing element is dependent on the diameter of the reinforcing elements of the deformation modulus of the soil and the level of stress. Also called coefficient varies along the reinforcing member.

In determining the rate of soil foundation under the bed reinforcing element, the expression

$$K = \frac{q}{\int_{0,5d_a}^r \frac{2q \cdot d_a}{\pi \cdot r \cdot E_0} \cdot dr}, \quad (3)$$

where $q = Q_{c\pi}/d_a$; d_a – diameter of the reinforcing member; $Q_{c\pi}$ – shear force on the shear plane; E_0 – modulus of total deformation of the soil.

Area of maximal normal stress from bending the reinforcing member located at a distance L_x from the plane shear (Figure 4). This distance is also the area of force transfer from reinforcing elements on the ground. According to the decision of the problem of a semi-infinite long arm in elastic half-space in the perception of the force acting on the rod, takes an active part only of the base length L_x .

The length of the active zone of soil deformation is essential in assessing the carrying capacity of the reinforcing element and depends on the geometry and deformation characteristics, coefficient of bed of soil foundation and is determined by the formula:

$$L_x = \frac{\pi}{2} \cdot \sqrt[4]{\frac{4E_a \cdot I_a}{K \cdot d_a}}, \quad (4)$$

where E_a – elasticity modulus reinforcing member; I_a – moment of inertia of the cross-sectional the reinforcing element.

Assuming that stress in the ground beneath the reinforcing element are distributed uniformly on the area L_x , the resultant stress distribution, i.e. effort perceived by ground foundation beneath the reinforcing element can be defined by the expression

$$R_{rp} = q_{ult} \cdot L_x. \quad (5)$$

The value q_{ult} for each zone along the length of the shear plane is determined from expression

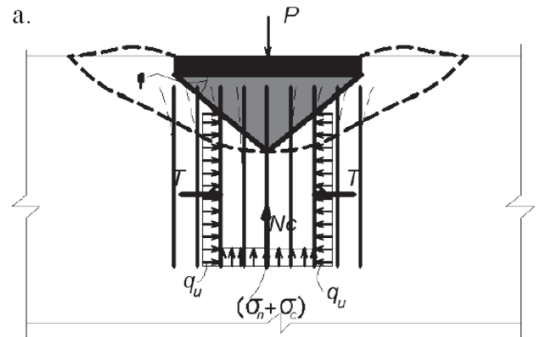
$$q_{ult} = \sigma_{zp}(\varepsilon_{zp}) \cdot d_a. \quad (6)$$

where σ_{rp} – function of bulk stress in the ground under the reinforcing elements, depending on the volume strain of the soil under the reinforcing elements.

Substituting the Equation (6) in the Equation (5) obtain

$$R_{rp} = \sigma_{zp}(\varepsilon_{zp}) \cdot d_a \cdot L_x, \quad (7)$$

where ε_{rp} – volumetric soil deformation corresponding to the joint deformation of the soil and reinforcing element.



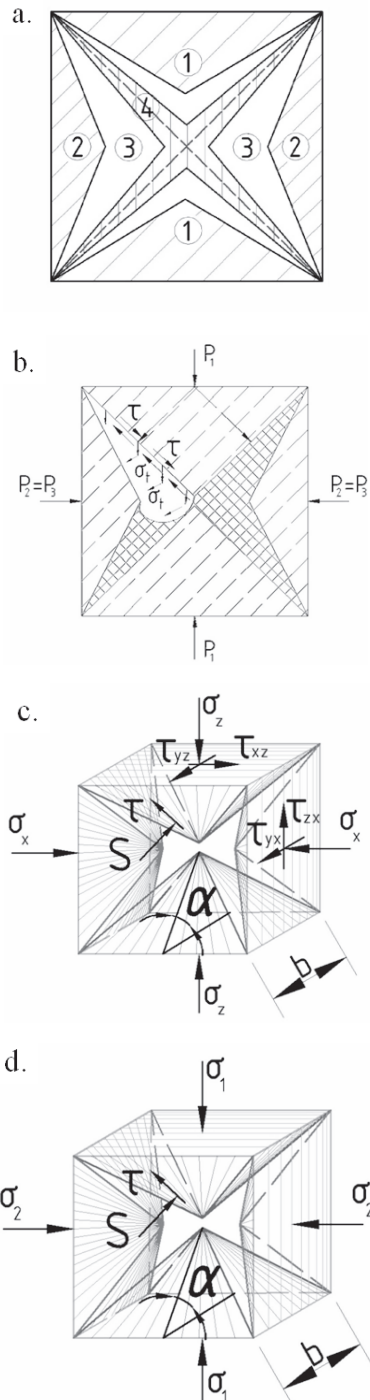
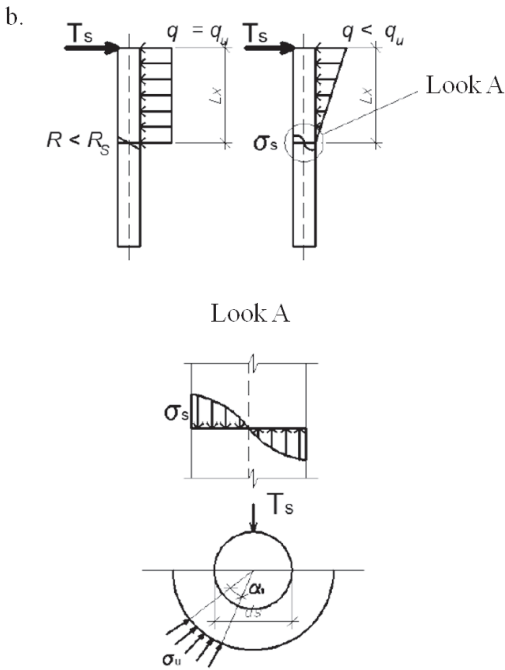


Figure 4. a – Design scheme for the determination of the bearing capacity of reinforced base, b – Design scheme for determining the bearing capacity of the reinforcing element

Limiting bearing capacity of the soil under the reinforcing element can be determined by tensile strength in a three dimensional stress, as the ground under the reinforcing element is working in cramped conditions, so that will be an increase soil resistance to compression.

On the basis of the established scheme of destruction and areas of stress-strain state is proposed generalized scheme of inelastic deformation of the ground under the reinforcing elements on the basis of the modified model of non-associated plastic flow by Nikolaevsky [Mirsayapov I.T. & Koroleva I.V., 2011, №2], according to which the strength of the dry Coulomb friction deviates from the site of limit equilibrium and acts in the plane of purely tangential slip of physical particles. Orientation detection of such potentially dangerous areas requires consideration of the deformed state of the soil (Figure 5).

Figure 5. a – consolidated areas of different density of a specimen in triaxial tests: 1-vertical consolidated pyramids; 2 – consolidated pyramids at specimen's

sides; 3 – uniformed deflected state area; 4- area of dilatancy; b – deformed state of clay between pyramids formed; c – deflected state of volume element in space in random moment of time at preultimatecondition (stresses and tensions are not shown); d – deflected state of volume element in space at ultimate condition (stresses and tensions are not shown)

Considering that, regardless of the degree of heterogeneity in the beginning of the loading stress-strain state of an elementary volume of soil destruction always occurs in the space of principal stresses, combining the space of the principal stresses $\sigma_1, \sigma_2, \sigma_3$ and space principal strains $\varepsilon_1, \varepsilon_2, \varepsilon_3$, and preserving the principle of the coaxial stress tensor and strain rate [Mirsayapov I.T. & Koroleva I.V., 2011, № 2], we assume that the law of dry Coulomb friction binds projection of the forces acting on the grounds of limiting equilibrium on the normal to the area and sliding to itself. The condition of the current under load is written as

$$|t| = S \cdot \operatorname{tg} \varphi + c_0, \quad (8)$$

where $S = \sigma_1 \cdot l \cdot l' + \sigma_2 \cdot m \cdot m' + \sigma_3 \cdot n \cdot n'$,

$$t = \sqrt{\begin{aligned} & (\sigma_1 \cdot l \cdot m' - \sigma_2 \cdot l' \cdot m)^2 + \\ & + (\sigma_2 \cdot m \cdot n' - \sigma_3 \cdot m' \cdot n)^2 + \\ & + (\sigma_3 \cdot n \cdot l' - \sigma_1 \cdot n' \cdot l)^2 \end{aligned}}$$

φ – angle of internal friction; c_0 – specific cohesion; l, m, n – cosines to platforms of limit equilibrium; l', m', n' – cosines to platforms of gliding.

Special orientation of limit equilibrium platforms is defined by equations below [Mirsayapov I.T. & Koroleva I.V., 2011, №2]:

$$l^2 = \frac{\bar{I}_3}{\bar{I}_2 \cdot \bar{\sigma}_1}; \quad m^2 = \frac{\bar{I}_3}{\bar{I}_2 \cdot \bar{\sigma}_2}; \quad n^2 = \frac{\bar{I}_3}{\bar{I}_2 \cdot \bar{\sigma}_3}; \quad (9)$$

where $\bar{I}_2 = \bar{\sigma}_1 \cdot \bar{\sigma}_2 + \bar{\sigma}_2 \cdot \bar{\sigma}_3 + \bar{\sigma}_3 \cdot \bar{\sigma}_1$ and $\bar{I}_3 = \bar{\sigma}_1 \cdot \bar{\sigma}_2 \cdot \bar{\sigma}_3$ – second and third invariants of tensors of modified main stresses $\bar{\sigma}_i = \sigma_i + H$ ($i = 1, 2, 3$);

$H = \frac{c}{\operatorname{ctg} \varphi}$ – uniform compression defined

by Mohr-Coulomb's hypothesis;

φ – angle of internal friction.

Expressions for cosines to gliding platform's

normal are as in [Mirsayapov I.T. & Koroleva I.V., 2011, №2]:

$$\left. \begin{aligned} (l')^2 &= \frac{1}{3} \cdot \frac{3 \cdot d\varepsilon_2 \cdot d\varepsilon_3 - I_2 + \sqrt{I_2^2 - 3 \cdot I_1 \cdot I_3}}{(d\varepsilon_1 - d\varepsilon_2) \cdot (d\varepsilon_1 - d\varepsilon_3)}; \\ (m')^2 &= \frac{1}{3} \cdot \frac{3 \cdot d\varepsilon_1 \cdot d\varepsilon_3 - I_2 + \sqrt{I_2^2 - 3 \cdot I_1 \cdot I_3}}{(d\varepsilon_2 - d\varepsilon_1) \cdot (d\varepsilon_2 - d\varepsilon_3)}; \\ (n')^2 &= \frac{1}{3} \cdot \frac{3 \cdot d\varepsilon_1 \cdot d\varepsilon_2 - I_2 + \sqrt{I_2^2 - 3 \cdot I_1 \cdot I_3}}{(d\varepsilon_3 - d\varepsilon_1) \cdot (d\varepsilon_3 - d\varepsilon_2)}; \end{aligned} \right\}, \quad (10)$$

where $d\varepsilon_1, d\varepsilon_2, d\varepsilon_3$ – increments of main deformations;

$$I_1 = d\varepsilon_1 + d\varepsilon_2 + d\varepsilon_3,$$

$$I_2 = d\varepsilon_1 \cdot d\varepsilon_2 + d\varepsilon_2 \cdot d\varepsilon_3 + d\varepsilon_3 \cdot d\varepsilon_1,$$

$I_3 = d\varepsilon_1 \cdot d\varepsilon_2 \cdot d\varepsilon_3$ – first, second and third invariants of deformation increments.

As stated above, potentially available platform's orientation is not constant in general, and changes in the process of inelastic deformation of soil according to equation [Mirsayapov I.T. & Koroleva I.V., 2011, № 2].

$$\alpha = \arccos \sqrt{\frac{1}{1 - \frac{\mu_{de}}{de_3^p}} - \frac{\mu_{de}}{6}}, \quad (11)$$

where $\mu_{de} = \frac{2de_2^p - de_1^p - de_3^p}{de_1^p - de_3^p}$ – deformed

state characteristic (Lode-Nadai characteristic);

de_1^p, de_2^p, de_3^p – increments of plastic deformations;

$$de_1^p = de_1^p - de_m^p;$$

$$de_2^p = de_2^p - de_m^p; \quad ,$$

$$de_3^p = de_3^p - de_m^p$$

$\varepsilon_1, \varepsilon_2, \varepsilon_3, \varepsilon_m$ – linear and volumetric deformations.

Based on the above described model and the results of experimental studies [Mirsayapov I.T. & Popov A.O., 2008, Mirsayapov I.T. & Popov A.O., 2010] (Figure 1-3), the condition of soil strength by reinforcing elements under triaxial compression is represented as

$$4 \cdot \left[\begin{aligned} & \sigma_V \cdot A_{sh} \cdot \cos \alpha_1 + \\ & + \tau_V \cdot A_{sh} \cdot \sin \alpha_1 \end{aligned} \right] \geq \sigma_1 \cdot A_1, \quad (12)$$

where $A_{sh} = \frac{b^2}{4\cos\alpha_2(t)}$ – surface area of the

side faces of the pyramid;

$A_1 = b^2$ – the area of the cube;

α_1 – angle of the site limit equilibrium;

α_2 – angle of the area of shear;

$$\sigma_v(t) = \sigma_1 \cdot l(t) \cdot l'(t) + \sigma_2 \cdot m(t) \cdot m'(t) + \sigma_3 \cdot n(t) \cdot n'(t) + \sigma_d(t) \quad -$$

normal stress;

$$\sigma_d(t) = \frac{E}{(1+\nu) \cdot r} \cdot \Delta\delta_d \quad - \text{dilatants stress};$$

$\tau_v = S \cdot \text{tg}\varphi + c_0$ – shear stress at the site of the limit equilibrium.

In determining the carrying capacity of reinforced soil foundation is also necessary to pay attention to the shape of stress distribution in the soil along the reinforcing element. In real cases, the epure is different from the rectangular, which was adopted at the beginning. Depending on the stage at which the ground is deformed, the shape of epures can be different. This change takes into account the introduction of the estimated coefficient of completeness epures ω , which is defined by the formula

$$\omega = \frac{\int_0^{L_x} \sigma_{rp}(\varepsilon_{rp}) dL}{\sigma_{rp}^{\max}(\varepsilon_{rp}^{\max}) \cdot L_x} \quad (13)$$

where σ_{rp}^{\max} – the maximum stresses corresponding to the limit deformations in the ground; ε_{rp}^{\max} – ultimate strains in the soil.

The value of the limiting shear force, the perceived reinforcing elements is determined from the equation of equilibrium moments of the external and internal forces of the loaded section of the cantilever beam clamped along the shear line of the soil. This simulates the beam reinforcement structure in the edge region, which crosses the shear plane. When calculating taken curved linear epure of compressive stresses in the soil under the reinforcing element with the maximum value $q \leq q_{ult}$ based on the conditions of joint deformation and soil reinforcing element:

$$R(a) = 3 \frac{M_u}{L_x} n \quad (14)$$

where $M_u = \frac{\sigma_a(\varepsilon_a) \cdot A_a \cdot \omega_a}{4} d_a$ – limiting the

bending moment resisted by reinforcing element crossing the shear plane reinforced array; A_a – cross sectional area of reinforcing element; n – the number of reinforcements crossing the shear plane; $\sigma_a(\varepsilon_a)$ – the stress function in the reinforcing element, depending on the joint deformations reinforcing element ε_a and the soil under the reinforcing element ($\varepsilon_{rp} = \varepsilon_a$); ω_a – coefficient of block stress distribution in the cross sectional reinforcing member.

Reinforced soil resistance to compression in the central portion is defined by the formula

$$N_c = (\sigma_u + \sigma_c) \cdot \sin\varphi \cdot \text{tg}\varphi \cdot A_f + \sigma_a \cdot A_{ap} \cdot n_1 \quad (15)$$

where

$\sigma_u = 4(\sigma_v \cdot A_{sh} \cdot \cos\alpha_1 + \tau_v \cdot A_{sh} \cdot \sin\alpha_1)$ – limiting stresses in the ground in a spatial stress state (Figure 5); $\sigma_c = c \cdot \text{ctg}\varphi$ – pressure connection; A_{sh} – area of shear surface, m^2 ; A_f – area of the core compression, m^2 ; σ_a – tension in the reinforcing element; A_a – sectional area of the reinforcing elements arranged in the core compression, m^2 ; n_1 – number of reinforcing elements in the core compression.

4. DEFORMATION OF THE REINFORCED SOIL BASIS.

Engineering methods of calculation should include elements of accounting trajectory bases loaded, while considering not only the features of soil deformation, which can be determined by the compression dependencies, but also those which are caused by the spatial condition of the soil.

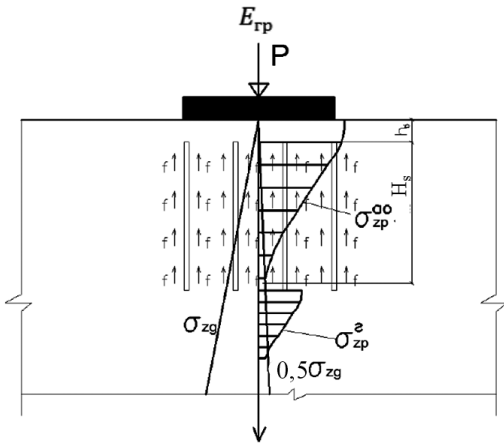


Figure 6. The scheme for the calculation of deformations reinforced vertical elements soil foundation

Engineering method is proposed to calculate the sediment reinforced base, which is based on the method of layering with regard to the spatial summation of the stress-strain state reinforced soil mass [Mirsayapov I.T. & Koroleva I.V., 2011, №4].

The total sediment reinforced base is written as follows (Figure 6)

$$S = S_n + S_{aa} + S_y, \quad (16)$$

where S_n – sediment ground pillows; S_{aa} – sediment within the reinforced zone; S_y – sediment below the zone of reinforcement.

Draft dirt cushion is determined by summing the layering with the restriction of the compressible stratum with dirt pillows:

$$S_n = \frac{0,8 \sum_{i=1}^m \sigma_{zp,i}^{cp} \Delta_{n,i}}{E_n}, \quad (17)$$

where $\Delta_{n,i}$ – elementary layer thickness in the range ground pads; m – the number of individual layers within ground pad.

Deformation within the reinforced zone and the lower zone of the reinforcement is determined by the following procedure.

The natural state of stress on the action of its own weight of soil accept the conditions of the one-dimensional compression by a factor of lateral pressure

$$\xi = \frac{K_v - 2G_v}{K_v + 4G_v}, \quad (18)$$

where K_v – bulk modulus of soil; G_v – shear modulus of the soil.

Bulk modulus of soil within the reinforced zone is defined by the formula:

$$K_{v_{rp}}^{\text{эKB}} = \left[\frac{K_{v_{rp}} (V_{rp} - V_a) (\gamma_{ei} + \gamma_{\mu i})}{V_{rp}} + \frac{(\gamma_{ei} + \gamma_{\mu i}) \sum f_i \cdot u_i \cdot l_i^{aa}}{\varepsilon_{v_{rp}}^{\text{эKB}}} \cdot \frac{\alpha_k}{V_{rp}} \right] \cdot \gamma_n, \quad (19)$$

where $K_{v_{rp}}$ – modulus volume deformations within the reinforced soil zone; V_{rp} – the volume of soil within the reinforced zone; V_a – the volume of reinforcing elements within the reinforced zone; f_i – resistance of the shift between the reinforcing element and the ground; u_i – girth cross section the reinforcing element; α_k – the ratio of the deformation modulus of the material the reinforcing element and the soil; γ_n – coefficient taking into account the inelastic properties of fiber-reinforced base; γ_{ei} , $\gamma_{\mu i}$ – coefficients that take into account the length and reinforcement percentage by volume:

$$\gamma_{ei} = 1,6 + 0,3 \frac{l_{aa}}{H_s},$$

$$\gamma_{\mu i} = 1,07 \frac{\mu_1 - \mu_i}{\mu_1},$$

where l_{aa} – the length of the reinforcing elements, m ; H_s – height of the compressible strata, m ; μ_i – reinforcement percentage of a base of soil; μ_1 – percentage of reinforcement at the length of the reinforcing elements equal to the width of the base of the foundation slab.

In calculating rainfall reinforced an array within the reinforced zone for the height of the compressible strata accepted height reinforcing element. The height of the compressible strata below the zone of reinforcement determined by the regulatory procedure:

$$H_s = Z; \quad \sigma_z = 0,5\sigma_{zp}, \quad (20)$$

where H_s – power compressible thickness received at depth Z ;

σ_z – vertical normal stress at depth Z of the additional load on the base along the axis of facilities;

σ_{zp} – vertical normal stress from the weight of the foundation soil depth Z .

Values for diagrams additional vertical

stress axis of the foundation (square stamp) at a depth Z can be determined by conventional one-regulatory manner. The values of horizontal stress components along the central axis can be determined from the solutions of the theory of elasticity. It should be noted that the central axis of the vertical and horizontal stresses are the main ones

Knowing the components of the vertical stress at different points of the base, to determine the average tension and stress intensity:

$$\sigma = \frac{\sigma_x + \sigma_y + \sigma_z}{3}, \quad (21)$$

$$\sigma_i = \frac{1}{\sqrt{2}} \sqrt{(\sigma_x - \sigma_y)^2 + (\sigma_y - \sigma_z)^2 + (\sigma_z - \sigma_x)^2 + 6 \cdot (\tau_{xy}^2 + \tau_{yz}^2 + \tau_{zx}^2)}. \quad (22)$$

From the values of the average voltage and the stress intensity determine the increment of the strain tensor invariants: the increment of volumetric strain and intensity of deformation.

The transition from tensor invariants deformations to the axial strain ε_z in the case of calculating the deformation along the central axis of the foundation, given the coincidence of the axes of the principal stresses and principal strains with the central axis of the foundation can be made:

- at coincidence of the axes of principal stresses and strains from the central axis of the stamp

$$\left. \begin{aligned} \varepsilon_v &= \varepsilon_1 + \varepsilon_2 + \varepsilon_3, \\ \varepsilon_i &= \frac{2}{3}(\varepsilon_1 - \varepsilon_3), \end{aligned} \right\} \quad (23)$$

- in other cases, use the condition of alignment tensor increments of stress and strain

$$\begin{aligned} \frac{\Delta(\varepsilon_x - \varepsilon_y)}{\Delta(\sigma_x - \sigma_y)} &= \frac{\Delta(\varepsilon_y - \varepsilon_z)}{\Delta(\sigma_y - \sigma_z)} = \\ &= \frac{\Delta(\varepsilon_z - \varepsilon_x)}{\Delta(\sigma_z - \sigma_x)} = \frac{\Delta\varepsilon}{\Delta\sigma} = \chi \end{aligned} \quad (24)$$

Determine the conditional modules that characterize the transition from the natural condition of the substrate in the state after the application of local load

$$K_v = \frac{\Delta\sigma}{\Delta\varepsilon_v}, \quad (25)$$

$$G_v = \frac{\Delta\sigma_i}{3\Delta\varepsilon_i}. \quad (26)$$

Modules (25) and (26) may be represented parameters by the Hooke's law incremental stress and strain for the loading step.

Then the increment of axial strain obtained from Hooke's law in increments of:

$$\Delta\varepsilon_z = \frac{\Delta\sigma_z}{G_v} - \Delta\sigma \cdot \frac{3K_v - G_v}{3K_v \cdot G_v}. \quad (27)$$

The values obtained for the strain increments central axis and a corner point are the result of the action of the local load as an additional loading base, being under the influence of the initial state of stress due to its own weight of the soil.

Sediment base, divided into equal layers of depth to the conventional compressible strata, described by

$$S = \sum_{i=1}^n \varepsilon_{zi} \cdot h_i. \quad (28)$$

5. CONCLUSION

Developed computational models bearing capacity and precipitate reinforced base including the expression for the resistance of reinforced soil mass shear resistance of reinforced soil mass in the middle of compression, the values of maximum shear force perceived by the reinforcing elements limit values of shear perceived reinforced soil foundation. The proposed model for calculating the load capacity makes it possible to reliably calculate bearing capacity of reinforced foundation at all stages of loading, taking into account the joint strength and deformation of the reinforcing elements of the soil.

The developed computer model precipitation reinforced soil foundation with the joint deformation of the soil mass and reinforcements into account the joint deformation of the soil and the reinforcing elements and allows you to more accurately predict the amount of rainfall vertical elements reinforced soil foundation.

The analytical expression for the resistance of reinforced array in the middle of compression and shear in the edge zone of limit values of shear perceived soil and reinforcing elements, the expression for determining the length of the

reinforcing elements and the anchoring of the bending moment, a function taking into account the deformation of the reinforcing elements and a partial shift expressed in terms of length and percentage of reinforcement.

Comparison of the results of the calculation of bearing capacity and sediment, soil reinforced with vertical elements of reasons for the proposed settlement models are in good agreement with the results of the tests (a deviation of not more than 15%). The validity and reliability of the results of the calculation is confirmed by comparison with the data of field observations of precipitation reinforced base cylindrical tank, the test results of four large-scale stamps on the reinforced basis, the three models of reinforced bases in the field and more than 20 models in the laboratory.

6. REFERENCES

- Mirsayapov I.T. & Koroleva I.V. 2011. Calculation model of long nonlinear deformation of clay soils under complex stress state. *News of the KSUAE*, No. 2 (16), pp. 121-128.
- Mirsayapov I.T. & Koroleva I.V. 2011. Prediction of deformation of foundations taking into account the long-term non-linear deformation of soil. *Soil Mechanics and Foundation Engineering*, No. 4, pp. 16-23.
- Mirsayapov I.T. & Popov A.O. 2008. Experimental and theoretical study of work reinforced soil masses. *News of the KSUAE*, No. 2 (10), pp. 75-80.
- Mirsayapov I.T. & Popov A.O. 2010. Estimation of strength and deformability of reinforced soil bases. *International Journal of Geotechnics*, No. 4, pp. 58-67.

Understanding Long-Term Effect of Tunnel-Soil Interaction

C.W. Ong

Managing Director, KIMARO Geotechnical Engineering (Singapore & Malaysia) Pte Ltd, Singapore,
Managing Director, J.Pro Consulting Engineers (S'pore & M'sia) LLP, ong@kimaro.com.sg

C. F. Leung

Professor, National University of Singapore, ceelcf@nus.edu.sg

K.Y. Yong

Vice President, National University of Singapore, uciyky@nus.edu.sg

Professor, Department of Civil Engineering, National University of Singapore

ABSTRACT: Tunnel excavations generally cause ground settlement and deformation nearby, especially in soft clay. Although many studies have been conducted to investigate tunnel-soil interactions in the short-term, impacts in the long-term are still not well understood. The centrifuge test results reveal that in the short term, an immediate shear zone with large soil movement above tunnel can be identified. In the long term, the significant soil movement zone extends much wider resulting in a wider surface settlement trough and the soil settlement is noted to be dominant rather than the lateral soil movement. Qualitative assessment on the excess pore pressure responses has provided an understanding on the development of negative excess pore pressure in the immediate shear zone and positive excess pore pressure in the support zone.

1. INTRODUCTION

Tunnel excavations generally cause ground settlement and deformation nearby, especially in soft clay. Although many studies have been conducted to investigate tunnel-soil interactions in the short-term, impacts in the long-term are still not well understood. A published field study covering an 11-year period of post-tunnelling monitoring for the Haycroft Relief Sewer in Grimsby, UK, (O'Reilly et al., 1991) in very soft clay recorded that the soil settlement in the long-term had increased significantly. In view of the complexity of field instrumentation and monitoring, physical modelling can be an attractive mean to study the tunnel-soil interaction problem in both short-term and long-term. One effective way is to conduct centrifuge model tests employing artificial gravitational field to replicate the prototype stress level as experienced by the ground in the field. Under a well-controlled environment, centrifuge tests can provide flexibility and repeatability to study tunnel-soil interaction problems that could not be achieved in field tests (Mair et al., 1984; Loganathan et al., 2000; Ran, 2004; Jacobz et al., 2004).

Many research studies have been carried out to investigate tunnelling-induced soil movements. Peck (1969), Schmidt (1969), O'Reilly

and New (1982), Lake et al. (1992), Mair et al. (1993) and others developed empirical formulae from field studies to predict the soil movements induced by tunnelling. In addition, several centrifuge model studies including Loganathan (2000) and Ran (2004) were conducted to examine soil movements due to tunnelling.

Besides empirical formulae and centrifuge model studies, analytical solutions have been developed by researchers including Sagaseta (1987), Verrujit and Booker (1996), Loganathan and Poulos (1998), Park (2005) and Osman et al. (2006a) to predict the ground displacements for various shapes of tunnel deformation. However, such analytical solutions cannot account for all aspects, in particular the time effects. Many researchers reported field measurement results for soil movements induced by tunnelling. However, most of these studies did not report field measurements during the post-tunnelling period despite some reports on significant long-term settlements after tunnelling in soft clay; see for example, Haycroft Relief Sewer in Grimsby, UK, (O'Reilly et al., 1991) and Shanghai Metro Tunnel No.2, China, (Zhang et al., 2004).

Based on the above review, it is evident that the mechanism and calculation of tunnelling-induced soil movements in the short-term are reasonably well studied. However, the long-

term tunnel-soil interaction in soft clay clearly needs further investigation.

2. CENTRIFUGE EXPERIMENTAL SET-UP AND PROCEDURES

2.1. NUS Geotechnical Centrifuge Facility

Recently, there has been rapid development in geotechnical centrifuge modelling technology world-wide, and centrifuge testing is now commonly used to study geotechnical and geo-environmental problems. Geotechnical centrifuge modelling has also been employed to complement conventional numerical analysis and field monitoring (Schofield, 1998; Ng et al., 1998; Kimura, 1998). Each approach has its own advantages in terms of quality of result, time and cost. Particularly in cases where there are uncertainties in the applicability of a proposed design methodology, use of more than one approach permits calibration of results against each other and verification of conclusions drawn.

Figures 1, 2 and 3 show the National University of Singapore (NUS) centrifuge facilities. The centrifuge primarily consists of a conical case, a driven shaft, and rotating arm, and two swinging platforms. It has a capacity of 40,000 g-kg and operates up to a maximum g-level of 200g, implying that the allowable payloads at 200g and 100g are 200 kg and 400 kg, respectively. The structure of the centrifuge is based on the conventional dual swing platform design.

The model package is normally loaded onto one of the swing platforms with the opposing platform counter balanced by either counter-weights or the other model package with identical weights. When fully spun up during test operation, the distance from the axis of rotation to the base of the platform is 1.871 m. The centrifuge is driven by a hydraulic motor delivering up to about 37 kW power. The swing platform has a working area that measures 750 mm x 700 mm and headroom of 1180 mm. A stack of electrical slip rings is mounted at the top of the rotor shaft for signals and power transmission between the centrifuge and the control room.

DC voltage is transmitted through the slip rings to the transducers mounted on the centrifuge or the model package from the

control room. Similarly, registered signals from the transducers are then transmitted via the slip rings. The signals are first filtered by an amplifier system at 100 Hz cut-off frequency to reduce interference or signal noise pick-up through the slip rings. The amplified signals are then collected by a data acquisition system at a regular interval in the control room. Software called DasyLab © is used to process the signals whereby the signals are smoothed using a block average. Two closed circuit cameras, which are mounted on the centrifuge, enable the entire in-flight test process to be monitored in the control room. The NUS centrifuge is described in detail by Lee et al. (1991) and Lee (1992).



Figure 1. Photograph of NUS geotechnical centrifuge with the model package mounted on the platform

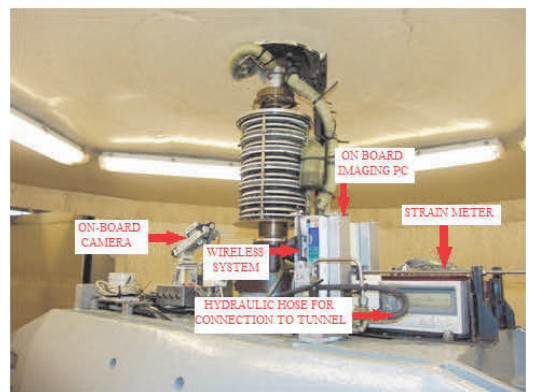


Figure 2. NUS Geotechnical Centrifuge On board set-up

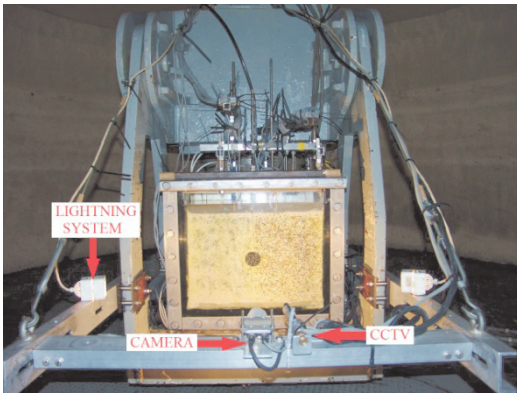


Figure 3. Set-up of the entire model package in 1g

2.2. Model Tunnelling Technique

There are many modes of ground movement associated with tunnel construction. In a situation where the tunnel excavation has passed a particular section is considered, the vectors of the ground movement developed will be more or less in the plane perpendicular to the tunnel axis. Consequently it is reasonable to assume that a plane strain model of long tunnel section would be a good representation of tunnelling-induced soil movements; this is usually referred to as a two-dimensional simulation (Taylor, 1998).

In the present study, an innovative model tunnelling technique has been developed to simulate the inward tunnel deformation due to over-excavation. An oval-shape ground deformation pattern is imposed as the boundary condition and the gap parameter (GAP) proposed by Lee et al. (1992) is used to quantify the amount of tunnel over-cut. Loganathan & Poulos (1998) and Park (2005) evaluated that an oval-shape deformation pattern is in reasonable agreement with tunnel deformations observed in the field.

The cross section of the innovative model are shown in Figure 4. The model tunnel is made of a circular rigid outer plate and a hollow metallic circular tube of 60 mm diameter, simulating a 6-m diameter prototype tunnel at 100g. The rigid plate helps to maintain a uniform GAP for the entire model tunnel. The two radial bearings inside the model tunnel help to facilitate a smooth movement of the sliding rod and provide support to the solid aluminium



Figure 4. Cross-section of model tunnel

sliding rods. There are nine small rods which are inserted into the respective holes of the model tunnel. A rigid circular plate is then used to encircle the model tunnel and an oval-shape GAP is created between the rigid circular plate and the point of contact of nine small rods. The whole mechanism works as such when there is a force pushing the aluminium sliding rod, the small rods will fall onto the three thinner parts of sliding rod of smaller cross-sectional area. As such, the GAP in cross-sectional view will close up and this simulates the inward tunnel deformation of the oval-shape GAP. There are advantages of such model tunnel. Firstly, the present model tunnel is able to simulate the precise volume loss when the GAP closes up after tunnelling. The percentage of volume loss has been calibrated by calculating the area of surface settlement against the GAP created in the model tunnel at the undrained stage. Secondly, the circular rigid outer plate can provide a very uniform oval-shaped of the GAP throughout the entire length of the model tunnel. As such, a constant volume loss around the model tunnel can be ensured.

2.3. Kaolin Clay

The Malaysian kaolin clay used in the present study has a liquid limit (LL) of 80%, plastic limit (PL) of 40 % and hence a plasticity index (PI) of 40%, and a specific gravity, G_s , of 2.65. The coefficient of consolidation C_v and permeability at pressure of 100 kPa, are 40 $m^2/year$ and 2×10^{-8} m/s, respectively. The effective internal friction angle, ϕ' , is 23° . Kaolin clay has critical state parameters λ of

0.244, average κ of 0.053, N of 3.35 and M of 0.9.

2.4. Toyoura Sand

The sand that underlies the clay serves as drainage channel and socket for the pile. It has an average particle size of 0.2 mm and specific gravity, G_s , of 2.65. The minimum and maximum density of the sand is 1335 kg/m³ and 1645 kg/m³, respectively. The critical state friction angle is 32°.

2.5. Experimental Procedure

The model ground was remoulded from Malaysian kaolin clay powder and water at a weight ratio of 1 to 1.2 in a de-airing mixer. The clay was then pre-loaded under a pressure of 20 kPa. The container was then placed on the centrifuge platform and accelerated to 100g. After the ground settlement and pore water pressure readings stabilized, the centrifuge was stopped and the front wall of the container was removed to install the model tunnel, pore pressure transducers (PPTs) and to place marker beads onto the soil facing the Perspex window. Different colours of 1-mm diameter beads were randomly embedded on the surface to produce an artificial texture for the subsequent analysis of PIV. These beads are made of light PVC so that they could move with the soil freely. The beads were pushed into the soil by the highly greased Perspex window of the strong box to ensure a full perfect contact and the beads can move together with the soil. Permanent control markers dots with known centre to centre distance were marked on the Perspex window in order to provide reference points to the subsequent image analysis by PIV. The entire model package was then spun up to 100g for reconsolidation of the clay. The test began by pushing the sliding rod forward with the small rods lying on the sliding rod dropping onto the thinner part of the sliding rod. As a result, the gap between the rigid aluminium plate and the model tunnel closes and inward tunnel deformation was simulated. The model tunnel was left in place to simulate the tunnel lining to study the post-excavation ground deformation and pile responses. The centrifuge was kept at 100g for 2 hours (2.3 years in prototype scale)

and instruments were monitored regularly during this period.

3. TUNNEL-SOIL INTERACTION

In order to interpret the building or pile behaviour due to tunnelling-induced soil movement, it is important to examine the mechanism of tunnel-soil interaction. Particle Image Velocimetry (PIV) technique (White et al., 2003; Zhang et al., 2005) has been used in centrifuge model tests to obtain more accurate and detailed information on soil displacements. With a better understanding and results obtained in free-field experimentally in the present study, further evaluations can then be made on tunnelling-induced building and pile responses.

The magnitude of volume loss depends primarily on the method of tunnelling and soil conditions. The typical volume loss design values for tunnels of up to 6.6m diameter in marine clay are in the range of 2% to 3.5%, depending on the method of tunnelling (15% volume loss should be considered if using TBM with compressed air) (LTA, 2010). In view of the above, a volume loss of 3% (Test 1) is simulated in the present study. To evaluate the detrimental effects of higher volume loss, 6.5% (Test 2) is also simulated. The tunnel cover C (distance from ground surface to tunnel crown) and tunnel diameter D is 12 m and 6 m, respectively. The digital image of a typical test is shown in Figure 5.

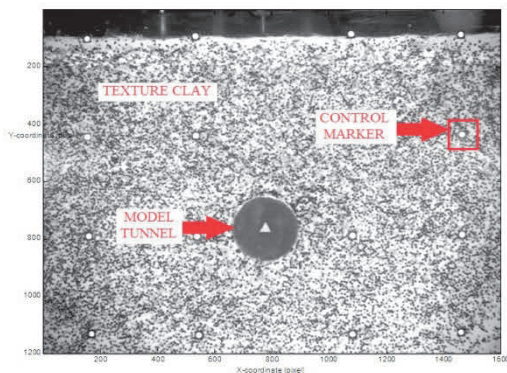


Figure 5. Example of digital images taken during test for PIV analysis

In the present study, the terminology “short-term (ST)” refers to the stage in which tunnel excavation has just been completed, under undrained condition. On the other hand, “Long-term (LT)” refers to the stage when the soil has completed consolidation due to tunnelling. After 720 days, it was observed that changes in the ground movement and pile responses are negligible. Hence the time of 720 days after tunnel excavation is taken as reaching the long-term stage.

Test 1 has been repeated to evaluate the repeatability and consistency of the test. During the tests, the beads were randomly embedded on the surface to produce an artificial texture for the subsequent analysis of PIV. Images captured in days 2, 180, 360, 540 and 720 were analyzed. It is observed that the results are consistent for all tests.

3.1. Cumulative Soil Movements

The cumulative soil displacement vectors and contours at different times after tunnel excavation can be obtained using the PIV technique. Figures 6 shows the cumulative soil movement contours and vectors over time for Test 1 (volume loss of 3%). For ease of comparison, the contour of cumulative soil movement of 10 mm is highlighted as bold dash lines in the plots. The 10 mm movement is selected as the bench mark because the maximum allowable settlement for shallow foundation as specified by the Civil Design Criteria for Road and Rail (LTA, 2010) is 20 mm and 10 mm is often set as the alert level. In the short-term, principal soil movements are concentrated within a zone indicated in Figure 6a. This zone may be identified as the ‘Immediate Shear Zone’ as the soil within this zone has likely been ‘unloaded’ due to tunnel excavation. For clay, the soil does not settle as a rigid body but gradually deforms by arching, causing the radial stress in the immediate shear zone to be reduced due to stress relief. This leads to the observed soil movement pattern and the settlement trough at the ground surface. On the other hand, the zone outside the immediate shear zone may be identified as the ‘Support Zone’, as the circumferential soil stresses increase within this zone to support the arches formed in the immediate shear zone.

Qualitatively, it is expected that volumetric soil strain in the long-term would increase due to soil consolidation. This might cause the soil movements to increase in both the horizontal and vertical directions, as observed in Figures 7. It can be observed from the figures that the shear zone propagates with time and becomes wider over time due to post-tunnelling soil reconsolidation, as shown in Figure 7a to 7d.

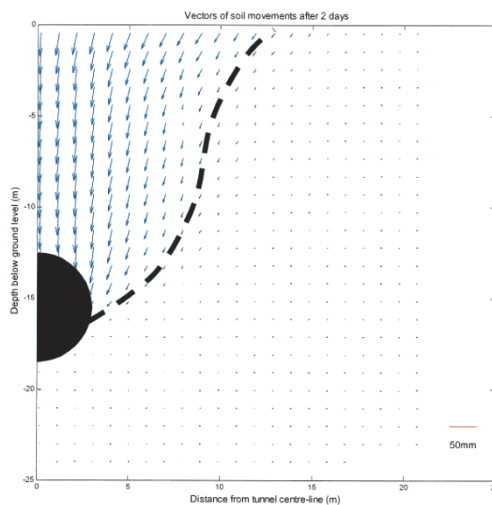


Figure 6a. Cumulative soil movement vectors over time for Test 1, Volume loss=3% (after 2 days)

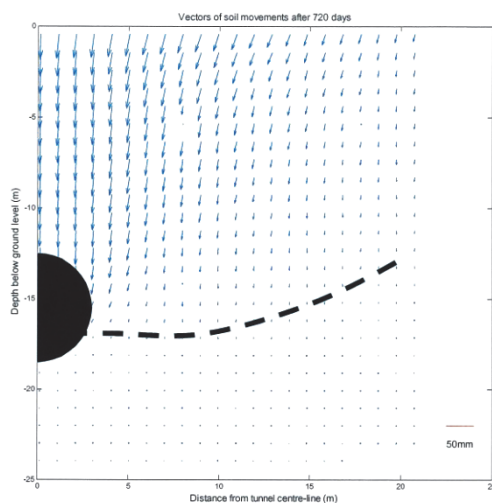


Figure 6b. Cumulative soil movement vectors over time for Test 1, Volume loss=3% (after 720 days)

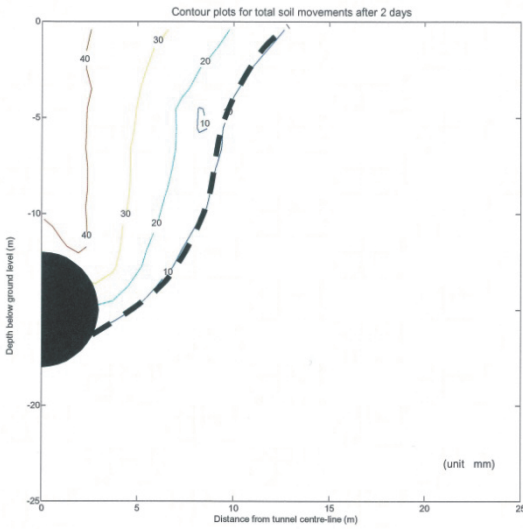


Figure 7a. Contour plots of soil movements after 2 days (Test 1, Volume loss=3%)

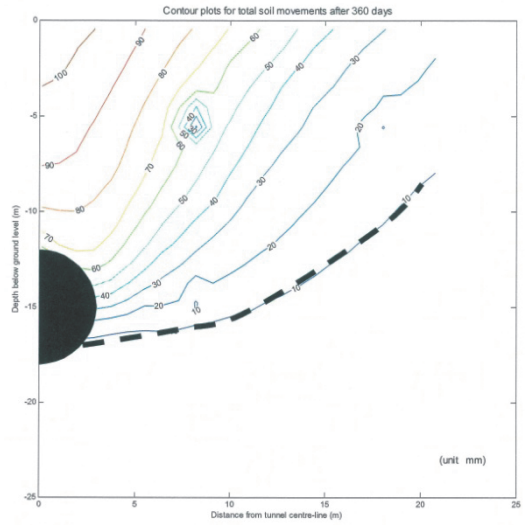


Figure 7c. Contour plots of soil movements after 360 days (Test 1, Volume loss=3%)

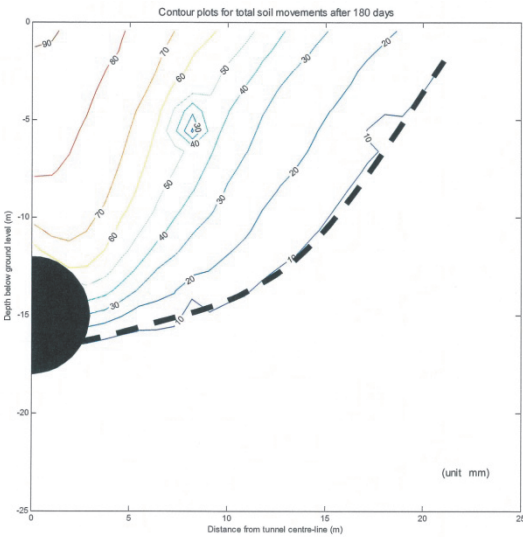


Figure 7b. Contour plots of soil movements after 180 days (Test 1, Volume loss=3%)

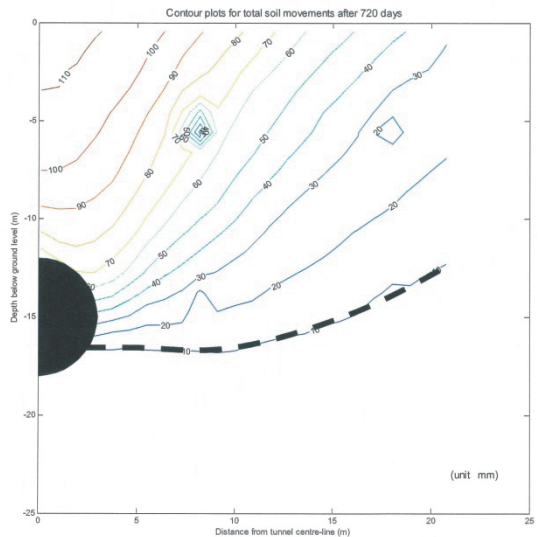


Figure 7d. Contour plots of soil movements after 720 days (Test 1, Volume loss=3%)

3.2. Soil Surface Settlement Troughs

The surface settlement trough along a plane transverse to the tunnel can be described by the Gaussian curve (Peck, 1969). The popularity of the Gaussian curve as a prediction tool for the magnitude of surface settlement due to tunnelling lies in its simplicity and efficiency.

The surface settlement curve, S , is given in Equation (1).

The surface settlement, S , is given by

$$S = S_{\max} \exp\left(-\frac{x^2}{2i^2}\right), \quad (1)$$

where S_{max} is maximum is maximum ground surface settlement at the tunnel vertical centre-line, x is the offset distance from the centre-line, and i is the offset distance of the inflection point from the centre-line.

Figures 8 and 9 show the measured surface settlement troughs over time obtained from PIV and potentiometers with volume loss of 3% and 6.5%, respectively. It is evident that in the short-term (2 days), the surface settlement troughs follow a Gaussian distribution curve with a maximum ground surface settlement of 41 mm for a volume loss of 3% and 92 mm for a volume loss of 6.5%. This corresponds to the respective imposed volume loss with simulated tunnel opening of approximate GAP = 100 and 200 mm. Based on the above findings, there is further evidence that the accuracy of volume control of the model tunnel is good and reliable. As expected, the volume loss at the ground surface is close to the tunnel volume loss under such undrained condition. The point of inflection, i , is determined from the settlement trough at the point when the change of gradient is zero. The point of inflection, i , of the settlement trough is determined to be approximately 7.5 m for both tests. This value is identical to the prediction of 7.5 m by Peck (1969), using a trough width parameter k of 0.5 suggested by Mair et al. (1993) for tunnels in clay. Thus it can be established that the observed settlement trough in the short-term can be reasonably predicted using existing methods.

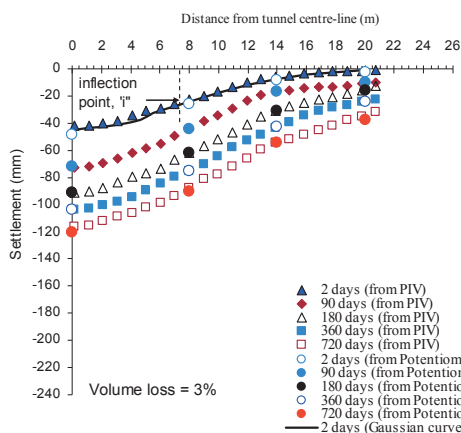


Figure 8. Surface settlement troughs over time (Test 1, Volume loss=3%)

In the long-term, the ground settlement continues to increase with time, as shown in Figures 8 and 9. It should be noted that the soil has practically completed its self-weight consolidation before tunnel excavation. The remaining self-weight consolidation settlement of the soil should be very small. Hence the long-term soil movement is mainly due to stress relief of clay due to tunnel excavation and the settlement trough S are noted to become wider over time. Shirlaw (1993) presented case studies of long-term settlements and reported that the ground settlement due to tunnelling and the extent of settlement trough can increase significantly in the long-term in some cases. In contrast, Gaussian distribution curve is found to be inappropriate for representing the long-term surface settlement trough with a wider parabolic shape. Nevertheless, although the magnitude of maximum long-term ground settlement is larger, the differential settlement for a wider settlement trough is not as significant as that in the short-term.

3.3. Subsurface Vertical Soil Movements

The vertical soil movements can provide clues on the mechanisms associated with tunnel-soil-pile interaction, particularly on the induced pile axial forces and settlements.

Figures 6a indicate that in the short-term (ST, 2 days), the largest vertical soil movements are spotted in the immediate shear zone above

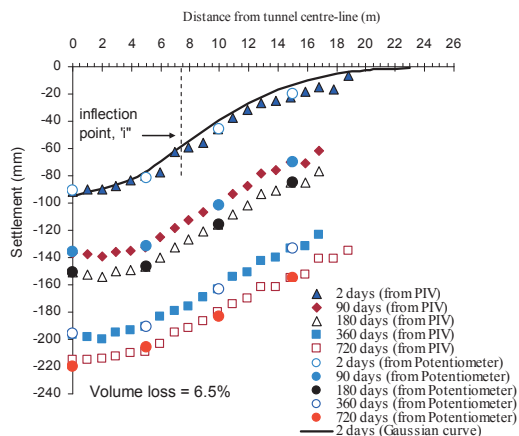


Figure 9. Surface settlement troughs over time (Test 2, Volume loss=6.5%)

the tunnel. However, this zone becomes wider in the LT as shown in the contour plots over time in Figures 7a to 7d. The propagation of vertical soil movement trough seems to be an inverted ‘half-ripple’. This large vertical deformation zone is critical and must be taken into consideration.

Figures 10 and 11 show the ST surface and subsurface settlement troughs for Tests 1 and 2, respectively, in comparison with existing predictive methods proposed by Mair et al. (1993) and Loganathan and Poulos (1998). Mair et al. (1993) proposed that at a depth z below the ground surface, and above a tunnel depth of z_o , the trough width parameter for tunnels constructed in clays are given by Equations (2) and (3).

$$i = K(z_o - z) \quad (2)$$

$$K = \frac{0.175 + 0.325\left(1 - \frac{z}{z_o}\right)}{\left(1 - \frac{z}{z_o}\right)} \quad (3)$$

where i is the trough width parameter for tunnels constructed in clay.

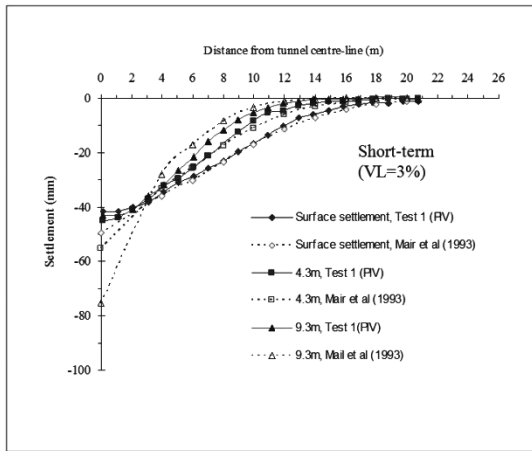
The solution of vertical displacement around a tunnel excavation proposed by Loganathan and Poulos (1998) is given in Equation (4).

$$\varepsilon_{x,z} = \varepsilon_0 \exp\left\{\left[\frac{1.38x^2}{(H + R)^2} + \frac{0.69z^2}{H^2}\right]\right\} \quad (4)$$

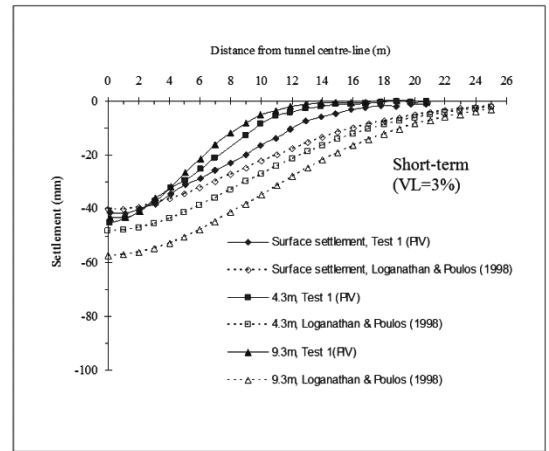
where ε_0 is the ground loss ratio, H is the tunnel depth, z is the depth below ground surface and x is the lateral distance from tunnel centre-line.

It is noted that the method proposed by Mair et al. (1993) yields a better prediction as compared to the method proposed by Loganathan and Poulos (1998). In addition, the influence zone predicted by Loganathan and Poulos (1998) is much greater than the measured data and prediction by Mair et al. (1993). Hence, care should be exercised when employing quasi-analytical methods to predict soil displacements due to tunnelling as certain conditions in the derivation of analytical solutions may not be valid (e.g. volume loss may not be conserved (Loganathan and Poulos, 1998)).

For the subsurface settlement troughs at various depths, the subsurface settlement profiles generally follow the prediction by Mair et al. (1993). It should be noted that the

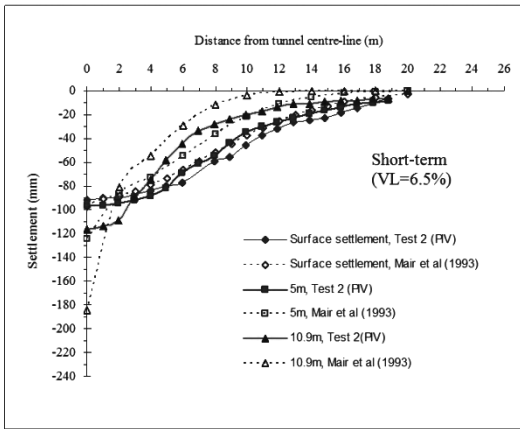


(a)

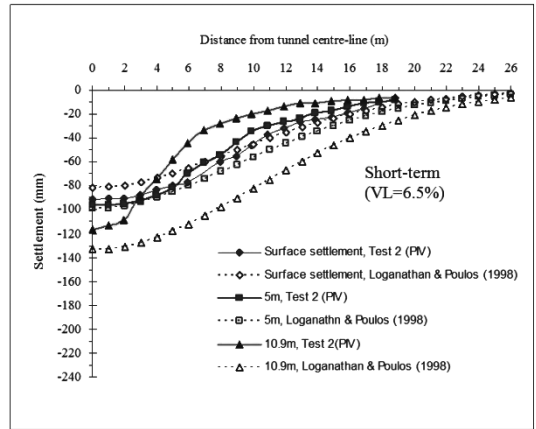


(b)

Figure 10. Settlement troughs at surface, 4.3m and 9.3m depths (Test 1, Volume loss=3%): (a) comparing with Mair et. al (1993) (b) comparing with Loganathan and Poulos (1998)



(a)



(b)

Figure 11. Settlement troughs at surface, 5m and 10.9m depths (Test 2, Volume loss=6.5%): (a) comparing with Mair et. al (1993) (b) comparing with Loganathan and Poulos (1998)

maximum subsurface settlements measured in the experiments, especially when close to the tunnel, may not be accurate. This is mainly due to the over-sizing of the tunnel end cap to prevent water seepage. The over-sized tunnel end cap greatly influenced the tracking of soil displacements which were subsequently analysed by PIV. Despite the above shortcoming, the back analysis generally validates the use of Mair et al.'s (1993) method to predict the subsurface settlements in the short-term.

3.4. Subsurface Horizontal Soil Movements

The short-term and long-term lateral soil movements at various distances from tunnel centre-line are plotted in Figures 11 & 12. The proportion of horizontal to vertical movements at the surface is considerably greater than that at greater depths, especially when the distance from the tunnel centre-line increases. This observation is similar to the finding obtained from the centrifuge model tests conducted by Grant and Taylor (2000).

As expected, the horizontal soil movement caused by tunnelling diminishes with increasing distance away from the tunnel. It is noted that the lateral soil movements form a bulb shape at the tunnel spring line. However, the soil

movements diminish rather rapidly in the horizontal direction and become negligible at distance of approximately 1.5D from the tunnel circumference, i.e 12 m from tunnel centre-line.

The results from the analytical solution proposed by Loganathan and Poulos (1998) are also presented in the figures. However, the predictions by Loganathan and Poulos (1998) do not agree well with the measured data. This may be attributed to the condition that volume loss has not been conserved for undrained cases in their formulation and other factors.

3.5. Qualitative Assessment on Excess Pore Pressure Responses

Pore water pressure changes in the ground are monitored using pore pressure transducers (PPTs) during Test 1. To minimize the effect of reinforcement that the PPTs have on the ground, only 2 PPTs were used, of which one PPT is located within the immediate shear zone and the other one is located outside the zone. Figure 13 shows the schematic location of the PPTs placed in the clay near the tunnel lining and the trend of the pore water pressure changes obtained from the PPTs throughout the test.

For the first 50 minutes of the test, the pore water pressure increases in 10 steps. This is because the acceleration of the centrifuge from 0g to 100g is divided into 10 steps with an interval of 5 minutes per step. Subsequently, the pore water pressure starts to drop and stabilize. This is because the excess pore water pressure induced by the increased acceleration field

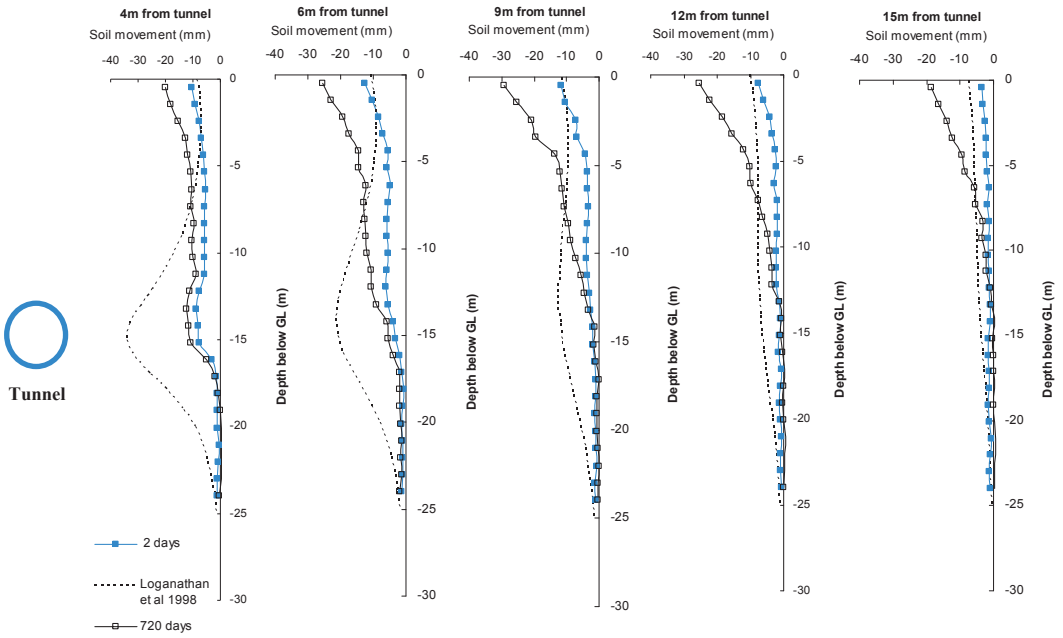


Figure 11. Horizontal soil movements at different distance from tunnel center-line at 2 and 720 days - Test 1, Volume loss=3%

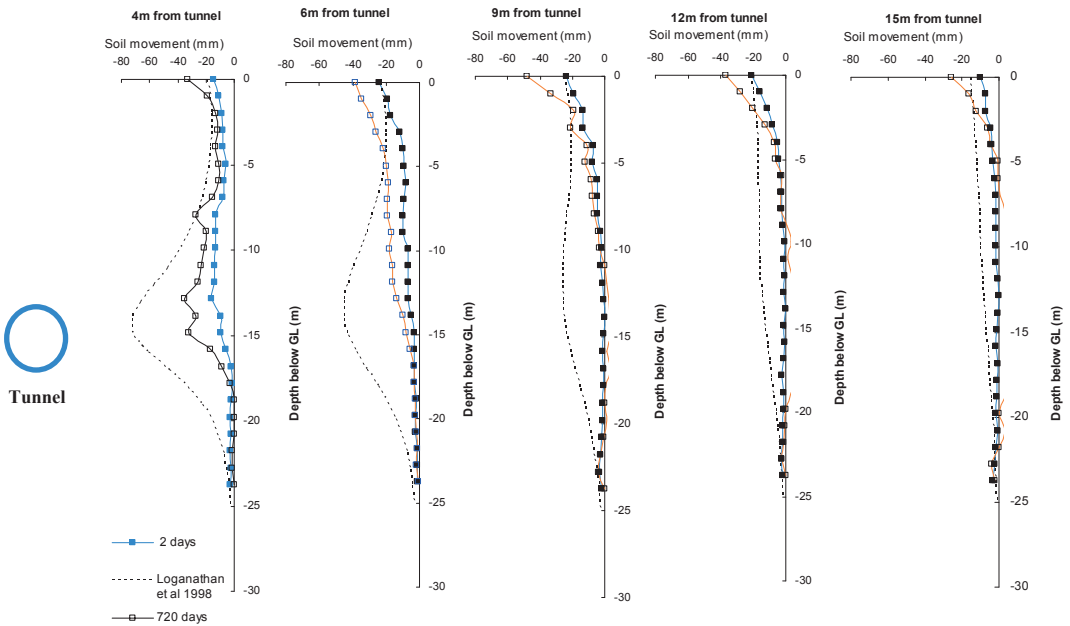


Figure 12. Horizontal soil movements at different distance from tunnel center-line at 2 and 720 days - Test 2, Volume loss=6.5%

dissipates. This process continues until the effective stress in the ground is equivalent to the preconsolidation pressure. At this state, the soil sample is normally consolidated. As PPT1 is at a higher elevation, the initial pore pressure at PPT1 is lower than that at PPT2.

Tunnel excavation causes stress relief on the clay surrounding the tunnel lining and thus a sharp drop in the pore water pressure is observed immediately after the tunnelling process for PPT1 which is located inside the immediate shear zone. Subsequently, the pore water pressure gradually increases over time due to dissipation of pore water pressure. In contrast, an opposite trend is observed for PPT 2 located outside the immediate shear zone. It is observed that additional excess pore pressure is being induced in the clay, as indicated by a sharp increase in pore water pressure immediately after tunnel excavation, caused by the shearing process of the affected soil due to soil arching.

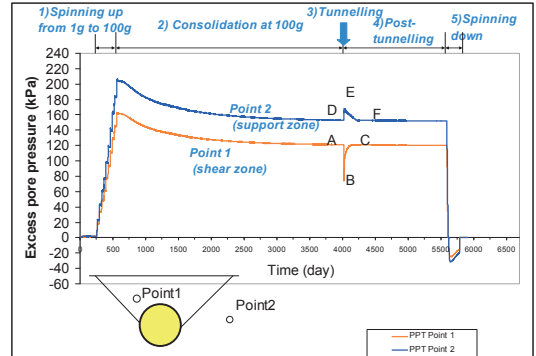
Further observation suggests that the pore water pressure stabilizes about after two and a half hours (720 days in prototype scale) after the tunnel excavation. This observation shows that the excess pore water pressure due to tunnelling has practically fully dissipated and approaches the steady state pore pressure.

The above observation can be explained with an analogy of soil responses due to tunnelling with virtual loading of beam resting on elastic foundation (Winkler spring), as shown in Figure 14a. At the initial stage before tunnel excavation, the virtual loaded beam is supported by the outer plate of the model tunnel placed during 1g, while the rest of the virtual beam is supported by the virtual Winkler spring. During tunnel excavation, the virtual beam moves downward due to contraction of the tunnel in the centrifuge. At this stage, the soil above the tunnel is unloading and inducing excess negative pore pressure, while the soil outside the immediate shear zone is being loaded, as illustrated in Figure 14b. This causes the Winkler spring to be compressed by the virtual loaded beam. Thus, positive excess pore pressure is induced.

The above changes in the pore water pressure regime once again confirm that the behaviour of clay can be time-dependent due to low permeability of the clay sample. The soil will continue to deform with time as a result of

dissipation of excess pore pressures. This observation reiterates the importance of studying the long-term behaviour of tunnelling-induced soil movement and pile responses for tunnels with relatively large volume loss.

Figure 13. Pore pressure changes due to tunnelling



(Test 1)

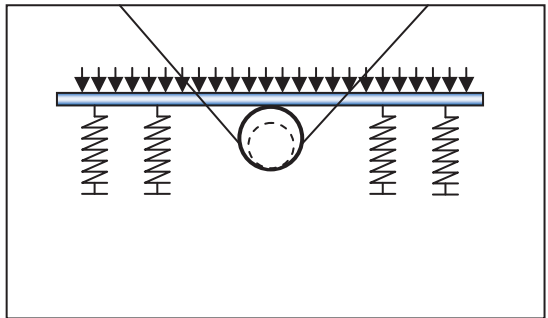


Figure 14a. Analogy of soil responses due to tunnelling with virtual loading of beam resting on foundation before tunnelling

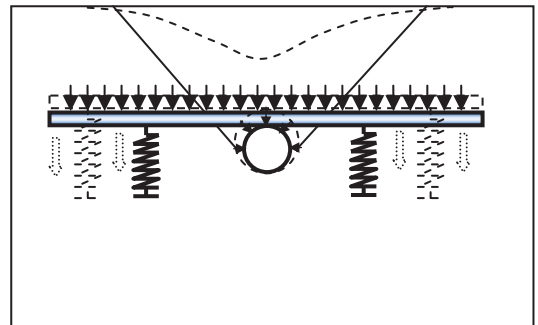


Figure 14b. Analogy of soil responses due to tunnelling with virtual loading of beam resting on foundation after tunnelling

4. CONCLUDING REMARKS

The centrifuge model tests with the application of PIV have provided useful data to examine the patterns of soil movements induced by tunnelling in soft clay. The main aim is to investigate the induced soil movement patterns over time.

The surface settlement trough in clay generally follows the Gaussian distribution curve in the short-term. The magnitude of maximum ground surface settlement increases with time and tunnel volume loss. The settlement magnitude is larger in the long-term and the settlement trough is wider as compared to that in the short-term. The data confirmed that the empirical equation proposed by Mair et al. (1993) is applicable in the prediction of the subsurface settlement troughs in clay in the short-term. On the other hand, an immediate shear zone with large soil movement above the tunnel can be identified in the short-term. In the long term, the significant soil movement zone extends much wider. In addition, soil settlement is noted to be more dominant than lateral soil movement in the long term. Qualitative assessment on the excess pore pressure responses has provided an understanding on the development of negative excess pore pressure in the immediate shear zone and positive excess pore pressure in the support zone.

5. REFERENCES

- Grant, R. J. and Taylor, R. N. 2000. Tunneling-induced ground movements in clay. *Geotechnical Engineering, Proc. Institutions of Civil Engineers*, Vol. 143, No. 1, pp. 43-55.
- Jacobsz, S.W., Standing, J.R. and Mair, R.J. 2004. Tunnelling effects on pile groups in sand. *Proc. Advances in geotechnical engineering: The Skempton Conference, ICE*, Vol 2, 1056-1067.
- Kimura, T. 1998, "Development of Geotechnical centrifuge in Japan", *Proc. Centrifuge 98, Tokyo*, Pre-print volume, pp. 23-32.
- Lake, L. M., Rankin, W. J. and Hawley, J. 1992. Prediction and effects of ground movements caused by tunneling in soft ground beneath urban areas. *CIRIA Project Report 30, Construction Industry Research and Information Association, London*.
- Lee, F. H., Tan, T. S., Leung, C.F., Yong, K.Y., Karunaratne, G. P. and Lee, S. L. 1991. Development of geotechnical centrifuge facility at the National University of Singapore. *Proc., Int. Conf. Centrifuge 91, Boulder, USA*, 11-17
- Lee, K. M., Rowe, R. K. and Lo, K. Y. 1992. Subsidence due to tunneling: Part I – Estimating the gap parameter. *Canadian Geotechnical Journal*, Vol. 29, No. 5, pp. 929-940.
- Loganathan, N. and Poulos, H. G. 1998. Analytical prediction for tunneling-induced ground movements in clays. *Journal of Geotechnical and Geoenvironmental Engineering*, Vol. 124, No. 9, pp. 846-856.
- Loganathan, N., Poulos, H. G. and Stewart, D. P. 2000. Centrifuge model testing of tunneling induced ground and pile deformations. *Geotechnique*, Vol. 50, No. 3, 283-294.
- LTA, 2010. *Civil design criteria for road and rail transit systems revision A1, Rail & Engineering Group, Land Transport Authority, Singapore*
- Mair, R. J., Philips, P., Schofield, A.N. and Taylor, R.N. 1984. Application of centrifuge modeling to the design of tunnels and excavations in soft clay. *Proc.Int.Symposium on application of centrifuge modeling to geotechnical design. Manchester, Craig, W.H.* (edit),pp.356-366.
- Mair, R. J., Taylor, R. N. and Bracegirdle, A. 1993. Subsurface settlement profiles above tunnels in clay. *Geotechnique*, Vol. 43, No. 2, pp. 315-320.
- Ng, C.W.W., Springman, S.M. & Norrish, A.R.M. 1998, "Centrifuge modelling of spread-base integral bridge abutments", *Journal of Geotechnical and Environmental Engineering, ASCE*, Vol. 124, No. 5, pp. 376-388.
- O'Reilly, M. P. and New, B.M. 1982. Settlements above tunnels in the United Kingdom – their magnitude and prediction. *Tunneling 82, London, IMM*, pp 173-181.
- O'Reilly, M. P., Mair, R. J. and Alderman, G. H. 1991. Long-term settlements over tunnels; an eleven year study at Grimsby, *Tunneling 91, London, IMM*, pp. 55-64.
- Osman, A. S., Mair, R. J. & Bolton, M. D. 2006a. On the kinematics of 2D tunnel collapse in undrained clay *Geotechnique* 56, No. 9, 585–595
- Park, K. H. 2005. Analytical solution for tunneling-induced ground movement in clays. *Tunneling and Underground Space Technology* Vol. 20, pp. 249-261.
- Peck, R. B. 1969. Deep excavations and tunneling in soft ground. *Proc. 7th International Conference*

Soil Mechanics and Foundation Engineering, Mexico City, State of the Art Volume, pp. 225-290.

- Ran, X. 2004. Tunnel pile interaction in clay. *M Eng thesis, National University of Singapore*.
- Sagaseta, C. 1987. Analysis of undrained soil deformation due to ground loss. *Geotechnique*, Vol. 37, No. 3, pp. 301-320.
- Schmidt, B. 1969. Settlements and ground movements associated with tunnelling in soil. *PhD thesis, University of Illinois*.
- Schofield, A.N. 1998, "Geotechnical centrifuge development can correct a soil mechanic error", *Proc. Centrifuge 98, Tokyo, Preprint volume*, pp. 1-8.
- Shirlaw, J. N. 1993 Pore pressures around tunnels in clay: Discussion. *Canadian Geotechnical Journal*. Vol. 30, pp. 1044-1046.
- Taylor, R. N. 1998. Modelling of tunnel behaviour. *Proc. Institutions of Civil Engineers*, Vol. 131, pp. 127-132.
- Verrujit, A. and Booker, J. R. 1996. Surface settlements due to deformation of a tunnel in an elastic half plane. *Geotechnique*, Vol. 46, No. 4, pp. 753-756.
- White, D.J., Take, W.A. & Bolton, M.D. 2003. Soil deformation measurement using particle image velocimetry (PIV) and photogrammetry. *Geotechnique*, Vol. 53, No. 7, 619-631.
- Zhang DM, Huang HW Hicher PY 2004 Numerical Prediction of Long-term settlements over Tunnels in Clay, *ITA 2004*
- Zhang, Y.D., Tan, T.S. & Leung, C.F. 2005. Application of particle imaging velocimetry (PIV) in centrifuge testing of uniform clay. *International Journal of Physical Modelling in Geotechnics*, 15-26.

Inclined Reinforcement-Backfill Interactions to Transverse Pull

Pavan Kumar

Osmania University, Hyderabad, India

Madhav Madhira

Center for Geoenvironmental Engg, J.N.T.U College of Engineering, Hyderabad, India,

madhavmr@gmail.com

ABSTRACT: Geosynthetic materials reinforce the retaining walls, steep slopes and embankments are commonly aligned horizontal relative to the sliding surface. Inclined reinforcement in the form of grouted nails is widely used for repair and strengthening of tunnels, deep cuts, existing slopes etc. Most of the available methods of analysis and design of reinforced earth structures consider the axial resistance of reinforcement. However, the kinematics of failure of reinforced earth structure clearly demonstrates that the reinforcement is subjected oblique pull. The paper presents response of inclined geosynthetic reinforcement subjected to normal force/displacement at shallow end. Assuming a simple Winkler type response for the ground and the reinforcement to be inextensible, a relation is established between the pullout resistance and normal displacement applied at shallow end. The response of reinforcement depends on interface shear characteristics and deformational response of ground. A parametric study is carried out to study the significance of inclination of reinforcement, depth of embedment, length and interface shear characteristics reinforcement and stiffness of ground. The influence of oblique pull on inclined reinforcement is demonstrated by quantifying the factor of safety against pullout in case of reinforced earth wall. The analysis infers that the inclined reinforcement mobilizes higher pullout resistance compared to horizontal reinforcement.

1. INTRODUCTION

Earth reinforcement in the form of strips, bars, grids or sheets fabricated or manufactured from metal or geosynthetics are widely used to reinforce the geotechnical structures such as retaining earth walls, slopes, embankments and foundation soils etc. In these structures reinforcement is commonly aligned horizontal and use of inclined geosynthetic reinforcement is limited due to construction difficulties. Instead inclined reinforcement in the form of grouted nails is driven to support tunnels and to stabilize existing slopes or excavations where the construction proceeds from top to bottom. The present paper illustrates use of inclined reinforcement in reinforced earth wall and its interaction with granular backfill.

Most of the procedures for the design of geosynthetic reinforced earth walls (Claybourn and Wu 1993) are based on limit state analysis; i.e the reinforced earth structure is assumed to be on the verge of failure and, subsequently, the strength and layout of the geosynthetic is determined. These limit equilibrium analysis compare the horizontal forces due to lateral earth pressures tending to cause instability to the stabilizing tensile force in reinforcement

along an assumed failure surface. The stabilizing tensile force is limited by its own tensile strength and bond resistance developed behind a potential failure surface. The axial pullout tests or direct shear tests are carried out to determine the bond resistance (Jewell, 1996; Alfaro et al. 1995; Farrag et al. 1993; Hayashi et al. 1994; Juran et al. 1988; Lopes and Ladeira 1996; Ochiai et al. 1996; Sobhi and Wu 1996).

The inclination of reinforcement and orientation of reinforcement force is one of the factors that influence the design of reinforced earth wall. The kinematics of failure (Fig. 1) is usually such that the failure surface intersects the reinforcement obliquely and reinforcement is subjected to both axial and transverse components of force by the sliding mass of soil. Most of the available theories for analysis and design of reinforced soil structures consider only axial resistance to pullout (Flower, 1982; Jewell, 1992) and not the transverse one. The inclination of reinforcement is considered to vary between the direction of reinforcement and tangent to the slip surface (Gray and Ohashi 1983, Leschinsky and Reinschmidt 1985, Degencamp and Dutta 1989, Shewbridge and Sitar 1989, Leschinsky and Boedeker 1989, Athanasapoulous 1993, Burd 1995, Bergado et al. 2000).

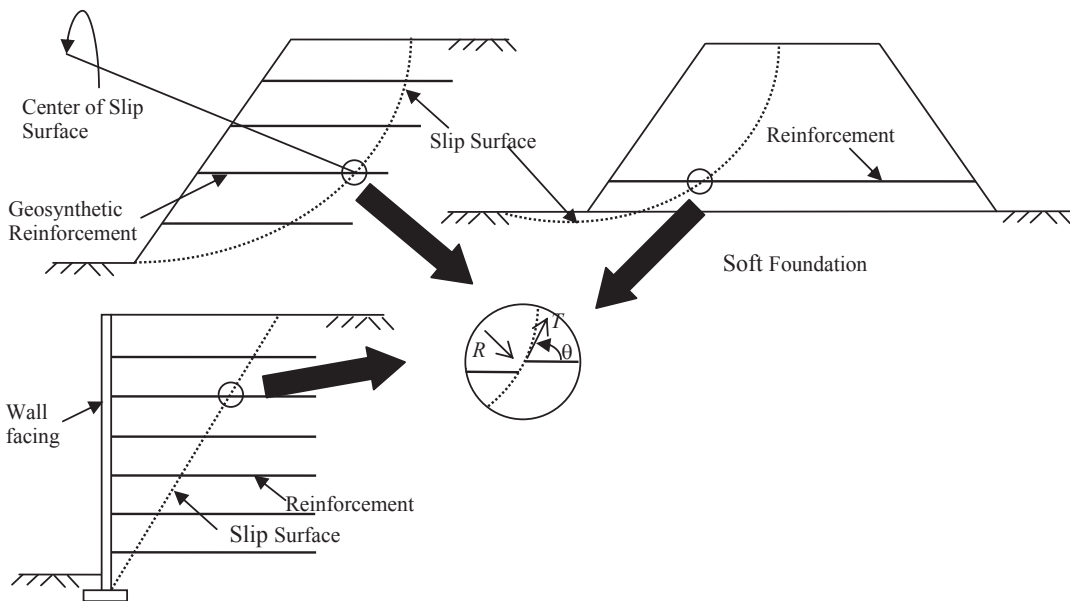


Fig. 1 Kinematics of reinforced slopes, embankments and retaining walls

The transverse pull/displacement at one of the extremes of reinforcement mobilizes additional normal stresses on the reinforcement as the reinforcement deforms transversely. The response to transverse force/pull is evaluated for linear and nonlinear subgrade response (Madhav and Umashankar, 2003), full and non linear shear mobilization along the interface. The formulation is applicable only for small deformations i.e. transverse displacements up to 1% of the length of the reinforcement. The analysis is extended to large displacements up to 10% length of reinforcement by Madhav and Manoj (2004). The improvement in the factor of safety against pullout of reinforcement varied from 1.19 to 1.27 by considering the influence of transverse pull in reinforced earth wall (Madhav and Kumar, 2007).

2. PROBLEM DEFINITION AND ANALYSIS

The inextensible sheet reinforcement inclined at an angle α with horizontal having length L is acted upon by a normal force P or a normal displacement, w_L at the shallow end (Fig. 2a). The interface angle of shearing resistance between the reinforcement and soil is ϕ_r . The

response of the reinforcement to the normal force is to be obtained in terms of a relation between the force, P , and the normal displacement, w_L at shallow end. The model proposed for the analysis is shown in Fig. 2b. The reinforcement and the underlying soil responses are represented, respectively, by a rough membrane and a set of Winkler springs. The sheet reinforcement is subjected to varying overburden stress of intensity γz_1 at shallow end and γz_2 at deeper end respectively. A'B' represents the deformed profile of the reinforcement; σ_t and σ_b , τ_t and τ_b are the normal and shear stresses acting on the top and bottom surfaces of reinforcement respectively. The equilibrium of forces is considered on an infinitesimal length of Δx and unit width located at a distance x from deeper end of reinforcement, B (Fig. 2d).

The reinforcement is considered as inextensible i.e. sheet reinforcements made of geogrids are considered to be inextensible. The linear normal stress – displacement relation of backfill soil is characterized by the relation

$$q = k_s w \quad (1)$$

where k_s is the modulus of subgrade reaction (Terzaghi, 1955) and w is the normal displacement. Full shear resistance (rigid plastic behaviour) is assumed to be developed along the

interface irrespective of its horizontal displacement (i.e. $\tau_t = q_t \tan \phi_r$, $\tau_b = q_b \tan \phi_r$) as in several axial pull-out studies (Jewell et al.,

1984). The inclination of reinforcement mobilizes an additional shear resistance obtained from following equations

Fig. 2a Reinforcement subjected to normal force at shallow end

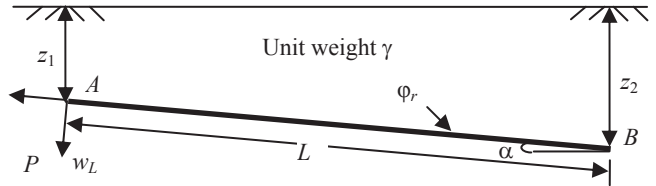


Fig. 2b Model for analysis

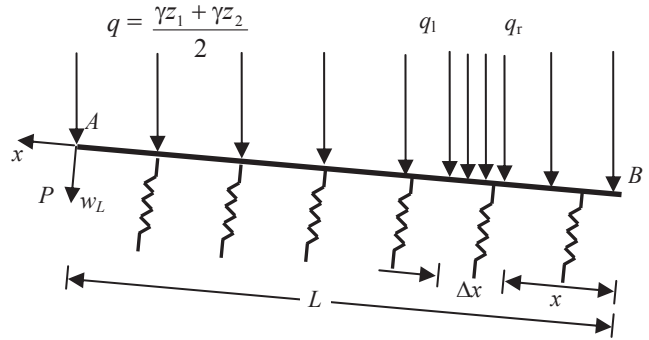


Fig. 2c Deformed Profile of reinforcement

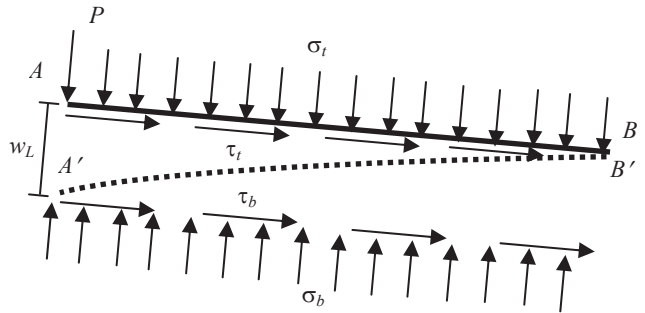
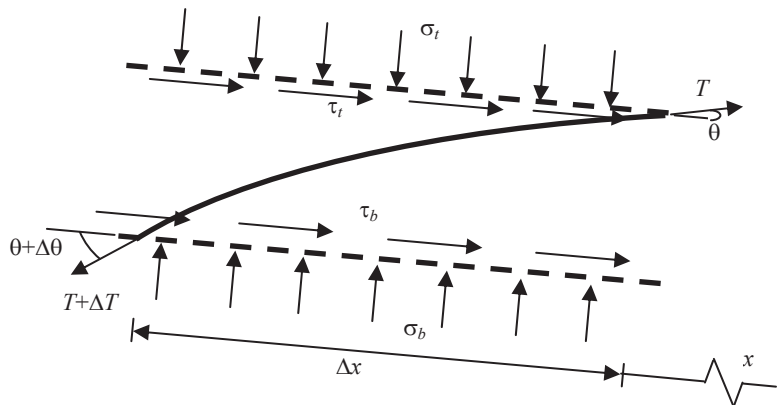


Fig. 2d Forces on an element



The gravity stresses acting at right and left end of infinitesimal length Δx (Fig. 2b) are respectively

$$q_r = \gamma(z_2 - x \sin \alpha) \quad (2)$$

$$q_l = \gamma(z_2 - (x + \Delta x) \sin \alpha) \cong \gamma(z_2 - x \sin \alpha) \quad (3)$$

(since Δx is small)

The normal stress acting on the top and bottom surface of reinforcement are respectively

$$\sigma_t = \gamma(z_2 - x \sin \alpha) \cos \alpha \quad (4)$$

$$\sigma_b = \gamma(z_2 - x \sin \alpha) \cos \alpha + k_s w \quad (5)$$

The shear stress acting on the top and bottom surface of reinforcement are respectively obtained from following equations

$$\tau_t = \sigma_t \tan \varphi_r + \gamma(z_2 - x \sin \alpha) \sin \alpha \quad (6)$$

$$\tau_b = \sigma_b \tan \varphi_r + \gamma(z_2 - x \sin \alpha) \sin \alpha \quad (7)$$

Substituting the normal stresses in the above equations

$$\tau_t = \gamma(z_2 - x \sin \alpha) \cos \alpha \tan \varphi_r + \gamma(z_2 - x \sin \alpha) \sin \alpha \quad (8)$$

$$\tau_b = \gamma(z_2 - x \sin \alpha) \cos \alpha \tan \varphi_r + k_s w \tan \varphi_r + \gamma(z_2 - x \sin \alpha) \sin \alpha \quad (9)$$

The equilibrium of forces along tangential and normal to the reinforcement are respectively

$$\frac{dT}{dx} = [k_s w + 2\gamma(z_2 - x \sin \alpha) \cos \alpha] \tan \varphi_r \cos \theta + [2\gamma(z_2 - x \sin \alpha) \sin \alpha] \cos \theta + k_s w \sin \theta \quad (16)$$

$$T \cos^2 \theta \frac{d^2 w}{dx^2} = k_s w \cos \theta - [k_s w + 2\gamma(z_2 - x \sin \alpha) \cos \alpha] \tan \varphi_r \sin \theta - [2\gamma(z_2 - x \sin \alpha) \sin \alpha] \sin \theta \quad (17)$$

The original problem is to derive the response of the reinforcement in terms of w and T for a given applied transverse force, P . However, it was found simpler to obtain the force, P , for a given free end displacement, w_L . The boundary conditions are: at $x = 0$ (at point B in Fig. 2a), the slope, dw/dx , and tension in the reinforcement, T , are zero, and at $x = L$ (at point A in Fig. 2a), the displacement $w = w_L$.

The normal force, P , required to cause the displacement, w_L , is obtained by integrating the soil reaction mobilized as

$$(T + \Delta T) \cos(\theta + \Delta \theta) - T \cos \theta - (\tau_t + \tau_b) \Delta x = 0 \quad (10)$$

and

$$(T + \Delta T) \sin(\theta + \Delta \theta) - T \sin \theta + (\sigma_t - \sigma_b) \Delta x = 0 \quad (11)$$

Equation (10) and (11) on simplification reduce to

$$-T \sin \theta \frac{d\theta}{dx} + \frac{dT}{dx} \cos \theta - (\tau_t + \tau_b) = 0 \quad (12)$$

$$T \cos \theta \frac{d\theta}{dx} + \frac{dT}{dx} \sin \theta + (\sigma_t - \sigma_b) = 0 \quad (13)$$

Multiplying Eq. (12) with $\cos \theta$ and Eq. (13) with $\sin \theta$ and adding the two, one gets

$$\frac{dT}{dx} - (\tau_t + \tau_b) \cos \theta + (\sigma_t - \sigma_b) \sin \theta = 0 \quad (14)$$

Similarly, multiplying Eq. (12) by $\sin \theta$ and Eq. (13) by $\cos \theta$ and subtracting the former from the latter, one gets

$$-T \frac{d\theta}{dx} - (\tau_t + \tau_b) \sin \theta - (\sigma_t - \sigma_b) \cos \theta = 0 \quad (15)$$

$$\text{But } \tan \theta = \frac{dw}{dx} \text{ and } \frac{d\theta}{dx} = \cos^2 \theta \frac{d^2 w}{dx^2} \text{ and}$$

the Winkler spring response to the increase in normal stress, $\sigma_b - \sigma_t = k_s w$

Substituting normal and shear stresses in Eq. (14) and Eq. (15), the coupled governing equations for the reinforcement subjected to normal force are

$$P = \int_0^L k_s w dx \quad (18)$$

Non-dimensionalising Eq. (16), (17) and (18) with $X = x/L$, $W = w/w_L$, $T^* = T/T_{\max}$ where

$$T_{\max} = 2\gamma \frac{(z_1 + z_2)}{2} L \tan \varphi_r \cos \alpha, \text{ the pullout}$$

capacity of inclined reinforcement and

$$P^* = \frac{P}{\gamma \left(\frac{z_1 + z_2}{2} \right) L}, \text{ one gets}$$

$$\frac{dT^*}{dX} = \frac{1}{2} \mu \frac{w_L}{L} W \left[\cos \theta + \frac{\sin \theta}{\tan \varphi_r} \right] + \frac{\frac{z_2}{L} - X \sin \alpha}{\frac{z_2}{L} - \left(\frac{\sin \alpha}{2} \right)} \left[\cos \theta + \frac{\tan \alpha \cos \theta}{\tan \varphi_r} \right] \quad (19)$$

$$T^* \cos^2 \theta \frac{d^2 W}{dX^2} = \frac{1}{2} \mu W \left[\frac{\cos \theta}{\tan \varphi_r} - \sin \theta \right] - \frac{\frac{z_2}{L} - X \sin \alpha}{\frac{z_2}{L} - \left(\frac{\sin \alpha}{2} \right)} \left[\frac{\sin \theta}{w_L / L} - \frac{\tan \alpha \sin \theta}{\tan \varphi_r (w_L / L)} \right] \quad (20)$$

$$P^* = \mu W_L \int_0^1 W dX \quad (21)$$

where $\mu = \frac{k_s L}{\gamma \left(\frac{z_1 + z_2}{2} \right) \cos \alpha}$, relative backfill stiffness factor and $W_L = w_L / L$

The boundary conditions in non-dimensional form becomes: at $X = 0$, $T^* = 0$ and $dW/dX = 0$ and at $X = 1$, $W = 1.0$. As the coupled equations cannot be solved analytically, a finite difference approach is adopted.

$$\frac{T^*_{i+1} - T^*_i}{\Delta X} = \frac{1}{2} \mu \frac{w_L}{L} W_i \left[\cos \theta_i + \frac{\sin \theta_i}{\tan \varphi_r} \right] + \frac{\frac{z_2}{L} - X \sin \alpha}{\frac{z_2}{L} - \left(\frac{\sin \alpha}{2} \right)} \left[\cos \theta_i + \frac{\tan \alpha \cos \theta_i}{\tan \varphi_r} \right] \quad (22)$$

$$T^*_i \cos^2 \theta_i \left(\frac{W_{i-1} - 2W_i + W_{i+1}}{\Delta X^2} \right) = \frac{\mu}{2} W_i \left(\frac{\cos \theta_i}{\tan \varphi_r} - \sin \theta_i \right) - \frac{\frac{z_2}{L} - X \sin \alpha}{\frac{z_2}{L} - \left(\frac{\sin \alpha}{2} \right)} \left[\frac{\sin \theta_i}{w_L / L} - \frac{\tan \alpha \sin \theta_i}{\tan \varphi_r (w_L / L)} \right] \quad (23)$$

$$P^* = \mu W_L \frac{1}{n} \left[\frac{W_1 + 1}{2} + \sum_{i=2}^n W_i \right] \quad (24)$$

where $\Delta X = 1/n$ and n the number of sub-elements in to which the reinforcement strip is divided into, W_i and T^*_i are, respectively, the normalized displacement and normalized tension at node 'i'. Solving for normalized displacement and normalized tension, one gets

$$T^*_{i+1} = \frac{\mu}{2n} \frac{w_L}{L} W_i \left[\cos \theta_i + \frac{\sin \theta_i}{\tan \varphi_r} \right] + \frac{\frac{z_2}{L} - X \sin \alpha}{\frac{z_2}{L} - \left(\frac{\sin \alpha}{2} \right)} \frac{1}{n} \left[\cos \theta_i + \frac{\tan \alpha \cos \theta_i}{\tan \varphi_r} \right] + T^*_i \quad (25)$$

$$W_i = \frac{T^*_i n^2 \cos^2 \theta (W_{i-1} + W_{i+1}) + \frac{\frac{z_2}{L} - X \sin \alpha}{\frac{z_2}{L} - \frac{\sin \alpha}{2}} \left(\frac{\sin \theta_i + \frac{\tan \alpha \sin \theta_i}{\tan \varphi_r}}{w_L / L} \right)}{2T^*_i n^2 \cos^2 \theta_i + \frac{\mu}{2} \left[\frac{\cos \theta_i}{\tan \varphi_r} - \sin \theta_i \right]} \quad (26)$$

Arbitrary initial values are assigned for normalized displacements and tensions (W_{iold} and T_{iold}) at each node. Eqs. (24) and (25) are then solved along with the boundary conditions to obtain the new normalized displacements and tensions (W_{inew} and T_{inew}). The convergence for displacement and tension at each node is checked using the criterion $\varepsilon_W \leq 10^{-6}$ and $\varepsilon_T \leq 10^{-6}$ where

$$\varepsilon_W = \left| \frac{W_{inew} - W_{iold}}{W_{inew}} \right| \text{ and } \varepsilon_T = \left| \frac{T_{inew} - T_{iold}}{T_{inew}} \right|$$

If the convergence criterion is not satisfied, the values of W_{inew} and T_{inew} become W_{iold} and T_{iold} for the next iteration and this procedure is repeated until both the convergence criteria are satisfied.

The simultaneous equations 25 & 26 are solved till the following conditions are satisfied

$$\left| \frac{W_{new} - W_{old}}{W_{new}} \right| \leq 10^{-6} \quad \left| \frac{T_{new} - T_{old}}{T_{new}} \right| \leq 10^{-6}$$

3. RESULTS AND DISCUSSION

A parametric study is carried out for quantifying normalized displacement, $W^*(=w/L)$, normalized tension, T^* , normalized normal force, P^* , normalized maximum tension at shallow end, T^*_{max} , slope or inclination of reinforcement at shallow end, θ_L in terms of μ , φ_r , w_L and α . Parametric studies have been carried out for $\alpha = 0^\circ - 20^\circ$; $w_L/L = 0.001 - 0.1$; $z_1 = 1 - 10$ m; $L = 2 - 8$ m; $\varphi_r = 20^\circ$ to 30° and $\gamma = 15 - 20$ kN/m³. The values of coefficient of subgrade reaction, ks, considered (Scott 1981) are shown in Table 1. For the above ranges of parameters, the relative subgrade stiffness factor, μ ranges between 50 and 100,000.

Displacement and Tension Profiles – Effect of μ

The variation of normalized displacement profiles, W^* , with normalized distance, X , for $\mu = 50, 200, 500, 1000$ and $10,000$ and for a typical value of inclination of reinforcement, $\alpha = 10^\circ$, interface friction angle, $\varphi_r = 30^\circ$ and shallow end displacement, $W_L = 0.01$ are presented in Fig. 3. The normalized displacements are negligibly small for $X \leq 0.9$ and

increase sharply beyond $X > 0.9$, indicating, the localized deformation of reinforcement for stiff backfills ($\mu = 10,000$). Where as for softer backfill ($\mu = 50$) the normalized displacement, W^* increases beyond $X > 0.3$ and the profile extend over a larger area to reach further end. The displacement profiles for horizontal reinforcement and for an inclined reinforcement with $\alpha = 20^\circ$ are compared (Fig. 4) for a given backfill stiffness factor, $\mu = 1000$, normalized shallow end displacement, $W_L = 0.01$ and interface friction angle, $\varphi_r = 30^\circ$. The two curves nearly coincide with an exception that the normalized displacements, W^* for an inclined and horizontal reinforcement are initiated at $X = 0.75$ and 0.85 respectively. This marginal increase in the spread of normalized displacement curve is observed to improve with increase in inclination of reinforcement.

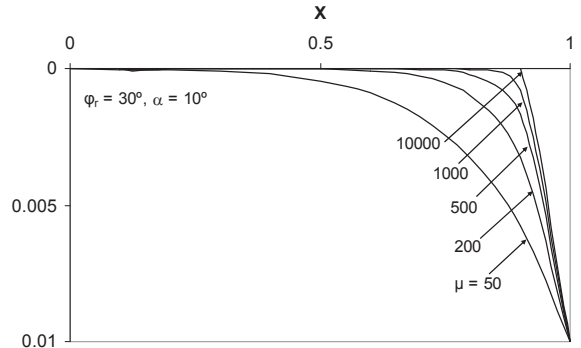


Fig. 3 Effect of μ on displacement profiles

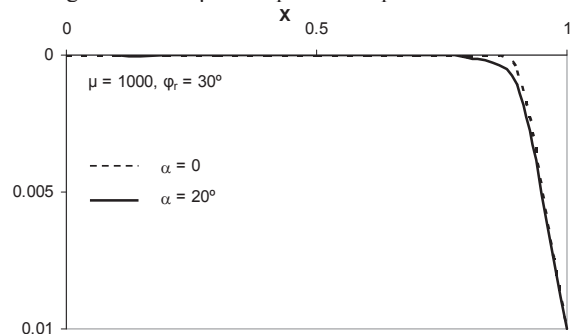


Fig. 4 Effect of α on displacement profiles

Tension in the reinforcement increases almost linearly with distance over the stretch of reinforcement that does not deform transversely as in the axial pullout case (Fig. 5). The increase in stiffness of backfill, μ beyond 1000 results in localized displacement of reinforcement at

shallow end (Fig. 4), tension increases sharply only in that part of the reinforcement length i.e. due to large normal stresses acting on the reinforcement. Thus tension increases sharply for $0.9 < X < 1.0$ and reaches a maximum value of 2.32 for $\mu = 10,000$, whereas it varies almost linearly and reaches a maximum value of 1.35 for $\mu = 50$, $W_L = 0.01$ and $\phi_r = 30^\circ$. Similar variation of tension profile is observed for horizontal and inclined reinforcement for a given backfill stiffness factor, $\mu = 1000$, normalized displacement, $W_L = 0.01$ and interface friction angle, $\phi_r = 30^\circ$. The increase in inclination of reinforcement, α from 0 to 20° increases the normal stresses acting on the reinforcement thus improving the maximum tension (at $X = 1$) from 1.21 to 1.89 (Fig. 6).

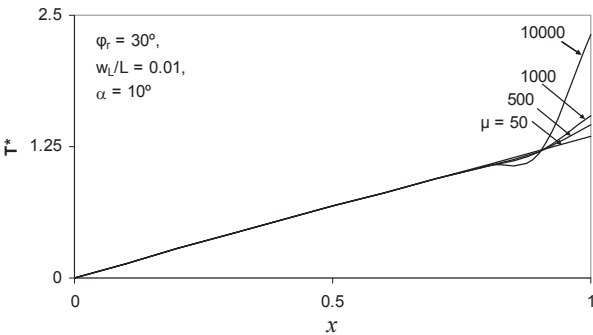


Fig. 5 Effect of μ on tension profiles

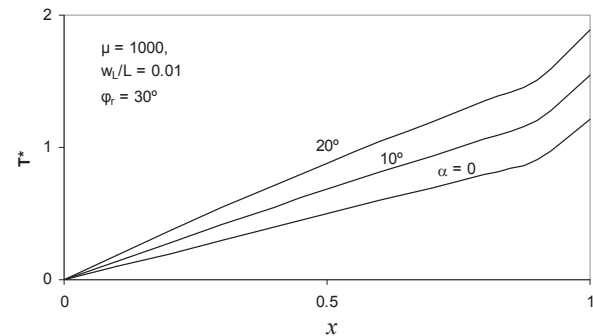


Fig. 6 Effect of α on tension profiles

Variations of P^* , T^*_{max} , and θ_L with μ – Effect of α

Large normal stresses and hence large shear resistances are developed at the reinforcement – soil interface with increase in inclination of reinforcement and/or increase in relative stiffness of backfill. Thus the normal force, P^* , required to cause a given shallow end displace-

ment increases with μ . For softer backfills ($\mu \leq 50$), the influence of inclination of reinforcement is insignificant on the normal force and P^* remains constant at 0.1 (Fig. 7). The influence of inclination of reinforcement on the mobilized normal force is clearly depicted for backfills with relative stiffness factor, $\mu > 1000$. The normal force P^* increased from 1.27 to 1.57 with increase in inclination of reinforcement from $\alpha = 0^\circ$ to 20° for $\mu = 10,000$.

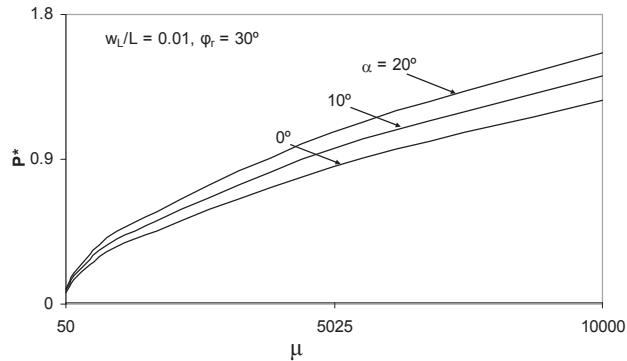


Fig. 7 Normalized normal force versus μ

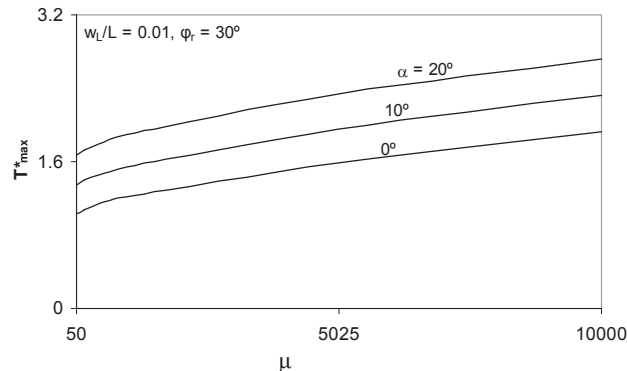


Fig. 8 Normalized maximum tension versus μ

The maximum tension, T^*_{max} developed in the reinforcement also increases with increase in stiffness of backfill, μ similar to the normal force, P^* (Fig. 8). The improvement of T^*_{max} with increase in inclination of reinforcement, α is uniform irrespective of μ . The maximum tension, T^*_{max} in horizontal reinforcement improved from 1.04 to 1.92 with increase in relative stiffness of backfill, μ from 50 to 10,000; whereas in case of an inclined reinforcement with $\alpha = 20^\circ$ the maximum tension developed in reinforcement increased from 1.68 to 2.72. The trends of variation of slope of

reinforcement at shallow end, θ_L with μ and α are similar to the variation of normal force, P^* (Fig. 9).

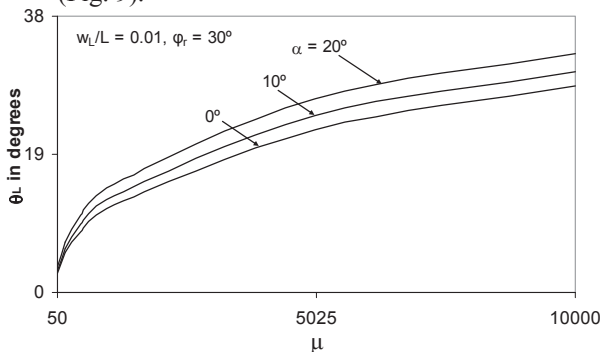


Fig. 9 Inclination of reinforcement at shallow end versus μ

Variations of P^* , T^*_{max} , and θ_L with W_L – Effect of α

The variation of normalized normal force, P^* with normalized shallow end displacement, W_L is presented in Fig. 10 for different inclinations of reinforcement, α relative stiffness factor, $\mu = 1000$ and interface friction angle, $\phi_r = 30^\circ$. The curves are concave upward indicating larger normal forces are required to mobilize larger displacements. For low values of normalized displacement ($W_L \leq 0.01$), the influence of inclination of reinforcement is insignificant on the normal force and P^* remains constant at 0.45. Further increase in W_L beyond 0.01 improved P^* marginally with increase inclination of reinforcement, α from 0° to 20° . The normal force, P^* increased from 5.46 to 6.39 with increase in inclination of reinforcement from $\alpha = 0^\circ$ to 20° for $W_L = 0.1$.

Similar to the variation with relative subgrade stiffness factor the improvement of T^*_{max} with increase in inclination of reinforcement, α is uniform irrespective of W_L (Fig. 11). The maximum tension, T^*_{max} in horizontal reinforcement improved from 1.02 to 5.97 with increase in normalized displacement at shallow end, W_L from 0.001 to 0.1; whereas in case of an inclined reinforcement with $\alpha = 20^\circ$ the maximum tension developed in reinforcement increased from 1.65 to 7.29.

The slope of reinforcement at shallow end, θ_L increased sharply with normalized displacement, W_L and the influence of inclination of

reinforcement, α is marginal (Fig 12). At a low value of normalized shallow end displacement of 0.001, the change in orientation of reinforcement is small and slope at shallow end is limited to 1.26 irrespective of initial inclination of reinforcement. In case of large displacements of order 0.1, the reinforcement undergoes a localized deformation based on stiffness of backfill and θ_L increases from 49° to 52° for horizontal and inclined reinforcement with $\alpha = 20^\circ$ respectively.

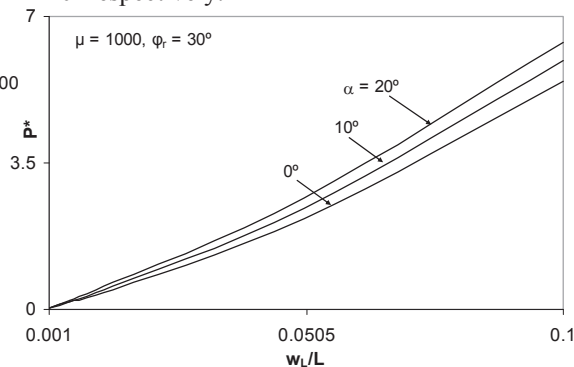


Fig. 10 Normalized normal force versus w_L/L

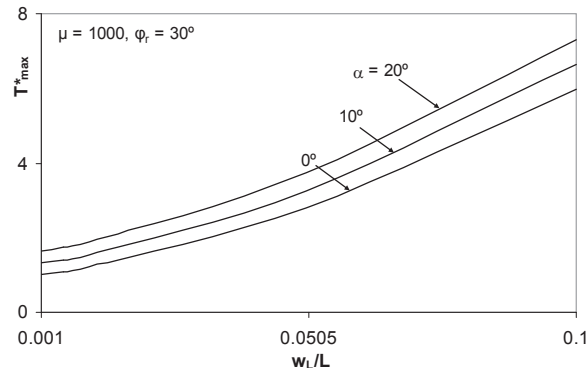


Fig. 11 Normalized maximum tension versus w_L/L

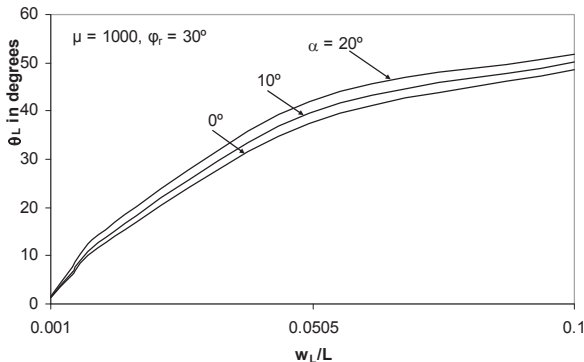


Fig. 12 Inclination of reinforcement at shallow end versus w_L/L

Variation of P^* with ϕ_r – Effect of α

The normal force, P^* , required to cause a given shallow end displacement, $W_L = 0.01$ increases linearly with interface friction angle (Fig. 13). The rate of increase of P^* with ϕ_r marginally decreased with increase in inclination of reinforcement. For an interface friction angle, $\phi_r = 30^\circ$ the mobilized normal force increased from 0.36 to 0.45 with increase of α from 0° to 20° .

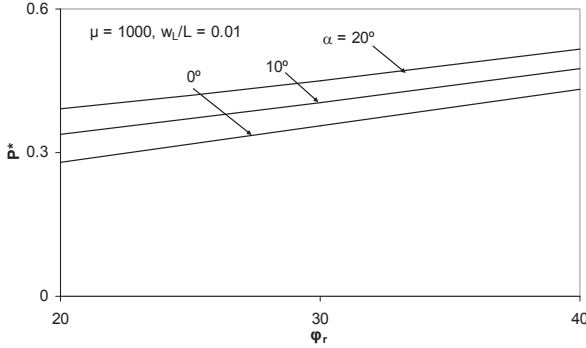


Fig. 13 Normalized normal force versus ϕ_r

4. APPLICATION OF OBLIQUE PULL IN REINFORCED SOIL WALL

In the present section the stability of reinforced earth wall subjected to oblique pull is considered and a comparison between factors of safety against pullout of horizontally aligned reinforcement with inclined reinforcement is demonstrated. A reinforced soil wall (Fig. 14) of height ' H ' is considered of ' n ' number of reinforcement layers. The friction angle of backfill is ' ϕ ', reinforcement soil interface friction angle is ' ϕ_r ', and unit weight of fill is ' γ '. The reinforced fill is divided into active and resistant zone by coulomb failure surface making an angle $[45 + \phi/2]$ with horizontal. The reinforcement is inclined at angle ' α ' with horizontal and arranged at a uniform spacing of $S_v = H/n$ within the backfill.

The depth of horizontal/inclined reinforcement from top of wall

$$z_i = \left(i - \frac{1}{2}\right) \frac{H}{n} \quad (26)$$

The active earth pressure force acting on reinforced fill is obtained as

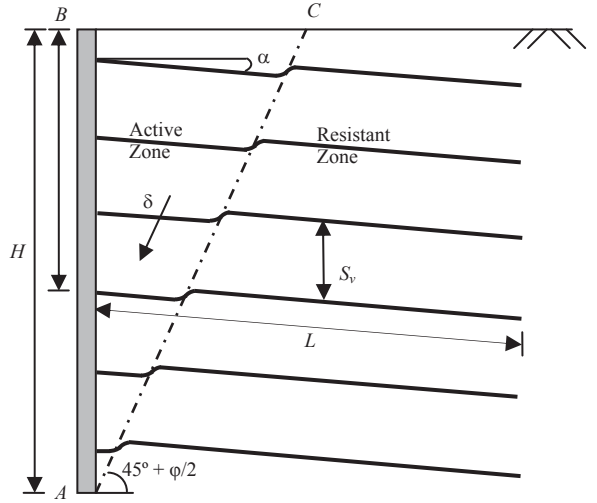


Fig. 14 Inclined reinforcement subjected to oblique pull

$$P_a = W \tan\left(45 - \frac{\phi}{2}\right) \quad (27)$$

Where W is the weight of failure wedge

The pullout resistance developed at depth ' z_i ' from top of the fill

$$T_i = 2\gamma z_i L_{ei} \tan \phi_r \quad (28)$$

The ratio of total pullout resistance developed in all layers to the active earth pressure force is defined as conventional factor of safety, FS_{conv}

$$FS_{conv} = \frac{\sum_{i=1}^n T_i}{P_a} \quad (29)$$

But the kinematics of failure demonstrates that the active wedge ABC undergoes an oblique displacement ' δ ' resulting in an oblique force/displacement at the intersection of failure surface with reinforcement layer. The oblique displacement is resolved into normal and tangential components to the inclined reinforcement (Fig. 15). Under the action of tangential displacement of $\delta \cos(\alpha + \theta)$, reinforcement in resistant zone is assumed to mobilize full shear resistance and the improved pullout resistance is obtained as (Madhav & Kumar, 2009)

$$T_{imp} = \gamma(z_{1i} + z_{2i}) \cos \alpha \tan \varphi_r L_{eia} + \gamma(z_{1i} + z_{2i}) \sin \alpha L_{eia} \quad (30)$$

Where L_{eia} is the effective length of inclined reinforcement

$$L_{eia} = L - \left[\frac{(H - z_i) \tan \left(45^\circ - \frac{\varphi}{2} \right)}{\cos \alpha} \times \left[1 - \frac{\sin \left(45^\circ - \frac{\varphi}{2} \right) \sin \alpha}{\cos \left(45^\circ - \frac{\varphi}{2} - \sin \alpha \right)} \right] \right] \quad (31)$$

and z_{1i} is the depth of the point below ground surface where inclined reinforcement intersects the failure surface at i^{th} level

$$z_{1i} = z_i + \left(\frac{(H - z_i) \sin \left(45^\circ - \frac{\varphi}{2} \right)}{\cos \left(45^\circ - \frac{\varphi}{2} - \alpha \right)} \right) \quad (32)$$

and z_{2i} is the depth of the other end of reinforcement

$$z_{2i} = z_i + L \sin \alpha \quad (33)$$

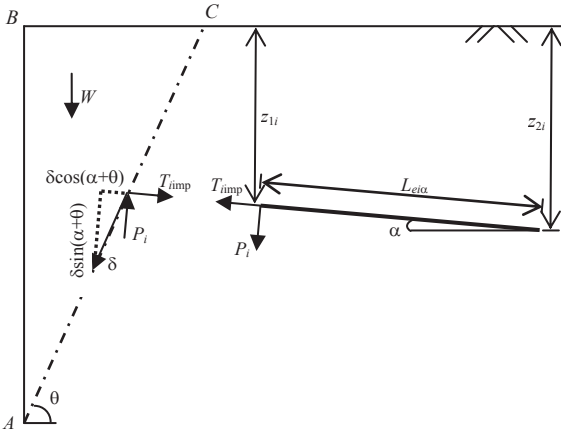


Fig. 15 Resolving of oblique force into normal and tangential components

Under the action of normal displacement of $\delta \sin(\alpha + \theta)$, the soil beneath the reinforcement also deforms and mobilizes an additional normal reactive force of P_i . In the preceding

sections the methodology to evaluate the normal force, P and its variation with backfill stiffness factor, μ , oblique displacement, δ and interface friction angle, φ_r is demonstrated. The above factors are computed corresponding to each layer as follows

Normalized displacement at i^{th} layer

$$W_{Li} = \frac{\delta \sin(\alpha + \theta)}{L_{eia}} \quad (34)$$

Relative stiffness factor for i^{th} layer:

$$\mu_i = \frac{k_s L_{eia}}{\gamma \left(\frac{z_{1i} + z_{2i}}{2} \right) \cos \alpha} \quad (35)$$

substituting the above values of normal displacement and stiffness factor in Eqn. 24 the normalized force, P^*_i is obtained in each layer and normal force is obtained as

$$P_i = P^*_i \times \gamma \times \left(\frac{z_{1i} + z_{2i}}{2} \right) L_{eia} \quad (36)$$

The total pullout resistance mobilized in inclined reinforcement is

$$T_{iT} = \gamma(z_{1i} + z_{2i}) \cos \alpha \tan \varphi_r L_{eia} + \gamma(z_{1i} + z_{2i}) \sin \alpha L_{eia} + P_i \tan \varphi_r \quad (37)$$

The modified factors of safety without and with oblique pull are respectively obtained from

$$F_\alpha = \frac{\sum_{i=1}^n T_{iimp}}{P_a} \quad (38)$$

$$F_{\alpha o} = \frac{\sum_{i=1}^n T_{iT}}{P_a} \quad (39)$$

The variation of factors of safety with inclination of reinforcement is presented in Fig. 16 for backfill stiffness factor, $\mu = 1000$, oblique displacement, $\delta = 0.01L$ and interface friction angle, $\varphi_r = 30^\circ$. Both factors of safety with and without oblique pull, increased with inclination of reinforcement. In case of horizontal reinforcement ($\alpha = 0$) subjected to pure axial pullout, $F_\alpha = FS_{conv} = 4.49$. With increase in inclination of reinforcement to 20° , factor of safety, F_α increased to 9.73. Considering the oblique pull and the response of backfill to the

normal displacement, further improvement in factor of safety is observed. Increase in inclination of reinforcement, α from 0° to 20° increased the factor of safety $F_{\alpha 0}$ from 5.47 to 11.46.

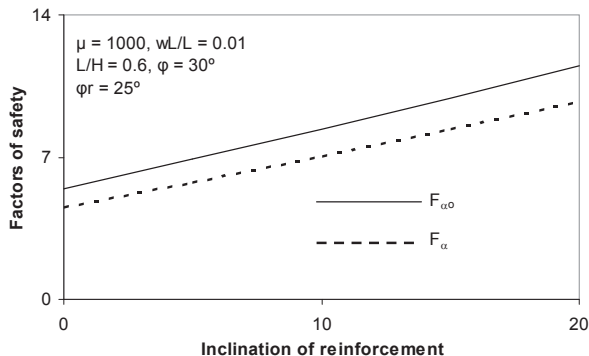


Fig. 16 Factor of safety versus inclination of reinforcement

5. CONCLUSIONS

The use of inclined reinforcement embedded in soil and subjected to normal force/displacement at shallow end is proposed by considering reinforcement to be inextensible, linear backfill response and full shear mobilization along reinforcement soil interface. The governing equations are normalized and solved numerically. The variations of parameters such as normal displacements and tension with distance, and of normal force, maximum tension and slope of reinforcement at shallow end with normalized shallow end displacement, relative backfill stiffness factor is quantified for different inclinations of reinforcement.

The displacement curves for inclined and horizontal reinforcement nearly coincide with an exception that an increase in inclination of reinforcement shifted the initiation of normalized displacement towards shallow end. Thus a marginal increase in length of reinforcement undergoing a change in orientation under similar backfill condition and normalized displacement is observed with increase in inclination of reinforcement. The increase in normal force, P^* is insignificant for soft backfills ($\mu \leq 50$) and in case of stiff backfills ($\mu = 10,000$) P^* increased by 24% with increase in inclination of reinforcement, α from 0° to 20° . Similarly for low values of shallow end displacement ($W_L \leq 0.001$) the influence of

inclination on normal force, P^* is negligible and same is increased by 17% with increase in inclination of reinforcement, α from 0° to 20° .

The use of inclined reinforcement in reinforced earth wall and significance of oblique pull is demonstrated by quantifying the factor of safety against pullout of reinforcement for different inclinations. The factors of safety without oblique pull increased from 1.27 to 2.17 and with oblique pull increased from 1.27 to 2.55 with increase in inclination of reinforcement from 0° to 20° . It is therefore established that geosynthetic reinforcement at miniature inclinations practically feasible in place generates pullout resistances larger than conventional horizontal reinforcement in reinforced earth construction.

REFERENCES

- Alfaro, M.C., Miura, N., Bergado, D.T., 1995. Soil-geogrid reinforcement interaction by pull out and direct shear tests. *Geotechnical Testing J. ASTM* 18 (2), 157–167.
- Athanasopoulos, G.A. 1993. Effect of particle size on the mechanical behavior of sand Geotextile composites. *Geotextiles and Geomembranes*, 12, 252 – 273.
- Bergado, D.T., Teerawattanasuk, C., and Long, P.V., 2000. Localized mobilization of reinforcement force and its direction at the vicinity of failure surface. *Geotextiles and Geomembranes*, 18, 311 – 331.
- Burd, H.J., 1995. Analysis of membrane action in reinforced unpaved roads. *Canadian Geotechnical Journal*, 32, 946 – 956.
- Claybourn, A.F., and Wu, J.T.H., 1993. Geosynthetic reinforced soil wall design, *Geotextiles and Geomembranes*, 12, 707 – 724.
- Degenkamp, G., and Dutta, A., 1989. Soil resistance to embedded anchor chain in soft clays. *Journal of Geotechnical Engineering*, ASCE, 115, 1420 – 1437.
- Farrag, K., Acar, Y. B. & Juran, I., 1993. Pull-out resistance of geogrid reinforcements. *Geotextiles and Geomembranes*, 12, 133–159.
- Flower, J., 1982. Theoretical design considerations for fabric reinforced embankments. *Proceedings of 2nd International Conference on Geotextiles*, 3, 665-670.

- Gray, D.H., and Ohashi, H., 1989. Mechanics of fiber reinforcement in sand. *Journal of Geotechnical Engineering*, ASCE, 109, 335 – 353.
- Hayashi, S., Makiuchi, K., Ochiai, H., 1994. Testing methods for soil-geosynthetic frictional behaviour Japanese Standard. In: *Proceedings of the Fifth International Conference on Geotextiles, Geomembranes and Related Products 1*, 411–414.
- Jewell, R.A., Milligan, G.W.E., Sarsby, R.W., Dubois, D., 1984. Interaction between soil and grids. In: *Polymer Grid Reinforcement*. Thomas Telford, London, pp 18–30.
- Jewell, R.A., 1992. Keynote Lecture: Links between the testing modeling and design of reinforced soil. In: *Proceedings of the International Symposium on Earth Reinforcement Practice, Fukuoka Japan*, Vol. 2, pp. 755–772.
- Jewell, R.A., 1996. Soil reinforcement with geotextiles. *CIRIA*, Publication No. 123, 332pp.
- Juran, I., Knochennmus, G., Acar, Y.B., Arman, A., 1988. Pullout response of geotextiles and geogrids. In: *Holtz, R.D. (Ed.), Geosynthetics for Soil Improvement*, ASCE. Geotech. Spl. Publ. no.18, pp. 92–111.
- Leshchinsky, D., Reinschmidt, A.J., 1985. Stability of membrane reinforced slopes. *Journal of Geotechnical Engineering*, ASCE 111 (11), 1285–1300.
- Leshchinsky, D., Boedeker, R.H., 1989. Geosynthetic reinforced soil structures. *Journal of Geotechnical Engineering*, ASCE 115 (10), 1459–1478.
- Lopes, M.L., Ladeira, M., 1996. Role of specimen geometry, soil height and sleeve length on the pull-out behaviour of geogrids. *Geosynthetics International 3* (6), 701–719.
- Madhav, M.R., and Umashankar, B., 2003. Analysis of inextensible sheet reinforcement subject to transverse displacement/force: Linear subgrade response. *Geotextiles and Geomembranes*, 21, 69 – 84.
- Madhav, M.R., and Manoj, T.P., 2004. Response of geosynthetic reinforcement to transverse force/displacement with linear subgrade response. *Proceedings of International Conference on Geotechnical and Geoenvironmental Engineering, Mumbai*: 13 – 18.
- Madhav, M.R., and Kumar, P.V.S.N.P., 2007. Effect of oblique pull of reinforcement in RE wall – Coulomb failure mechanism, Proc., *First Indian Young Geotechnical Engineers Conference, Hyderabad*: 283 – 289.
- Ochiai, H., Otani, J., Hayashi, S., Hirai, T., 1996. The pull-out resistance of geogrids in reinforced soil. *Geotextiles and Geomembranes 14*, 19–42.
- Scott, R.F., 1981. Foundation Analysis. *Prentice-Hall Inc., Englewood Cliffs, NJ*, 249pp.
- Sobhi, S., Wu, J.T.H., 1996. An interface pull out formula for extensible sheet reinforcement. *Geosynthetics International 3* (5), 565–582. Sobhi and Wu 1996
- Shewbridge, S.E., and Sitar, N., 1989. Deformation characteristics of reinforced sand in direct shear. *Journal of Geotechnical Engineering, ASCE*, 115:1134 – 1147.
- Terzaghi, K., 1955. Evaluation of coefficient of subgrade reactions. *Geotechnique, Institute of Engineers, London 5* (4), 197–226.

Bearing Capacity of Piles in a “Soil-Pile-Structure” System

Paramonov V.N., Kravchenko P.A.
Georeconstruction Engineering Co, St.Petersburg, Russia

ABSTRACT: The paper features presentation of small-scale modeling results for piles behavior in different conditions of their use. It is shown that there is a significant difference between load distribution between the piles and the raft in a strengthened and a pile-raft foundation types. The authors also describe the effect of the essential bearing capacity increase of piles in a strengthened and a pile-raft foundation in comparison with a single pile and a pile in a pile group is described.

1. INTRODUCTION

In many megacities in the world with long history of existence there are plenty of historic buildings preserved as heritage, or there are buildings and structures, located in adjacency to other existing buildings, which lost their designated applicability. Thus, the use of such buildings as initially intended no longer being advisable, their historic value makes one retain their architecture.

As a rule, in such cases reconstruction is required, which is often accompanied with replacement of bearing structures, construction of covered atria within buildings themselves and so on. Such actions, as a rule, lead to increase of loads on foundations, and, as a result, to their necessary strengthening. In case of buildings on pile foundations it is often necessary to evaluate a possibility of pile load increase. The necessity to evaluate bearing capacity of piles arises for structures constructed incompletely, when the superstructure undergoes design changes when the foundations have been already constructed.

2. PRECONDITIONS TO CARRYING OUT RESEARCH

A number of research cases demonstrate that bearing capacities of piles installed into clays

increase in time [1]. In Saint-Petersburg there was a unique possibility to estimate bearing capacity of piles in months and even decades after their installation. The effect of pile bearing capacity increase on construction sites was identified repeatedly [4, 5, 6]. The authors described a number of projects on which the increase in bearing capacity of piles in time was registered. The bearing capacity of piles in the considered cases increased 1,6 times and more.

The results of static tests of piles are given in papers for piles being a part of structures which have existed by the time of the tests from several months to several decades. On construction sites considered, the estimation of bearing capacity of piles was carried out already as a part of a pile-field under the erected constructions. As a rule, there were results of static load tests at the time of construction and later in a considerable period of time that allowed to note an increase of bearing capacity of piles due to the load influence from the superstructure. For the "final" pile tests the pile heads were cut down from the raft and loaded by a jack supported against the raft. According to results of the research the bearing capacity of the piles increased up to 2 times and sometimes more in comparison with the initial values.

3. SMALL-SCALE MODELING

Small-scale tests allow to research interaction between different types of foundations and soil without resorting to expensive full-scale in-situ experiments. Small-scale modeling allows to carry out series of experiments, from time to time modeling the same conditions, excepting mistakes and influence of casual factors which is not a feasible task in the field.

In our case small-scale modeling was used as the basis for creation and improvement of engineering calculation methods.

The size of the raft model in plan used in the modeling was assumed as 150×150 mm. The arrangement of the piles in plan was taken as 2×2 , the spacing being $3d$. The pile diameter was $d=16$ mm. Piles were installed into soil medium to the level of 300 mm below the surface.

Small-scale modeling of the raft foundation, the pile-raft foundation and the foundation strengthened by piles were carried out in laboratory conditions. The results and methodology of the laboratory tests were provided in a number of publications [2, 3]. In process of experimental investigations the dependence of the loads transferred by piles to the soil and influence of the raft on the pile bearing capacity were determinates.

Experiments were conditionally split up into the main and additional series. The main series included raft modeling, raft strengthening by piles and the pile-raft foundation.

In the additional series the bearing capacities of the piles in various conditions of their work (for a single pile, a pile as a part of a pile group, a pile as a part of a strengthened and pile-raft foundation) were investigated. For an exception of systematic mistakes all experiments were made with triple repetition. In this article we consider the results of the additional series of experiments.

In the process of small-scale modeling the methodology which allows to estimate the “key factor” for design of pile foundations – distribution of loads between piles and the raft was developed.

4. LOAD DISTRIBUTION IN PILE STRUCTURES

The measurements of the part of the load transferred to the soil by the piles were carried out during modeling. The results are shown in Figure 1.

It was noted that the value of the load part transferred by piles comes to stabilization both in case of the pile-raft and the strengthened foundation. In case of the strengthened foundation the part of the load transferred by the piles

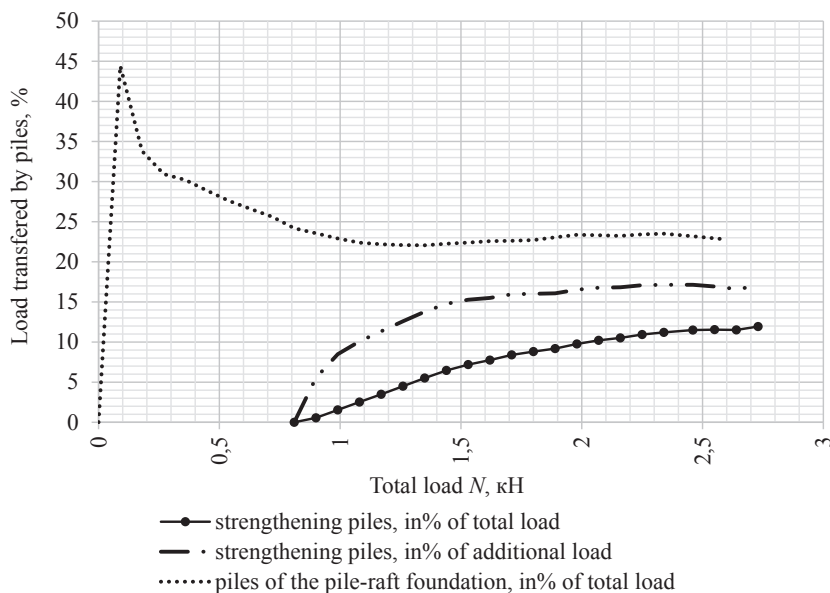


Figure 1. Load distribution in pile structures

increases from zero to a constant value, whereas in case of the pile-raft foundation the part of the load transferred by piles decreases from an immediate maximum to a constant value.

The value of distribution of loads in these cases can be determined by the following ratios:

- in the case of the pile-raft foundation:

$$\varepsilon_{pile}^{PRF} = \frac{F_d^{pile}}{(F_d^{pile} + F_d^{raft})} \cdot 100\% = \frac{0,492}{(0,492 + 1,84)} \cdot 100\% = 22\%$$

- in case of the strengthened foundation:

$$\varepsilon_{pile}^{StrF} = \frac{F_d^{pile}}{(F_d^{pile} + F_d^{raft})} \cdot 100\% = \frac{0,420}{(0,420 + 1,84)} \cdot 100\% = 18,6\%$$

The divergence between the calculated and the measured values in case of the pile-raft

foundation does not exceed 12%, in case of the strengthened foundation – 6%.

5. THE BEARING CAPACITY OF THE PILES

Bearing capacity of a pile as a part of the pile group was equal to 122,5 N, the bearing capacity of the raft is reached at load value being 1,83 kN. By the “Superposition approach”, total bearing capacity of the pile-raft foundation should be equal to: $0,1225 \cdot 4 + 1,83 = 2,32$ kN. However, experiments show that its bearing capacity is never below 2,70 kN.

To explain this effect, additional series of experiments was carried out. Static load tests results are shown in Figure 2.

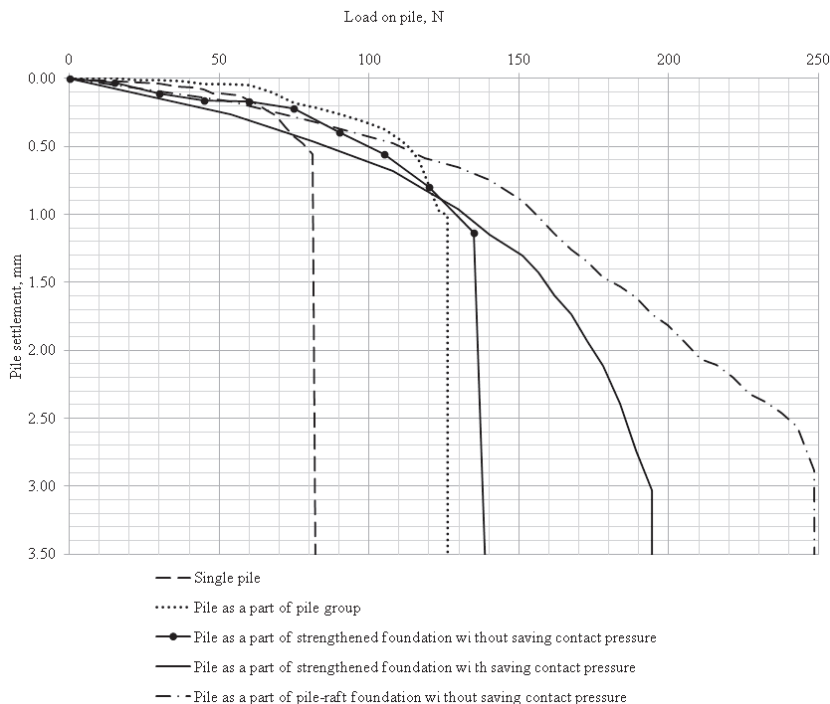


Figure 2. Results of pile static tests in different conditions

Bearing capacity of a single pile is equal to 80 N, of a pile in group due to the effect of pile group – 126 N. Bearing capacity of a pile in the pile-raft foundation is equal to 250 N, in the strengthened foundation – 195 N. It may be supposed that the increase of the bearing capacity can be attributed to soil compaction under the raft or due to additional stress under it. To

confirm the first hypothesis the pile-raft foundation was totally unloaded and a pile was tested. In this case the bearing capacity of a pile was equal to 135 N which is close to the bearing capacity of a pile in a pile group (126 N). Thus we can conclude that the soil compaction does not essentially affect the increase of the bearing capacity of a pile. Contact pressure under the

raft leads to a more significant increase of bearing capacity.

Actually the increase of bearing capacity of piles is caused by increasing values of horizontal pressure in the space between the installed piles. Additional horizontal pressure can be calculated by the lateral pressure coefficient:

$$\sigma_{xi} = \xi \cdot \sigma_{z1} \quad (1)$$

The value of the additional friction can be determined multiplying the horizontal pressure by the friction coefficient which is equal to the tangent of the internal angle of the soil:

$$\Delta F_{tp} = \sum \sigma_{xi}^{non} \cdot u \cdot h_i \cdot tg \varphi \quad (2)$$

Results of the calculations are shown in Figure 3.

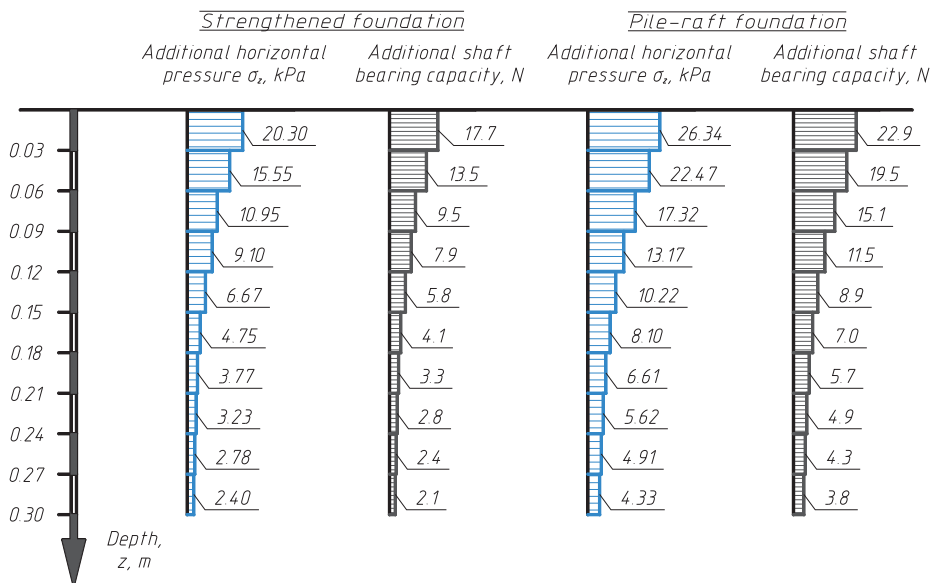


Figure 3. Calculated additional horizontal pressure and shaft bearing capacity

Thus the calculated bearing capacity of a pile in the pile-raft foundation is equal to 244 N (the difference with the experiment 2%). For a pile in the strengthened foundation the calculated value of bearing capacity is equal to 192 N (4% less than the experimental value).

6. PREDICTING BEARING CAPACITY INCREASE FOR PILES, BEING A PART OF A FOUNDATION OF A RECONSTRUCTED BUILDING

One of the buildings in Saint-Petersburg was constructed in 1986. The size of the building in plan is 197×49 m. The building is short-listed for reconstruction.

At the design stage (27 years ago) 14 static load tests of the piles were carried out. Results of in-situ tests showed that the bearing capacity of the piles was equal to 1100 kN.

According to the new design materials, in the process of reconstruction of the building new towers will be erected on the existing raft with the 16-m long piles, their toe-level being at 19,5 m.

Calculation of load distribution on the 50 existing piles was performed. The load transferred by the piles to the subsoil, as a percentage of the general load can be determined by the following ratio:

$$\varepsilon_{pile} = \frac{n_d \cdot F_d^{pile}}{(n_d \cdot F_d^{pile} + F_d^{raft})} \cdot 100\% = \frac{1100 \cdot 50}{(1100 \cdot 50 + 126592)} \cdot 100\% = 30\%$$

Then the part of the load transferred by the raft to the soil is equal to 70%.

Calculation of the additional bearing capacity of piles with the use of the formulas 1 and 2 for different load values was carried out. The calculation results of the increased bearing capacity of the piles are given in Figure 4.

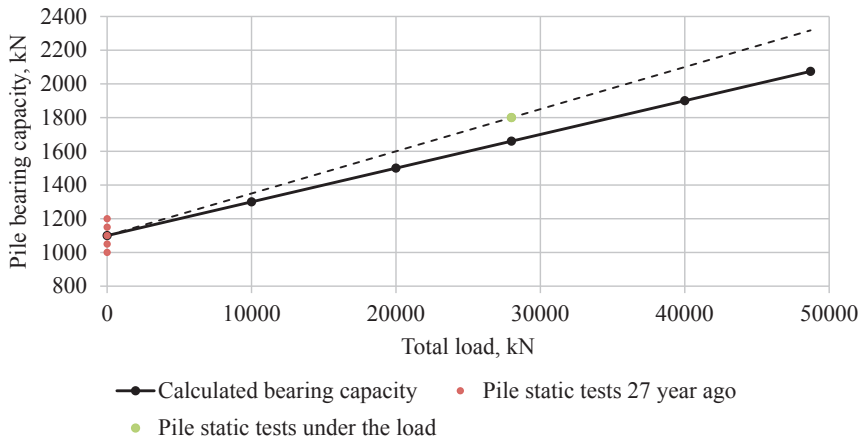


Figure 4. Calculated pile bearing capacity in comparison with static tests

The value of the total load on the foundation is equal to 27997 kN. Under such load the expected bearing capacity of a pile is equal to 1660 kN. Static tests of the piles carried out in current conditions while preserving contact pressure under the raft showed the increased bearing capacity as being more than 1800 kN. So the calculated bearing capacity of a pile is less than in reality but the value of the divergence is equal to 7,8%.

7. REFERENCES

1. Bartolomey A.A., Omelchak I.M., Jushkov B.S. Forecast of settlements of pile foundations. – M.: Stroyizdat, 1994 (In Rus).
2. Kravchenko P.A. Distribution of loads in pile-raft and strengthened foundations/News of Petersburg State Transport University 3(32)//SPb, 2012, pp. 132-137.
3. Kravchenko P.A., Paramonov V.N. Effect of increasing of bearing capacity of piles under the load/News of high schools. Construction. №7-8 (643-644)// Novosibirsk: NGASU, 2012, pp. 117-121.
4. Paramonov V.N., Dunaevskaya T.A. Change of bearing capacity of driven piles in time at the open sites and at sites loaded by structures/Reconstruction of cities and geotechnical engineering №. 8 //SPb: Georeconstruction, 2004, pp 102-106.
5. Paramonov V.N., Tihomirova L.K. Change of bearing capacity of driven piles in time // Reconstruction of cities and geotechnical engineering.

№1 // SPb: Georeconstruction, 2000, pp. 127–131.

6. Paramonov V.N., Ulitsky V.M., Shashkin A.G. Bearing capacity of bored in geological conditions of Saint-Petersburg / Reconstruction of cities and geotechnical engineering. № 3 // SPb: Georeconstruction, 2000, pp 8-12.
7. Улицкий В.М., Шашкин А.Г., Шашкин К.Г. Геотехническое сопровождение развития городов./Группа компаний «Геореконструкция»./ Санкт-Петербург. 2010.

Determination of Cracking Characteristics of Soils for Various Geotechnical Engineering Problems

Prathyusha, J., Uday, V.K. and Singh, D.N.

Dept. of Civil Engineering, Indian Institute of Technology Bombay, Powai, Mumbai, India-400076

ABSTRACT: Investigations were conducted on soils of entirely different characteristics and their cracking characteristics, under varied environmental conditions, were studied by resorting to 'image analyses'. The test results and observations have been critically evaluated and importance of these conditions has been demonstrated. Also, by resorting to laser microscopy, cracking characteristics of these soils, particularly the depth of crack, has been studied. This study has been found to be quite useful in correlating dimensions of the crack with each other and its volume.

1. INTRODUCTION

Cracking of fine-grained soils, which normally occurs in both natural as well as man-made structures such as excavations, earth slopes, dams, highway embankments, hydraulic barriers, top covers of the landfills, clay liners, cricket pitches and turfs, and agricultural lands, leads to their failure. This phenomenon can be attributed, primarily, to the loss of moisture from the soil mass, as a result of severe environmental conditions (viz., humidity and temperature) that may result in non-uniform distribution of moisture and temperature, which further causes differential stresses within the soil mass. This loss of moisture is responsible for shrinkage of fine-grained soils, which results in building up of the negative pressure or suction in the soil mass, and the cracks appear when soils are restrained from undergoing volumetric changes, termed as shrinkage. As such, cracking of the soil influences its overall engineering behaviour (in particular seepage, consolidation, compressibility and shear strength characteristics).

Furthermore, tension cracks developed within the backfill of the retaining structures and foundations is a major concern to the professionals involved with the *soil-structure interaction analysis*. Though, many theories

have been developed to incorporate the effect of tension cracks for such analyses, they could not be validated due to lack of instrumentation for measurement of cracks or mathematical models which could be employed for estimating them.

Hence, it becomes important to investigate the mechanism(s) of soil cracking and the parameters that influence it significantly. In this context, several researchers have studied cracking characteristics viz., crack intensity, width and depth (Lakshmikantha et al., 2009; Uday and Singh, 2013a,b), cracking moisture and tensile strength (Nahlawai et al., 2004), initiation of secondary cracks (Birle et al., 2008) and geometry of cracks of the soil mass (Nahlawi and Kodikara, 2006) experimentally as well as numerically. Based on these studies, it has been demonstrated that cracks can develop due to various processes such as desiccation and shrinkage, freezing and thawing, penetration by plant roots, differential settlement and different types of loadings such as mechanical, thermal and chemical on the soil mass.

Incidentally, most of the studies on cracking characteristics of fine-grained soils have been confined to image analysis (2-D), to quantify the crack geometry, and based on the results mathematical models have been developed. However, these studies cannot be employed for determining depth of the cracks and their

propagation in the soil mass, and are soil specific as well. Needless to say, such studies (i.e., 3-D) require a special attention of the researchers to model cracking characteristics of fine-grained soils, precisely.

This paper presents details of the methodology employed for studying the cracking characteristics of soil, under different conditions of temperature and humidity, which becomes essential for several geotechnical engineering related problems as stated above.

2. EXPERIMENTAL INVESTIGATIONS

In the present study, two commercially available soils, white clay (Kaolin) designated as WC and bentonite (designated as BT), and three natural soils collected from western part of India, designated as S1, S2, S3 have been used. Certain amount of these soils was mixed with the desired amount of distilled water, thoroughly, by using an electric operated stirrer for 24 hours, to obtain slurry of good consistency and with predetermined initial moisture content, defined as liquid to solid ratio, L/S. Later, this slurry was poured in a petri-dish and in order to

remove the entrapped air the dish was tapped on a wooden platform appropriately. It was made sure that the petri-dishes used for this study are defect free (viz., no concentric depressions and protrusions on the inner side). Later, the dish was placed on the weighing balance, of 0.01 g accuracy and the whole assembly was installed in an environmental chamber (refer Fig. 1), which can be set at desired values of temperature and humidity with the help of electronic controls.

This device (Uday and Singh 2013a) helps in simulating varied environmental conditions (20 to 60°C and 40 to 95% Rh over a control volume of 90 l) and these parameters can be data logged along with the weight of the specimen over prolonged durations. The weight of the petri-dish with slurry, W , was subjected to drying under the different environmental conditions, and the weights of the specimen is data logged over a period of time, t , until three consecutive weights were observed to be same. During the whole process of drying, condition of the specimen was observed by live streaming of the images from the Image Acquisition and Analysis System, IAAS.

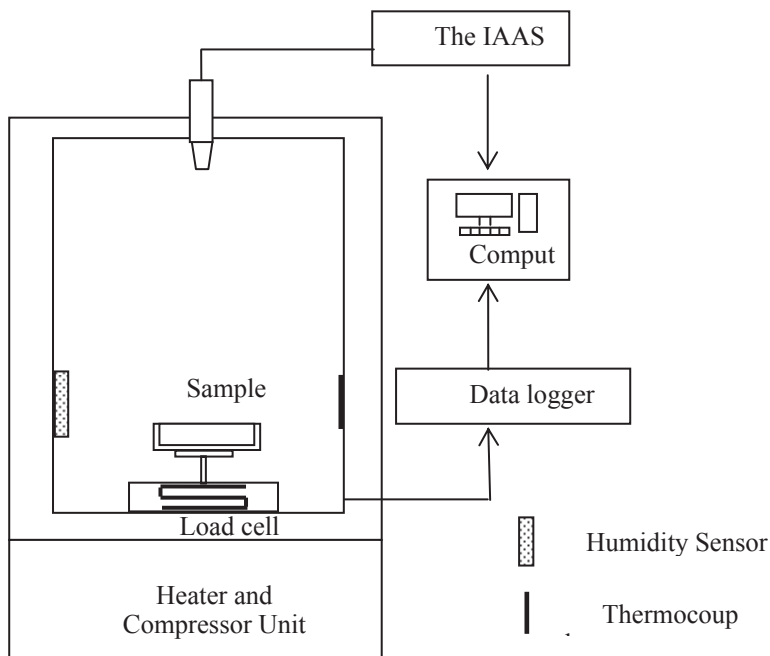


Fig. 1. The environmental test chamber along with the attached IAAS

The image analysis system, developed to suit the requirement of the study, comprises of (a) Charge Coupled Device (CCD), camera, (Sony, SSC-G818) (b) lighting arrangement (a ring light and a diffusion cell) and (c) image analysis system. The image analysis system is software designed according to the need of the study. The software has two major functions, (i) acquisition of images (manual or prefixed time intervals) and (ii) analysis of the image captured to obtain various parameters. Image analysis module has various options to obtain various parameters viz., shrinkage percentage, particle count, angle measurement, linear measurement, arc measurement. From these parameters, the required cracking characteristics/indices, (i) shrinkage percentage, defined as the percentage decrease in the surface area of the soil in the process of drying/shrinkage, (ii) average length of the crack, defined as the ratio of the total crack length (l_t) to the number of cracks in the specimen, n_c , (iii) crack intensity factor, defined as the ratio of the area of cracks, A_c , to the final effective area of the specimen, A_s , and (iv) time of crack initiation, defined as the time corresponding to the initiation of the crack can be obtained. For this study, these indices are considered as the cracking characteristics.

Later, by resorting to a laser microscope, LEXT OLS 4000, (Olympus, Japan), attempt has been made to study the 3-D cracking characteristics of fine-grained soils (Uday and Singh, 2013b).

3. RESULTS AND DISCUSSIONS

3.1. Drying Tests

From the results of the drying tests, a relationship between the weight of the specimen, W_t (in mg), corresponding to drying time, t , (in hour) was developed (refer Fig. 2).

The plot between W_t and t represents a typical drying response of the soil, where the initial straight line depicts the CRP (constant rate period) as enunciated by earlier researchers (Tang et al. 2010; Shinde et al. 2012), and the same can be represented by the following relationship (Uday and Singh 2013a).

$$W_t = A \cdot t + B \quad (1)$$

where, A is the slope of the initial portion of the W_t versus t relationship, and is equal to the

evaporation rate, E_r , (Shinde et al. 2012) and B is empirical constant, which is equal to W_0 , the initial weight of the specimen (corresponding to $t=0$).

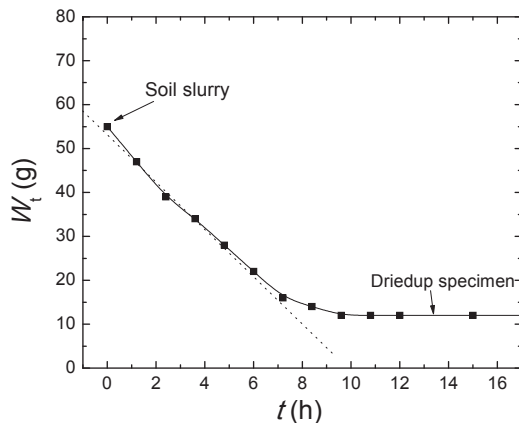


Fig. 2. The weight loss of the soil specimen during its air-drying

Further, to establish the influence of the factors which affect drying of the specimens, investigations were conducted for various specimen specific parameters (i.e., initial thickness, t_i ; initial water content, L/S , boundary conditions); exposure conditions (ambient temperature, θ ; humidity, R_h), and the soil type (i.e., mineralogy). The results obtained from the various conditions are presented and discussed in the following.

3.2. Effect of L/S and Boundary Conditions

To begin with, and to establish the influence of initial L/S and boundary conditions on drying of fine-grained soils, tests were conducted on soils WC and BT (the two soils which exhibit large difference in their liquid limit, LL , and plasticity index, PI) and drying was allowed in lubricated (by applying silicone gel) and non-lubricated petri-dishes, respectively. It has been reported by Uday and Singh (2013a) that E_r is independent of the L/S , which is in accordance with the findings reported by Birle et al. (2008). However, it has been observed that specimens dried without lubrication exhibit cracking (Fig. 3).

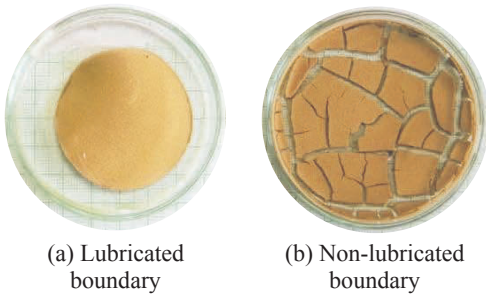


Fig. 3. Difference in cracking patterns of the soils due to different boundary conditions

3.3. Effect of Temperature

The variation of evaporation rate with ambient temperature, θ , during drying of soil specimens was investigated at different temperatures ($\theta=30, 35, 40, 45, 50, 55$ °C), under constant humidity ($R_h=40\%$) and from the results it has been reported by Uday and Singh (2013a) that the weight loss of the soil specimen due to its drying has been found to be highly dependent on the temperature. Interestingly, from the cracking patterns of the soil BT, it can be observed that severity of the cracking, in terms of number of segments formed, increases with an increase in exposure temperature (Fig. 4).

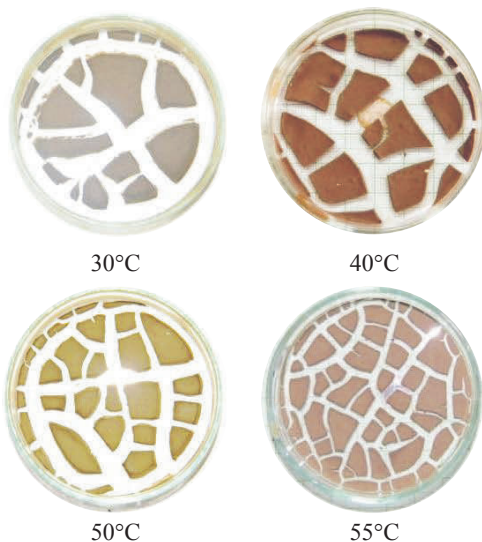


Fig. 4. The cracking patterns of the specimens of the soil BT (initial thickness, $t_i=4$ mm) corresponding to different temperatures

3.4. Effect of Specimen Thickness

It has been observed by Uday and Singh 2013a that E_r is quite dependent of t_i , for soils S1, S2, S3 and WC as compared to the soil BT. Furthermore, in order to understand the influence of t_i , on cracking characteristics of fine-grained soils under similar ambient conditions the cracking patterns of soil BT was compared (Fig.5) and it has been observed by Lakshmi-kantha et al. (2009, 2012) that the intensity of cracking decreases with increase in t_i .

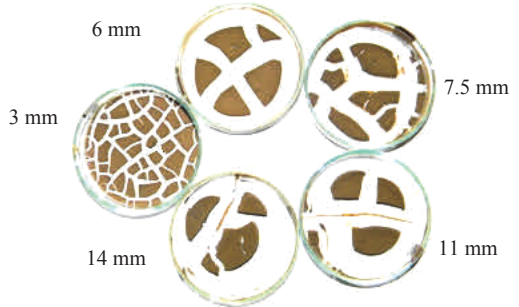


Fig. 5. The cracking patterns of the specimens of the soil BT corresponding to different initial thickness

3.5. Effect of Humidity

In order to study the influence of humidity on cracking characteristics of fine-grained soils, specimens were subjected to drying under different humidity conditions ($R_h=40, 50, 60, 70$ and 90%) and by maintaining constant temperatures. It has been reported by Uday and Singh (2013a) that, in general, with an increase in R_h , the E_r decreases for all the soils considered in this study. This can be confirmed from Fig.6, depicting the cracking patterns of soil BT under different humidity levels, which indicates the decrease in the intensity of cracking corresponding to higher values of humidity.

The crack specific parameters for the soil specimens were measured by employing the laser microscope, LEXT OLS 4000. A critical synthesis of the measurement results (viz., width of crack, W ; length of crack, L and depth of crack, D) by employing Mathematics 5.2 yields the following relationship:

$$D = a \times W^b \times L^c \quad (2)$$

a and b are related to clay content, CL ; plasticity index, PI ; free swell index, FSI and specific

gravity, G and c is equal to 0.5 as reported by Uday and Singh (2013b).

Eq. 2 can be employed for determining D , from easily measurable parameters, W , L and soil properties. Further, with an intention to determine the volume of the crack, V_c , the relationship proposed by Ringrose-Voase and Sanidad (1996), refer Eq. 3, were employed.

For Triangular Model (TM)

$$V_c = 0.5 \times D \times W \times L \tag{3a}$$

Square Root Model (SM)

$$V_c = 0.67 \times D \times W \times L \tag{3b}$$

The crack volumes measured by OLS 4000, designated as V_m , and those computed by employing Eq. 3, designated as V_c , are found to be matching very well (refer Fig. 7). The discrepancy in Soil BT can be attributed to the irregular surface of the crack, the effect of which is not included in Eq. 3.

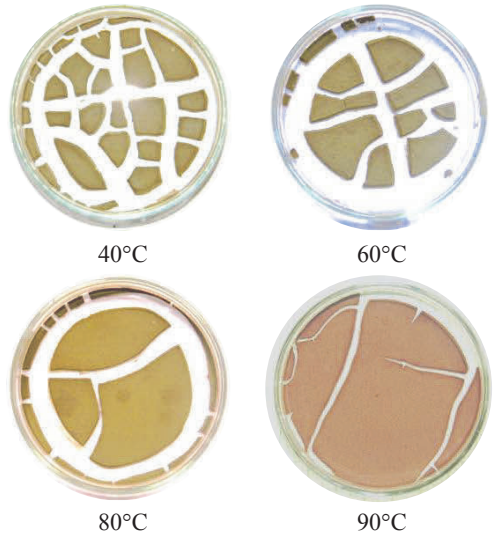


Fig. 6. The cracking patterns of the specimens of the soil BT ($t_i=4$ mm) corresponding to different humidity levels

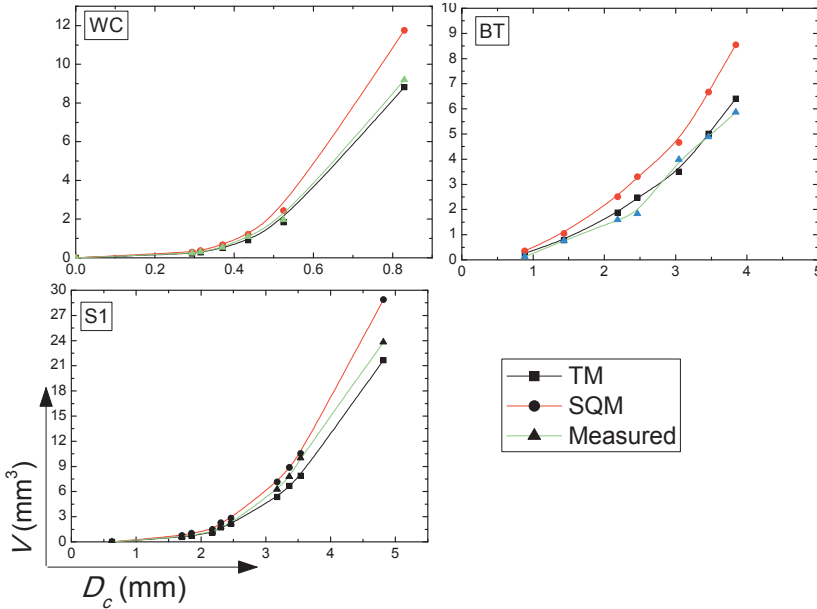


Fig. 7. Variation of V_m and V_c for different soils

4. CONCLUSIONS

Based on the extensive investigations related to drying, and subsequent, cracking characteristics of fine-grained soils, the following conclusions can be derived:

1. It has been demonstrated that the effect of (a) environmental factors (i.e., temperature and humidity), (b) dimension of the specimen and (c) soil type (defined in terms of mineralogy) on drying and cracking characteristics of the fine-grained soils is quite significant.

2. It has been observed that the evaporation rate remains unaffected by the initial moisture content and boundary conditions of the soil specimen. However, it increases with an increase in temperature and thickness of the specimen and decreases with an increase in humidity level.
 3. The mineralogy of fine-grained soils has a very significant influence on their cracking characteristics.
 4. In author's opinion cracking of fine-grained soils can be controlled by limiting their evaporation rate, which in turn can be achieved by addition of appropriate chemicals (viz., nano-materials, minerals, surfactants, polymers etc.). Hence, the methodology developed, and presented in this study, would be of great help in achieving this objective.
 5. Based on these studies, an empirical model has been proposed, which has been found to be quite efficient and useful for estimating the depth and volume of the crack, if its length and width, and other soil specific properties are known.
6. Ringrose-Voase, A.J., and Sanidad, W.B., (1996), A Method for Measuring the Development of Surface Cracks in Soils: Application to Crack Development after Lowland Rice, *Geoderma*, Vol. 71, pp. 245-261.
 7. Shinde, S.B., Kala, V.U., Kadali, S., Tirumkudulu, M.S. and Singh, D.N., 2012, "A Novel Methodology for Measuring the Tensile Strength of Expansive Clays" *Geomechanics and Geoengeering: An International Journal*, Vol. 7, No. 1, pp. 15-25.
 8. Tang, C. S., Cui, Y. J., Tang, A. M. and Shi, B., 2010, "Experiment Evidence on the Temperature Dependence of Desiccation Cracking Behaviour of Clayey Soils", *Engineering Geology*, Vol. 114, pp. 261-266.
 9. Uday, K.V. and Singh, D.N., 2013a, "Investigations on Cracking Characteristics of Fine-grained Soils under Varied Environmental Conditions". *Drying Technology*. In Print.
 10. Uday, K.V. and Singh, D.N., 2013b, "Application of Laser Microscopy for Studying Crack Characteristics of Fine-grained Soils," *Geotechnical Testing Journal*, ASTM, 36(1), 146-154.doi:10.1520/GTJ20120004.

REFERENCES

1. Birlle, E., Heyer D. and Vogt, N., 2008, "Influence of the Initial Water Content and Dry Density on the Soil-Water Retention Curve and the Shrinkage Behavior of a Compacted Clay", *Acta Geotechnica*, Vol. 3, pp. 191-200.
2. Lakshmikantha, M. R., Prat, P. C. and Ledesma A., 2012, "Experimental Evidence of Size Effect in Soil Cracking", *Canadian Geotechnical Journal*, Vol. 49, pp. 264-284.
3. Lakshmikantha, M. R., Prat, P. C. and Ledesma, A., 2009, "Image Analysis for the Quantification of a Developing Crack Network on a Drying Soil", *Geotechnical Testing Journal*, Vol. 32, pp. 1-11.
4. Nahlawi, H. and Kodikara, J. K., 2006, "Laboratory Experiments on Desiccation Cracking of Thin Soil Layers", *Geotechnical and Geological Engineering*, Vol. 24, pp. 1641-1664.
5. Nahlawi, H., Chakrabarthi. S. and Kodikara, J., 2004, "A Direct Tensile Strength Testing Method for Unsaturated Geomaterials", *Geotechnical Testing Journal*, Vol. 27, No. 4, pp.1-6.
6. Ringrose-Voase, A.J., and Sanidad, W.B., (1996), A Method for Measuring the Develop-

Finite Element Modelling to Study Soil Structure Interaction of Asymmetrical Tall Building

B. Pallavi Ravishankar

Research student, GTE, Earthquake Engineering Research Centre, IIIT Hyderabad, INDIA,
pallavi.badry@gmail.com

Neelima Satyam D.

Assistant Professor, GTE, Earthquake Engineering Research Centre, IIIT Hyderabad, INDIA,
neelima.satyam@iiit.ac.in

ABSTRACT: Tall asymmetric buildings experience more risk during the earthquakes (Ming, 2010). This happens mainly due to attenuation of earthquake waves and local site response which get transferred to the structure and vice versa. This can be well explained by the Dynamic Soil Structure Interaction (DSSI) analysis. In this research paper 150 m tall asymmetrical building with two different foundation systems like raft and pile is considered for analysis and assuming homogeneous sandy soil strata results are studied for input of Bhuj ground motion (2001, $M=7.7$). The response of structure in terms of SSI parameters under dynamic loading for a given foundation systems has been studied and compared to understand the soil structure interaction for the tall structures. It has been clearly identified that the displacement at top is more than that at bottom of the building and stresses are more at immediate soil layer under foundation than the below layers .

1. INTRODUCTION:

Most of the civil engineering structures involve some type of structural element which are in direct contact with ground. When the external forces, such as earthquake, act on these systems, neither the structural displacements nor the ground displacements, are independent of each other. The process in which the response of the soil influences the motion of the structure and the motion of the structure influences the response of the soil is explained by the phenomenon Dynamic soil-structure interaction (DSSI). During Earthquake loading the waves travels always with kinetic energy from ground to the surrounding soil mass as well as the structural part in contact with it. A fraction of the kinetic energy released from earthquake waves is transferred into buildings through soil. The exact estimation of transfer of wave energy from soil to structure and again from structure to soil broadly can be divided into two phenomena like a) kinematic interaction and b) inertial interaction. Soil structure interaction parameters such as stresses and displacements in both structure and support systems (Foundation + Soil mass in contact) are depends up on relative stiffness superstructure, foundation system and supporting soil mass. Type of foundation system

is one of the governing parameter n which interaction parameter depends.

In this paper asymmetrical high rise building modelled along with the homogenous sandy soil strata. The building is provided with two different type of foundation systems viz. raft foundation and pile foundation and interaction parameters like displacements and stresses are studied at different points under consideration. It has been observed that displacements and stresses varies with foundation system provided.

2. MODELLING

A Finite element modelling is done for super-structure along with the supporting system using finite element software Ansys-13 (ANSYS Inc). The material models is defined using material library in Ansys for a different linear , nonlinear and contact material for the soil and structure.

In this paper soil and structure modelled integrally with introducing appropriate interface material as per meshing of foundation surface in contact with soil beneath and soil structure interaction parameters like displacements and stresses are studied.

2.1. Soil Properties

A local unbounded homogeneous deep sandy soil volume of 200m x 100m x50 m as shown in Figure1 is considered with the following engineering properties is modelled with Ansys .

Table 1. Parameters of the non-linear soil model

Soil Type	Sandy soil
Eref	19000 kN/m ²
Possion's ratio (η)	0.3
cohesion (C)	23kN/ m ²
internal friction angle (Θ)	230
Mean shear velocity (Vs)	290 m/s

The soil structure interaction is modelled with the concept of elastic half space theory. There are two ways to model the soil structure interaction problem viz. Direct method and Substructure method. In direct method superstructure, foundation system and unbounded soil mass is modelled together with a proper interface element. In substructure method superstructure and foundation system is modelled separately with proper consideration of load transfer from superstructure to the foundation system.

In this paper superstructure and support system is modelled by direct method.

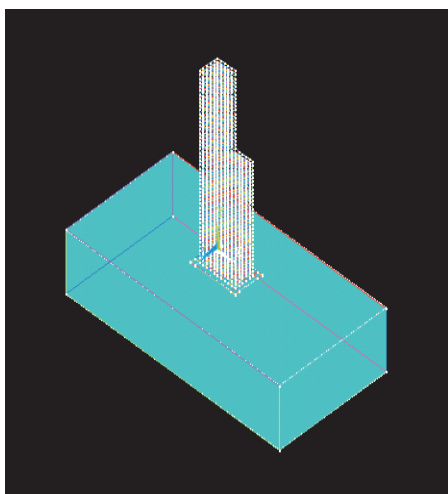


Figure 1. Finite Element non linear soil model.

2.2. Description of structure

A 150 m tall superstructure as shown in Figure 2 of base dimension 40mx20m is considered with a loading asymmetry in such a way, left half portion of building raised to 150 m(50 storeys) and right half raised to 90m (30 storeys). Initial framed structure is modelled in Finite element program Ansys-13.

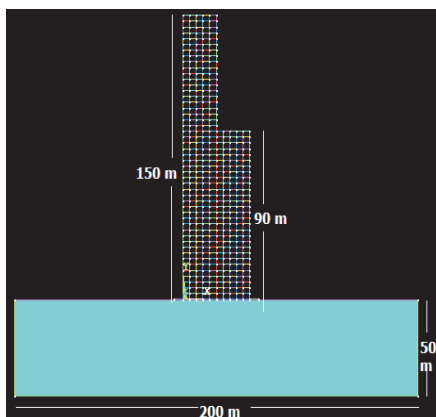


Figure 2. Finite Element model of structure and support system

2.3. Foundation System

Two type foundation system is modelled viz raft and pile foundation.

Raft foundation system (Figure.3) with a dimension 50m x 30m with design uniform thickness 0.5m and a concrete Grade M-20 with rebar material Fe-415 is provided for the modelling.

For pile foundation system (Figure 4) pile cap of 0.2 m thickness is provided with 4m pile spacing in both direction. Pile of diameter 0.25 m and length 10m is modelled.

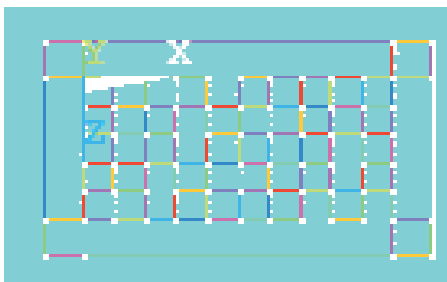


Figure 3. Raft with planer dimension 50m x 30m

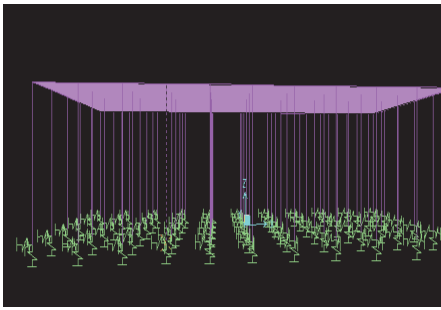


Figure 4. Pile foundation with pile cap dimension 45m x 25m

2.4. Elements selection in Ansys-13

In Ansys framed superstructure is modelled with 2D-Beam element BEAM188 and Piles with SOLID 185, interface element with CONTA175 and TARGE170. Soil is modelled with SOLID 65 and *Drucker-Prager* non linear material model is for soil behaviour.

BEAM188 is suitable for analyzing slender to moderately thick beam structures. The element is based on Timoshenko beam theory which includes shear-deformation effects and element provides options for unrestrained warping and restrained warping of cross-sections. SOLID185 is eight noded 3-D element gives translations in 3-directions used for solid modeling. CONTA175 is ideal to use when there is sliding between two elements in contact (either node to node or line to line). Contact occurs when the element surface penetrates one of the target segment elements, TARGE170 on a specified target surface. Soil is modeled with SOLID 65 which is used for the 3-D modeling of solids with or without reinforcing bars (rebar). The solid is capable of cracking in tension and crushing in compression. Material model *Drucker-Prager* for soil describes the non linear plasticity behavior which depends on the engineering soil properties given as a input data of this model.

2.5. Dynamic analysis of the soil structure interaction model

The dynamic analysis carried out by considering Bhuj input ground motions at the bottom of the soil mass and stresses and displacement at different locations like A,B,C,D,E as shown in Figure 5 of the building and the soil are studied.

For the static analysis of structure the self weight, gravity weight is considered and initial stresses are observed which serves as initial stress conditions for dynamic analysis (Figure.6). The ground motion with PGA 0.31g is given to the model to find the displacements and stresses for the soil strata.

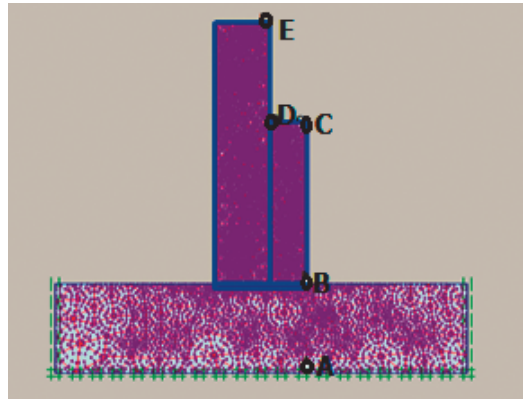


Figure 5. Different points under consideration along elevation of the model

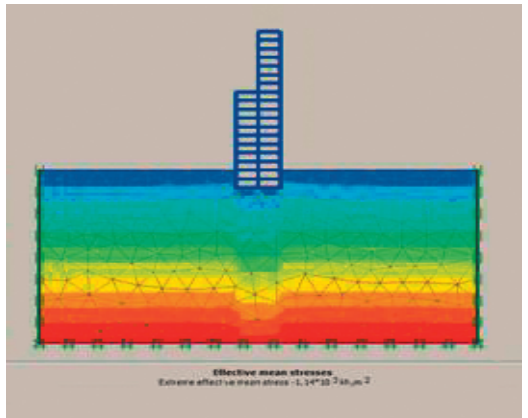


Figure 6. Initial stress contours before applying dynamic loading with stress 200 kN/m²

3. RESULTS

Displacements in x, y and z direction is calculated for the dynamic loading and at each point from bottom to top of model is been plotted .Figure 7,8 and 9 explains the displacement curves in x , y and z directions supported by raft foundation.

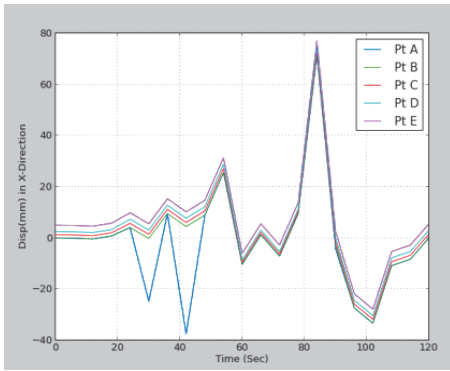


Figure 7. Displacements at different location calculated in X-direction

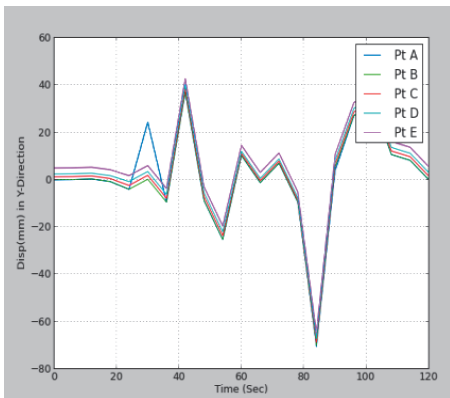


Figure 8. Displacements at different location calculated in Y-direction

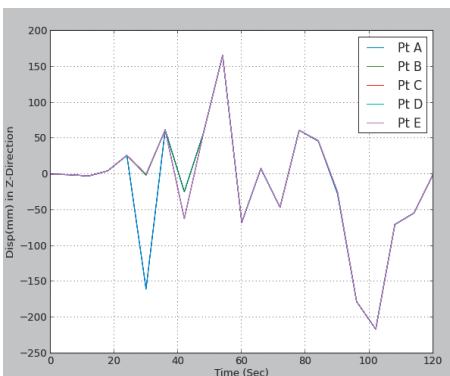


Figure 9. Displacements at different location calculated in Z-direction

Table 2. Maximum displacements under dynamic load conditions for raft foundation system

Locations	Comparative displacement w.r.t point A (%)	
	X-Disp	Y-Disp
A	71.39 mm	37.10 mm
B	0.42 %	0.34 %
C	2.51 %	4.39 %
D	4.61 %	8.43 %
E	8.12 %	14.29 %

When the soil mass and support system is subjected to the dynamic loading it undergoes the deformations which creates the stresses. The stresses in x, y and z direction is calculated for each point mentioned in Table.3. Stress plots at different locations under consideration along the elevation are shown in Figure 10, 11 and 12.

Table 3. Maximum Stress value under dynamic load conditions for raft foundation system

Locations	Comparative stresses w.r.t point A (%)	
	X-Stress	Y- Stress
A	428.39 kN/m ²	222.6 kN/m ²
B	994 %	990 %
C	20.52 %	0.44 %
D	14.61 %	8.43 %
E	-8.11 %	8.29 %

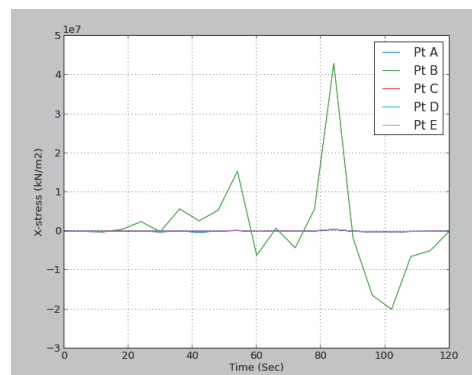


Figure 10. Stresses at different location calculated in X-direction

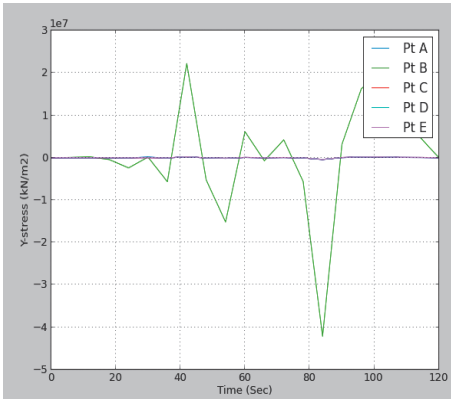


Figure 11. Stresses at different location calculated in Y-direction

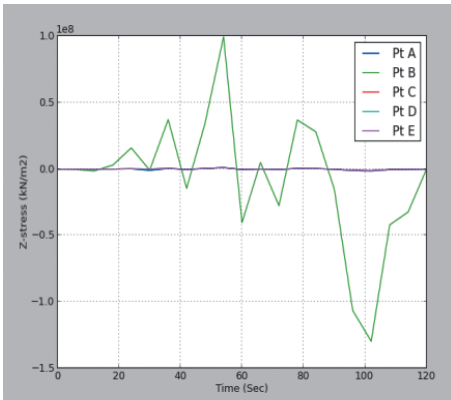


Figure 12. Stresses at different location calculated in Z-direction

An interactive modelling is done for the same soil properties and same structural configuration and foundation system is altered by a pile type and again results are studied. Table 4, and 5 explains the displacements and stress respectively at different points under consideration for the pile foundation system with initial pile configuration mentioned in foundation system.

Table 4. Maximum Displacements under dynamic load conditions for pile foundation system

Locations	Comparative displacement w.r.t point A (%)	
	X-Disp	Y-Disp
B	0.21 %	0.20 %
C	2.09 %	4.07 %
D	4.11 %	9.22 %
E	7.57 %	15.27 %

Table 5. Maximum Stress value under dynamic load conditions for pile foundation system

Locations	Comparative stresses w.r.t point A (%)	
	X-Stress	Y- Stress
B	763 %	812 %
C	1.18 %	0.24 %
D	2.52 %	8.55 %
E	6.61 %	11.29 %

4. CONCLUSION

In order to carry out SSI parametric study an asymmetrical building with respect to loading of 150 m height with base dimension 40 m x 20m is analysed for raft and pile foundation systems separately. The soil mass beneath foundation is modelled as per *Drucker-Prager* nonlinear theory in Ansys-13.

The interactive response is studied for the input Bhuj ground motion with PGA 0.31g. The SSI response is studied for both pile and raft foundation systems. The response of building at different key location at different elevation are noted. It has been observed that for a given ground motion the displacements increases as from soil mass to superstructure top in both X and Y direction, but this change is very minute for the Vertical(Z)-direction displacements. Stress concentration is found to be much more in immediate soil layer below the foundation and it decreases evenly in both directions as moving away down and up from foundation. It is noted that for the same soil strata displacements and stresses in case of pile foundation system is comparatively less than raft foundation system.

5. REFERENCES

1. Zhang Chuhan and John P. Wolf, Elsevier (1998) "Dynamic Soil-Structure Interaction" Chapter 1 and 4
2. M Çelebiand C.B. Crouse (2001) "Recommendations for soil structure interaction effect for instrumentations" *Workshop Documentation Emeryville, Ca.* November 14-15, 2001
3. Ming Ming Yao(2010) Earthquake Wave-Soil-Structure Interaction Analysis of Tall Buildings Ph.D. Thesis, University of Victoria

4. Wegner J.L., Yao M.M., and Bhullar S.K. "Dynamic wave soil structure inter-action analysis of a two-way asymmetric building system DSSIA-3D" *Journal of Engineering and Technology Research Vol. 1 (2)*, pp. 026-038, May 2009.
5. Wu W.H., Wang J.F. and Lin C.C. (2001) "Systematic assessment of irregular building-soil interaction using efficient modal analysis" *Earthquake Engineering and Structural Dynamics* Vol. 30, pp. 573-594, 2001.
6. Georgios N. Petropoulos (2008) "Large- Scale simulation of Soil-Structure interaction on building response in region" *The 14th World Conference on Earthquake Engineering* Oct 12-17, 2008, Beijing, China.

Reciprocal Influence of Inclined Subway Tunnels Constructed by Means of Artificial Freezing and Above-Ground Structures

I.I. Sakharov, V.N. Paramonov

Design Institute Georeconstruction, St.Petersburg, Russia

ABSTRACT: This paper deals with specificity of construction and maintenance of buildings located above inclined escalator tunnels in Saint Petersburg. In soft soil conditions characteristic of the city inclined tunnels as a rule are constructed by means of artificial freezing which causes significant settlements of the ground surface during thawing of the ice-soil cylinder. One of the problems reviewed in the paper is estimation of soil thawing influence on settlements of above-ground structures. The other featured problem is influence of buildings constructed above inclined tunnels on the tunnel linings.

INTRODUCTION

The presence of thick soft soil strata underlying the upper layer of silty sands is characteristic of the city centre in Saint Petersburg. This situation forces to construct the running subway tunnels and underground subway stations at depths of 40-60 m from the ground surface. The consequence of that is the necessity to construct long (quite often min 100 m) inclined escalator tunnels which connect stations with the ground-based vestibules. In view of the necessity to pass through great thicknesses of soft saturated soils, tunnels are constructed by means of artificial freezing.

The method of artificial freezing presupposes formation of ice-soil cylinders the thickness of walls of which can exceed 2-3 m. Such significant sizes of frozen soil layers lead to considerable absolute values of heaving deformations (during artificial freezing) and especially to large thawing settlements (during degradation of the ice-soil cylinder).

The processes of thawing of the ice-soil cylinder around the tunnel are accompanied by settlements of the ground surface and by deformations of buildings located in settlement trough. The absolute values of the settlements of the ground surface above the axis of the tunnels can reach 50 cm (Fig. 1), however

sometimes the displacements of greater values (up to 74 cm) were noted. The dimensions of the settlement trough in the transverse direction can reach 75 m from the axis of the tunnel, in the lengthwise direction the dimensions of the trough are close to the length of the inclined tunnel.

Thawing usually completes in 2-4 years after the end of tunnel construction and it is precisely during this period that the most intensive increase of deformations of the ground surface is observed. In view of involvement of the very large volume of soil in the settlement process after the complete thawing of ice-soil cylinder the development of the consolidation processes of the territory is observed which one has to take into account in design of buildings above the subway structures.

In addition to this, design of buildings in the tunneling zones needs an estimation of additional influence on these tunnels. In these cases it is necessary to calculate the additional pressures on the tunnel lining and the bending moments therein. In this case it is also necessary to exclude excessive settlement differentials of tunnel which can provoke its bending and opening of joints between the liners.

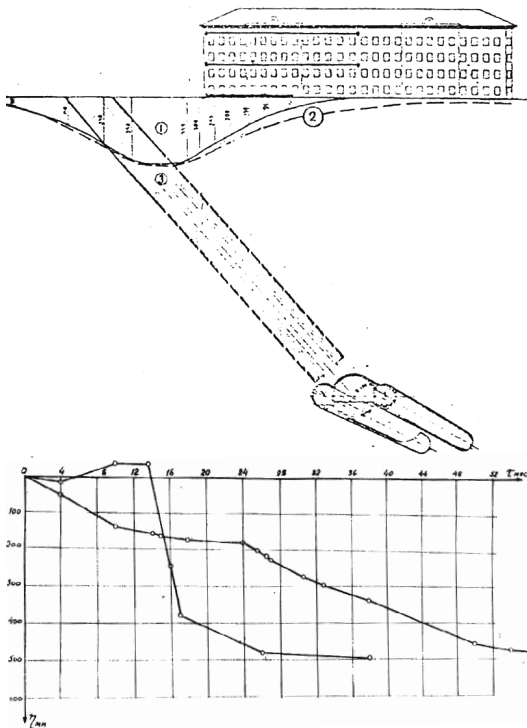


Figure 1. Vertical displacements of a building in the zone of influence of the inclined tunnel constructed by means of artificial freezing.

1. EVALUATION OF TUNNEL THAWING INFLUENCE ON SETTLEMENTS OF ABOVE-GROUND STRUCTURES

The main negative effect of construction of inclined tunnel is in the ice-soil cylinder thawing. Nevertheless, to estimate the duration of its initial formation, structural calculations of its lining, *etc* it is advisable to follow the complete cycle of formation and degradation of the cylinder. This means that the process of freezing and thawing must be considered in three-dimensional conditions, taking into account the duration of the processes.

The calculations of strains and stresses which occur in the system "structure-freezing (thawing) soil" should be based on mathematical models which schematize these processes. Let us briefly consider some features of the schematization.

It is obvious that solutions of all problems of soil freezing and thawing have to be based on a primary solution of the *temperature field*

problem. These solutions have to include the heat of phase transition with the moving boundary of the freezing front taken into account. In comparison with the classical Stefan problem the solution has to take into account the fact that the process of water becoming ice in thin pores of the soil is not instantaneous but gradual in the so-called spectrum of subzero temperatures.

The process of *frost heaving* is the complex process because of absence of any progress in the investigations of the structure of water, unknown properties of the fixed ground water, continuity of structural and textural changes during the freezing process and other factors. Therefore the analysis of the mechanism of *frost heaving* can be considered only from a phenomenological standpoint. The undeniable consequences of freezing are the volume changes of soils caused by the process of water becoming ice (of the pore water and water migrating into the freeze area). In addition, many experiments have confirmed the increase of the soil volume due to the frost caving. Hence the vertical deformation of heaving can be represented by some polynomial which includes the listed components.

Thawing of the frozen soil accompanied by melting of ice and incomplete reduction of pores causes settlements of soils. The value of the strain of thawing can be simply calculated with the use of models based on the physical properties of soils. It is also possible to use the models based on the results of special tests on thawing with splitting up the settlement into the so called "thermal-" and "load-" related settlements. The time of the settlements of thawing is determined by taking into account the consolidation of soils during thawing.

The program «Termoground» [1] is developed by the authors based on the above said assumptions. The main features of the program are as follows.

In order to establish the temperature distribution in a three-dimensional space the equation of the heat conduction with the phase transition is used:

$$\rho_d (C_{th(f)} + L_0 \frac{\partial W_w}{\partial T}) \frac{\partial T}{\partial t} = \lambda_{th(f)} \left(\frac{\partial^2 T}{\partial x^2} + \frac{\partial^2 T}{\partial y^2} + \frac{\partial^2 T}{\partial z^2} \right) + q_v, \quad (1)$$

where $C_{th(f)}$ – heat capacity of thawed or frozen soil; ρ_d – dry unit weight, T – temperature; t –

time; L_0 – specific heat of phase transition; λ – thermal conductivity of thawed or frozen soil; x, y, z – coordinates; q_v – power of the internal heat sources; W_w – water content due to unfrozen water in soil.

Relative vertical deformations of frost heave, perpendicular to the freezing front, are calculated from the following equation:

$$\varepsilon_{fh\perp} = 0.09(w_{tot} - w_w) \frac{\rho_d}{\rho_w} + 1.09 \int_0^{t_c} q_{wf} dt + \varepsilon_{cr} \quad (2)$$

Here the three-term formula includes the deformations due to freezing of the pre-winter water, originally located in the pores of the soil ($w_{tot}-w_w$); due to freezing of the migrating water (q_{wf}) and due to the frost cracks (ε_{cr}). The calculation of the first component of the formula is straightforward. The second and third components depending on the water level and soil type are calculated by special expressions derived from the numerous experimental data handling. Frost deformations parallel to the freezing front are calculated with the use of experimentally or analytically determined coefficient of anisotropy ψ .

The Ψ values obtained based on multiple laboratory data analyses of freezing clay soil of variable grading and moisture content at different temperatures can for the first approximation be determined by means of the following equation:

$$\Psi = -2.4 - 0.1 \cdot T + 3.3 \cdot W + 0.06 \cdot I_p. \quad (3)$$

Thawing deformations of soils are determined from the special oedometric tests by the expression:

$$\varepsilon_{th} = A_{th} + \delta_{ith} \quad (4)$$

where A_{th} – the "thermal" thaw deformation, δ_{th} – the "load" thaw deformation:

$$\delta_{ith} = m_{0th} \cdot p_i \quad (5)$$

where m_{0th} – the compressibility of the thawed soil, p_i – normal pressure.

If there are no special tests the thawing deformations are determined by the formula:

$$d\varepsilon_{th} = \frac{W - W_p - K_d \cdot I_p}{\gamma_w / \gamma_s + W_{tot}}$$

where: I_p – plasticity index; γ_w – specific gravity of pore water; γ_s – specific gravity of soil particles; K_d – compressibility ratio which depends on dispersion property of the soil and the normal stresses calculated by the empirical relation.

A situation where estimation of the effect of "freezing - thawing" is required is shown in Fig. 9. A new building was being built in the area of influence of the existing inclined subway tunnel.

The contour lines of the temperature of soil at the moment of the end of freezing (through 10 months) are shown in the Figure 3. According to the calculation the overall thickness of the frozen soil with the temperature lower than zero is 3 meters. The zero isotherm is shown in the Figure 3 and the rule notes the distance from it to the outline of future lining. The thickness of the ice-soil cylinder with the temperature on the outline of -2°C is 2,5 m, which was established experimentally and confirms the correctness of the executed thermophysical calculation.

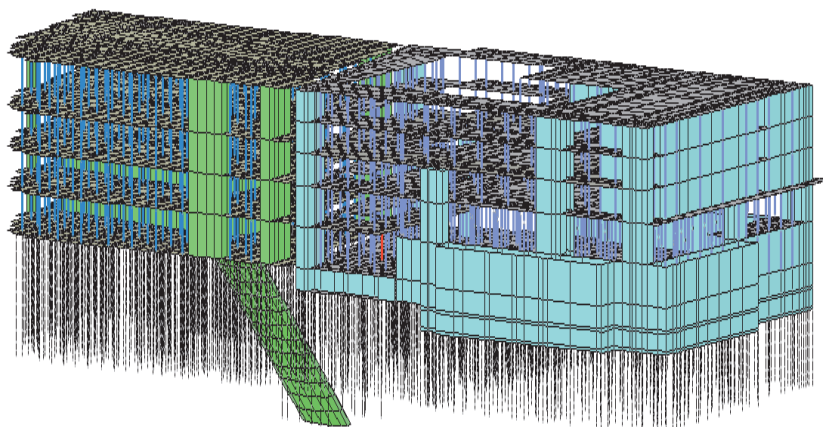


Figure 2. Location of the designed building above the previously constructed inclined subway tunnel (design detail)

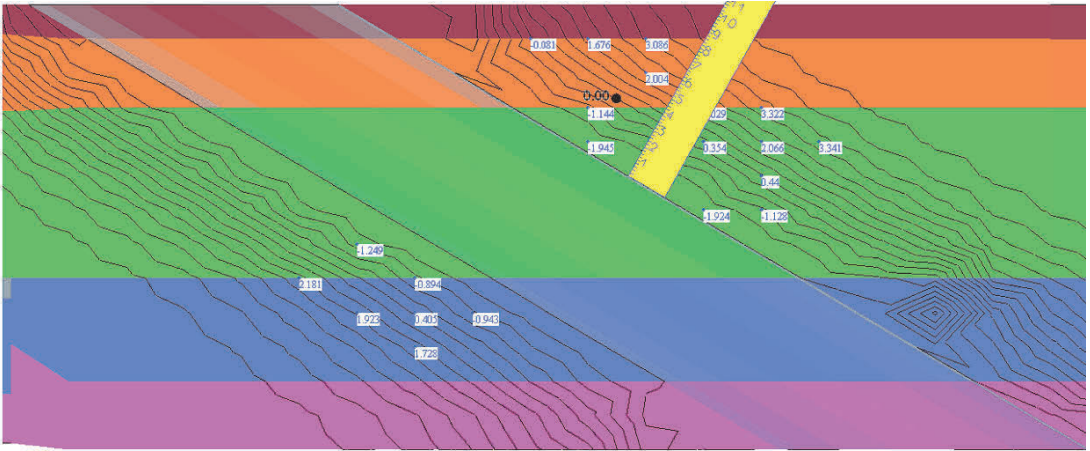


Figure 3. Contours of temperature around the inclined tunnel after freezing

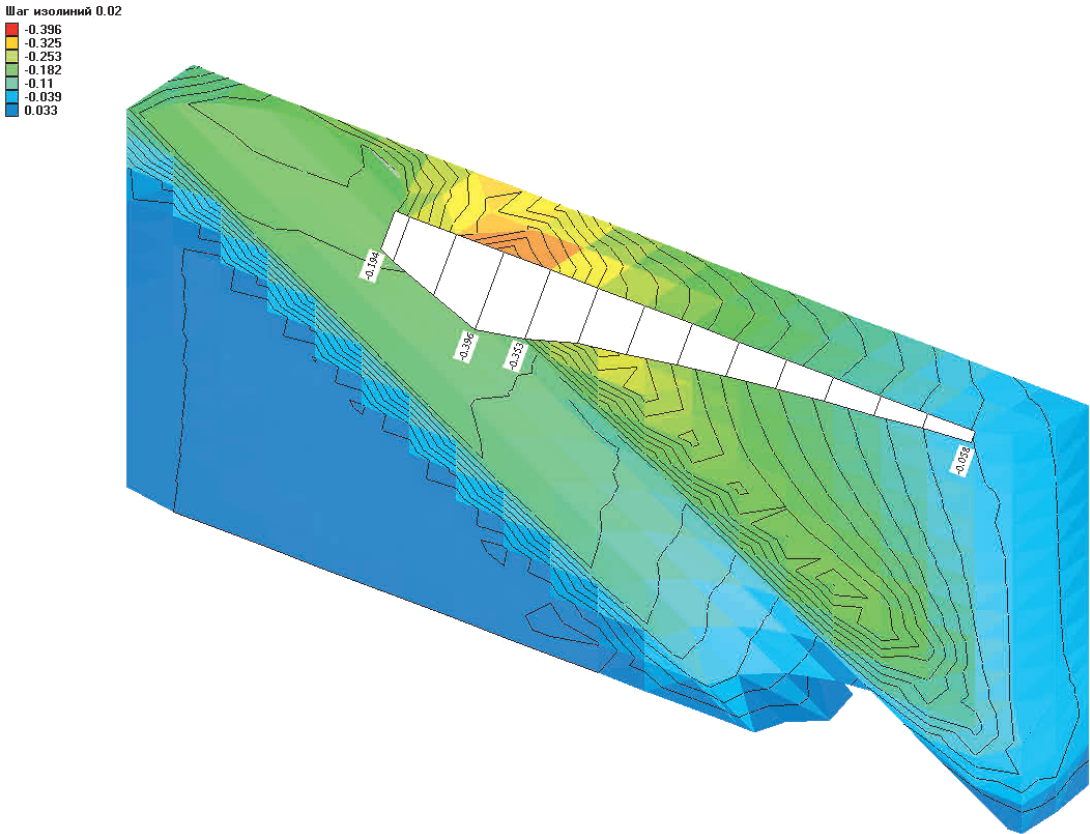


Figure 4. Diagram of the settlements of the ground surface above the axis of the inclined tunnel after thawing of the ice-soil cylinder

Шаг изолиний 0.02

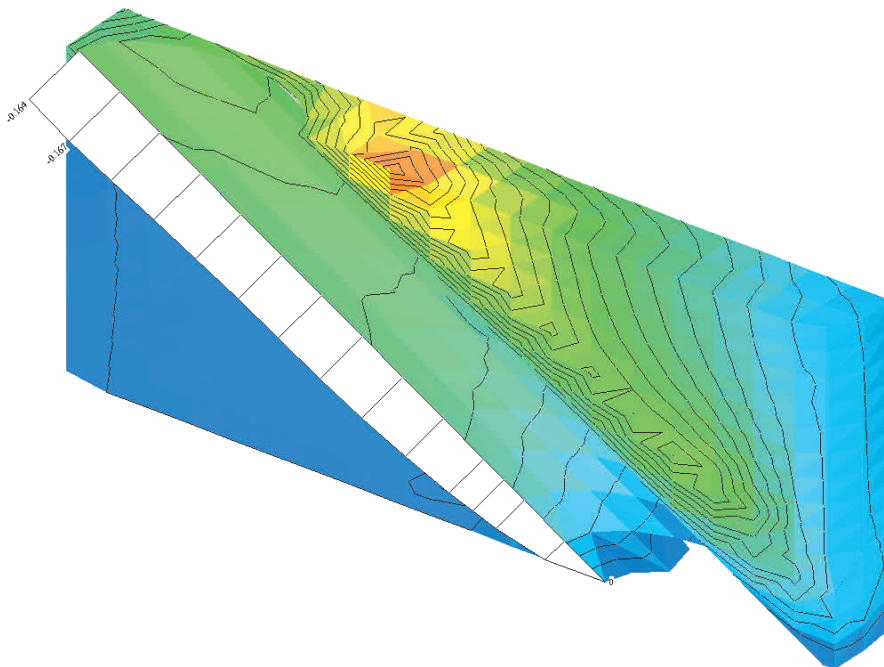


Figure 5. Diagram of the settlements of the inclined tunnel after thawing of the ice-soil cylinder

Шаг изолиний 0.001

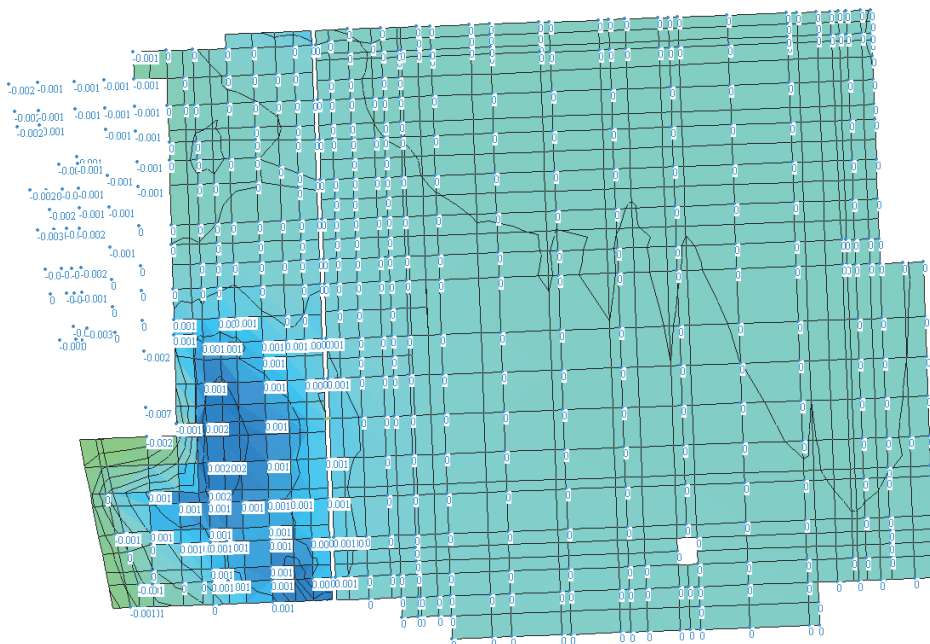


Figure 6. Settlements of the building due to the ice-soil cylinder thawing effect

Figures 4-6 show diagrams of the maximum settlement of the ground surface above the inclined tunnel, the settlement of the tunnel and possible settlements of the building due to the effects of thawing of the protective ice-soil cylinder. Maximum estimated settlement of the ground surface during thawing is about 40 cm, which is correlated with the numerous experimental data in St. Petersburg. Maximum settlement of the tunnel after thawing is 16.4 cm. In case of construction of the building on pile foundations in the early thaw, that is, in the most unfavorable case, the maximum expected settlement of the building due to the thawing of the soil does not exceed 1.6 cm, which is quite acceptable.

2. EVALUATION OF THE INFLUENCE OF THE BUILDING ON THE INCLINED SUBWAY TUNNEL

As an example we shall consider a construction project near metro station “Dostoevskaya” in Saint Petersburg. The existing wing of a building located above the inclined metro tunnel is listed for demolition in view of its unsatisfacto-

ry condition and a new building with an underground scope is intended in its place.

Let us specify the main difficulties of designing a new building on the site under consideration. They are as follows: undoubtedly, the great thickness of soft structurally unstable subsoil, and also three existing buildings in adjacency, allowing additional settlements not to exceed 2 cm. However, the presence of the inclined subway tunnel, which passes practically under the center of the new building, is by far the greatest design difficulty. The design had to limit additional pressures on the tunnel lining and the bending moments, and also to exclude tunnel deformations, capable of causing its bend and opening of the seams between the tubes.

It should be noted that the presence of the tunnel forces to transmit the load from the constructed object onto piles, located beyond the limits of the inclined tunnel, which leads to formation of a centrally oriented span in the constructed building with the width of more than 16 m. The remaining parts of the building, located out of the inclined tunnel zone, permit to arrange piles with essentially greater uniformity and to construct them at smaller lengths.

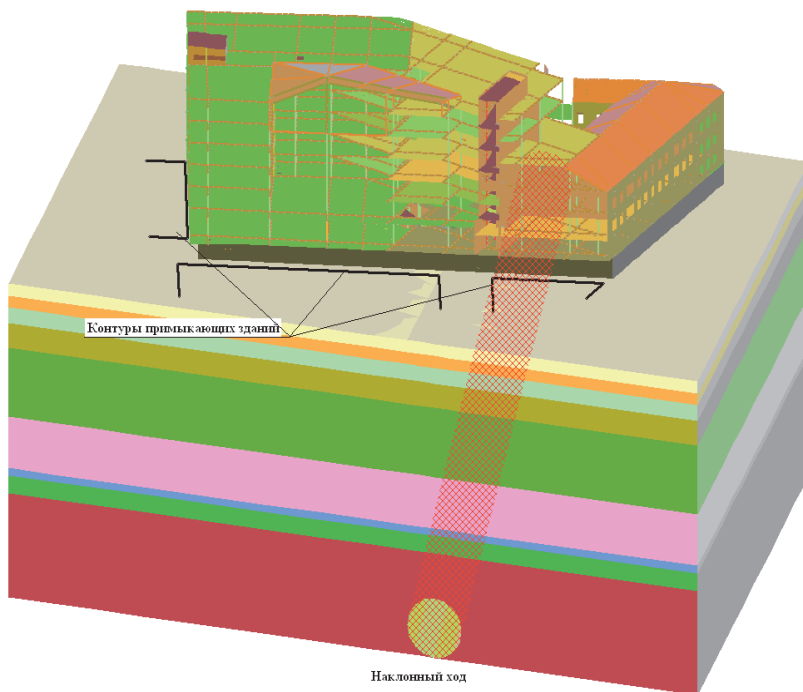


Figure 7. Finite element mesh.

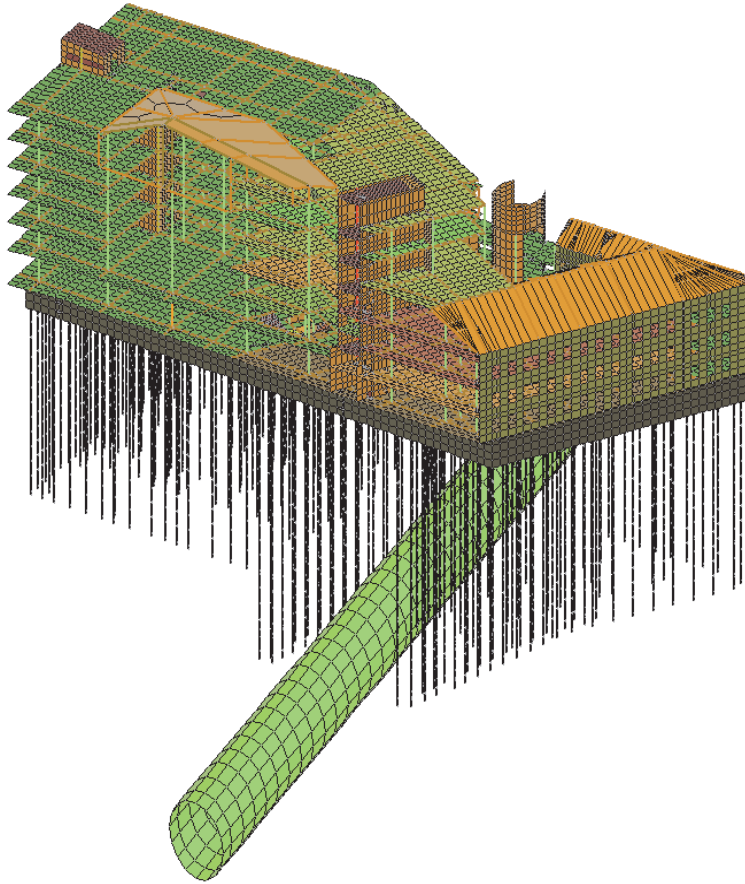


Figure 8. Design details (subsoil not shown).

The evaluation of the influence of the designed building on the inclined tunnel was produced with the use of Finite Element Method. The finite element mesh is shown in Figure 7. The design details of the building and the tunnel are given in Figures 8 and 9. The diagram of longitudinal pressures on the lining is given in Fig. 10. As can be seen from the diagrams of pressures, their maximum values do not exceed 20 kPa which is within the permissi-

ble range. Other calculated parameters (moments in two directions, settlements of the tunnel) also do not exceed the limiting values. Settlements of adjacent buildings do not exceed several millimeters (Fig. 11). The design loads transferred to the piles were in the range from 850 to 1800 kN (for the piles around the tunnel) and from 770 to 1840 kN (for the piles of the remaining part of the building).



Figure 9. Design details (subsoil not shown).

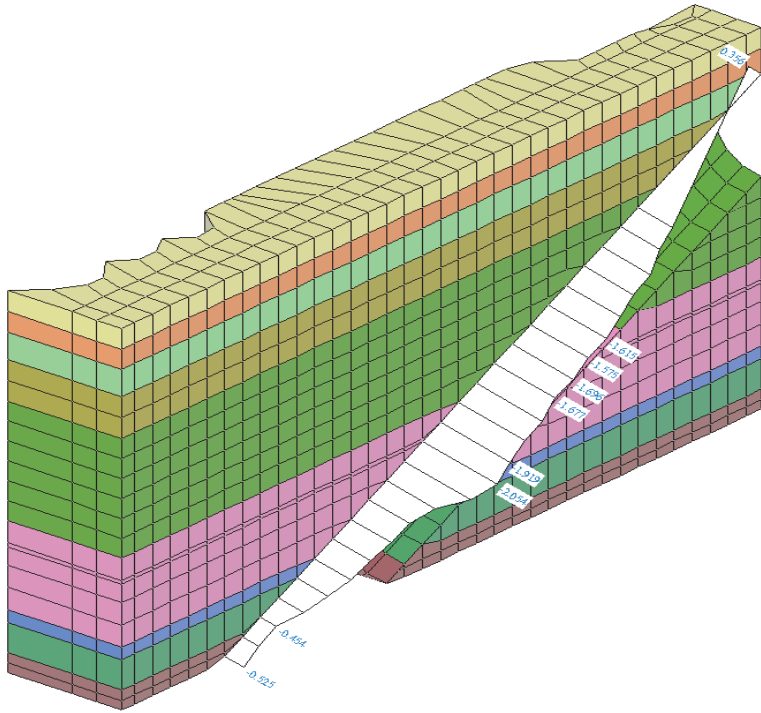


Figure 10. Diagram of longitudinal pressures on the lining, kPa.



Figure 11. Settlements of adjacent buildings, m.

3. CONCLUSION

The deep position of running subway tunnels and the large length of inclined tunnels are the specific problems of Saint Petersburg. The zones of influence of escalator tunnels are great, and in fact their construction by means of artificial freezing will still be used in the future, in spite of the obvious danger for the existing buildings and structures. At present, no reliable theoretical base or experimental data on this mutual influence are now in place, therefore the design scheme for the simulation of reciprocal influence of the building and the underground structure must consider the most unfavorable conditions of the solution. The examples given in the paper show that neither the analytical solution methods for the enumerated cases exist, nor can they be obtained, which requires development of special models based on the finite element method.

4. REFERENCES

1. Kudryavtsev S.A, Sakharov I.I., Paramonov V.N. Numerical predictions of freezing, heave and thawing of soils under footings in three-dimensional mode. Permafrost engineering. Proceeding of the fifth International symposium on permafrost engineering (2-4 September 2002, Yakutsk, Russia). - Yakutsk: Permafrost Institute Press, 2002. - Vol.1. P.198-202.
2. Улицкий В.М., Шашкин А.Г., Шашкин К.Г. Геотехническое сопровождение развития городов./Группа компаний «Геореконструкция»// Санкт-Петербург. 2010.

Behaviour of Barrage Foundation Due to Presence of Rock Including Soil-Structure Interaction

N.K. Samadhiya & Kumar Venkatesh

Professor, Department of Civil Engineering IIT Roorkee, India, nksamfce@iitr.ernet.in & Asstt. Professor, Department of Civil Engineering MNNIT, Allahabad-India, venkatesh@mnnit.ac.in

A.D. Pandey

Asstt. Professor, Department of Earthquake Engineering, IIT Roorkee, India, adpanfeq@iitr.ernet.in

ABSTRACT: Field conditions with regard to foundation media do not present uniform characteristics throughout its extent. It becomes important to examine the situation when the foundation media is non homogeneous. In order to investigate the effect of non-uniform foundation condition a typical barrage system has been selected, located at the site where the subsoil is partly river bound material and partly rock. Three dimensional eight noded isoparametric element have been employed for modeling the barrage component with foundation media, whereas the raft floor has been modeled using the plate bending element using finite element technique. Presence of the rock has been considered from the bottom of the models vertically as well as laterally. The finite element analysis has been performed to find out the variation of moments and deformations at the three sections of the raft floor which include the soil-structure interaction behaviour. The study has represented that presence of rock has affected the moments and deformations behaviour of the foundation.

1. INTRODUCTION

A barrage is a diversion headwork, which is employed to divert inflows into the canal from a river. In a barrage the crest is kept at low level and the gates alone affect heading up of water. During the floods, the gates are raised to pass the high flood flow. When the flood recedes, the gates are lowered and the flow is obstructed, thus maintaining the required pond level at the upstream of the barrage for feeding the main canal under gravity. Barrages are usually made of masonry, plain cement concrete or reinforced concrete, depending on the nature of foundation encountered, availability of construction material, dewatering problems, economy of construction, etc. A barrage can have gravity or a raft floor. In recent years, the hydraulic and structural engineers have taken up are seized upon the important task of evolving safe and economic design criteria for barrage raft floor due to several advantages such as less excavation and dewatering, lesser construction time, superior flexural behavior etc.

A number of analytical methods are available for the design of raft floors, viz., conventional method (Bowles, 1982), Baker's method

(Baker, 1948), Hetenyi's method (Hetenyi, 1964) and numerical methods (Desai et al 2000). Out of the above Hetenyi's method (Verma, 1981) is widely adopted for analysis and design of barrages raft floor in India as this method has also been recommended by Indian standard code (IS:11130-1984). The finite element analyses of barrages have been carried out by Sarkar (2001) and Sasidhar (2002). A comparative analysis of a barrage raft floor has also been carried by Venkatesh et al (2004) and Pandey et al (2005) on homogeneous media. However, this paper is an attempt to analyze the behaviour of barrage foundation on varying soil/rock media.

2. FINITE ELEMENT METHOD

The finite element method is a numerical procedure for analyzing structures and continua. It is a powerful tool in structural analysis of simple to complicated geometries. In the recent years with the advent of compact and powerful computers, the analyses performed by finite element method have become more acceptable. Finite element program has been employed in the present study.

The basic steps involved in the finite element method are as mentioned below.

- I. Discretization of the continuum.
- II. Calculation of the element stiffness matrices.
- III. Assembling the element stiffness matrices.
- IV. Calculation of the element load vectors.
- V. Assembling the element load vectors.
- VI. Imposition of boundary conditions.
- VII. Imposition of external forces.
- VIII. Calculation of the displacement vectors.
- IX. Calculation of the strains and stress field.

A detailed discussion on finite element analysis is beyond the scope of this paper but well documented in standard literature. (Desai and Abel, 2000; Krishnamurthy, 2002; Cook et al., 1989; Bathe, 1982; Zienkiewicz, 1977).

3. IDEALIZATION OF BARRAGE

Typical barrage bays 3-4, have been selected for this study. The barrage foundation of bays 3-4 is separated by expansion joints from rest of the bays. The plan of bays 3-4 (figure 1) with three sections of the barrage foundation in transverse direction (across the flow) i.e. Upstream section (a-a), section (b-b) and downstream section (c-c) at different distances from upstream edge have been chosen for the comparison of behaviour. The barrage raft floor with cut-off of bays 3-4 are completely resting on alluvial soil with single and double pier but suddenly at the edge of bay 4 towards bay 5 there is discontinuity in foundation soil media due to presence of hard rock as shown in typical transverse section of the bays 3-4 (figure 2).

4. ANALYSIS CRITERIA

The investigations are based on linear elastic model for representative load cases. The self-weight of the soil and rock media has not been considered as it has been assumed that entire soil and rock media is already settled by its own weight. It has also been assumed that within the entire soil & rock media, elastic modulus and poisson's ratio remain the same as well as soil and rock junction has been assumed to be in contact with each other. The presence of the rock has been taken up to study the effect of intruded rock on barrage foundation of bays 3-

4, if it extends toward the barrage foundation of bay 4 and bay 3 from bottom and side. The presence of rock is taken in to consideration from the bottom towards the foundation and from the edge of bay 4 towards bay 3. The vertical extent of rock is studied in 3 cases and the lateral extent of rock is studied in 2 cases thus making a total of 6 cases as given in table 1.

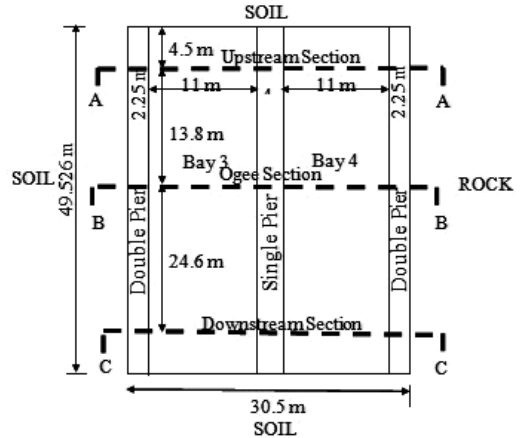


Figure 1. Plan of barrage.

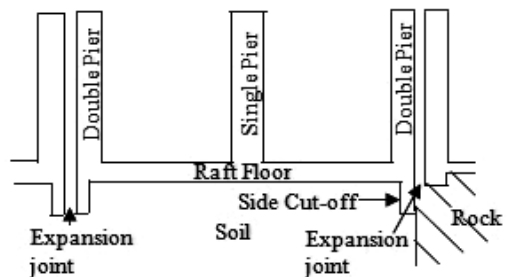


Figure 2. Transverse section of barrage.

Table 1. Vertical and lateral intrusion of rock below bays 3-4 raft floor.

Barrage Bays 3-4	Vertical extent of rock (From bottom in m)	Lateral extent of rock (From edge of the bay-4 double pier side in m)
Case 1 (Figure 3)	20	15.25
Case 2		30.5
Case 3	40	15.25
Case 4		30.5
Case 5	60	15.25
Case 6 (Figure 4)		30.5

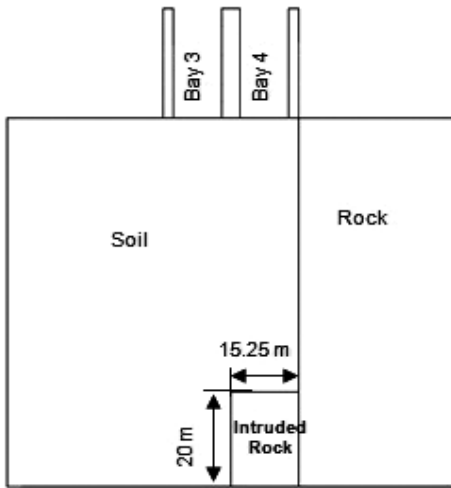


Figure 3. Intrusion of rock (Case1) in bays 3-4.

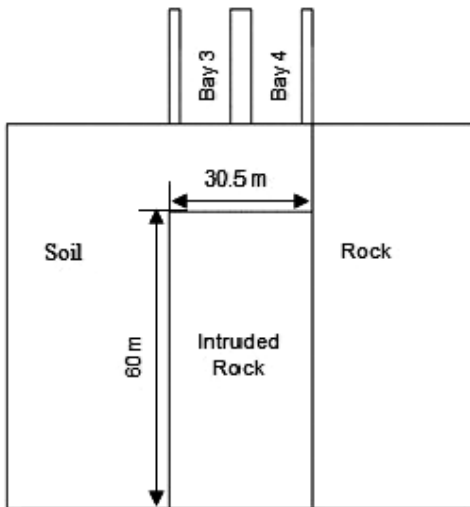


Figure 4. Intrusion of rock (Case 6) in bays 3-4.

5. MODELLING AND MESHING

Three-dimensional eight noded isoparametric elements have been used for the modeling of soil and rock media (king, 1977). The cut-off, pier, abutment wall and beam have also been modeled using eight noded isoparametric brick elements. The element is defined by eight nodes having three degrees of freedom at each node, translations in the nodal x, y, and z directions. The four noded three-dimensional isoparametric shell elements have been used for barrage foundation modeling to simulate the behaviour of foundation as plate bending element (king, 1977), having six degrees of freedom per node capable of taking loads normal to the plane. In this model the depth of the soil and rock media considered is 80m from the crest level. The extent of surrounding soil and rock up to 35m on both sides of the transverse section of the raft and 50m on both in upstream and downstream side equivalent to the length of the foundation along the flow has been considered. Several iterations were made for refining the mesh of the models from coarser to finer till the values of moments at the same section under study in the two consecutive models converged under gravity load. The material properties of various components of barrage as well as for soil and rock media are as given in table2. The adopted model with finite element mesh consisting of the pier and beam structure with the supporting foundation and soil/rock media has been presented in figure 5 considering soil structure interaction. The dark grey portion in the figure resembles the rock portion. The total number of elements used for the adopted finite element model is 18744, which resulted in 21204 nodes in the model.

The boundary condition imposed on the finite element models consist of restraining the limiting boundary of the soil and rock in such manner that displacement normal to the boundary surface are restrained i.e. The ends along and across the direction of flow, soil/rock media is restrained against the horizontal displacement but the base of the soil/rock media at the depth of 80 m have been restrained against vertical and horizontal displacement.

Table 2. Material properties used in bays 3-4 model.

Components	Modulus of Elasticity (E) (kN/m ²)	Unit Weight (γ) (kN/m ³)	Poisson's Ratio (μ)
Pier/Abutment	2.5×10^7	25	0.15
Raft Floor	2.5×10^7	25	0.16
Cut-off	2.4×10^7	25	0.18
Foundation soil	1×10^5	20	0.3
Foundation rock	1×10^7	26	0.25

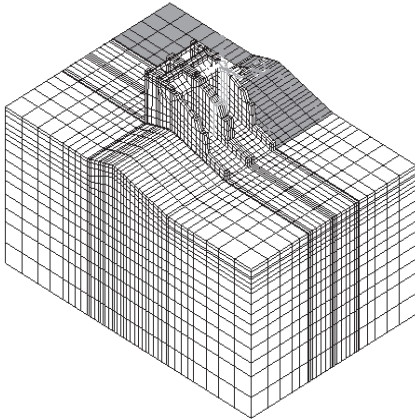


Figure 5. 3D-Finite element discretization of the Barrage with soil and rock system for bays 3-4.

6. RESULTS AND DISCUSSION

Analyses have been carried out for intruded and non-intruded cases. The effects of intrusion of rock on the moments of the foundation for all the six cases have been shown in Figures 6 to 8 for upstream, ogee and downstream sections respectively. The compared moments for all the cases indicates that there is a significant difference in the moments when rock is intruded beyond 40 m from the bottom of the soil/rock media. The moments obtained from first four cases resemble the non-intruded condition whereas the last two cases represent the change in the magnitude of the moments at upstream, ogee and downstream sections of barrage foundation which considers the soil-structure effect. The quantitative variations at the centre of foundation between first four and last two cases at upstream and ogee section are around 16% whereas for downstream section the

variation is about 25% which specify that intrusion is affecting the moments largely at downstream section compared to upstream and ogee section.

Figures 9 to 11 represents deformations of foundation at different sections considering intruded and non intruded cases. Differential settlement of foundation can be seen as barrage foundation is resting on varying soil/rock media. Significant reductions in the deformations have been seen with the increase in the intrusion of the rock. Deformations of the first four cases resemble the non-intruded condition, whereas the last two cases which are at the height of 40 to 60 m indicate the large quantitative difference at all the section compared to the other cases. The moments and deformations of foundation have reduced as the overall stiffness of the foundation media has also increased.

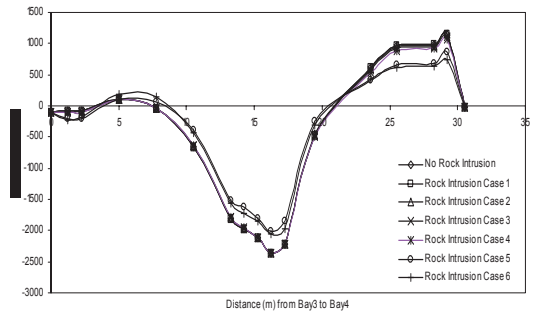


Figure 6. Moments 'Mz' at upstream section (A-A) considering gravity load with and without rock intrusion.

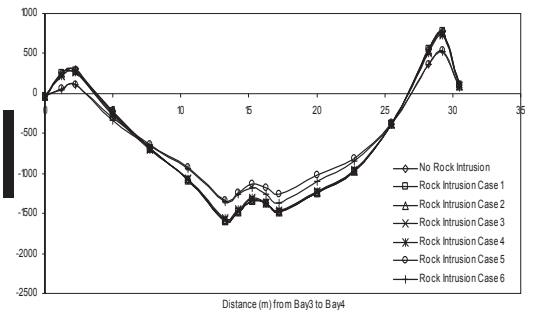


Figure 7. Moments 'Mz' at ogee section (B-B) considering gravity load with and without rock intrusion.

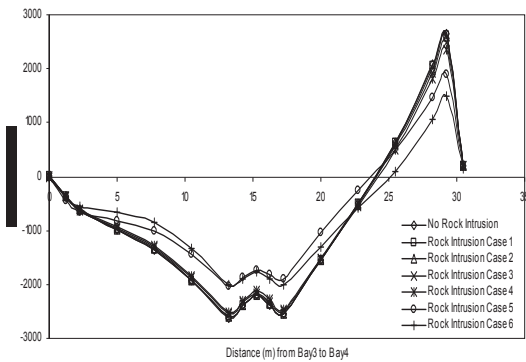


Figure 8. Moments 'Mz' at downstream section (C-C) considering gravity load with and without rock intrusion.

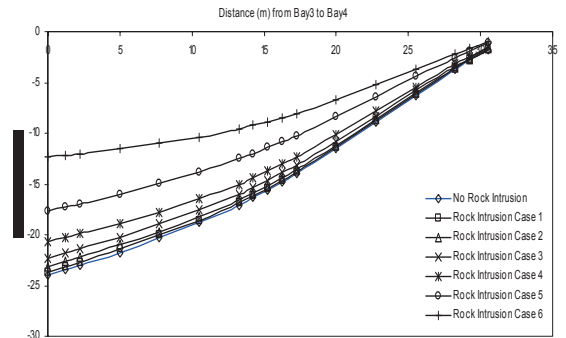


Figure 11. Deformation at downstream section (C-C) considering gravity load with and without rock intrusion

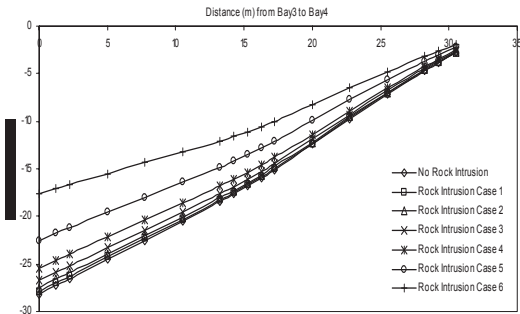


Figure 9. Deformation at upstream section (A-A) considering gravity load with and without rock intrusion

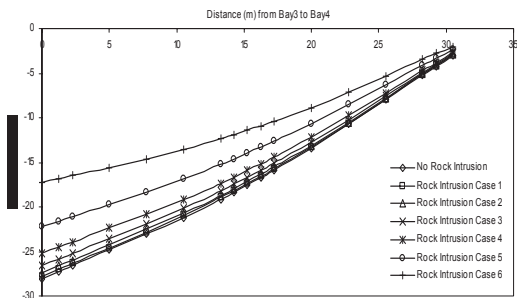


Figure 10. Deformation at ogee section (B-B) considering gravity load with and without rock intrusion

7. CONCLUSIONS

Based on the comparison of moments and deformations at a various sections of the barrage raft floor for intrusion and non-intrusion of rock, the following conclusions may be drawn:

- i) The moments and deformations reduces with the intrusion of rock and it has been attributed to the increase in the stiffness of soil/rock media which influenced the behaviour of foundation at every section.
- ii) The intrusion of rock from 40 m to 60 m was most critical from the base which signifies that intrusion of rock within the 40 m of ground level is going to change the behaviour of foundation significantly.
- iii) The intrusion of rock also affecting the soil-structure interaction behaviour which are depicted through change in moments and deformations.
- iv) The three-dimensional system as represented by finite element method is able to account for the geometrical disposition of the barrage foundation and spatial variation of stiffness for soil/rock media.

8. REFERENCES

- Baker, A.L.L. 1948. *Raft foundations, the soil line method of design*, Concrete publications limited, London.
- Bathe, K.J. 1982. *Finite element procedures in engineering analysis*, Prentice-hall, Eaglewood cliffs, New Jersey.
- Bowles, J.E. 1982. *Foundation analysis and design*, Mcgraw Hill, New York.
- Desai, C.S. & Abel J.F. 2000. *Introduction to the finite element method*, CBS publisher and distributors, New Delhi.
- Verma, C.V.J. 1981. *Design and construction features of selected barrages in india*, Publication no. 149, Central board of irrigation and power, New Delhi.
- Hetenyi, M. 1964. *Beams on elastic foundations*, seventh printing, The university of michigan press, USA.
- IS: 11130: 1984. *Criteria for structural design of barrages and weirs*, Bureau of indian standards, New Delhi.
- King, G.J.W. 1977. An introduction to superstructure/raft/soil interaction, Proc. Int. Symposium on soil-structure interaction, University of Roorkee, Roorkee, PP. 453-466.
- Krishnamoorthy, C. S. 2002. *Finite element analysis, theory and programming*, Tata Mcgraw Hill, New Delhi.
- Pandey, A.D., Sharma, N., Venkatesh K. & Kulkarni M.D. 2005. Comparative study on analysis of barrage raft by hetenyi's method and FEM, *Water and Energy International Journal*, Vol. 62 No.1, pp.40-47.
- Sarkar, S. 2001. *FEM analysis of barrage under varying subsoils condition*, M. Tech. Dissertation, Department of Earthquake Engineering, IIT Roorkee (India).
- Sasidhar, T. 2002. *3-d finite element analysis of a barrage*, M. Tech. Dissertation, Department of Earthquake Engineering, IIT Roorkee (India).
- Venkatesh, K., Pandey, A. D. & Samadhiya, N. K. 2004. Comparative analysis of raft foundation for a barrage in india. Proc. Int. Conf. On Geotechnical Engineering, Sharjah (UAE), pp. 468-473.
- Zienkiewicz, O.C. 1977. *The finite element method*, Mcgraw-Hill, London.

Evaluating Current Movements of the Earth Surface for the Purposes of Proving Referential Integrity of the Principal Markers in the Levelling Network of St. Petersburg and Definition of Long-Term Settlements of Buildings and Structures

V.A. Vasenin
Design Institute Georeconstruction, St.Petersburg, Russia

ABSTRACT: The paper deals with issues capable of causing changes in level indications of the fundamental benchmark of Russia – the Kronstadt Gauge. The author considers the processes of the Baltic Sea rise and the uplift of Fennoscandia, comparing time-related tidal gauge level variations in multiple locations along the Baltic coast. The study identifies contemporary prevalent uplift trends in the earth crust in St.Petersburg area and defines their rates.

A vast practical interest exhibited by designers and builders working in complicated ground conditions in St.Petersburg is focused upon proper evaluation of settlements of contemporary and historic buildings. For such evaluations to be reliable the researcher must be in possession of long-term settlement monitoring data.

To render proper long-term settlement evaluations it would be technically sensible to re-levell geodetic stations and wall benchmarks comprizing the local levelling network. This method is considerably wide-spread and has been used repeatedly to establish both deformation rate and stability of survey markers [8].

The all-important issue in this respect is a study of possible deformability of the primary survey markers of the city levelling network. Correspondingly, it is necessary to thoroughly consider the initial primary levelling point used in the Russian Federation and a number of CIS countries – the Kronstadt Gauge. The present paper presents a study of the levelling network development, contemporary vertical movement of the regional earth's surface, and stability of the primary survey markers.

The inception of level measuring systems is traditionally related to the mean sea level. It used to be believed that the mean sea level is the same for all locations (save a certain amount of average annual fluctuations). However, the state-of-the-art level of expertise in understand-

ing changes in the level of the global ocean proves this assumption to be far from reality.

Monitoring of the Baltic Sea level commenced as early as in 1703 in line with a ruling of tsar Peter the First of Russia on the island of Kotlin (in the Marine Canal of the city of Kronstadt). However, regular monitoring began only in early 19th century. The water levels were monitored in the same way as nowadays, using notched vertical planks indicating various heights, known as tidal gauges, that were installed at gauge stations.

The results of annual measurements of the average at the gauge station allowed the hydrographer vice-admiral M.V. Reineke to define the average annual level of the Baltic Sea over the period 1825–1839 which was mounted on a granite pier of the Siniy Bridge over the Obvodny Canal in Kronstadt. As had been suggested by the Department of Military Topography of the General Staff in 1872, that point was taken as primary in establishing all heights in Russia.

Over the period between 1805 and 1929 level monitoring was conducted with the help of timber gauge-planks. As of 1930 until 1941 monitoring was ongoing in Kupecheskaya Haven in Kronstadt. Since 1951 water levels have been taken off the gauge mounted on a pier of the Siniy Bridge (Fig. 1, *a*). Near to the Kronstadt Gauge there is a pavilion of the

Marine Depth Gauge, built in the architectural fashion prevalent in the times of tsar Peter The First (Fig. 1, *b*). A marine depth gauge is an automatic recorder with which to measure the water level. Its meter is immersed into a 7-m depth standpipe, linked to the water surface in the canal. The device was installed in 1897 and is still in operation. The result measurements according to the Kronstadt Gauge and according to the Marine Depth Gauge are regularly compared [10].

Based on the results of water measurement in Kronstadt over the entire monitoring period it is possible to plot water levels in the Baltic Sea (Fig. 2). Annual average fluctuations of the sea level give the researcher an opportunity to assess earth's crust movement around Kronstadt.

A high degree of interest is incited by mean levels of the Baltic Sea calculated by various researchers over a given period of measurements (Table 1). The data contained in Table 1, prompted a conclusion that the level of secular uplift of the earth's crust around the Kronstadt Gauge reached about 2 cm over the past 100 years (1839–1939 – see also Fig.2).

In Fig. 2, where annual mean water level changes in the Baltic Sea are represented until 2006, their general linear trend is identifiable as constituting a rise of 0,51 mm/year. However, that curve can be more correctly represented by two consecutive trends: (1) a long absence of any change in the annual mean level of the Baltic Sea (1835–1947); (2) its rise at the rate of maximum 1,75 mm/year (1947–2006).

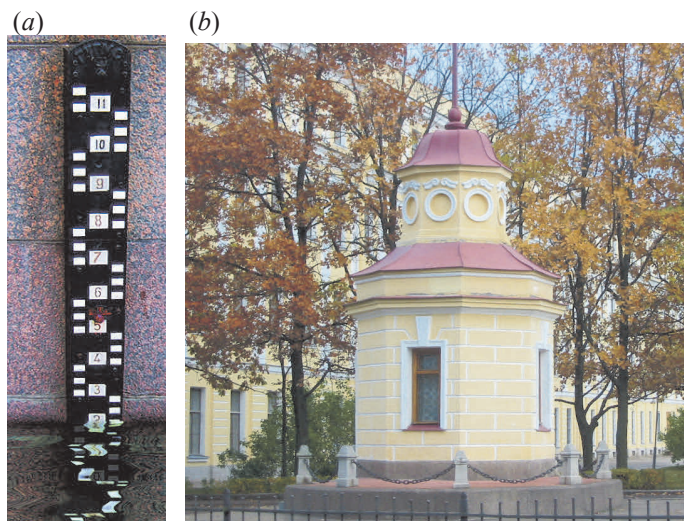


Fig. 1. The Kronstadt Gauge on the pier of the Siniy Bridge over the Obvodny Canal in Kronstadt (*a*) and the Marine Depth Gauge pavilion (*b*)

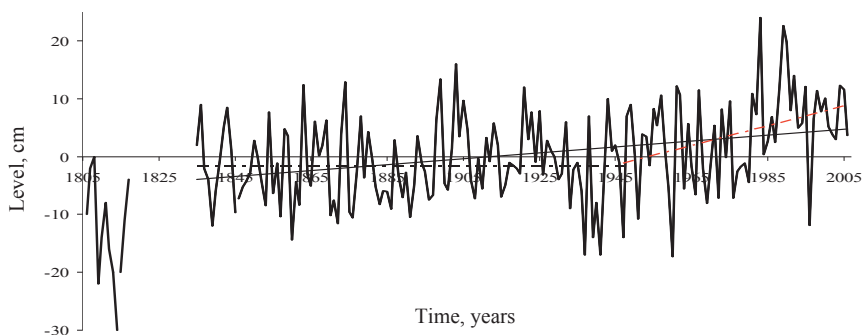


Fig. 2. Change of the Baltic Sea water levels in Kronstadt since 1806 until 2006 [12]: the black solid line – linear approximation 1835–2006; the black dotted line – linear approximation 1835–1947; the red dotted line – linear approximation 1947–2006

Table 1. Height (H) of the mean level of the Baltic Sea read from the nought of the Kronstadt Gauge [8]

Researcher	H , m	Period of measurements, years
M. F. Reineke	0,0000	1825–1839
V. E. Fuss	-0,0127	1841–1850
N. Saltykov	-0,0216	1841–1886
V. E. Fuss	-0,0102	1863–1872
A. N. Bronsdorf	-0,0338	1841–1885
S. D. Rylke	-0,0350	1841–1890
V. E. Fuss	-0,0234	1841–1895
N. Saltykov	-0,0145	1841–1850, 1863–1885
N. Saltykov	-0,0190	1873–1885
V. E. Fuss	-0,0127	1841–1910
L. F. Rudoviz	-0,0151	1841–1913
TSNIIGAiK	-0,0170	1841–1939

Amongst the main factors contributing to water rise at that monitoring station the following are normally listed:

- Eustatic rise of the global ocean (influenced by intensified glacial retreat, rise in precipitation volumes, increased tributary contribution by rivers, etc);
- Global uplift of the earth’s crust in the region of the station;
- Possible local deformation of the bridge piers resulting from intensified traffic over the bridge;
- Overall sinking of the area due to increased dewatering activities;
- Construction of St.Petersburg Flood Prevention Complex (“The Dam”).

Below, we shall deal with all the above factors, potentially leading to a change of Baltic water trends at the monitoring station under consideration.

To evaluate secular rise of the earth’s crust it is necessary to study changes of the Baltic Sea water level over time as measured by other

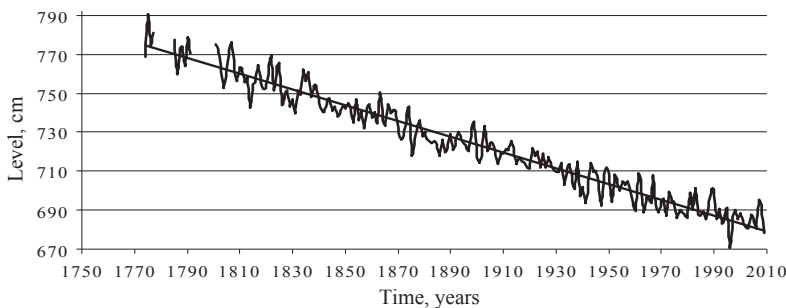


Fig. 4. Mean annual water level of the Baltic Sea in Stockholm since 1774 until now, courtesy of the Swedish Meteorological Institute [16]

monitoring stations in the area under consideration. Fig. 3 shows the major stations located on the Baltic Sea (marked with squares).

First, I shall consider changes of annual average levels of the Baltic Sea in time as provided by stations with long-term standing records. Amongst those the stations of particular interest are the ones in Stockholm (Fig. 4); Helsinki (Fig. 5), Hamina (Finland) (Fig. 6) and Świnoujście (Poland) (Fig. 7). Long-term charts of the Baltic Sea level change, as shown by the first three, identify apparent trends towards its lowering. It must be noted at this point that a similar trend is exhibited by the Valamo Monitoring Station, the data from which is used to define the water level in the Ladoga Lake (Fig. 8). However, in Poland the major trend seems to be directed towards rising of the sea level (see Fig. 7).

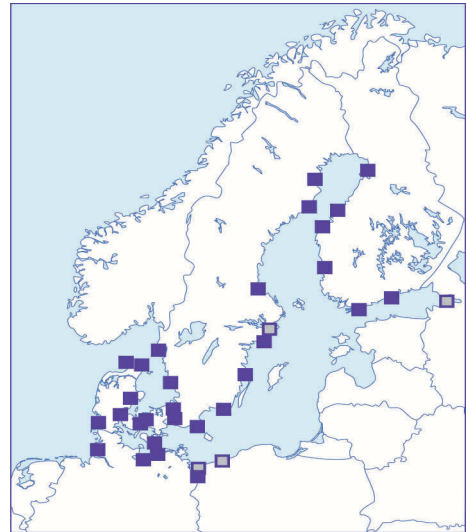


Fig. 3. Locations of level gauges on the Baltic coast: grey squares – measuring stations with long-term monitoring history; black squares – measuring stations with shorter-term monitoring history [17]

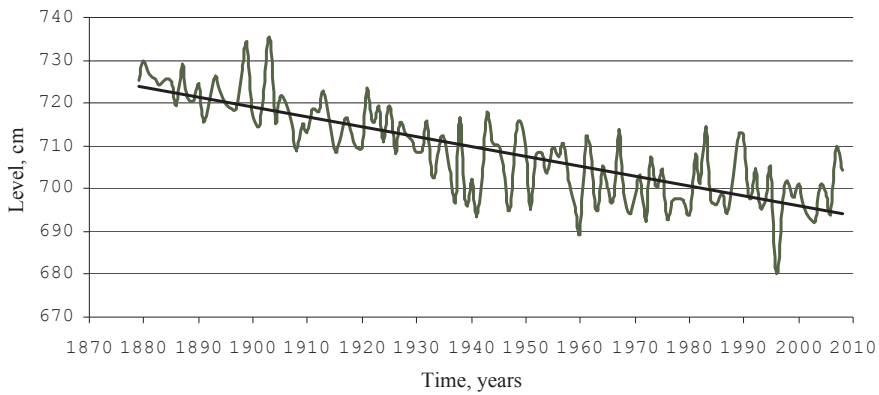


Fig. 5. Mean annual water level of the Baltic Sea in Helsinki since 1879 until now, courtesy of the Finnish Meteorological Institute [24]

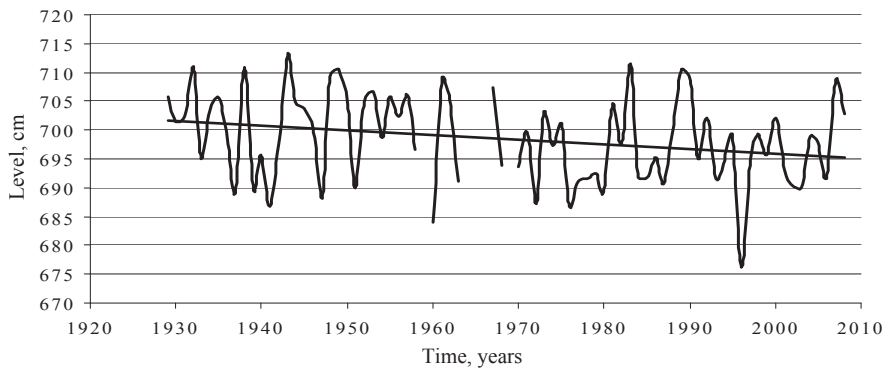


Fig. 6. Mean annual water level of the Baltic Sea in Hamina since 1930 until now courtesy of the Finnish Meteorological Institute [24]

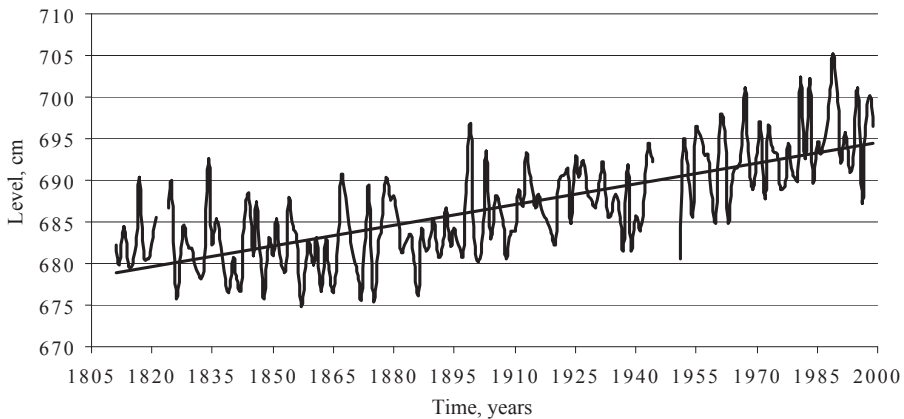


Fig. 7. Mean annual water level of the Baltic Sea in Świnoujście, courtesy of the Polish Meteorological Institute [24]

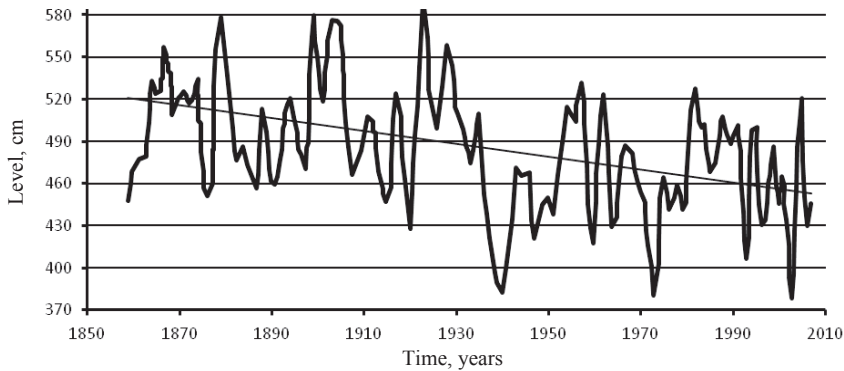


Fig. 8. Mean annual water level in the Ladoga Lake since 1859 until now [1]

The trend towards sea retreat in the Gulf of Bothnia has been known for quite a long time. Slow movements of the coastline became a subject for study as early as in 17th-18th centuries. To understand the nature of this phenomenon I shall describe the conditions prevalent in the region in more detail. This region is commonly referred to as Fennoscandia. This natural country comprises Scandinavian Peninsula, the territory of Finland, Kola Peninsula and a part of the Russian Federation to the north-west of the line “The Gulf of Finland of the Baltic Sea – the Ladoga and Onega Lakes – the Onega Bay of the White Sea”.

The history of formation of Fennoscandia is more or less unified – there for a long time processes of transport and erosion (by actions of water, wind ice, etc) of crushed solid crystalline and metamorphic rock with their gradual accumulation in lowered areas of the earth’s surface have been ongoing.

During the Quaternary period Fennoscandia was the centre of repeated formation of glaciers. The “young” character of its terrain and landscape is essentially defined by a lengthy stay of glaciers and their relatively recent retreat (the northern areas of Fennoscandia became glacier-free around 8–9 thousand years ago, whereas its southern areas were released from ice approximately 12–14 thousand years ago. It is by the recent presence of the glacier that the large number of lakes and glacial deposits in the area can be explained.

The retreat of the sea registered at many monitoring stations was initially (one may boldly say until the beginning of the 19th century) related to the overall lowering of the

global ocean. Later another possible explanation “surfaced”, *i.e.* the general rise of the earth’s crust in Fennoscandia. There are at least three hypotheses wherewith the observed rise can be explained [4, 5]: (1) general tectonic activity of the Baltic Shield; (2) glacio-isostatic rise of the terrain; (3) a combined effect of both the tectonic processes and the isostatic rise. The most popular amongst researchers is the second hypothesis, of which the gist is roughly as explained below. As the load from the glacier increases the earth’s crust is depressed and lowered, whereas with the lifting of the load the earth rebounds. In view of the fact that the melting of the glacier masses took a rather continuous time to occur and came to natural conclusion quite recently (by geological time standards), the observed phenomenon of the uplift of Fennoscandia and its rate are determined by the viscosity parameter of both the earth’s crust and its underlying strata [23].

Based on the results of sea level measurements at meteorological stations located alongside the entire perimeter of the Baltic Sea, numerous researchers were able to map the supposed uplift of the surrounding area. For such mapping it is important that the considered measurements should coincide in time. However, as a rule, the available records obtained at different monitoring stations correspond to different periods of time. Therefore, it becomes rather difficult to collate the measurements for the whole area. Correspondingly, the uplift maps should be plotted not so much in terms of vertical movements, as in terms of rates (velocities) of those movements. Several of such maps are now available [28]. The most comprehen-

sive regional map of post-glacial rebound was compiled by M. Ekman (Fig. 9). When charting such maps, the trends of water level changes in the Baltic Sea at the monitoring stations used to assess the uplift rate, are assumed as linear. To chart a postglacial map, like the one presented in Fig. 9, data was obtained from such monitoring stations as having reasonably long observation periods (roughly 100 years, 1892–1991).

Considering the map adduced in Fig. 9, the maximum vertical movements are instantly noticeable as prevalent in the northern part of the Gulf of Bothnia, totalling 8,8 mm/year. Their minimum values are registered on the south coast of the Baltic Sea. During the period considered (1892–1991), the rate of the crust uplift in Kronstadt [13, 14, 26] reached 0,09 mm/year.

The map of the vertical movements of the earth's surface in Fig. 9 is charted relative to the sea level. However, as has been noted above, the sea level itself is liable to instability. It was as early as in 1940 and 1941 that Torarinson

and Guttenberg demonstrated the annual rate of the global ocean rise (between 1807–1939) to be 1,1 mm/year, and concluded that it had eustatic nature [13, 15].

Figure 10 contains graphs representing reconstruction of the global change in sea level over the last 300 years (1700–2000) [18]. The graphs demonstrate that the dependency of the rate of change in average annual sea level on time is a non-linear function. In 2000 this dependency reached approximately 2 mm/year.

Figure 11 contains a map of movement rate contours plotted based on data as contained in [25, 28] with account of the first and the second class levelling results. The contours on the Russian side (in the area of the Ladoga Lake) are based on Russian monitoring data over the past twenty years and have not been finally verified (even a minor error in measurement results can significantly affect the distribution of contours on the map). The map was complemented with third grade levelling results.

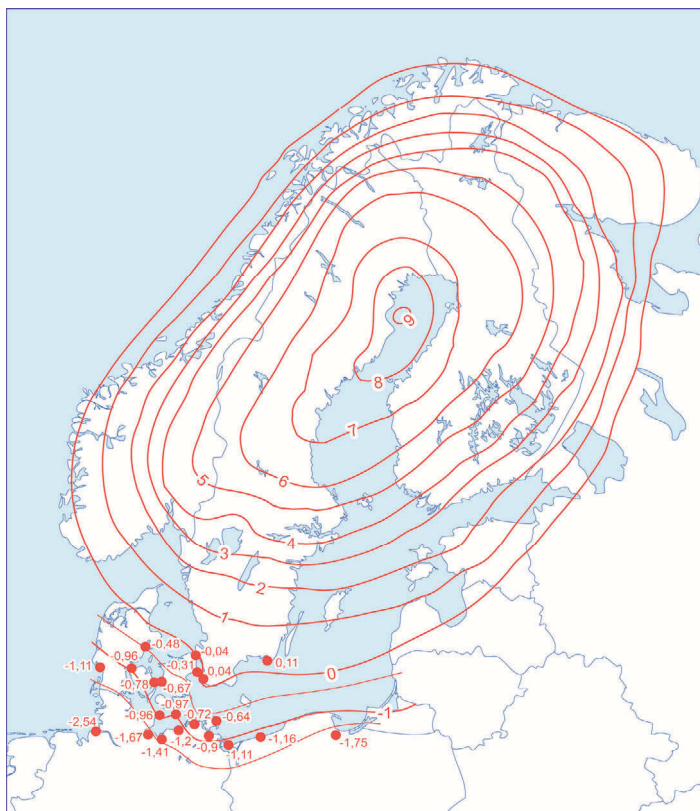


Fig. 9. Rate contours (mm/year) of postglacial rebound in Fennoscandia (according to [13, 14, 26])

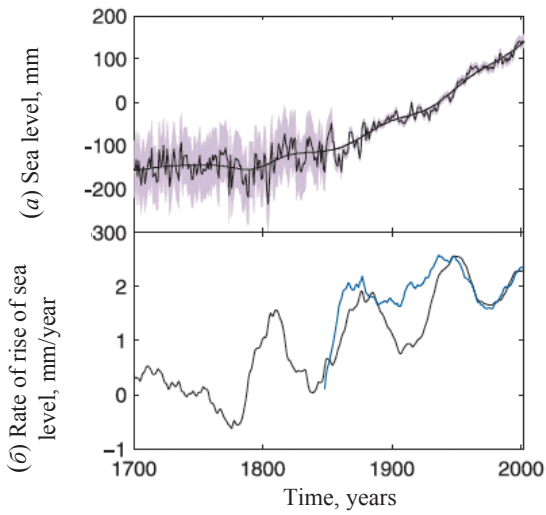


Fig. 10. Change of mean annual global sea water level (a reconstruction): (a) – change of sea level (a smoother black line – the general trend of change; grey shading being a possible mean quadratic displacement); (b) – corresponding changes of the rate of sea rise (blue line – changes of the sea level in the north-east region of the Atlantic, for the purposes of comparison) [18]

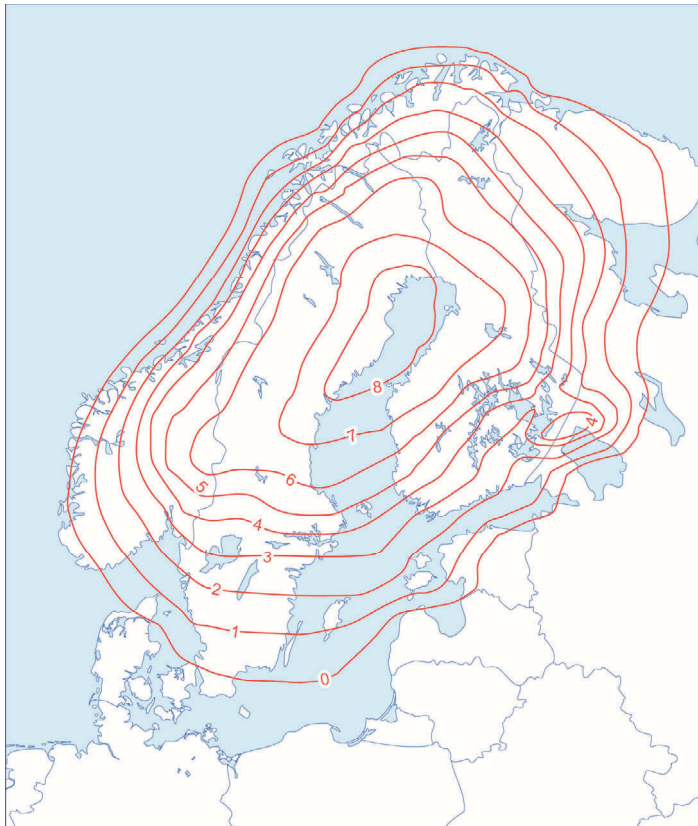


Fig. 11. Rate contours (mm/year) of postglacial rebound in Fennoscandia (according to [25, 28])

Apart from level gauging, in Fennoscandia since 1993 continuous GPS (Global Positioning System) measurements have been underway within the framework of BIFROST Project (The Baseline Inferences for Fennoscandian Rebound Observations Sea Level and Tectonics). The data collected by stationary GPS-stations provide a possibility to build spatial vectors of their displacements thus enabling one to chart maps of the earth's movements both in vertical and in horizontal directions. Figure 12 contains contours of vertical displacements and displacement vectors of separate GPS-stations in Fennoscandia over the last 7 years of observations [22, 23].

That map was prepared using the data from 34 GPS-stations of the Swedish SWEPOS network (21 receivers) and the Finnish FinnRef network (12 receivers). Based on such maps many researchers develop and verify numerical models of the earth's crust uplift, reconstructing a space-time history of the latest ice age and distribution of viscosity in the underlying mantle [24].

Figure 13 contains collated comparison results [26] of the Baltic Sea level gauging at mo-

onitoring stations [13, 14] and the GPS-measurements within the extended GPS network [20, 21]. The figure demonstrates the rates of the GPS-measured earth's crust uplift in various areas to be 1,0-1,5 mm/year higher than the corresponding level-gauging data. O. Vestol [27] suggested an empirical model of the earth's crust uplift. According to his research the eustatic rise of the Baltic Sea amounts to average 1,32 mm/year with addition of 6% on account of changes (uplift) of the geoid.

Thus the values of the absolute velocities of the earth's crust uplift (h_{abs} , mm/year) can be calculated approximately like this:

$$h_{abs} = (h_{rel} + 1,3) \times 1,06,$$

where h_{rel} – rate of sea level rise based on level-gauging monitoring (mm/year).

Considering the constant rate of eustatic sea level rise and the verified data obtained based on levelling and GPS networks, one of the latest maps of earth's crust uplift rate contours was charted (Fig. 14). This map is of a higher accuracy compared to the ones reflecting uplift of Fennoscandia and based on the above-described approaches [10, 19, 25, 27]).

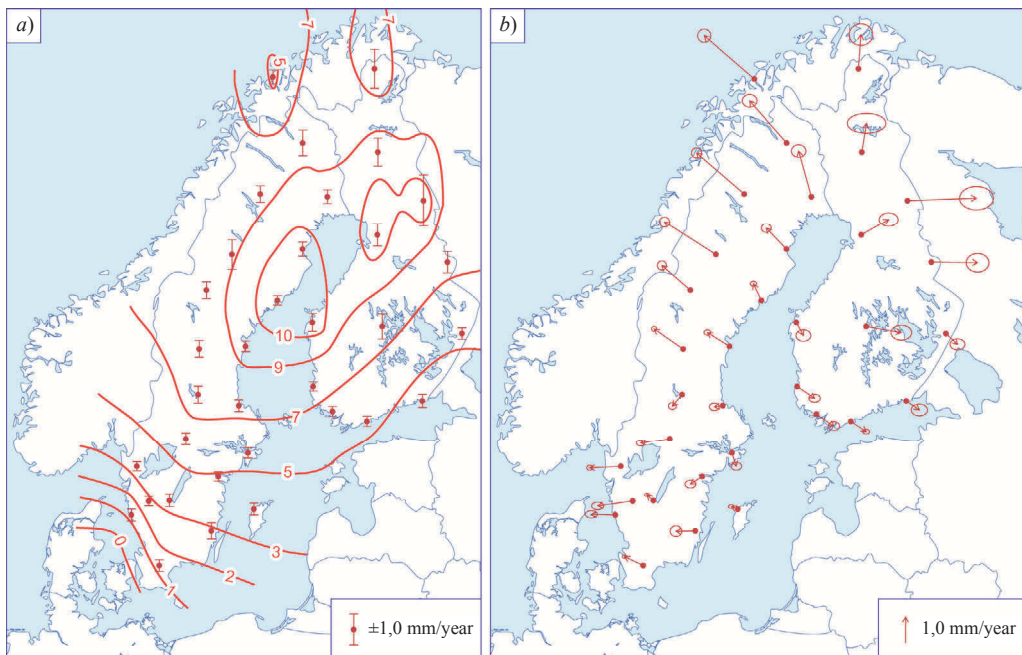


Fig. 12. Rate contours (mm/year) of postglacial rebound in Sweden and Finland (based on interpretation of stationary GPS-receivers: (a) – contours of vertical movements; (b) – spatial vectors of surface movement (according to [22, 23] for the years 2001–2004)

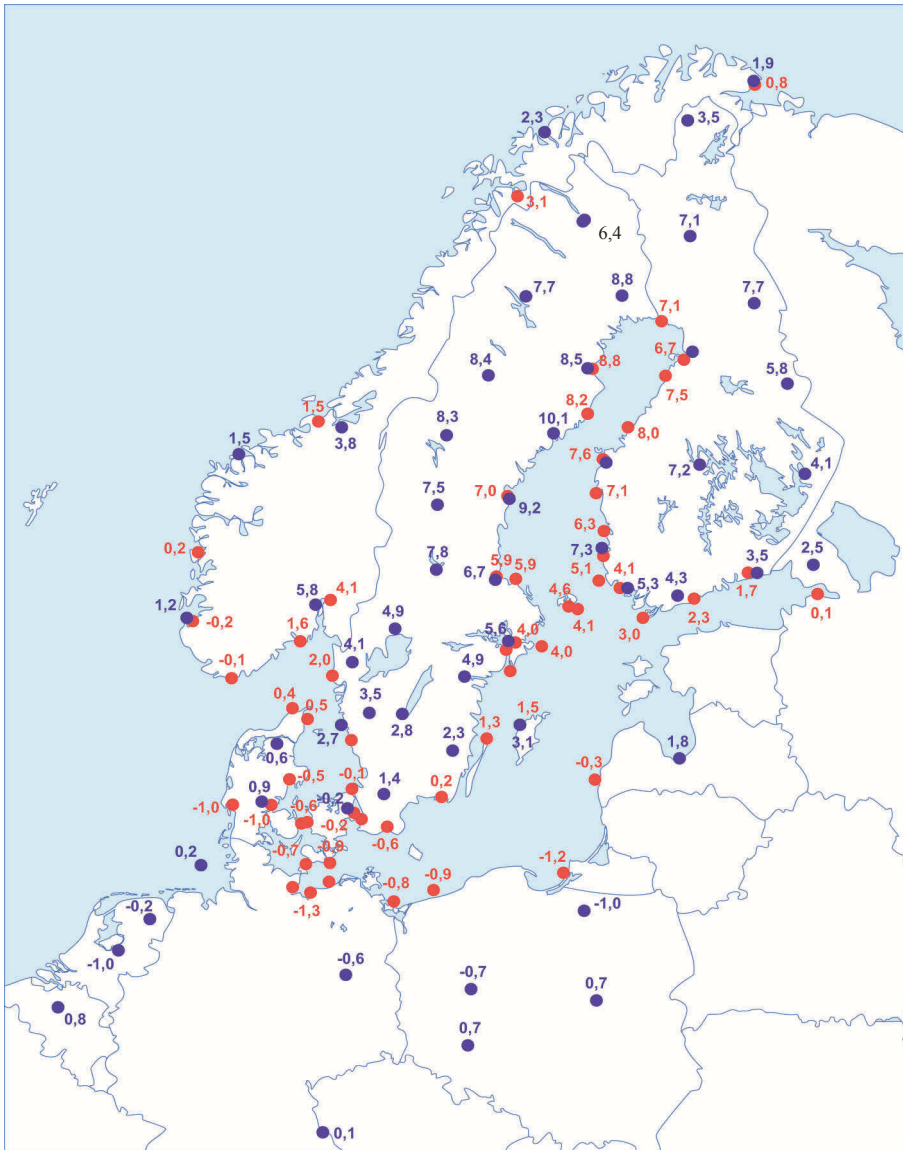


Fig. 13. Values of postglacial rebound vertical rates (mm/year) based on level gauging (red dots) and regular GPS (blue dots) [27]

I have already mentioned the construction of the St.Petersburg Dam, resulting from which the nought-benchmark of Russia was practically cut off from the high sea. In this respect a decision was taken to construct a contingency gauge in the village of Shepelevo, located 40 km to the west from the town of Lomonosov, which was put into operation in 1988. To monitor possible deformations of the quaternary and bedrock strata near the level-gauging station, boreholes

in the major aquifers were constructed. To register soil deformations in the strata above the aquifers, a group of borehole extensometers was installed (a network of in-depth gauges in four boreholes).

Fig. 15 presents the major part of St.Petersburg geodynamic range. To evaluate accuracy of the monitoring results of the water-level changes in the Baltic Sea at the Kronstadt Gauge, I shall compare mean annual sea-levels

in other parts of the Gulf of Finland and the Neva Bay. Fig. 16 contains data over the period 1977–2006 (nearly 30 years) for the Kronstadt, Lomonosov, Neva Estuary and Vyborg stations, as well as the stations in the villages of Ozerki

and Lisiy Nos (including the Shepelevo contingency gauge) (since 1989 until 2006). It is visible from the figure that the curves of annual mean sea level changes in the designated locations are similar to each other.

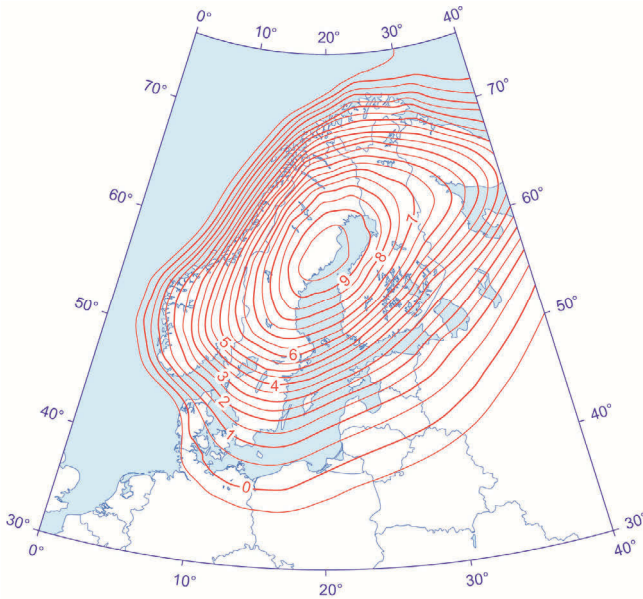


Fig. 14. Map of absolute rates contours (mm/year) of post-glacial rebound of the area (relative to the Earth mass centre) [25, 28]

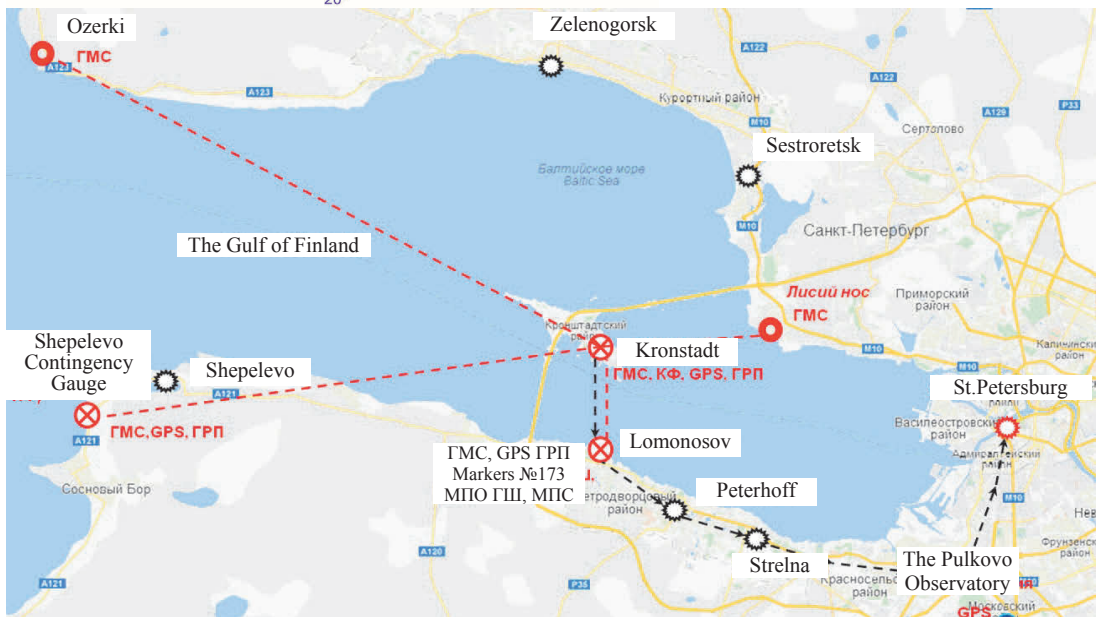


Fig. 15. St.Petersburg Geodynamic Range. The main part: ГМС – hydrometeorological stations, ГПИ – in-depth benchmark stations (1987), КФ – Kronstadt Gauge, the black lie – the tie-in of the Gauge with St.Petersburg

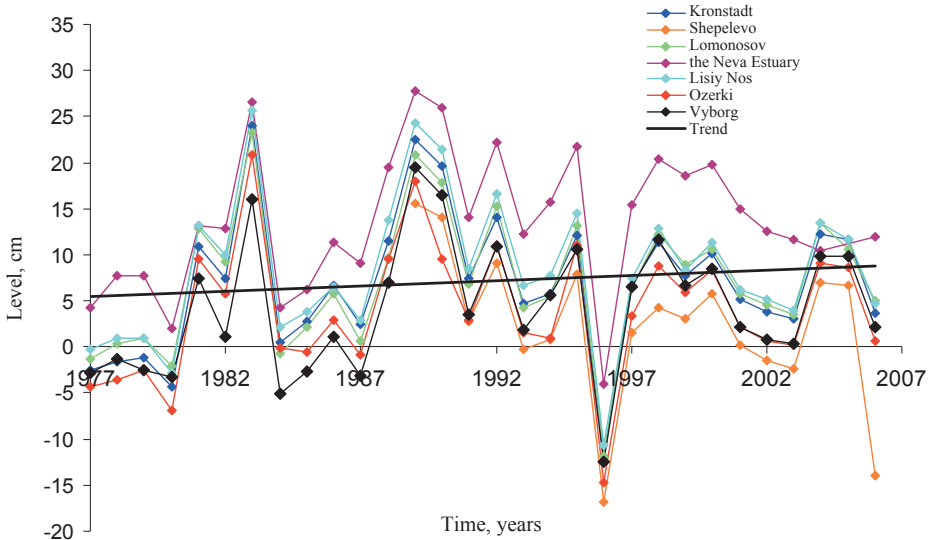


Fig. 16. Mean annual level of the Baltic Sea based on measurements at various monitoring stations since 1977 until 2006, as well as at the Shepelevo contingency benchmark since 1989 until 2006, based on the unified governmental oceanologist information system [[www:http://data.oceaninfo.ru](http://data.oceaninfo.ru)]

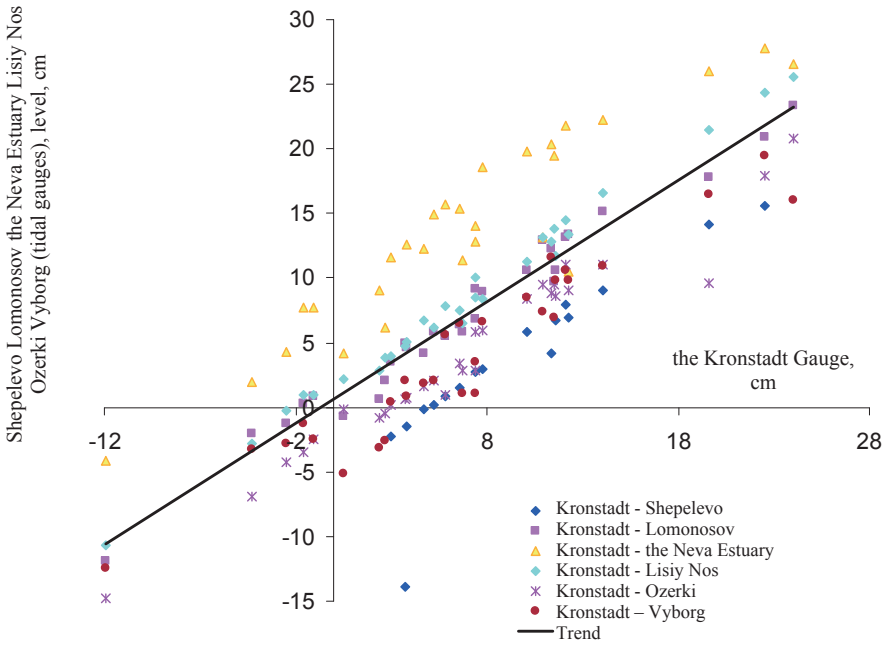


Fig. 17. Connection between mean annual water levels based on the Kronstadt Gauge and gauges of the Neva Bay and the Gulf of Finland in St.Petersburg and the Leningrad Region, over the period 1977–2006

In Figure 17 the reader will find the corresponding diagrams reflecting the connection between the Kronstadt Gauge and the above-mentioned monitoring stations. A clear correla-

tion between the results of sea-level measurements at various stations becomes visible. The best correlation is observed between points located in the Neva Bay (in paired points

“Kronstadt – Lomonosov”, “Kronstadt – Lisiy Nos). Figure 18 contains differences in mean annual levels of the Baltic Sea at the designated locations. The trends of the given curves are practically horizontal. Insignificant differences in mean annual levels of the Baltic Sea such as the ones displayed between those locations can be explained by variability of their hydrogeological conditions. Figure 18 also contains differences in mean annual water levels for the pairs “Kronstadt – Vyborg” and “Kronstadt – Lomonosov”. For those differences there are tendencies towards their reduction with time. Such trends in the displayed curves can be attributed to a whole range of causes:

- Variable hydrogeological conditions at different stations;
- A short period of conducted observations;
- A possible sinking of soil around the monitoring station located in the Neva Bay;
- A possible uplift of soil around the Vyborg Hydrometeorological Station over the observed period.

The last of the mentioned causes for the appearance of the trend towards reduction of differences in the considered locations appears the most realistic and can be confirmed by the

above-mentioned maps representing distribution of Fennoscandian post-glacial rebound velocities (Fig. 9, 11).

Summing up my consideration of stability of the primary level-gauging stations and benchmarks, it appears as certain that on the territory of St.Petersburg and the surrounding Leningrad Region currently there prevails a vertical uplift of the earth’s crust occurring at the rate of approximately 0,5–1,5 mm/year. The observed movement is caused by the overall uplift of the crest of the Baltic Shield brought about by glacio-isostatic factors (post-glacial rebound). However, this prevailing regional trend of postglacial rebound can be coupled with contemporary local tectonic movements, which in turn can be related to possible warps in the earth’s crust occasioned by postglacial crest uplift, as well as to human activities (such as construction of hydroelectric facilities, large-scale backfilling, drainage and city development, as well as industrial use of aquifers). The last group of causative factors is often the most influential in being conducive to appearance of localized spots in cities, where there is prevalence of vertical settlement even in areas where no construction has been ongoing.

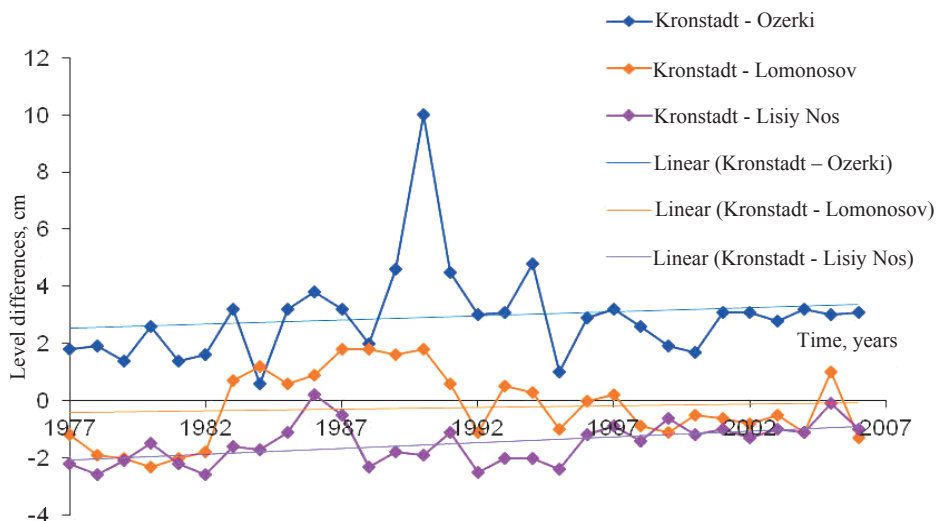


Fig. 18. Differences of the mean annual levels of the Baltic Sea based on various gauges over the period 1977–2006

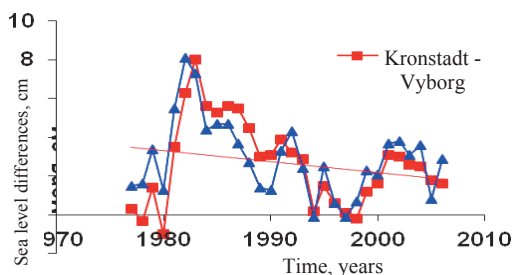


Fig. 19. Differences of the mean annual levels of the Baltic Sea based on various gauges over the period 1977–2006

The adduced results did not identify any considerable discrepancies in the registered sea levels at the level-gauging stations in the Gulf of Finland, the Neva Bay and the Kronstadt Gauge, which, albeit indirectly, points towards deformation-resistant property of the latter over the last 30 years (1977–2006). In view of the fact that this analysis spanned the area of a considerable size (along the line “Shepelevo – Lomonosov – Kronstadt – Lisiy Nos – Ozerki – Vyborg”), various localities within which possess different geological properties, it becomes possible to assume the settlement factor related to industrial aquifer dewatering around the Kronstadt Gauge not to have had any significant contribution towards its instability, remaining a purely local phenomenon.

In conclusion I shall briefly dwell on the history of the Kronstadt Gauge. Its use as the primary reference point of the USSR was decreed by Ruling № 760 of the Ministerial Council dated 7 April 1946.

However, it may be interesting to point out that even long before the official ruling, the Kronstadt Gauge had been repeatedly used in that capacity. When there appeared a necessity to establish the primary nought reference for the entire levelling network of the Russian Empire the attention of the authorities was directed towards that particular gauge as having had the lengthiest measurement history. Apart from that, the Kronstadt Gauge enjoyed a rather convenient location (in the Obvodny Canal where there were practically no waves, and besides the gauge was the nearest to both capitals of the Russian Empire – St.Petersburg and Moscow). However, it is worth pointing out that a significant drawback of the gauge was its

insular location, as it was necessary to tie it in with the coast of Oranienbaum. Additionally, the water level in the canal where the gauge was mounted was somewhat different to that of the Gulf of Finland due to atmospheric circulation (*viz.* wind action).

In 1840 the Department Head of the Hydrographic Board M.F.Reineke sorted the results of water level measurements in the Gulf of Finland over the period 1825–1839. He ordered a notch to be etched on a pier of the Siniy Bridge over the Obvodny Canal in Kronstadt, corresponding to the mean level of the Baltic Sea over that period of measurements. It was with that notch that all other noughts in the country were subsequently tied in. Later in 1886, an astronomer-surveyor of the Pulkovo Observatory F.F. Vitram had the notch marked with a special copper plate which existed until 1913. It later disappeared with a new one being put in its place by the Manager of the Instruments Chamber of the Kronstadt Port H.F.Tohnberg, and in contemporary geodetic descriptions of the Kronstadt Gauge it is referred to as “The Tohnberg Plate”. To identify any possible deformations of the Siniy Bridge pier a levelling was done between the Tohnberg Plate and the horizontal stroke of the Russian letter «П» as contained in the word «польза» (“benefit”) on the monument to P.K.Pakhtusov (Fig. 20), located 100 m away from the Kronstadt Gauge.



Fig. 20. The monument to P.K. Pakhtusov in Kronstadt

Increments between the working benchmark on the Pakhtusov monument and the nought of the Kronstadt Gauge are contained in Table 2, taken from a number of references [12 etc.]. It is visible from the table that the discrepancies between the measured increments (making account also of the substitution of the levelling marker on the monument in 1968) and the possible errors during mountings of the plates are negligible.

In 1872 the primary nought point of the Kronstadt Gauge was used by a surveyor of the Military Topography Department of the Headquarters of the General Staff N. Y. Zinger to level the marker № 173 mounted on the Oranienbaum Coast (this marker is known in the catalogues as the marker of the Military Topography Department of the General Staff - BTO ГИИ). It was subsequently used to be tied

in with the main grade lines of St. Petersburg suburbs [7].

Stability of the primary nought point of the Kronstadt Gauge can be ascertained by the results of its levelling link with marker №173 BTO ГИИ on the Oranienbaum Coast. However, in view of the fact that the Kronstadt Gauge was located on a practically isolated island, natural problems appeared in maintaining integrity of the inter-coastal levelling network. The results of the levelling link of the of the primary nought point of the Kronstadt Gauge with the Oranienbaum Coast are contained in Table 3 [12]. One can see that since 1872 until 1994 the primary nought point of the Kronstadt Gauge was tied in with the mainland 12 times. The table also lists the type of levelling and the Head Surveyors in charge of works.

Table 2. Changes in levelling increments * of the working benchmark of the level gauge on the monument to P.K. Pakhtusov over the nought marker of the Kronstadt Gauge [12 and others]

Year	Surveyors, surveying organizations	Δh_1 , m	Δh_2 , mm	Δh_3 , mm
1886	F.F. Vitram, The Pulkovo Observatory	5,2251	+1,0	+1,0
1892	F.F. Vitram, N.O. Shchetkin	5,2251	+1,0	+1,0
1903	H.F. Tohnberg	5,2266	+2,5	+2,5
1905	H.F. Tohnberg	5,2239	-0,2	-0,2
1907	H.F. Tohnberg	5,2246	+0,5	+0,5
1911	H.F. Tohnberg	5,2254	+1,3	+1,3
1912	H.F. Tohnberg	5,2230	-1,1	-1,1
1913	H.F. Tohnberg	5,2241	0,0	0,0
1931	V. Shavrov, V. Koposov	5,2250	+0,9	+0,9
1934	Morokov, Hydrography Board VMC USSR	5,2260	+2,0	+2,0
1945	Butenko, Hydrography Board VMC USSR	5,2280	+4,0	+4,0
1947	V. S. Klimakhin, A. P. Kamensky	5,2266	+2,5	+2,5
1951	C. I. Sundukova	5,2252	+1,1	+1,1
1968	A. Ya. Durnov, Organization 10 GUGK, Leningrad	5,2376	+13,5	+3,5
1976	M. P. Pavlov, Organization 10 GUGK, Leningrad	5,2395	+15,4	+5,4
1977	M. P. Pavlov, Organization 10 GUGK, Leningrad	5,2423	+18,2	+8,5
1978	V. A. Волков, Organization 10 GUGK, Leningrad	5,2388	+14,7	+4,7
1981	V. N. Petrov, PO "North-West Aerogeodeziya"	5,2446	+20,5	+10,5
1982	V.A. Sechkov, PO "North-West Aerogeodeziya"	5,2445	+20,4	+10,4
1987	L. M. Gorbatov, PO "North-West Aerogeodeziya"	5,2417	+17,6	+7,6
1994	L. M. Gorbatov, GP "Aerogeodeziya" FSGiK	5,2415	+17,4	+7,4

* Δh_1 – measured increment; Δh_2 – increment relative to 1913; Δh_3 – increment with account of the change in 1968 of the observed marker of the levelling point on the monument to P. K. Pakhtusov; during the routine governmental levelings in 1931 and 1947 the horizontal stroke of the letter "П" in the word "Полезьа" (benefit) was surveyed (Павлов, 1937; Шерман, Буланов, 1949); there has still been no information on which of the three notches of that etching had been monitored until 1931; since 1968 monitoring has been done on its upper notch.

Table 3. Results of levelling tie-ins of the nought point of the Kronstadt Gauge with the mainland (the data take from [12])

Years	Increments of markers on the Oranienbaum Coast over the Nought of the Kronstadt Gauge, m		Δh_1 , m	Δh_2 , mm	Surveyors, main method of levels transfer over the water, references
	173 VTO GSh	MPS			
1872	5,571 ± 0,017	–	5,753	+110	Ignatyev, Fedotov ; Simultaneous level definition with a level-theodolite (Цингер, 1878)
1875	5,512 ± 0,015	–	5,694	+51	A. A. Tillo, V. E. Fuss ; Geometric levelling on ice (Тилло, 1876)
1886	5,493 ± 0,022	–	5,675	+32	V. E. Fuss, V. A. Astafyev ; Geometric levelling on ice (Витрам, 1894)
1886	5,462 ± 0,013	–	5,644	+1	V. E. Fuss, V. A. Astafyev ; Water levelling in doldrums condition (Витрам, 1894)
1888	5,494 ± 0.014	–	5,676	+33	V. E. Fuss, V. A. Astafyev ; Geometric levelling through fort structures (Витрам, 1894)
1890	5,465 ± 0,010	–	5,647	+4	F.F. Vitram, N. A. Novgorodtsev et al. ; Level definition by vertical Repsold circles (Витрам, 1894)
1892	5,4663±0,0029	5,6420±0,0029	5,642	–1	F.F. Vitram, N. O. Shchetkin ; Geometric levelling from a ferry pontoon (Витрам, 1894)
1931	5,4608±0,0041	5,6427±0,0041	5,643	0	V. Shavrov, V. Kuposov, V. Stepanov ; Geometric levelling on ice and on piles (Павлов, 1937)
1947	–	5,6352±0,0016	5,635	–8	V. S. Klimakhin, A. P. Kamenskiy ; Geometric levelling on ice, (Шерман, Буланов, 1949)
1969	–	5,6480±0,0016	5,649	+6	L. Ya. Tamme et al. ; Hydrostatic levelling over water (Тамме, 1971)
1988-89	–	5,6677±0,0065	5,668	+25	V. L. Averin, L. M. Gorbatov, V. N. Telepaev ; Levelling on ground through Gorskaya Railway Station and the Dam, 172,7 km
1994	–	5,6456±0,0011	5,646	+3	L. M. Gorbatov, E. A. Bykova ; Geometric levelling through the Dam and through 900-m long through-run (Archives of GP “Aerogeodeziya”)

Δh_1 – conditional increment of the MPS marker (the Russian Transport Ministry), calculated in light of the possibility of increment difference distribution (1931) of this marker and the marker 173 of the Military Topography Department of the General Staff for the entire preceding period; Δh_2 – same for the year 1931

The results of the conducted levelling demonstrate that over the last 100 years the value of increment of the marker МПС on the Oranienbaum Railway Station appears relatively stable. The actual fluctuations of the increment value are caused by errors in level-

ling and assumptions in the methodology of the levelling works.

Thus, the results of linking the primary nought point of the Kronstadt Gauge with the Oranienbaum Coast confirm the relative resistance to deformations of the Kronstadt Gauge. Therefore, to tie in the city levelling works

conducted in the second half of the 19th century it is possible to use the results of the levelling link of the primary nought point of the Kronstadt Gauge with Oranienbaum coast conducted in 1892. (Ф. Ф. Витрам [2]).

In view of the fact that the works on the linking of the nought point of the Kronstadt Gauge were extremely complicated and labour consuming, in the early 1950-s, to carry out levelling of the city, as well as for the needs of reconstruction and development of the levelling network, a concept of secular and fundamental

benchmarks (and their clusters) was introduced, those benchmarks being tied in with the nought of the Kronstadt Gauge. Comparing results of the levellings of the fundamental and secular gauges in the region over a long period of time it becomes possible to evaluate the contemporary vertical movements of the earth's crust in the area under consideration. To identify the prevailing character of distribution of contemporary vertical movements of the earth's crust on the Karelian Peninsula S. V. Enman [26] prepared a map of those movements (Fig. 21).

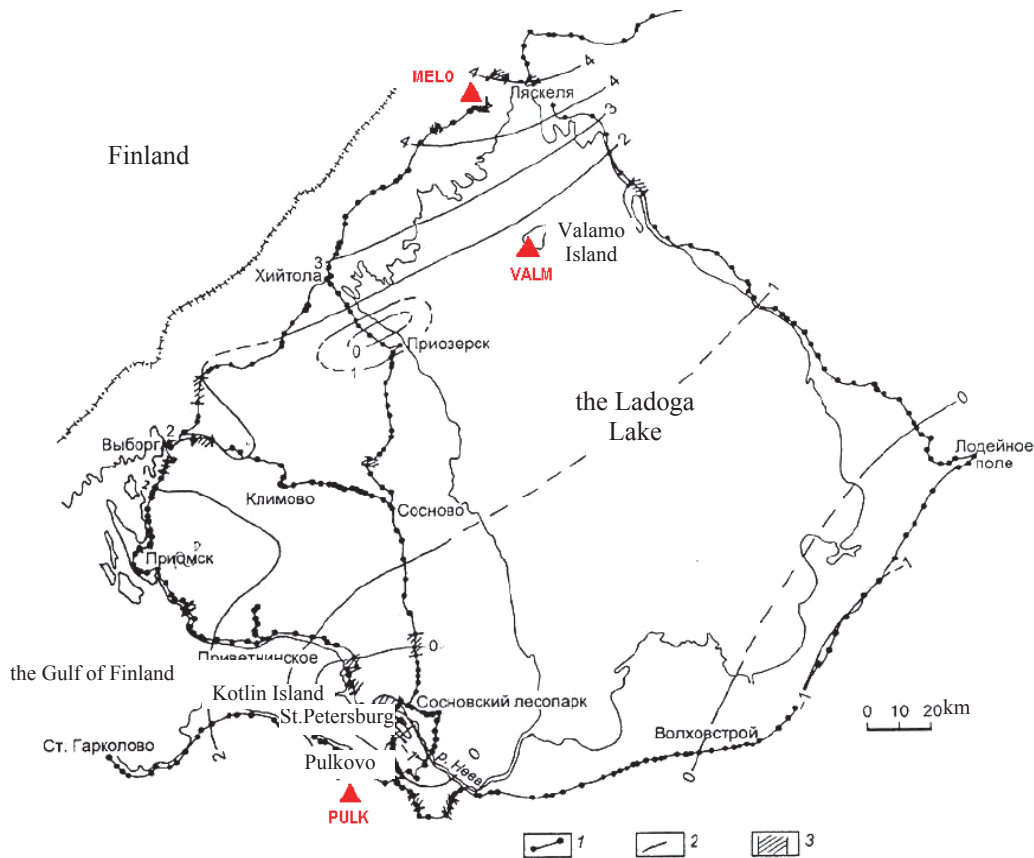


Fig. 21. The lines of the high-accuracy governmental levelling and the contours of contemporary vertical movements of the earth's crust (SVDZP) of the Karelian Peninsula. Drawing by C.V. Enman (Энман [10]): 1 – contours of high-accuracy governmental levelling; 2 – contours of rates of contemporary vertical movements of the earth's crust (mm/year); 3 – zones of contrast movements; the triangles denote the main GPS stations (see Table 4)

The map was charted based on analysis of high-precision re-levelling along the lines, forming four closed-up ranges. The network was tied in in those four ranges based on the results of re-

levelling of 1960–1980-s. Based on the results of equated movement values a map was plotted for the area under consideration. It was established that on the Karelian Peninsula the pre-

vailing trend was towards rising of the area at the rate of 4 mm/year. However, there are also lowering areas – along the floodplain of the River Neva and around the town of Priozersk. The fact that there are such areas on the map can be explained by man-made factors, which determine development of settlement phenomena in the upper areas of the settlement-prone quaternary mantle.

Using the nought of the Kronstadt Gauge to calculate levels of suburban markers was widespread largely before 1894–1896. After that V.E. Fuss and S.D. Rylke introduced systems of primary referencing from the mean level of the Baltic Sea for the period 1841–1895 and from the mean Baltic-Black Sea level for the same period of time. So, over more than 30 years following the introduction of those levels the use of the nought point of the Kronstadt Gauge was somewhat constrained. Later it was used to establish levels of surveying markers in 1920–1940-s.

At this point it is necessary to point out that the main advantage of the nought point of the Kronstadt Gauge when compared with others is that it used to be the only one physically fixed (the others being counted off it, *i.e.* in essence having a virtual character).

Apart from the glacio-isostatic rebound of the terrain, for a geodynamic researcher it is also quite interesting to consider horizontal components of the GPS station movements in the region under consideration (see Table 4).

Understanding the distribution of horizontal movements of the earth's crust along with seismology data gives one a possibility to evaluate distribution of tectonic deformations of the area in question.

In the regions of the Gulf of Finland and the Ladoga Lake seismic activity is traditionally very low. The epicentres of the 42 events with magnitudes 1,2...4,0 had foci at the depths of 5...12 km [11]; 39 of these events are designated in Fig. 22 (since 1956 until 2009 they were registered at magnitudes 0,1...3,5 with foci at the depths of 5...10 km). Analyzing distribution of the earthquakes foci in the region under consideration one can notice (see Fig. 22) that in the area of the Ladoga Lake they are mostly associated with the cluster of the Valamo Group (10 earthquakes over the last 55 years), with 6 more earthquakes being distributed along the periphery of the lake. Five earthquakes over the last 30 years with magnitudes up to 2,6 with foci at the depths of 5...10 km occurred to the north-west direction of the Ladoga Lake. Other 30 epicentres had been registered in the coastal areas of the Gulf of Finland. Out of those 30, 16 earthquakes with magnitudes 0,6...2,1 were associated with the focus located in Anjalankoski at the depth of less than 2 km (see Fig. 21). The epicentre of the strongest local earthquake of Narva which occurred in 1881 was located in the southern part of the Gulf of Finland.

Table 4. Mean rates at GPS stations around the Gulf of Finland and the Ladoga-Onega region [11].

Name of station, country	Latitude $N, ^\circ$	Longitude $E, ^\circ$	Time of measuring, years	Horizontal rates North N , mm/year	Horizontal rates East E , mm/year	Vertical rates, mm/year
BOTS (Petrozavodsk), Russia	61,842	34,381	1999–2009	10,72±0,16	20,31±0,17	1,44±0,38
GIRS (Girvas), Russia	62,458	33,667	2001–2009	10,00±0,20	22,28±0,31	5,61±0,79
MELO (near Sortavala), Russia	61,783	30,785	1999–2009	10,26±0,15	21,91±0,26	4,24±0,39
PULK (Pulkovo), Russia	59,772	30,328	2002–2010	11,78±0,02	21,34±0,02	1,48±0,06
SVTL (Svetloe), Russia	60,533	29,781	2006–2010	10,81±0,06	21,13±0,06	2,71±0,16
VALM (Valamo), Russia	61,360	30,886	1999–2009	10,89±0,14	22,47±0,31	3,29±0,42
JOEN (Joensuu), Finland	62,391	30,096	1999–2010	11,71±0,02	20,35±0,02	4,17±0,06
METS (Metsähovi), Finland	60,218	24,395	1999–2010	12,54±0,02	19,79±0,02	4,94±0,04
VIRO (Virolahti), Finland	60,539	27,555	1999–2007	11,90±0,14	19,95±0,16	3,95±0,3
SUUR (Suurpea), Estonia	59,464	24,380	2007–2010	12,97±0,10	18,91±0,11	7,63±0,25
TOIL (Toila), Estonia	59,422	27,536	2008–2010	12,43 0,14	20,87±0,14	3,90±0,31

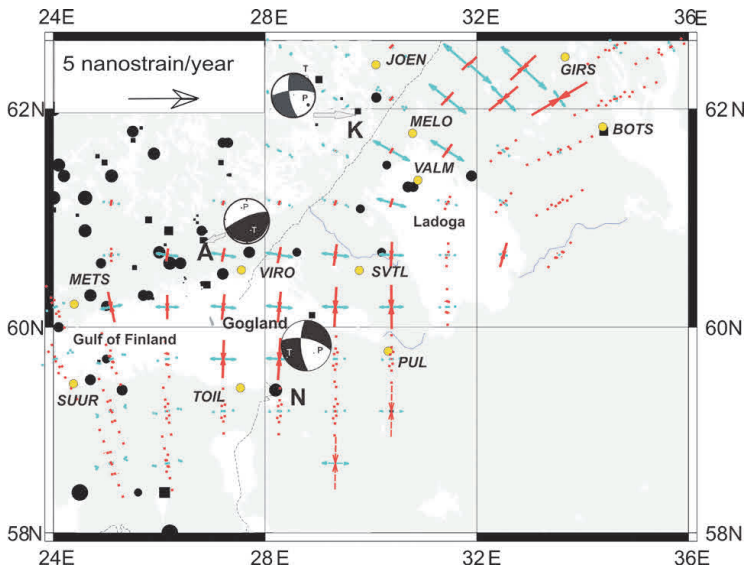


Fig. 22. Distribution of rates of main deformations, calculated based on results of GPS monitoring and seismic activity in the region The Gulf of Finland – The Ladoga Lake [11]. Blue lines – direction of tensile deformations, red lines – compressive deformations. Deformations are calculated through grid of 50×50 km. The earthquakes foci shown are: Kesälahti (K), Anjalankoski (A), and the Gulf of Finland (F). Black zones in circles – compression, white zones – tension. Grey arrows show links between epicentres and foci of earthquakes. Smaller black circles and squares denote locations of historically and instrumentally registered earthquakes (with magnitudes of 0,1...4). The corresponding value of signs is proportional to the magnitudes. The “N” stands for the location of Narva Earthquake of 1881. The yellow points denote the GPS stations.

Horizontal movements of various GPS stations allowed to assess distribution of relative deformations in the considered area. It must be noted that for an objective judgement density of station locations is very low which means the results obtained so far can only be deemed preliminary. Fig. 22 contains distribution of rate intensities of the main relative deformations in conjunction with the epicentres and the foci of the earthquakes in the region.

Considering distribution of deformation rates one can single out minimum three zones. The first zone – the Ladoga and Onega Lakes are characterized by insignificantly low compressive deformations. The second zone is in the north part of the Ladoga Lake. This area is associated with large scale tensile deformations. The third zone is the Karelian Peninsula and the Gulf of Finland and manifests approximately equal principal rates of tensile and compressive deformations. The borders of these areas featuring different character of movements may be associated with development of rift/shear areas, which can be explained by development of the Ladoga Lake Trough. Multidirectional move-

ments within the boundaries of the considered areas and also development of shear deformations are the main factors in determining seismic character of the region. Such areas are the north-west boundaries of the Ladoga Trough (Fig. 21) – the area of transition from tensile to shear deformations, and also, possibly, the south coast of the Gulf of Finland – the area of transition from shear to compressive deformations. The mechanisms of earthquakes point towards more complicated deformations ongoing in the areas of the epicentres. In this respect, in the Ladoga tensile area shear deformations occurred in the focus, in Anjalankoski there occurred a falling shear, and in the area *F* deformations can be classified as being of the fault-shear type. The discrepancies between the seismic and the geodynamic data can be explained by a difference in the level of deformation assessment – GPS measurements are done on the surface, whereas earthquakes appear at the depths of 2...17 km. It is worth adding at this point that if additional GPS stations had been used the field of deformations would certainly have been more complicated.

For the purposes of evaluating long-term settlements (settlement rates) of buildings and structures in St.Petersburg it is necessary to tie in the absolute geodetic levels to one primary point, for which putting together a special scheme of tie-ins is required. For this an important factor was investigation of contemporary vertical movements in the region as well as of stability of the nought-point of the Kronstadt Gauge. To provide more accurate evaluation of contemporary vertical movements in the region it is necessary to broaden the geodynamic range and to include into the study levelling results of in-depth benchmarks in Lomonosov, Shepelevo and Kronstadt, in conjunction with results of GPS monitoring of the city markers. However, it must be remembered that the in-depth fundamental benchmarks were installed only in the late 1980-s, and the network of GPS receivers in the city is only now being formed. To obtain accurate verifiable results and their evaluation at least 15 years will be required.

Based on results of the conducted research the tying in of the main levelling works to the primary nought of the Kronstadt Gauge can be done for all city levellings since 1872 without specific corrective coefficients taken to account for deformations of the Siniy Bridge piers. This will give a possibility to create a system of tie-ins for the main levelling works with reference to a primary point and to evaluate long-term settlements of historic buildings in St.Petersburg. The proper evaluation of long-term settlements of buildings will be highly important for fulfilment of the following purposes:

- **Condition surveys of buildings** – settlement curves obtained for the last 25...130 years will be highly valuable in establishing causes for possible deformations, as well as for identifying the condition category of buildings and conditions of subsoil behaviour.
- **Monitoring of buildings** – settlement propagation curves for buildings obtained even for the recent 15...25 years of their life will be instrumental in selection of primary nought geodetic points, as well as for evaluation of the accrued proper deformations of existing buildings (e.g. during construction).
- **Establishing geotechnical backgrounds for construction projects** – in this respect paragraph 8.8 of the Russian Technical

Codes TCH 50-302-2004 “Foundation Design in St.Petersburg” acquires a new sense, viz. **the retrospective analysis of the actual geotechnical situation**, which implies evaluation of the degree of completed settlements of existing buildings and evaluation of their completed deformations (with consideration of natural and man-made factors). The last requirement is practically impossible to fulfil by numerical methods.

- **Reconstruction design** – settlements propagation curves of buildings assist in proper evaluation of subsoil strengthening;
- **Development of rheological soil models** – the materials on settlement propagation rates will be highly important in evaluating rheological parameters of soil models.
- **Justification of potential needs to remove separate structural elements of historic buildings** – the settlement propagation curves will either justify or disprove the necessity to remove separate structural elements of historic buildings.
- **Selection of locations for in-depth fundamental benchmarks in the city to preserve markers of levelling networks** – defining distribution of extreme settlement rates in the city, in view of its constant reconstruction, development, and building of underground structures will be crucial for selecting locations of fundamental benchmarks in the territory of St. Petersburg.

REFERENCES:

1. Богданов В. И., Кравченкова Т. Г., Малова Т. И., Маринич М. А., Трубицина А. А. *Валаамский ряд уровневых наблюдений. 1859–2001 гг.* // Тезисы докладов 5-й Международной конференции по проблемам физической метрологии. Санкт-Петербург, 17–21 июня 2002 г. СПб: Изд-во Санкт-Петербургского политехнического ун-та, 2002. С. 78–83.
2. Витрам Ф. Ф. *Нивелировка между Кронштадтом и Санкт-Петербургом.* Записки по гидрографии. Вып. XV. Санкт-Петербург, 1894.
3. Галаганов О. Н., Горшков В. Л., Гусева Т. В., Розенберг Н. К., Передерин В. П., Щербакова Н. В. *Парадокс отличий в вертикальных движениях по данным определений разными методами* // Геодезия, картография і аэрофотознімання. Львів, 2009. Вип. 71. С. 241–248.

4. Николаев Н. И. *Новейшая геотектоника и геодинамика литосферы*. М.: Недра, 1988.
5. Никонов А. А. *Голоценовые и современные движения земной коры*. Геолого- и геоморфологические вопросы. М.: Наука, 1977.
6. Фус В. Е. *Средний уровень моря у Кронштадта по наблюдениям с 1841 по 1895 г.* // Записки по гидрографии. Вып. XVII. СПб, 1896.
7. Цингер Н. Я. *Опыт работ с нивелир-теодолитом по железным дорогам Балтийской и С-Петербургско-Варшавской от Динабурга до станции Лапы* // Записки ВТО Гш. Часть XXXVI. СПб., 1878.
8. Шабаров С. Н. *Нивелирные сети Санкт-Петербурга – Ленинграда* // Автореф. дисс. на соиск. уч. ст. канд. техн. наук. М., 1972.
9. Энман С. В. *Современные вертикальные движения земной поверхности на карельском перешейке и близлежащих территориях*. Бюлл. Московского общества испытателей природы. Отд. Геолог. Т.81. Вып. 6, Москва, 2006.
10. Agren J, Svensson R. *Land uplift model and system definition used for the RH 2000 adjustment of the Baltic Levelling Ring* / Proceedings of the 15-th General Meeting of the Nordic Geodetic Commission (NKG). Copenhagen, Denmark, 2006.
11. Assinovskaya B., Shchukin J., Gorshkov V., Shcherbakova N. *On recent geodynamics of the Eastern Baltic Sea region*. BALTICA, Volume 24. Number 2.
12. Bogdanov V. I., Medvedev M. Yu., Solodov V. A., Trapeznikov Yu. A., Troshkov G. A., Trubitsina A. A. *Mean monthly series of sea level observations (1777–1993) at the Kronstadt gauge* // Reports of the Finnish Geodetic Institute. 2000. V. 1. 34 p.
13. Ekman M. *A concise history of postglacial land uplift research (from its beginning to 1950)* // Terra Nova. 1991. V. 3–4. P. 358–365.
14. Ekman M. *A Consistent map of the postglacial uplift of Fennoscandia* // Terra-Nova. 1996. V. 8. № 2. P. 158–165.
15. Gutenberg B. *Changes in sea level, postglacial uplift and mobility of the Earth's interior* // Geological Society of America Bulletin. 1941. V. 52. P. 721–772.
16. Hammarklint T. *Swedish sea level series – a climate indicator*. Stockholm: Swedish Meteorological and Hydrological Institute (SMHI), 2009. Hammarklint, T. 2009. December. http://www.smhi.se/polopoly_fs/1.89631/Swedish_Sea_Level_Series_-_A_Climate_Indicator.pdf
17. Huenicke B. *Atmospheric forcing of decadal Baltic Sea level variability in the last 200 years: A statistical analysis* / PhD thesis. Hamburg: International Max Planck Research School on Earth System Modelling, 2008.
18. Jevrejeva S., Moore J. C., Grinsted A., Woodworth P. L. *Recent global sea level acceleration started over 200 years ago?* // Geophysical Research Letters. 2008. V. 35. L08715.
19. Lambeck K., Smither C., Ekman M. *Test of glacial rebound models for Fennoscandia based on instrumented sea and lake-level records* // Geophysical Journal International. V. 133. P. 375–387.
20. Lidberg M., Johansson J. M., Scherneck H.-G., Milne G. A., Davis J. L. *New results based on re-processing of 13 years continuous GPS of the Fennoscandia GIA process from BIFROST / Earth: Our changing planet: Proceedings of the IAG/IUGG symposia, Perugia, Italy, 2–13 July, 2007*.
21. Lidberg M., Johansson J. M., Scherneck H.-G., Davis J. L. *An improved and extended GPS derived velocity field for the glacial isostatic adjustment in Fennoscandia* // Journal of Geodesy. 2007. V. 81. № 3. P. 213–230.
22. Milne G. A., Davis J. L., Mitrovica J. X., Scherneck H.-G., Johansson J. M., Vermeer M., Koivula H. *Space-geodetic constraints on glacial isostatic adjustment in Fennoscandia* // Science. 2001. V. 291. P. 2381–2385.
23. Milne G. A., Mitrovica J. X., Scherneck H.-G., Davis J. L., Johansson J. M., Koivula H., Vermeer M. *Continuous GPS measurements of post-glacial adjustment in Fennoscandia. 2. Modelling results* // Journal of Geophysical Research. American Geophysical Union, 2004. V. 109. № B2. P. 1–19.
24. *Permanent Service for Mean Sea Level (PSMSL)* / Official website. Swindon, UK: Natural Environment Research Council, <http://www.psmsl.org/>
25. Poutanen M. *GPS measurements in Satakunta Area* / Working Report 2010-Oct. Eurajoki, Finland: Finnish Geodetic Institute, POSIVA OY, 2010.
26. Rosentau A., Meyer M., Harff J., Dietrich R., Richter A. *Relative sea level change in the Baltic Sea since the littorina transgression* // Zeitschrift für Geologische Wissenschaften (Journal for the Geological Sciences). 2007. V. 35. № 1–2. P. 3–16.
27. Vestol O. *Determination of postglacial land uplift in Fennoscandia from levelling, tide-gauges and continuous GPS stations using least squares collocation* // Journal of Geodesy. 2006. V. 80. P. 248–258.
28. Vuorela A. *Review of Bothnian Sea shore-level displacement data and use of a GIS tool to estimate isostatic uplift* / Working Report 2009-17. Eurajoki, Finland: Finnish Geodetic Institute, POSIVA OY, 2009.
29. Улицкий В.М., Пашкин А.Г., Пашкин К.Г. *Геотехническое сопровождение развития городов. Группа компаний «Геореконструкция»*. // Санкт-Петербург. 2010.

RETAINING WALLS

Analysis of Lateral Earth Pressures on Anchored Sheet Pile Walls Using Conventional and Finite Element Methods

Ö. Bilgin

University of Dayton, Dayton, Ohio, U.S.A., bilgin@udayton.edu

ABSTRACT: Conventional methods used for the design of anchored sheet pile walls are based on lateral force and moment equilibrium of active and passive earth pressures and anchor force. The stress concentration around the anchor level due to the restricted wall movements is not considered in determining the lateral earth pressures. A parametric study using conventional and numerical methods was performed to investigate the behavior of single level anchored sheet pile walls. The study results indicate that the conventional methods overestimate the wall bending moments while the anchor forces are underestimated. New lateral earth pressure coefficients were developed by taking into account the stress concentration due to an anchor and they are discussed in this paper.

1. INTRODUCTION

The conventional methods generally used in the design of anchored sheet pile walls are free earth support and fixed earth support methods. Because of its simplicity, free earth support is the more preferred method. These conventional design methods use active and passive earth pressures that are concerned with the failure condition based on Mohr-Coulomb failure criterion. Active and passive earth pressures are based on the rotation or translation of walls as rigid body and triangular active and passive lateral earth pressure distributions assumption. However, the anchor causes stress concentration in the surrounding soil at the anchor level resulting from restricted wall movements which is not considered by the conventional methods used for design.

Due to the stress concentration at the anchor level, the location of the active resultant force would actually be at higher elevation compared to the triangular pressure distribution. Goel and Patra (2008) also state that the Rankine and Coulomb theories underestimate the height of the center of lateral earth pressure. This would affect the design due to the changed moment arm when the moment equilibrium is considered to determine the wall penetration depth, anchor force, and maximum bending moments. Nataraj

and Hoadley (1984) proposed a simplified lateral earth pressure diagram where both active and passive pressures were idealized as rectangular pressure distributions.

The design components of anchored sheet pile wall, such as penetration depth, anchor force, bending moment, and pile section, depend on the lateral earth pressure distribution behind and in front of the wall. Therefore, using inaccurate pressure distributions would result in either unsafe or over-designed walls.

With the advances in computing technology, the use of continuum mechanics numerical methods in the analysis and design of sheet pile walls has been increasing in recent years. Although the finite element is primarily being used as numerical method, the finite difference method is also being used. The finite element method has been utilized by researchers to study and understand the behavior of cantilever, braced, and anchored sheet pile walls under static and dynamic loading conditions.

The objective of this paper is to present new lateral earth pressure coefficients that would provide more realistic lateral earth pressures for the single level anchored sheet pile walls rather than the assumed triangular stress distribution. This paper presents the analyses results and provides recommendations for the lateral earth pressure coefficients to be used in the design of

anchored sheet pile walls to have more realistic earth pressure distributions acting on the wall and therefore resulting in better wall designs.

2. CONVENTIONAL DESIGN METHOD

Current common design practice of sheet pile walls is based on limit equilibrium approach. Free earth support method is the most common method used for design. This design method is based on active and passive earth pressures as shown in Figure 1(b) that are concerned with the failure condition based on Mohr-Coulomb failure criterion. A typical wall section, the lateral earth pressures, and resulting forces acting on the wall are shown in Figure 1.

The anchored sheet pile wall design using the free earth support method is summarized below. The wall penetration depth required below the bottom of excavation is determined by considering moment equilibrium about the anchor elevation. Using the notation in Figure 1 moment equilibrium is given as

$$P'_A d_A + P_{WA} d_{WA} = \frac{P'_P}{FS} d_P + P_{WP} d_{WP} \quad (1)$$

where P'_A and P'_P =resultant effective active and passive earth forces, respectively; P'_{WA} and P'_{WP} =resultant hydrostatic forces on the active and passive sides of the wall, respectively; d_A , d_P , d_{WA} , d_{WP} =moment arms with respect to anchor elevation; and FS=factor of safety. Factor of safety is applied to the passive loads

during wall design (U.S. Navy 1986; U.S. Army 1994). The safety factors are used to take into account for the uncertainties in soil conditions, the method of stability analysis, the loading conditions, as well as to restraint soil movements to an acceptable level (Potts and Fourie 1984).

Since the water level is assumed to be at the same elevation behind and in front of the wall during this study, hydrostatic forces cancel each other. Then Eq. (1) can be simplified as

$$P'_A d_A = \frac{P'_P}{FS} d_P \quad (2)$$

Once the wall penetration depth is determined from Eq. (2) anchor force A_p is calculated from horizontal force equilibrium is given as

$$A_p = P'_A - \frac{P'_P}{FS} \quad (3)$$

Based on the active and passive pressure distributions and calculated anchor force, the wall maximum bending moment is determined. Design moment is calculated by applying moment reduction factor (Rowe 1952) to the maximum bending moment. Steel sheet pile section is selected based on the design moment and the wall design is completed by selection and design of the anchorage system.

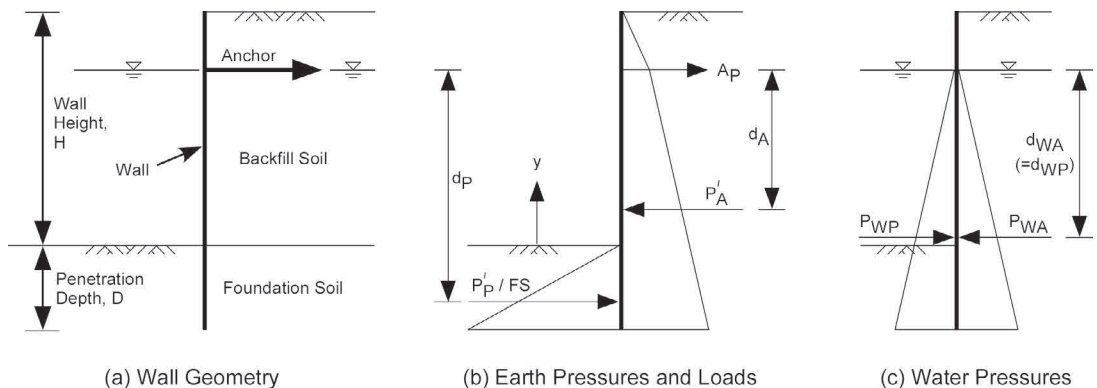


Figure 1. Typical sheet pile wall section and forces acting on the wall used in free earth method

3. METHOD OF APPROACH

Comparative study of lateral earth pressures, wall bending moments, and anchor forces obtained using conventional design method and continuum mechanics numerical method is performed. Finite element analysis was used as continuum mechanics numerical method. Walls with different heights and surrounding soil conditions were analyzed to investigate the effect of these parameters. Total of twelve cases with different soil conditions and wall heights were studied using both conventional and finite element methods. The details of the cases studied and the analysis methods are given in the following.

4. WALL AND SOIL PROFILES STUDIED

The behavior of single anchored sheet pile walls with heights up to 12 m have been studied by others (Bilgin 1994; Dawkins 2001). Three different wall heights (6, 9, and 12 m) were used in this study to include size effect. The design and analyses were performed for these three wall heights and for the soil profile combinations using conventional and finite element methods.

Two different soil types were considered during this study; medium dense sand and loose sand. One-letter code designations are used to refer to the soil types throughout the paper. Letter codes “D” and “L” represents medium dense sand and loose sand, respectively. The properties selected for the two soil types are given in Table 1. A study performed by Bilgin and Erten (2009) showed that the best position for the anchor location to have minimum wall deformations was approximately $25 \times H$ below from the top of wall. Therefore, the anchor location was fixed and it was at 25 percent of the wall height below the top of wall in all cases. Groundwater table elevation was assumed to be at the anchor level on both sides of the wall. A typical wall section used in the analyses is shown in Figure 1(a).

Three different wall heights (6, 9, and 12 m) were analyzed and four different soil type configurations were considered for each wall height. Two of the cases involved same soil type throughout the site, i.e. both backfill and foundation soils had same soil type, either

medium dense or loose sand. The other two cases consisted of different soil types for backfill and foundation soils. One case involved medium dense sand for backfill soil with loose sand for foundation soil and the other case involved loose backfill sand over medium dense sand foundation soil. Each case analyzed was given a two-letter identification code using the soil types’ one-letter codes followed by a number indicating the wall height in meters. The first letter in a two letter code indicates the backfill soil and the second letter indicates the foundation soil. Therefore, the four cases analyzed for 12 m wall were DD12, LL12, DL12, and LD12. Case LD12, for example, refers to the case where backfill soil is loose sand, foundation soil is medium dense sand, and the wall height is 12 m.

Table 1. Soil Properties Used in Analyses

Property	Medium	Loose
	dense sand (D)	sand (L)
Unit weight (kN/m^3)		
Saturated	18	16
Unsaturated	17	16
Friction angle ($^\circ$)	36	30
Dilatancy angle ($^\circ$)	6	0
Modulus of elasticity (kPa)	35,000	15,000
Interface strength, R_{int}	0.65	0.67

4.1. Conventional design calculations

The twelve cases first were designed using conventional free earth support method. The lateral earth pressure coefficients were calculated by using non-linear log spiral failure surface (U.S. Navy 1986) which represents the actual failure surface more accurately. For active conditions the log spiral shape is reasonably approximated by a straight failure line and therefore Coulomb’s active lateral earth pressure coefficients can also be used. On the other hand, the actual failure surface is significantly non-linear for passive conditions. The passive resistances calculated using the straight failure line can be much higher than those calculated using non-linear log spiral surfaces and should not be used for values of relatively high wall friction angles (Clough and Duncan 1991).

The wall penetration depth and steel sheet pile sections obtained from the conventional design were used in finite element models. Analyses were performed using a safety factor applied to the passive pressures. The safety factor used in the conventional design methods usually ranges between 1.5 and 2.0. The calculations in this study were performed using a safety factor of 1.5. The wall penetration depths calculated using free earth method and pile profiles selected for each case are given in Table 2.

Table 2. Wall Penetration Depths and Pile Sections Used in Analyses

Case	Penetration Depth <i>D</i> (m)	Pile Section
DD12	2.47	PZ27
DL12	4.01	PZ27
LD12	2.50	PZ27
LL12	3.96	PZ27
DD9	1.85	PZ27
DL9	3.01	PZ27
LD9	1.88	PZ27
LL9	2.97	PZ27
DD6	1.23	PZ22
DL6	2.00	PZ22
LD6	1.25	PZ22
LL6	1.98	PZ22

The pile sections were selected among four different sections of PZ type piles, which are the most commonly available and used ones for sheet pile walls. In addition, the same pile sections were selected for the cases of same wall height. Table 2 shows that the wall penetration depth and the pile section needed to satisfy the maximum bending moments get smaller as the wall height decreases, as expected. The table also shows that the cases where the wall height and foundation soil types are the same have almost the same wall penetration depth, i.e. the retained soil has lesser effect in determining the penetration depth. For example, for 12-m-high walls, while DD12 and LD12 cases have almost the same penetration depth of approximately 2.5 m, DL12 and LL12 cases have almost the same penetration depth of approximately 4.0 m. The cross-sectional area and moment of inertia were 136.9 cm²/m and 11,500 cm⁴/m, respectively, for PZ22 and 168.1

cm²/m and 25,200 cm⁴/m, respectively, for PZ27, with elastic modulus of 200 GPa.

4.2. Finite element analysis

The finite element modeling comprised two-dimensional plane strain analysis and analyses were carried out using Plaxis finite element code (Brinkgreve et al. 2006). Because of cohesionless soils, analyses were performed considering fully drained conditions.

When using a liner elastic soil in finite element analysis, depth of the model boundary below the dredge line has a linear effect on the vertical movement of the ground surface at the top of the wall during construction simulation, but relatively very little influence on the horizontal movement of the wall face (Briaud and Lim 1999). In this study, the depth of the numerical model boundary assumed to be two times the wall height below the dredge line. It was shown by Bilgin (1994) that the model boundary width has an affect on wall behavior up to a certain distance on both sides of the wall. Increasing the model boundary width beyond eight times of the wall height (four times the wall height both behind and in front of the wall) almost does not have any effect on wall deformations, bending moments, and anchor forces. Therefore, the model width was selected as eight times the wall height (and the wall was located in the middle of the model width) for cases analyzed in this study.

Soil layers were modeled using 15-node triangular elements. 15-node elements provide a fourth order interpolation for displacements and the numerical integration involves twelve stress points. Sheet pile wall was modeled using five-node plate elements. Interface elements had ten nodes, five on soil elements and five on wall elements. A typical finite element model mesh consisted total of 1,500 ± 30 elements (1,350 ± 25 soil elements, 51 ± 3 wall elements, and 102 ± 6 interface elements). Due to a stress concentration in and around the wall, a finer finite element mesh used in these areas and mesh became coarser in the zones away from the wall.

An elastic-plastic model is used to describe soil-structure interface behavior and the interface strength, R_{int} , is given as

$$R_{int} = \frac{\tan \delta}{\tan \phi'} \quad (4)$$

where δ =interface friction angle and ϕ' =soil friction angle. Interface strength values used for the two soil types are given in Table 1.

The soil excavation was simulated by removing soil in lifts. Total soil depth removed was performed in eight steps, i.e. the thickness of the soil lifts was equal to one-eighth of the total wall height. This resulted in 0.75, 1.125, and 1.50-m-thick soil lifts for 6, 9, and 12-m-high walls, respectively. The anchor was installed when the soil excavation reached anchor level.

4.3. Mohr-Coulomb model

The Mohr-Coulomb constitutive model for soils has been commonly used in finite element modeling of retaining walls (Potts and Fourie 1985; Day and Potts 1993; Grande et al. 2002; Karlsrud and Andresen 2005; Krabbenhoft et al. 2005; Tan and Paikowsky 2008; Potts and Fourie 1984). Because of its simplicity and limited number of parameters needed for modeling, the Mohr-Coulomb soil model also was used to simulate the response of soil layers in this study.

Mohr-Coulomb model is a linearly elastic and perfectly plastic constitutive model. The total strain, ε , that accompany the stress change is divided into elastic (recoverable), ε^e , and plastic (irrecoverable), ε^p , strain components as

$$\varepsilon = \varepsilon^e + \varepsilon^p \quad (5)$$

Similarly, strain rate, $\dot{\varepsilon}$, is also divided into elastic (recoverable), $\dot{\varepsilon}^e$, and plastic (irrecoverable), $\dot{\varepsilon}^p$, strain rate components as

$$\dot{\varepsilon} = \dot{\varepsilon}^e + \dot{\varepsilon}^p \quad (6)$$

In the elastic perfectly plastic models, the material behavior is elastic within a region of stress space below the yield surface, where recoverable deformations occur. When the stress states reach the boundary of elastic region, i.e. yield surface, then the material starts to deform under constant stress and ideal plastic deformations occur. The yield function, f , is defined by Mohr-Coulomb criterion using the

soil stresses (normal stress, σ , and shear stress, τ) and effective strength parameters (cohesion, c' , and friction angle, ϕ') as

$$f = |\tau| - \sigma \tan \phi' - c' \quad (7)$$

and when the yield function is equal to zero ($f=0$), plastic yielding occurs. The elastic soil behavior below the yield surface is characterized by Hooke's law to relate the stresses to strains.

The parameters needed for Mohr-Coulomb model are the Young's modulus, E , and Poisson's ratio, ν , for the elastic strain component of soil behavior. The effective strength parameters cohesion, c' , and friction angle, ϕ' , as well as the dilatancy angle, ψ , are needed for plastic strain component of soil behavior. Cohesionless soils ($c' = 0$) are used in this study. However, because of the numerical calculation complications that may occur in performing some of the options in finite element analysis software used (Brinkgreve et al. 2006) small soil cohesion value of 0.3 kPa was used in the analyses.

5. RESULTS AND ANALYSIS

The results of the analyses performed for twelve cases are studied in regards to active earth pressures, passive earth pressures, wall bending moments, and anchor forces. Figure 2 shows the final wall deformed shapes at the end of excavation obtained from finite element analyses for all the cases analyzed. The deformed shapes indicate that most of the walls move away from the soil towards the excavation through the height of the wall indicating active conditions behind the wall. There are two cases, DL12 and LL12, where the top of the wall moves back towards the soil, indicative of localized passive conditions. Since most of the walls move away from the soil, soil lateral earth pressures behind the wall are referred to as active earth pressures in this paper. The lateral earth pressures in the front of the wall are referred to as passive earth pressures since the wall movements within the penetration depth are always towards the excavation.

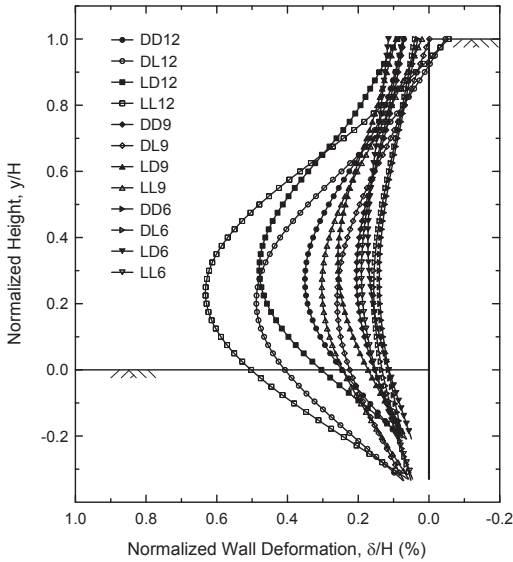


Figure 2. Wall deformations from finite element analyses

5.1. Active earth pressures

The lateral earth pressures behind the wall obtained from conventional and finite element methods are shown in Figure 3. The earth pressures are normalized by the atmospheric pressure. Finite element analysis results show

higher active earth pressures at higher wall elevations, compared to conventional method which uses Coulomb active pressure distribution. This is due to the stress concentration caused by the anchor restricting wall movements. The pressures obtained from finite element analyses are lower through the rest of wall height, except at the tip of the wall finite element analyses give slightly higher pressures. The stress concentration magnitude is bigger for higher walls, e.g. higher stress concentration occurs in 12-m-high walls compared to 9-m-high walls. In addition, the stress concentration zone moves towards the top of the wall as the wall height gets shorter. The center of the stress concentration zone is at about $0.8 \times H$ for 12-m-high walls, $0.85 \times H$ for 9-m-high walls, and $0.9 \times H$ for 6-m-high walls.

Figure 4(a) shows the comparison of active earth loads obtained from conventional and numerical methods for all twelve cases analyzed. In all the cases, the earth forces behind the wall for both methods are in good agreement, within three percent on average. The effect of method used is more significant when the locations of the resultant of lateral earth loads are considered.

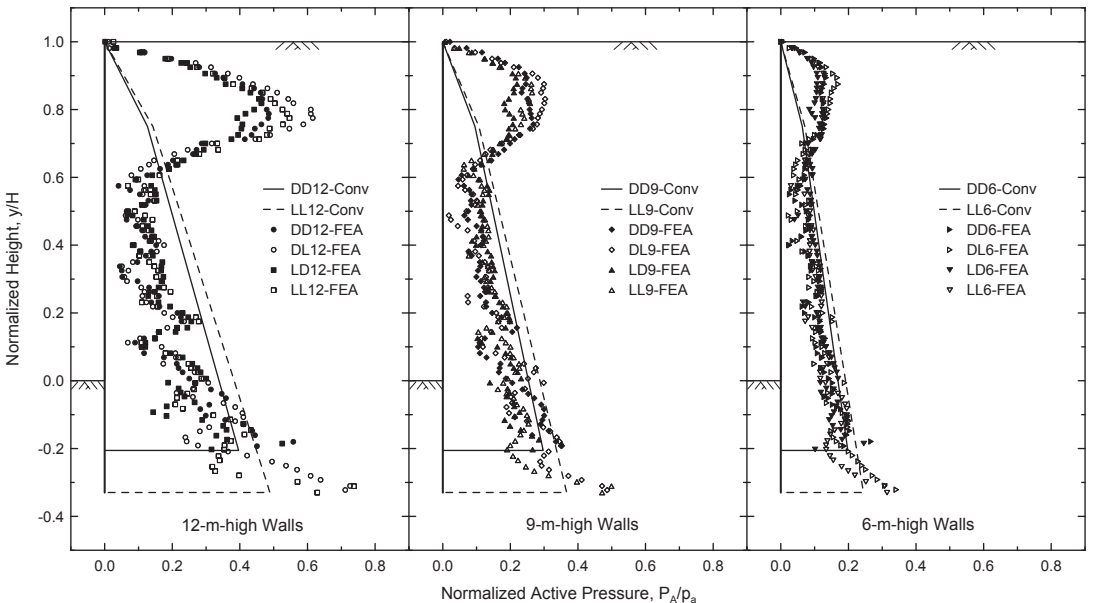


Figure 3. Normalized active earth pressure comparisons of conventional and numerical methods

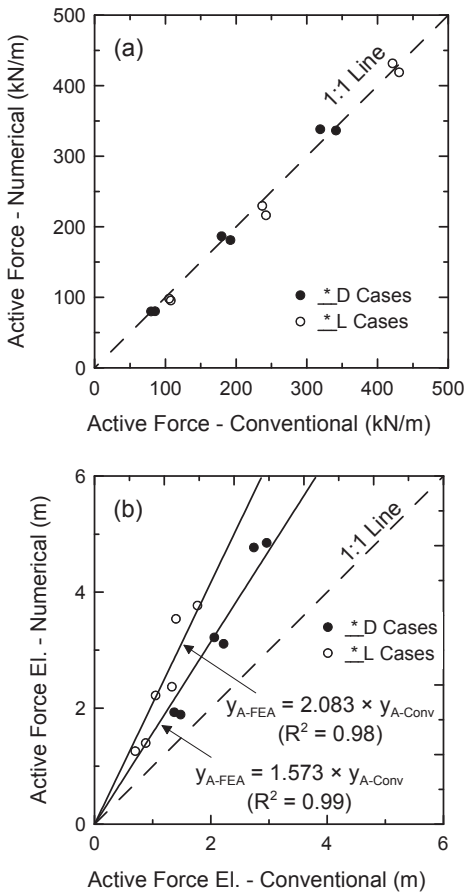


Figure 4. Active earth load comparisons of conventional and FEA methods (a) magnitude (b) location

Figure 4(b) shows the comparison of the active earth load application elevations for all the cases analyzed. The location of the resultant active force was approximately 83 percent, on average, higher than the ones assumed by the free earth support method. The difference was more significant (108 percent on average) when loose foundation soils were present. These results indicate that when the moment equilibrium is used to determine the wall penetration depth and the maximum wall bending moments during conventional design process, triangular lateral earth pressure distribution assumption would result in inaccurate designs due to the actually shorter moment arms.

5.2. Passive earth pressures

The lateral earth pressures, normalized by atmospheric pressure, in front of the walls obtained from conventional and finite element methods are shown in Figure 5. It should be noted that the pressures of free earth support method shown in the figure include the already applied factor of safety of 1.5. The passive pressures of free earth support method increase as the depth increases along the wall penetration. The finite element analyses results are in good agreement with the conventional method results within the top 70 percent of penetration depth, after which the passive pressures starts to decrease. The same behavior was observed in all twelve cases analyzed.

Figure 6(a) shows the comparison of passive earth loads obtained from conventional and numerical methods for all twelve cases analyzed. In all cases, the passive earth forces obtained from finite element analyses were lower than the ones obtained using the free earth support method. The difference is due to the lower passive pressure distributions occurring within the lower 30% of wall penetration depth as shown in Figure 5. The finite element analyses result in approximately 24%, on average, less passive earth loads compared to the free earth support method, where the passive forces already reduced by the applied safety factor of 1.5. Figure 6(b) shows that the passive earth load resultant location obtained from finite element analysis is at slightly higher elevation because of the reduced stresses toward the tip of the piles compared to conventional methods. The elevation of passive load resultant obtained from finite element analysis is approximately 11% higher when dense foundation soils are present and approximately 6% higher when loose foundation soils are present. These results indicate that the moment and horizontal force equilibriums used to determine wall penetration depth and anchor force, respectively, during conventional design process would lead to inaccurate designs due to the actually lower passive earth pressures.

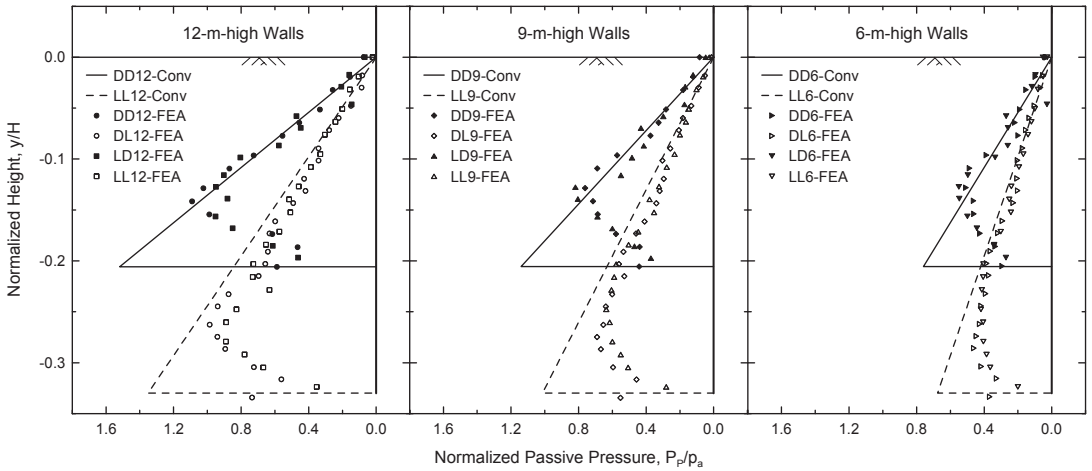


Figure 5. Normalized passive earth pressure comparisons of conventional and numerical methods

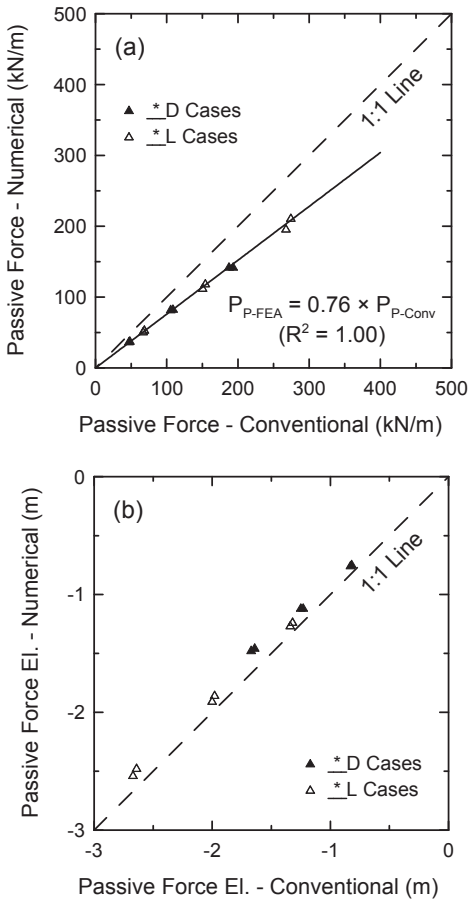


Figure 6. Passive earth load comparisons of conventional and FEA methods (a) magnitude (b) location

5.3. Wall bending moments

Figure 7 shows comparative analysis of wall bending moments obtained using free earth support and finite element methods. Figure 7(a) and (b) show the comparison of maximum moments and the location of maximum moment along the wall height, respectively. Finite element analysis resulted in much lower wall bending moments compared to the design moments obtained from free earth support method. The results show that the finite element analysis results are approximately 35% lower than the one obtained from free earth support method. The analyses results showed that the maximum bending moment along the wall height occurs at slightly lower elevation than the ones obtained from free earth support method. It should be noted that the moments from conventional methods are the design moments, i.e. values after the Rowe moment reductions applied to the maximum moments calculated using conventional lateral earth pressures and free earth support method. The maximum moments calculated before the moment reduction using the triangular earth pressure distributions are actually much higher than the moments obtained from finite element analyses (approximately 100 percent more, on average).

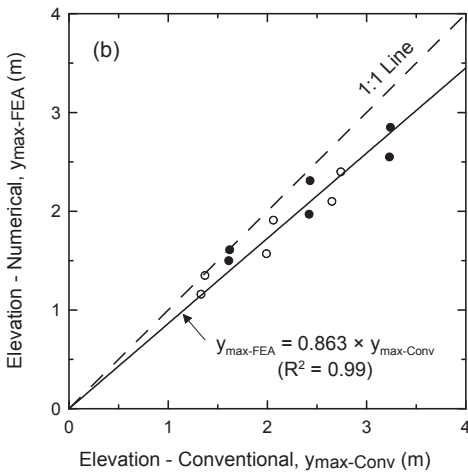
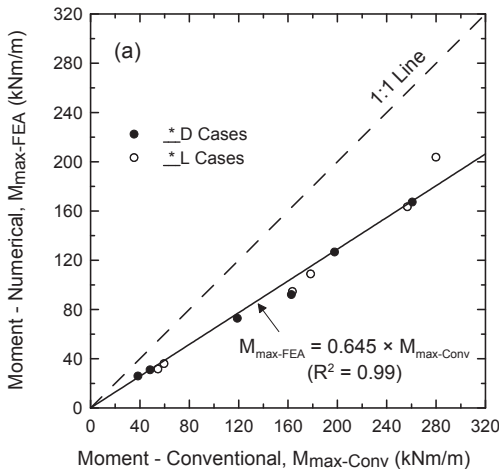


Figure 7. Wall bending moment comparisons of conventional and FEA methods (a) magnitude (b) location

5.4. Anchor forces

Since both active and passive earth pressure distributions obtained using conventional and finite element methods differ from one another, anchor forces obtained from two methods are also expected to be different. The anchor forces obtained from the analysis of all twelve cases using conventional and finite element methods are shown in Figure 8. The figure shows that the anchor forces are approximately 40 percent higher than the ones calculated from conventional method, indicating that the anchor forces are underestimated when designed using the conventional methods.

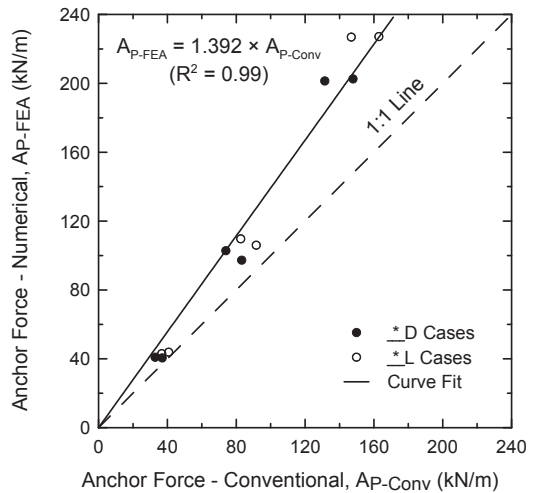


Figure 8. Anchor force comparisons of conventional and FEA methods

6. CASE STUDY OF LARGE SCALE MODEL TESTS

The results of large scale model tests performed by Grande et al. (2002) was used to verify the methods and modeling employed during the parametric study presented in this paper. Grande et al. (2002) conducted large scale model tests to study the deformation and moment distribution behavior of sheet pile wall supported with struts. Aluminum plate was used as wall material in the model. The wall was 2.06 m high with penetration depth of 0.44 m. Similar to parametric study cases performed in this study the anchor was approximately 25 percent of the wall height below the top of the wall. The model geometry, wall construction sequence, as well as soil, wall, and anchor properties were reported by Grande et al. (2002) in their paper. They have reported the wall bending moments obtained from their model tests.

A finite element modeling and analysis of the large scale wall model tested was performed using the test model geometry and material properties. Free earth support method was also used to calculate bending moments of the model wall. The wall bending moments obtained from free earth support method and the finite element analysis were compared to the measured values obtained from the model tests.

Figure 9 shows the bending moments obtained from free earth support method, finite

element analysis, and the large scale testing. Both finite element analysis and measured values are in very good agreement and both indicate that negative moment at the anchor level is maximum and governs the design. However, with the conventional design methods it is not possible to determine when the negative moment is the governing design moment because of the assumed triangular earth pressure distribution. The free earth support method gives the highest moment value among all the three values. When the positive moments are studied, the maximum moment obtained from finite element analysis is 35 percent less than the one obtained from free earth support method and it is consistent with the results of parametric study of twelve cases analyzed earlier in this study. The moment obtained from model test is even lower than the finite element value and it is about 57 percent less than the free earth support method. The model tests performed by Grande et al. (2002) also show that the free earth support method gives higher moments than what the wall actually experiences. This conclusion agrees with the parametric study findings of this study.

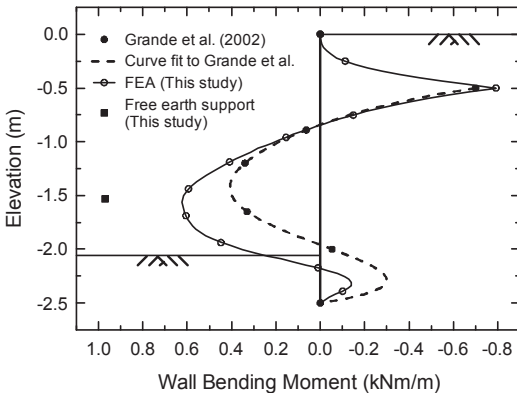


Figure 9. Wall bending moments obtained for case study

7. PROPOSED LATERAL EARTH PRESSURE COEFFICIENTS

For the cases and parameters considered the parametric study results showed that free earth support method, method commonly used for the design of anchored sheet pile walls, gives always higher wall bending moments and lower anchor forces. The same trend was observed in

all cases and there was a good correlation in the results. It is no surprise that finite element analyses give different results compared to free earth support method, because the whole design is based on the triangular lateral earth pressure distribution in front and behind the wall. However, it has been long known that both active and passive pressure distributions are actually not triangular in shape. The stresses at the tip of the wall change because of the wall tip movements and more importantly there is a stress concentration in soils around the anchor level due the restricted wall movements at that location.

The results of finite element analysis of twelve cases studied were used to develop lateral earth pressure coefficients that would provide more realistic earth pressure values to be used in the design of anchored sheet pile walls. The lateral earth pressures obtained from finite element analyses both in the front and behind the wall are divided by the effective overburden pressure to obtain the lateral earth pressure coefficient along the wall height. Earth pressure coefficients behind and front of the wall are shown in Figure 10 and Figure 11, respectively.

Earth pressures used in conventional design methods assume constant active lateral earth pressure coefficient along the height of the wall, including the depth of penetration as shown in Figure 10. The K_{A-Conv} values shown in the figure were obtained considering the non linear log spiral failure surface (U.S. Navy 1986). For the active conditions, the Coulomb earth pressure coefficients can also be used as they yield approximately same values. The figure shows that the conventional methods significantly underestimate the lateral earth pressure coefficient at higher elevations along the wall height and slightly overestimate at lower elevations. Based on the results obtained and the data presented in Figure 10, it appears that for the normalized heights below 0.6 the lateral earth pressure coefficient is almost constant, except towards the tip where it increases slightly. For the normalized heights of more than 0.6, the lateral earth pressure coefficient increases almost linearly up to the ground surface. The coefficient decreases when very close to ground surface, within the top $0.1 \times H$. The increase in the lateral earth pressure coefficient was ex-

pected since it has been long known that there is a stress concentration in soils around the anchor level due the restricted wall movements by the anchor. The active lateral earth pressure coefficient trends obtained from the analysis of twelve cases of this study are shown in Figure 10.

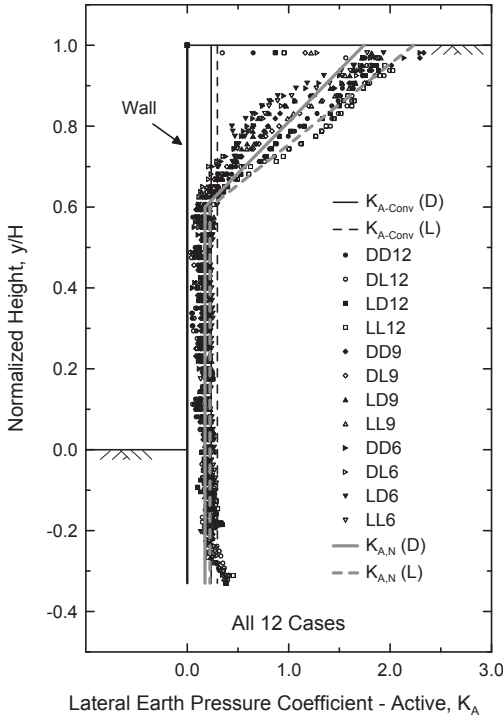


Figure 10. Active earth pressure coefficient ($\sigma'_{H-FEA} / \gamma'z$)

Earth pressures used in conventional design methods also assume constant passive lateral earth pressure coefficient along the depth of wall penetration as shown in Figure 11. The K_{P-Conv} values shown in the figure were obtained from U.S. Navy (1986) design manual considering the non-linear, logarithmic spiral, failure surface. The Coulomb passive earth pressure coefficient gives even higher values than the ones given by U.S. Navy (1986). Figure 11 shows that the lateral earth pressure coefficients obtained from finite element analyses are significantly lower than the ones given by conventional methods. The results in Figure 11 show that although there are some fluctuations the passive earth pressure coefficient is almost

constant within the normalized depths of up to 0.7. Beyond this depth, the coefficient decreases almost linearly until the pile tip. The active lateral earth pressure coefficient trends obtained from the analysis of twelve cases of this study are shown in Figure 11.

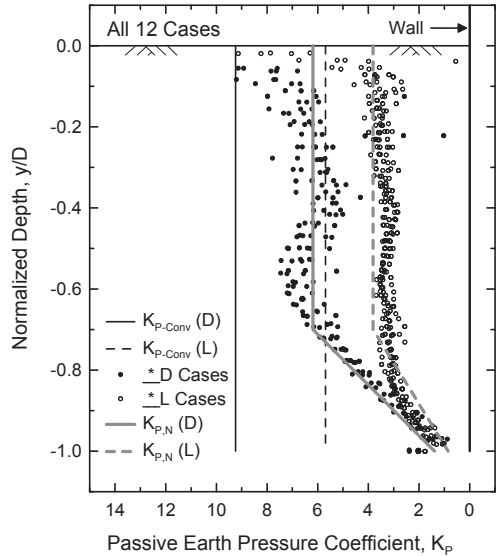


Figure 11. Passive earth pressure coefficient ($\sigma'_{H-FEA} / \gamma'z$)

The lateral earth pressure coefficients shown in Figure 10 and Figure 11 for different soil types yield unique trends for active and passive conditions when normalized by the coefficients obtained from conventional methods where constant coefficient is assumed through the height of the wall. The proposed lateral earth pressure coefficients to be used in the design of anchored sheet pile walls normalized by the ones obtained from conventional methods are given in Figure 12, for both active and passive conditions. The active earth pressure coefficients behind the wall are normalized by the Coulomb earth pressure coefficients. The passive earth pressure coefficients in front of the wall are normalized by the coefficient obtained considering non-linear failure surface as given by U.S. Navy (1986). For active conditions, the Coulomb lateral earth pressure coefficients can also be used.

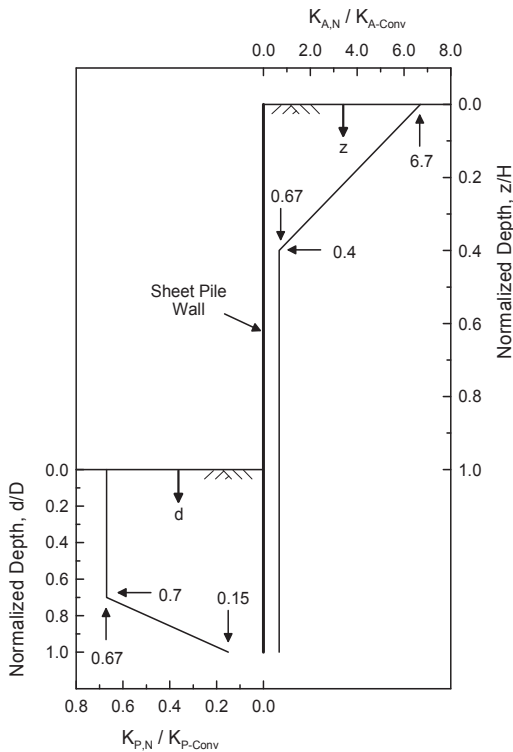


Figure 12. Proposed active and passive lateral earth pressure coefficients

Based on the results of this study and Figure 12, the proposed lateral earth pressure coefficient behind the wall (active lateral earth pressure coefficient) is given as

For $0 < z < 0.4 \times H$:

$$K_{A,N} = \left(6.7 - 15.08 \frac{z}{H} \right) \times K_{A-Conv} \quad (8)$$

For $0.4 \times H < z < H + D$:

$$K_{A,N} = 0.67 \times K_{A-Conv}$$

where $K_{A,N}$ =proposed active earth pressure coefficient; K_{A-Conv} =active lateral earth pressure coefficient using non-linear log spiral failure surface (U.S. Navy 1986) or Coulomb active lateral earth pressure coefficient; z =depth from the wall top; H =wall height; and D =wall penetration depth.

Similarly the proposed lateral earth pressure coefficient in front of the wall (passive lateral earth pressure coefficient) is given as

For $0 < d < 0.7 \times D$:

$$K_{P,N} = 0.67 \times K_{P-Conv} \quad (9)$$

For $0.7 \times D < d < D$:

$$K_{P,N} = \left(1.88 - 1.73 \frac{d}{D} \right) \times K_{P-Conv}$$

where $K_{P,N}$ =proposed passive earth pressure coefficient; K_{P-Conv} =passive lateral earth pressure coefficient using non-linear log spiral failure surface (U.S. Navy 1986); and d =depth from the bottom of excavation (i.e. dredge line).

8. DISCUSSION OF RESULTS AND DESIGN IMPLICATIONS

There have been several anchored sheet pile wall failures reported in the literature. Sowers and Sowers (1967) presented several cases of anchored bulkhead failures. They have concluded that excessive earth pressures, inadequate support, inadequate consideration of or allowance for deflection, and lack of consideration of effect of construction operations were among the factors leading to anchored sheet pile wall failures. Rieke et al. (1988) reported failure of 300-ft-long anchored sheet pile wall during the placement of backfill behind the wall. Barley (1997) reported failure of 15.6-m-high anchored sheet pile walls due to an anchor component failure. Endley et al. (2000) reported unexpectedly larger than the originally calculated deformations for a 12-m-high anchored sheet pile wall. None of the wall failures reported was a result of a bending moment failure of sheet pile sections, indicating that the pile sections selected based on the design bending moments have more safety factors compared to the other components of wall system. This is consistent with the findings of the parametric study presented in this paper. The finite element analysis results showed that the conventional methods result in approximately 50 percent more bending moments. The parametric study results also showed that the conventional methods underestimate the anchor forces

approximately 28 percent. The anchor failures reported in the literature mentioned above could very well be the reason of this underestimation of the actual forces that the anchor system experience. If the anchors have been designed for 40 percent more loads as obtained from the parametric study (Figure 8), it is very likely that some of the anchor failures, e.g. 15.6-m-high wall reported by Barley (1997), resulting in overall wall failure could have been prevented.

As discussed earlier, the finite element analysis results showed that free earth support method, even after Rowe moment reduction, results in higher wall bending moments. On the other hand, parametric study results indicate that the free earth support method actually underestimates the anchor forces. This is because of the inaccurate lateral earth pressures used in the conventional design methods. The design performed using the new proposed lateral earth pressure coefficients given in Figure 12 takes into account the stress concentration at the anchor level that would be the better representative of soil stresses acting on the wall. A sheet pile wall designed using these earth pressures will result in more accurate wall bending moments and anchor forces.

9. SUMMARY AND CONCLUSIONS

Although the existence of stress concentration at the anchor level due to the restricted wall movements has been long known, the conventional design methods assume lateral earth pressures linearly increase with depth and do not consider the stress concentration/ reduction. Since the whole design depends on the lateral earth pressures, the design based on an inaccurate earth pressure distribution will result in designs which are either conservative or more importantly unsafe.

A comparative parametric study using conventional design method and finite element method was performed to investigate the lateral earth pressures, bending moments, and anchor forces of anchored sheet pile walls in cohesionless soils. For the parameters and the ranges considered, the following conclusions were drawn from this study:

- Neither active nor passive earth pressures do not linearly increase with depth as assumed in conventional design methods. The stress

concentration occurs at the anchor level due to the restricted wall movements. There is also a stress increase in the active pressures and reduction in passive pressures close to the pile tip.

- Conventional design method overestimates the wall bending moments. For the cases studied, conventional design methods resulted in approximately 50 percent more wall bending moments compared to the finite element analysis results.
- Conventional design method underestimates the anchor forces. Anchor forces obtained from finite element analysis were approximately 40 percent more than the ones obtained from conventional design method.
- The proposed lateral active and passive earth pressure coefficients consider the stress concentration/reduction and result in more accurate lateral earth pressure distributions along the wall height. Therefore the proposed earth pressure coefficients and the pressure distributions should be used for more accurate wall bending moment and anchor force calculations.

10. REFERENCES

- Barley, A. D. (1997). "The failure of a 21 year old anchored sheet pile quay wall on the Thames." *Ground Engineering*, 42-45.
- Bilgin, Ö. (1994). *The behavior of anchored sheet pile walls constructed by excavation and backfilling*. Thesis, School of Civil and Environmental Engineering, Oklahoma State University, Stillwater, Oklahoma.
- Bilgin, Ö., and Erten, M. B. (2009). "Analysis of anchored sheet pile wall deformations." *Proc., International Foundation Congress & Equipment Expo '09*, Orlando, FL.
- Briaud, J. L., and Lim, Y. (1999). "Tieback walls in sand: numerical simulation and design implications." *Journal of Geotechnical and Geoenvironmental Engineering*, ASCE, 125(2), 101-109.
- Brinkgreve, R. B. J. et al. (editors) (2006). *Plaxis 2D – Version 8 users manual*. Rotterdam: A.A. Balkema.
- Clough, G. W., and Duncan, J. M. (1991). Earth Pressures. In *Foundation Engineering Handbook*, ed. H-Y. Fang, pp. 223–235. Van Nostrand Reinhold, New York.

- Dawkins, W.P. (2001). "Investigation of wall friction, surcharge loads, and moment reduction curves for anchored sheet pile walls." *ERDC/ITL TR-01-4*, US Army Corps of Engineers.
- Day, R. A., and Potts, D. M. (1993). "Modelling sheet pile retaining walls." *Computers and Geotechnics*, 15(3), 125-143.
- Endley, S. N., Dunlap, W. A., Knuckey, D. M., and Sreerama, K. (2000). "Performance of an anchored sheet pile wall." *Proc., GeoDenver 2000 Geotechnical Measurements - Lab and Field, GSP No. 106*, ASCE, 179-197.
- Goel, S., and Patra, N. R. (2008) "Effect of arching on active earth pressure for rigid retaining walls considering translation mode." *International Journal of Geomechanics*, ASCE, 8(2), 123-133.
- Grande, L., Soreide, O. K., and Tefera, T. H. (2002). "Large scale model testing on the moment distribution and deformation behaviour of a sheet pile wall." *Proc., 2nd Int. Conference on Soil Structure Interaction in Urban Civil Engineering*, Zurich, Switzerland, 389-394.
- Karlsruh, K., and Andresen, L. (2005). "Loads on braced excavation in soft clay." *International Journal of Geomechanics*, ASCE, 5(2), 107-113.
- Krabbenhoft, K., Damkilde, L., and Krabbenhoft, S. (2005). "Ultimate limit state design of sheet pile walls by finite elements and nonlinear programming." *Computers and Structures*, 83(4,5), 383-393.
- Nataraj, M. S., and Hoadley, P. G. (1984). "Design of anchored bulkheads in sands." *Journal of Geotechnical Engineering*, ASCE, 110(4), 505-515.
- Potts, D. M., and Fourie, A. B. (1984). "The behavior of a propped retaining wall: results of a numerical experiment." *Geotechnique*, 34(3), 383-404.
- Potts, D. M., and Fourie, A. B. (1985). "The effect of wall stiffness on the behavior of a propped retaining wall." *Geotechnique*, 35(3), 347-352.
- Rieke, R. D., Crowser, J. C., and Schroeder, W. L. (1988). "Bulkhead failure investigation and redesign." *Journal of Geotechnical Engineering*, ASCE, 114(10), 1110-1125.
- Rowe, P. W. (1952). "Anchored sheet-pile walls." *Proc., Institution of Civil Engineers*, London, Part I, Vol. 1, No. 5788, 27-70.
- Sowers, G. B., and Sowers, G. F. (1967). "Failures of bulkhead and excavation bracing." *Civil Engineering*, 37(1), 72-77.
- Tan, Y., and Paikowsky, S. G. (2008). "Performance of sheet pile wall in peat." *Journal of Geotechnical and Geoenvironmental Engineering*, ASCE, 134(4), 445-458.
- U.S. Army (1994). *Design of sheet pile walls, EM 1110-2-2504*, U.S. Army Corps of Engineers, Washington, D.C.
- U.S. Navy (1986). *Design Manual, 7.02, Foundations and Earth Structures*, U.S. Navy, Naval Facilities Engineering Command (NAVFAC), Alexandria, Virginia.

Differential earth pressure against combined sheet pile walls: Full-scale tests and numerical simulations

Fang LIU, Mingjing JIANG, Wei ZHOU

Department of Geotechnical Engineering, Tongji University, Shanghai 200092, China.

E-mail: liufang@tongji.edu.cn, mingjing.jiang@tongji.edu.cn, 15371778967@126.com

Hiroaki NAKAYAMA

Nippon Steel & Sumitomo Metal Corporation, Chiba, Japan 293-8511.

E-mail: nakayama.8q7.hiroaki@jp.nssmc.com

ABSTRACT: Full-scale tests and the finite element simulations were undertaken for investigating the differential earth pressures against the combined steel sheet pile walls formed by steel sheet piles intermittently welded with H-sections. The comparison between the simulations and the field measurements shows a good agreement in terms of the ultimate wall deflection. Apparent differential earth pressures were seen at the same elevation due to soil arching caused by the different properties of primary and secondary elements of the walls as well as the corrugated surface of the walls. The stiffness and spacing of the primary elements significantly affect the earth pressure re-distribution between the primary and secondary elements of the walls.

1. INTROCUITION

Steel sheet pile (SSP) wall is a common type of flexible retaining system used in waterfront structures such as quay walls of ports. This type of wall is formed by sequentially connecting prefabricated steel sheet piles (with variable shapes e.g. U-profile, Z-profile, and Hat-profile), and receives particular attention in the field of coastal engineering due in part to its exceptional performance in terms of space-saving and reusability. Sheet piles can be also used in combination with steel tubular piles or H sections to form combined walls, which can provide an economic solution for larger bending stiffness than that of pure SSP walls.

Calculation of earth pressure in sheet pile design is usually based on classical soil mechanics (USACE 1994, BSI 2009); however the actual earth pressure distribution along sheet pile walls have not been very well understood. Variation in stiffness and shape of different members forming a combined wall could further complicate the earth pressure distribution against the wall.

Extensive studies have been conducted on the plastic bending/hinge of SSP in order to embrace plastic design of SSP in Eurocode 3 (Bourne-Webb 2007, 2011a). Pertinent effort has also been made to investigate the reduced

modulus action and in-plane bending resulting from interlocking between adjacent steel sheet piles (SSPs) (Crawford & Byfield 2002, Byfield & Mawe 2004, Bourne-Webb 2011b). All these studies are very beneficial to highly improve the principle used in SSP design. However, as an important input factor, the load associated with earth pressures are oversimplified in SSP design based on the framework of the ultimate limit state design, where active or passive earth pressures based on the classical soil mechanics were assigned according to a rough estimate of wall movement by ignoring the soil-wall interaction (USACE 1994, Kort 2002). The distribution of earth pressures against SSP walls has been more realistically evaluated using the finite element simulation under excavation conditions in several studies by considering the plasticity in soils and/or SSPs (e.g., Tan & Paikowsky 2008, Bourne-Webb 2011a), but these studies were in two-dimensional context, which can not simulate the differential earth pressure at the same depth resulting from the corrugated cross section of SSP walls.

The actual earth pressure distributed on a SSP wall could be distinct from that on a planar wall being considered in the classical theories of earth pressure. DiBiagio (1977) reported that the earth pressures measured at the same depth but on the protruding and indented corrugations

of a propped SSP wall were almost equal immediately after pile installation, but deviated from each other during excavation. This difference was hypothetically attributed to the consolidation and arching or movements of sheeting (DiBiagio 1977). Tan & Paikowsky (2008) also found the pressure difference between inside and outside webs of a SSP wall at the same depth according to a two-year field instrumentation. Although there are few in situ measurements of earth pressures against a combined SSP wall, we suspect more noticeable differential earth pressures to be seen on different members of the wall in this case due to more distinction in geometry and stiffness of the members forming the wall.

Eurocode 3 explicitly states that the primary and secondary elements of a combined wall should be designed based on their functionality: (1) the primary elements (normally tubular piles, H sections, or built up box types, etc.) act as the retaining elements against earth pressures; and (2) the secondary elements (generally steel sheet piles of various types) only fill the gap between primary elements and transmit loads resulting from the earth pressures to the primary elements. However, it is still unclear on how to implement this general guideline to accurately compute earth pressures between different elements, although Eurocode 3 addresses that it can be advantageous to take into account the arching effects leading to a supplemental loads to the primary element and a reduction in earth pressure against the secondary elements.

This paper presents some preliminary results from a collaborative effort between Tongji University and Nippon Steel & Sumitomo Metal Corporation with the aim of a better understanding on the differential earth pressures against combined SSP walls. Full-scale tests were conducted on Japanese side for two combined walls using Hat-type piles (Hat piles for short), some of which were welded with H sections of variable length as the primary elements. The finite element method (FEM) was then used to simulate the full-scale tests on the combined walls in order to attain complete information of the earth pressure distribution in the transversal and vertical direction of the walls. Finally a parametric study using FEM was also present to discuss the impact of wall configuration parameters such as the stiffness of

the primary elements and the spacing between primary elements.

2. SUMMARY OF FULL-SCALE TESTS

A total of three full-scale walls (one pure SSP wall and two combined SSP walls) were monitored with respect to their performance during excavation. These full-scale tests are recapped in this section for completeness, and more detailed information on the tests can be found in Nakayama et al. (2013).

2.1. Test procedure

In order to place the instrumentation on the retained side of the walls, excavation was imitated in a man-made embankment following the procedure illustrated in Fig. 1. The sheet piles were first driven into the ground with a height of 6 m being remained above the ground using the vibratory hammer method without water jetting. After that, earth pressure cells and other sensors were attached on the surface of the wall on the retained side. In order to attain a uniform ground, the embankment was constructed up to a total height of 5 m by layers with 0.4 m raising for each, leaving 1 m height wall above the surface for the sake of safety. The ground was compacted by running a bulldozer, and the soils adjacent to the piles were rammed down using a tamper. After consolidation, the embankment was excavated using a backhoe on one side of the wall by six steps with an excavation depth of 1 m each.

Figure 2 presents the plane view of the embankment, occupying an area of $50\text{ m} \times 24\text{ m}$ at the original ground level and forming a plateau of $38\text{ m} \times 12\text{ m}$ in area on the top. Three walls formed by SSPs are 7.2 m each in length, and they are aligned along the central line of the embankment.

2.2. Wall specifications

All three walls being tested are 13.5 m in height. Figure 3 illustrates the cross sections of the walls including two combined SSP walls (i.e., case 1 and 2) and one pure SSP wall (i.e., case 3). In case 1, four Hat piles and four enhanced Hat piles with H sections are alternatively connected together forming a 7.2 m wide wall. The Hat piles are pre-manufactured products,

called NS-SP-10H. Each Hat pile is 900 mm in width and its geometry data is given in Fig. 4(a). Figure 4(b) shows the combination of a Hat pile and an H section forming a primary element. The length of the H sections is differently selected in case 1 and 2. H sections in case 1 cover the full length of the Hat piles, while those in case 2 only cover a length of 7.5 m of the Hat piles, starting at the distance of 3.5 m from the top of the Hat piles. The wall in case 3 is composed of twelve U-profile piles with a width of 600 mm each. The test results of case 3, which can be read from Nakayama et al. (2013), are omitted here because combined SSP walls are the focus of this paper.

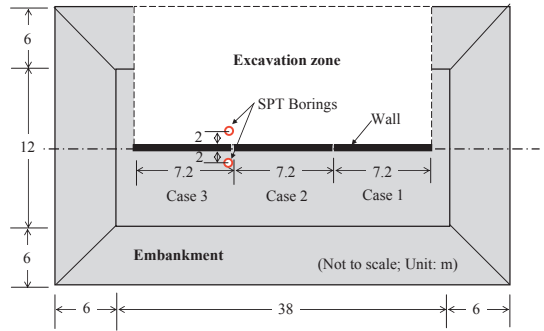
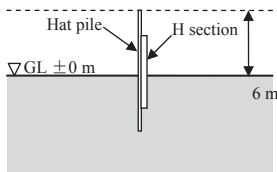
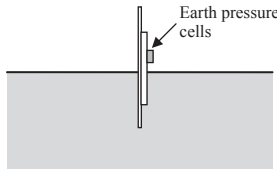


Figure 2. Plane view of the embankment and three walls

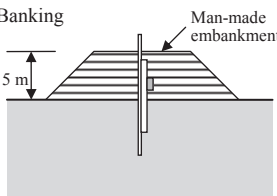
Stage I: Pile installation



Stage II: Instrumentation



Stage III: Banking



Stage IV: Excavation

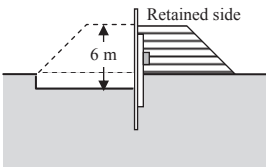
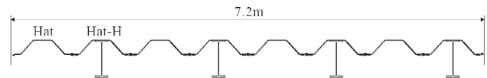


Figure 1. Construction procedure of the full-scale tests

Case 1 & 2



Case 3



Figure 3. Cross sections of three walls

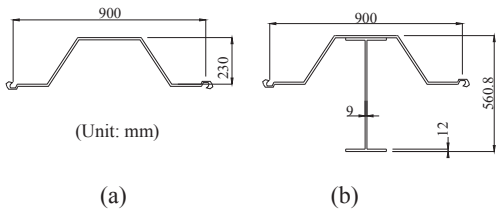


Figure 4. Geometry of the wall elements used in case 1 and 2: (a) secondary element (NS-SP-10H Hat pile); and (b) primary element (NS-SP-10H Hat pile welded with an H section)

2.3. Instrumentation

Figure 5 shows the positions of the instruments used to monitor the performance of the walls during excavation.

For each wall, a total of four earth pressure cells were placed on the retained side of the walls, two at the original ground surface (i.e., $GL \pm 0$ m), and the other two at 1 m above the ground surface (i.e., $GL +1$ m). At the same elevation level, one earth pressure was attached to the web of a Hat pile, and the other attached to an H-section. The wall deflection was

measured from two inclinometers attached on the excavation side of the wall. The horizontal displacement of the wall at the embankment surface level was detected through the three-dimensional measurement by a digital camera taking pictures on the target points attached at the top of the piles.

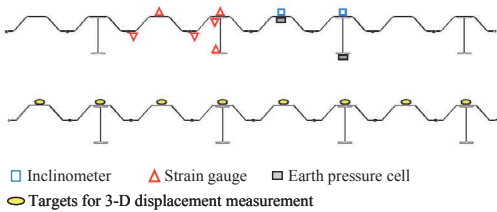


Figure 5. Instrumentation layout (lower side is the retained side)

3. SOIL PROPERTIES

After the embankment was constructed, two standard penetration tests (SPT) were conducted on the retained and excavation sides of the walls, and the positions of SPT borings are shown in Fig. 2.

Figure 6 presents the SPT blow counts at various depths. The ground water table was seen at 2 m below the original ground surface. Above the original ground surface, the blow count increases with the increase of the embankment depth. This seems reasonable since the lower part of the embankment received more compaction energy and surcharge loads than the upper parts. It is plausible that the two curves above the ground surface obtained from different side of the walls are close to each other with small variation. This indicates that the soils on both sides were uniformly constructed.

Two soil samples were collected from each SPT boring at 2.5 m above the ground surface and 1.5 m below the ground surface. The consolidated drained triaxial compression test (CD test) was conducted on each soil samples. The stress-strain response and volumetric strain response curves are presented in Fig. 7. The strength parameters resulting from the CD tests are tabulated in Table 1. The angle of the internal friction, ϕ , ranges from 35.1° to 42.4°. The cohesion, c , is small in all samples, indicating that sandy soils were encountered in the field.

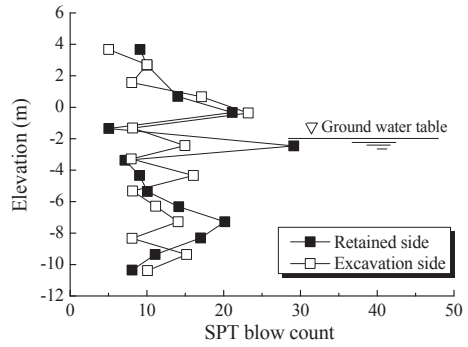


Figure 6. SPT boring logs

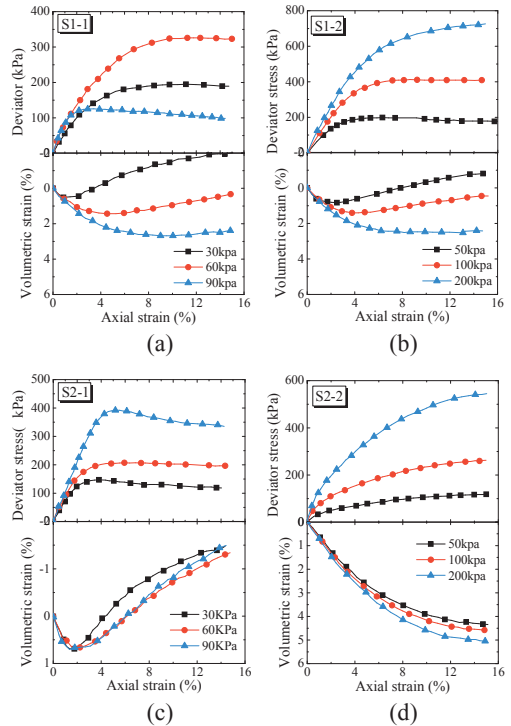


Figure 7. Stress-strain response curves and volumetric strain response curves obtained from CD tests on four soil samples

Table 1 Strength parameters of soils obtained from CD test

No.	S1-1	S1-2	S2-1	S2-2
Position	Excavation side	Retained side		
Elevation (m)	+2.5	-1.5	+2.5	-1.5
c (kPa)	4	10	0	0
ϕ (°)	38.5	39.3	42.4	35.1

4. FINITE ELEMENT ANALYSIS

The numerical simulation of the full-scale tests were conducted using the commercial FEM software ABAQUS. Figure 8 shows the geometry and boundary conditions of the FEM model. The wall was truncated into 4.5 m wide in the model consisting of three secondary elements interlocked with two primary elements. The wall is 12.5 m in height. The upper portion of the wall above the embankment surface was not considered in the analysis, because this part will not significantly affect the results of earth pressures. The embankment was simplified as part of the ground providing lateral confining to the wall. The ground was simulated up to a depth and lateral expansion twice as large as the wall height in order to minimize possible boundary effect. Considering the ground water lower than the excavation level, pore water pressure was not considered in the simulations and the analysis was performed with respect to the total stress rather than the effective stress.

Figure 9 shows the three-dimensional (3D) mesh of one symmetrical half of the model composed of 115450 elements in total.

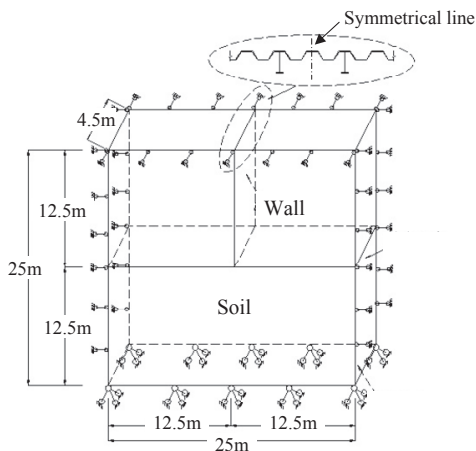


Figure 8. Geometry of the finite element model

The wall was simplified as a continuous wall without physically modelling the interlocks between Hat piles, but the interlocking effect was considered by reducing the modulus of the wall. The Hat piles were modelled using solid cell elements with finite thickness. The H sections were simplified using linear beam

elements, which were tied to Hat piles and assigned with the sectional properties according to the actual H sections. The wall elements were assumed to be elastic with a Poisson ratio of 0.3 and an elastic modulus of 100 GPa (after considering a modulus reduction factor of 0.5 due to interlocking effect).

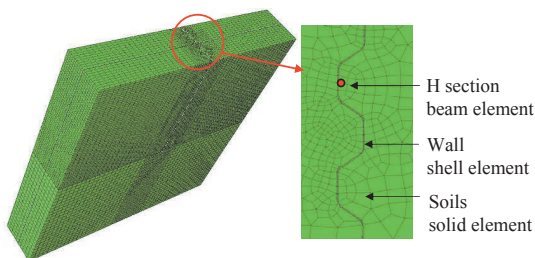


Figure 9. 3D mesh used in the simulation

Soils were modelled using solid elements with eight nodes each. A simple Mohr-Coulomb model was used for soils, although other rigorous elastic-plastic models of soils, which will be implemented in future study, are advantageous especially in simulating the stress-dependency and plasticity of soil properties. The model parameters of soils are given in Table 2. The averaged strength parameters, c and ϕ , obtained from CD tests were used in the simulation. The angle of dilation, ψ , was set as a half value of the angle of internal friction in soils corresponding to dense soils. A typical value of the Poisson ratio was picked according to the early stage of the volumetric strain responses in CD tests. The elastic modulus was first estimated from the stress-strain response curve, ranging from 5 to 30 MPa, and then justified in the simulation in order to attain a wall deflection as close as possible to the field data at the end of excavation. The results corresponding to the elastic modulus of 30 MPa agree relatively well with the field data, so are presented in the subsequent section for comparison.

Table 2 Parameters of Mohr-Coulomb model used for soils in the simulation

γ (kN/m ³)	ν	E (MPa)	c (kPa)	ϕ (°)	ψ (°)
20	0.3	30	3.5	38.5	19

The wall-soil interface was assumed to be rough with an angle of interface friction, δ , as

large as a half value of the angle of internal friction in soils, ϕ . The wall-soil interface was modelled using zero thickness interface element in which the shearing resistance was defined using a Mohr-Coulomb failure criterion.

Before excavation, an initial stress field was obtained from the geostatic step by assigning a predefined coefficient of lateral pressures, i.e., 0.42 in this case. The excavation procedure was simulated by six steps with 1 m removal each. The soil and interface elements within the removal zone were sequentially killed in each excavation step.

5. COMPARISON BETWEEN TESTS AND ANALYSES

Figures 10 and 11 compare the wall deflection obtained from FEM simulations to the measurements acquired by the full-scale tests. As shown in Fig. 10, the wall deflection at the top of the wall during excavation is larger in case 2 than in case 1, because shorter H sections were used in case 2. The simulated deflection is in good agreement with the field data when the excavation depth exceeds 5 m, below which, however, much less deflection is seen in the simulation. This variation is due in part to the excessive heave of the excavated ground estimated by Mohr-Coulomb model, which assumes the same pre-failure deformation modulus during loading and unloading so that the unloading modulus could be underestimated leading to a larger rebound deformation than it should be. Lifting force due to ground heave could be induced and transmitted to the wall on the excavation side through the rough wall-soil interface, endowing the wall a slight rotation, which will partially compensate the wall deflection towards the excavation side at the top of the wall. A parametric analysis with respect to the elastic modulus of soils also demonstrated that this rotation can be more evident if a smaller value of the modulus was used. One of the consequences resulting from this unexpected rotation is that, although the ultimate wall deflection estimated by the simulation is in nearly the same magnitude as the field data at the end, less simulated deflection is seen in the case of shallow excavation where the wall deflection due to unbalanced lateral earth

pressures from the retained side have not yet become dominant.

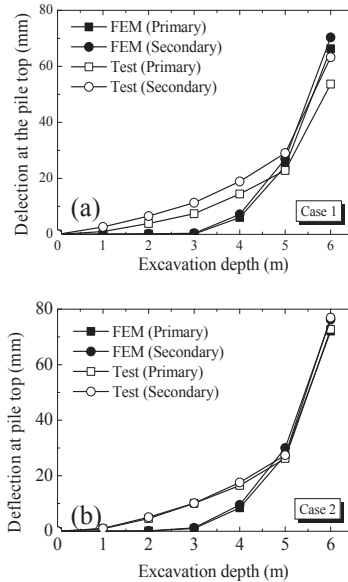


Figure 10. Comparison of the deflection at the top of the wall obtained from the field tests and FEM simulations for: (a) case 1; and (b) case 2

Figure 11 also demonstrates a good agreement between the simulation and the field data in terms of the deflection of the full-length wall, particularly above the excavation level (i.e., GL -1 m). However, below the excavation level, a slight deflection up to 5 mm towards the retained side of the wall was seen in the simulations, which could also be caused by soil rebound on the excavation side due to unloading.

Despite the distinction with respect to wall deflection during the intermediate phase of excavation, the simulated earth pressures after the completion of excavation are regarded acceptable to some extent, because the simulation produced an ultimate wall movement generally agreeing well with the field measurement, which will control the magnitude of earth pressures according to the classical well-known soil mechanics.

Figure 12 and 13 compare the simulated earth pressures to the field measurement obtained from the earth pressure cells placed on the secondary elements and primary elements (see Fig. 5), respectively.

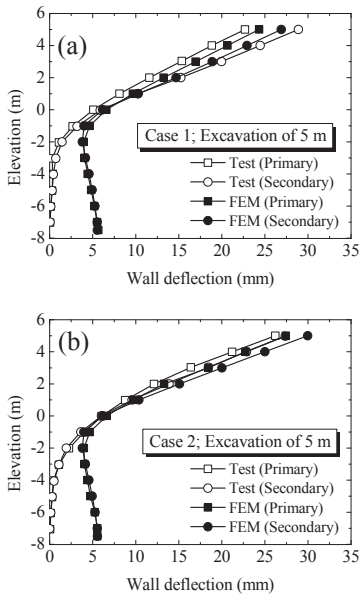


Figure 11. Comparison of wall deflection obtained from the field tests and FEM simulations under an excavation depth of 5 m for: (a) case 1; and (b) case 2

As shown in Fig. 12, for a given elevation, when the excavation depth is less than 3 m, no significant decrease is found in the simulated earth pressures against the secondary elements, which however rapidly drop to a reasonable range close to the field data at the end.

As shown in Fig. 13, the simulated earth pressures against the primary elements are found to apparently deviate from the field measurements when the excavation depth is less than 3 m. Before excavation started, the field instrumentation provided earth pressure already much larger than the theoretical value of the earth pressure at rest. Note that the observation points on the primary elements in the simulations are different from those in the field. The earth pressure cells in the field were attached behind the H sections of the primary elements (see Fig. 5), while the observation points in the simulation were set directly behind the web of the Hat piles of the primary elements (see point A in Fig. 14), because the H sections were not physically modelled in the simulation but simplified as beam elements. However this difference will not cause such larger deviation of the earth pressure before excavation. Therefore, this inconsistency was considered due to excess compaction near the wall in the

field as addressed by Nakayama et al. (2013). When the excavation depth reaches 3 m, the simulation and field data seem to coincide gradually.

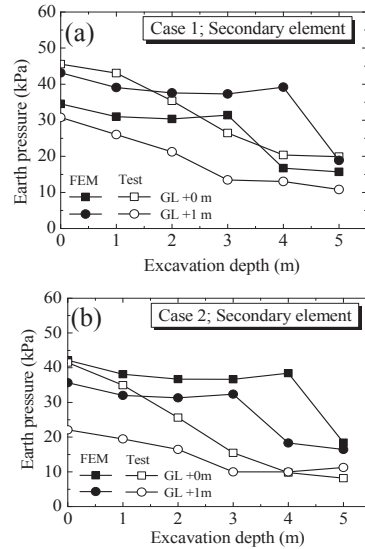


Figure 12. Comparison of earth pressures against the secondary element obtained from the field tests and FEM simulations for: (a) case 1; and (b) case 2

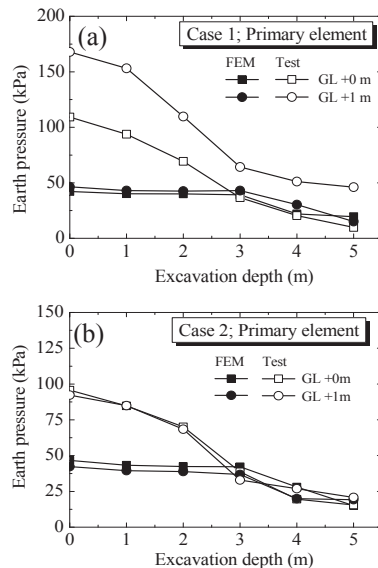


Figure 13. Comparison of earth pressures against the primary element obtained from the field tests and FEM simulations for: (a) case 1; and (b) case 2

In order to show the differential distribution against the primary and secondary elements of the walls, the transversal distribution of the earth pressures at the same elevation are given in Fig. 14, in which the results obtained from case 1 at the elevation of 2 m and the excavation depth of 5 m are presented as an example. The theoretical solution based on Coulomb's theory of the active earth pressure is superimposed in the figure for comparison. As shown in Fig. 14, the earth pressure behind the web of the secondary element (i.e., point C) is close to the theoretical value, but the earth pressure behind the primary element is about 50% higher. This upward jump of earth pressures is due to earth pressure re-distribution between the secondary and primary elements as a result of soil arching caused by differential soil movement behind different elements of the wall. Another interesting finding is the differential earth pressures between point B and C, which will be also seen in pure SSP walls without H sections (Liu et al. 2012). This is due to soil arching solely attributed to the impact of the corrugated surface of the wall (Liu et al. 2012).

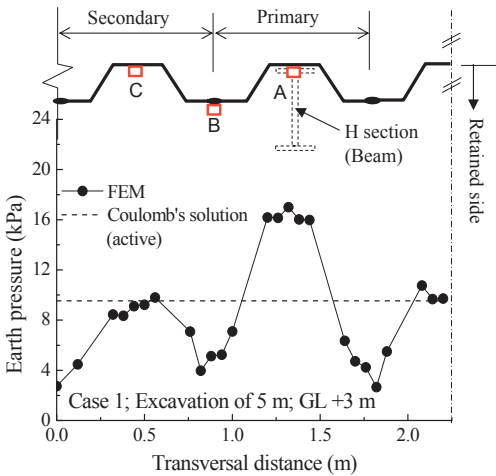


Figure 14. Differential earth pressures in the transversal direction of the wall

The earth pressure of points A, B, and C at different elevations can be found in Fig. 15. Since very little difference is found between case 1 and 2, we concluded that appropriately shortening H sections will not cause extra detrimental earth pressures against the wall.

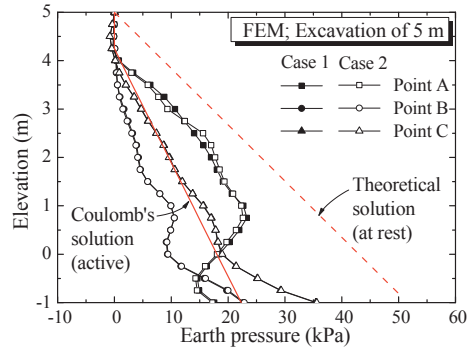


Figure 15. Earth pressure distribution along the depth of the walls

6. PARAMETRIC ANALYSES OF WALL SPECIFICATIONS

Parametric analyses were also conducted through FEM simulations with the aim to investigate differential earth pressures on SSP combined walls with different configurations of the wall elements, such as the spacing between primary elements and the stiffness of primary elements.

Considering the majority usage of SSP walls in soft soils, soils were modelled in this parametric study using the modified Cam-clay model with a parameter set (see Table 3) obtained from a typical silty clay, which can be extensively found in the fifth stratum below the ground surface in Shanghai area. The wall-soil interface is assumed to be frictionless to avoid the interface effect at this moment.

Table 3. Parameters of modified Cam-clay model for a typical silty clay in Shanghai area

γ (kN/m ³)	ν	c (kPa)	Φ ($^{\circ}$)	K	λ	M
18.0	0.33	21	23.7	0.016	0.12	1.2

As shown in Fig. 16, for simplicity, all simulations used a unified model of the wall (12 m in height and 8.1 m in width) composed of nine Hat piles. Enhancement of the bending stiffness of wall due to the presence of the H sections was imitated by assigning a large value of the elastic modulus to the webs (i.e., E_2 , normally larger than the elastic modulus of the Hat piles, E_1), where H sections were welded

(i.e., dark zones in Fig. 16). This enhancement of stiffness can be characterized by the modulus ratio $\xi = E_2/E_1$. Note that $\xi=1$ stands for a pure SSP wall without any H sections being used. Another important factor in wall configuration, the spacing between the primary elements can be characterized by the number of the Hat piles between two H sections, N_s , and examples of $N_s = 1$ (dense case), and 3 (sparse case) are shown in Fig. 16.

The excavation proceeded in five steps in the simulations to reach a total excavation depth of 5 m. The wall deflections and differential earth pressures on the wall at the same elevation were analyzed with respect to different configurations of the wall.

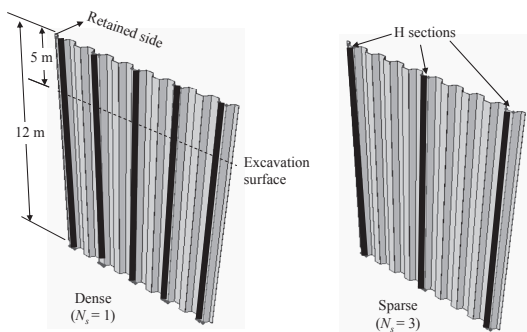


Figure 16. Illustration of two combined walls with different values of the spacing between primary elements

6.1. Effect of stiffness ratio

Figure 17 presents the deflections at the top of the wall under different stiffness ratios if three Hat piles are used between two primary elements (i.e., $N_s = 3$). When the stiffness of the primary element is 10 times as large as that of the secondary element (i.e., $\xi = 10$), the reduction of the maximum deflection (at the secondary element) is about 6% of that produced by a pure SSP wall. However much less reduction in the wall deflection is noticed when the ratio is increased further from 10 up to 1000. This infers that increasing the stiffness of the primary elements will not effectively reduce the wall deflection if the stiffness ratio is already larger than 10.

Figure 18 presents the earth pressures against the primary elements (i.e., point A in Fig. 14) and secondary elements (i.e., point C in Fig. 14). As for the case of SSP wall (i.e., $\xi=1$), the pressures against the inside web (i.e., point C in Fig. 14) are presented in Figs. 18(a) and (b). Little variation is found in the earth pressure distributions when the stiffness ratio exceeds 10. Differential earth pressures in the transversal direction are seen because the stiffness of the primary and secondary elements varies. Above the excavation surface, the earth pressures against the primary elements on the retained side of the wall are larger than the secondary elements, while smaller below the excavation surface.

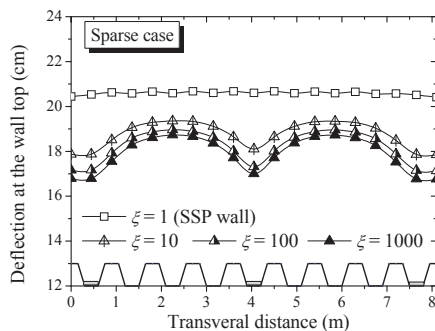


Figure 17. Deflection at the top of the wall at different stiffness ratios

Figure 19 plots the ratio of the earth pressure against the combined wall at various depths to that against the pure SSP wall (point C in Fig. 14) at the same depth, termed as the re-distribution ratio. This ratio can be used to characterize the re-distribution of earth pressure between primary and secondary element. This ratio is equal to one for the case of pure SSP walls. Larger this ratio is, more loads associated with earth pressures are withstood by that element. As shown in Fig. 19, the re-distribution ratio for secondary element ranging from 0.8 to 1.0 decreases with the increase of stiffness ratio ξ . In the contrast, the re-distribution ratio for primary elements ranging from 1.0 to 1.8 increases with the increase of stiffness ratio.

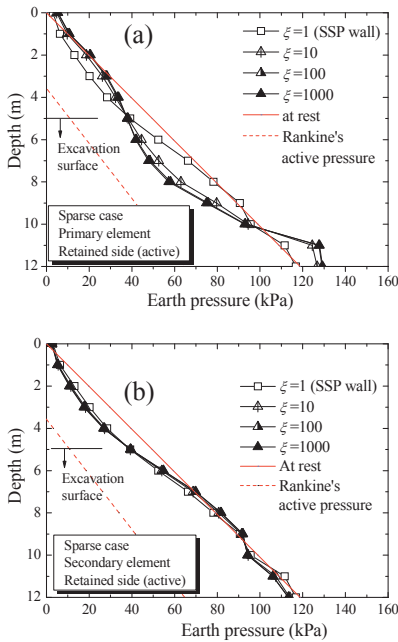


Figure 18. Earth pressures against: (a) the primary element; and (b) the secondary element at different stiffness ratios

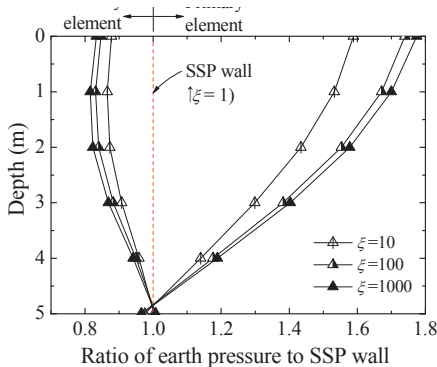


Figure 19. Redistribution ratio against the primary and secondary elements at various stiffness ratios

6.2. Effect of spacing of primary elements

Figures 20 and 21 presents results obtained from different values of the spacing between primary elements under a stiffness ratio of 1000. Note that a stiffness ratio of around 10 is more common in the practice.

As shown in Fig. 20, 17% and 7% reduction of the maximum wall deflection (at the second

ary elements) is seen when one and three Hat piles are placed between two primary elements, respectively.

As shown in Fig. 21, the spacing of the primary elements will also affect the redistribution ratio. For the case of $N_s = 3$, the results of the secondary element are obtained from the one in the middle between primary elements. With the increase of the spacing, the redistribution ratio will increase for both secondary and primary elements. As the spacing is enlarged, the redistribution ratio for secondary elements approaches one, because soil arching between the primary and secondary elements can not be effectively formed and differential earth pressures appear only adjacent to the primary elements but not far way. However earth pressure redistribution always happen surrounding the primary elements, and, as a result, the redistribution ratio increases with the spacing but we expect it will reach a steady value at a certain spacing, which requires further investigation.

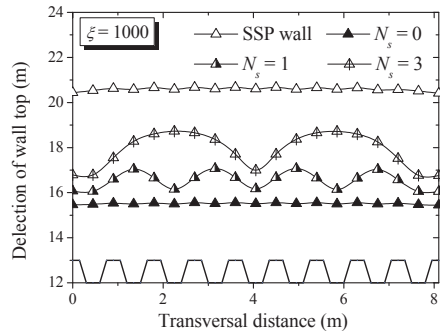


Figure 20. Deflection at the top of the wall at different spacing settings between primary elements

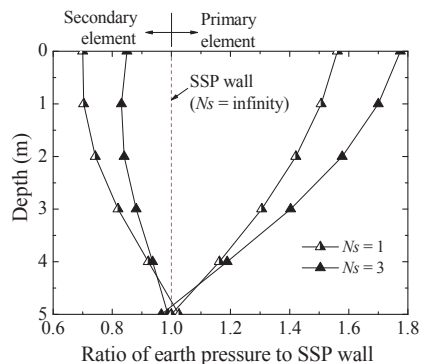


Figure 21. Redistribution ratio against the primary and secondary elements at variable spacing

7. CONCLUSIONS

Full-scale tests and the finite element simulations were conducted for investigating the differential earth pressures against the combined steel sheet pile walls using Hat-type piles and H sections. In addition, parametric analyses were performed to examine the effect of different wall configurations. The major conclusions are as follows.

(1) The simulated ultimate deflections of the wall after the completion of the excavation are in good agreement with the field measurements. However the simulated intermediate deflections during shallow excavation are less than field data due to excessive ground heave estimated by Mohr-Coulomb model which underestimates the deformation modulus during unloading.

(2) Differential earth pressures are seen at the same elevation due to earth pressure redistribution between the secondary and primary elements as a result of soil arching caused by differential soil movements behind different elements of the wall. The earth pressure against the primary elements can be 50% higher than that against the secondary element. Moreover, differential earth pressures can also be induced by the corrugated surface of the wall.

(3) Appropriately shortening H sections in the primary elements of a combined SSP wall will not cause extra detrimental earth pressures against the wall.

(4) The stiffness of the primary elements relative to that of the secondary element affects the earth pressure distribution between the primary and secondary element. The redistribution ratio of earth pressures decreases with increasing stiffness ratio for the secondary elements, while increases for the primary elements. However, to increase the stiffness of the primary elements will not effectively reduce the wall deflection if the ratio is already larger than 10.

(5) The increase of the spacing between two primary elements will enlarge the maximum wall deflection and the redistribution ratio of earth pressures.

ACKNOWLEDGEMENT

The study is part of the collaboration project financially supported by Nippon Steel & Sumi-

tomo Metal Corporation. Support from National Science Foundation of China (No. 41102173 and 51025932) is also appreciated.

REFERENCES

- Bourne-Webb, P. J., Potts, D. M. & Rowbottom, D. 2007. Plastic bending of steel sheet piles. *Proceedings of the Institution of Civil Engineers-Geotechnical Engineering*, Vol. 160, No. 3, pp. 129-140.
- Bourne-Webb, P. J., Potts, D. M., KÖNig, D. & Rowbottom, D. 2011a. Analysis of model sheet pile walls with plastic hinges. *Géotechnique*, Vol. 61, No. 6, pp.487-499.
- Bourne-Webb, P. J., Potts, D. M. & Rowbottom, D. 2011b. Eurocode reduction factors for U-profile sheet pile walls. *Proceedings of the Institution of Civil Engineers-Structures and Buildings*, Vol. 164, No. 6, pp. 377-390.
- Byfield, M.P. & Mawer, R.W. 2004. Analysis of reduced modulus action in U-section steel sheet piles. *Journal of Constructional Steel Research*, Vol. 60, pp. 401-410.
- Crawford, R.J. & Byfield, M.P. 2002. A numerical model for predicting the bending strength of Larsen steel sheet piles. *Journal of Constructional Steel Research*, Vol. 58, pp. 1361-1374.
- Nakayama, H., Toshihiko, S., Noriyoshi, H., Kei, T. & Ryosuke, N. 2013. Full-scale embankment load test on retaining walls combined with hat-type sheet piles and hat-type sheet piles and hat-type +H-shape sheet piles. *Proceedings of the 5th China-Japan Geotechnical Symposium*, Chengdu, China, pp. 411-420.
- Dibiagio, E. 1977. Field instrumentation-A geotechnical tool. Norwegian Geotechnical Institute Pub. No. 115, pp. 29-40.
- Liu, F., Zhang, G. Q., Jiang, M. J. & Nakayama, H. 2012. Shape effect on active earth pressure against a sheet pile wall with different displacement modes. *Proceedings of the International Symposium on Coastal Engineering Geology*, Shanghai, China, pp. 245-249.
- Tan, Y. & Paikowsky, S. G. 2008. Performance of sheet pile wall in peat. *Journal of Geotechnical and Geoenvironmental Engineering*, Vol. 134, No. 4, pp. 445-458.
- US Army Corps of Engineers (USACE). 1994. *Design of Sheet Pile Walls*, EM 1110-2-2504, Department of the Army, U.S. Army Corps of Engineers, Washington, D.C.

- British Standards Institution (BSI). 2009. *Eurocode 3: Design of Steel Structures, Part 5: Piling*. BS EN 1993-5: 2007, BSI, Milton Keynes.
- Kort, D. A. 2002. *Steel Sheet Pile Walls in Soft Soils*. PhD thesis, Delft University of Technology, Netherlands
- Krabbenhoft, K., Damkilde, L. & Krabbenhoft, S. 2005. Ultimate limit state design of sheet pile walls by finite elements and nonlinear programming. *Computers and Structures*, Vol. 83, pp. 383-393.

Numerical Modelling of Anchored Retaining Structures in Medium Stiff to Stiff Soils

I. Sokolić

Geotehnički studio d.o.o. – Zagreb, CROATIA, igor.sokolic@geotehnicki-studio.hr

ABSTRACT: The modern approach to numerical modelling of anchored retaining structures is described in this paper, with special concern on computer software Plaxis 2D and advanced hardening constitutive soil model (Hardening Soil small model - HSs). The basic characteristics of soil behavior are described for cohesive and non-cohesive stiff to medium stiff soils, both in drained and undrained conditions. The critical overview on the capabilities of advanced soil models is given, taking into account the complex change of stress state in the soil around the excavation pit. The strategy for determination of HSs soil parameters is described for soil conditions typical in the area of City of Zagreb. The strategy is developed by monitoring retaining wall displacement and by performing back analysis and parametric analysis in computer program Plaxis 2D.

1. INTRODUCTION

The design of anchored retaining structures is very complex geotechnical problem in which the aspect of soil-structure interaction is pronounced. For making the quality construction design it is necessary to make the range of specific stability and serviceability calculations such as control for: global stability, overturning, anchor resistance, anchor grouted body resistance, structural element resistance, the stability of basal heave, hydraulic failure due to seepage, uplift stability, structure deformation and the deformation of the surrounding ground and audience buildings. Some examples of design situations are shown on Figure 1. (according to BSI: Eurocode 7, 2004).

Classical design approach of retaining structures imply a number of different types of calculations and methods for each stability, resistance and serviceability control. For example the global stability is controlled by comparing the moment effect of the actions toward the moment effect of resistance to the center of rotation. The calculation can be made by using some of the limit state methods for soil stability such as the method according to Bishop, Jambu, Spencer or similar. The control of structural element resistance can be modelled by structural beam resisting on the linear spring (at the

positions on anchors), and on the Winkler spring bedding (in the area of passive soil resistance). The same method can be used for prediction of retaining wall displacement. It is recommended that the results of displacement calculations are double checked with some of the empirical methods that are calibrated on monitoring of similar structures in similar ground conditions.

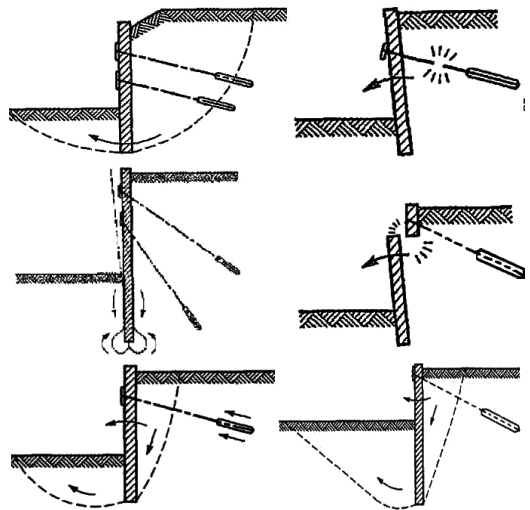


Figure 1. Examples of different design situations from Eurocode 7 (2004).

The method proposed by Clough & O'Rourke (1990) is one of such empirical method widely used for prediction of the horizontal wall movement and the settlement of the ground behind the wall. For the calculation of the hydraulic failure of the ground it is necessary to construct complex flow nets for describing the hydraulic flow of underground water and the field of flow gradients in the critical areas around the wall.

The main disadvantage of the classical approach is the grate number of different methods and recommendations that must be used for different design situations and stability calculations (Gaba et al. 2003, Twine and Roscoe 1999, German Society for Geotechnics 2003). There are many different assumptions and restrictions on how to define the soil pressure distribution on the wall (Figure 2.), which depends on: Soil type, Retaining wall type (diaphragm wall, sheet pile wall, secant pile wall etc.) and Anchor type (stiffness, disposition and installation sequence).

The specific problem in classical approach for retaining wall design are the assumptions to define the stiffness of the soil (Winkler springs) and stiffness of the anchors. Those values are not the constants for the soil material but depends on the soil-structure interaction.

Beside the many assumptions and restrictions of the classical design approach, those methods are constantly used in every day praxis, due to the fast calculation process and simplicity of the calculation methods. Those methods are developed and calibrated based on the results of measurements of physical models and monitoring of the performance of real structures. That provides great confidence for their use in similar ground conditions, and for similar retaining structures.

But due to great evolution of technologies in the field of retaining structures, the modern excavation pits are going beyond the boundaries of comparable experience (much deeper excavations, complex soil profiles and different soil conditions). For that reason there is a constant need for developing the unique design method for design of modern retaining structures. Such a method should enclose all stability, resistance and deformation controls in the same process. It should account for all aspects of real soil and structural elements behavior, and should imply for their interaction. One of such modern methods is the Finite Element numerical Method (FEM) for geotechnical modelling that enable the wide range of design controls in a simple model (Figure 3).

The development of the method was initiated by the development of constitutive sols models, which started in early 1970. Also, developments in computer hardware and, more importantly, in geotechnical software enable the geotechnical engineer to perform very advanced numerical analyses at low cost and with relatively little computational effort. Commercial codes, fully integrated into the PC-environment, have become so user-friendly that little training is required for operating the software. They offer sophisticated types of analysis, such as fully coupled consolidation analysis with elasto-plastic material models. However, for performing such complex calculations and obtaining sensible results a strong background in numerical methods, mechanics and, last but not least, theoretical soil mechanics is essential. This is sometimes overlooked in practice because glossy brochures give the impression that achieving reliable results is as easy as operating the software and this is certainly not true (Schweiger 2002)!

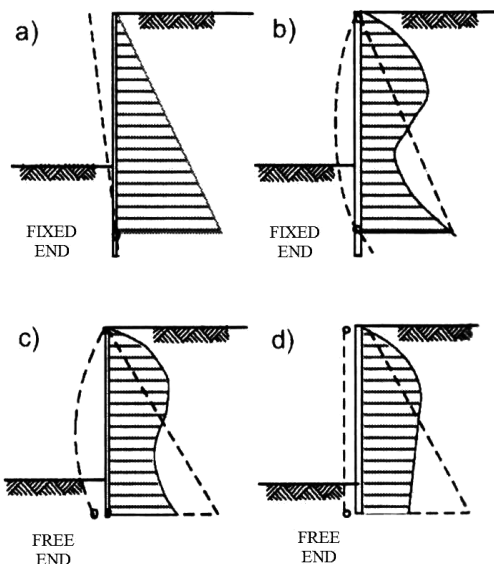


Figure 2. Schematic view on the effect of anchor disposition on the soil pressure distribution.

Due to complexity of the process, there are many difficulties that arise from of numerical modelling of geotechnical structures. The results of the research performed by De Vos and Whenhman (2006), show that the main problems are related to:

- Soil parameters (23% of examinee)
- Initial stress in the ground (16%)
- Type of constitutive soil model (15%)
- Interpretation of the results (13%)
- Discretization of finite element mesh (11%)
- Boundary conditions (10%)
- Type of calculation (9%)
- Type of mesh element (5%)
- Other (1%)

The first three elements are the core of the FEM numerical modeling, so it is a great concern that they gain problems in the everyday praxis for more than 50% of examinee. Additional problem is that the customers that are using the same calculation methods, that are modelling the same retaining structure based on a same geotechnical investigations, produce the wide range of different results that cannot be expected from the engineer point of view. Such observations can be observed in benchmarks performed by Schweiger (2002) and von Wolfersdorff (1994) on anchored retaining structures in sand.

The great contribution to the development of the numerical modelling of retaining structures provided the research in the field of constitutive soil models (Pots et. All 2002), theory of soil mechanics (Mitchell et al. 2005), Soil investigation (Mayne et al. 2001) and monitoring of geotechnical structures (Duncliff 1993). The complete interaction of those research fields is required to be able to make the quality benchmarks, back analysis and parametric analysis, and it provides the development of the modern approach of modelling geotechnical structures.

The computer software Plaxis 2D is very common in the everyday praxis and it is widely used around the Globe (Brinkgrave 2010). The hardening model (Hardening Soil Model – HS) available in Plaxis 2D and its extension with small strain stiffness (Hardening Soil Small – HSs) are very applicable for modeling the cohesive and non-cohesive materials. From that reason they are widely used for modelling

geotechnical structures in the area of City of Zagreb where the gravel and stiff clay are dominant in the soil profile. Additionally there is constant increase in monitoring of the performance of the retaining walls during the construction (Sokolić & Plepelić 2010), that enabled the performance of quality back analysis and parametric analysis (A. Szavits-Nossan 2008, Sokolić 2007, A. Szavits-Nossan et al. 2009, Tomac & Marić 2006, Sokolić 2008).

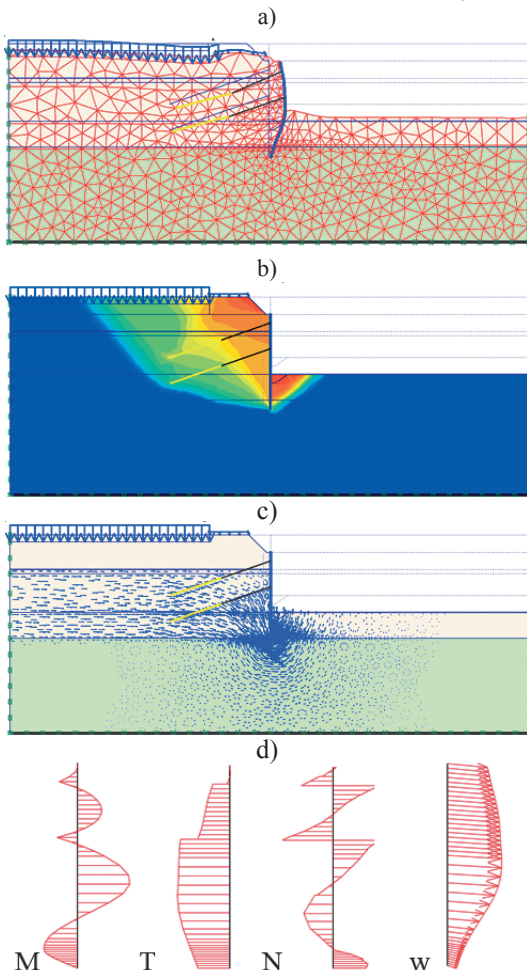


Figure 3. Examples of the stability and serviceability controls performed by FEM modelling in computer software Plaxis 2D. a) the serviceability calculation (the deformation of the structure and surrounding soil); b) the global safety control; c) control of hydraulic failure; d) the control of structure resistance (internal forces: Moment, Shear Force and Axial Force); e) serviceability check (wall displacement)

2. ELEMENTS OF NUMERICAL MODELING

Numerical model of anchored retaining wall consists of soil elements, retaining structure elements (retaining wall, free anchor length, grouted anchor length) and boundary conditions (kinematic displacement conditions and static conditions of external forces or anchor prestress forces). Based on great number of research in the field of numerical analysis of retained structures, some basic guidance can be defined for basic elements of numerical modeling.

From the aspect of numerical modeling, the triangle elements are more stable than rectangle elements, while the elongated and irregular shapes should be avoided (De Vos and Whanhman 1999). When using triangle elements it is important to have six stress knots to gain sufficient precision of the calculation. When the failure is expected to accrue in the calculation, the elements with more knots should be used (Brinkgrave 2010). The density of the finite element mesh should be adjusted to the each model so that it is denser in the area of stress concentration (at the bottom of the retaining wall, beside the wall and the anchor bond length, at the boundary of applied external loads or displacements). In the rest of the model the mesh should be light to save the calculation time. Optimal density of the finite element mesh should be defined iteratively by gradual increase of density until there is no more effect to the final results of the calculation (De Vos & Whanhman 1999). The same principle is valid for the size of the element. The research performed by Potts and Zdravković (2001) on the model of retaining structure in the clay with the stiffer, shows that the height of the model affects much the results of wall displacement. The effect is more pronounced on for the soil model with linear stiffness than for the model with small strain stiffness, and it can be neglected for the height / width ratio of excavation pit model bigger than 10. The effect of the width of the model on the soil settlement behind the wall is greater than the effect of the model height. For the soil model with small strain stiffness the effect can be neglected for the width of the model / width of the excavation pit ratio bigger than 20, while for the soil model with linear stiffness, at the ratio bigger than 40.

Kempfert and Gebreselassie (2006) performed the numerical simulation of anchored retaining structure with three rows of anchor in soft clay. The results of analysis show that the width of the model has small influence on the horizontal deformation on the wall and bending of the wall. The dominant effect on the soil settlement behind the wall and the bottom heave has the height of the model / width of the model ratio. The influence on the results can be neglected for the height of model / width of the pit ratio and width of the pit / width of the model ratio bigger than 10.

When modelling retaining wall it must be considered that the thickness of the wall can influence the results of analysis, which is often neglected when modeling the wall by plate elements. Potts and Zdravković 2001 have shown that when using the volume elements for modelling the wall, the shear stress appears on the face of the wall, causing the smaller final displacement of the wall and smaller internal moment. For that reason, it is on the 'safe side' when modelling sheet pile walls or diaphragm walls by using plate elements. The plate elements are also used when modelling the pile walls. In such conditions great care must be taken to define the effective axial and bending stiffness of such walls (Brinkgrave 2010, Potts and Zdravković 2001).

The contact between the soil and wall or soil and anchor grouted body is modelled by using interface elements. Those elements can reduce the stiffness and strength of the soil on the contact. The research shows that the stiffness reduction has minor effect on the results of the analysis (Potts and Zdravković 2001), while the strength reduction has the minor effect on the active pressure and the horizontal displacement of the wall at the toe of the wall, small effect on the internal moment and big effect on the rotation and vertical displacement of the wall (Freiseder 1998).

The problem to define the type of the calculation (drained, undrained, coupled consolidation calculation) and the initial state of stress in the ground is much more complicated. It is well known that the ideal elastic model results in unrealistic deformations of the retaining structure and the surrounding soil, leading to great basal heave and the unrealistic rotation of the bottom of the wall (Schweiger 2002, Sokolić

2008, Pots and Zdravković 2001). Unrealistic tensile stress appears in the active area behind the wall and to big compression in the passive zone. Those effects can be reduced by introducing the Mohr-Coulomb failure criteria (Mohr-Coulomb soil model – MC). But the MC model doesn't have the capability to account for dilatancy effects on strength that can be a problem especially in undrained analysis.

Generally, the main trend in modern numerical modeling of anchored retaining structures is the use of advanced soil models which enables the performance of coupled consolidation analysis by using effective soil strength parameters. They account also for the stiffness reduction due to shearing, small strain stiffness, kinematic and isotropic hardening etc. (Gaba et al. 2003, De Vos and Whenhman 2006, Schweiger 2002, Pots et al. 2002, A.Szavits-Nossan 2008, A.Szavits-Nossan et al. 2009).

3. STATE OF STRESS IN THE GROUND AND THE EFFECTS OF EXCAVATION

Due to pit excavation and anchor installation the surrounding ground exhibits grate change in stress and strain. The surrounding soil can be divided in four characteristic zones according to the change of stress state (Figure 4). Zone 1 in which the vertical stresses remain almost the same while horizontal stresses reduces due to excavation in front of the wall and the movement of the wall toward the pit (Active Zone); Zone 2 in which the vertical stresses remain almost the same while the horizontal stresses increase due to anchor forces; Zone 3 in which the vertical stresses decrease due to excavation, while the horizontal stresses increase due to wall movement toward the soil (Passive zone); Zone 4 in which the vertical stresses decrease due to soil excavation, while the horizontal remain almost the same.

The change in stress state can be described by stress trace (Figure 5 b and c). The starting point of stress trace is defined by initial state of stress in the ground which is defined by effective weight of the soil γ' and the coefficient of the horizontal stress K_0 . In both cohesive and non-cohesive normally consolidated soil the K_0 coefficient can be calculated by using Jaky's expression:

$$K_0 = K_0^{nc} = 1 - \sin(\varphi') \quad (1)$$

where φ' is effective angle of internal friction, and in preconsolidated soils by using the expression according to Mayne and Kulhawy (1982):

$$K_0 = K_0^{nc} OCR^{\sin(\varphi')} \quad (2)$$

where OCR is the coefficient of overconsolidation that can be measured by confidence in odometer.

Care must be taken when testing high overconsolidated clays when great vertical pressure must be used, that is rather rear in conventional geotechnical laboratory. The results of investigation on such clays performed by Burland (1979) shows that the value of the overburden removal effects great on the K_0 value, but its effect is negligible for the horizontal stress in the ground. In such condition the near the surface the value of K_0 is much close to the passive value K_p , deeper below the surface the value is around 1.0. The value of K_0 and OCR can be investigated with 'in-situ' field tests such as CPT (Lune et al. 1997), pressuremeter or dilatometer.

Figure 1c. shows the stress trace around the excavation pit due to excavation in stiff clay where the starting point of stress (point O) assumes that $\sigma_h' > \sigma_v'$. The starting state came from the initial stress for normally consolidated soil (point O') by removing the overburden pressure. In the case that the installation of the retaining structure imply the excavation of the soil (when installing diaphragm wall or secant piles) first there is decrease of stress in the area near the retaining wall (point 1A and point 1B). After the wall installation the stress returns almost in the same starting position (Point 2a and 2B). Due to excavation there is decrease in the stress behind the wall (point 3A) and increase in the front of the wall (point 3B). The pore pressure decreases and the underground water starts to seep. The pore pressure in over consolidated clays reached initially after excavation is less than for the final state of static seepage. In the process of the pore pressure 'relaxation', the effective stress in the soil decrease which can lead to the active failure (point 4A) or even passive failure (point 4B).

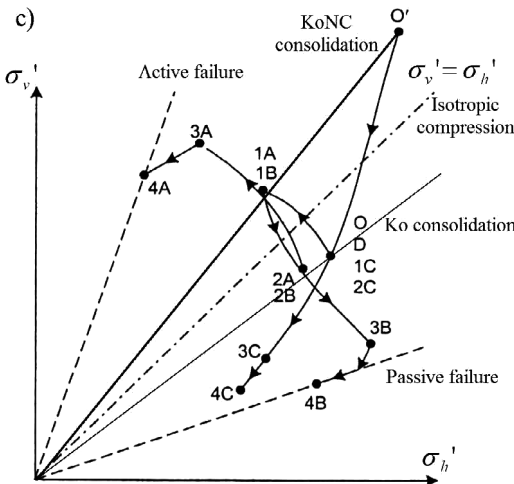
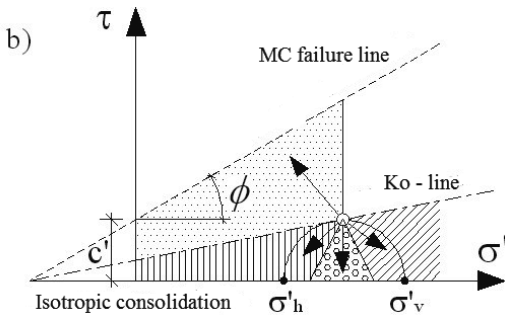
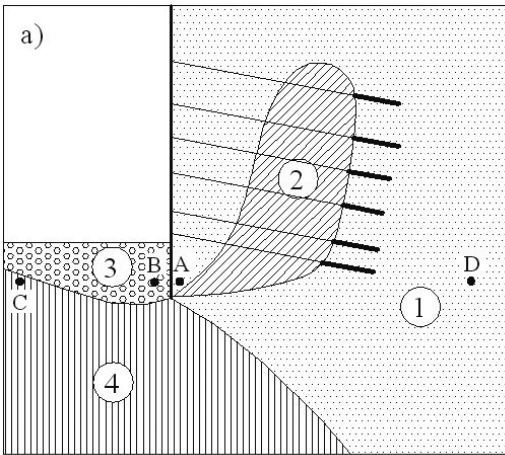


Figure 5. a) Zones of characteristic stress traces due to pit excavation; b) stress trace in corresponding zones; c) active and passive failure in stiff clay behind the wall and in front of the wall (after Gaba et al. 2003 and Kempfert and Gebresselassie 2006)

The complexity of change in the stress state around the excavation pit is one of the main reason that makes the numerical modeling of anchored retaining structures very complex process. The calculation of effective stress change depends most on the initial state of the stress in the ground (Figure 5c). Additionally it is effected by the calculation of the pore pressure in undrained analysis, which causes the main problem when choosing the right soil constitutive soil model to gain the most realistic results of analysis.

4. THE SOIL BEHAVIOUR AND THE APPROPRIATE CONSTITUTIVE MODEL

In the classical approach of modelling anchored retaining structures that is based on MC soil model, the most important is to determine the equivalent strength and stiffness parameters for the final stage of limit equilibrium. The modelling approach is the same both in the case of drained and undrained conditions, while the type of strength parameters should be adopted to the type of analysis (drained or undrained).

On the other hand, the numerical calculation with final element model is performed in steps (step by step implementation of boundary conditions) so there is a need to model the stress-strain behavior of soil for the wide range of state of stress and strain. The final result is obtained by gradually integrating the soil response by applying the boundary conditions.

Due to extremely nonlinear and plastic behavior of the soil and the effect of dilatation (characteristic effect for the granular material), there is still no constitutive model developed that could model all aspects of real soil behavior. Although some advanced soil models can be used for modelling some specific groups of soil. The Cam-Clay model is widely used for modeling the soft soils, HS soil model for modelling sand, gravel and stiff clay (Brinkgrawe 2010).

Each constitutive soil model is based on stress-strain curve of soil shearing that describe the strength and stiffness for arbitrarily state of stress and strain. The typical stress-strain curve for shearing of soil is shown on Figure 6a. The corresponding change of stress and the strength of soil for different rate of deformation are shown on Figure 6b.

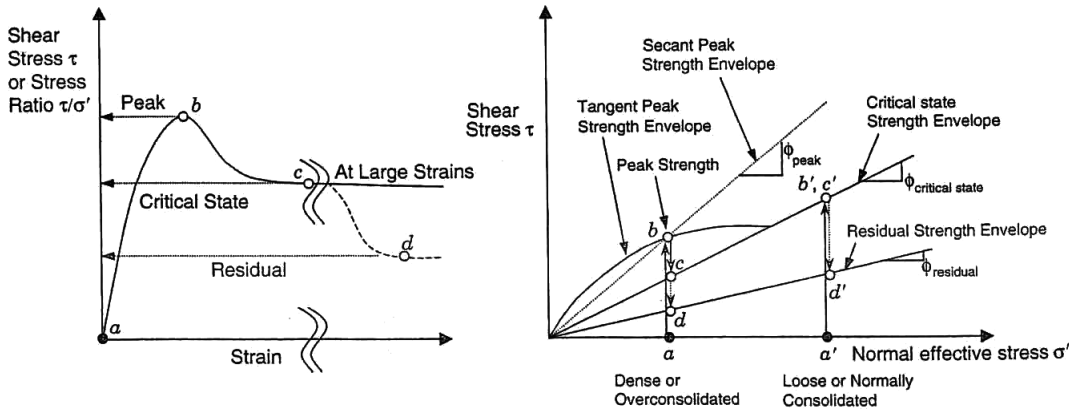


Figure 6. a) Stress strain curve for shearing of soil b) Peak, critical and residual strength of soil (according to Michell 2005)

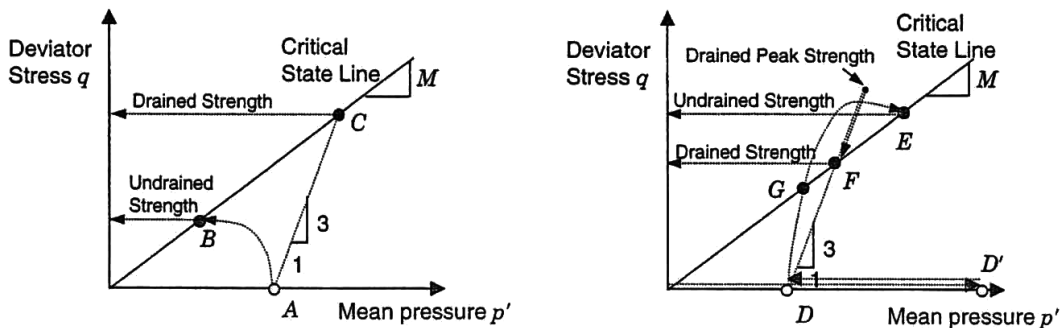


Figure 7. a) Drained strength of clay; b) undrained strength of clay (according to Michell 2005)

For dense noncohesive soils and overconsolidated cohesive soils the peak strength appears due to interlocking and the dilatancy effects. For further shearing the soil dilates which results in strength reduction towards the strength in the critical state.

In the critical state the soil deforms under constant deviatoric stress and without change in the volume. The final volume in the critical state can be expressed by mean of critical void ratio e_{cv} , and its value depends on effective isotropic stress p_{cv} . For the different types of soil the points of critical state $e_{cv} - p_{cv}$ can be approximated with so called Critical State Line (Roscoe et al. 1985, Jefferies and Been 2006).

Due to shearing, loose sand and normally consolidated clays reach the critical state by gradually increase of strength, while the volume of the soil sample reduces. For further shearing of the clay materials, failure plane occurs. Due to the alignment of the clay minerals along the failure plane, the strength even reduces reaching the residual strength.

The Figure 6b) shows that the critical strength and residual strength can be well approximated with line, while the envelope of peak strength is curved. The type and curvature of the envelope depends on the type of the soil. Hvorslev (1960) has defined the envelope for the overconsolidated clays based on the odometer test and the OCR coefficient. Bolton (1986) defined the shape of peak strength envelope for sands by using the relative density and the dilatancy of sand.

The shape of the peak strength envelope depends mostly on the dilatancy effect. The same effect causes the change in pore pressure during the shearing in undrained conditions, while the total volume of the same is retained. When pore pressure changes, the effective stresses change as well. On the Figure 6b) the stress traces are shown for triaxial shearing of clay in drained and undrained conditions for different type of clay overconsolidation.


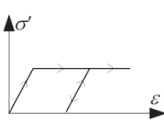
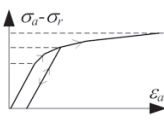
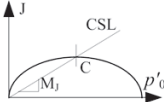
Normally consolidated clays reach the bigger strength in drained conditions (point C) than in undrained conditions (point B) while it is opposite for overconsolidation clays (points F and E). The shape of stress-strain curve for shearing of clays also depends on the overconsolidation of the clay and the drainage conditions. When shearing the overconsolidated clays the reduction of the strength appears after reaching the peak strength followed by the brittle failure both in drained and undrained conditions. The brittle failure in undrained conditions is more pronounced for the fissured clays (Mitchel and Soga 2005). The methodology to define the undrained strength for fissured clays in Zagreb is described by A.Szavits-Nossan (2008).

It is characteristic for the soil that the material is hardening due to increase of stress. It results in stiffer behavior when subjected to unloading and reloading process. The limit boundaries in the stress space that surrounds the unloading / reloading area (where the soil behaves almost elastic) are called the surface of plastic failure, and they are the basic elements of the advanced constitutive soil models.

The example of such soil behavior is well pronounced on the example of the odometer test on clay. The stiffness of the soil can be well approximated by using compression and recompression coefficients in the $e - \log \sigma_p$ diagram, while the surface of plastic failure is described by the overconsolidation pressure σ'_p .

The advanced soil models usually accounts for two separate plastic failure surfaces, one for shearing and one for volume change. Table 1 shows the example of the constitutive models that are most used in every day geotechnical praxis. The basic elements of soil models are shown together with the area of implementation of each constitutive soil model.

Table 1. Example of constitutive models of soil: Linear Elastic; Ideal Elastoplastic; Hardening; Critical State Model.

Soil model	Stress-strain curve	Aspects of behavior	Limitations	Example (Application)
LINEAR ELASTIC		- linear elastic behavior	- unlimited strength - no dilatation - unique stiffness for loading / unloading - direct link between volumetric and shear stiffness	- LE model (Plaxis) - Hooke (for rough estimate of deformation) (for analysis of monolithic rock)
ELASTIC PERFECTLY PLASTIC		- linear elastic to the failure (plastic) - unique strength line - unique dilatation at failure	- unique stiffness for loading / unloading - unique stiffness for different stress and strain state	- Mohr-Coulomb MC (Plaxis) - Von Mises - Druker-Prager (rough estimate of stability)
SOIL HARDENING		- soil hardening - stiffness reduction due to shearing - stress dependent stiffness	- no peak strength reduction - no critical state line - additional rules for unloading	- Hardening soil HS (Plaxis) - BRICK model - NOVA model (sand, gravel, stiff clay)
CRITICAL STATE MODEL		- critical state - isotropic hardening - peak strength reduction	- large number of soil parameters - model specifics	- Cam-Clay (Plaxis) (soft clay)

5. HARDENING SOIL SMALL MODEL

Hardening soil model (HS), available in computer program Plaxis, is originally developed for modeling the behavior of sand (Shanz et al. 1999). In the Plaxis 2D v.7 the model is expanded for modeling also the cohesive soils, while in version v.8 the extension for small strain stiffness is added: (Benz 2007). The basic elements of Hardening Soil model (HSs) are (Brinkgrave 2010):

- Stress dependent stiffness
- Plastic volumetric strain due to primary compression
- Plastic shear strain due to primary shearing
- Strength according to Mohr-Coulomb failure criteria
- Dilatancy effect
- Elastic behavior due to unloading and re-loading
- Small strain stiffness
- Nonlinear elastic behavior for small deformations below limit strain $\gamma_{0.7}$

The basic idea in formulation of HSs soil model is the hyperbolic relationship between vertical deformation σ_1 and deviatoric stress q in drained triaxial test (Figure 7).

$$-\varepsilon_1 = \frac{q}{2E_{50}(2 - R_f)(1 - qR_f / q_f)} \quad (2)$$

where R_f is the coefficient of failure (the ratio of shear strength q_f according to asymptotic value of stress-strain curve q_a), E_{50} (stress dependent Young's modulus of elasticity), and q_f (shear strength) which are defined by following expressions:

$$E_{50} = E_{50}^{ref} \left(\frac{c \cos \varphi - \sigma'_3 \sin \varphi}{c \cos \varphi + p^{ref} \sin \varphi} \right)^m \quad (3)$$

$$q_f = (c \cot \varphi - \sigma'_3 \frac{2 \sin \varphi}{1 - \sin \varphi}) \quad (4)$$

where E_{50}^{ref} is reference stiffness at the reference pressure p^{ref} , σ'_3 minor principle stress, m coefficient of stiffness over stress, and c i φ are strength parameters. Figure 8 shows the comparison of stress-strain curve for different soil models: MC, HS and HSs.

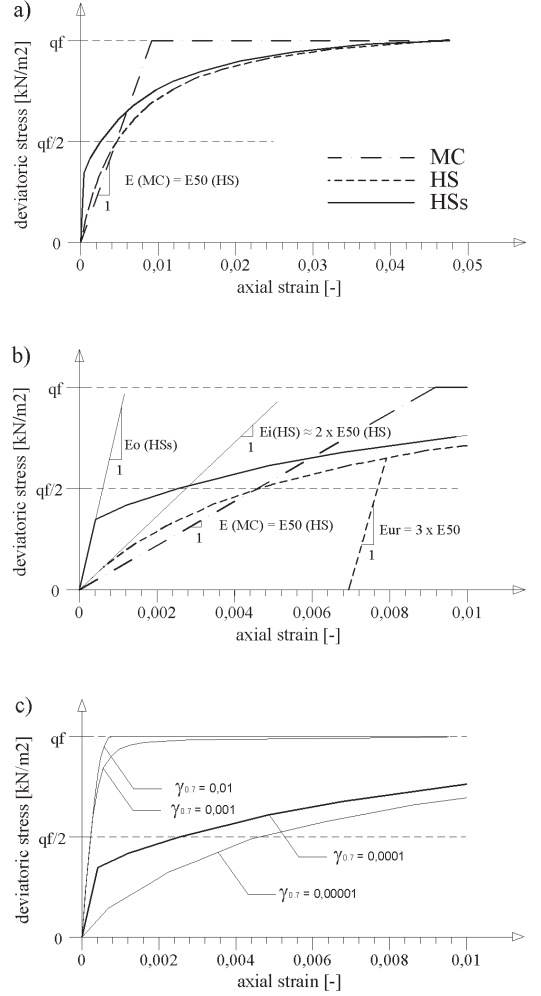


Figure 8. Standard drained triaxial test simulation performed by three different soil models MC, HS and HSs (Sokolic 2006). a) global view on type of deformation, b) insight view in the zone of small deformation, c) influence of limit strain parameter $\gamma_{0.7}$ on the shape of the deformation curve.

The stiffness of the soil for unloading and reloading E_{ur} , volumetric stiffness E_{oed} and shear stiffness at small deformations G_0 are defined according to following expressions:

$$E_{ur} = E_{ur}^{ref} \left(\frac{c \cos \varphi - \sigma'_3 \sin \varphi}{c \cos \varphi + p^{ref} \sin \varphi} \right)^m \quad (5)$$

$$E_{oed} = E_{oed}^{ref} \left(\frac{c \cos \varphi - \sigma'_1 \sin \varphi}{c \cos \varphi + p^{ref} \sin \varphi} \right)^m \quad (6)$$

$$G_0 = E_0^{ref} \left(\frac{c \cos \varphi - \sigma'_3 \sin \varphi}{c \cos \varphi + p^{ref} \sin \varphi} \right)^m \quad (7)$$

where σ'_1 is major principle stress.

Additionally parameters for HSs model are the same as for all soils in Plaxis 2D: unit weight for dry and saturated conditions (γ_{dry} , γ_{sat}), coefficient of permeability in two directions (k_x i k_y), dilatancy parameter ψ and limit strain parameter $\gamma_{0.7}$ ($\gamma_{0.7} \approx 10^{-5}$ for sand).

It can be concluded from the expression (2) and (7) that the strength and stiffness are different in the same point for the different step of calculation, and depend on state of stress σ'_1 and σ'_3 in each stress point of finite element mesh. As it was previously described in paragraph 2, it is very important to accurately define the initially state of stress in the ground (K_0 -procedure in computer software Plaxis). The reference stiffness parameters must be defined according to initial stress in the soil, to match the stiffness in each layer of soil for given depth. The example of defining the reference stiffness parameters of soil for pit excavation in the area of Zagreb is shown on Figure 9. The method is described in more detailed in Sokolić (2006).

Beside the grate advantages of HSs soil model mentioned above, the model has also some disadvantages that one should take care of (Sokolić 2011). HSs soil model doesn't have the capability to model the strength reduction due to shearing (brittle failure at peak strength). For that reason, grate care must be taken when modeling the retaining structures by using peak strength parameters of soil. The magnitude of shear strain must be checked during the calculation. This disadvantage is typical for dense noncohesive materials and for overconsolidated cohesive materials in drained conditions, but also for overconsolidated clays in undrained conditions (Figure 10).

When using undrained type of calculation, special care must be taken for defining dilatancy parameter ψ . The parameter has the great influence on the stress trace and the undrained strength (Figure 11). For the value $\psi > 0$

undrained strength is increasing to infinity ∞ , while for value $\psi < 0$ it reduces to zero 0. That can lead to very unrealistic results when checking the global stability by use of strength reduction method in undrained conditions ($\varphi - c$ reduction).

The HSs soil model doesn't account for Critical State Theory. From that reason the strength, stiffness and rate of dilatancy doesn't depend on the change of volume or void ratio of soil. The soil parameters must be adopted for initial density of the soil, and the change in volume should be checked during the calculation.

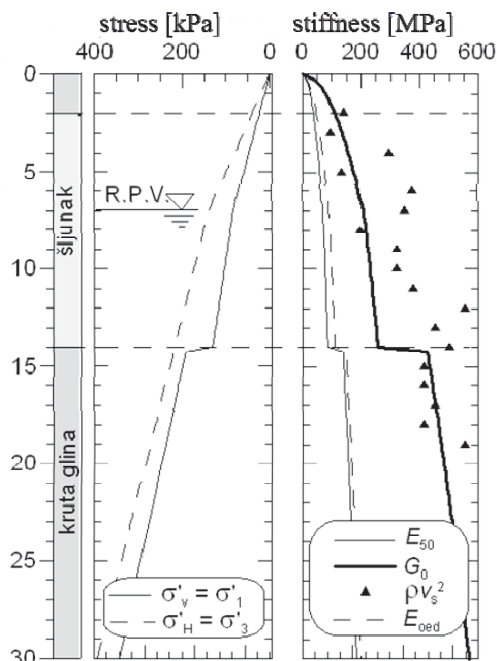


Figure 9. Initial stress state in the ground (left) and initial stiffness profile (right)

6. HSS SOIL MODEL PARAMETERS FOR SOIL PROFILE IN ZAGREB

The excavation of deep pits for Business centers and underground parking areas in the City of Zagreb started early nineties. The first calculations were made according to classical approach (Škacan et al. 1994, Šilhard et al. 2002). With the expansion of FEM the modern computer software were used such as FLAC

(A.Szavits-Nossan 1999) and Plaxis (A.Szavits-Nossan 2008, Sokolić and Vukadinović 2007).

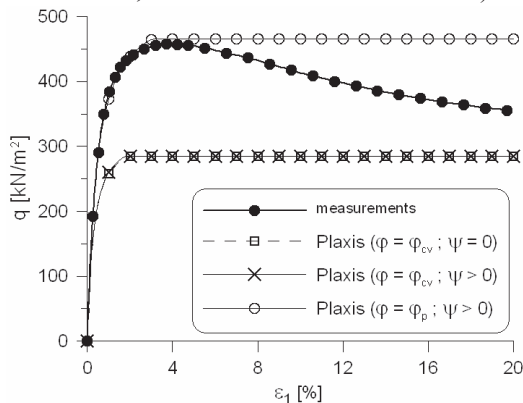


Figure 10. Numerical simulation of triaxial CID test on Erksak sand by using HS model (Sokolić 2011)

is possible to make first approximation of HSs soil model parameters.

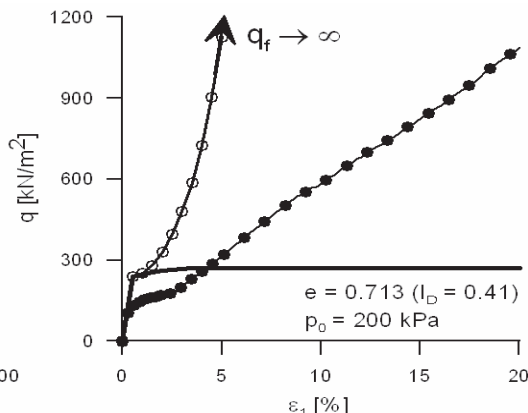
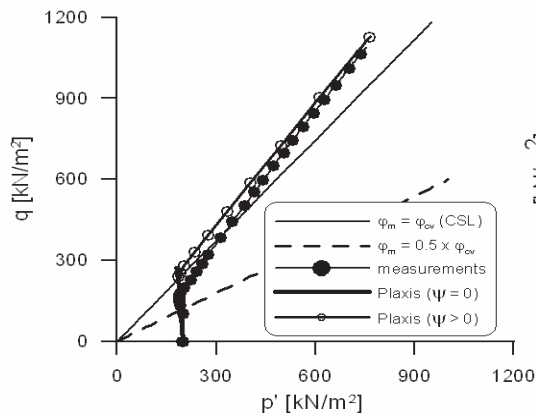
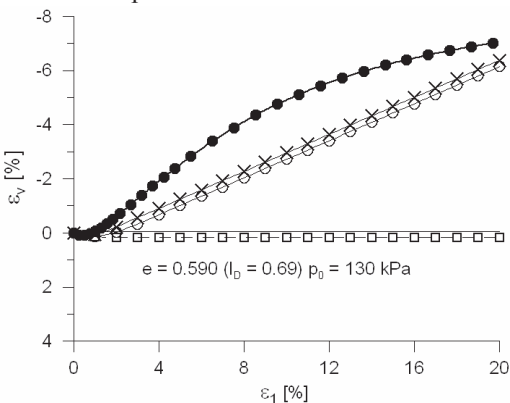


Figure 11. Numerical simulation of triaxial CIU test on Erksak sand by using HS model (Sokolić 2011)

The soil profile typical for alluvium of River Sava in the City of Zagreb consists dominantly of gravel layer and the stiff clay in the bottom. The geotechnical investigations that are usually performed consists of simple laboratory tests (physical properties of soil, direct shear test, odometer test and UU triaxial test) together with 'in-situ' tests, mostly SPT test and in recent times the measurement of shear wave velocity (SASW, down-hole, cross-hole).

The characteristic soil profile is shown on Figure 12. that consists of: seewe analysis, plasticity limits together with initial water content, undrained shear strength, standard penetration test results (normalized values are indicated by best approximation line) and shear wave velocity profile. Based on those results it

To define the undrained strength of clay c_u and the stiffness of the clay E the correlations according to SPT number is usually used. After the Stroud this approach provides good estimation for the stiff clays taking into account the value of the SPT value normalized to the standard energy N_{60} and the plasticity index of the soil I_p , according to following expressions (Clayton 1995):

$$c_u = f_1 N_{60} \quad (8)$$

$$E = f_2 N_{60} \quad (9)$$

where f_1 is the coefficient that correlates to the plasticity index, and it is in the between 4 to 6 for I_p in the range between 10 to 70 %. Coefficient f_2 depends additionally on the strength mobilization value q/q_f and it is in the range

between 1 to 2 for $q/q_f = 0.5$. Effective strength parameters for clay can be examined in the direct shear test and triaxial test or even correlated to the mineral content of the clay.

Based on normalized SPT value $(N_1)_{60}$, for example according to expression proposed by Skempton (1986):

$$(N_1)_{60} = N_{60} \sqrt{p^{ref} / \sigma'_v} \quad (10)$$

where σ'_v is vertical effective stress, it is possible to predict the peak strength for gravel, for example according to expression proposed by Hatanaka i Uchida (1996):

$$\varphi'_p = 20^\circ + \sqrt{15.4(N_1)_{60}} \quad (11)$$

The stiffness of the gravel can be correlated to the N_{60} value according to expression (9) by using the factor f_2 for non-cohesive soils.

The initial state in the ground can be defined according to soil weigh tested in laboratory and by using K_0 procedure described in Paragraph 3. The OCR coefficient can be well tested in the odometer. Due to geological history of the sediments in the alluvium of river Sava, it can be expected to have the overconsolidation of the clays. According to back analysis performed on retaining structures the values of overconsolidation are $OCR \approx 3$ for clas and $OCR \approx 2$ for gravels (A.Szavits-Nossan 2008, A.Szavits-Nossan et al. 2009).

The small strain stiffness can be calculated from shear wave velocity profile v_s (Figure 8) according to expression:

$$G_0 = \rho \cdot v_s^2 \quad (12)$$

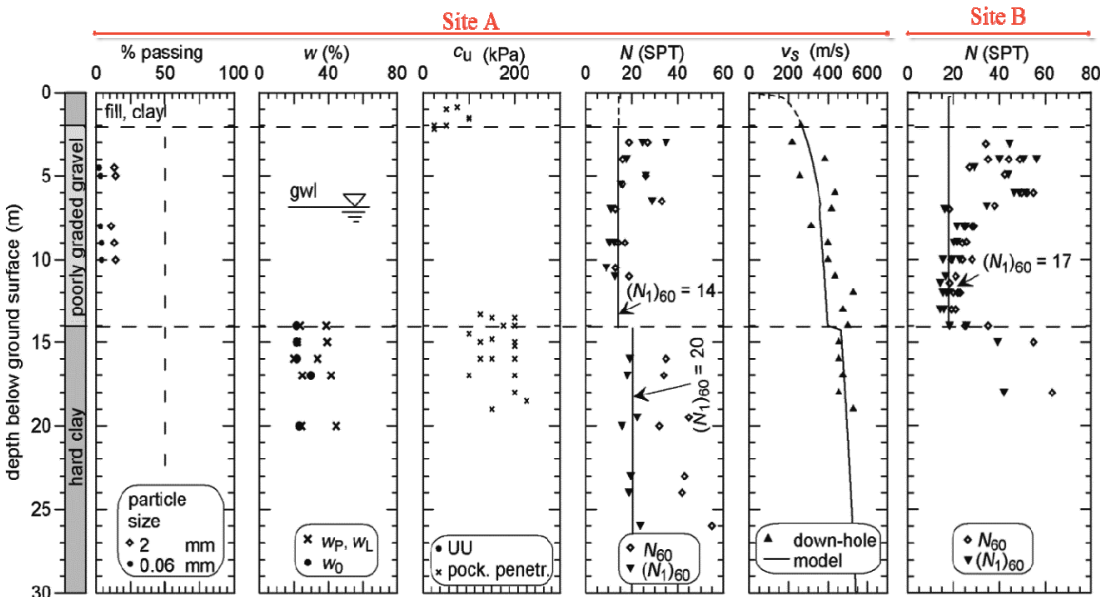
$$E_0 = 2G_0(1 + \nu) \quad (13)$$

where G_0 is initial shear stiffness modulus, ρ soil density, E_0 initial Young modulus, and ν Poisson number. According to the research the stiffness ratio $E_{50}^{ref} / E_{ur}^{ref}$ is in the range between 2 to 5, E_0^{ref} / E_{50}^{ref} between 5 to 10, while for $E_{oed}^{ref} / E_{50}^{ref}$ around 1 (Brinkgrave 2010, Kempfert and Gegrelassie 2006).

According to results of parametric studies performed on retaining structure of sheet pile wall (Sokolić 2008), the most important stiffness parameter is E_{50} , while the effect of variation of other stiffness parameter E_0 i E_{ur} in above mentioned boundaries is less pronounced. The same is observed in parametric study or diaphragm wall performed by A.Szavits-Nossan (2008). According to results of beck analysis, the stiffness of the soil is somewhat greater than predicted by conventional correlations.

Soil parameter m accounts for stiffness reduction due to stress value. The value is usually used $m = 0.5$ for gravel, and $m = 1$ for clay.

Figure 12. Typical soil profile for the alluvium of Sava River in the area of City of Zagreb



According to results of several back analysis performed on different retaining structures (A. Szavits-Nossan 2008) the reference stiffness parameters can be defined according to expression:

$$E_{50}^{ref} [MPa] = 5 \cdot (N_1)_{60} \quad (14)$$

$$G_0^{ref} [MPa] = 15 \cdot (N_1)_{60} \quad (15)$$

The value of dilatancy parameter ψ can be estimated according to expression proposed by Bolton (1986), taking into account relative density of soil and the level of stress in the ground. Special care must be taken when using the value $\psi \neq 0$, because it has great influence on the stress trace and strength in undrained conditions. It is recommended to use value $\psi = 0$, which is on safe side of calculation.

7. EXAMPLES OF BACK ANALYSIS OF RETAINING STRUCTURES AND PARAMETRIC STUDY

The strategy of selecting HSs model parameters for medium stiff to stiff soil described in Paragraph 6 was first proposed by A. Szavits-Nossan 2008. It was calibrated on the example of horizontal movement of diaphragm wall and validated afterwards on two other retaining structures in the similar soil conditions (A. Szavits-Nossan et al. 2009). For one of those structure (sheet pile wall with passive anchors) a very detailed parametric study was performed (Sokolić and Vukadinović 2007, Sokolić 2008). The main goal was to validate the influence of basic HSs model parameter on the performance of the retaining structure model. The basic concept and the results of back analysis and parametric study are shown in this paper.

7.1. Back Analysis

Three retaining walls used in back analysis were constructed as temporary structures securing two excavation pits for underground car parks of two commercial buildings in Zagreb, Croatia. A strategy for modelling soil behaviour and selecting relevant soil parameters was first established and calibrated against Wall No. 1. Then, the same strategy was used in modelling Wall No. 2 and Wall No. 3 followed by a

comparison of calculated and measured wall displacements.

The basic parameters of the foundation soil deposits encountered at two close sites are shown in Figure 12. At the site A two types of anchored retaining walls were used (Wall No. 1 and Wall No. 2), while at site B a third wall type was used (Wall No. 3). All sites are characterized by a thin surface layer of manmade fill and medium stiff clay, underlain by a layer of medium dense poorly graded gravel with rounded grains, which rests on a very thick layer of stiff, overconsolidated clay of medium to high plasticity. Although a noticeable drop in the normalized SPT blow count $(N_1)_{60}$ below the ground water level in the gravelly layer is apparent, a common peak friction angle was used in the analysis. Although the two sites are stratigraphically similar and not very far from each other, they yet slightly differ with relation to SPT blow counts at respective depths. Site A was more extensively tested (SPT and down-hole geophysical measurements of shear wave velocities up to 30 m depth, triaxial consolidated drained tests on undisturbed clay samples), whereas at site B no triaxial tests and no geophysical in situ tests were performed. Based on similar profiles of SPT blow counts in the stiff clay layers at both sites, it was assumed that effective strength parameters for these layers were the same at both sites, while differences in blow counts rendered different peak friction angles for gravelly layers.

Three different anchored retaining walls were constructed at sites A and B. Their cross sections are shown in Figures 13. The retaining wall No. 1 is a reinforced diaphragm of cast in place concrete, anchored by three rows of BBR type prestressed high grade steel ground anchors. The excavation depth, measured from the top of the wall, was 13.5 m. The retaining wall No. 2 is a Larsen type sheet pile wall driven into the ground and anchored by two rows of BBR type high grade steel prestressed ground anchors. The excavation depth, measured from the top of the wall, was 9 m. The retaining wall No. 3 is also a Larsen type sheet pile wall driven into the ground with two rows of Ischebeck Titan type ground anchors. The excavation depth, measured from the top of the wall, was 7 m.

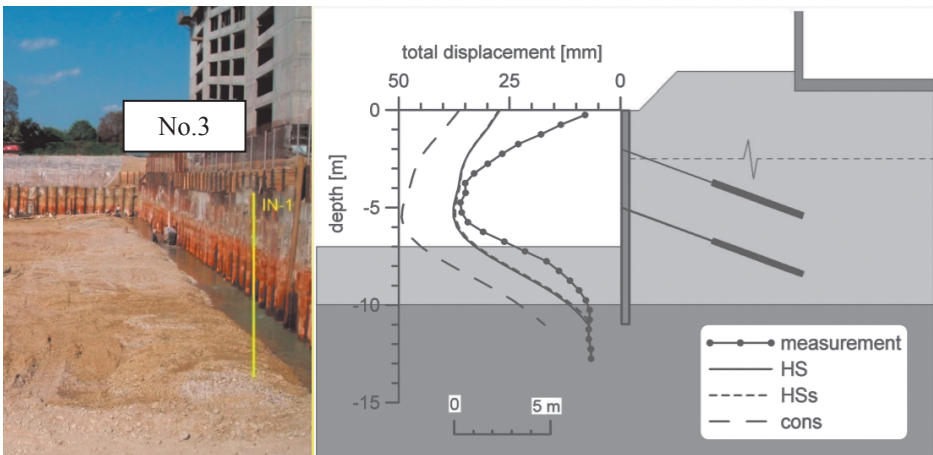
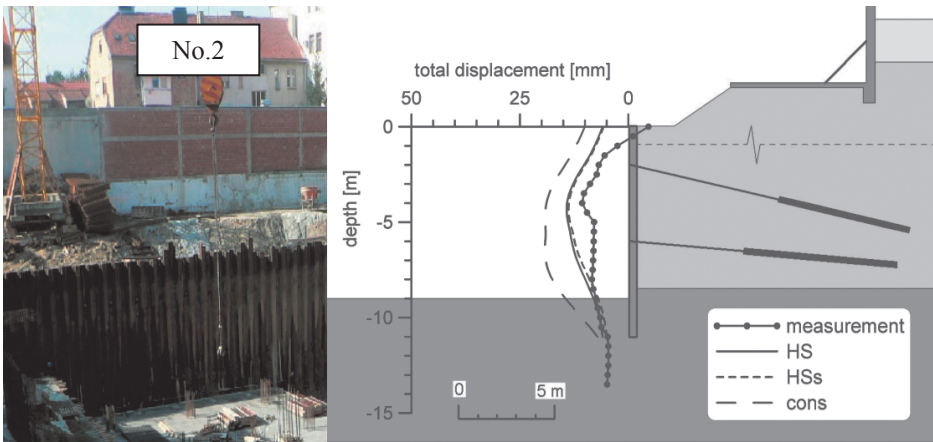
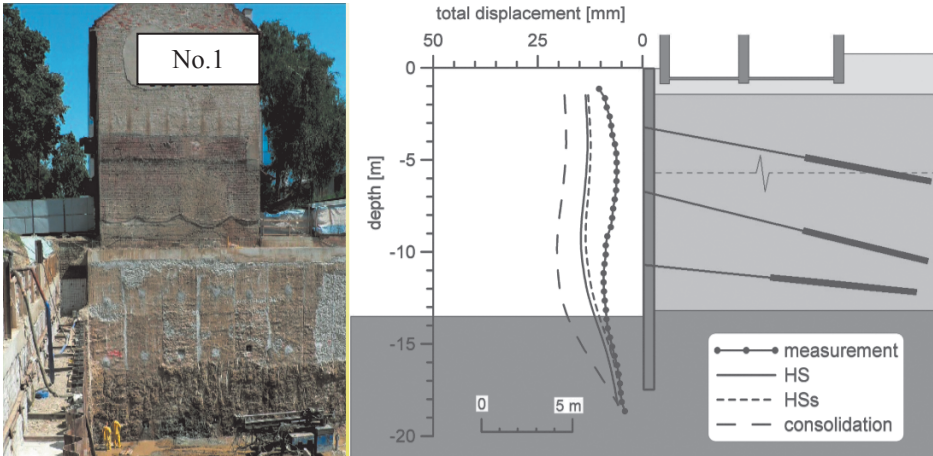


Figure 13. Excavation pits and beck analysis results

The soil-structure interaction analyses for all three anchored retaining walls were performed by the program Plaxis 2D Version 9 using the stage construction option. This allowed detailed modelling of various construction sequences: excavation and ground water lowering, anchor installation, anchor prestressing, etc. Figure 12 show calculated total horizontal displacements in the bottom stiff clay stratum after reaching the final excavation phase for undrained conditions (full lines) and after full dissipation of induced excess pore water pressures (long dashed lines). Both, the undrained and drained analyses were performed by disregarding the strong nonlinear soil behaviour at small strains (soil model HS). The undrained analyses were also performed by taking into account the small strain behaviour (soil model HSs). These results are shown in Figure 13 by short dashed lines. Despite opposite expectations, they differ very little from the results with the HS soil model for the undrained analyses. The probable reason for the small difference is the high mobilization of the soil shear strength where small strain behaviour has little influence.

The calculated horizontal displacements of the anchored walls were compared with measurements taken during excavation stages by inclinometers, with tubes which were either embedded into the reinforced concrete diaphragm wall or installed into the ground on the back side of the wall. Since inclinometers measure only the relative horizontal displacements (displacements only up to the rigid body translation), the comparison with calculated displacements was obtained by adding a constant value to measured results so as to match measurements with the calculated horizontal displacement at the bottom of the retaining wall. Such "corrected" measurements are shown in Figure 13 by dotted lines. According to the present general prediction quality in geotechnical engineering, particularly regarding anchored retaining structures, a remarkable agreement of calculated and measured wall displacements was achieved. This is a promising result for the proposed modelling strategy for anchored retaining structures in medium stiff to stiff soils.

7.2. Parametric study

The detailed parametric study was performed on retaining wall No. 3 by using three

deferent soil models (MC, HS, HSs) with equal strength parameters (c , φ and ψ). The stiffness parameter E for the MC model was based on results from geotechnical investigation works and from correlations.

For the MC model, the stiffness for each layer is constant with depth and remains the same for all phases of calculation. For the HS model, which accounts for stress dependent stiffness, initial stress distribution is not constant with depth and it changes its value during the calculation. From the aspect of comparison of results, it is very important to match the initial stiffness for both models, i.e. $E_{50}(\text{HS}) = E(\text{MC})$, in certain points of model. To calculate E_{50} distribution with depth it is necessary to first calculate the minor principal stresses according to K_0 procedure (effective horizontal stresses σ_3' with depth). By using $p_{\text{ref}} = 100 \text{ kN/m}^2$ for all materials and the power parameter m , the matching reference stiffness E_{50}^{ref} can be calculated according to eq. (3). This procedure gives the initial stiffness distribution that is comparable to initial stiffness profile modelled by MC soil model (Figure 19). Unloading-reloading stiffness parameters for the HS model were used according to Plaxis manual instructions $E_{\text{ur}}^{\text{ref}} = 3 \times E_{50}^{\text{ref}}$ and $\nu_{\text{ur}} = 0.2$. In the HSs model all stiffness parameters from the HS model were retained. The two additional parameters for small strains were chosen in the following way. G_0^{ref} was chosen as $E_0^{\text{ref}} = 5 \times E_{50}^{\text{ref}}$. The threshold strain $\gamma_{0.7}$ was calculated according to Plaxis manual.

To evaluate the influence of each stiffness parameter on the final calculation results, 14 parameter analyses were performed:

- A. Four MC model analyses varying parameter $E(\text{MC}) \times 1; 2.5; 5; \text{ and } 10$.
- B. Four HS model analyses varying parameter $E_{50}^{\text{ref}}(\text{HS}) \times 1; 2.5; 5; \text{ and } 10$.
- C. Two HS model analyses varying $E_{\text{ur}}^{\text{ref}} \times 5; 10$ and for $E_{50}^{\text{ref}} = 5 \times E(\text{MC})$.
- D. Two HSs model analyses taking $E_0^{\text{ref}} = (5; 10) \times E_{50}^{\text{ref}}$ for $E_{50}^{\text{ref}} = 5 \times E(\text{MC})$.
- E. Two HSs model analyses varying parameter $\gamma_{0.7} \times 10; 100$ for $E_{50}^{\text{ref}} = 5 \times E(\text{MC})$ and $E_0^{\text{ref}} = 10 \times E_{50}^{\text{ref}}$

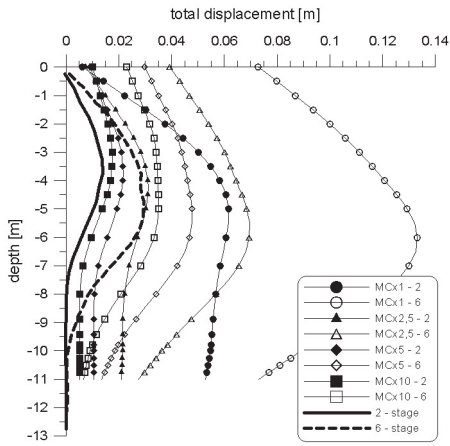


Figure 14. Parameter analysis A

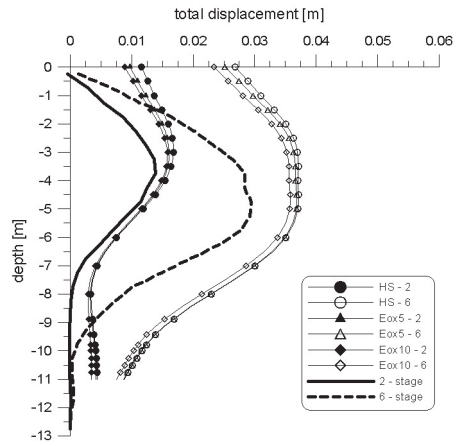


Figure 17. Parameter analysis D

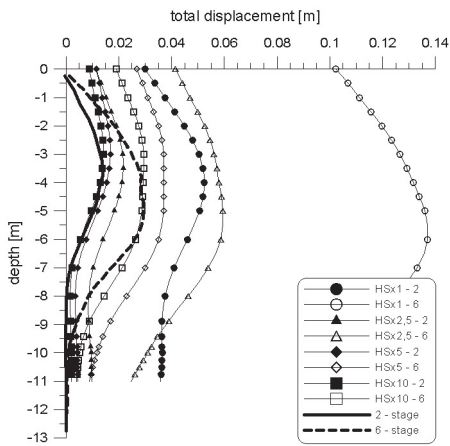


Figure 15. Parameter analysis B

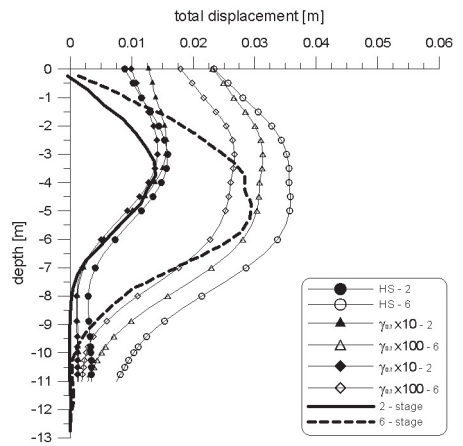


Figure 18. Parameter analysis E

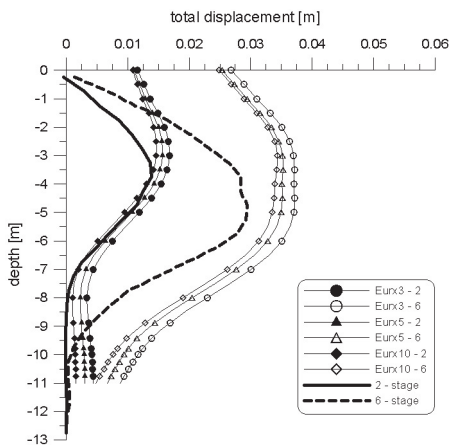


Figure 16. Parameter analysis C

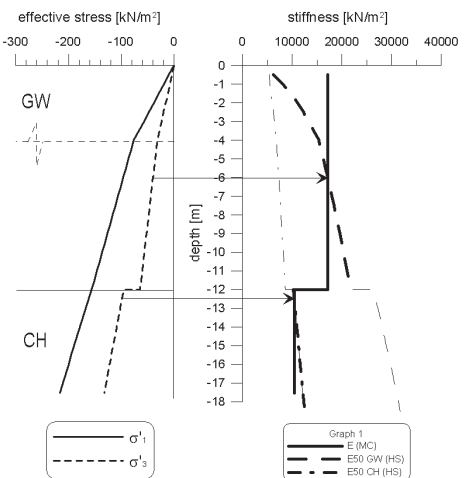


Figure 19. Initial stiffness profile

The results of the parametric study are shown on Figures 14 to 18. It can be observed that by using the MC model, calculated global displacements are unreal, especially the bottom heave. Total displacements of the wall are far too over predicted for the first set of estimated stiffness parameters. Increasing modulus E up to ten times (in this example) it is possible to fit the measurements in both excavation stages. On the other hand, the HS model improves global deformations significantly, especially the bottom heave. By increasing modulus E_{50}^{ref} 'curve fitting' is progressing faster and appearing more realistic than with the MC model. By increasing E_{ur}^{ref} , the horizontal displacement shape is translated towards measured values but the curvature is almost the same as before leaving internal forces in the sheet pile wall almost unchanged. The HSs model does not change the results much in this case, probably because the global safety factor of structure is around 1,3. It means that soil shear strains are extremely plastic and far away from small-strain region. Increasing parameter $\gamma_{0.7}$ in the HSs model on the other hand, has a very big influence on the results compared to increasing G_0^{ref} , but that parameter variation leads to an unreal small-strain region.

Generally, while modeling temporary flexible retained structures with computer program Plaxis2D it is better to use HS model than MC model. In that case displacement of the model are most sensitive to the stiffness parameter E_{50}^{ref} and it is very important how the modulus E_{50} is distributed at the initial stage. That depends significantly on power parameter m and the initial stress distribution. Compared to that, 'playing' with other stiffness parameters, out of recommendations given in the Plaxis manual, is unnecessary. Using HSs soil model for modeling structures with very low safety factor is only time consuming and does not lead to more accurate results.

8. CONCLUSION

The modern approach for numerical modeling of anchored retaining structures in medium stiff to stiff ground is presented in this paper. It is based on detailed understanding of the real soil behavior and requires quality geotechnical investigations to determine soil parameters for

advanced constitutive soil models. The general problems related to numerical modeling of retaining structures are presented. Most of the problems arise from extremely complex change in stress-strain change and trace of stress in the audience of the excavation pit, which requires powerful constitutive soil models to account for real stress-strain behavior of soil in wide range of stress and strain. The sensitivity of the modeling to the initial state of stress in the ground is described, together with the grate effect of the drainage conditions to the results of analysis. The basic elements of HSs soil model are presented together with its grate advantages for modelling medium stiff to stiff soils characteristic for alluvium of Sava River in the area of City of Zagreb. The main disadvantages of the model are also discussed, especially from the aspect of dilatancy parameter.

Based on the experience on the beck analysis, performed on several retaining structures, the strategy for determining soil parameters of gravel and stiff clay is detailed elaborated. From the results of performed back analysis, it can be concluded that proposed strategy gives reliable results, from the engineering point of view. According to the results of parametric study performed, it can be concluded that the most important is to quality determine the reference stiffness parameter E_{50}^{ref} directly from the geotechnical investigations. That can be done reliably by using the correlation to the normalized number of standard penetration test $(N_1)_{60}$. Other stiffness parameters (E_{ur}^{ref} , E_{ocd}^{ref}) can be taken according the recommendations given in Plaxis Manual. The initial shear stiffness should be fitted to the results of in-situ measurements of shear wave velocity profile.

Although the proposed strategy for soil parameter determination provides reliable results, it is recommended that it is used only as the first estimate for the model parameters. For each project, some specific site conditions can be expected, that should be determined by quality geotechnical investigations including modern laboratory and in-situ tests.

9. REFERENCES

- BSI (2004). –BS EN 1997-1:2004; Eurocode 7: Geotechnical design – Part 1: General rules. British standard.

- Benz, T. 2007. Small-strain stiffness of soils and its numerical consequences. *PhD Thesis. Stuttgart: Institute of Geotechnics, University of Stuttgart*
- Brinkgrave, R.B., Swolfs, W.M., Engin, E., 2010. Plaxis 2D Manual 2010. *Delft: Plaxis bv. P.O. Box 572.*
- Bolton, M.D., 1986. The strength and dilatancy of sands, *Géotechnique*, Vol.36, No. 1.
- Burland, J.B, Simpson, B. & St John, H.D., 1979. Movements around excavations in London Clay. *Proc 17 Euro conf soil mechanics and foundation eng*, vol 1.
- Clayton, C.R.I., 1995. The Standard Penetration Test (SPT): Methods and Use. Report 143, *CIRIA*, London.
- Clough, G.W. & O'Rourke, T.D. 1990. Construction induced movements of insitu walls, *Proc., ASCE Conf. on Design and Performance of Earth Retaining Structures, Geotechnical Special Publication No. 25, ASCE, New York*, pp. 439-470.
- De Vos, M. & Whanhman, V.: Workpackage 3 – Innovative design methods in geotechnical engineering. Background document to part 2 of the final WP3 report on the use of finite element and finite difference methods in geotechnical engineering. Geotechnet <http://www.geotechnet.org>, 2006.
- Dunnicliff, J. 1993: Geotechnical instrumentation for monitoring field performance. John Wiley & Sons, Inc. New York.
- Freiseder, M.G., 1998. Ein Beitrag zur numerischen Berechnungen von tiefen Baugruben in weichen Boden. *Gruppe Geotechnik Graz, Institute für Bodenmechanik und Grundbau*, Heft 3.
- Gaba, A.R., Simpson, B., Powrie, W. & Beadman, D., 2003. Embedded retaining walls - guidance for economic design. *London: CIRIA C580.*
- German Society for Geotechnics, 2003. Recommendations on Excavations. *Ernst & Sohn*, Berlin.
- Hatanaka, M. i Uchida, A., 1996. Empirical correlation between penetration resistance and effective friction of sandy soil. *Soils & Foundations*, Vol. 36(4).
- Hvorslev, M.J., 1960. Physical components of the shear strength of saturated clays, *Proc ASCE Research Conference on the Shear Strength of Cohesive Soils*, Boulder, CO, pp. 169-273.
- Jefferies, M & Been, K., 2006. Soil liquefaction - A critical state approach. *Oxon: Taylor & Francis.*
- Kempfert, H.-G. & Gebreselassie, B. 2006. Excavations and Foundations in Soft Soils. *Springer*, Berlin.
- Lunne, T., Robertson, P.K. & Powell, J.J.M., 1997. Cone Penetration Testing in Geotechnical Practice. *Blackie Academic and Professional*, London UK.
- Mayne, P.W. & Kulhawy, F.H., 1982. K₀-OCR relationships in soil. *Journal of Geotechnical Engineering*, 108 (GT6): 851-872.
- Mayne, P.W., Christopher, B.R. & DeJong, J., 2001. Manual on Subsurface Investigations. Publication No. FHWA NHI-01-031, *Washington, DC: National Highway Institute*, Federal Highway Administration.
- Mitchell, J. K., & Soga, K., 2005: Fundamentals of Soil Behavior (Third Edition ed.). Hoboken, New Jersey: John Wiley & Sons, Inc.
- Potts, D.M., Axelsson, K., Grande, L., Schweiger, H. & Long, M. 2002. Guidelines for the use of advanced numerical analysis. *London: Thomas Telford.*
- Potts, D. M., & Zdravković, L. 2001. Finite element analysis in geotechnical engineering - Application. *London: Thomas Telford.*
- Roscoe, K.H., Schofield, M.A. & Wroth, M.A., 1985. On the yielding of soils. *Géotechnique*, 8 (1), 22-53.
- Schweiger, F.H.: Benchmarking in geotechnics 1. Report No.CGG_IR006_2002. Computational Geotechnics Group, Institute for soil Mechanics and Foundation Engineering, Graz University of Technology, Austria, 2002.
- Skempton, A.W. 1986. SPT procedures and the effects in sand of overburden pressure, relative density, particle size, aging, and overconsolidation. *Géotechnique*, Vol.36(3).
- Shweiger, H.F., 2002. Note on pore pressure. *Plaxis Bulletin* No.12.
- Schanz, T., Vermeer, P.A. & Bonnier, P.G.: The hardening soil model - formulation and verification. *Plaxis Symposium "Beyond 2000 in Computational Geomechanics"*. Amsterdam: Balkema, 1999.
- Sokolić, I. & Vukadinović B., 2007. Soil parameter analysis based on inclinometer measurements of sheet pile displacement. *14th European Conference on Soil Mechanics and Geotechnical Engineering*, Madrid, Vol. 4.
- Sokolić I., 2008. Sheet pile wall analysis by computer program Plaxis using different constitutive

- models for soil. *International Geotechnical Conference Development of Urban Areas and Geotechnical Engineering*, Saint Petersburg, Vol. 1.
- Sokolić, I. 2010. A send model embedded into the Iwan System. *PhD Thesis, University of Zagreb, Faculty of Civil Engineering*.
- Sokolić, I. & Plepelić, G. 2010. Retaining wall movements due to deep excavation in Zagreb, *Int. Geotech. Conf. Geotechnical Challenges in Megacities*, Moscow, Russia, Vol.3, 951-957.
- Sokolić, I., 2011. Triaxial test simulation on Erksak sand using hardening soil model. *XVth European conference on soil mechanics and geotechnical engineering*, Athena.
- Sokolić, I., Krajnović, D., Vukadinović, B.: Komparacija projektnih i izmjerenih veličina na zaštiti građevne jame u Zagrebu. *Građevinarstvo, nauka i praksa, Žabljak, knjiga 2, 787-790*.
- Szavits-Nossan, A.: Advances and uncertainties in the design of anchored retaining walls using numerical modeling, *Acta Geotechnica Slovenica* 5 (1), 2008.
- Szavits-Nossan, A., Sokolić, I. & Plepelić, G., Design of anchored retaining structures by numerical modeling, 17th International Conference on Soil Mechanics & Geotechnical Engineering, Alexandria, Egypt. Vol. 3, 2009.
- Szavits-Nossan, A., Kovačević, M.S. & Szavits-Nossan, V., 1999. Modeling of an anchored diaphragm wall. *Proc. Interntl. FLAC Symposium on Numerical Modeling in Geomechanics: FLAC and Numerical Modeling in Geomechanics*. Minneapolis.
- Tomac, I. & Marić, B. Deep excavation case histories in the city of Zagreb. 13th Danube-European conference on geotechnical engineering, Ljubljana, Slovenia, 2006.
- von Wolffersdorff P.-A.: Feldversuch an einer Spundwand in Sandboden: Versuchsergebnisse und Prognosen. *Geotechnik* 17(2), 73-83, 1994.
- Škacan, B., Verić, F. & Szavits-Nossan, A. Retaining structure for the open excavation of Esplanade center. *Geotehnika prometnih građevina*, Novigrad, Croatia, Vol. 1, 1994.
- Šilhard, V., Verić, F. & Ivšić, T. Protection of deep excavation for the "Branimir" Center. 3rd Conference of the Croatian Society for Soil Mechanics and Foundation Engineering, *Geotechnics through Eurocode 7*, Hvar, Croatia, 2002.
- Twine, D. & Roscoe, H.: Temporary propping of deep excavations – guidance on design. London: CIRIA C517, 1999.

Deep Pit Excavation in Special Geotechnical Conditions

Y. El-Mossallamy¹, A. Wahby² & W. Eltahawy¹

¹ Geotechnical Laboratory at Faculty of Engineering – Ain Shams University

² BAUER Egypt

ABSTRACT: The need of construction of underground structures such as basements, main stations and tanks in big cities is increased in the last decades due to the lack of construction areas in crowded cities. The deep pit excavation with the appropriate support systems is a geotechnical challenge in most cases; where controlling the groundwater and the deformation of adjacent structures are the main design criteria. The performance of deep excavation in soft soil is demonstrated through a case history in Port-Said in north of Egypt. The subsoil conditions represent a double layer system where the upper layer is stiffer than the deep extended layer of soft clay. Another case history of deep excavation in Cairo will be also presented.

1. INTRODUCTION

Deep excavations are generally conducted using laterally supported shoring system. Two case histories will be demonstrated: one case history in Port-Said, north of Egypt, where the subsoil conditions are stratified layers including soft clay. The upper layer with depth of about 15m consists of medium to dense silty sand followed with soft clay. The second case history is in Cairo on the Nile River dealing with relatively deep excavation just beside existing neighboring high rise buildings. The upper layer with depth of about 13m consists of sandy silt and silty clay followed with very dense sand.

It can be seen that the two case histories dealing with pit excavation in stratified soil, one time the upper layer is stiffer and in the second case the lower layer is the stiffer one. The low shear strength and high compressibility of the weaker layer may cause excessive deformations in soil which lead to damage of adjacent structures and affect the whole excavation stability. Therefore, the support system and sequence of excavation should be carefully designed in order to control the ground deformation below allowable limits to prevent adjacent building damage and ensure the required factor of safety regarding shoring stability (El-Mossallamy, 2005).

2. FIRST CASE HISTORY

2.1. Description

A cultural center located near the beach in Port-Said, north Egypt. It is a multi-story building with one basement as a deep garage and founded on large diameter bored piles with pile length of about 42 m. The foundation level lies about 5.5 m beneath the ground surface. The subsoil at the site consists mainly of five layers. The upper layer was medium dense sand with thickness 7 m followed with a silty sand layer which extended down to about 15 m beneath ground surface. A soft clay layer with a thickness of about 30 m was then followed down to a depth of 45 m below the ground surface. Then, another medium dense sand layer extends for 5.0 m beneath the soft clay. Finally, a stiff clay layer with thickness 10 m was found at the end of the deep boreholes. The groundwater table lies about 0.50 m below the ground surface. The project is located about 500 m from the beach.

Adjacent neighboring buildings exist at the south part of the building area. The neighboring buildings are multi-story reinforced concrete structures that are founded on shallow raft foundation with foundation depth of about 1.5m. The building height reaches about 36.0 with slenderness ratio of about 3.0 (Fig. 1).

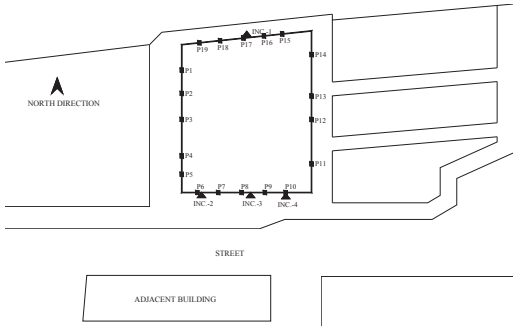


Figure 1. General layout

The shoring system consists of a secant large diameter bored piles with two rows of inclined anchors extended to 9.0 m below ground surface. The diameter of secant piles are 0.9 m with overlap 0.6 m and the total length of the anchors is 21.0 m including 15.0 m free length and 6.0 m grout length. The first row of anchors installed at depth 0.50 m below ground surface with 23° inclination angle while the second row installed at depth 4.0 m with 18° inclination angle (Fig. 2). The working capacity of the anchor is 350 kN and the spacing between anchors in the upper row was 2.4 m while the spacing between anchors in the lower row was 1.2 m.

2.2. Measurements

Lateral and vertical deformations of shoring system and vertical displacements of adjacent buildings were monitored during execution of the excavation works. Four inclinometers with 20 m length were installed to measure the lateral deformations. Results of horizontal displacements at head of shoring system from surveying measurements and results of horizontal displacement with depth from inclinometers readings are shown in figure 3.

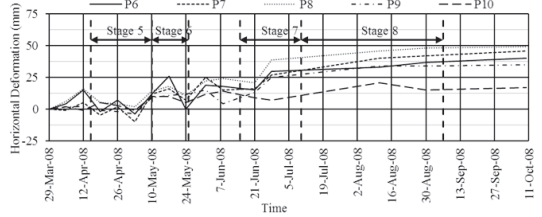


Figure 3.a. Lateral movements of the south reference points

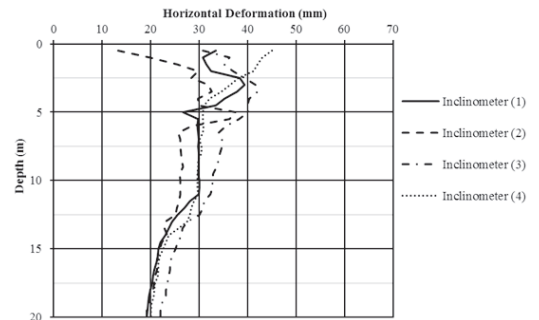


Figure 3.b. Lateral displacements

2.3. Numerical Analysis

A numerical model was conducted to investigate the response of deep excavation in the existing layered soil. Both hardening soil model (HSM) and soft soil models (SSM) were used to simulate the soil behavior. The Hardening Soil model is an advanced model for simulating the behavior of different types of soil, both soft soils and stiff soils. On the other hand, soft soil model was used only for the soft clay layer (PLAXIS Manual, 2013). Program package Plaxis was used applying an effective stress analysis considering the change of excess pore pressures with time due to consolidation. The advantage of using effective strength

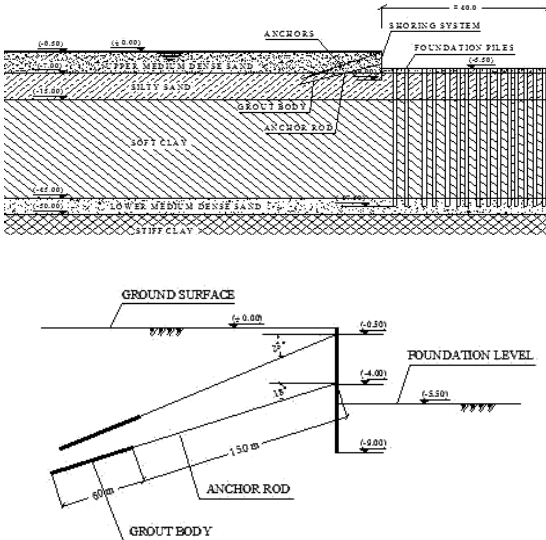


Figure 2. Shoring system

parameters is that the change of shear strength with consolidation can be considered in a coupled analyses (Schanz et.al, 1999).

However, especially for soft soils, effective strength parameters are not always available, therefore, the designer has to deal with measured undrained shear strength c_u as obtained from undrained tests. The available data on the undrained shear strength are used to back-calculate the corresponding effective shear parameters of the soft clay applying Equation (1).

$$c_u = c' \cos \phi' + \frac{1}{2}(\sigma_3' + \sigma_1') \sin \phi' \quad (1)$$

Comparisons between the undrained shear strength of the soft clay using different in-situ tests, lab tests and the results of the above equation are given in figure 4. These comparisons prove the reliability of assumed

effective friction angle of the soft clay of about 7° to 13° .

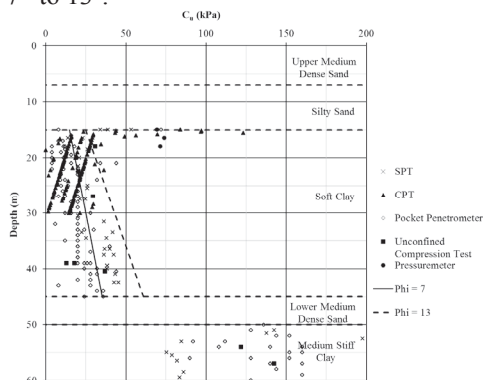


Figure 4. Comparison between measured and calculated undrained shear strength of the soft clay

The applied soil parameters of different models are summarized in the following table.

Table 1. Parameters of the non-linear model

Soil Type	Soil Model	Material Type	γ (kN/m ³)	k (m/day)	E_{50}^{ref} (kPa)	E_{oed}^{ref} (kPa)	E_{ur}^{ref} (kPa)	Power (m)	c_{ref} (kPa)	ϕ°
Upper Medium Dense Sand	HSM	Drained	18	15	30000	30000	90000	0.50	1	38
Silty Sand			18	6.4	8000	8000	24000	0.50	1	34
Lower Medium Dense Sand			20	0.864	25000	25000	75000	0.50	1	36

	Soil Type	Soil Model	γ (kN/m ³)	k (m/day)	E_{50}^{ref} (kPa)	E_{oed}^{ref} (kPa)	E_{ur}^{ref} (kPa)	Power (m)	c_{ref} (kPa)	ϕ°	$C_{increment}$
Model (1)	Soft Clay	HSM	16	0.016	6000	12280	18000	1.00	1	7	-
	Stiff Clay		20	8.64E-05	40000	40000	120000	0.75	15	25	-
Model (2)	Soft Clay	HSM	16	0.016	6000	12280	18000	1.00	25	0	1
	Stiff Clay		20	8.64E-05	40000	40000	120000	0.75	138	0	2.3
Model (3)	Soft Clay	SSM	16	0.016	$C_c = 0.72, C_s = 0.14$ and $e_o = 1.56$				1	7	-
	Stiff Clay	HSM	20	8.64E-05	40000	40000	120000	0.75	15	25	-
Model (4)	Soft Clay	SSM	16	0.016	$\lambda^* = 0.09, \kappa^* = 0.0199$				1	7	-
	Stiff Clay	HSM	20	8.64E-05	40000	40000	120000	0.75	15	25	-

2.4. Results of Numerical Model

Four models were performed, two models using hardening soil model (HSM) and the other two models using soft soil model. In case of using hardening soil model, the first model was analyzed with effective strength parameters ϕ' and c' , while, the second model was analyzed using undrained strength parameters ($\phi = \phi_u = 0$ and $c = c_u$). In case of using soft soil model (SSM), the first model was analyzed using oedometer test results for estimating value λ and κ , while, the second model was analyzed using adjusted values of λ and κ estimated from following empirical correlations according to Yudhbir and Wood (1989):

$$\lambda = 0.217 G_s I_p$$

$$\kappa = 0.048 G_s I_p$$

The effective shear parameters are used in both models applying the SSM.

A comparison between the numerically predicted response and the monitored response is presented to assess the adequacy of the adopted numerical modeling. Figures 5 to 8 show the comparison between predicted soil deformation from numerical modeling using HSM and measured deformations at different inclinometers. In addition, the comparison between estimated soil deformation from numerical modeling using SSM and measured deformations at different inclinometers are presented in figures 9 to 12 respectively.

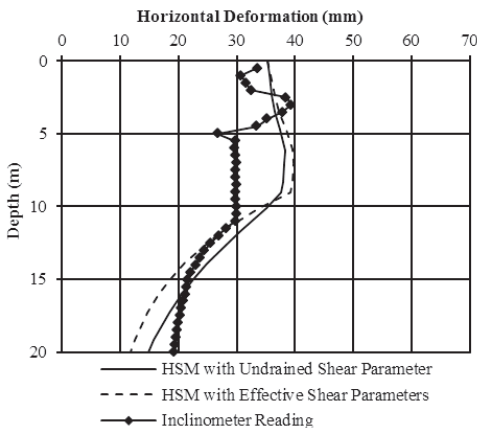


Figure 5. Verification of HSM with Inclinometer (1) readings

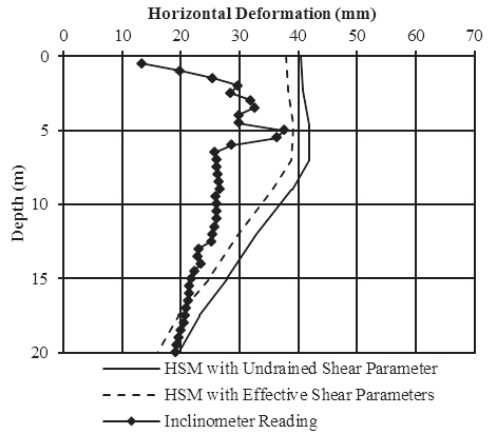


Figure 6. Verification of HSM with Inclinometer (2) readings

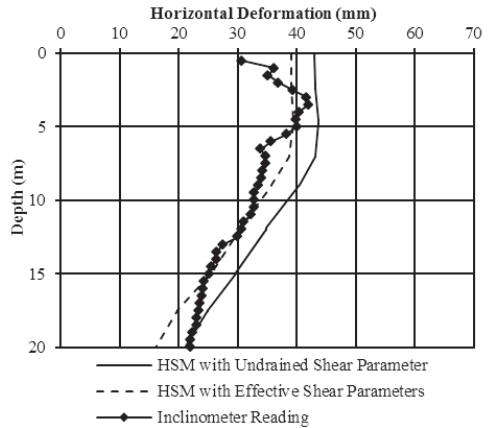


Figure 7. Verification of HSM with Inclinometer (3) readings

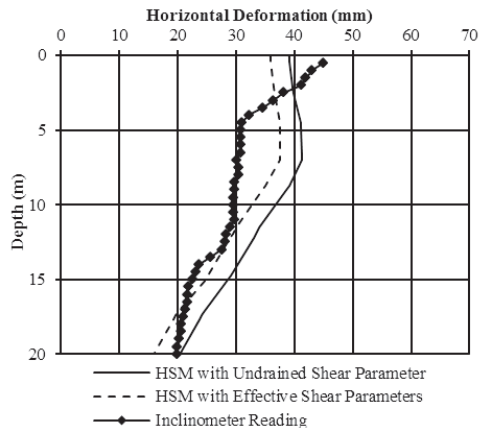


Figure 8. Verification of HSM with Inclinometer (4) readings

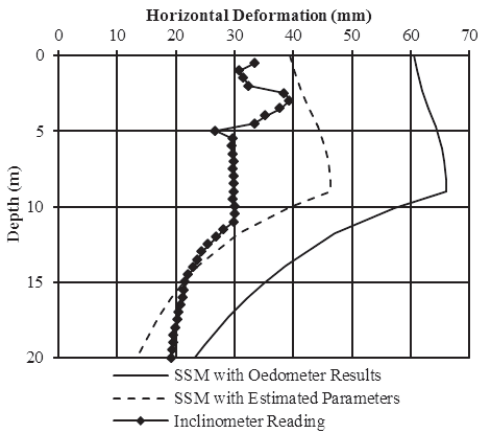


Figure 9. Verification of SSM with Inclinometer (1) readings

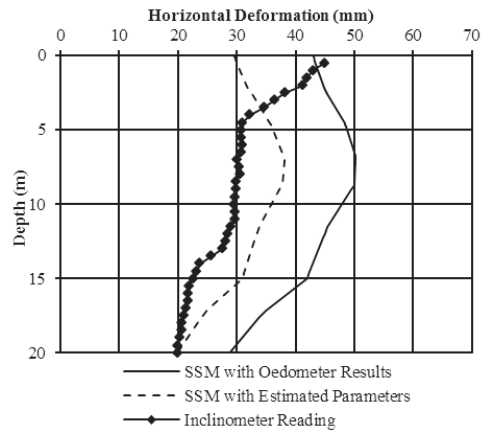


Figure 12. Verification of SSM with Inclinometer (4) readings

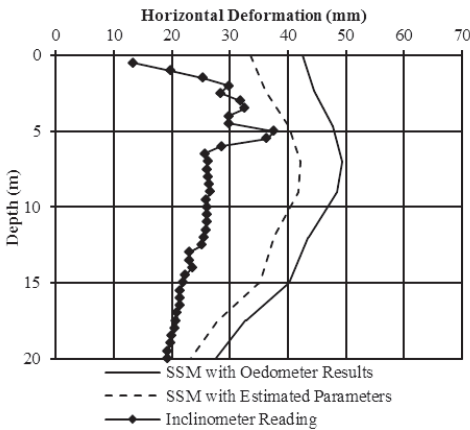


Figure 10. Verification of SSM with Inclinometer (2) readings

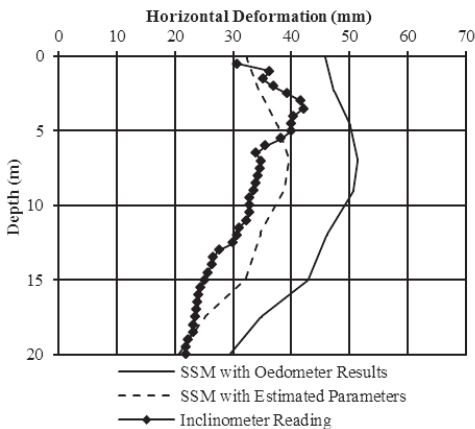


Figure 11. Verification of SSM with Inclinometer (3) readings

The results show the ability of different models and application of either effective shear strength parameters or undrained shear strength value. The application of effective shear strength parameters in undrained analyses with consolidation calculation is a rational model that considers the change of shear strength with time due to consolidation. Nevertheless, the application of this model must be based on realistic estimation of the effective shear strength parameters of the soft clay. This case history approves the methodology (Equation 1) to estimate the effective shear parameters of the soft clay using the measured undrained shear strength of it.

The performance of deep excavation in the double layer system depends mainly on the condition of the lower layer. Although the excavation of about 5.5 m and the total length of the shoring piles of 9.0m lie in the upper stiffer layer, the deeper soft clay layer governs the excavation performance. Two row- pre-stressed tie-back anchors were needed to control the horizontal displacement of the shoring system and hence control the effect of the excavation on the neighboring buildings.

3. SECOND CASE HISTORY

3.1. Description

It is planned the construction of a double towers in Maadi, Cairo direct at the Nile River. The two towers have a common three underground basement that cover the whole project area as shown in figure 13.

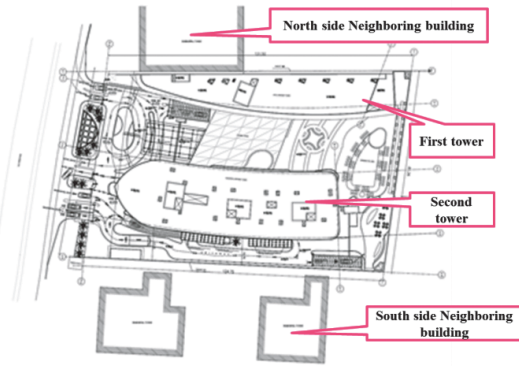


Figure 13. General layout

According to the conducted site investigation, the subsoil consists of a surface fill layer down to depth of about 2.0m below street level followed with a silty clay, clayey silt layer with depth of about 10 to 11m. A silty sand layer with depth of about 7m is found beneath the silty clay, clayey silt layer followed with a dense to very dense sand layer that extends to deeper depths. The conducted CPT tests were evaluated to get the main design parameters of the silty clay / clayey silt and silty sand layer in conjunction with the conducted in-situ and laboratory test results. The SPT (standard Penetration Test) in conjunction with the conducted laboratory test results were used to develop the geotechnical parameters of the dense to very dense sand layer. The ground water table is found about 2.0m to 2.5m below ground surface that is equivalent to level of -4.5 regarding the Nile Corniche road level. This level is affected seasonally by the Nile water level.

For the whole perimeter, diaphragm wall with wall thickness of 0.64m and 0.8m is suggested to be used as the main support element of the deep pit excavation. Two lines of anchors were applied to support the Diaphragm

wall. The upper anchor level is chosen at elevation -4.0 and the lower anchor level is at -8.5. These levels are chosen to have the optimum straining actions in the diaphragm wall and to have free height for the construction of the raft and the basement slabs. The spacing between the upper anchors is about 3.0m and for the lower anchors is about 1.5m. The numbers of strands as well as the reinforcement of the wall depend on the position of the wall. For parts of the shoring system adjacent to the neighboring buildings, especial solutions are developed. For the north side, the suggested shoring system is demonstrated in figure 14.

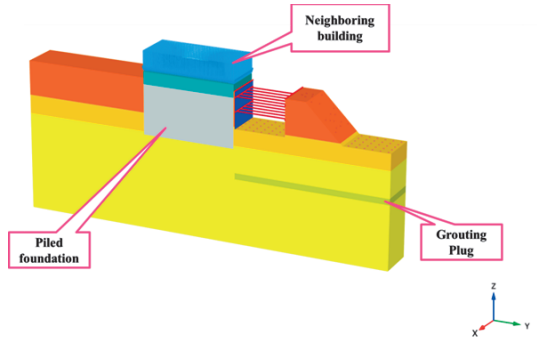


Figure 14. Shoring system at the north side

The neighboring building beside the north side is a high rise building with about 28 floors and only one basement. Its shapes in the plan are rectangular form with length parallel to the pit excavation of about 30m. According to available data, the high rise building is founded on driven piles that are penetrated in the dense to very dense sand with pile tips at level -20.0. The shoring system in this part consists of the main diaphragm wall (external DW) with thickness 800mm, another parallel diaphragm wall 640mm (internal DW) at the boundary of the first tower to form a type of cofferdam. The internal 640mm DW will be supported by slopes where the slope toe lies at the boundary of the second tower. The slopes will be stabilized by existing foundation piles that shall be extended in the slope. The piles act as dowels increasing the slope stability to reach the project requirements.

The excavation of the first tower will be conducted inside the cofferdam using struts of

steel pipes with total length of about 16.0m. The shoring system in north side has been modeled applying three dimensional finite element analyses. All construction stages were modeled to investigate the deformation performance and determine the maximum straining actions acting on the supposed shoring system. It was suggested to use the double hardening soil model to represent the soil stress-strain performance. Following table summarizes the soil parameters used in the analyses.

Layer	Fill	Silty clay	Silty sand	Dense sand
Top level	0.0	-2.0	-13	-19
c' (kPa)	1	5	1	1
ϕ' (°)	30	25	33	36
γ' (kN/m ³)	18	18	19	20
E_{50}^{ref} (MPa)	10	15	50	80
E_{ur}^{ref} (MPa)	30	45	150	200
Power m	0.6	1.0	0.7	0.5

Figure 15 demonstrates the results of the conducted three dimensional analyses of the north side of the suggested shoring system.

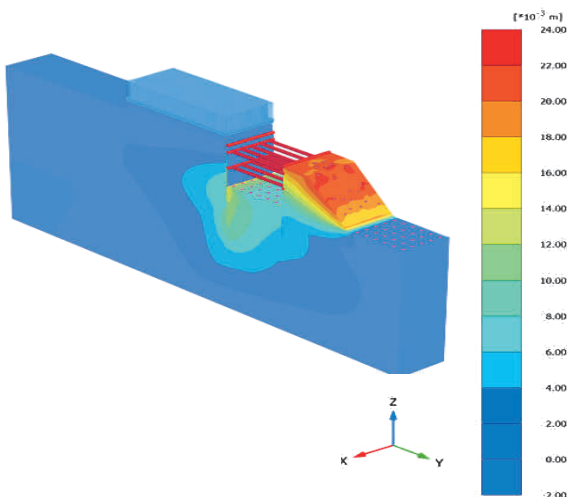


Figure 15. Horizontal displacement

The maximum induced vertical displacement of the piled founded neighboring buildings reaches about 5mm with maximum differential settlement of about 5mm within the whole building. The maximum induced

horizontal displacement of the piled founded neighboring buildings reaches about 8mm.

The additional bending moments of the neighboring piles are shown in figure 16.

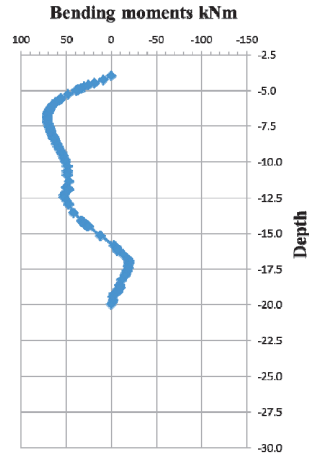


Figure 16. Additional bending moments of the neighboring piles due to recent excavation activities

The dowel effect of the piles to stabilize the slope adjacent to the cofferdam increases the slope stability to fulfill the design requirements and reduce the horizontal displacements. Additional bending moments are developed in the dowel piles figure 17.

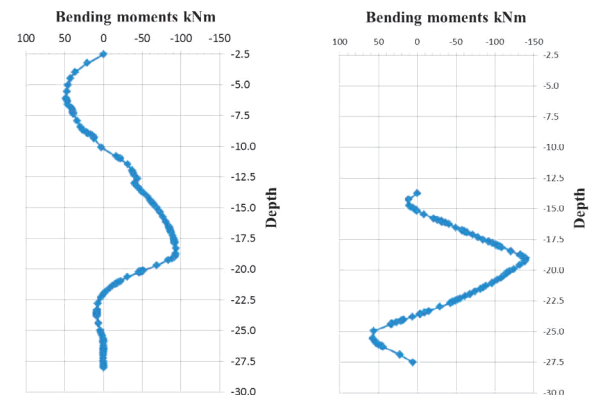


Figure 17. Induced bending moments in the dowel piles

A monitoring program included precise surveying, piezometers and inclinometers are

developed and will be installed to observe the real performance of the special complex shoring system.

4. CONCLUSION

The performance of deep pit excavation in layered soil depends on the conditions of the soil layers. In case of deep soft layer, its effect on the horizontal displacement performance of the shoring system can govern the structural design of the whole system. Applying enhanced numerical models with the corresponding constitutive laws to simulate the stress-strain relationship of the different soil layers are essential in such cases. The double hardening soil model approves its ability to simulate the performance of both soft clay as well as very dense sand. The effective shear parameters of the soft clay in conjunction with consolidation analyses can be applied successfully considering the changing of soil shear strength with time due to consolidation. In this case, the estimation of the effective angle of internal friction of the soft clay is a main design parameters that must be calibrated regarding the undrained shear strength of the soft clay.

Using the deformation parameters evaluated directly from Oedometer test leads to overestimate the deformation performance. This is due to the sample disturbance during drilling, sampling and preparing the test in the lab. Therefore, the application of verified correlation can help adjusting the design parameters.

The foundation piles inside the excavation boundary, which acts as dowels, have a pronounced effect reducing the total horizontal displacement of the shoring system. The three dimensional analyses can help detecting the real performance of complex deep pit excavation. The dowel effect of existing pile can reduce the displacements and increase the total stability of the shoring system.

5. REFERENCES

El-Mossallamy, Y. (2005) "Deep pit excavation in complex geological conditions: measures to optimize the performance of the support system", International Symposium "GeoCityNet / Lille.

PLAXIS Manual, 2013, A. A. Balkema, Rotterdam.

Schanz, T., Vermeer, P. A. and Bonnier, P. G., (1999). "The hardening soil model: formulation and verification". In : Brinkgreve, R.B.J, eds, Beyond 2000 in Computational Geotechnics: 10 years of PLAXIS international, A.A. Balkema, Rotterdam.

Yudhbir, Wood, D. M., (1989). "General Report Recent developments in laboratory strength and deformation testing". Proc.12th ICSMFE 1989, Rio de Janeiro, Vol.4

6. RELATED REFERENCES

Briaud, J. L., (1992). "The pressuremeter". A.A. Balkema, Rotterdam, Netherlands.

Clough, G. and O'Rourke, T., (1990). "Construction induced movements of in-situ walls". Proceedings of ASCE Special Conference on Design and Performance of Earth Retaining Structures, Cornell University, New York, pp. 439-470.

Kempfert, H. G. and Gebreselassie, B., (2006). "Excavations and foundations in soft soils". Springer-Verlag, Berlin.

Kulhawy, F. H. and Mayne, P. H., (1990). "Manual on estimating soil properties for foundation design". Electric Power Research Institute, EPRI.

Ou, C. Y. and Hsieh, P. G., (2011). "A simplified method for predicting ground settlement profiles induced by excavation in soft clay". Computers and Geotechnics, El-Sevier, Amsterdam.

Peck, R. B., (1969). "Deep excavations and tunneling in soft ground". State of the Art Report, Proceedings of 7th ICSMFE, Mexico, pp. 225-290.

Robertson, P. K. and Campanella, R. G., (1983). "Interpretation of cone penetrometer tests, Part I sand". Canadian Geotechnical Journal, Vol. 20, No. 4, pp. 718 - 733.

Skempton, A. K., (1986). "Standard penetration test procedures and the effects in sands of overburden pressure, relative density, particle size, aging, and overconsolidation." Geotechnique, London, Vol. 36, No. 3, pp. 425-447.

Vermeer, P. A. and De Borst, R., (1984). "Non associated plasticity for soils, concrete and rock." HERON, Vol. 29, No. 3.

Von Soos, P., (1990). "Properties of soil and rock (in German)". In: Grundbautaschenbuch Part 4, 41th edition. Ernst and Sohn, Berlin.

**GUIDELINES FOR SOIL-
STRUCTURE INTERACTION:
FIRST DRAFT FOR DISCUSSIONS
AND FURTHER DEVELOPMENT**

Soil-Structure Interaction

V.M. Ulitsky

St. Petersburg State Transport University, Russia, ulitsky.vladimir@gmail.com

A.G. Shashkin, K.G. Shashkin, V.A. Shashkin, M.B. Lisyuk, V.N. Paramonov, V.A. Vasenin
Georeconstruction Engineering Co, St.Petersburg, Russia, mail@georec.spb.ru

INTRODUCTION

Taking into account reciprocity (interaction) of subsoil and superstructure is a fundamental principle of calculation (i.e. computation and numerical analysis) and design. In Russia this principle received the status of a clause in the Federal law Ref. 384-ФЗ «Technical regulations of safety of buildings and structures». The law makes one liable to consider «*aspects of interaction of structures between themselves and with their subsoil*», «*plastic and reological properties of [construction] materials and soils*», as well as «*spatial work of structures*».

According to the Russian Codes (22.13330 «The foundations (*taken in the broadest sense, incl. footings and subsoil*), of buildings and structures») «the structure and its foundation/footing/subsoil should be considered as a single unity, i.e. an account should be made of interaction between a (super)structure and its subsoil»; «loads and impacts on subsoil rendered by foundations of structures, should be established by calculation/computation, as a rule being based on studying interactions between subsoils and superstructures».

Similar requirement is found in Standard Procedure Ref. 24.13330 «Piled foundations»: «a structure and its foundations should be considered jointly, i.e. an interaction between a

structure and a compressible subsoil» should be taken into account; «calculation/computation of a structural system «piled foundation – flexible slab – superstructure», in general, should be made in a spatial setting, taking into account interaction between the superstructure and the underground sections of buildings, as well as between piled foundations and the [associated] subsoil».

1. THE NATURE OF STRESS CONCENTRATION EFFECTS IN THE INTERACTION ZONE OF THE SUPERSTRUCTURE AND THE SUBSOIL

When designing foundations and underground parts of structures practitioners aspire to balance out settlement epures (diagrams), and to exclude development of settlement differentials caused both by heterogeneity of geological conditions, and by uneven character of subsoil loading. The aspirations are fulfilled by limiting settlements, relative settlement differential, and the structure's tilt by the corresponding limiting subsoil deformation values (combined deformation of the subsoil and the superstructure). Thereby they are able to resolve the important issue of limiting the additional loads in the superstructure generated by the settlement differential.

However, providing a uniform epure does not mean there will be no additional loads in the superstructure caused by its interaction with the subsoil. To explain this effect one may simply consider interaction of a stiff plate and its underlying stratum (the sublayer).

Under the loading from the plate the sublayer develops a contact pressure epure which, according to the famous analytical Bussinesque solution (1) for an absolutely rigid round plate, has the appearance of a parabola with asymptotes associated with the plate edges (see Curve 1 on Fig. 1):

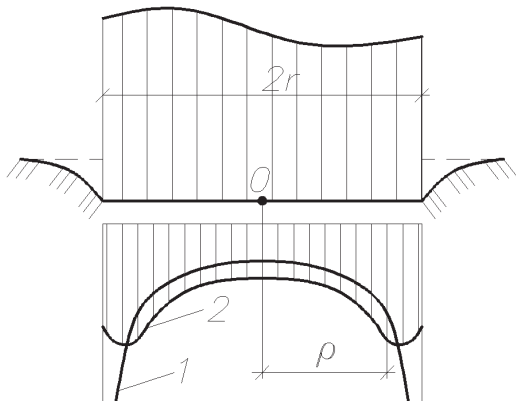


Fig. 1. The contact epure of pressure in subsoil under a plate: 1 – according to the analytical solution, 2 – in reality, taking into account development of plastic deformations.

$$p_{\rho} = \frac{p_m}{2\sqrt{1 - \frac{\rho^2}{r^2}}} \quad (1)$$

where p_{ρ} – pressure along the round plate footing at distance ρ from its centre at $\rho < r$ (r – plate footing radius); p_m – mean pressure along the plate footing.

In reality the contact epure assumes a characteristic "saddle" outline (Epure 2 on Fig. 1), which is proved by numerous *in situ* measurements (Fig. 2). Formation of such the epure under a plate is caused by development of plastic deformations in the edge associated areas of the sublayer where stress exceeds the strength of the soil.

The plate, possessing absolute rigidity, has an absolutely uniform epure of settlements. And it follows from the condition of equilibrium that

in the plate itself there appears an epure, which completely repeats the contact epure of pressure in the sublayer.

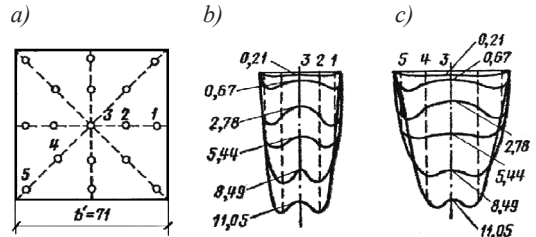


Fig. 2. Experimental epures of reactive pressures: under a square plate of 71×71 cm on a sandy subsoil at pressures from 0,2 to 8 kgfs/cm² (from 20 to 800 kPa) (Murzenko tests): a – arrangement of strain gauges; b – epures along the centre axis; c – diagonal epures.

The appearance of the contact epure of normal vertical stresses (both in the sublayer, and its "reflection" in the plate) depends on pliability of the sublayer and rigidity of the plate itself. Two extreme situations, practically unattainable in reality, are when the plate has correspondingly absolute rigidity and zero rigidity (in the latter case it morphs into flexible loading). In the first case the contact epure in the sublayer will assume the shape of Curve 2 on Fig. 1, in the second case it will look like an evenly distributed epure of pressure under flexible loading.

Because in solutions of real construction design problems it is not the idealized plate that is normally considered, but rather some actual superstructures having final rigidity, the contact epure will assume some intermediate shape between two noted extreme examples.

The type of the contact epure depends also on subsoil yielding properties. At absolutely unyielding subsoil equivalent to rigid supports, the contact epure will be identical to a result of collecting loads over loaded areas, as it is done in usual design practice. In this case there will be no place for the load concentration effects, caused by soil-structure interaction. In reality any subsoil except solid rock rocky has a specific yielding. The interaction effect will be realized in such a way that rigidity of superstructure will tend to level out the settlement epure, resulting from which additional loads will appear in the superstructure.

2. THE GENERAL PRINCIPLES OF SOLVING SOIL-STRUCTURE INTERACTION PROBLEMS

2.1. Soil-structure interaction calculations are generally carried out by numerical methods in a spatial setting with modeling of the bearing structures, the foundation and the subsoil in a single calculation profile. Normally practitioners consider a «structure – soil» system, or more precisely, a «superstructure – underground part – subsoil» system, covering all elements of the project interacting with one another.

2.2. Structural elements of a building are represented with rod, shell or volumetric final elements. The subsoil is modeled with spatial final elements. The flat deformed state scheme is only allowed in cases when deformations, perpendicular to the profile, are negligible (a structure is of the extended type and all sections are similar to each other).

2.3. Construction materials' behavior is represented by a linear or a nonlinear model, as required by the relevant normative documents/codes. Behavior of soil is represented by a nonlinear model relevant to site conditions.

2.4. The dimensions of the calculation profile of a subsoil are chosen in such a way that they do not influence calculation results. The dimension of the calculation profile in the vertical direction should be no smaller than the depth of deformation development in the subsoil (the active zone). For the model of linearly deformable medium the active zone is defined by thickness of the compressible stratum. In this case a restriction to the calculation profile from below is applied, according to the depth of the compressible stratum defined by local construction and design codes.

In the horizontal direction, the dimension the calculation profile should be no smaller than the size of the surface settlement trough around the structure. For the model of linearly deformable medium in the horizontal direction the sizes of the calculation profiles around the building should be no smaller than the width of the building and/or the depth of the compressible stratum.

2.5. It is acceptable if soil-structure interaction calculations are performed by means of iterative procedure of reducing separate calculations for the structure and for the subsoil to a

joint soil-structure calculation. This procedure is carried out by realization of the following algorithm:

(1) Define loads on the subsoil.

(2) Define subsoil settlement from the applied loads without rigidity of the building (the practitioner here considers the “foundation-subsoil” system in which the influence of superstructure is present as loads on the foundation).

(3) Define factors of rigidity (stiffness coefficients) of the subsoil as relation of active loads to obtained settlement values.

(4) Recalculate subsoil loads taking into account the factors of subsoil rigidity variable in plan view.

(5) Repeat steps (2)..(4) until the results collate at the required level of accuracy (for structural loads the usual accuracy level is taken as $\pm 5\%$).

The number of necessary iterations to achieve the required precision depends on structural strength and deformability of the subsoil. The more rigid the subsoil and the more pliable the subsoil, the higher the number of required iterations. Usually, to achieve the $\pm 5\%$ accuracy of structural stresses it is required to perform from 10 to 50 iterations. At smaller number of iterations the solution accuracy appears insufficient.

The disadvantage of the iterative method of solving soil-structure interaction problems is the division of the analysis between the domains of the superstructure and the subsoil in various software products. In case the iterative method is realized in separate software codes not connected with each other, when assigning intermediate input parameters for each calculation stage “manually”, there appears a risk of additional errors at each iteration of the problem solution, those errors being related to assigning new loads. Correspondingly, it is necessary to use such software products which incorporate “converters”, allowing for an automatic application of the entire range of solution results obtained for yielding supports as initial loads to the subsequent solution of a subsoil deformation problem. From this it follows that the models of subsoil behaviour not equipped with such converters are not popular. Thus, the iterative mechanism appears labor-consuming and inconvenient for realization. A consequence of

this is that practitioners are inclined to reduce the number of labor-consuming iterations, the result being a drop of calculation quality. In this regard, preference should be given to the kinds of software capable of calculating the «superstructure – underground sections – subsoil» complex in one calculation profile.

3. FACTORS WHICH INFLUENCE LOADS CONCENTRATION IN THE SUBSOIL-SUPERSTRUCTURE INTERACTION ZONE

3.1. The calculation profile for the system «superstructure – underground part – subsoil» should be chosen taking into account the most essential factors which define the stressed condition and deformations of subsoil and superstructures. The most essential factors defining the stressed-strained condition of subsoil and superstructures are as follows below:

(1) superstructure rigidity defined by:

(1.1) spatial rigidity of the structural layout (structural layout) of the building;

(1.2) deformation properties of the materials from which the superstructure is (to be) constructed;

(1.3) particulars of the construction process, primarily, any changes to the structural layout that might have been introduced in the course of construction;

(2) rigidity of foundations (foundations on natural subsoils, piled foundations, etc);

(3) rigidity of subsoil (subsoil yielding), defined by the geological structure and deformation properties of the subsoil strata, as well as by a possibility of their change in the process of construction and subsequent use of the finished project.

3.2. The effect of soil-structure interaction manifests in the form of loads concentration in the contact epure. The effect of soil-structure interaction depends on a ratio of strengths in the superstructure and the subsoil.

To understand the regularities of formation of the soil-structure interaction effect, depending on the factors listed in 3.1 (1) ... (3) above, we will consider a number of specific types of idealized structural layouts of extended and free-standing (“dot”) buildings with bearing walls (Fig. 3).

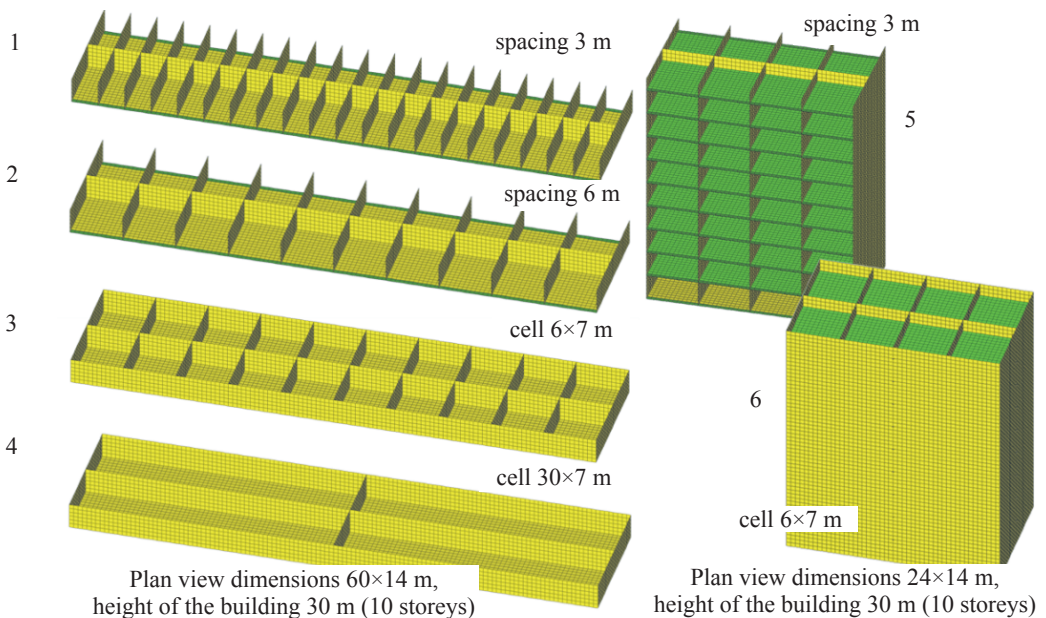


Fig. 3. Numerical modeling of idealized structural layouts of buildings with different structural strengths (extended buildings: 1, 2 – with transverse bearing walls; 3 – cellular type; 4 – with longitudinal bearing walls; “free-standing” (“dot”) buildings: 5 – with transverse bearing walls; 6 – cellular type)

In view of the fact that the interaction effects manifest within several lower floors, we will consider 10-floor tall buildings in their floor-by-floor construction.

Let us consider a range of change in material strength in structures from the minimum value, characteristic of brickwork (constructed, for example, of M100 class brick on M100 class mortar, of which the strain modulus is 1350 MPa), to the maximum value, which can correspond the initial modulus of elasticity of concrete (for example, monolithic reinforced concrete, class B25, of which the initial modulus of elasticity (instant deformation modulus) is equal to 30000 MPa). The instant modulus manifests in limited periods of time at rather quick loading application. Therefore, in the interval between the designated values it is logical to consider a concrete structure under long load application, which, according to the formula 5.3 of the Russian Normative Documents СП 52.101 «Concrete and reinforced concrete structures», imparts to B25 concrete the strain modulus of 8500 MPa. The moduli given above differ in magnitude several times and cover the main range of changes of material strength of superstructures.

Solving the problem of soil-structure interaction we shall consider floor-by-floor construction of buildings, each being a representative of every structural layout/structural layout (in this example reinforced concrete walls are assumed as having thickness 200 mm, brick walls – 380 mm; intermediate floors are taken as being reinforced concrete monolithic spans with thickness of 180 mm for all schemes).

Let us consider the following foundation types:

(1) a continuous reinforced concrete raft on natural subsoil (raft thickness 500 mm);

(2) piled foundations topped with a raft (length of piles 20 m, cross-section 400×400 mm, raft thickness 500 mm) with variable pile spacing: (3 ... 5) d and (8 ... 9) d.

When modeling behavior of the building on the raft we will be varying the parameters of subsoil deformability. Let us consider the options covering the whole range of possible change in subsoil strength of and corresponding to:

(1) soils with a high degree of deformability – weak soils (for example, loose sands,

water saturated clay with consistencies ranging from fluid to soft-plastic);

(2) soils with medium degree of deformability (for example, medium density sands, clay with firm-plastic consistency);

(3) soils with low degree of deformability (for example, dense sand, clay with firm to semi-firm consistency).

When solving soil-structure interaction problems it appears necessary also to find out how rheological properties of the soil medium can influence the interaction effect between structures and subsoil. Rheological properties of soil are defined by mechanical characteristics, which display non-linear changes from instant values, actual for the moment of load application to a subsoil, to stabilized values, corresponding to long-term action of soil under loading [9]. We shall assume instant values of mechanical soil properties as being by a factor of magnitude greater than the long-term values given in Table 1.

Table 1. Settlement parameters of subsoil

Degree of soil deformability	E , kPa	η	c_u , kPa	φ°	γ , kN/m ³
High	5000	0.3	50	8	19.5
Medium	10000	0.3	100	23	20.5
Low	20000	0.3	200	22	21.0

When modeling work of piled foundations we shall assume a two-layer subsoil with the top stratum having thickness of 8 m, representing a medium with high or medium degree of deformability and the bottom bearing stratum with medium or small degree of deformability.

Performing numerical analysis of soil-structure interaction, we shall use an elastic model to represent the superstructure, and an elastoplastic model with independent strain hardening at consolidation and form-change deformation to represent subsoil behavior.

To identify interaction effects we shall compare calculations results for each building on an elastoplastic subsoil with corresponding calculation results on an absolutely unyielding subsoil (on rigid supports). For convenience of analysis, we shall use a relation of a load in some point of the superstructure obtained through the solution with a yielding subsoil, to a

load in the same point obtained through the solution on rigid supports, which we will term *the soil-structure interaction index* and designate it as K_{SSI} in our notation (where SSI stands for “Soil-Structure Interaction”).

3.3. Influence of the structural layout on the soil-structure interaction effect

When designing buildings with bearing walls it is necessary to bear in mind that the greatest the interaction effect between structures and non-linearly deformable media will manifest in structural layouts with an open-end (unclosed) contour of walls. Moreover, creation of closed contours by means of intermediate floors (overspans) is not capable to considerably reduce stress concentration in the contact epure, as strength of intermediate floors in the vertical plane is considerably inferior to strength of walls.

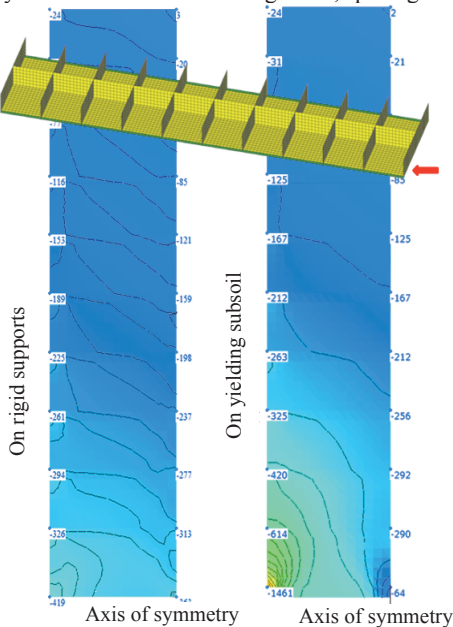
For the example under consideration in the transverse walls which are not “tied” along the edges by longitudinal walls (schemes 1 and 2 on Fig. 3), the K_{SSI} index for gable walls = 3.7 (see Fig. 4 a, 5 a). If the transverse walls are “tied” by longitudinal walls (schemes 3 and 4 on Fig. 3), concentration of vertical loads in the

lower part of transverse walls is characterized by K_{SSI} index = 1.8, i.e. by a twice smaller value (see Fig. 4 b, 5 b). It is worth pointing out here that such effect is observed regardless of spacing between transverse walls. It is identical both for a cellular scheme of the building (scheme 3 in Fig. 3) with grid size of 6x7 m, and for Scheme with longitudinal bearing walls (scheme 4 in Fig. 3), forming cells with dimensions of 30x7 m (Fig. 5).

The described effect can be explained by the fact that reflection of the contact pressure epure on the foundation footing for the cellular scheme is shared at the same time by longitudinal and transverse walls, whereas in the open-ended scheme the contact loads concentrate entirely in transverse walls.

The contact epures for longitudinal walls of buildings with transverse walls and those of cellular profile are quite close to each other (Fig. 6). The external longitudinal wall in the cellular building appears considerably more loaded, than the wall in the middle. For a building with longitudinal bearing walls the outline of the contact epure is similar to the shape of the epure in the transverse wall of the cellular structure, which becomes evident if you stretch the latter’s scale horizontally.

Layout with transverse bearing walls, spacing 6 m



Layout with longitudinal and transverse bearing walls

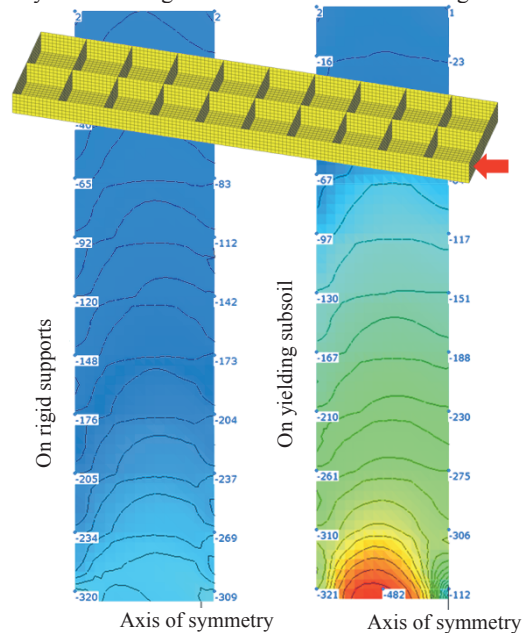


Fig. 4. Distribution of vertical stresses in the gable wall of a building (kN).

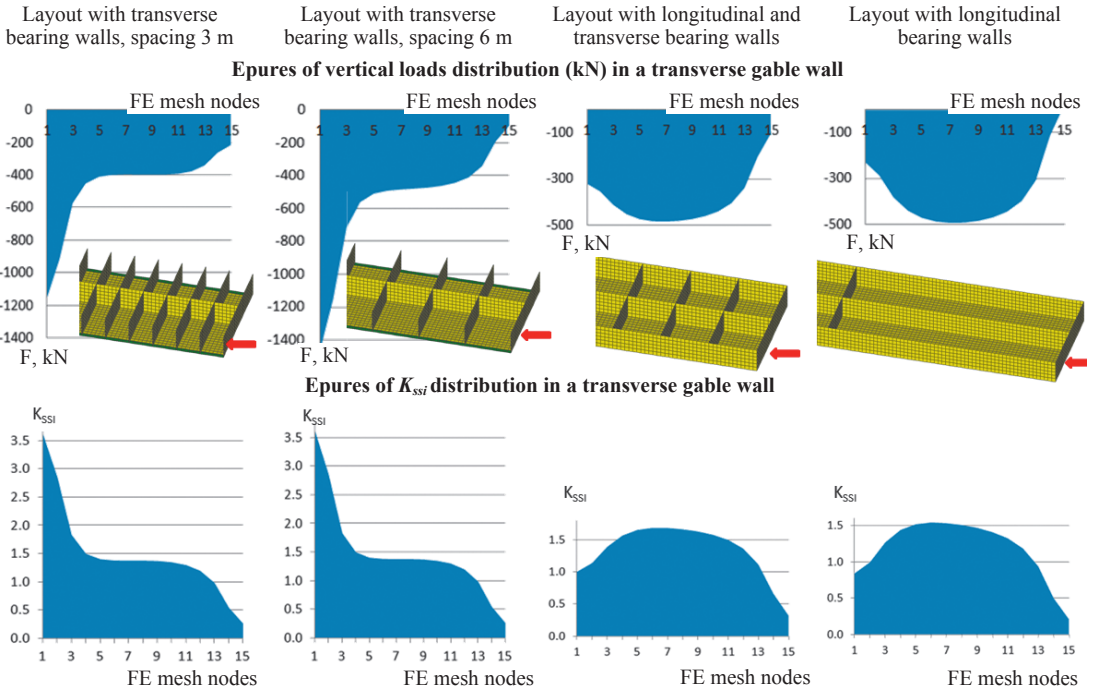


Fig. 5. An extended building. Epures of vertical loads distribution (kN) in a transverse wall on the building's gable end, calculated on the nonlinear and deformable subsoil, consisting of deposits of medium degree of deformability, and epures of K_{SSI}

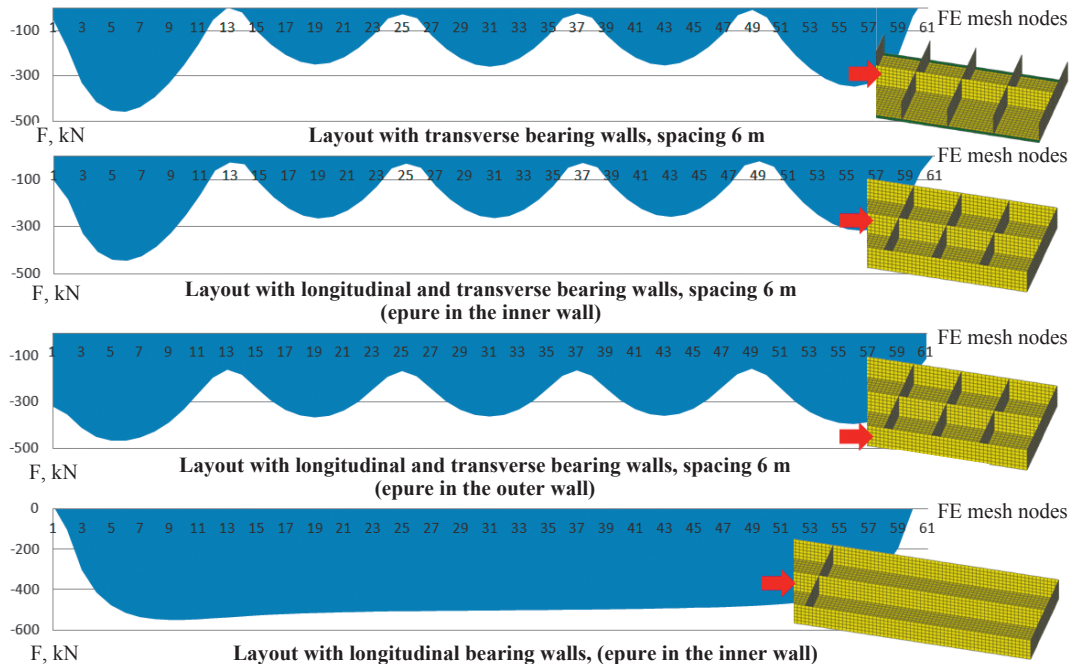


Fig. 6. An extended building. Epures of vertical loads distribution (kN) in longitudinal walls of the building calculated on the nonlinear and deformable halfspace consisting of soil of medium degree of deformability.

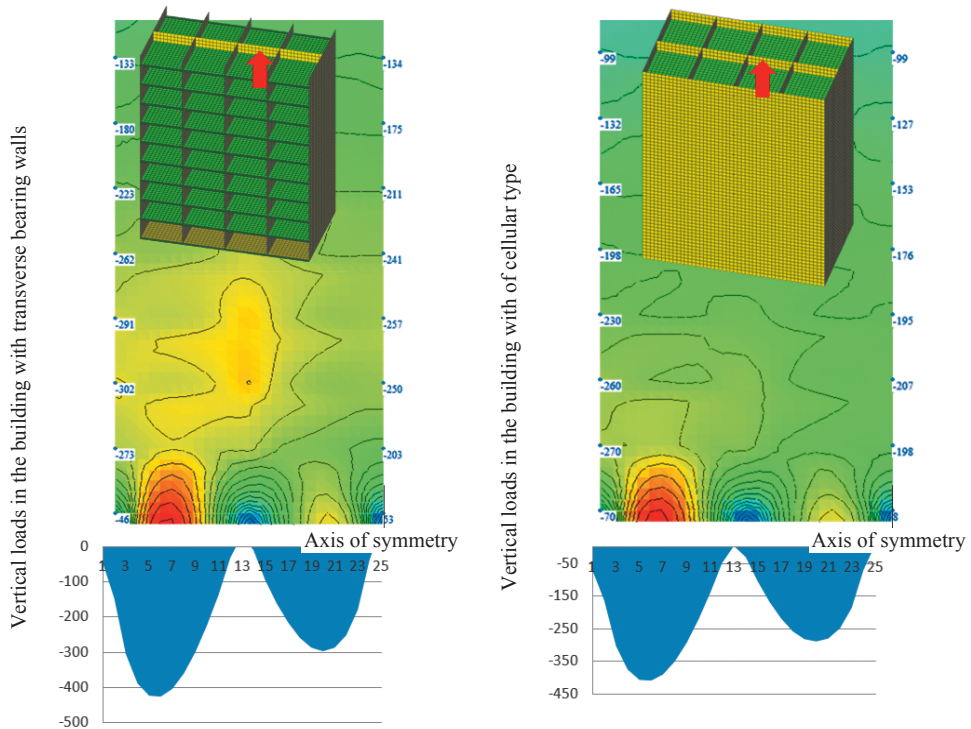


Fig. 7. A free-standing (“dot”) building. Epures of vertical loads distribution (kN) in longitudinal walls of the building calculated on the nonlinear and deformable halfspace consisting of soil of medium degree of deformability.

When considering free-standing («dot») buildings (schemes 5 and 6 in Fig. 3) it becomes obvious that shortening of longitudinal walls increases their load-assuming “competitiveness” in relation to transverse walls. Reducing the extent of a cellular building to full symmetry in two directions, the loads in orthogonal systems of walls become identical (Fig. 7).

3.1. Taking into account floor-by-floor construction sequence

The analysis of stressed-strained conditions of structures of a building with accounts taken of its floor-by-floor construction allows to establish that starting from the 3rd floor there appears an affinity between contact epures, which change in the process of construction only numerically, retaining their outline. The contact epure of loads for a 1-floor high building has an excellent outline, however, owing to the small scale of loads they are not a defining factor in design of wall structures.

In the considered example, for the structural layouts of buildings *with transverse bearing walls* (schemes 1 and 2 in Fig. 3) the character of the contact epure arising in the transverse gable wall practically does not change from the very beginning of construction. It is practically when the building reaches 1-floor height that the epure becomes final (Fig. 8 a, b). In the similar way there is a likelihood in the epures of contact stresses arising in the process of construction in longitudinal walls for all structural layouts of buildings (Fig. 9).

A somewhat different situation is observed in transverse walls of buildings *with cellular structure* (scheme 3 in Fig. 3), *and also with longitudinal bearing walls* (scheme 4 in Fig. 3). At the initial stage of construction, after completion of 1-2 floors, the character of the contact stress epures is similar to those appearing in buildings with transverse bearing walls (there is a concentration of stresses along the edges of transverse walls) (Fig. 8 c, d). As construction continues, the epure is gradually leveled, reaching its final outline upon

completion of the 4th floor, like the epure appearing from a 10-floor loading.

It is natural that the K_{SS} increases in process of construction as the strength of walls in their plane also increases. Therefore, if walls of a

building are calculated to assume loads conditioned by interaction of the building of a designed height with its subsoil, no intermediate construction situations will present any danger for such a building.

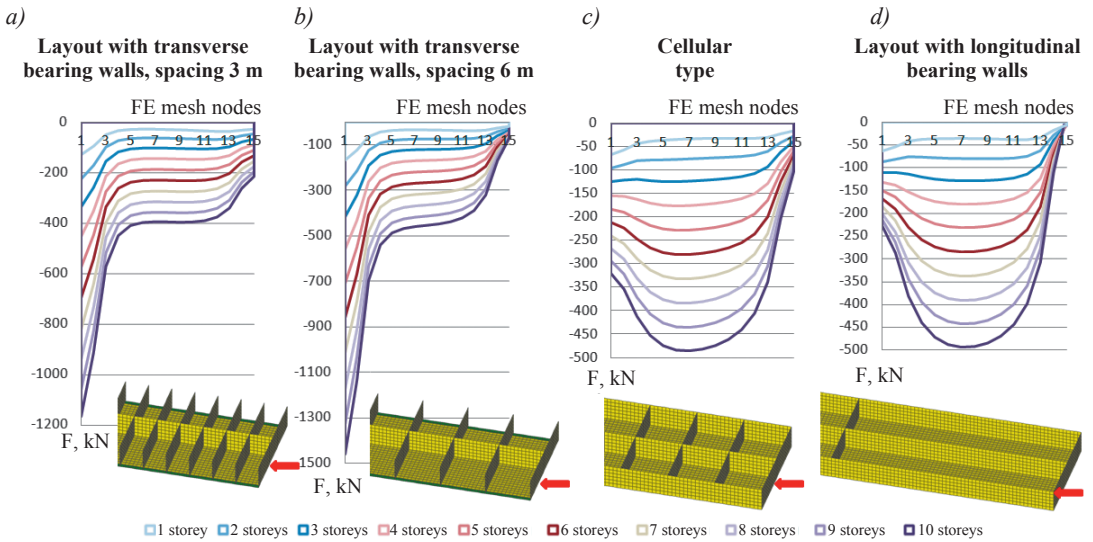


Fig. 8. Epures of vertical loads distribution (kN) in gable walls at floor-by-floor construction of a building calculated on the nonlinear and deformable halfspace consisting of soil of medium degree of deformability.

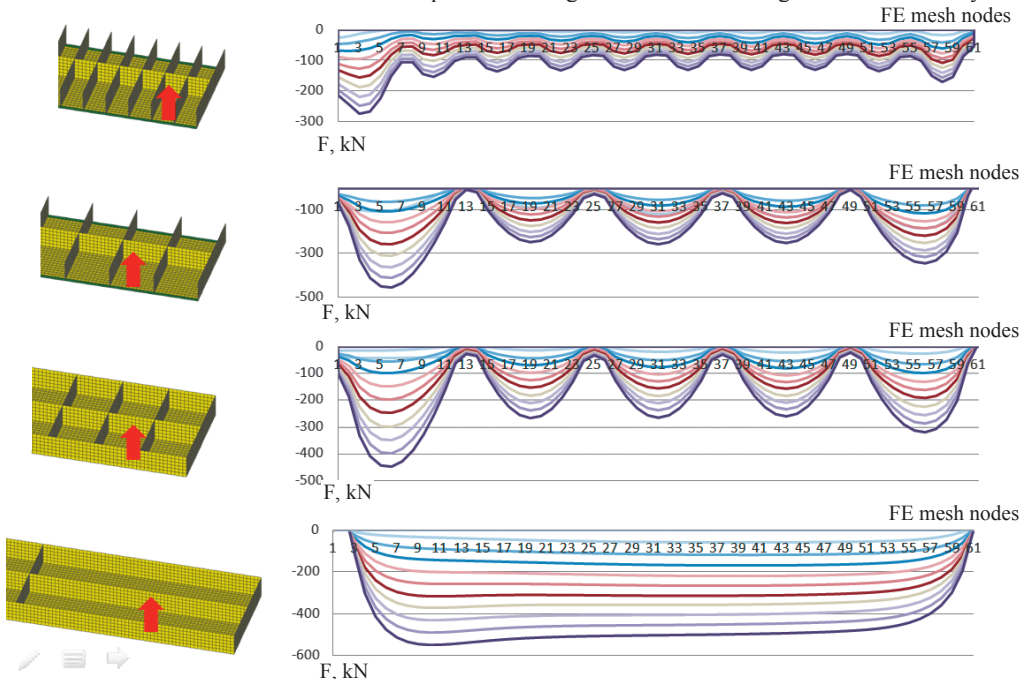


Fig. 9. Epures of vertical loads distribution (kN) in longitudinal walls at floor-by-floor construction of a building calculated on the nonlinear and deformable halfspace consisting of soil of medium degree of deformability.

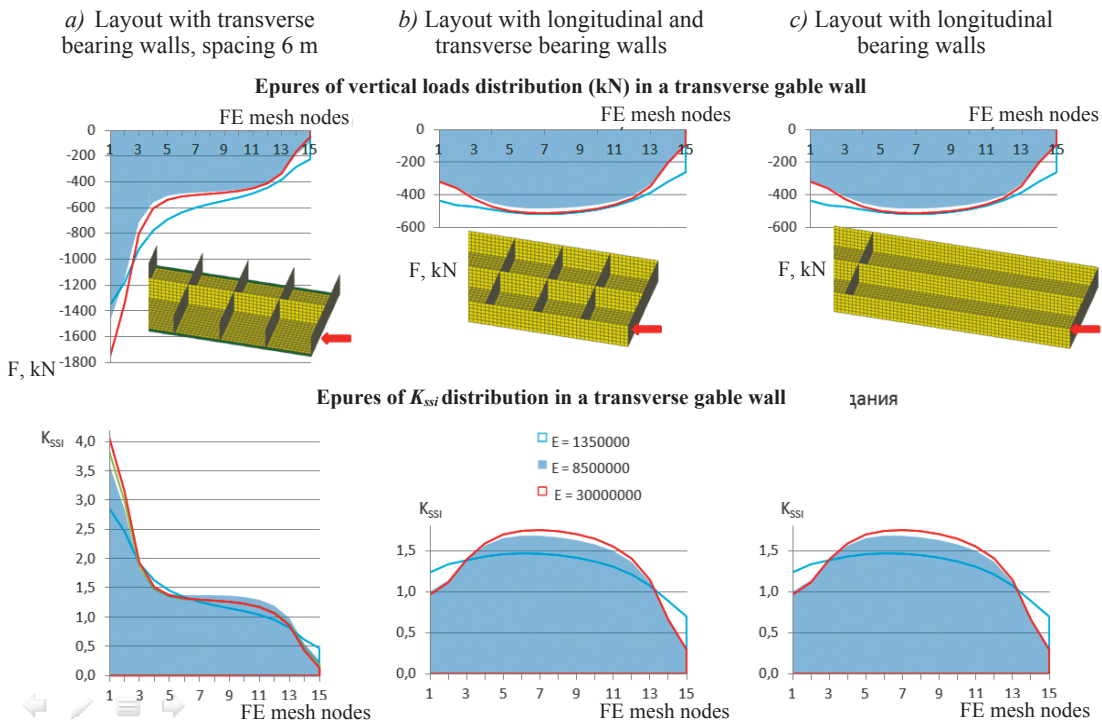


Fig. 10. Epures of vertical loads distribution (kN) and K_{SSI} in gable walls at various mechanical characteristics of constructional materials calculated on nonlinear and deformable subsoil consisting of deposits of medium degree of deformability.

3.2. Influence of stiffness (strength) parameters of structural materials

Increase of strength parameters of superstructure while the other equal conditions remain unchanged are conducive to an increase of interaction effects between structures and nonlinearly deformable medium.

For all structural layouts considered in the example (see Fig. 3) there is a tendency towards an increase of K_{SSI} with increasing strain modulus of the superstructure material. At the other equal conditions (particularly at medium deformability of subsoil) for Scheme with transverse bearing walls (scheme 2 in Fig. 3) the max value of loads and, correspondingly, the max value of $K_{SSI}=4.06$ are observed for the strongest material, this being concrete, which works with the instant strain modulus. The lowest value is observed with brickwork ($K_{SSI}=2.85$), having the lowest of all considered strain moduli (Fig. 10 a). For the layouts of cellular type with longitudinal bearing walls

(schemes 3 and 4 in Fig. 3) $K_{SSI}=1.45$ for brickwork and 1.7 for reinforced concrete with instant strain modulus (Fig. 10 b, c).

This tendency is displayed more clearly when considering problems with subsoils of low deformability.

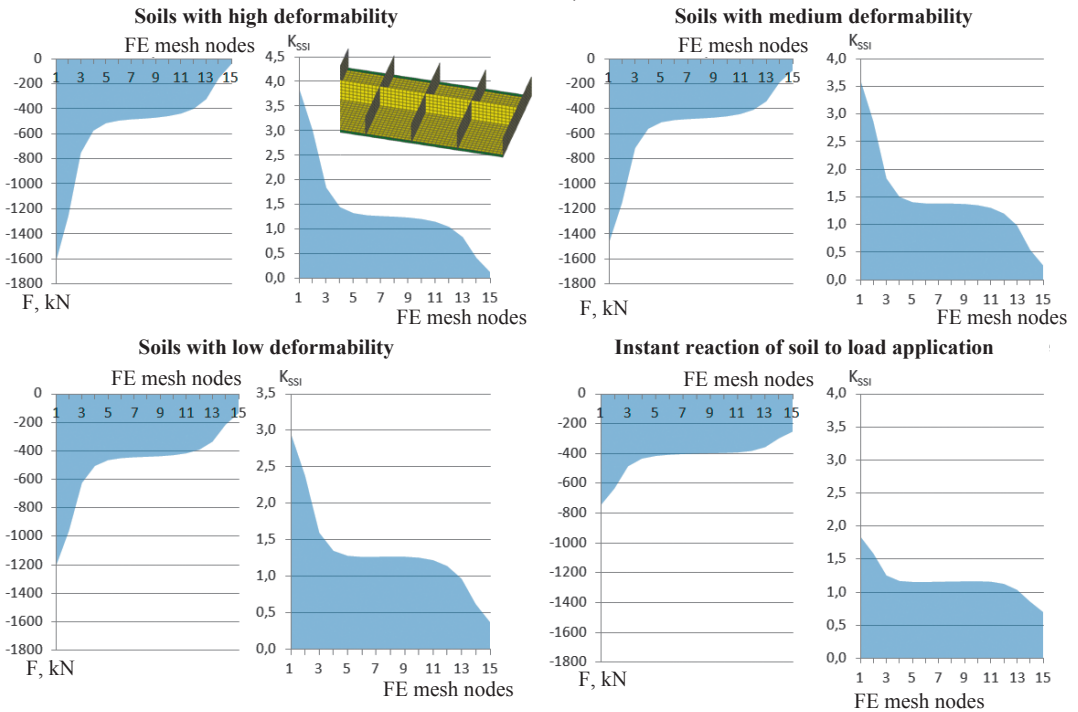
3.3. Taking into account the subsoil stiffness

An increase in deformability of subsoil, with other conditions remaining equal, correspondingly increases effects of soil-structure calculations.

For all structural layouts considered in the example (see Fig. 3) the interaction effect essentially depends on subsoil deformability. Other conditions remaining equal, (particularly, in considering behaviour of monolithic reinforced concrete with the long strain modulus of 8500 MPa) in the structural layout with transverse bearing walls (Scheme 2 on Fig. 3), and with subsoil represented by weak (soft) deposits, the index of K_{SSI} reaches 3.8, dropping to

3.5 kN/m at medium degrees of soil deformability, further decreasing to 2.7 in low-deformable soils, and at instant reaction of soil to loading K_{SSI} is reduced to 1.8 (Fig. 11). Thus, it appears that the effect of rheological behavior

a)



c)

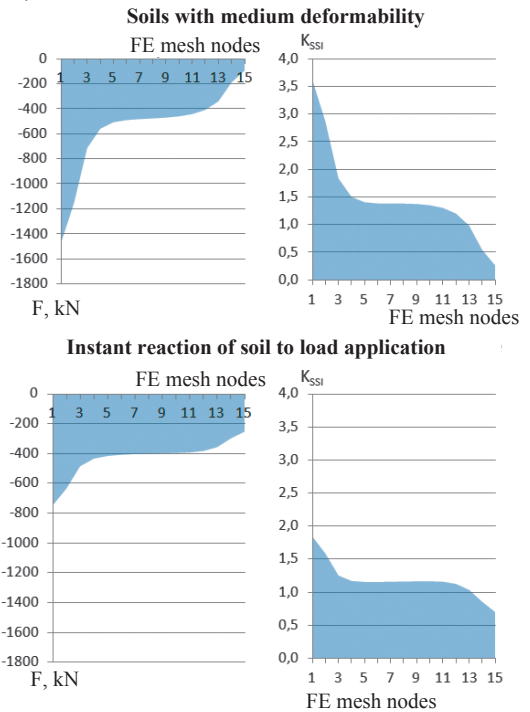
Fig. 11. Epures of vertical loads distribution (kN) and K_{SSI} in gable walls at various deformability of soil (other conditions remaining equal: in particular, numerical analysis of building from monolithic reinforced concrete with long-term strain modulus of 8500 MPa).

Considering the same scheme with transverse walls constructed from brick, similar tendencies of load concentration decrease along the edges of transverse walls with reduction of a halfspace deformability are observed. The similar picture can be traced also with the instant strain modulus of reinforced concrete being 30000 MPa for the given calculation profile.

Despite a somewhat more blurred situation for the structural layout of cellular type (Scheme 3 on Fig. 3), the interaction effect has, largely, the same tendency, as for the structural layout with transverse walls. It increases in a more deformable subsoil, and drops with reduction of deformability (Fig. 12). For soil of high, medium and small degrees of deform-

ability (with the maximum mechanical characteristics at the initial period) does not lead to increase in K_{SSI} in comparison with the calculation performed for stabilized condition of subsoil.

b)



d)

ability with buildings from monolithic reinforced concrete featuring a long strain modulus of 8500 MPa the index of K_{SSI} changes within 1.75-1.65, whereas at instant reaction of the medium to loading we observe a decrease in K_{SSI} to 1.4. For a brick building with the cellular structural layout, the tendency towards decreasing stress concentration and K_{SSI} with reduction of subsoil strength is more pronounced: at the high degree of deformability K_{SSI} is equal to 1.62, further decreasing to 1.47 at the medium degree, to 1.25 at the low degree, and to 1.05 at instant reaction to loading. With an increase of strain modulus in a structure, for example, up to the strain modulus of reinforced concrete in instant loading applications (30000 MPa), the tendency towards change of interaction effects

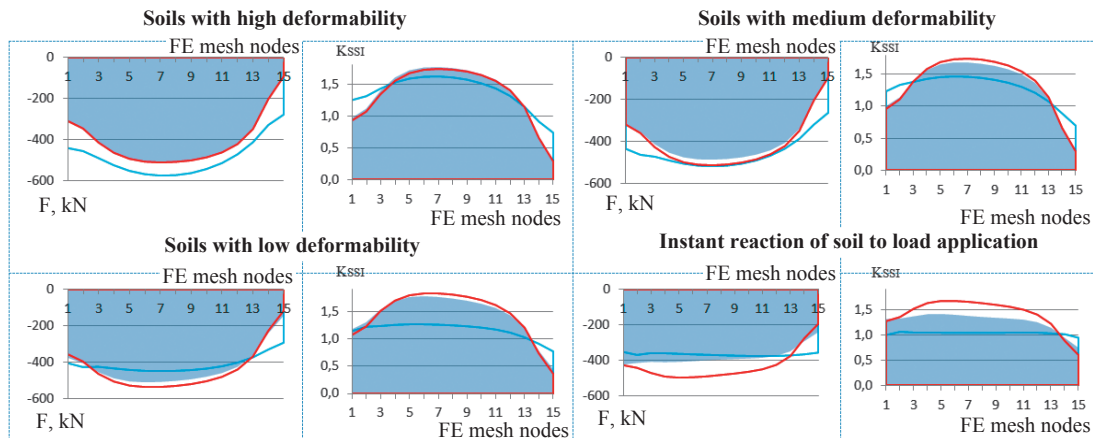


Fig. 12. Epures of vertical loads (kN) and K_{SSI} epure in a transverse wall on the building's gable end for scheme of cellular type at various subsoil deformabilities and various strain moduli of superstructures. Showing the epure for half of the wall, nodes of the FE mesh (spaced at 0.5 m), the symmetry axis being at point 15.

with increasing strength of the subsoil medium is no longer perceptible: the K_{SSI} then varies within 1.7-1.8.

A similar picture is observed also for the structural layout with longitudinal bearing walls (Scheme 4 on Fig. 3).

Thus, for any structural layout with bearing walls we should expect manifestation of the maximum interaction effect between the structure and the non-linearly deformable halfspace with strength reduction of the medium.

3.4. Stressed-strained condition of a raft foundation

Loads in the raft can be established based on analysing the system «superstructure – raft – subsoil», as well as using simplified subsoil calculation methods based on coefficients of subgrade reaction. Most attention while calculating the raft should be given to bending moments. Soil-structure interaction effects as relevant to the superstructure should be analysed based on spatial finite-element subsoil models. Concentrations of soil pressure below the edge of the building lead to increased moments in the edge areas.

Fig. 13 contains fields of bending moments for buildings with transverse bearing walls, of cellular profile, as well as for buildings with longitudinal bearing walls (see Fig. 3 for Schemes), obtained through calculations on non-linearly deformable halfspace and the

Winckler's base. The variants for the superstructure construction materials are the same as in the above examples (see 3.2 above). For the buildings with transverse bearing walls (scheme 2 in Fig. 3) the highest moments are concentrated in the middle of the span in the edge area of the building's raft, whereas for the cellular building (Scheme 3 in Fig 3) the highest moments are concentrated in the middle of the cell.

For a scheme with transverse reinforce concrete bearing walls with the long-term strain modulus of 8500 MPa the bending moment is undervalued approx. 1.6 times (Fig. 13 a), whereas for structural layouts with longitudinal and transverse bearing walls and with longitudinal bearing walls calculating on the Winckler's base yields bending moment overvaluation of 7% (Fig. 13 b) and of 11% (Fig.13 b) respectively. Thus, the simplified calculation methodologies reveal their approximate character and imprecision.

When analyzing calculations it becomes evident that the maximum moments in the raft defined through Winckler's hypothesis for all considered structural layouts depend little on strength correlation between the superstructure and the subsoil. On the contrary, for each of the considered structural layouts on elastoplastic subsoil such dependency is present.

Design of foundation rafts requires definition of moments in the raft related to the overall bending of structures and the moments condi-

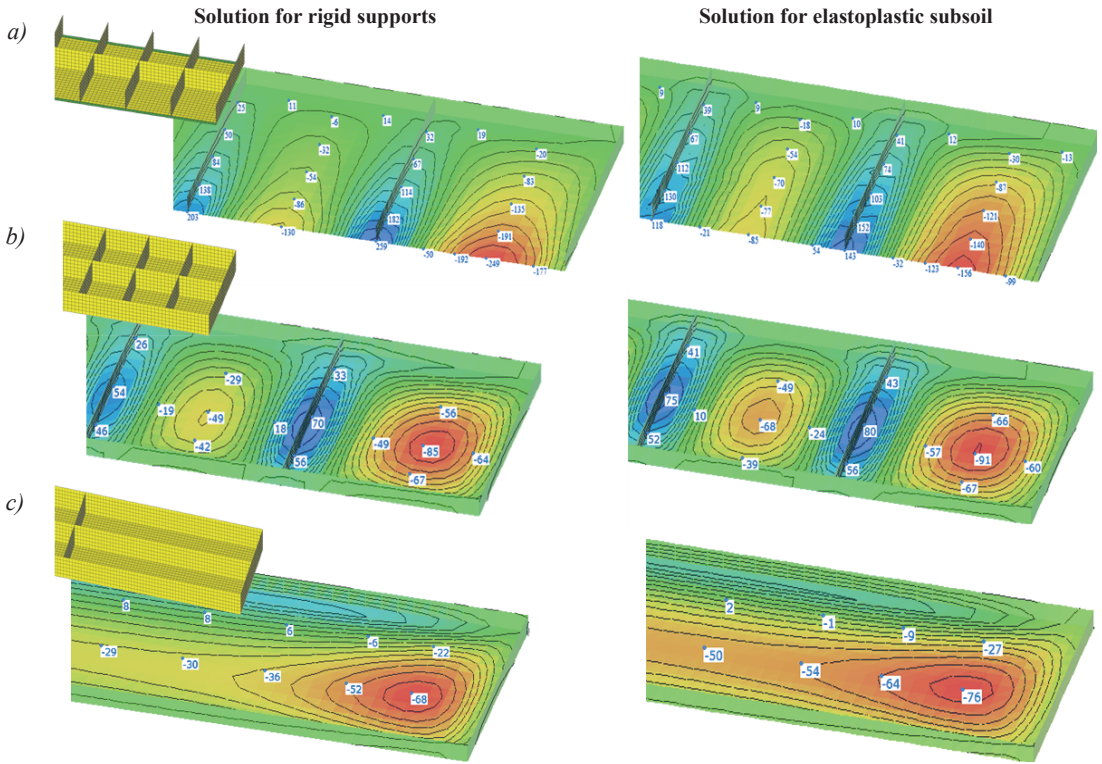


Fig. 13. Distribution of bending moments as calculated on elastic support (Winckler's base) and on elastoplastic subsoil, kNm.

tioned by action of soil pressure between the bearing elements of the superstructure. Moments in the raft, related to the overall bending of structures are reduced with a corresponding reduction of structural strength. Moments conditioned by action of soil pressure between the bearing elements can increase (compared to calculations on constant strength coefficients of subgrade reaction) due to concentrations of stresses in the contact epure near the edges of buildings on in the edges of rigid structural elements.

4. SPECIFICS OF INTERACTION BETWEEN THE BUILDING ON A PILED FOUNDATION AND ITS SUBSOIL

4.1. Using piled foundations is capable of essentially changing the contact epure of loads in walls, in comparison with the natural subsoil foundation, which is caused by the maximum load concentration in walls constructed on top of edge piles.

For an illustration of this effect, in addition to the example of the raft foundation on natural subsoil considered in section 3 above, we will look at the pile-raft foundation with two options of pile arrangement for the structural layouts of the buildings presented on Fig. 3. In the first option the spacings between the piles is equal to (3-5) d , in the second – (8-9) d . Let us consider 3 options of subsoil stratification:

(1) the base layer is represented by soil medium with small (low) degree of deformability, and the top layer has a medium degree of deformability;

(2) the base layer is represented by soil medium with small degree of deformability, but the top layer has a high degree of deformability;

(3) the base layer is represented by soil of medium degree of deformability, however the top layer has a high degree of deformability.

The thickness of the top layer is 8 m. The length of piles is taken as equal to 10 m (the model featured prismatic piles with section of 40×40 cm). Bearing capacity of piles according

to numerical modeling test results produced 3200 kN for the 1st subsoil stratification option, 1975 kN for the 2nd option and 1645 kN for the 3rd.

Epures of load distribution within the walls of the buildings constructed on a piled foundation, considerably differ from the similar epures for the foundation on natural subsoil (Fig. 14). The broken outline of these epures demonstrates that the biggest part of loading is transferred to halfspace by means of piles, the piles acting as the concentrator of loads. Thus, it is in places of interface between the piles and the raft that the sharp increase in loads is observed.

Considering the structural layout of the cellular type (Scheme 3 on Fig. 3) it is possible to observe the contact epure to change its outline (Fig. 14), becoming more and more similar to the epure for a building with transverse bearing walls (Scheme 2 on Fig. 3, Fig. 14 and). Such

alteration of the epure outline is caused by emergence of the load concentration effect in edge piles. The contact epure in this case becomes a result of a competition between two phenomena: loads concentration in an edge pile and the tendency of the superstructure to redistribute the load to adjoining walls.

With reduction of piles spacing from (3-5) d to (8-9) d loading from the superstructures for each pile increases. Thus, loads concentration sharply increases in places of piles interface, which substantially changes the contact epure of load distribution in transverse walls with piles spacing increase (Fig. 14 d-f).

The similar picture is observed also in consideration of longitudinal walls of buildings. Comparing contact epures for a longitudinal wall, it is visible that piled foundations considerably change the epure outline which at the spacing (8-9) d acquires a "sawtooth" pattern

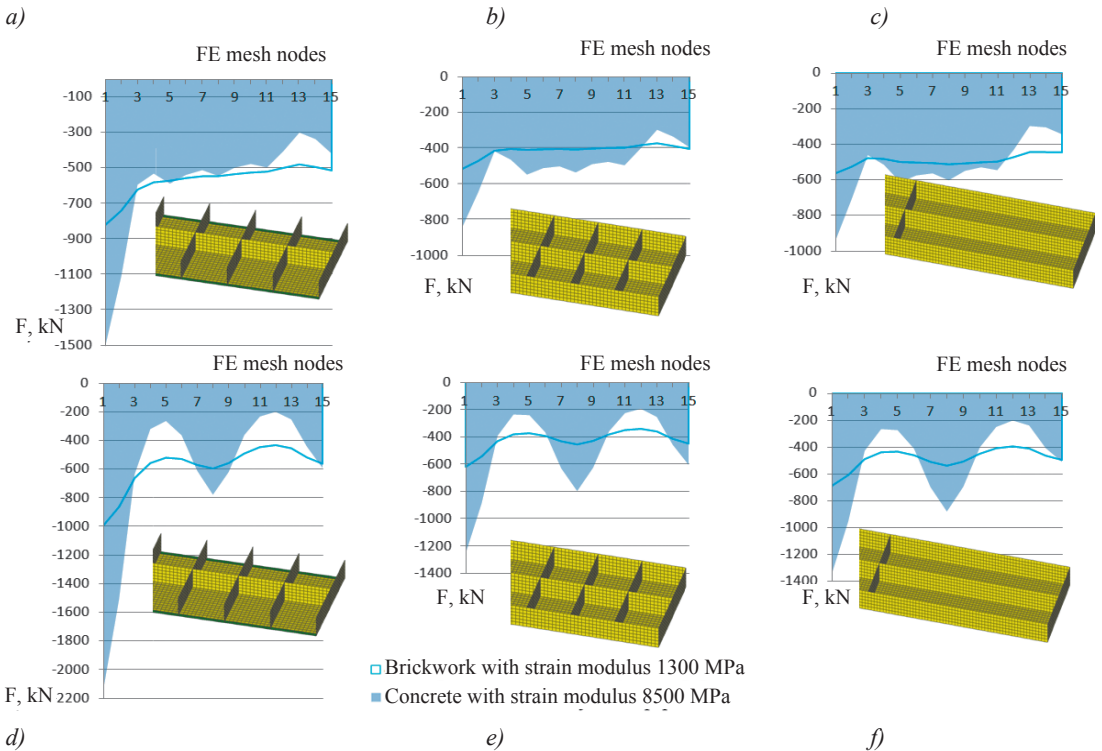


Fig. 14. Vertical loads distribution (kN) in a transverse wall on the building's gable end calculated for a piled foundation for various structural layouts. Superstructure materials – reinforced concrete with strain modulus of 8500 MPa and brick with strain modulus of 1350 MPa, subsoil according to option 1, piles spaced at (3-5) d (a – c) and (8-9) d (d – f). Showing half of the wall, nodes of the FE mesh marked horizontally (spaced at 0.5 m), the symmetry axis being at point 15.

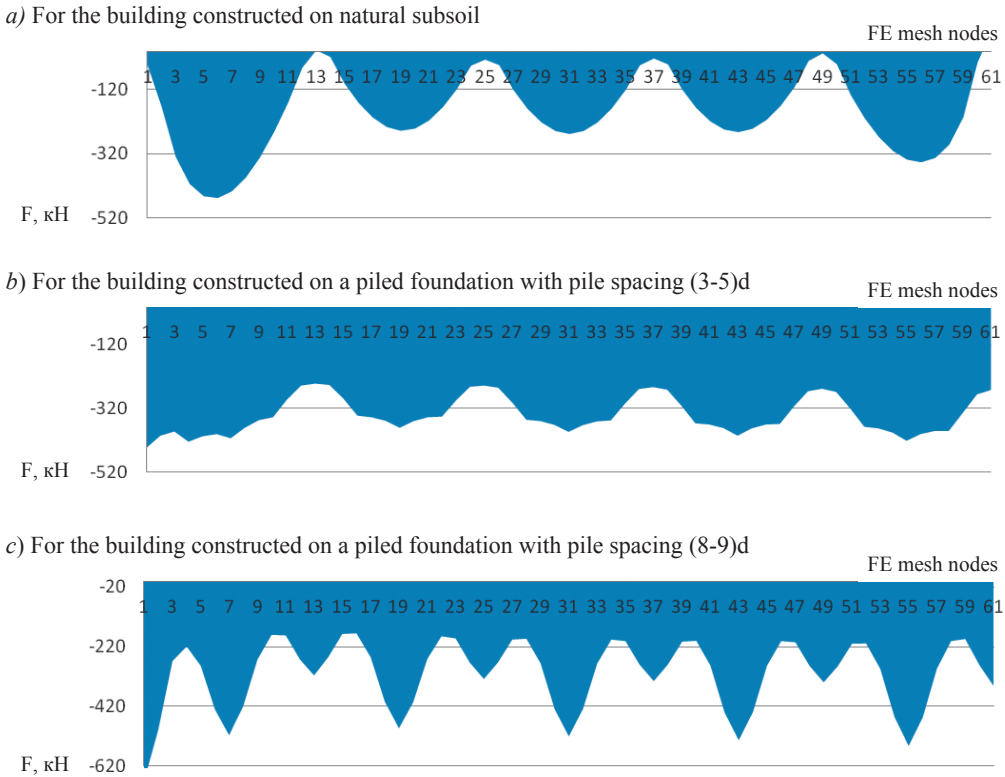


Fig. 15. Comparison of distribution of contact vertical loads (kN) in a longitudinal wall of the building calculated on piled foundations and natural subsoil for the scheme with transverse bearing walls. Superstructure material – reinforced concrete with strain modulus of 8500 MPa, subsoil according to option 1. Showing half of the wall, nodes of the FE mesh marked horizontally (spaced at 0.5 m), the symmetry axis being at point 61.

(Fig. 15). Nevertheless, except for the zones over the edge piles, the maximum loads are observed in flights (overspans) between the transverse walls. With increase of pile spacing, provided that other conditions remain unchanged, these maxima also increase.

4.2. Piled foundations exhibit the same regularity, as foundations on natural subsoil – the higher the strength of superstructure material, the higher the loads concentration in the contact epure. The effects of loads concentration in the zone over the piles decrease with replacement of walls material from reinforced concrete for brick.

In the considered example for the piled foundation with pile spacing (3-5) d and for subsoil stratification according to option 1 (see section 4.1) the decrease in strain modulus of superstructures leads to a loads concentration decrease in the edge zone of transverse walls

(Fig. 14 a–c): for buildings with transverse bearing walls the load decreases 1.8 times, for buildings of cellular type – 1.6 times, and for buildings with longitudinal bearing walls – 1.5 times (layouts of buildings are contained in Fig. 3). Apart from the decrease in load concentration value in the edge zone, there is also a flattening of "peaks" under internal piles that leads to alignment of the contact epure. At less dense arrangement of piles – (8-9) d the value of loads concentration decreases approximately 2 times for all considered structural layouts of buildings.

If deformability of halfspace increases according to option 2 or 3 (see section 4.1), the same tendencies for loads concentration decrease are seen with reduction of the strain modulus of the superstructure.

4.3. The lower the strength of the interacting “piles-subsoil” system, the stronger the effect of

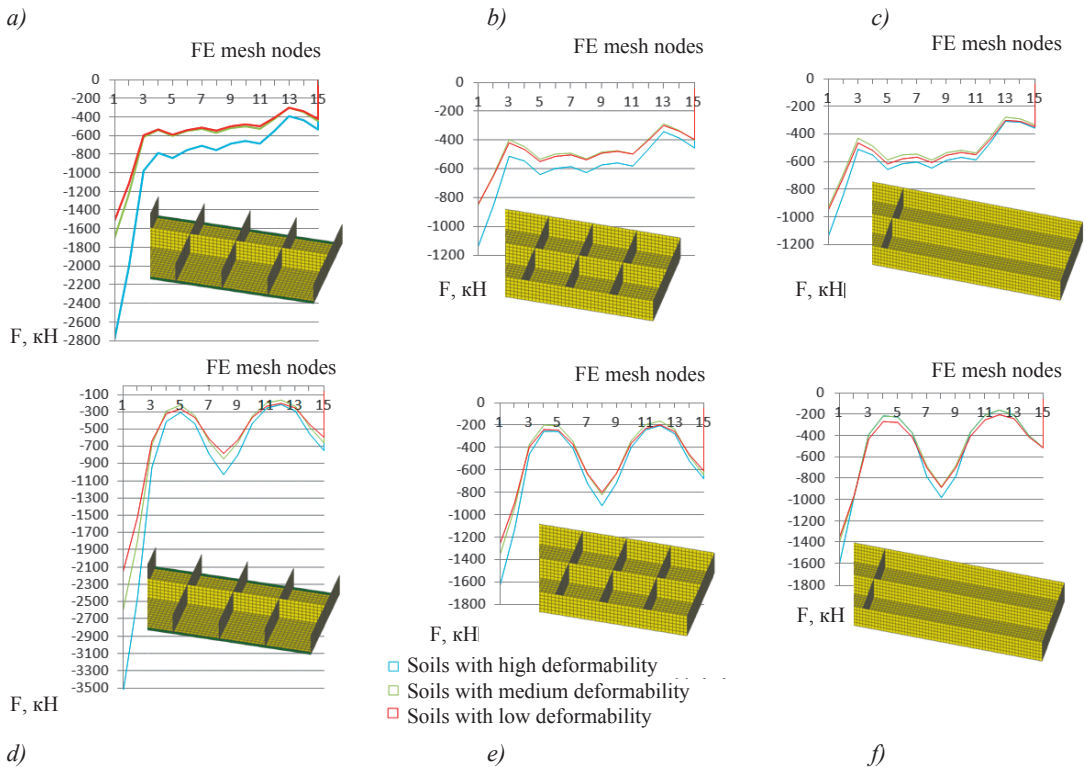


Fig. 16. Vertical loads distribution (kN) in a transverse wall on the building's gable end calculated for a piled foundation for various structural layouts. Superstructure material – reinforced concrete with strain modulus of 8500 MPa, subsoil according to options 1, 2 and 3, piles spaced at (3-5) d ($a - c$) and (8-9) d ($d - f$). Showing half of the wall, nodes of the FE mesh marked horizontally (spaced at 0.5 m), the symmetry axis being at point 15.

this system's interaction with the superstructure, causing an increase in loads in the contact epure of bearing walls.

In the considered example, a change of subsoil deformability renders the highest influence on distribution of loads in a transverse wall in the structural layout with transverse bearing walls (Scheme 2 on Fig. 3, Fig. 16). Increasing pile spacing from (3-5) d to (8-9) d causes loads on the edge of a transverse wall to increase 1.3 – 1.4 times (cf. Fig.16 $a - c$ and $d - f$).

The outline of the contact epure for a building of cellular type (Scheme 3 on Fig. 3) is similar to the epure for a building with transverse bearing walls – considerable loads concentration arises in the edge zones. This effect is connected with redistribution of loads in the piled foundation. In this respect, the less deformable the subsoil medium, the greater the possibility to effect this redistribution and to level out the load concentration phenomenon.

As a result, the greatest loads concentration over an edge pile is observed for the case of the most deformable subsoil, when the pile cuts through a subsoil with a high degree of deformability and has its toe in deposits characterized by the medium degree of deformability (subsoil stratification option 3 – see section 4.1).

Contact epures for buildings with longitudinal bearing walls (Scheme 4 on Fig. 3) are close to similar epures for buildings with cellular structure (Scheme 2 on Fig. 3) both in outline, and in the actual numerical values.

Epures of loads distribution in a transverse wall with subsoil stratification options 1 and to option 2 (see section 4.1) slightly differ from each other for the whole considered variety of problems. This feature can be explained with the fact that distribution of loads in structures of a building constructed on a piled foundation is influenced by deformability of the base layer to a greater extent greater than by deformability of

intermediate layers. With an increase in deformability of the base layer, concentrations of loads in the superstructure will also increase. The pile having reached its bearing capacity bordering on ultimate, growth of loads concentration in the superstructure with subsequent increase of subsoil deformability stops.

5. REGULARITIES IN MANIFESTATION OF INTERACTION EFFECTS BETWEEN STRUCTURES AND NON-LINEARLY DEFORMABLE MEDIA DEPENDING ON CORRELATION OF THEIR STIFFNESS VALUES

Value of vertical loads in structures in the area where they interact with the subsoil depends on the ratio between the strain modulus of the structure and the secant strain modulus of soil. Vertical loads in structures in the zone of stresses concentration, related to the subsoil interaction effect, monotonously increase with strength ratio change and are asymptotically limited. In this respect, there are no such ratios of strengths, at which the interaction effect is of

no importance as far as the loads concentration in the contact zone is concerned.

It is possible to illustrate this effect with the help of the considered example. For each structural layout (see Fig. 3) of the building on natural subsoil we build dependency graphs of K_{SSI} on the ratio of strain moduli E_{struct}/E_{secant} (the strain modulus of superstructure material to the secant strain modulus of nonlinearly deformable halfspace) (Fig. 17). For all considered structural layouts of buildings the K_{SSI} graph, depending on the “superstructure strength – subsoil strength” ratio, has a characteristic outline with a sharp increase at the initial site and a further flattening out.

It is characteristic that on all graphs there is no initial horizontal fragment. Therefore, there are no such E_{struct}/E_{secant} ratios, at which the interaction effect is of no importance as far as the loads concentration in the contact zone is concerned. In all cases, except when calculating buildings founded on non-deformable rock, there is always a load concentration in superstructure in the contact zone.

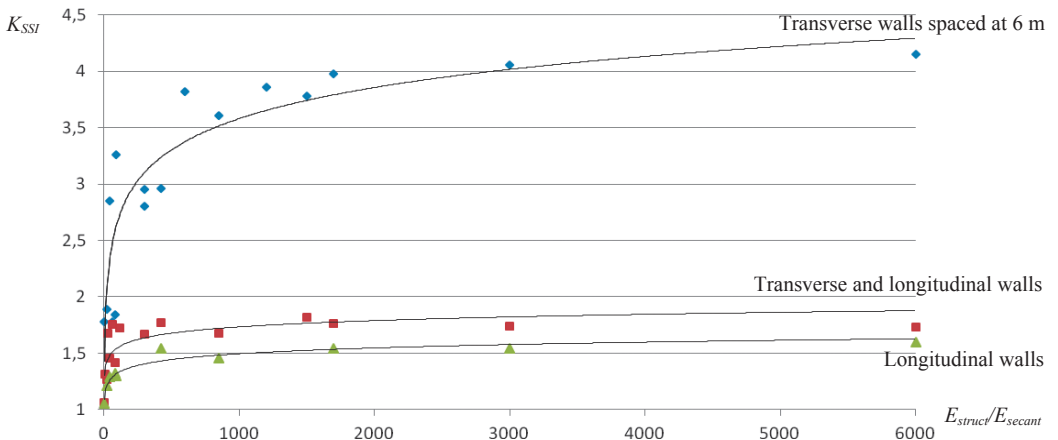


Fig. 17. The graph showing dependency of the index of interaction between structures and non-linearly deformable subsoil on the ratio of their strengths for various structural layouts of buildings.

Starting from a certain value of material strength of the superstructure, halfspace stiffness ceases to have any significant impact on K_{SSI} practically through the entire range of real changes of physicommechanical characteristics of halfspace. Differently put, increasing the strength (stiffness) of superstructure materials, it is possible to cross the border of the area

close to the maximum K_{SSI} value in a wide range of halfspace strengths. Thus, the statement that interaction of a building and halfspace depends on their ratio of strengths is true only in a certain range of their change.

Use of piled foundations is capable to change essentially the contact epure of loads in the walls, in contrast with the foundation on a

natural subsoil, which can be explained by the maximum loads concentration in the wall over a pile at the edge. For piled foundations the same regularity is true, as for foundations on a natural subsoil, *viz.* the higher the strength of the superstructure material, the higher the loads

concentration in the contact epure (Fig. 18). The lower the strength of the interacting system “piles-subsoil”, the higher the effect of this system’s interaction with the superstructure, leading to the loads increase in the contact epure of the bearing walls.

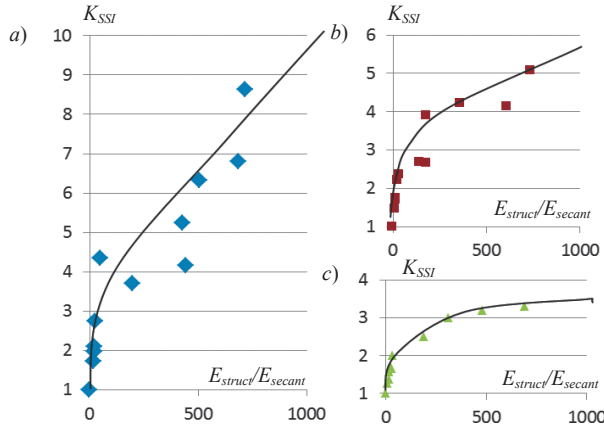


Fig. 18. Graphs showing dependency of the index of interaction between structures of the building on a piled foundation and non-linearly deformable subsoil on the ratio of their strengths for various structural layouts of buildings: *a* – layout with transverse bearing walls, *b* – layout with longitudinal and transverse bearing walls, *c* – layout with longitudinal bearing walls.

Recommendations on taking into account interaction effects between a building and non-linearly deformable halfspace in practical design

5.1. Soil-structure interaction should be taken into account at any ratio of strengths between the structure and the subsoil. This is so, because the dependency of K_{SSI} on the ratio of strengths between the structure and the halfspace does not have any initial fragment at which the interaction effect is absent. In all cases, except when calculating buildings on non-deformable rock, there is a load concentration in the superstructure contact zone, caused by the interaction between the building and the halfspace.

5.2. For practical purposes, soil-structure calculations of buildings with bearing walls and subsoils should be carried out with the strain modulus of reinforced concrete, which allows for long-term load applications.

Dependence of K_{SSI} on the ratio of strengths between the structures and the halfspace has well pronounced nonlinear character, and,

beginning from a certain strength ratio, the flattening out of the graph representing this dependence is observed. For the structural layouts of buildings considered as examples the following observation is true: the effect of loads concentration in the interaction zone between the structures and the subsoils ceases to increase, if strength of bearing walls is defined by the long-term strain modulus of reinforced concrete.

5.3. For practical purposes, it is sufficient to carry out soil-structure calculations of buildings and subsoils with the deformation characteristics of the soil corresponding to the stabilized condition. There is no necessity to consider rheological behavior of soil for soil-structure calculations.

This conclusion follows from the revealed regularity of the interaction effect increasing alongside the associated growth of subsoil deformability.

5.4. For practical purposes, it is sufficient to perform soil-structure calculations for uniform construction of buildings with bearing walls for buildings erected full-height, consideration of

floor-by-floor construction in this case is not required.

5.5. For cases of non-uniform construction of a building, construction in several phases, adjoining construction or in proximity to existing buildings, it is necessary to consider rheological properties of structural materials and subsoils. For non-uniform construction of a building it is necessary to consider non-uniform loading of the subsoil and the corresponding concentrations of loads in the soil-structure interaction zone.

5.6. In order to account for the interaction effects between structures of a building with bearing walls and natural subsoil the following recommendations can be given.

If there are untied walls in level of the first two floors and the foundations, when choosing the material and thickness of the wall it is necessary to consider a possibility of 4-fold concentration of vertical loads in edge zones. It is necessary to increase wall thickness and/or to install additional quantities of rebar in reinforced concrete walls, or to reinforce the masonry/brickwork.

Designing buildings with longitudinal and transverse bearing walls within the level of the first two floors and the foundations, and choosing the material and thickness of the walls it is necessary to consider a possibility of 2-fold concentration of vertical loads in the middle of a span/overhang/flight.

5.7. Designing buildings with bearing walls on piled foundations, to account for the soil-structure interaction effects it is advisable to follow the following recommendations.

In the level of the first two floors and rafts of piled foundations, when choosing the material and thickness of the walls it is necessary to consider a possibility of 2-fold increase in concentration of vertical loads in edge zones in comparison with a building on natural subsoil; (for a building with untied walls it can result in 8-fold concentration of vertical loads, and for a buildings with a cellular arrangement of walls and with longitudinal walls – in 4-fold or 3-fold concentration, respectively). It is necessary to increase wall thickness and/or to install additional quantities of rebar in reinforced concrete walls, or to reinforce the masonry/brickwork.

Following the recommendations provided in sections 5.6 and 5.7 for buildings with orthogo-

nal vertical bearing walls (i.e. for the traditional schemes of residential buildings) ensures safety in terms of possible generation of loads within the walls of the building, which might exceed the corresponding permissible values practically for any characteristics of non-linearly deformable halfspace. Introduction of such safety factors allows to consider the interaction effect for any strength ratios between structures and halfspace. To adopt a more economically viable and effective structural solution it is necessary to perform soil-structure calculations for the designed building and its subsoil.

6. DISTRIBUTION OF PILE LOADS IN THE PILED FOUNDATION

6.1. Distribution of loads between piles within a piled foundation is characterized by unevenness, with loads concentration in the edge piles and unloading in the central part.

6.2. Distribution of loads between piles within a piled foundation depends on pile spacing and bearing capacity of a separate pile. This effect is more pronounced in piled foundations with the low raft, transferring the of load to the subsoil.

6.3. There can be such a small pile spacing at which piles and soil around the piles work as a uniform solid, resembling to a stiff plate, forming a “theoretical” foundation with “footing” at the toe-level of the piles. Such foundation has the highest bearing capacity among piled foundations with raft and various pile spacing. At that, the piles assume loads considerably smaller than the ultimate bearing capacity of a single pile.

As an example to elucidate this effect, we will consider numerical analysis of a piled foundation with a low raft (a problem with the contact between the raft and the subsoil) and a piled foundation with an elevated raft (a problem without the contact between the raft and the subsoil). In all schemes for each pile let us assume contact zones (by means of the interface elements).

The raft and the piles we will model with elastic elements of the first order without consideration of their nonlinear behaviour (dimensions of the raft in plan view 10×20 m, cross-section section of the piles 400×400 mm, length of the piles of 20 m). We will assume

physicomechanical characteristics of the final elements, representing the piles, as corresponding to class B25 concrete, and for the elements modeling the raft, we will assume infinite stiffness for the uniform transfer of load onto the piles.

For numerical modeling we will assume the top layer as having thickness of 19 m, featuring the physicomechanical characteristics as contained in Table 1, for the subsoil stratification options given in section 4.1 above.

Calculation graphs «specific* loading – settlement» of piled foundations with a low raft at variously spaced piles are placed within the interval limited to "extreme" problems, i.e. the curves for a plate on the surface and for an embedded plate (Fig. 19).

* Specific load here is equal to the ratio of the overall plate (raft) load and its square area.

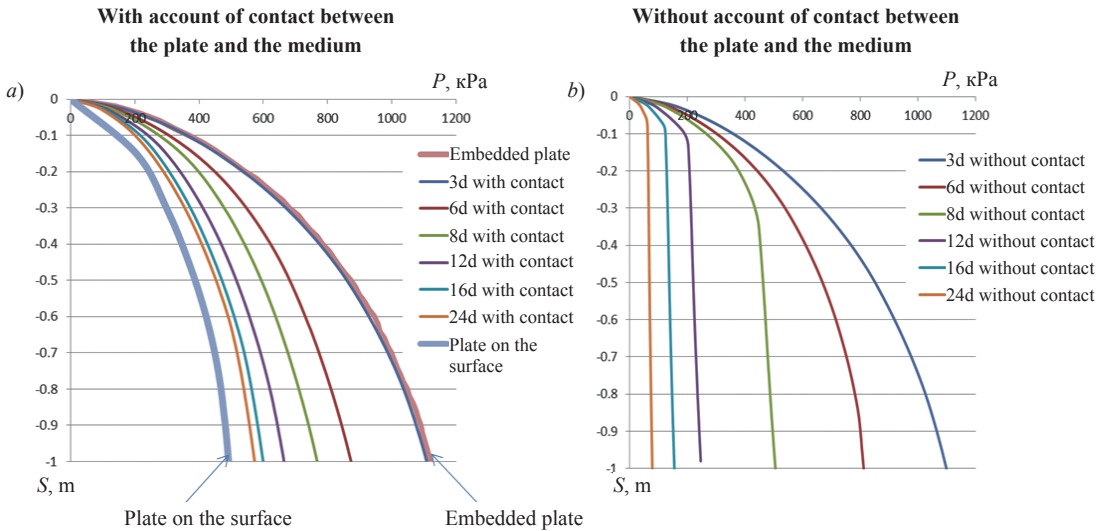


Fig. 19. Computed graphs «specific load – settlement» for the piled foundation with a low raft (a) and for the piled foundation with the elevated raft (b)

At pile spacing 3d piles and soil in the inter-pile space work as a uniform «theoretical foundation» (Fig. 20). Graphs «specific loading – settlement» and fields of movements distribution in the subsoil for piled foundations with the low and the high rafts coincide both with one another and with the corresponding graph and fields of movements distribution for a plate with the footing depth corresponding to the toe-level of the piles. In all cases under the foundation footing (or at the toe-level of the piles) we can observe formation of «the condensed nucleus», along with formation of characteristic slip surfaces.

6.4. There exists a pile spacing at which bearing capacity of a single pile ceases to counterbalance the pressure rendered on its load bearing area along the footing of the theoretical

foundation. Correspondingly, there occurs a pushing of the pile through the theoretical foundation. With increase in pile spacing, bearing capacity of a piled foundation with a low raft, as a whole, decreases, whereas the loading assumed by each pile, increases. We can observe alignment of the loads transferred by the piles to the subsoil.

The loading assumed by each pile comes nearer to the bearing capacity of a single pile.

In the considered example, pile spacing being 6d, we begin to observe "slipping" (displacement) of piles in the soil. With an increase in pile spacing it is possible to track naturally reasonable migration of «the condensed nucleus» in the direction from the pile toes towards the raft (Fig. 21).

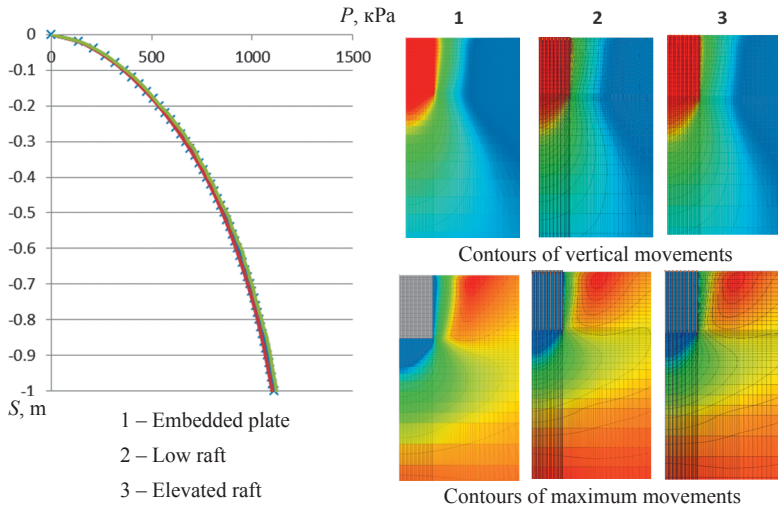


Fig. 20. Computed graphs «specific load – settlement» and the fields of movements – for the piled foundation with pile spacing $3d$ on low raft (with contact), an elevated raft (without contact) and for the embedded plate.

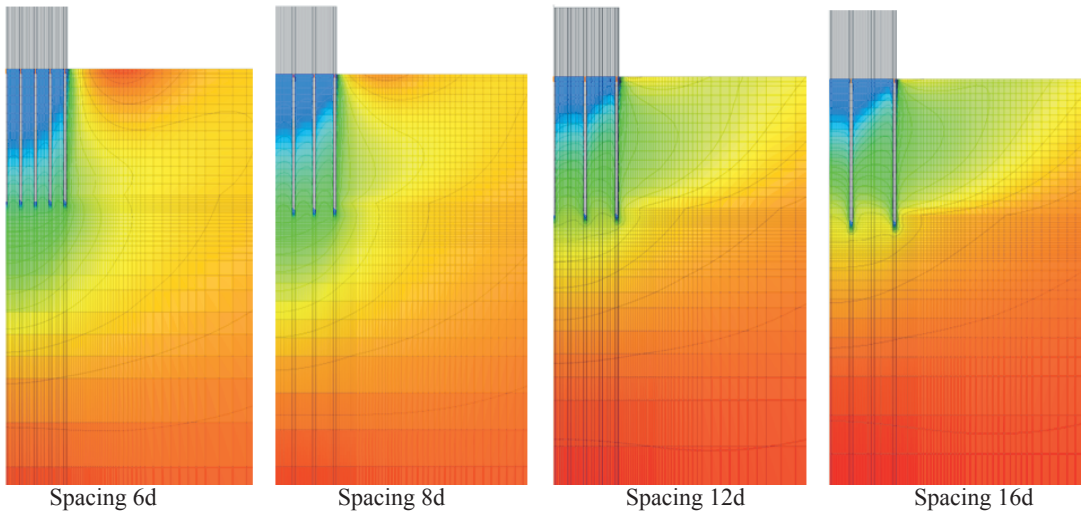


Fig. 21. Contours of vertical movements for piled foundations with a low raft at various pile spacings.

Let us compare behavior of a plate on a surface and a foundation with large pile spacing of $24d$. In Fig. 22 it is visible that "load – settlement" graphs for a piled foundation with a low raft with spacing $24d$ and for a slab are close, the difference between maximum assumed loads being about 14%. The difference is caused by a small contribution of piles towards increasing bearing capacity of the foundation. The graph shows that bearing capacity of a piled foundation with an elevated raft is much less the

maximum load assumed by the slab and the piled foundation with a low raft.

The type of movement fields arising from a piled foundation with a low raft, is almost similar to movements from a plate on a surface (see Fig. 22). Formation of «the condensed nucleus» occurs directly under the raft, similar slip surfaces also appear, leading to formation of considerable uplifts of soil. In a piled foundation with an elevated raft the maximum movements are local and concentrated under the toe of each pile.

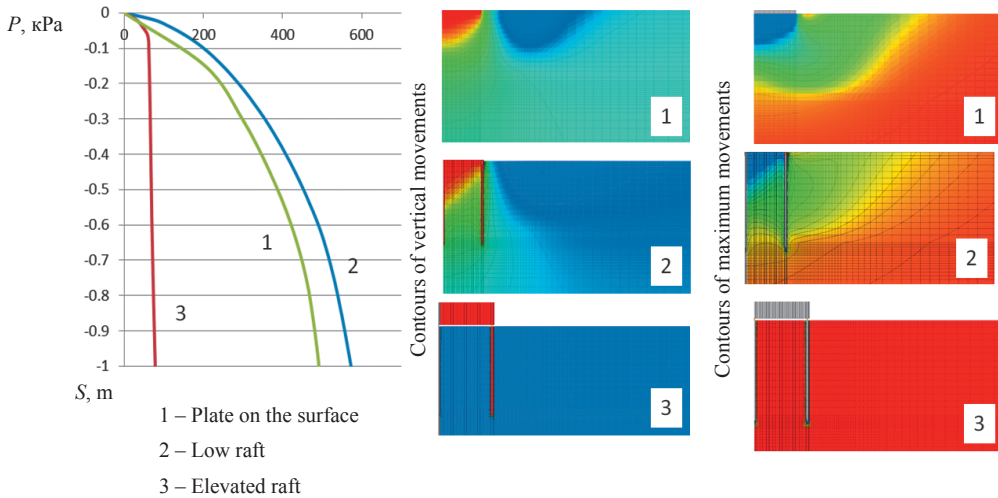


Fig. 22. The computed graphs «specific load – settlement» and fields of movements for a piled foundation with pile spacing $24d$ with low (with contact), an elevated raft (without contact) and for the embedded plate.

6.5. Bearing capacity of a piled foundation with a low raft at any pile spacing within a foundation is less the bearing capacity of a raft and piles.

In the considered example, as obvious from the results of the numerical analysis, manifestation of the effect of engaging the slab of a piled foundation with a low raft is visible in the range of spacings between its piles from $6d$ to $16d$, where d – cross-section square area of a pile (Fig. 23). At distance between the piles, equal or less than $6d$, the bearing capacity of the piled foundation with a low raft is not different from the bearing capacity of the corresponding piled foundation with an elevated raft, and at the distance equal to or exceeding $24d$ – from the bearing capacity of a slab.

Let us compare the ultimate bearing capacity of a piled foundation with a low raft F_{pr} and the sum f_p+f_r , where f_p – total bearing capacity of piles, f_r – bearing capacity of a slab on a natural subsoil. From Fig. 24 it follows that superposition f_p+f_r yields unreasonably overvalued expectation of bearing capacity of a piled foundation with a low raft and it cannot be applied even to an approximate assessment of efficiency of such foundation.

For loading distribution between elements of a piled foundation – the raft and the piles, as shown by calculations from the considered example, at pile spacing less than $6d$ decrease of

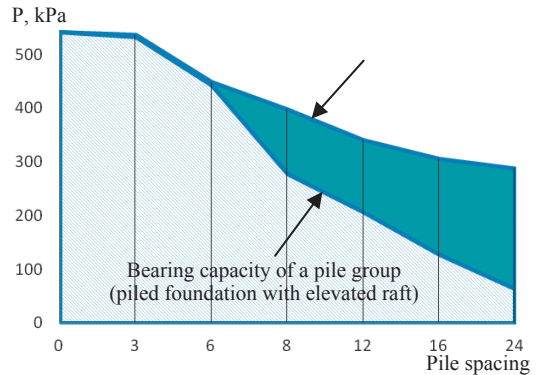


Fig. 23. Ultimate bearing capacity of a foundation depending on pile spacing.

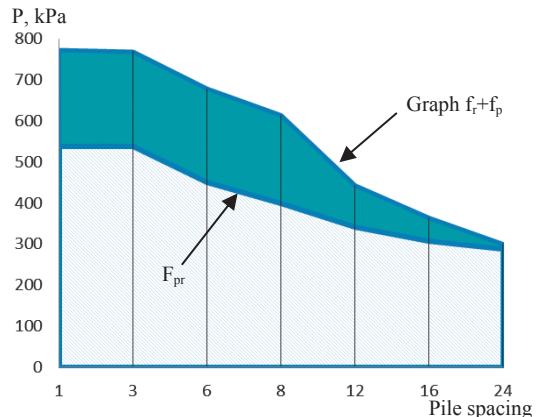


Fig. 24. Collation of graphs F_{pr} and f_r+f_p .

loading transferred to the piles and increase of loading assumed by the raft are typical. At pile spacing more than $6d$ there is a constant increase of the loading assumed by the raft up to a complete transfer of loading by the raft to the subsoil (at pile spacing more than $24d$) (Fig. 25).

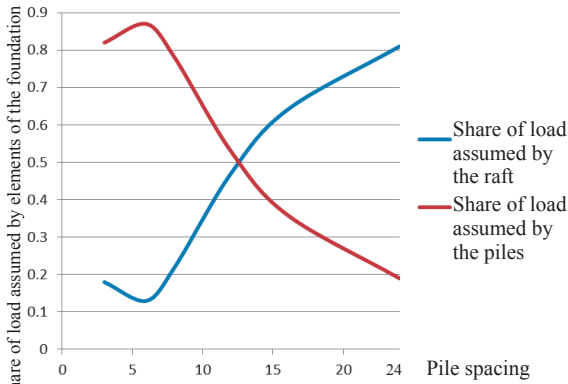


Fig. 25. Loading distribution between the raft and the piles in a piled foundation with a low raft at various pile spacings.

Decrease of the share of load transferred onto the piles in the range of values of pile spacing $3d$ and $6d$ can be explained by the fact that the piles and the subsoil within the theoretical foundation work as a deeply embedded plate. A feature demonstrative of such work is the distribution of loading between piles and the raft footing, distinct from a tendency observed at the spacing more than $6d$. Distribution of loads between the elements of the «theoretical foundation» (the raft, the piles and the subsoil contained between them) occurs in proportion to their stiffness values.

6.6. Distribution of loads between piles within a piled foundation displays certain unevenness: at uniform arrangement of piles through «the loaded areas» the edge piles appear overloaded, and the ones in the middle – underloaded. The overload of piles in the edge zones can reach 2-3 times. Therefore, during design of piled foundations it is necessary to check whether or not the load for an edge pile exceeds the ultimate strength of the chosen material. The piles along the edges should be designed so as to be able to assume the load (i.e. material load), being in excess of the calculated design load and the bearing capacity of a pile in the soil. And arrangement of piles should be

designed based on calculation of loadings for «the loaded areas».

Having analyzed distribution of loads between the piles, observed in the considered example, it should be noted that distribution of loads to piles for the piled foundation with an elevated raft and the piled foundation with a low raft at a spacing $3d$ appear similar (Fig. 26). In the case corresponding to the ultimate condition of the piled foundation with a low raft, the pile spacing being $3d$, the outer piles assume load of 3000 kN, the ones nearby – 1400 kN, and the others from 1100 kN to 900 kN (bearing capacity of a single pile is about 3200 kN). Let us point out here that the concept the maximum load for this system is relative owing to the big radius of the "load-settlement" curves.

For a piled foundation with an elevated raft with pile spacing $6d$ when considerable settlements develop the loads assumed by the piles are leveled out and begin to tend towards the ultimate bearing capacity of a single pile, whereas at spacing $12d$ and more the "load-settlement" graphs for all piles are almost identical. The load assumed by piles makes about 4000 kN which exceeds ultimate bearing capacity of a single pile. At further increase of pile spacing in the foundation with an elevated raft the loads between piles are distributed evenly, thus each pile of a pile group separately assumes a bigger load than a single pile is capable to assume.

In a piled foundation with a low raft at spacing $12d$ the load is about 4000 kN, as well as in the problem with an elevated raft, internal piles assume the load of about 3200 - 3400 kN. With a further increase in pile spacing in a piled foundation with a low raft, the edge piles assume the most part of the load, and likewise it exceeds the maximum load for a single pile. However, with increasing pile spacing the load assumed by internal piles is leveled out and approaches the bearing capacity of a single pile.

Based on the foregoing, it follows that for the considered example pile spacing in excess of $6d$ is more effective from the point of view of utilizing the reserves of bearing capacity of a single pile. In a piled foundation with a low raft with pile spacing $3d$, piles are utilized in the least effective way as far as their bearing capacity is concerned (however, such foundation as a whole possesses the highest bearing capacity of all).

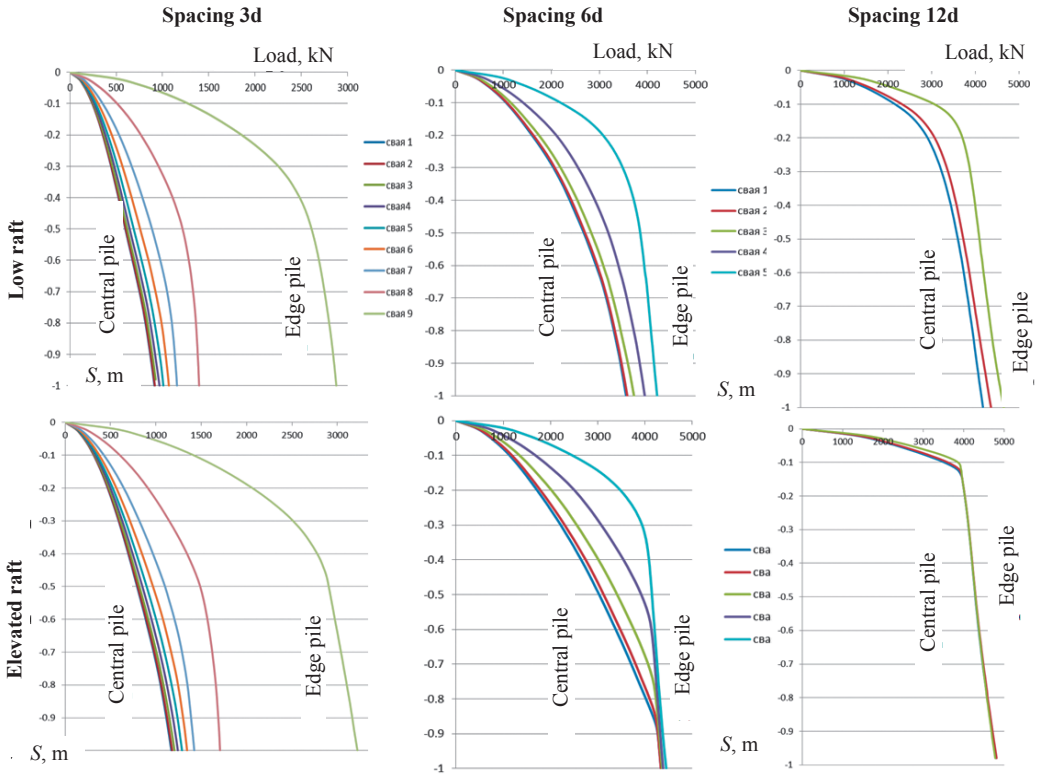


Fig. 26. Distribution of loads between piles within a piled foundation with a low and a high raft at various pile spacings.

Fig. 27 contains an example of soil-structure calculation for a multistorey building on piled foundations and its subsoil.

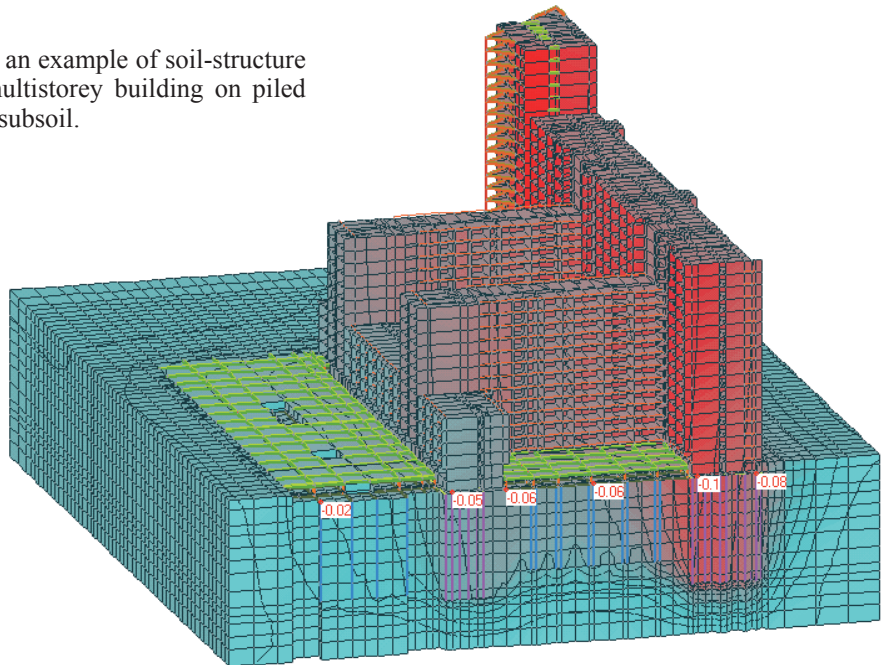


Fig. 27. An example of soil-structure calculation of a multistorey building on piled foundations and its subsoil. Showing a cross-section of settlement contours of the buildings (m).



Fig. 28. Loads on piles (tonne/force) in the area of an adjoining 20-storeyed building.

The most loaded are the edge and, especially, the corner piles (Fig. 28). Loads in the edge piles often exceed bearing capacity of an individual pile (about 100 tonne/force). It is considered that taking into account the nonlinear behavior of the soil should lead to alignment of loads in the piles. As shown by nonlinear calculations, some redistribution of loads in piles does not occur.

When comparing pile load values as obtained through soil-structure numerical analysis with bearing capacity of a separate pile it is necessary to remember that in the absence of the obviously expressed "failure" of a pile, its bearing capacity is defined by a theoretical limit corresponding to some degree of its movement. A building's settlement, as a rule, exceeds movements during a pile test, which means that the actual loads in piles can be above the corresponding loads on the "load-settlement" curve obtained during a static tests of a single pile.

Tests of piles under constructed buildings show that bearing capacity of piles within a loaded pile field considerably increases. This effect can be explained by the fact that during a test of a single pile the pile interaction effect is

absent. Presence of other loaded piles at small distance increases the pile's toe resistance just as the actual load increases settlement resistance of subsoil under the foundation. Additionally, in the loaded soil under a building there is an increase of vertical and horizontal stresses which also enhance skin-friction resistance of a pile.

A long-standing design experience in the area of piled foundations with pile arrangements based on "collecting loads through the loaded areas" shows that insufficient bearing capacity of piles in the soil, being observed in the edge zones, is substantially compensated by the undervalued real bearing capacity of piles in the soil within a fully loaded piled foundation. However, for the purposes of design, it is not recommended to employ the effect of bearing capacity increase of piles in the loaded pile field. For its reasonable application in design practice special theoretical and experimental studies are still necessary. It is recommended to arrange piles based on calculating loads through "the loaded areas".

In practical design of buildings it is necessary to consider also the negative side of the noted effect, *viz.* that the actual structures of the raft and the piles along the edges of the building

should be capable of assuming the load exceeding the design loads and bearing capacity of piles in soil. Otherwise it may be possible that the piles or the raft structures will fail which will entail complete elimination of their bearing input.

7. EXAMPLES OF PRACTICAL MANIFESTATION OF SOIL-STRUCTURE INTERACTION EFFECTS

7.1. An extended building with bearing walls

Let us consider an extended building of a series u-5733 with bearing longitudinal and transverse walls on a natural subsoil, with the so-called «incomplete framework» in level of the ground floor, permitting to house trading facilities and to do full glazing of windows (Fig. 29).

In St. Petersburg in the second half of the 1960s several dozens of buildings of this type were constructed in various districts. It is interesting to note that in the early eighties, i.e. some 20 years after their construction, some of these buildings were strengthened by reinforced concrete shells in the edge zones of gable walls on the ground floor level (Fig. 30).

As an example we will consider a real residential building of this series constructed in St. Petersburg. Site conditions are given in Table 2. Walls of the building are constructed from hollow brick with the strain modulus of brickwork being 1350 MPa that corresponds to brick grade M100 and mortar grade M100. The strain modulus of reinforced concrete elements of the first floor and of the intermediate floors, taking into account long-term load application is equal to 8500 MPa.

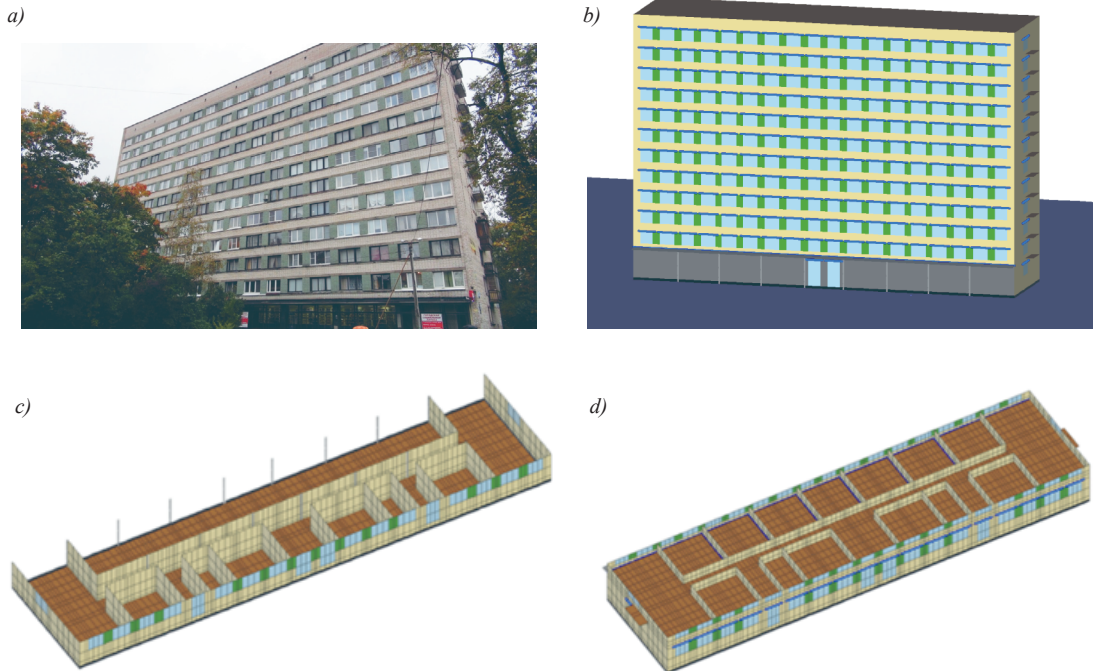


Fig. 29. Extended brick building of the standard series u-5733 ; a) – photograph of the building; b) – the settlement model; c) – the ground floor plan; d) – a standard floor plan.



Fig. 30. Reinforced concrete strengthening patches in edge zones of gable walls on the building of the standard series *u* -5733.

Table 2. Site conditions.

Geol. index	Definition of deposits	Plast. value., I_p	Natural moist. cont., W	Soil density, kN/m^3	Porosity factor, e	Liquid index, I_L	Strength parameters		Strain mod. E_s , kg/cm^2
							ϕ , degree	c , kg/cm^2	
tg IV	Made ground	Resistance $R_c = 1.0 kg/cm^2$							
lg III b	Sands, large grain, dense, moist and saturated			21.1	0.5		41	0.02	450
lg III b	Sands, silty, dense, moist			18.8	0.55		32	0.05	230
lg III b	Clay sand, light, silty, laminated, firm plast.	0.1	0.28	19.3	0.809	0.73	15	0.1	85
lg III b	Sands, medium grain, dense moist and saturated			21.1	0.5		39	0.03	450
g III lz	Sand clay, silty, with gravel and pebbles, firm pl.	0.04	0.14	21.9	0.4	0.21	28	0.2	130

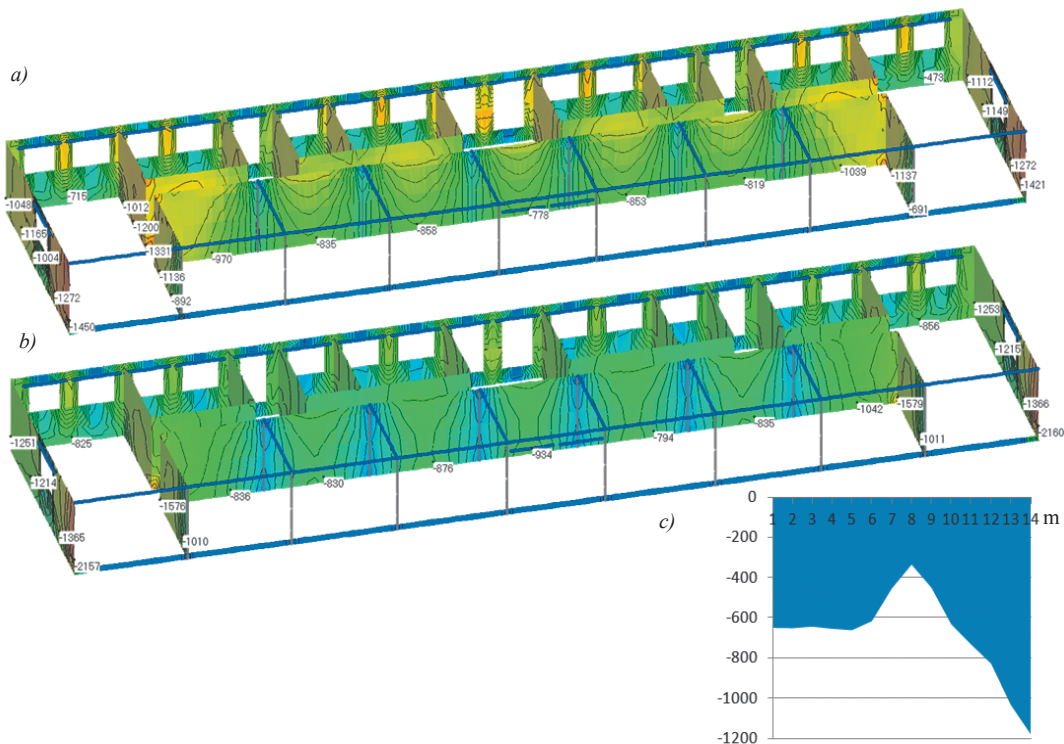


Fig. 31. Contours of vertical stresses distribution (kPa) calculated on rigid supports (a) and non-linearly deformable subsoil (b); the epure of vertical loads (kN) in a gable wall of the building of the standard series *u* -5733.

Calculated design resistance of brickwork with depreciating indices is about 1460 kPa which meets the strength criteria, but only in case the calculation was done on rigid supports (the maximum stress in the edge zone reaches 1450 kPa – Fig. 31 a), which obviously corresponds to design assumptions with traditionally applied technique of collecting loadings through “the loaded areas”. After consideration of the contact epures it becomes apparent that mostly the soil-structure interaction effect is revealed in the gable wall on the ground floor level where this wall is not “reinforced” with any longitudinal walls. The maximum loads arising in that location reach 1165 kN (Fig. 31, c) which 1.5 times exceeds calculation results for an absolutely rigid subsoil. Stress values in the edge zone (2157 kPa) 1.48 times exceed compressive strength of brickwork (Fig. 31). Thus, the strengthening of that spot on the wall undertaken in the 1980s appears quite reasonable.

7.2. An example of a free-standing (“dot”) building with bearing walls

The building of series *u*-5833/14 is a 12-storeyed brick free-standing (“dot”) building on natural subsoil, consisting of two crossed, almost square sections shifted in relation to each other by a half-floor (Fig. 32). At the crossing point of the two sections there is a lift/staircase block, consisting of two staircases and two lift shafts. The building is constructed of clay hollow bricks with thickness of internal and external walls being 380 mm and 510 mm, respectively.

In Leningrad, in the late sixties and early seventies 94 houses of this series were constructed. In some years after construction, in a number of buildings representing this series cracks began to appear, the greatest concern of experts being associated with vertically oriented cracks showing development of limit states in brickwork. As a result, the condition of a number of buildings of this series was recogni-

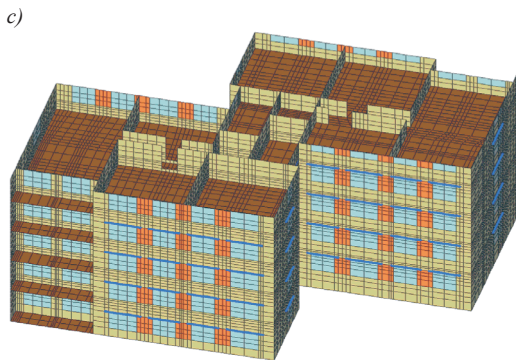
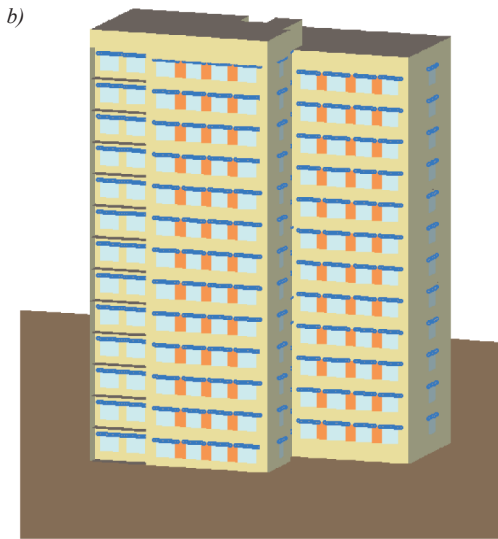


Fig. 32. Free-standing (“dot”) brick building of the standard series *u-5833/14*: *a* – photograph of the building; *b* – settlement model; *c* – bearing and self-bearing walls of a standard floor.

zed as critical, from some of them the residents were evacuated, and the buildings' front walls were strengthened by means of installing steel frames in gable walls on the levels from the ground to the sixth floor (Fig. 33).

Analysis of a building on rigid supports produced a rather uniform distribution of vertical loads (Fig. 34). Thereat stress values in the walls and the intermediate walls (about 1440 kPa) do not exceed compression strength of the brickwork.



Fig. 33. Example of strengthening on the building of the standard series *u-5833/14*

Analysis results for the building constructed *in situ*, for which the ground conditions are provided in Table 3, show that taking into account its interaction with the subsoil, loads in the intermediate walls 1.2 to 1.8 times exceed those computed for an absolutely rigid substratum (Fig. 34). Tension values in the most loaded locations amount to 2000 ... 2800 kPa. It is natural that strengths of the brick walls constructed of grade 100 brick, widely used in civil construction at the time, are not relevant to assume the acting vertical loads without introduction of any ancillary measures.

Table 3. Site conditions

Geol. index	Definition of deposits	Plast. value., I_p	Natural moist. cont, W	Soil density, kN/m^3	Porosity factor, e	Liquid index, I_L	Strength parameters		Strain mod. E_s , kg/cm^2
							ϕ , degree	c, kg/cm^2	
tg IV	Made ground	Resistance $R_0=1.0\text{kg/cm}^2$							
lg III b	Sands, medium grain, dense, moist			21.0	0.55		38	0.01	420
lg III b	Sands, silty dense, moist			19.8	0.55		32	0.05	210
lg III b	Clay sand, light, silty, laminated, firm plast.	0.1	0.28	19.5	0.800	0.75	15	0.1	80
g III lz	Sand clay, silty, with gravel and pebbles, firm plast.	0.04	0.15	21.1	0.4	0.20	25	0.2	110

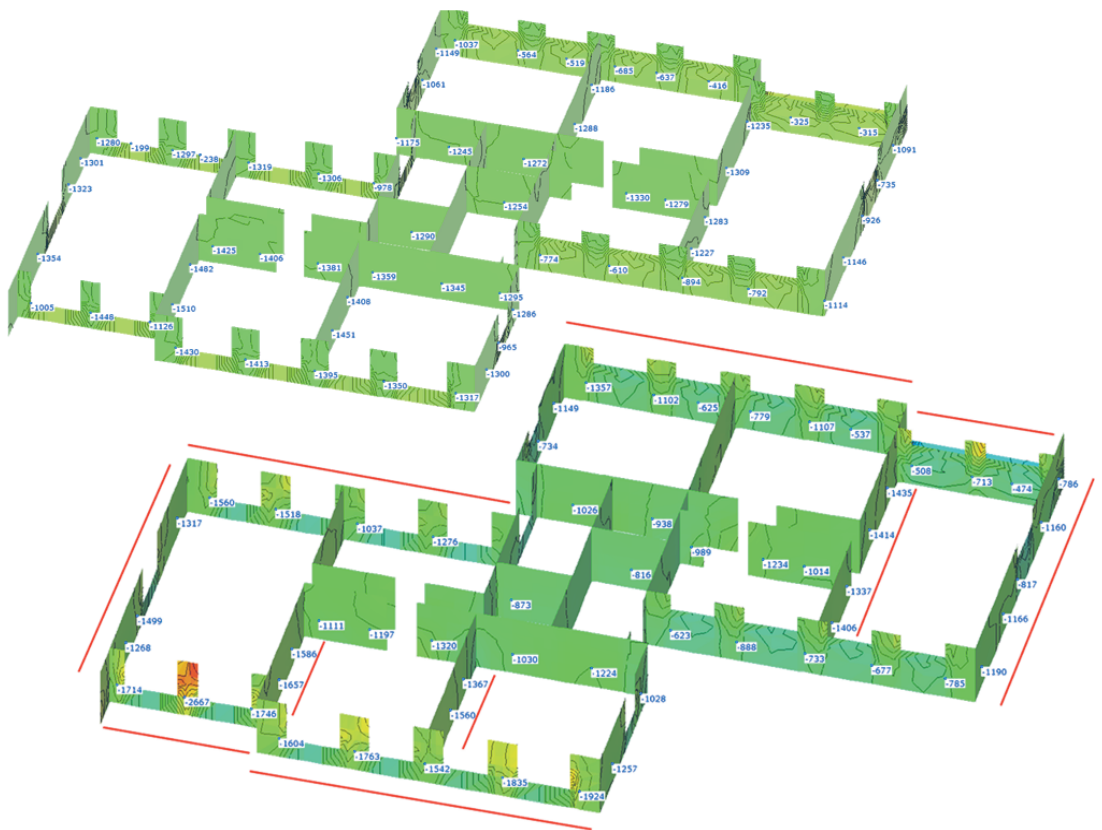


Fig. 34. Contours of vertical loads distribution (kN) calculated on rigid supports (a) and non-linearly deformable subsoil (b); building series *uu-5833/14* (red lines indicate the walls where stresses exceed compressive strength of brickwork)